Towards mid-infrared fibre lasing

Thesis submitted to the University of Nottingham for the degree of

Doctor of Philosophy, 2024.

Joel Nunes

Supervised by:

Professor Trevor Benson

Professor Angela Seddon

Dr David Furniss

Professor Mark Farries

Dr Sendy Phang

Abstract:

This thesis focused on the development of trivalent lanthanide doped chalcogenide glasses intended for the fabrication of MIR (*mid-infrared*) fibre lasers operating at wavelengths beyond 4 µm. The fabrication and spectroscopic evaluation of separate trivalent 'Ce' (*cerium*), 'Pr' (*praseodymium*), 'Sm' (*samarium*), 'Tb' (*terbium*), and 'Dy' (*dysprosium*) cation doped chalcogenide glass samples was undertaken as the first step towards achieving this goal. These RE^{3+} (*rare-earth*) doped chalcogenide glass samples were produced using the 'melt/quench' technique, then drawn into single material fibres (*fibre without a glass cladding*) and/or fabricated into a SIF (*step-index fibre*) using the 'rod-in-tube' technique. Emerging from the production and fabrication of these RE^{3+} doped samples was a novel non-destructive evaluation technique using either NIR or MIR imaging to detect internal defects and inhomogeneities in glass samples. As a result of this work the capability to produce RE^{3+} doped bulk chalcogenide glass, single material fibre SIF and extruded glass rods and tubes was demonstrated with some RE^{3+} doped glass compositions exhibiting optical losses as low as 1.81 ± 0.29 dB/m. Additionally, the ability to cause permanent photoinduced refractive-index changes in RE^{3+} doped glass was also demonstrated. There was also evidence of defects within several chalcogenide glass samples during their production and fabrication, alluding to room for improvement in the employed methodology.

Absorption spectra, PL (*photoluminescence*) spectra, and PL lifetime measurements were then performed on the RE^{3+} doped chalcogenide glass samples in the NIR (*near-infrared*) to the MIR spectral region to assess their spectroscopic behaviour during photoexcitation. These spectroscopic measurements inspired the development of a novel variation on the 'pump and probe' technique using an FTIR (*Fourier transform infrared*) spectrometer to evaluate latent ESA (*excited state absorption*) in RE^{3+} doped fibre samples. Importantly, knowledge of these ESA bands offers an opportunity to either avoid or utilise them. As a result of these spectroscopic measurements several absorption and PL emission bands in the NIR and MIR spectral regions were detected and evaluated from Ce^{3+}, Pr^{3+}, Sm^{3+}, Tb^{3+}, and Dy^{3+} cation doped samples. Notably, some of the RE^{3+} dopants, exhibited PL emission bands comprised of emissions from disparate transitions each with overlapping wavelengths. Additionally, up-conversion, the transfer of longer wavelength pump energy (*lower photon energy*) to shorter wavelength PL emissions (*higher photon energy*), was demonstrated in both the 'Pr^{3+}' and 'Tb^{3+}' cations while employing 'in-band' pumping of their lowest excited state manifolds, the $^3H_5$, and $^7F_5$ manifold, respectively. Furthermore, latent ESA measurements of Pr^{3+}, Sm^{3+}, Tb^{3+}, and Dy^{3+} cation doped chalcogenide glass fibre samples revealed several prominent transitions from excited RE energy levels for each dopant for the first time. The corresponding absorption measurements and PL emission measurements were used to propose RE energy level transitions for the observed ESA. These results showed the influence of latent ESA on the behaviour of the upper energy levels of RE^{3+} dopants under excitation.

Finally, and importantly, this thesis presents the results for the first demonstration of room temperature MIR lasing in a chalcogenide SIF with a 'Ce' cation doped core at wavelengths greater than 5 µm.

Table of Contents

Glossary of acronyms, symbols, and frequently used abbreviations:

Symbol	Meaning
Al	Aluminium
As	Arsenic
a.u.	Arbitrary units
BP	Band pass
c	Speed of light in a vacuum
CaF_2	Calcium fluoride
Ce	Cerium
CO_2	Carbon dioxide
CW	Continuous wave
dB	Decibels
Dy	Dysprosium
EDX	Energy Dispersive X-ray
ESA	Excited state absorption
FBG	Fibre Bragg grating
FTIR	Fourier transform infrared
Ga	Gallium
Ge	Germanium
GLS	Gallium lanthanum sulphide
GPa	Giga-pascal
GSA	Ground state absorption
GSD	Ground state depletion
N_2	Nitrogen
NA	Numerical aperture
NIR	Near-infrared
OD	Outer diameter
[-OH]	Hydroxyl group
Pa	Pascal
PL	Photoluminescence
ppm	Parts per million
ppmw	Parts per million by weight
Pr	Praseodymium
QCL	Quantum cascade laser
QCW	Quasi-continuous wave
RE^{3+}	Trivalent rare earth cation
RF	Radio frequency
RMSE	Root mean square error
S	Sulfur
Sb	Antimony
Se	Selenium
SE	Stimulated emissions
[-Se-H]	Selenium hydride group
SEM	Scanning electron microscopy

Symbol	Meaning	Symbol	Meaning
h	Planck's constant	**SIF**	Stepped index fibre
H	Hydrogen	**Sm**	Samarium
H_2O	Water	**SNR**	Signal to noise ratio
ID	Inner diameter	**SWP**	Short wave pass
In	Indium	**t**	Time
InSb	Indium-antimonide	**Tb**	Terbium
IR	Infrared	**$TeCl_4$**	Tellurium tetrachloride
k_b	Boltzmann constant	**T_g**	Glass transition temperature
K	Degrees Kelvin	**TIR**	Total internal reflection
KBr	Potassium bromide	**Xe**	Xenon
La	Lanthanum	**ZBLAN**	Fluoride glass (ZrF_4-BaF_2-LaF_3-AlF_3-NaF)
LED	Light emitting diode	**µm**	Micron
LWP	Long wave pass	**τ_{rad}**	Radiative lifetime
MCT	Mercury cadmium telluride	**° C**	Degrees Celsius
MIR	Mid-infrared	**λ**	Wavelength
mm	Millimetre	**ν**	Frequency
ms	Millisecond	**$\sigma_{abs}(\nu)$**	Absorption cross-section
mW	Milliwatt	**$\sigma_{em}(\nu)$**	Emission cross-section
n	Refractive index	α	Absorption coefficient

The term '**single material fibre**' refers to a fibre consisting of a core with uniform refractive index without a glass cladding.

Acknowledgements

I would like to express my gratitude to my supervisors Professor Trevor M. Benson, Professor Angela Seddon, Professor Mark Farries, Dr David Furniss, and Dr Sendy Phang for their guidance and support. I am grateful for the freedom and encouragement provided to me in pursuing the ideas and techniques that are presented in this thesis. I would like to thank the following people, who helped and supported me during this endeavour. Thank you to Richard Crane, and Dr Zhuoqi Tang for training me to make chalcogenide glass, and for their support in the laboratory. I also would like to extend my sincere gratitude to Dr David Furniss and Professor Mark Farries, both of which were tomes of technical wisdom and support. Thanks to Dr Łukasz Sojka, Professor Slawomir Sujecki, Dr Frédéric Maes, Dr Martin Bernier, and Dr Nikolaos Kalfagiannis for their support. I am also grateful for the funding provided by the EPRSC (*Engineering and Physical Research Sciences Council*) I thank them for enabling this endeavour. Finally, I would like to thank my friends and family back home in Trinidad and Tobago for supporting me.

Thank you all.

1 Thesis introduction:

The overall aim of this work was towards the development of RE^{3+} (*rare-earth*) doped chalcogenide glass fibres for the purpose of achieving room temperature MIR lasing. Importantly, this entailed pursuing improvements to the manufacture of chalcogenide glass fibres and evaluating the spectroscopy of rare-earth dopants. To accomplish this goal a systematic assessment of several RE^{3+} doped chalcogenide glass samples, with an emphasis on their fabrication and spectroscopic characterisation was undertaken. This was done to demonstrate the capability of producing high purity RE^{3+} doped chalcogenide glasses along with its subsequent fabrication into usable fibres and optical components, while identifying and addressing the challenges encountered. Non-destructive evaluation using either NIR (*near-infrared*) or MIR (*mid-infrared*) imaging was carried out to detect hidden internal defects in glass samples. This employed low-cost components to achieve excellent imaging quality. The spectroscopic properties of several RE^{3+} doped chalcogenide glass samples were then evaluated using both absorption and emission spectroscopy along with a novel variation on the ‘pump and probe’ technique to evaluate latent ESA (*excited state absorption*). This was done to investigate the dynamics of transitions within the RE^{3+} energy levels, especially in the MIR spectral region, and yielded knowledge essential for the effective usage of these RE dopants.

1.1 Motivation:

MIR light sources are useful for a wide variety of current and future applications because many chemicals and biological materials exhibit spectroscopic interactions with IR (*infrared*) light, especially in the MIR spectral region [1–4]. The large wavelengths of MIR electromagnetic radiation can interact with most elements and compounds. Within the ‘fingerprint region’ between 6 to 15 µm, many molecules exhibit a unique set of characteristic spectral absorption bands enabling molecular sensing and identification for medical diagnostics and security applications, in addition to environmental monitoring of pollutants, and remote sensing [1–7]. Furthermore, within the MIR spectral region, between 3 to 25 µm [8], many chemicals exhibit their fundamental vibrational absorption bands, allowing for efficient transfer of MIR light energy to these materials. This makes MIR light sources ideal for cutting and sintering applications such as medical scalpels, along with metal, and polymer machining. Atmospheric transparency windows within the MIR spectral region enable line-of-sight transmission of MIR light. This enables free-space optical communication [9–12], directed energy weapons/countermeasures [13,14], and thermal imaging [6]. Additionally, MIR light sources are also employed within instrumentation as photoexcitation sources and seed lasers for supercontinuum generation [15,16].

Most trivalent lanthanides, RE^{3+} cations, can produce PL (*photoluminescence*) in the NIR and MIR spectral regions when excited [17]. Chalcogenide glasses are materials that are often transparent over large portions of the IR spectral region [18]. These materials are capable of being RE^{3+} doped and drawn into fibres. Thus, the chalcogenide host glass can facilitate photoexcitation of the RE^{3+} dopants with an IR pump source, while transmitting resulting PL due to its transparency in the IR spectral region. Furthermore, the properties of the chalcogenide glass system are often beneficial towards the IR PL emissions from RE^{3+} cations. Consequently, RE^{3+} doped chalcogenide glass can be used to realise low cost, compact, rugged, bright MIR light sources that can operate at room temperature, at wavelengths greater than 4 µm, as this thesis will show.

Development of IR light sources based on chalcogenide glass, especially MIR fibre lasers, depends on the quality of the host glass. Making low optical loss RE^{3+} doped chalcogenide glass presents a variety of challenges to their production and fabrication due to the presence of impurities and internal defects which cause additional optical losses. Thus, considerable effort must be devoted towards avoiding and eliminating impurities and defects.

Most RE^{3+} cations possess energy level structures that support NIR and MIR radiative transitions. These transitions could be utilised for implementing both incoherent and coherent IR light sources, when paired with a suitable excitation scheme. However, latent ESA bands can act as a depopulation mechanism for excited state energy levels, rendering seemingly feasible excitation schemes impractical. Thus, the selection of feasible emission wavelengths, and effective excitation schemes for the RE^{3+} cation requires consideration of the electronic transitions occurring within the RE^{3+} cations, inclusive of ESA and overlapping extrinsic impurity absorptions.

1.2 Thesis outline:

The chapters of this thesis present the synthesis, fabrication, and characterisation of several chalcogenide glass samples followed by their spectroscopic characterisation and their subsequent usage in optical cavity experiments. Figure 1-1 illustrates the layout of the thesis, which is divided into seven Chapters.

- Chapter 2 introduces the properties of trivalent lanthanides (*rare-earth*), chalcogenide glasses and MIR fibre lasers.

- Chapter 3 presents the production and evaluation of both undoped and RE^{3+} doped chalcogenide glasses. Five trivalent lanthanide dopants, namely: 'Ce' (*cerium*), 'Pr' (*praseodymium*), 'Sm' (*samarium*), 'Tb' (*terbium*), and 'Dy' (*dysprosium*), each incorporated into a separate chalcogenide host glass, were produced, and assessed. Glass production entailed chemical precursor purification, chalcogenide glass synthesis, and fabrication of chalcogenide bulk glass, glass extrusions and fibres. Optical evaluation entailed absorption, optical attenuation, and refractive index measurements, along with IR imaging of samples.
- Chapter 4 presents the spectroscopy measurements of five RE^{3+} doped chalcogenide glass samples, these RE^{3+} dopants included: Ce^{3+}, Pr^{3+}, Sm^{3+}, Tb^{3+}, and Dy^{3+} each in a separate chalcogenide host glass. This spectroscopic evaluation entailed PL measurements via laser induced photoexcitation, and ESA evaluation via a novel variation on the 'pump and probe' technique devised and implemented, by the author and the Mid-Infrared Photonics Group. ESA measurements were undertaken to evaluate the latent spectroscopic behaviour of the RE^{3+} dopant during photoexcitation.
- Chapter 5 investigates MIR lasing in SIF samples with either Tb^{3+} or Ce^{3+} cation doped cores. This chapter also presents results for MIR lasing at wavelengths greater than 5 µm from a SIF with a Ce^{3+} doped core.
- Chapter 6 summarises the work accomplished in this thesis and lists further actions to optimise glass production/fabrication and characterisation of chalcogenide glass, along with proposing potential future work.
- Chapter 7 is an appendix which catalogues the procedures and equipment configurations used for the various tasks and measurements performed in prior Chapters. This section only

catalogues tasks that were not developed or significantly modified by the author. In some cases, combinations of these pre-existing techniques were used in new and unique ways. Importantly, these details allowed the equipment configurations and procedures used to be properly critiqued in the discussion sections of prior chapters. The procedures in this section were either previously developed within the Mid-Infrared Photonics Group, George Green Institute for Electromagnetics Research, at the University of Nottingham or found in literature.

Note, Chapters 3 to 5 each contain a methodology sub-section. These sub-sections presented detailed procedures for either novel techniques or substantial modifications to pre-existing procedures developed by the author and the Mid-Infrared Photonics research group. Conversely, only the basic steps essential to properly describe how a task was performed, for tasks not developed by the author, were given in these sub-sections. The detailed procedures for tasks not developed by the author were included in Chapter 7 Appendix.

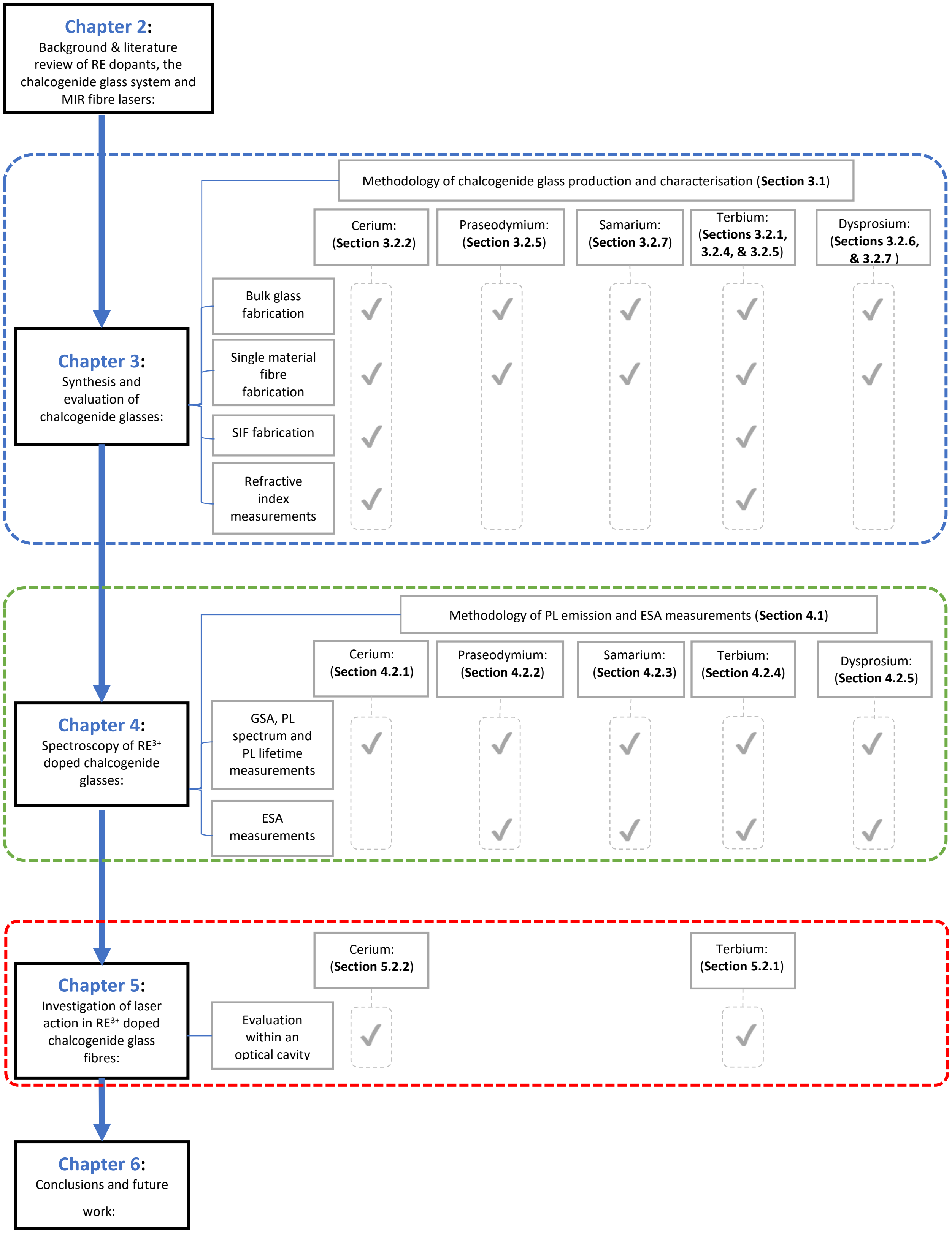

Figure 1-1:Illustration of thesis outline, showing Chapters and their major sub-items.

2 Background and literature review:

The following section presents a background and literature review. Section 2.1 introduces RE (*rare-earth*) dopants inclusive of their chemical and spectroscopic properties. Section 2.2 introduces the chalcogenide glass system inclusive of their compositions, production, fabrication, and their material properties along with common impurities and defects. Finally, Section 2.3 introduces the background theory on MIR (*mid-infrared*) fibre lasers.

2.1 RE (*rare-earth*) dopants:

Lanthanides or RE elements are metallic elements belonging to the 'f-block' of the periodic table. Their chemical and spectroscopic properties make them useful for a variety of commercial, industrial, and scientific applications. Each lanthanide can achieve a stable trivalent oxidation state [RE^{3+}] when incorporated into compounds. In addition to the trivalent state, some lanthanides can also assume a stable divalent [RE^{2+}] or a tetravalent [RE^{4+}] oxidation state, such as the RE cations Ce^{4+}, Sm^{2+}, Eu^{2+} and Yb^{2+} [19–21]. The co-existence of multiple valence states, and the interchangeability between these coexisting valence states in RE cations have been reported [22–25]. Thus, the usage of the 'RE^{3+}' abbreviation throughout this thesis refers to a predominantly trivalent RE^{3+} population, however this does not exclude the possibility of a minority of other valence states for the RE cations.

Metallic RE elements are chemically reactive and will oxidise when exposed to air at room temperature [19] necessitating their long-term storage in an inert atmosphere. RE elements are also reactive to halides, chalcogens, and pnictogens. Consequently, RE elements in the form of

RE metal foils, and RE halide salts can be used to dope chalcogenide glass. Furthermore, it has been reported that some RE elements can exhibit reactivity with silica [26–28]. Some RE metals can be used as chemical getters in high vacuum systems due to their high reactivity, for example the elements 'La' and 'Ce' can be used to efficiently sequester H_2 and O_2 gas [29,30].

2.1.1 Spectroscopic and vibrational interactions of RE cations:

Most RE^{3+} cations have an unfilled '4f' orbital which allows upward and downward transitions of electrons within the 4f energy manifolds to occur via spectroscopic and vibrational interactions. Electrons in the 4f orbital of RE^{3+} cations can be temporarily excited by absorbing either incident photons, in a process called 'optical absorption', or by absorbing quantised lattice vibration energy, called phonons, in a process called 'multi-phonon absorption', as illustrated in Figure 2-1 (a) and (b). During these transitions the law of conservation of angular momentum is maintained by the electrons [31]. Thus, the energy absorbed equals the difference between the initial and excited state energy levels (*see Figure 2-1 (a)*). The following equation describes optical absorption:

$$h\nu = E_2 - E_1 \tag{Equation 2-1}$$

where 'v' is the frequency of the incident photon and E_2 and E_1 denote the energy associated with each energy level.

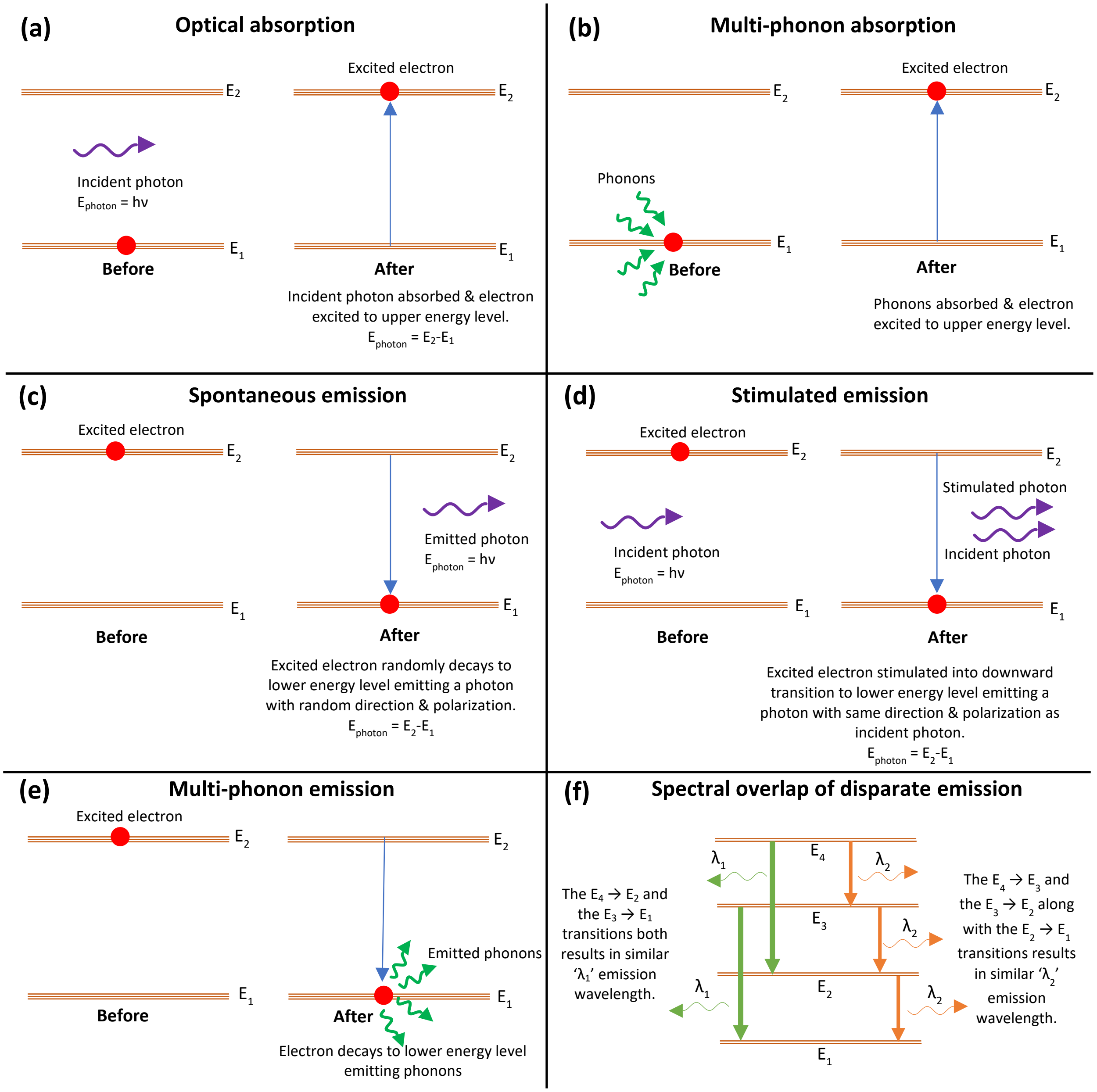

Figure 2-1: Showing simplified before and after illustrations for: ***(a)*** *optical absorption,* ***(b)*** *multi-phonon absorption,* ***(c)*** *spontaneous photon emission,* ***(d)*** *stimulated photon emission, and* ***(e)*** *multi-phonon emissions, along with simplified illustration of* ***(f)*** *spectral overlap of disparate emissions.*

The 'ground state' is the lowest energy state an electron can occupy within an electron orbital, while any state with greater energy than the ground state is an 'excited state'. Absorptions occurring from the ground state constitute a GSA (*ground state absorption*) while absorptions occurring from an excited state energy level constitute an ESA (*excited state absorption*).

Electrons in an excited state could undergo relaxation to a lower excited state or to the ground state by releasing energy, this transition could either be radiative, resulting in the emission of a photon, or non-radiative, resulting in the emission of phonons. The energy released during relaxation equals the difference between the excited state and the relaxed state (*see Figure 2-1 (c) and (e)*). Radiative transitions required that the energy gap between energy levels be bridged by the emission of a photon, with Equation 2-1 also describing the relaxation process. These radiative transitions could either occur spontaneously resulting in the emitted photon having random polarization and direction, called 'spontaneous emission' (*see Figure 2-1 (c)*), or they could be stimulated by an incident photon resulting in the emitted photon having identical phase and direction to the incident photon, in a process called 'stimulated emission' (*see Figure 2-1 (d)*). Non-radiative transitions required that the energy gap between energy levels be bridged by the emission of multiple phonons in a process called 'multi-phonon emission' (*see Figure 2-1 (e)*). Each RE^{3+} cation possess more than one excited state thus, the relaxation processes for an excited electron could occur via more than one decay path, resulting in the emission of a photon of a different wavelength to that of the incident photon (*see Figure 2-1 (f)*).

2.1.1.1 PL emission lifetimes:

The emission lifetime describes the rate with which electrons in an excited state relax to a lower energy level via radiative and/or non-radiative transitions. These downward transitions cause the electron population in the excited state to decrease exponentially. A single radiative decay path can be described by the following decay equation:

$$I(t) = I_o exp^{\left(\frac{-t}{\tau}\right)}$$ *Equation 2-2*

where ‘I(t)’ is the PL intensity as a function of time, ‘I_0’ is the initial PL intensity, and ‘τ’ is the PL lifetime. Note, spontaneous emissions can sometimes be comprised of multiple lifetimes due to spectral overlap of radiative emissions from disparate decay paths (*see Figure 2-1 (f)*). Wherein, excited state energy manifolds which possess decay paths, comprised of distinct branches with similar relaxation energies. This enables radiative emissions of similar wavelengths, each originating from different energy levels with distinct radiative lifetimes. For example, the 4.7 µm Pr^{3+} PL emission band has been shown to exhibit at least two lifetimes; 3.3 ms and 10.1 ms, each originating from different energy manifolds [32].

Non-radiative, multi-phonon emissions can compete with radiative transitions, reducing PL intensity, and thus alter PL lifetimes. The non-radiative relaxation rate is a function of the phonon energy of the host lattice and its temperature [33–35].

When photoexcited, or ‘pumped’, electrons within the RE cation 4f orbitals are excited into upper levels from which they can subsequently radiatively decay to lower levels. Spontaneous emission intensity and emission lifetimes both benefit from low phonon energy host environments, such as chalcogenide glass, as they facilitate a greater probability for radiative transitions occurring within the MIR spectral region. These transitions would otherwise be ‘quenched’ by competing non-radiative transitions in a host glass possessing a larger phonon energy, like oxide and fluoride glasses. Thus, numerous 4f → 4f radiative transitions occurring within the NIR and MIR spectral regions, in a chalcogenide glass host, have been reported in literature. The longest wavelength emissions reported, so far, are broad emissions > 8 µm from the: Sm^{3+} [36,37], Tb^{3+} [17,38], and Dy^{3+} [39] cations each in a chalcogenide host glass. Additionally, the longest PL emission lifetime reported, so far, is ~16.1 ms from the Tb^{3+} cation in a chalcogenide host glass [40].

Several of the RE cations exhibit interesting MIR emissions at wavelengths ≥ 4 µm, such as Ce^{3+} (see Section 4.2.1.2), Pr^{3+} (see Section 4.2.2.2), Sm^{3+} (see Section 4.2.3.2), Tb^{3+} (see Section 4.2.4.2), and Dy^{3+} (see Section 4.2.5.3). Additionally, it has been shown that the RE precursors used can affect both the chalcogenide glass and the MIR spectroscopic properties of the RE dopant [32].

2.1.1.2 Latent ESA (excited state absorption):

Excited electrons can sometimes absorb additional energy to be further excited to higher levels within the RE^{3+} cation in a process called ESA (*excited state absorption*). Notably, this type of absorption remains dormant when the excited state level is unpopulated, hence the term 'latent ESA'. Thus, the latent ESA band reveals itself once the excited state becomes populated. ESA measurements typically employ a 'pump and probe' technique, where an excitation source, the 'pump', causes the excitation of electrons to upper energy levels. This enables subsequent optical absorption between the excited electrons and a second excitation source, the 'probe'. Traditionally, the pump and probe technique employs a double modulation scheme as described in [41–43]. The ESA bands for several RE cations have been reported, these include:

- The ‘Er’ (*erbium*) cation exhibited NIR ESA bands around 0.55 µm, 0.81 µm, 0.97 µm, 1.7 µm and 1.95 µm [42,44,45].
- The ‘Nd’ (*neodymium*) cation exhibited NIR ESA bands around 1.054 µm, 1.238 µm, 1.325 µm [43,46].
- The ‘Tm’ (*thulium*) cation exhibited NIR ESA around 1.1 µm [47].

A low phonon energy host environment, such as chalcogenide glass, can minimise non-radiative relaxation rates, causing long radiative lifetimes in the excited state levels [17] thus facilitating an increase probability of ESA [42–47]. Thus, latent ESA bands are likely to be more prominent in the low phonon energy environment of a chalcogenide host as compared to other glass hosts with higher phonon energy. The phonon energies of various host glass systems are expanded upon in Section 2.1.1, and given in Table 2-1.

2.2 Chalcogenide glasses:

Section 2.2.1 introduces the composition and properties of chalcogenide glasses. Section 2.2.2 delves into the production and fabrication of chalcogenide glass and Section 2.2.3 examines optical loss of the chalcogenide glass system and some of the common impurities that afflict it.

2.2.1 Chalcogenide glass compositions and properties:

Chalcogenide glasses are X-ray amorphous materials predominately comprised of at least one chalcogen element from group 16 of the periodic table, excluding ‘O’ (*oxygen*) nor the radioactive elements below ‘Te’ (*tellurium*). The chalcogen elements can be combined with at least one other element, typically from the ‘p-block’ of the periodic table, such as a pnictogen, halogen, a metalloid, or a metal, to produce a stable covalently bonded glass. A wide variety of chalcogenide glass compositions have been reported, they are typically comprised of a sub-set of the following elements ‘S’, ‘Se’, ‘Te’ ‘As’, ‘Sb’ ‘Ge’, ‘Ga’ and ‘In’. Additionally, glass compositions containing transition metals and RE elements, such as GLS (*gallium lanthanum sulphide*) have also been extensively researched. Chalcogenide glasses can transparent over large portions of the IR spectral region [18] and are often completely opaque to visible light.

Chalcogenide glasses exhibit a glass transition occurring at the ‘T_g’ (*glass transition temperature*) [48]. The ‘T_g’ denotes the temperature were thermodynamic properties, such as heat capacity and expansion coefficient change from crystal-like values to liquid-like values. Additionally, these vitreous materials display no long-range structural periodicity. Under certain conditions chalcogenide glasses can undergo devitrification, which is the process by which these vitreous materials change their structure into that of crystalline solids, importantly this is undesirable.

Most RE^{3+} doped chalcogenide glasses reported are non-stoichiometric, multicomponent compositions comprised of three or more elements. These multicomponent compositions typically afford superior solubility for RE cations and greater resilience to devitrification during glass production and fabrication when compared to two-component stoichiometric compositions. Additionally, they allow the physical and spectroscopic properties such as ‘T_g’, and refractive index to be manipulated by varying components within the glass composition. For example, the refractive index of a glass composition can typically be lowered by the addition of a few atomic % of ‘S’ without significantly changing its thermal properties.

Chalcogenide glasses typically exhibit low phonon energies, high optical nonlinearity and a high refractive index [49,50]. The ‘T_g’ of a chalcogenide glass depends on its composition and can range from 174.2°C for As_2Se_3 [51] to above 400°C for $Ge_{28}As_{12}Se_{60}$ atomic % compositions [52]. Some of these glasses have been demonstrated as suitable for extrusion and fibre drawing [53].

2.2.1.1 Optical properties: phonon energies and refractive index:

Glasses exhibit a transparency window comprised of a region of low optical attenuation, flanked on both the longer wavelength and shorter wavelength regions by high optical attenuation. The short-wavelength limit of the transparency window is often defined by competing intrinsic absorptions due to Rayleigh scattering, Urbach tail, and the WAT (*weak absorption tail*) [54]. The 'multi-phonon edge' signifies the long-wavelength limit of the transparency window and occurs due to the fundamental vibrational absorptions of the chemical bonds making up the glass. Chalcogenide glasses can have a wide range of phonon energies depending on their composition. Glass compositions which contain elements with greater atomic mass, exhibit lower phonon energies resulting in greater transparency into the IR spectral region. For example, selenide glasses have lower phonon energies than sulphide glasses, glass composition containing 'Sb' have lower phonon energies than compositions containing 'As'. Table 2-1 lists the phonon energy and refractive index for several glass systems found in literature.

Table 2-1: Phonon energies and refractive index of glass systems reported in literature.

Glass system	Phonon energy / cm^{-1}	Refractive index	Reference
Selenide glass	~240 - 350	2.4 – 2.7	[55,56]
Sulfide glass	~350 - 450		[1,55,57]
Fluoride glass	~560	1.47 - 1.51	[17,58,59]
Silica glass	~1100	1.42 - 1.48	[60]

The phonon energies of chalcogenide glasses are less than their fluoride, and silica glass counterparts. This makes them ideal host materials for supporting MIR radiative transitions in RE dopants, which would otherwise be quenched by non-radiative transitions in a higher phonon energy host environment.

The relatively heavy constituent elements and weak bond strength causes chalcogenide glasses to be more fragile when compared to most other glass systems. The strength of chalcogenide glasses can vary widely, some compositions have been reported to exhibit a Vickers' hardness between ~0.5 GPa up to ~2.2 GPa [61,62], this is significantly less than the 13.1 GPa exhibited by silica glass [63]. Thus, chalcogenide glasses, such as selenide and telluride-based compositions, and compositions containing 'Sb' are often difficult to handle and cleave.

2.2.1.2 Solubility of RE dopants in chalcogenide glass:

Chalcogenide glass compositions which contain a RE dopant typically also possess a single metallic element, either 'Ga' or 'In'. This metallic element is used as a co-solubilizer to improve solubility of an RE dopant [64–66]. It has been theorised that the co-solubilizer stabilises the glass structure by preventing the RE^{3+} dopant from inducing devitrification due to phase separation or crystallization [65]. The RE dopant are sensitive to the co-solubilizer, too low concentration and the RE dopant precipitate out of solution, while too high concentration the co-solubilizer itself causes devitrification [64]. Additionally, it has been reported that the choice of metal co-solubilizer used can influence the RE cation PL emission intensity [65,66].

Most chalcogenide glasses exhibit poor solubility for RE dopants despite the use of co-solubilizers. Excluding the GLS glass system, sulfide-based glass compositions capable of being drawn to fibre, containing ≥ 1.2 atomic percent RE dopant have been reported [67,68]. Additionally, selenide-based compositions capable of being drawn to fibre, typically contain between 400 and 1500 ppmw dopant concentration (*see Table 2-5*), however there have been extreme cases were fibres containing ≥ 6000 ppm RE cation dopant have been reported [40]. Highly doped glasses are typically problematic to draw to fibre due to their propensity for devitrification, resulting in brittle non-uniform fibre with high optical loss. However, bulk glass samples can typically exceed the RE dopant concentration found in fibres, for example selenide-based bulk glass containing ≥ 13,000 ppmw RE cation dopant have also been reported [69].

Table 2-2 lists the RE dopant concentration for several glass systems capable of being drawn to fibre found in literature. The solubility of RE dopants in the chalcogenide glasses, excluding the sulphide-based glasses, is generally poor even when compared to their fluoride, and silica glass counterparts.

Table 2-2: RE doped glass fibres and their dopant concentration found in literature:

Glass system	RE dopant	Dopant concentration	Reference
InF_3	Ho^{3+}	10 mol. %	[58]
ZBLAN	Ho^{3+}	5000 ppm ~molar	[70]
ZrF_4	Er3+	1 mol. %	[71,72]
Silica	Yb^{3+}	2500 ppm	[73]
Silica	Yb_2O_3 (with Al_2O_3)	0.75 mol. %	[74]

Note, as an example, a dopant concentration of 1000 ppmw Ce cation in a common chalcogenide composition such as $Ge_{15.0}$ $As_{21.0}$ $Ga_{1.0}$ $Se_{63.0}$ atomic % is equivalent to 0.055 atomic %.

2.2.2 Chalcogenide glass production and fabrication:

Most elements and molecules exhibit strong and distinct spectroscopic and vibrational absorptions in the MIR spectral region. Thus, the production of chalcogenide glass, and its subsequent fabrication into optical components, ideally needs to be carried out under pristine conditions, without these extrinsic impurities, to achieve their minimum optical loss [75]. The 'melt-quench' technique, and chemical vapour deposition are two methods that can be used to produce chalcogenide glass.

The 'Melt-Quench' technique is a common method used to produce bulk chalcogenide glass. Wherein a molten solution of the purified constituent materials was heated while being mixed in a sealed silica ampoule, the resulting glass melt was then rapidly cooled into an amorphous solid. Typically, the melt quench technique employs an electric resistance rocking furnace. However, variations on the technique employing microwave heating have been demonstrated [76,77]. This method can produce large amounts of relatively homogenous glass, which can be comprised of precursor chemicals with disparate melting and boiling points. Table 2-3 list some of the thermal properties of the 'p-block' elements commonly used to make chalcogenide glass.

Table 2-3: thermal properties of common constituent elements used in chalcogenide glasses. Note, melting and boiling temperatures obtained from [78].

Element	**Melting point / °C**	**Boiling point / °C**	**Vapour pressure**	**Reference**
S (*sulfur*)	115	445	14.5 Pa at 140 °C	[79]
Se (*selenium*)	221	685	352 kPa at 797 °C	[80]
Te (*tellurium*)	449	988	188 Pa at 617 C	[81]
As (*arsenic*)	816	614	186 Pa at 403 °C	[82]
Sb (*antimony*)	631	1587	1.45 Pa at 548 °C	[83]
Ge (*germanium*)	938	2827	0.137 Pa at 1237 °C	[84]
Ga (*gallium*)	29	2204	0.77 Pa at 1000 °C	[85]
In (indium)	156 °C	2027	0.0127 Pa at 1000 °C	[86]

Chemical vapour deposition is an alternate chalcogenide glass production technique capable of producing high-quality glass [87–89]. In this method chemical precursors are vaporised and deposited onto a substrate. Notably, this technique can also be used to purify chalcogenide glass.

Bulk chalcogenide glass can be heated above its 'T_g' to a supercooled liquid state which can then be either extruded through a die into a variety of shapes or drawn into fibre. Extrusion of inorganic glass through a die, as a method to shape these materials, has been demonstrated [53]. This type of processing allowed for the glass to be fabricated into shapes which would otherwise be difficult to achieve via casting, blowing, or fibre drawing alone.

Extrusion of a glass melt enables the fabrication of cladding tubes and multilayer glass rods which are necessary to make structured chalcogenide fibres using the 'rod-in-tube' method. This coupled with the capability to control the refractive index of the core enables the fabrication of a SIF (*step-index fibre*). SIFs were comprised of a concentric inner core, with a uniform refractive index, and an outer cladding with a uniform, lower refractive index. Importantly, this configuration of the SIF enabled TIR (*total internal reflection*) within the core, as illustrated in Figure 2-2. The high refractive index of chalcogenide glasses (see Table 2-1) enabled the fabrication of high NA (*numerical aperture*) SIF, telluride-based SIF exhibiting an ultra-high NA of 1.88 ± 0.02 have been reported [15]. Additionally, the high optical nonlinearity of chalcogenide glass allows for broadband MIR super continuum generation [15,16].

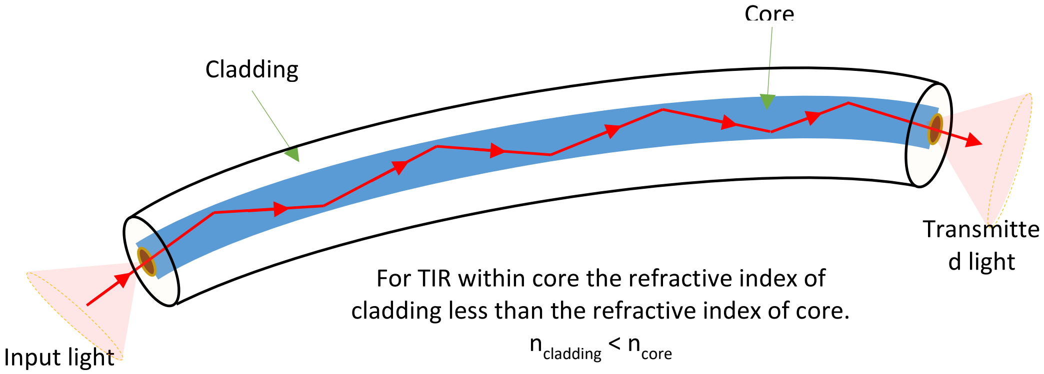

Figure 2-2: Simplified illustration of SIF (step-index fibre) showing TIR (total internal reflection) of light within the core. Note, that single material fibres consist of the core alone without any cladding.

2.2.3 Chalcogenide glass optical loss, impurities, and defects:

Chalcogenide glasses can exhibit small spectral regions of high optical attenuation within their transparency window due to either intrinsic absorptions in the glass or extrinsic absorptions from unwanted impurities. Minimising the optical loss of chalcogenide glass becomes increasingly difficult as more elements are incorporated into their composition. This is due to the unintentional inclusion of impurities during glass synthesis from each elemental constituent. These impurities cause extrinsic absorption bands in the resulting chalcogenide glass, resulting in an increase in optical attenuation. Stoichiometric glass compositions, such as As_2S_3 and As_2Se_3, exhibit lower minimum optical loss when compared to their non-stoichiometric, multicomponent counterparts due to their simple compositions. Two-component glass compositions have been shown to offer the lowest potential optical loss, with some reports of their theoretical and empirical minimum loss being less than 0.05 dB/km [90,91]. Regrettably, these two-component compositions often exhibit undesirable traits such as poor RE cation solubility. Thus, two-component compositions are typically used for undoped applications however, RE cation doped compositions, such as Ga_2S_3 [92] and As_2S_3 [67], have been reported.

The foremost extrinsic absorption bands within the NIR and MIR spectral region are attributed to hydride, oxide, and carbon impurities introduced via the chemical precursors during glass synthesis [93–95]. Additional impurities such as SiO_2, carbon, [-OH], and water could also be introduced during glass production and fabrication. Table 2-4 lists the absorption band positions of some common unwanted impurities in chalcogenide glasses within the 2.5 µm to 11 µm spectral region found in literature. Additionally, Figure 2-3 illustrates the impurity absorption bands listed in Table 2-4 along with the approximate wavelength ranges for the major hydride, and oxide impurities, namely: [-OH], [-Se-H], H_2O and [-Si-O].

The RE dopants are the most electropositive elements used in the glass composition, thus they are particularly susceptible to accumulating anionic impurities. Additionally, some elements can be inherently difficult to purify due to them having similar thermal properties to their impurities, such as low volatility, or exhibiting high melting/boiling temperatures. Thus, limiting the suitable types of purification methods for the precursors and their effectiveness.

Heat treatment of chemical precursors to remove high-volatility impurities has been shown to be advantageous in chalcogenide glass production [77,96,97]. However, this technique is ineffective for low volatility (refractory) impurities.

Vacuum distillation has been demonstrated as an effective method to remove impurities from chalcogenide glass by separating the high-volatility and refractory impurities from the purified glass [98,99]. This purification process is enhanced with the use of chemical getters such as oxygen getters 'Al' and 'Mg' and hydrogen getter '$TeCl_4$' [93,98,100,101] to encourage impurities to assume either a high-volatility or low-volatility form. Double-distillation and other multi-stage distillation have been shown to further improve the purification process, with each subsequent distillation removing residual impurities from prior distillations [102,103].

Table 2-5 lists some RE-doped chalcogenide glass fibres found in literature along with the specifications on their synthesis. The following can be observed:

- Glass compositions that were either distilled or had their constituent elements distilled had lower minimum optical loss compared to their undistilled counterparts.
- Glass compositions with a low RE dopant concentration (< 500 ppmw) tended to exhibit lower minimum optical loss (< 1 dB/m), these compositions also contained relatively small amounts of ‘Ga’ (< 1 atomic %).

Light scattering inclusions such as holes, voids, compositional inhomogeneities, heterogeneous and inhomogeneous crystallization can also adversely affect the optical attenuation of a glass system. These defects are simple to detect in glass systems transparent to visible light. However, the opacity of the chalcogenide glass system hampers the detection of these defects, despite this “heterophase” inclusions in chalcogenide glasses have been reported [104,105].

Table 2-4: Common unwanted impurities causing loss due to absorption within the 2.5 to 11 µm spectral region (adapted from [77,96]).

Wavelength / µm	Impurity	Reference
2.80 (*3571 cm*$^{-1}$)	[-O-H], H_2O, & Se-O-H	[56,86,106–110,95,111–115,91]
3.10 (*3226 cm*$^{-1}$)	[-S-H]	[91,108]
3.40 (*2941 cm*$^{-1}$)	[-C-H]	[56]
3.50 (*2857 cm*$^{-1}$)	[-Se-H]	[56,110,111,115,116]
4.00 (*2500 cm*$^{-1}$)	[-S-H]	[56,95]
4.05 (2469 cm^{-1})	SO_2	[117]
4.10 (*2439 cm*$^{-1}$)	[-Se-H]/ H_2Se	[56,95,110,111,113,115]
4.25 (*2353 cm*$^{-1}$)	CO_2	[86,91,106,107]
4.50 (*2222 cm*$^{-1}$)	[-Se-H]	[56,95,110,111,113–116,118]
4.90 (*2041 cm*$^{-1}$)	[-C-S], & [-Ge-H]	[39,95]

Wavelength / µm	Impurity	Reference
5.00 (*2000 cm*$^{-1}$)	[-As-H]	[91,95]
6.30 (*1587 cm*$^{-1}$)	H_2O	[56,86,91,106–112,114,115]
7.50 (*1333 cm*$^{-1}$)	As_4O_6 & As-S/S-S	[108,110,111,115]
7.80 (*1282 cm*$^{-1}$)	[-As-O], [-Ge-O], & H_2Se/Se-H	[56,91,108,110,111,115]
8.00 (*1250 cm*$^{-1}$)	SeO_2, [-As-O] & [-Ge-O]	[56,91,108,110,111,113]
8.70 (*1149 cm*$^{-1}$)	SeO_2 & [-As-O]	[110–112,115]
8.80 (1136 cm^{-1})	SO_2	[117]
8.90 (*1124 cm*$^{-1}$)	[As-O-As]	[110,115]
9.60 (*1042 cm*$^{-1}$)	[-Si-O]	[56,95,110,112]
10.70 (*935 cm*$^{-1}$)	[-Se-O]	[56]

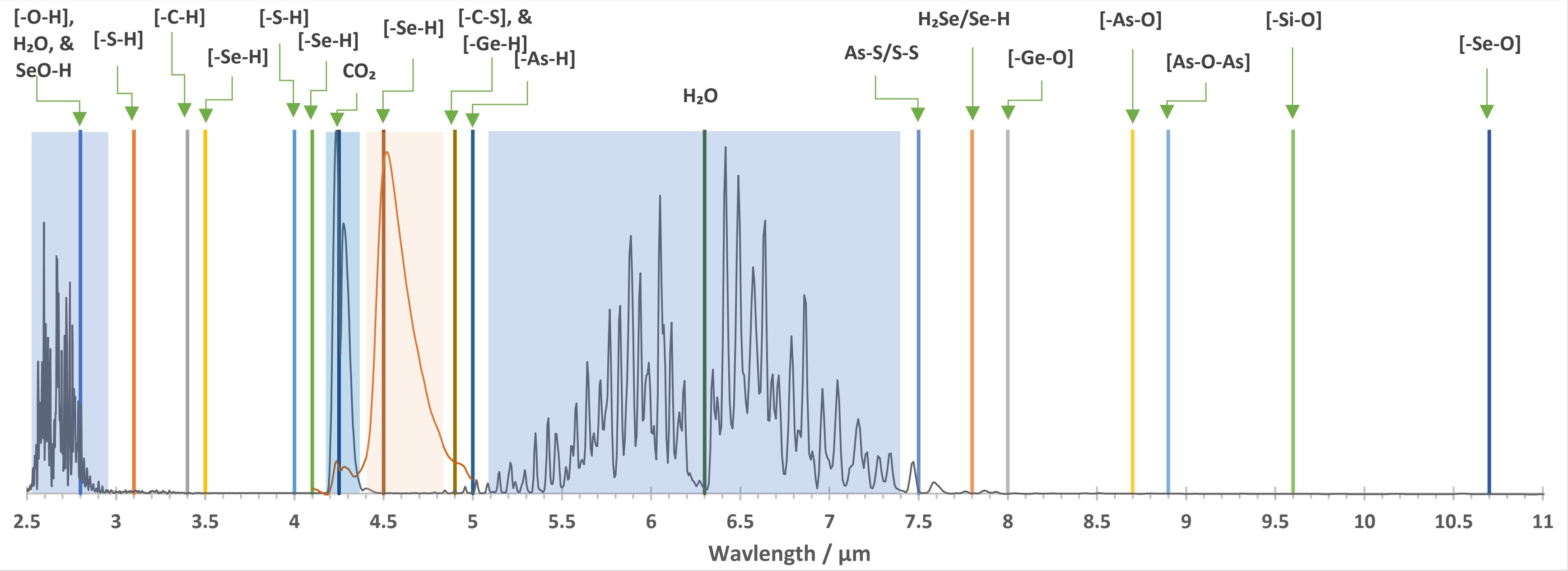

Figure 2-3: Showing absorption of unwanted impurities listed in Table 2-4. Note, [-Se-H] and H_2O absorption spectra obtained from [116] and via empirical measurement, respectively.

Table 2-5: Optical attenuation for RE^{3+} doped chalcogenide fibres found in literature.

Host glass composition / atomic %	Dopant source (*as quoted in reference*) and nominal concentration/ ppm	Type of fibre	Purification method of precursors and/or glass used	Minimum loss / (dB/m) @ wavelength / µm	Reference
Ge-As-Ga$_{1.0}$Se core/Ge-As-Ga-Se cladding	493 Pr^{3+}	SIF	Undistilled	2.8 @ 6.65	[119]
Ge-As-Ga$_{1.0}$Se	500 Pr (foil)	Unstructured	Undistilled	2.0 @ 6.77	[32]
	500 PrCl$_3$	Unstructured	Undistilled	1.8 @ 6.93	
	500 PrI$_3$	Unstructured	Undistilled	2.8 @ 6.75	
Ge-As-In$_{1.0}$ Se core/Ge-As-Ga-Se cladding	498 Pr^{3+}	SIF	Undistilled	4.3 ± 0.2 @ 6.58	[66]
$Ge_{16.5}As_{18.8}Ga_{0.2}Se_{64.5}$	200 Pr	Unstructured	'Se' and 'As' distilled	0.7 @ 6.61	[120]
$Ge_{16.5}As_{18.3}Ga_{0.7}Se_{64.5}$	2000 Pr	Unstructured		1.8 @ 6.07	
$(GeSbSe)_{97}Ga_3$	1000 Sm^{3+}	Unstructured	Undistilled	2.15 @ 6.04	[36]
$Ga_5Ge_{20}Sb_{10}Se_{65}$	500 Sm^{3+}	Unstructured	Undistilled	~15 between 7-8	[37]
$Ga_5Ge_{20}Sb_{10}Se_{65}$	500 Tb^{3+}	Unstructured	Undistilled	< 2.5 between 6.5 to 7.5	[38]
$Ga_5Ge_{20}Sb_{10}Se_{65}$	1000 Tb^{3+}	Unstructured	Undistilled	< 5 between 6.5 to 7.5	
$Ge_5As_{32}Se_{57.5}Ga_{0.5}I_5$	6000 Tb	Unstructured	Distilled	1.5 @ 9.0	[40]
$Ga_{3.2}Ge_{24.9}As_{15.3}Se_{56.6}$ core /$Ge_{18}As_{22}S_{60}$ cladding	1050 Tb^{3+}	SIF	Distilled	3 ± 0.3 @ 7.1	[121]
$Ga_5Ge_{20}Sb_{10}Se_{65}$	500 Tb^{3+}	Unstructured	Distilled	About 1.3	[122]
$Ga_5Ge_{20}Sb_{10}Se_{45}Te_{20}$	500 Tb^{3+}	Unstructured	Distilled	About 4.0	
$Ga_5Ge_{20}Sb_{10}S_{65}$	1000 Dy^{3+}	Unstructured	Distilled	< 2.0 between 2.0 to 2.5	[39]
$Ga_5Ge_{20}Sb_{10}Se_{65}$	1000 Dy^{3+}	Unstructured	Distilled	< 1.2 between 6.5 to 7.5	
$Ge_{12.5}As_{18.8}Ga_{0.2}Se_{58.5}S_{10}$	200 Dy	Unstructured	'Se' and 'As' distilled	2.6 @ 6.05	[120]
$Ge_{16.5}As_{18.8}Ga_{0.2}Se_{64.5}$	750 Dy	Unstructured		1.2 @ 6.19	
$Ge_{16.5}As_{18.5}Ga_{0.5}Se_{64.5}$	400 Dy	Unstructured	Distilled	0.8 @ 6.6	[123]

Note, ‘Unstructured’ refers to single material fibre.

2.3 MIR (*mid-infrared*) fibre lasers

Lasers are monochromatic, coherent light sources, typically characterised by outputs with high optical intensity, small spectral linewidth, along with good spatial coherence. The word laser is an acronym for "light amplification by stimulated emission of radiation" [124]. These devices operate on the principle of stimulated emission (*see Figure 2-1 (d)*) which was first theorised by Albert Einstein in 1916 [125,126]. The first practical implementation of amplification by stimulated emission was the 'maser' (*microwave amplification by stimulated emission of radiation*) which was developed in 1953 [127]. The first optical laser, operating at a wavelength of 0.6943 µm was built and operated by Theodore H. Maiman in 1960 [128].

Lasers are devices that achieve amplification by stimulated emission inside an optical cavity, which consists of a gain medium, bounded by mirrors. There are a variety of laser types, here we consider fibre lasers constructed using a step index fibre with a solid core, as illustrated in Figure 2-4. Fibre lasers typically produce a high-quality output beam, and they typically offer ease of beam delivery in a relatively inexpensive, robust, and compact form factor. The output power of these devices can range widely depending on their design, with output powers ranging from tens of milliwatts to several kilowatts from a single fibre in either a continuous or pulsed manner.

Figure 2-4 shows a gain medium consisting of the RE^{3+} doped core of a SIF, bounded at both ends by dichroic mirrors, while being photoexcited with a pump laser. The dichroic mirrors produced a 'Fabry–Perot' optical cavity at the lasing wavelength and they could either be discrete mirrors abutted to the gain medium or FBGs (*fibre Bragg-grating*) integrated into the gain medium. These dichroic mirrors were selected to possess reflectivity and transmission bands for the pump and lasing wavelengths, respectively. The SIF facilitated transmission and confinement of the pump laser(s) within the core of the SIF, while providing optical gain at the lasing wavelength. Photoexcitation of the gain medium resulted in optical absorption of the pump laser by the RE^{3+} cations (*see Figure 2-1 (a)*) causing their excited state level(s) to be populated with more electrons than their ground state in a process called population inversion. The processes of spontaneous and stimulated emission subsequently occurred from the excited state level(s).

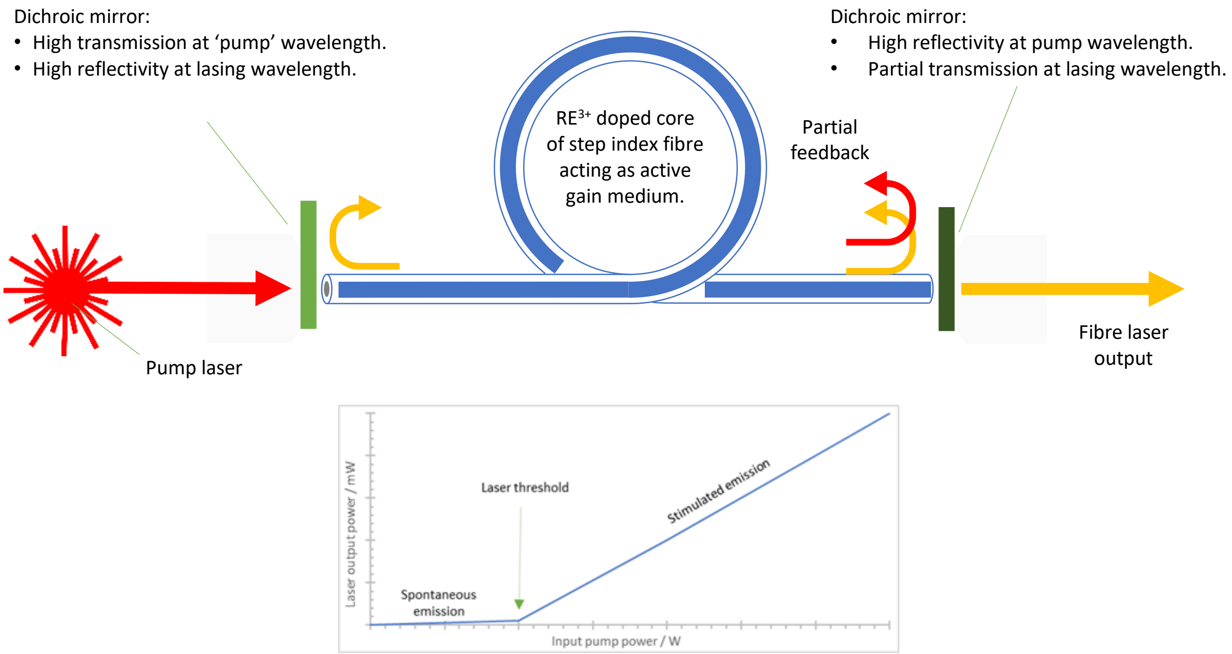

Figure 2-4: Simplified illustration of optical cavity using RE^{3+} doped core of SIF (step index fibre) as gain medium, along with hypothetical output versus input power for an optically pumped laser showing laser threshold.

The mirrors of the optical cavity reflected the emissions from the gain medium, this feedback light formed a standing wave cavity resonator, resulting in stimulated emissions within the gain medium. Lasing occurred at the 'lasing threshold', which was the lowest input pump power into the optical cavity where the output of the optical cavity was dominated by stimulated emission rather than by spontaneous emission. Beyond the laser threshold the slope efficiency described the relationship between the laser output power and the input pump power, as illustrated within the inset in Figure 2-4. Lasing occurred when the gain within the gain medium was greater than the optical attenuation within the optical cavity, namely due to optical losses of the RE^{3+} doped fibre, and the cavity mirrors. Thus, minimising the optical loss of the gain medium was beneficial for efficient laser operation.

2.3.1 Properties of MIR fibre lasers:

The low phonon energies, IR transparency, and capability to be fabricated into various shapes makes the chalcogenide glass system a suitable host material for room temperature MIR lasers operating at wavelengths greater than 4 µm. This glass system can be doped with RE^{3+} cations and drawn into SIF with relatively low optical loss, also their transparency allows the RE^{3+} dopant to be photoexcited by an IR pump source while transmitting the resulting PL. Some chalcogenide glass compositions have been reported to have optical damage thresholds as high as 12.2 MW/cm^2 of continuous wave irradiation [129]. Furthermore, photoinduced phenomena such as photobleaching and photodarkening have also been reported [49]. These photoinduced phenomena could be used to produce a dichroic mirror in the form of an FBG inscribed within a chalcogenide SIF. This could provide high reflectivity at a specific wavelength, ideal for an optical cavity. Each of these traits makes the chalcogenide glass system ideal for MIR fibre lasers.

MIR lasers have been demonstrated in bulk glass, crystals, SIF, hollow core fibres and gas cells [130–137]. Here we focus on MIR lasers using RE^{3+} doped glass or crystal as the gain medium operating with emission wavelengths greater than 3 µm. Table 2-6 lists some MIR lasers, found in literature employing the Ce^{3+}, Pr^{3+}, Tb^{3+}, Dy^{3+}, Ho^{3+} (*holmium*) and Er^{3+} (*erbium*) cations.

The RE-doped ZBLAN (*fluoride glass*) examples listed in Table 2-6 provided a relatively low phonon energy for their respective RE-cation dopants (see Table 2-1), which limited their infrared transmission edge to around 4 µm and likely caused some of the examples to require cryogenic cooling, at 77 K, to achieve MIR lasing. Conversely, the RE-doped chalcogenide host glass compositions listed provided a low phonon energy for the RE^{3+} dopants which allowed room temperature lasing at wavelengths greater than 5 µm.

The dichroic mirrors used for the lasers listed in Table 2-6 were either an FBG or, discrete mirrors. Notably, the MIR lasers which employed an FBG, see Table 2-6, achieved greater slope efficiencies when compared to their discrete mirror counterparts.

The MIR lasers which possessed a smaller quantum defect exhibited higher slope efficiencies, as evident by the Dy^{3+} MIR lasers operating at ~4.3 µm when comparing the 1.3, 1.7 and 2.83 excitation wavelengths. Interestingly, there are several examples of Dy^{3+} NIR lasers operating at ~2.9 µm in fibres [138]. However, to the best of my knowledge there currently have been no demonstrations of MIR fibre lasers operating at ~4.4 µm employing the Dy^{3+} cation, despite several demonstrations of lasing within the bulk crystals, see Table 2-6, and numerical modelling evaluating its feasibility [139].

Table 2-6: Specifications and characteristics for either bulk glass/crystals or fibre MIR lasers found in literature with emission wavelengths greater than 3 µm.

Description of gain medium	**Cavity mirrors**	**Excitation wavelength(s) / µm**	**Longest output wavelength / µm**	**Output power / W**	**Slope efficiency (%)**	**Year and reference**
Room temperature SIF with Ce^{3+} doped $Ge_{15}As_{21}Ga_1 Se_{63}$ core.	Butt coupled mirrors	4.150	5.280 (CW)	Not measured	Not measured	2021 [140]
Room temperature Ce^{3+} doped $Ge_{20}Sb_{10}Ga_5Se_{65}$ atomic % glass rod.	Mirrors	4.100	5.200 (CW)	Not reported	21.0	2021 [130]
Room temperature $Ge_{36}Ga_5Se_{59}$ atomic % glass rod doped with Pr^{3+} cations	Butt coupled mirrors	1.540	5-6	Not reported	Not reported	2021 [134]
Room temperature SIF with Tb^{3+} doped $Ga_3Ge_{25}As_{15}Se_{57}$ atomic % core.	Butt coupled mirrors	1.980	5.380 (CW)	Not reported	Not reported	2021 [141]
Room temperature SIF with Tb^{3+} doped $Ge_{20}Ga_5Sb_{10}Se_{65}$ atomic % core.	Butt coupled mirrors	1.980	~5.25 (CW)	0.0036	5.3	2022 [142]
Room temperature, double clad single mode ZBLAN fibre (*Le Verre Fluoré*) with Dy^{3+} doped core.	FBG	2.830	3.150 (CW)	1.06	73.0	2018 [137]
Room temperature Dy^{3+} doped YLF (*yttrium lithium fluoride*) crystal.	Mirrors	1.730	4.340	0.0002	> 0.05	1991 [135]
Room temperature Dy^{3+} doped PGS ($PbGa_2S_4$) crystal.	Mirrors	1.700	4.300	0.00067	8	2013 [143]
Room temperature Dy^{3+} doped $CaGa_2S_4$ (*calcium thiogallate*) crystal.	Mirrors	1.300	4.380	0.00012	1.6	1999 [136]
Room temperature Dy^{3+} doped KPb_2Cl_5 crystal.	Mirrors	1.700	4.500 µm	0.001	12	2022 [144]
Room temperature, double clad, InF_3 fibre (*Le Verre Fluoré*) with Ho^{3+} doped core.	Butt coupled mirrors	0.888	3.920 (CW)	0.20	10.2	2018 [58]
Ho^{3+} doped ZBLAN fibre cooled to 77° K.	Butt coupled mirrors	0.885	3.900 (CW)	> 0.0011	2.3	1997 [70]
Room temperature, double clad, single mode ZBLAN fibre (*Le Verre Fluoré*) with Er^{3+} doped core.	Butt coupled mirrors	0.980 and 1.973	3.780 (CW)	1.45	27.0	2016 [72]
Er^{3+} doped ZBLAN fibre cooled to 77° K	Butt coupled mirrors	0.653	3.480 (CW)	0.0085	3.0	1991 [145]
Room temperature, double clad, single mode fibre, ZrF_4 fibre (*Le Verre Fluoré*) with Er^{3+} dope core.	FBG	0.976 and 1.976	3.550 (CW)	5.6	26.4	2017 [71]

Note, **FBG** (*Fibre Bragg Grating*), and **CW** (*continuous wave*).

2.4 Chapter summary:

RE^{3+} cations exhibit numerous transitions from 3–12 µm that can be exploited for fibre lasers and amplifiers [17,20], however progress with their usage has been slow, especially for wavelengths greater than 5 µm (see Table 2-6). Demonstrations of room temperature MIR fibre lasing operating at wavelengths beyond 5 µm have only recently occurred using the Ce^{3+} and Tb^{3+} cations. Advancements in RE^{3+} doped chalcogenide glass production and fabrication along with availability of suitable pump sources could be partially attributed to these advancements.

The chalcogenide glass system is a suitable host material for RE^{3+} dopants, these materials exhibit high refractive index and low phonon energies and can be drawn into low-loss fibres [17]. Despite the desirable traits of the chalcogenide glass system there are very few examples of MIR laser action in chalcogenide glass fibres. Two reasons for this deficiency are:

i. The purification of RE^{3+} doped chalcogenide glass can produce single material fibres with relatively low-loss (see Table 2-5). However, deficiencies with the small core SIF fabrication processes can unintentionally introduce additional optical losses. Thus, a major limitation to chalcogenide fibre laser and amplifier development is the fabrication of low-loss small-core RE^{3+} doped fibres [17].

ii. RE^{3+} cations possess numerous latent ESA bands, these are sometimes-overlooked because of their latent nature. Regrettably, these latent ESA bands can render seemingly feasible excitation schemes impractical. Thus, the ESA bands of each RE^{3+} dopant presents a unique set of challenges in the selection of suitable pump and emission wavelengths, especially in the MIR spectral region. Consequently, knowledge of their location and strength offers an opportunity to either avoid or utilise them.

This thesis aims to evaluate excitation schemes and electronic transitions within RE^{3+} dopants that could be exploited for use as a MIR light source while striving to explore the properties and peculiarities of the chalcogenide glass system that may help or hinder MIR lasing. This entailed exploration of the interaction between the RE^{3+} dopant and the chalcogenide glass host, inclusive of its extrinsic impurities, and its influence on the spectroscopic properties of the RE^{3+} dopant for different pump wavelengths.

3 Synthesis and evaluation of chalcogenide glasses:

This Chapter presents the synthesis and evaluation of undoped and RE^{3+} (*rare-earth*) cation doped chalcogenide glasses, with the objective of giving a systematic assessment of several RE^{3+} doped samples while identifying deficiencies with the employed methodologies. Section 3.1.1 gives a description of the methodology employed in the preparation, purification, and synthesis of several chalcogenide glass compositions, along with the fabrication methods used to produce polished glass, glass extrusions, single material fibres, and SIF (*step index fibres*). Section 3.1.2 describes the methodology employed in the optical evaluation of chalcogenide glass samples. Section 3.2 presents the optical evaluation of bulk chalcogenide glass, glass extrusions, and fibre samples along with a discussion on the presented results. Note the following:

- ➢ Several of the purification and production methodologies used in this Chapter originated from techniques found in literature along with methods developed from previous work within the Mid-Infrared Photonics Group, George Green Institute for Electromagnetics Research, at the University of Nottingham [77,96,97]. A comprehensive description of each of these techniques can be found in Appendix 7.1 and 7.2.
- ➢ Most of the chalcogenide glass compositions evaluated in this thesis were based on previous on work done in [97] within the within the Mid-Infrared Photonics Group.

Additionally, throughout this thesis, a coding system was used to identify each glass sample evaluated. A description of the code structure and examples of its usage are given in Appendix 7.1.13.

3.1 Methodology for synthesis and evaluation of chalcogenide glass.

Section 3.1.1 describes the methodology employed in the production of bulk chalcogenide glass and its subsequent fabrication into single material fibre (*without a cladding*) and SIF, inclusive of intermediate glass extrusions. Section 3.1.2 describes the methodology employed in spectroscopic, and refractive index dispersion evaluation of glass samples along with a novel non-destructive evaluation method developed by the author and the Mid-Infrared Photonics Group.

3.1.1 Chalcogenide glass synthesis and fabrication of extrusions and fibres.

Section 3.1.1.1 describes the methodology employed to produce either undistilled or distilled, undoped or RE^{3+} doped bulk chalcogenide glass. Section 3.1.1.2 describes the processing of bulk chalcogenide glass into polished glass, glass extrusions, single material fibre, and SIF.

3.1.1.1 Methodology used in the production of bulk chalcogenide glass:

The chalcogenide host glass system used in the presented work were based on a sub-set of the elements ‘Ge’, ‘As’, ‘Sb’ ‘Ga’, ‘Se’, and ‘S’. Production of each bulk chalcogenide glass sample in this thesis employed the traditional ‘melt-quench’ technique with an electric resistance rocking furnace. After initial glass synthesis several of these chalcogenide glass compositions were doped with a single RE metal foil. Note, for the presented work only the metallic foil of the RE dopants were used. This was done to avoid introducing additional confounding factors to glass production and spectroscopic evaluation. Synthesis of bulk chalcogenide glass employed the flowchart illustrated in Figure 3-1 and was sub-divided into the following subsections:

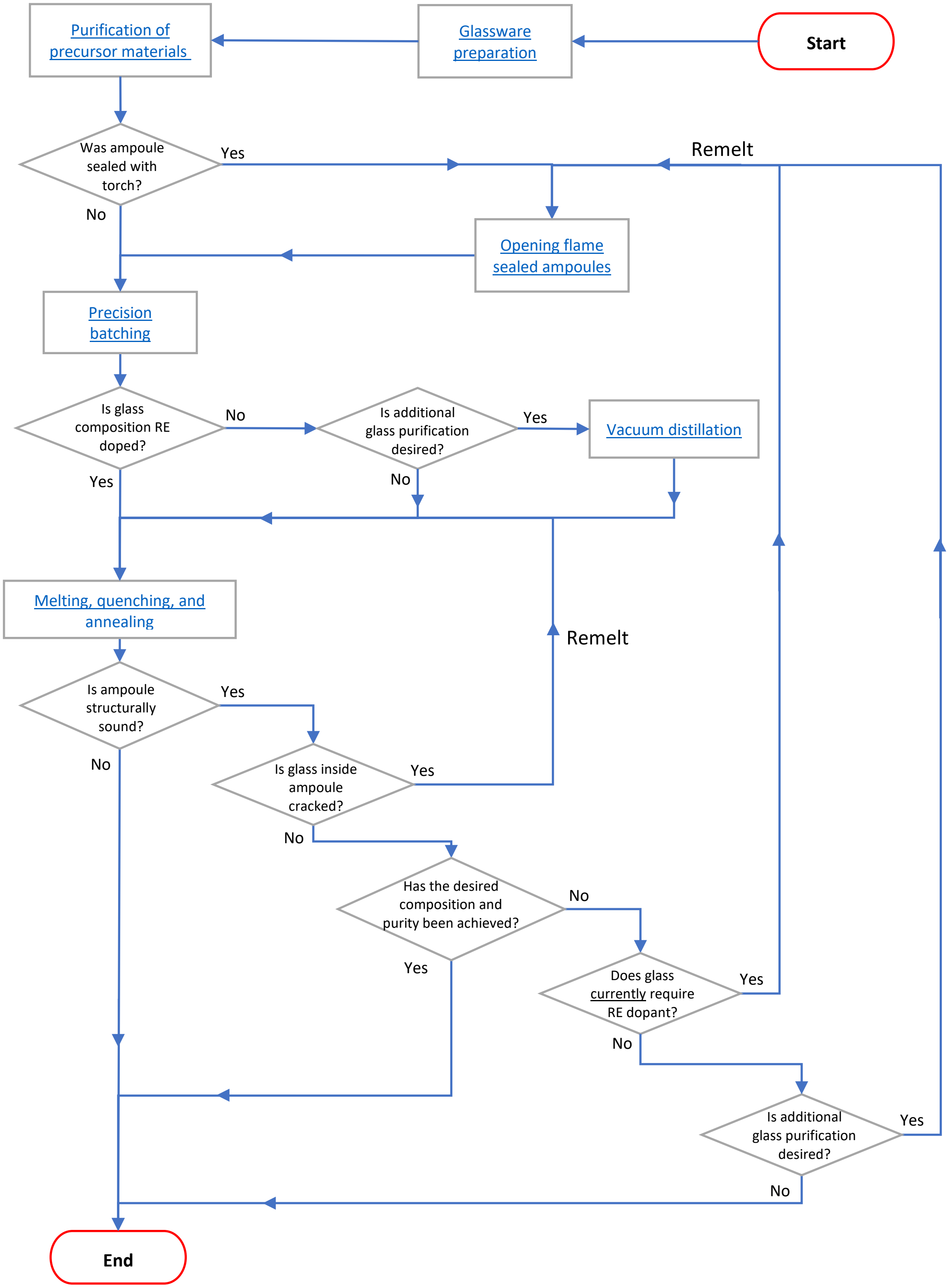

Figure 3-1: Process flowchart for production of either RE^{3+} doped or undoped bulk chalcogenide glass.

1. Glassware preparation: Stringent cleanliness of the silica glassware used in both the purification of chemical precursors and synthesis of chalcogenide glass was essential to minimise impurities in the chalcogenide glass produced. Thus, the silica glassware used were subjected to comprehensive cleaning and preparation steps. These steps entailed washing, rinsing, and heat treatments along with visual inspections. The specific preparation steps are given in Appendix 7.1.1.
2. Purification of the precursor chemicals: Purification of each precursor chemical was performed prior to chalcogenide glass production on small batches, with provisioning for losses occurring during the purification process. The purification method employed for each precursor chemical depended on their physical properties and the impurities present, Table 2-3 lists the properties of the constituent elements. Both the chalcogens and pnictogens were subjected to a bake-out while under continuous/dynamic vacuum to remove impurities with a high vapor pressure and to accelerate outgassing of physically or chemically adsorbed impurities from their surface. The metallic precursors liquid ‘Ga’, rare earth foils, and ‘Al’, each had their surface impurities mechanically removed. The steps used for the purification of each precursor chemical are given in Appendix 7.1.2.
3. Ampoule opening: It was sometimes necessary to open vacuum sealed silica glass ampoules to either add materials to their contents or to remove their contents for re-batching into another ampoule. Appendix 7.1.3 outlines the steps used to safely open ampoules.
4. Precision batching: This entailed batching of constituent chemicals of the chalcogenide glass into silica glassware intended as the ‘melt/quench vessel’, either a silica ampoule, or custom-

made silica distillation rig. Appendix 7.1.4 presents the steps used for calculation and batching of precursor material.

5. Melting, quenching, and annealing: Ampoules and their contents were subjected to a simultaneous heating and rocking schedule to melt and homogenise the contents. After melting the molten glass was rapidly cooled into an amorphous solid in a multi-stage quenching process then annealed at its 'T_g'. Upon completion of annealing, the silica glass ampoule and its chalcogenide glass contents were visually inspected for cracks and defects which could result in catastrophic failure of the ampoule if a remelt was required. If the chalcogenide glass, inside the ampoule, contained significant cracks, then it would be remelted inside the same ampoule, as these cracks could hamper subsequent fabrication processes. The steps for the melt quench and annealing process are given in Appendix 7.1.5.
6. Vacuum distillation: This was the procedure used to purify previously made undoped chalcogenide glass cullet without 'Ga'. The process was enhanced with the aid of chemical getters such as $TeCl_4$ and 'Al'. The steps for vacuum distillation are given in Appendix 7.1.6.

Glass synthesis employed the flowchart illustrated in Figure 3-1, production could entail more than one loop through the 'melt-quench' process via a 'remelt' depending on the desired composition and purity of the glass. These process steps were amenable to a variety of chalcogenide glass compositions and were used in the production of:

1. Undoped, undistilled glass: The melt-quench process was performed once.
2. Undoped, distilled glass: The melt-quench process step was performed twice, firstly to produce the undoped, undistilled glass followed by a distillation then remelting to homogenise the distilled glass.

3. RE doped, undistilled glass: The melt-quench process was performed twice, firstly, to produce the undoped, undistilled glass, followed by remelting with the dopant.
4. RE doped, distilled glass: The melt-quench process step was performed three times, firstly to produce the undoped, undistilled glass followed by distillation, then remelting to homogenise the distilled glass, and remelting with the RE-dopant and 'Ga' co-solubilizer.

3.1.1.2 Fabrication of chalcogenide bulk glass, extrusions, and fibres.

Glass fabrication employed the flowchart illustrated in Figure 3-2, these process steps were amenable to the fabrication of a variety of chalcogenide glass components such as polished bulk glass, glass extrusion along with single material fibres and SIF. The starting point for each of these items was bulk glass rod or billet and production could entail multiple steps to produce chalcogenide components. Fabrication of chalcogenide glass was sub-divided into the following:

1. Polished bulk glass: Bulk glass samples were disc shaped pieces of glass cut from larger annealed glass rods. Preparation of these glass samples could entail cutting, grinding, polishing, and pressing in a vacuum hot press until the desired surface finish was achieved. Appendix 7.1.7 describes the process used to prepare polished bulk glass samples. These glass samples could be used for spectroscopic evaluation (*see Section 3.1.2*), cladding tube extrusions and for the co-extrusion process, see Appendix 7.1.8 and 7.1.9, respectively.
2. Chalcogenide melt extrusion: Extrusions were performed on cylindrical bulk chalcogenide glass billets, to produce cladding tube extrusions, and co-extrusions. Wherein, chalcogenide glass samples were heated above their 'T_g', then pressure was applied to force the viscous fluid of the supercooled chalcogenide melt through a shaped die, to produce either a rod, or

tube. Sections 7.1.8, and 7.1.9 describes the extrusion process. Both rod and tube types of extrusions could then be used as an intermediate step in the fabrication of a SIF using the ‘rod in tube’ method, this process is described in Appendix 7.1.12.

3. Glass fibre/cane drawing: Glass rods were drawn into single material fibre, SIF, and cane. This process entailed heating a narrow region of the glass rod above its ‘T_g’. Axial tension was then applied to the glass rod while it was in a ‘supercooled liquid’ state to form a continuous stream of glass which rapidly solidified. The process for glass fibre drawing is described in Appendix 7.1.10. Single material fibre was drawn from a single chalcogenide glass rod, these fibres possessed an outer diameter of less than 400 µm. Conversely, SIFs were drawn from specially fabricated step-index glass rods comprised of at least one concentric inner core and an outer cladding. Glass drawn with an outer diameter greater than 400 µm was called ‘cane’ and could be either ‘single material’ or ‘step-index’. SIF were drawn from specially prepared glass rods comprised of two materials of differing refractive index using the ‘rod in tube’ method, as described in [146–149]. These specially prepared glass rods were fabricated using the ‘rod in tube’ method and utilised both the ‘cane’ drawing, and the cladding tube extrusion procedures described in Sections 7.1.8 and 7.1.9, respectively.
4. Propylamine etching: The logistics involved in glass production often resulted in glass samples being produced before they could be used, allowing time for the inclusion of impurities due to oxidation, absorption, and adsorption of atmospheric molecules. Thus, propylamine etching using the process described in Appendix 7.1.11 was carried out to remove any surface oxidation [150,151] which may have occurred, or to remove surfaces that were in contact with the inner wall of the silica ampoule. Glass rods were typically etched prior to fibre

drawing, while glass canes were etched prior to their use in the 'rod-in-tube' method to assemble a step-index glass rod. Note, extruded glass tubes were not etched due to the inability to properly clean their inner surface after etching.

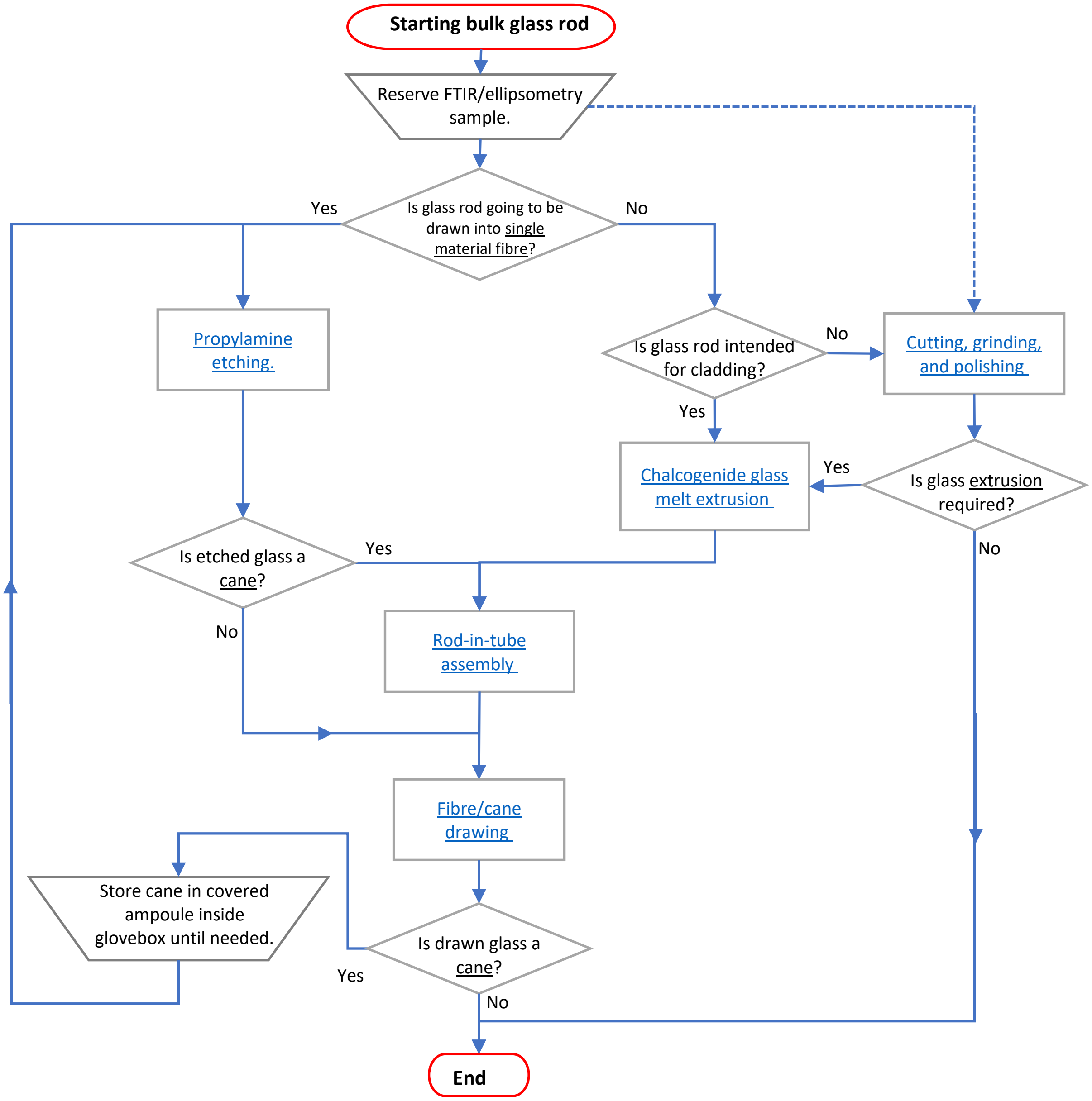

Figure 3-2: Flowchart to process bulk chalcogenide glass into polished bulk glass, single material fibre, glass extrusions, and SIF.

3.1.2 Optical, and compositional evaluation of chalcogenide glass.

Section 3.1.2.1 describes the methodology employed for the spectroscopic evaluation of chalcogenide glass samples using a FTIR (*Fourier transform infrared*) spectrometer. Section 3.1.2.2 describes the novel procedure employed for the non-destructive evaluation of various chalcogenide glass samples in the visible, NIR (*near-infrared*) and MIR (*mid-infrared*) spectral regions developed by the author. Section 3.1.2.3 explains compositional evaluation of chalcogenide glass samples. Section 3.1.2.4 describes the methodology employed to evaluate the MIR refractive index dispersion properties of bulk chalcogenide glass samples.

3.1.2.1 FTIR (Fourier transform infrared) spectral characterisation methodology:

The spectroscopic properties of chalcogenide glass samples were evaluated using a FTIR spectrometer. The spectrometer was used to simultaneously generate and analyse broadband IR light transmitted through either a bulk glass or fibre sample. Fourier analysis of the light transmitted through the entire optical path, inclusive of the sample, allowed for the evaluation of its intensity as a function of wavelength. This was used to identify spectral regions where the light was either absorbed/scattered/reflected and/or transmitted within the optical path. Importantly, this allowed for the identification and evaluation of both intrinsic and extrinsic absorption bands in a sample. The FTIR spectrometer was used in the following measurements:

<u>Bulk glass absorption measurements</u>: A FTIR spectrometer was used to measure the absorption spectrum of polished bulk chalcogenide glass samples over a large portion of the IR spectral region (*typically between 1 to 25 µm*). Separate NIR and MIR bulk glass absorption measurements

were each accomplished using the equipment setup and process described in Section 7.2.1 and combined. These absorption spectra were subsequently modified by having the absorptions for the host glass numerically removed, using the ‘Baseline Fit’ function in Matlab, to reveal the RE^{3+} cation GSA (*ground state absorption*) contributions. These modified absorption spectra are presented in Section 3.2, and were used to derive the RE^{3+} energy level diagrams presented in Chapters 4, and 5.

Optical loss measurements: The ‘cut-back’ method was employed to evaluate the optical attenuation of single material fibre samples over a portion of the IR spectral region (*typically between 1.5 to 11.5 μm*). Figure 3-3 illustrates the equipment configuration used for measurements (*designed and set up by Dr David Furniss*), while Figure 3-4 shows the flowchart used to perform fibre loss measurements.

The FTIR spectrometer, item 1, in Figure 3-3, was used to generate modulated broadband IR light, mirrors were then used to focus this light into the cleaved ‘launch-end’ of a fibre sample. The ‘cut-back’ method was employed to compare the intensity of broadband light transmitted through the fibre sample as it was incrementally cleaved towards the ‘launch end’. The detailed procedure for performing the loss measurement is described further in Appendix 7.2.2.

Note, the optics of this equipment configuration produces a large focal point (*~1 mm in diameter*) at the ‘launch end’ of the sample. Thus, the configuration was not suitable to evaluate the optical loss for small core SIF fibres due to the low intensity of IR light that would be launched into the core of the SIF. As a result, loss measurements of SIF samples were intentionally omitted.

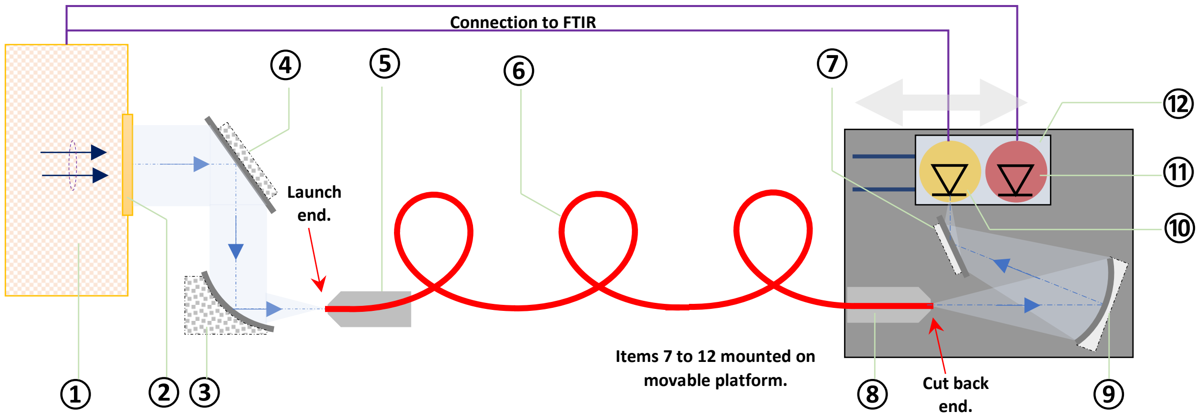

1. FTIR (*Fourier transform infrared*) spectrometer (*Bruker, IFS 66/S please see Figure 7-12*) equipped with Globar© source and 'KBr' (*potassium bromide*) beam splitter and using Bruker OPUS software (*version 3.1 build 3,0,19*).
2. 'KBr' window, 2 mm thick.
3. Aluminium 90° 'Off-axis' parabolic mirror, f = 69 mm on a kinematic mount.
4. Aluminium mirror on a kinematic mount.
5. Bare fibre holder (*Newport, 561-FH*) on XYZ translation stage.
6. Single material chalcogenide glass fibre sample, with both ends cleaved.
7. Flat aluminium mirror on a kinematic mount.
8. Bare fibre holder (*Newport, 561-FH*) on XYZ translation stage.
9. Parabolic aluminium mirror on kinematic mount.
10. Liquid nitrogen cooled InSb (*indium-antimonide*) detector (*InfraRed Associates, Inc. Model: ID413*) for the 1 to 5.5 µm spectral region, connected to Bruker IFS 66/S FTIR spectrometer.
11. Liquid nitrogen cooled MCT (*mercury-cadmium-tellurium 'Hg-Cd-Te'*) detector (*Kolmar Technologies, V100-1B-7/190*) for the 2 to 11 µm spectral region, connected to Bruker IFS 66/S FTIR.
12. Items 11 and 12 are mounted onto a home-made siding rail.

Figure 3-3: Diagram of equipment configuration used for optical attenuation measurements of solid core, single material fibres.

Between each 'cut-back' the intensity of the broadband light transmitted through the sample '$\mathbf{P_{out}}$' was measured by the FTIR spectrometer using both detectors, while '**L**', the length of fibre cleaved was measured to within a millimetre. Note, '$\mathbf{P_{out}}$' denoted an intensity measurement from the current cleave, and '$\mathbf{P_{in}}$' denoted the intensity measurement from a subsequent cleave. The 'cut-back' procedure (see Section 7.2.2) was repeated several times. The attenuation per unit length (dB/m) was calculated by individually ratioing each measured '$\mathbf{P_{out}}$' against each subsequent measured '$\mathbf{P_{in}}$' while dividing by the corresponding length between cleaves '**L**'. The calculation was given by the following equation:

$$Attenuation(dB/m) = \left(\frac{1}{L}\right) \times log_{10}\left(\frac{P_{out}}{P_{in}}\right) \qquad \textit{Equation 3-1}$$

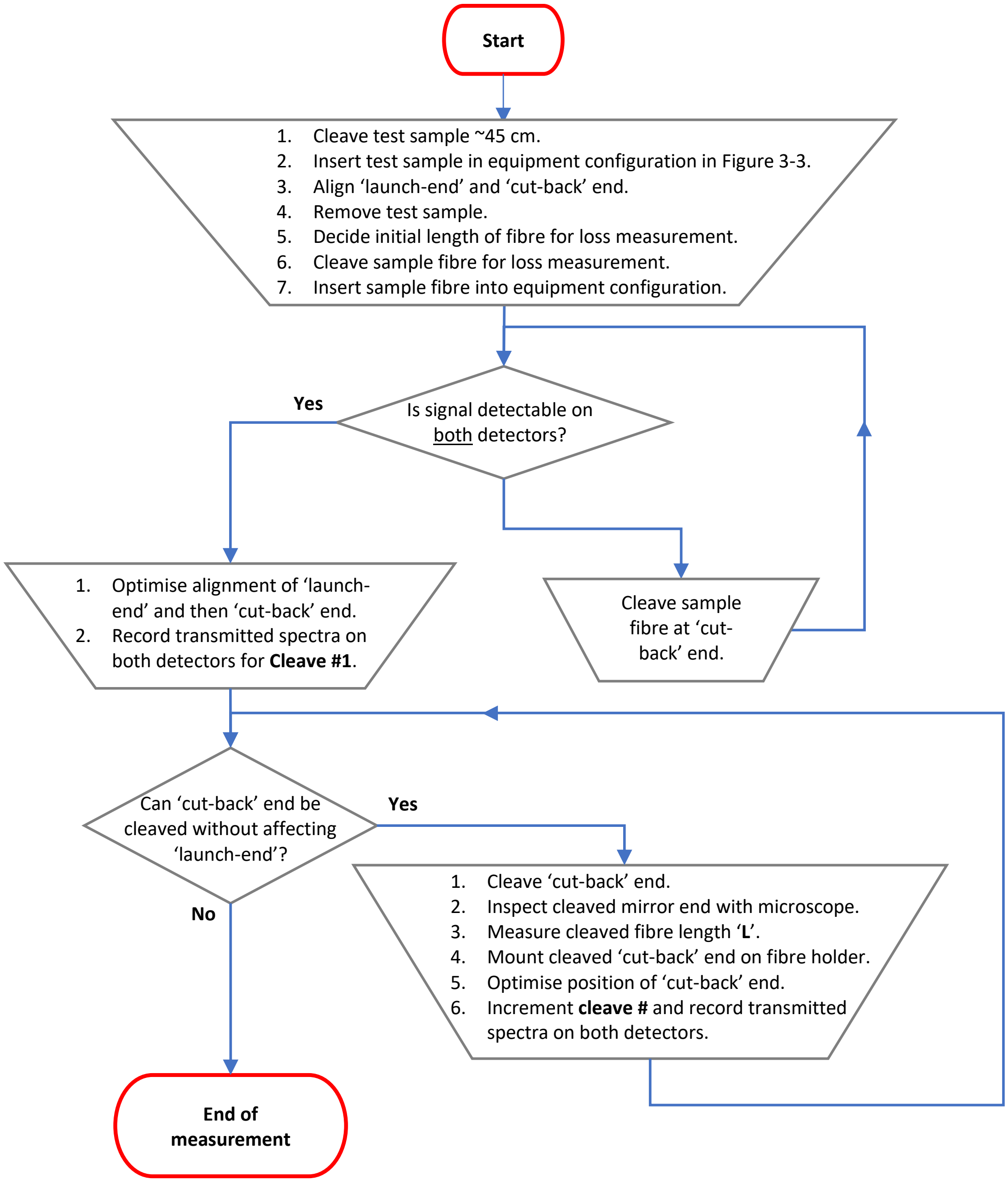

Figure 3-4: Flowchart for optical attenuation measurement of RE^{3+} doped single material fibre.

The attenuation spectra presented in Section 3.2 show the mean value of each attenuation spectrum calculated using Equation 3-1. Thus, each cut-back contributed towards the mean attenuation spectrum, due to this cross-calculation. This was done to account for variations in fibre diameter, fibre position (*at the 'cut-back' end*), cleave angle and the presence of surface debris into the overall loss measurement and typically resulted in slightly pessimistic, but more realistic results than compared to the method used in [103]. Note, in the presented attenuation spectra, in Section 3.2, spectral regions with high attenuation due to strong RE^{3+} GSA (*ground state absorption*) or impurity absorptions were omitted due to a lack of photons reaching the detector, making these spectral regions noisy.

3.1.2.2 Visible, NIR and MIR imaging methodology:

Bubbles, crystals, and other unwanted defects within chalcogenide glasses were usually hidden due to the opacity of selenide-based chalcogenide glasses to visible light. Thus, a non-destructive imaging technique employing low cost, NIR light source and NIR camera was developed to reveal such internal defects. Figure 3-5 illustrates four separate equipment configurations used to inspect chalcogenide polished bulk discs, glass rods, extruded rods, and fibres samples in the visible, NIR, and MIR spectral regions. The equipment configurations in Figure 3-5 (a), (b) and (c) employed a bright, low cost NIR LED to illuminate chalcogenide glass samples, and a low-cost NIR camera to image these samples. This combination of light source and camera offered a simple, versatile, and cost effective solution for imaging inside the otherwise opaque chalcogenide glass samples, as compared to an alternate method such as laser ultramicroscopy as described in [104,105]. This non-destructive inspection was used to detect the presence of both microscopic and macroscopic unwanted light-scattering defects including nucleated crystals; intrinsic defects such as refractive index striae; extrinsic defects such as debris and bubbles, and other imperfections.

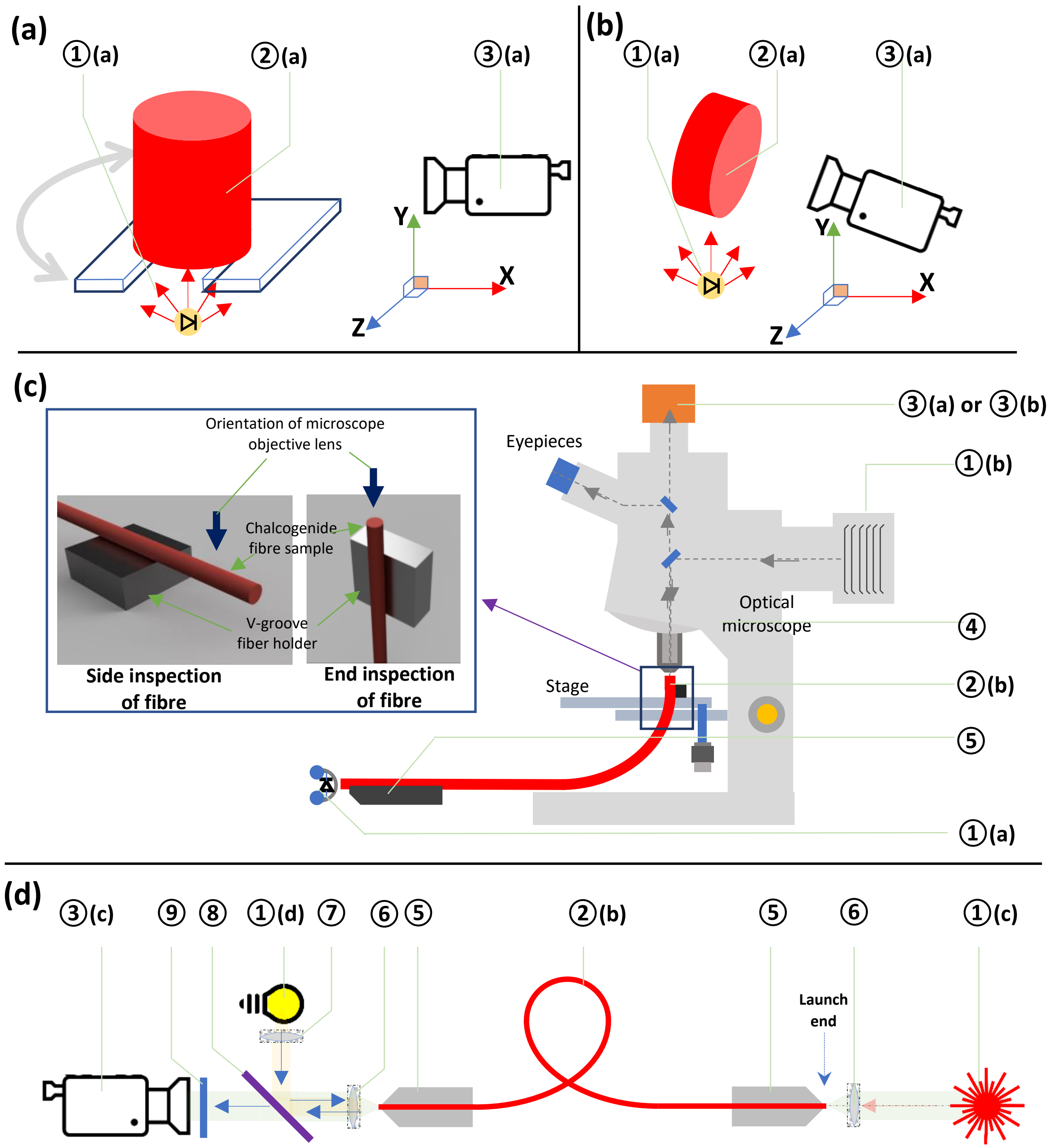

1. IR light sources:
   a. ~ 940 nm LED
   b. Tungsten lamp for visible illumination.
   c. Interchangeable laser:
      i. 3.390 µm HeNe laser (*Excelitas Technologies, 32172*).
      ii. 1.940 µm source (*m2K-BA-1940-E0500-MMF200_IG10*) with collimator (*Ocean Optics, 74-VIS*).
   d. Broadband MIR light source globar.
2. Chalcogenide glass sample:
   a. Glass rod or polished glass disk.
   b. Fibre sample with both ends cleaved.
3. Camera:
   a. Visible camera (GX).
   b. NIR camera (*ZWO, ASI120MM Mini*).
   c. MIR camera (*Xenics*).
4. Optical microscope (*Vickers Instruments, model M171484*)
5. Stainless steel V-groove fibre holder.
6. Aspheric lens, f = 5.95 mm (*Thorlabs, 39002-E*).
7. CaF$_2$ lens, f = 40 mm (*Thorlabs, LA5370*).
8. 50/50 CaF$_2$ beam splitter (*Thorlabs, SW510*) in kinematic mount, situated atop a XZ translational stage.
9. Interchangeable optical filter.

Figure 3-5: Equipment configurations used for the optical inspection of chalcogenide glass samples: ***(a)*** *and* ***(b)*** *glass rods and disks using visible/NIR illumination,* ***(c)*** *glass fibres using visible/NIR illumination, and* ***(d)*** *glass fibres using MIR illumination.*

Figure 3-5 (a) and (b), illustrates the equipment configuration used for visible/NIR imaging of polished bulk discs, glass rods (*either a bare glass rod or a glass rod still inside the melt-ampoule*), and extruded rods. In this configuration, samples were illuminated with either a NIR LED (*light emitting diode*), under-lit or backlit, item 1(a) in Figure 3-5, or with ambient, visible light. A visible/NIR camera, item 3 (a) in Figure 3-5, was mounted orthogonally relative to the light source through the sample to observe reflected/scattered light either in the visible or NIR spectral regions.

Figure 3-5 (c) shows the equipment configuration used for visible/NIR imaging of fibres. In this configuration a NIR LED, item 1 (a) in Figure 3-5, was abutted to a cleaved end of the fibre sample while the opposite end was positioned beneath the objective lens of a microscope, item 4 in Figure 3-5 where it could be illuminated with visible light from a tungsten lamp, item 1(b) in Figure 3-5.

A visible/NIR camera, item 3 in Figure 3-5, attached to the microscope, was then used to image the fibre sample either in transmission (*NIR light transmitted through fibre sample due to NIR LED*) or reflection (*visible light reflected from cleaved end of fibre due to the tungsten lamp*).

Figure 3-5 (d), illustrates the equipment configuration used for MIR imaging of fibres. In this configuration a MIR laser source, item 1 (c) in Figure 3-5, was launched into a cleaved end of the fibre sample while the opposite cleaved end fibre was illuminated by a thermal light source, item 1(d) in Figure 3-5. A MIR camera, item 3 (c) in Figure 3-5, was positioned to observe the cleaved end of the fibre sample through an interchangeable optical filter, item 9 in Figure 3-5. The fibre sample was then imaged either in transmission (*MIR light transmitted through fibre sample due to the laser*), in reflection (*MIR light reflected from cleaved end of fibre*), or in both reflection and transmission. Note, MIR inspection of SIF samples enabled direct observation of optical guiding properties of the core of SIF samples.

3.1.2.3 Composition and structural analysis of fibres:

Imaging and compositional analysis of chalcogenide glass fibre samples was carried out using a JEOL 6490LV SEM (*scanning electron microscope*) fitted with an X-Max 80 Oxford Instruments EDX (*Energy Dispersive X-ray*) spectroscopy detector. Compositional measurements were performed with an estimated ± 0.5 atomic % accuracy for elements heavier than oxygen. All fibre samples were carbon coated (*Edwards Coating System*) prior to either SEM imaging or SEM-EDX measurements. Note, all SEM measurements presented in Section 3.2 were graciously performed by PhD student Richard Crane.

3.1.2.4 MIR ellipsometry:

Refractive index dispersion measurements were performed using an IR ellipsometer (*J.A. Woollam, IR-VASE Mark II*). These measurements were performed on annealed, disc shaped samples. Note, all presented V.A.S.E (*variable angle spectroscopic ellipsometry*) measurements were performed on samples at angles of 55.00°, 65.00° and 75.00° at a measurement resolution of 2 cm^{-1} between the 1.55 to 40.00 µm spectral region. The empirical refractive index dispersion data was then fitted to a 2-term Sellmeier model using J.A. Woollam CompleteEASE software (*version 5.10*), according to instructions in [152]. The 2-term Sellmeier model utilised was defined by the following equation:

$$n = \sqrt{\left(\varepsilon + \frac{A\lambda^2}{\lambda^2 - B^2} - E\lambda^2\right)} \qquad \text{Equation 3-2}$$

where ‘n’ is the refractive index, ‘ε’ is an index offset, ‘A’ is the amplitude ‘B’ is the centre energy and ‘E’ is the position of a pole in the infrared. The 2-term Sellmeier model was found capable of fitting the 2.00 to 20.00 µm spectral region for each sample evaluated in Section 3.2. However, this model quickly became insufficient when considering the full 1.55 to 40.00 µm measurement window, which required a significantly more complex fitting model within the J.A. Woollam CompleteEASE software. Thus, the refractive index dispersion data presented throughout Section 3.2 was intentionally truncated to the 2.00 to 20.00 µm spectral region, allowing a convenient way for anyone else to reproduce the refractive index model without requiring proprietary software. Using the obtained refractive index dispersion model the NA (*numerical aperture*), was calculated using the following equation:

$$NA = \sqrt{\left((n_{core})^2 - \left(n_{cladding}\right)^2\right)} \qquad \text{Equation 3-3}$$

The ‘n_{core}’ and ‘$n_{cladding}$’ are the refractive indices of the core and cladding glass compositions, respectively. Note, all ellipsometry measurements performed were graciously aided by Dr Nikolaos Kalfagiannis of the School of Science and Technology, Department of Physics and Mathematics, Nottingham Trent University.

3.2 Evaluation of chalcogenide glass:

This section presents the synthesis, fabrication, and characterisation of several chalcogenide glass samples used in upcoming Chapters. This characterisation included absorption spectroscopy, compositional analysis, spectroscopic ellipsometry, non-destructive evaluation using IR imaging, and destructive evaluation. Sections 3.2.1 to 3.2.7 presents the production/fabrication specifications, and characterisation of six different sets of chalcogenide glass samples, each of which were subsequently used in the spectroscopy, and/or optical cavity measurements presented in Sections 4.2 and 5.2. Section 3.2.8 presents a discussion on the synthesis, and fabrication methodology employed in the presented work. Note the following:

i. Glass synthesis and fabrication followed the methodology presented in Sections 3.1.1.1 and 3.1.1.2, respectively.
ii. All bulk glass absorption measurements (see Section 7.2.1) and fibre loss (see Section 7.2.2) measurements were carried out to a 4 cm^{-1} resolution, unless otherwise stated.
iii. All optical characterisation measurement presented were carried out at room temperature, between 21 to 23 °C.
iv. Several of the fibre loss spectra included insets with the corresponding bulk glass absorption measurements overlayed using procedure described in Appendix 7.2.1.1.
v. MIR ellipsometry measurements (see Section 3.1.2.4) and carried out to a 4 cm^{-1} resolution.

3.2.1 Undistilled terbium cation doped samples:

Table 3-1 lists the specifications for two separate undistilled glass rods of differing composition, a 'Tb' (*foil*) doped core glass M228REJN(RC), and an undoped cladding glass M251JN. The core glass was drawn to single material fibre F103REJN(RC), while the cladding glass was extruded into a tube E088DF(JN). The core and cladding glass were subsequently assembled and drawn into a SIF F105REJN via the 'rod-in-tube' method. Section 3.2.1.1 presents the IR absorption spectrum, and refractive index measurements of polished bulk glass samples M228REJN(RC), and M251JN. Section 3.2.1.2 presents the evaluation of the single material fibre F103REJN(RC), and SIF F105REJN. Note, the SIF F105REJN was subsequently used for optical cavity work presented in Section 5.2.1.

Table 3-1: List of production and fabrication specifications for M228REJN(RC), M251JN, F103REJN(RC) and F105REJN. Note, the Tb^{3+} cation concentration calculations assumed several factors (see Section 3.2.8.2) and thus its accuracy should not be relied upon.

Glass type:	**Core**	**Cladding**
Glass melt code:	**M228REJN(RC)**	**M251JN**
Nominal composition (atomic %)	$Ge_{14.8}$ $As_{20.8}$ $Ga_{2.0}$ $Se_{62.4}$ (***undistilled***) + 500 ppmw Tb (foil)	$Ge_{14.8}$ $As_{20.8}$ $Ga_{2.0}$ $Se_{61.5}$ $S_{1.0}$ (***undistilled***)
Glass density	~ 4.5 g/cm^3	Not evaluated
Tb^{3+} concentration	8.53×10^{18} cations/cm^3	Undoped
Produced by:	The author (*supervised by* PhD student *Richard Crane*)	The author
Fibre and cane drawing code:	**F103REJN(RC)**	Not fibre drawn
Cladding tube extrusion code:	Not extruded	**E088DF(JN)**
SIF code:	**F105REJN**	

The glass density was estimated based on density measurements reported in [97,153,154].

SEM-EDX evaluation of a cleaved end of the SIF F105REJN, revealed the composition of the core (*nominally* $Ge_{14.8}$ $As_{20.8}$ $Ga_{2.0}$ $Se_{62.4}$ *atomic %*) was $Ge_{15.4}$ $As_{21.0}$ $Ga_{2.2}$ $Se_{61.4}$ atomic %, while the composition of the cladding (*nominally* $Ge_{14.8}$ $As_{20.8}$ $Ga_{2.0}$ $Se_{61.5}$ $S_{1.0}$ *atomic %*) was $Ge_{15.3}$ $As_{21.2}$ $Ga_{2.2}$ $Se_{60.5}$ $S_{0.8}$ atomic %.

3.2.1.1 Bulk glass M228REJN(RC) and M251JN evaluation:

Figure 3-6 shows the room temperature IR absorption spectrum for a polished M228REJN(RC) bulk sample measured to an 8 cm^{-1} resolution, with an inset showing the Tb^{3+} GSA bands within the 1.5 to 7.0 µm spectral region.

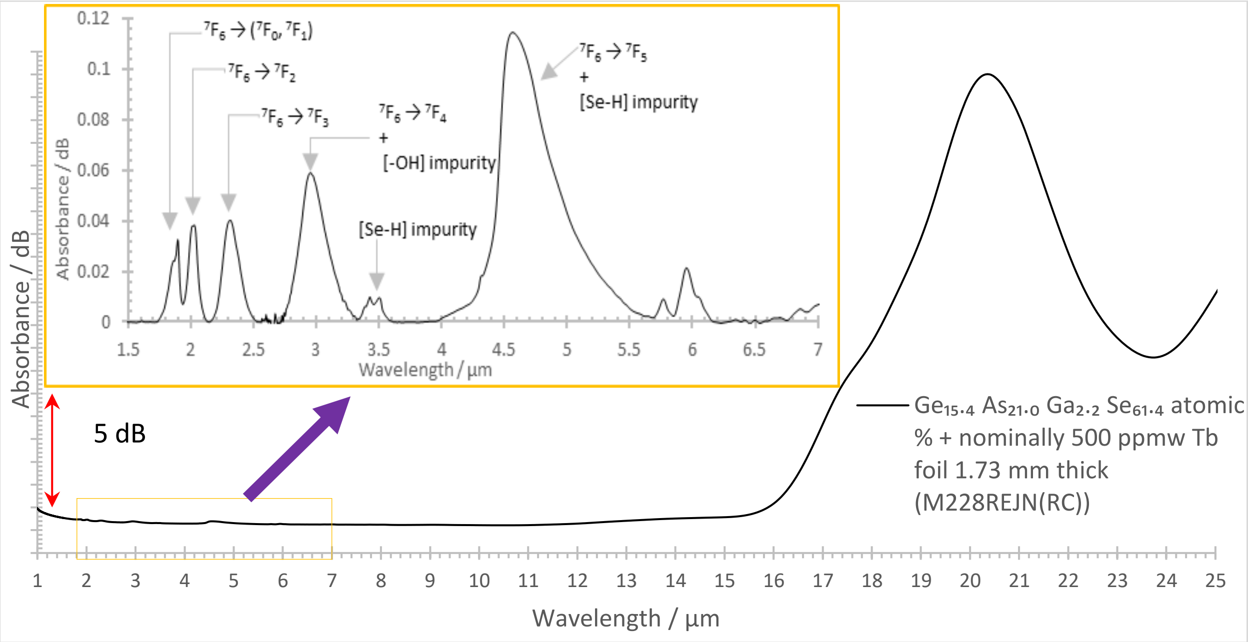

Figure 3-6: Showing room temperature IR absorption spectrum of undistilled nominally 500 ppmw Tb (foil) doped bulk M228REJN(RC) sample 1.73 mm thick, with inset showing Tb^{3+} ground-state electronic absorption bands within the 1.5 to 7.0 µm spectral region along with unwanted host glass impurities (see Table 2-4). Note, the as measured glass compositions, using SEM-EDX, for M228REJN(RC), is quoted in legend.

The Tb^{3+} doped sample exhibited several NIR and MIR GSA bands between the $^7F_6$ ground state and the $^7F_5$, $^7F_4$, $^7F_3$, $^7F_2$, $^7F_1$ and $^7F_0$ excited state levels, each ostensibly peaking at 4.58 µm, 2.94

µm, 2.31 µm, 2.01 µm, 1.89 µm, and 1.86 µm, respectively. Additionally, the ($^7F_6 \rightarrow {}^7F_0$), ($^7F_6 \rightarrow {}^7F_1$), and ($^7F_6 \rightarrow {}^7F_2$) GSA overlapped each other at room temperature. The $^7F_6 \rightarrow {}^7F_5$ GSA overlapped the extrinsic [-Se-H] impurity vibrational absorption, while the $^7F_6 \rightarrow {}^7F_4$ GSA overlapped the extrinsic [-OH] vibrational absorption.

Figure 3-7 shows the refractive index measurements for the bulk core glass M228REJN(RC) and bulk cladding glass M251JN samples. The core and cladding of the SIF F105REJN consisted of the M228REJN(RC) and M251JN glass compositions, respectively, and thus should possess a similar numerical aperture.

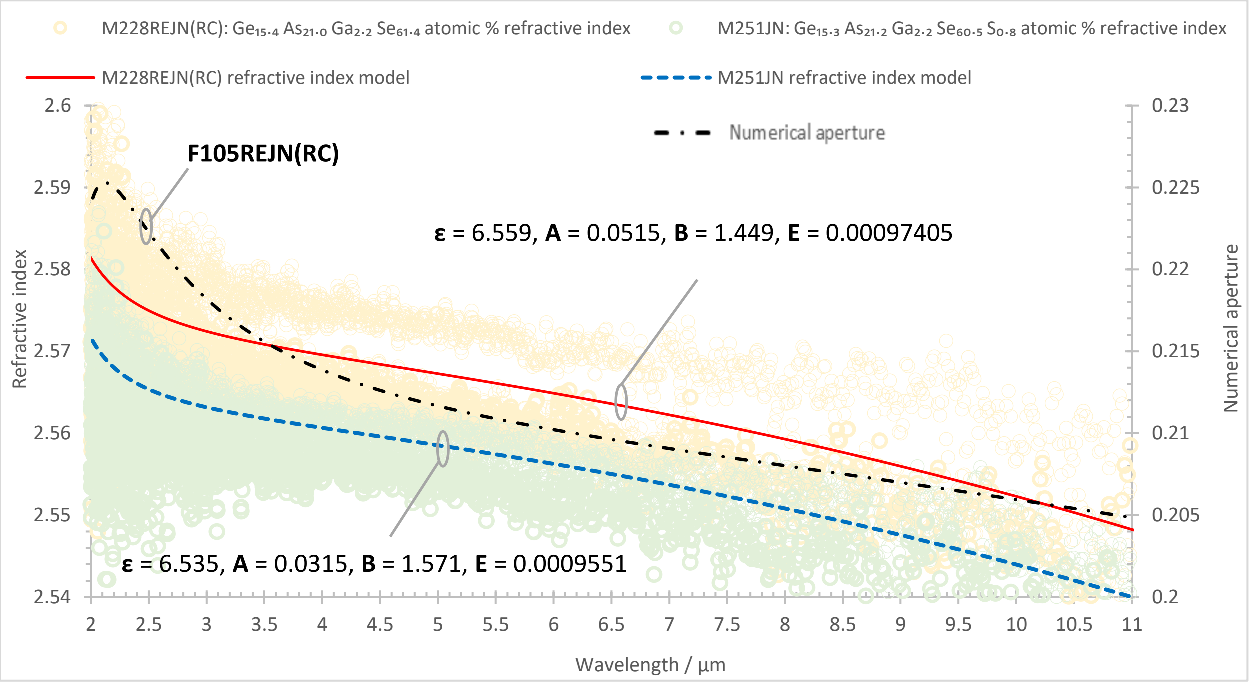

Figure 3-7: Showing refractive index dispersion of the bulk glass samples M228REJN(RC) and M251JN, along with their calculated numerical aperture. The M228REJN(RC) and M251JN constituted the core and cladding glass compositions, respectively, of the SIF F105REJN. Note, the as measured glass compositions, using SEM-EDX, for M228REJN(RC), and M251JN are quoted in legend, and the 2-term Sellmeier model coefficients included in annotations for refractive index measurements (see Equation 3-2).

3.2.1.2 F103REJN(RC) and F105REJN evaluation:

Figure 3-8 shows the attenuation spectrum for a nominally 500 ppmw 'Tb' foil doped undistilled single material fibre F103REJN(RC) with a diameter of 212 ± 2.3 µm and minimum optical loss of 3.61 ± 0.15 dB/m at a wavelength of 6.66 µm. The loss spectrum was measured to an 8 cm^{-1} resolution.

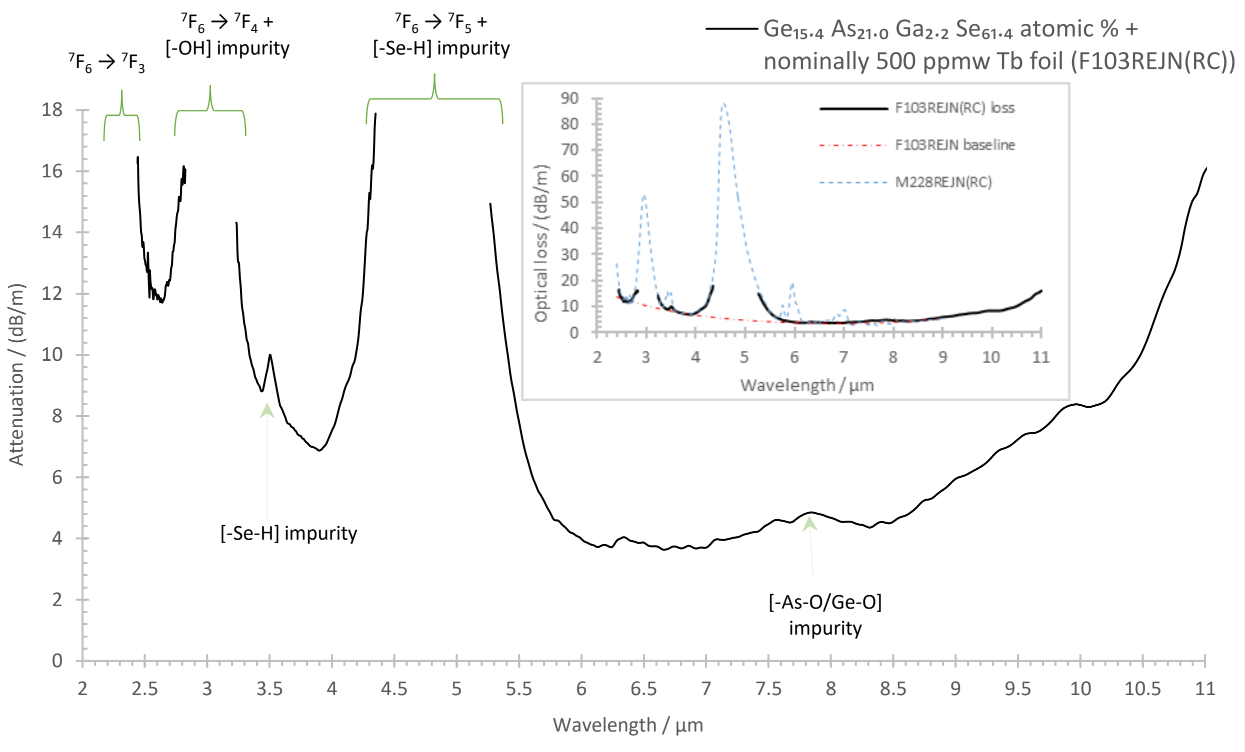

Figure 3-8: Attenuation (dB/m) vs. Wavelength (µm) for a nominally 500 ppmw Tb foil doped undistilled single material fibre F103REJN(RC) with a diameter of 212 ± 2.3 µm, 1.96 m long with a minimum loss of 3.61 ± 0.15 dB/m at 6.66 µm. With inset showing absorption data from M228REJN(RC) sample superimposed onto F103REJN(RC) loss spectrum. The Tb^{3+} ground-state electronic absorption and extrinsic vibrational absorption loss due to unwanted host glass impurities are identified (see Table 2-4). Note, the as measured composition, using SEM-EDX, for F103REJN(RC) quoted in legend.

Considering Figure 3-7, the SIF F105REJN likely possessed a numerical aperture of around 0.210 between the 4.00 to 7.00 µm spectral region. However, due to differences in thermal history between the annealed M228REJN(RC) and M251JN bulk glass samples and the unannealed SIF

F105REJN, the actual numerical aperture of the SIF possibly differed. Note, this is the lowest calculated NA of all the SIF samples evaluated in the presented work. Additionally, the core of the SIF, F105REJN probably possessed a similar attenuation spectrum, to that shown in Figure 3-8, by virtue of its core being comprised of single material cane produced from the same bulk glass rod as the fibre used for F103REJN(RC). However, there may be additional losses in the SIF due to differences in thermal processing and imperfections at its core/cladding interface.

The cleaved end face of a F105REJN SIF sample was evaluated by means of visible, NIR, and SEM imaging, using the procedures described in Sections 3.1.2.2 and 3.1.2.3, respectively. The SIF F105REJN(RC) exhibited good ovality of both the core and cladding, and concentricity of core, as shown in Figure 3-9. Additionally, this SIF could be handled delicately with little fear of unintentional breakage.

Due to the similarity of the core and cladding compositions, visible and SEM imaging struggled to display contrast between the core/cladding interface (*see Figure 3-9 (a)*). Fortunately, NIR imaging, revealed the core to be circular and centred within the cladding, as shown in Figure 3-9 (c). NIR imaging revealed striae within the cladding, and these defects were observed in several SIF samples taken from different portions of the drawn fibre and thus spanned a significant portion of the total SIF. The formation of the striae is discussed in Sections 3.2.8.4 and 3.2.8.6. Additionally, SEM imaging revealed holes, as shown in Figure 3-9 (b), unfortunately due to lack of contrast between the core and cladding the relative position of these holes was unknown. Samples of the SIF F105REJN were used to fabricate an optical cavity, which is further discussed in Section 5.2.1, these samples were subjected to a peak power of 842 mW from a 2.850 µm pump laser. Subsequent SEM imaging of the end face of the SIF after exposure to the laser revealed a 'goosebump' pattern on both the core and cladding, as shown in Figure 3-9 (d). Note, the absence of the goosebump pattern on the unexposed SIF sample in Figure 3-9 (b). The mechanism for the formation of these features is currently unknown.

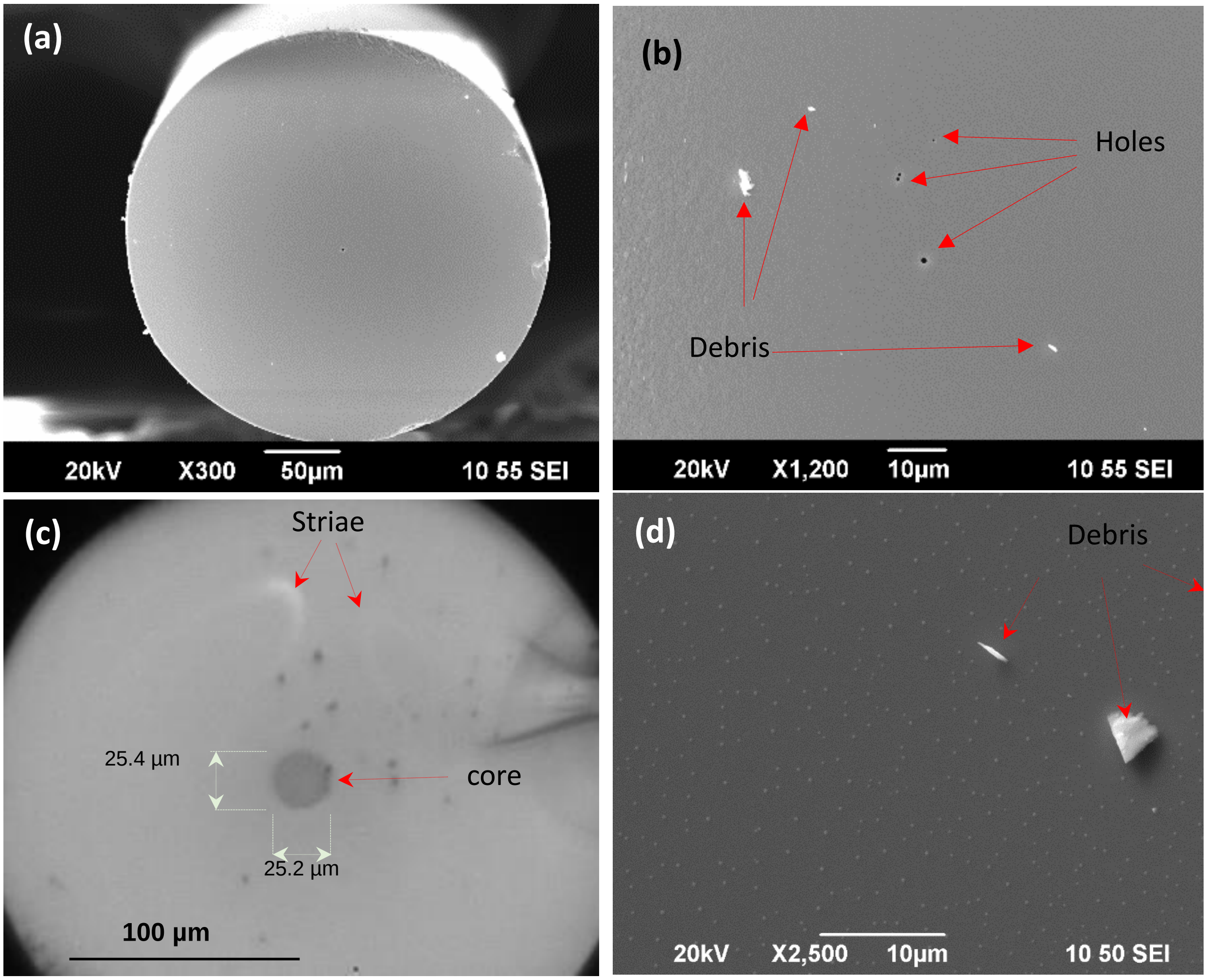

Figure 3-9: Images of the cleaved end of a SIF F105REJN sample with a 25 µm core: ***(a)*** *SEM image of cleaved end of SIF note core/cladding interface is not apparent due to the similarity of the core and cladding glass compositions,* ***(b)*** *SEM image showing holes in cleaved end of SIF (Note, SEM imaging struggled to display contrast between the core and cladding due to their similarity, hence the position of these holes relative to the core/cladding interface is unknown),* ***(c)*** *NIR image showing the core/cladding interface along with striae in the cladding, and* ***(d)*** *SEM image of 'goosebump' patterning (small white dots) on surface of cleaved end of SIF after being exposed to 2.85 µm pump laser at 842 mW. Note, images in Figures (a) & (b) are of the same sample, while Figures (c) & (d) are images of different samples.*

3.2.2 Undistilled cerium cation doped samples:

Table 3-2 lists the specifications for three separate undistilled glass rods of differing composition, a 'Ce' (*foil*) doped core glass M259REZQT, and two undoped cladding glasses M260JN and M287RC. The core glass was drawn to single material fibre F109REZQT(RC&JN), while the two cladding glass rods were separately extruded into two tubes E090DF(JN) and E093RC. The core and cladding glass tubes were subsequently assembled and drawn into two separate SIFs F113REZQT(JN&RC) and F130RERC via the 'rod-in-tube' method. Section 3.2.2.1 presents the optical evaluation, IR absorption spectrum, and refractive index measurements of bulk M259REZQT, M260JN and M287RC glass samples. Section 3.2.2.2 presents the evaluation of the single material fibre F109REZQT(RC&JN), and SIFs F113REZQT(JN&RC) and F130RERC. Section 3.2.2.3 evaluates the photoinduced refractive-index changes on core glass M259REZQT. Note, these photoinduced refractive-index experiments were intended as a first step towards inscribing a FBG into chalcogenide glass. The Ce^{3+} doped bulk core glass, single material fibre and SIFs produced were subsequently used for the PL emission measurements presented in Section 4.2.1.3.a while the SIF F130RERC was also used for optical cavity experiments presented in Section 5.2.2.

SEM-EDX evaluation of a cleaved end of the SIF F113REZQT(JN&RC) revealed the composition of the core (*nominally* $Ge_{15.0}\ As_{21.0}\ Ga_{1.0}\ Se_{63.0}$ *atomic % M259REZQT*) was $Ge_{16.2}\ As_{20.0}\ Ga_{0.9}\ Se_{62.9}$ atomic %, while the composition of the cladding (*nominally* $Ge_{16.5}\ As_{16.0}\ Ga_{3.0}\ Se_{61.5}\ S_{3.0}$ *atomic % M260JN*) was $Ge_{17.9}\ As_{15.4}\ Ga_{3.8}\ Se_{59.9}\ S_{3.0}$ atomic %. Additionally, SEM-EDX evaluation of a cleaved end of the SIF F130RERC, which shares the same M259REZQT core glass composition, revealed the composition of the cladding (*nominally $Ge_{21.0}$ $Sb_{10.0}$ $Se_{69.0}$ atomic % M278RC*) was $Ge_{21.5}$ $Sb_{11.2}$ $Se_{67.3}$ atomic %.

Table 3-2: List of production and fabrication specifications for M259REZQT, M260JN, M287RC, F109REZQT(RC&JN), F113REZQT(JN&RC) and F130RERC. Note, the Ce^{3+} cation concentration calculations assumed several factors (see Section 3.2.8.2) and thus its accuracy should not be relied upon.

Glass type:	**Cladding**	**Core**	**Cladding**
Glass melt code:	**M260JN**	**M259REZQT**	**M287RC**
Nominal composition: (atomic %)	$Ge_{16.5}$ $As_{16.0}$ $Ga_{3.0}$ $Se_{61.5}$ $S_{3.0}$ (***undistilled***)	$Ge_{15.0}$ $As_{21.0}$ $Ga_{1.0}$ $Se_{63.0}$ (***undistilled***) + 500 ppmw Ce (*foil*)	$Ge_{21.0}$ $Sb_{10.0}$ $Se_{69.0}$ (***undistilled***)
Glass density	Not evaluated	4.448 g/cm^3	Not evaluated
Ce^{3+} concentration	Undoped	9.56×10^{18} cations /cm^3	Undoped
Produced by:	The author	Dr Zhuoqi Tang	PhD student Richard Crane
Fibre and cane drawing code:	Not fibre drawn	**F109REZQT(RC&JN)**	Not fibre drawn
Cladding tube extrusion code:	**E090DF(JN)**	Not extruded	**E093RC**
SIF code:	**F113REZQT(JN&RC)**	**F130RERC**	

The density of M259REQT was based on gas pycnometer measurements reported in [97].

3.2.2.1 Bulk glass M259REZQT, M260JN and M287RC evaluation:

Figure 3-10 (a) and (b) show the NIR images of the M259REZQT glass rod, obtained using the equipment configuration in Figure 3-5 (a). These NIR images revealed two empty spherical inclusions (*bubbles*) originally hidden to the naked eye. The magnification imposed by the cylindrical chalcogenide glass rod made it difficult to measure the true diameters of these bubbles, thus scale bars were intentionally omitted from these images. The formation of these bubbles is discussed in Section 3.2.8.4.

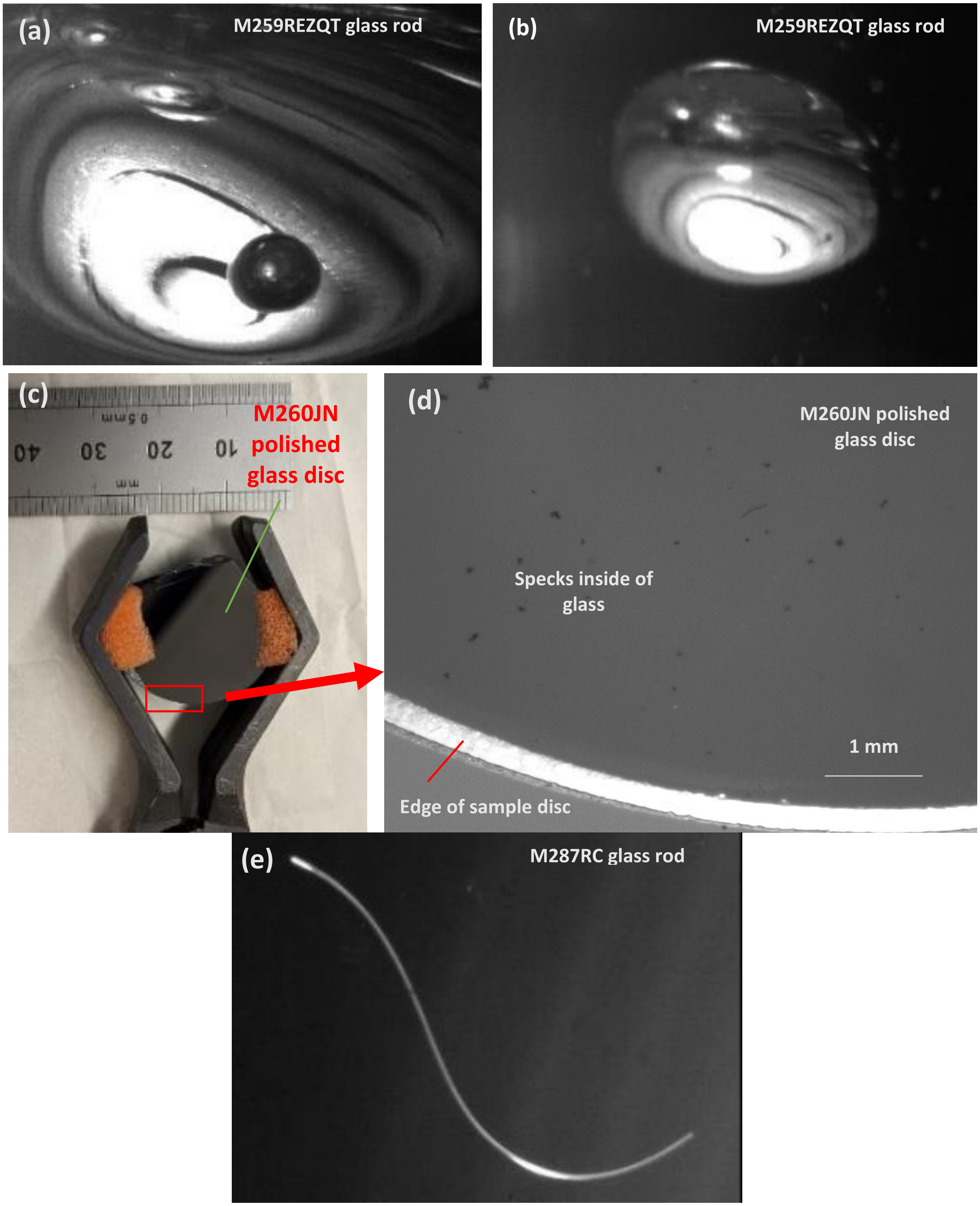

Figure 3-10: Showing: ***(a)*** *&* ***(b)*** *NIR images of M259REZQT glass rod showing bubbles,* ***(c)*** *&* ***(d)*** *visible and NIR image of polished M260JN sample, respectively, showing tiny specks inside of glass (Figure (d) is a higher magnification image under NIR illumination of the sample in Figure (c)), and* ***(e)*** *NIR image of M287RC glass rod showing filament. Note, the length scale on Figures (a), (b), and (e) have been intentionally omitted due to the magnification imposed by the cylindrical glass rod.*

Figure 3-10 (d) shows the NIR images of a polished M260JN disc sample, obtained using the equipment configuration in Figure 3-5 (b). These NIR images of the flat polished face of the sample, revealed tiny specks, originally hidden to the naked eye. Note, these features appeared to be evenly distributed within the glass and not on the surface, and resemble features observed in the M285RERC glass rod shown in Figure 3-30. Figure 3-10 (e) shows the NIR images of the M287RC glass rod, obtained using the equipment configuration in Figure 3-5 (a). These NIR images revealed a filament within the glass. This filament must have been refractory and was probably ceramic in origin to be capable of surviving the 900°C Melt-Quench processing of the Ge-Sb-Se glass (*see Table 7-12*).

Figure 3-11 shows the room temperature absorption spectra for M259REZQT, and M260JN bulk glass samples, with an inset showing the absorption bands within the 2 to 7 µm spectral region. Inset (a) in Figure 3-11, shows that the Ce^{3+} doped sample exhibited a single broad MIR GSA between the $^2F_{5/2}$ ground state and its single excited state $^2F_{7/2}$ level. Notably, both the $^2F_{5/2}$ and $^2F_{7/2}$ manifolds are known to exhibit extensive Stark splitting [155–158]. Additionally, the $^2F_{5/2} \rightarrow {}^2F_{7/2}$ GSA overlapped both extrinsic [-Se-H] impurity vibrational absorptions at 3.5 and 4.5 µm. Inset (b) in Figure 3-11, shows the extrinsic impurity absorption bands for [-OH] at ~2.7 µm, [-S-H] at 4.1 µm, and [-C-S] at 4.96 µm, along with the [-Se-H] absorption bands at 3.5 and 4.5 µm.

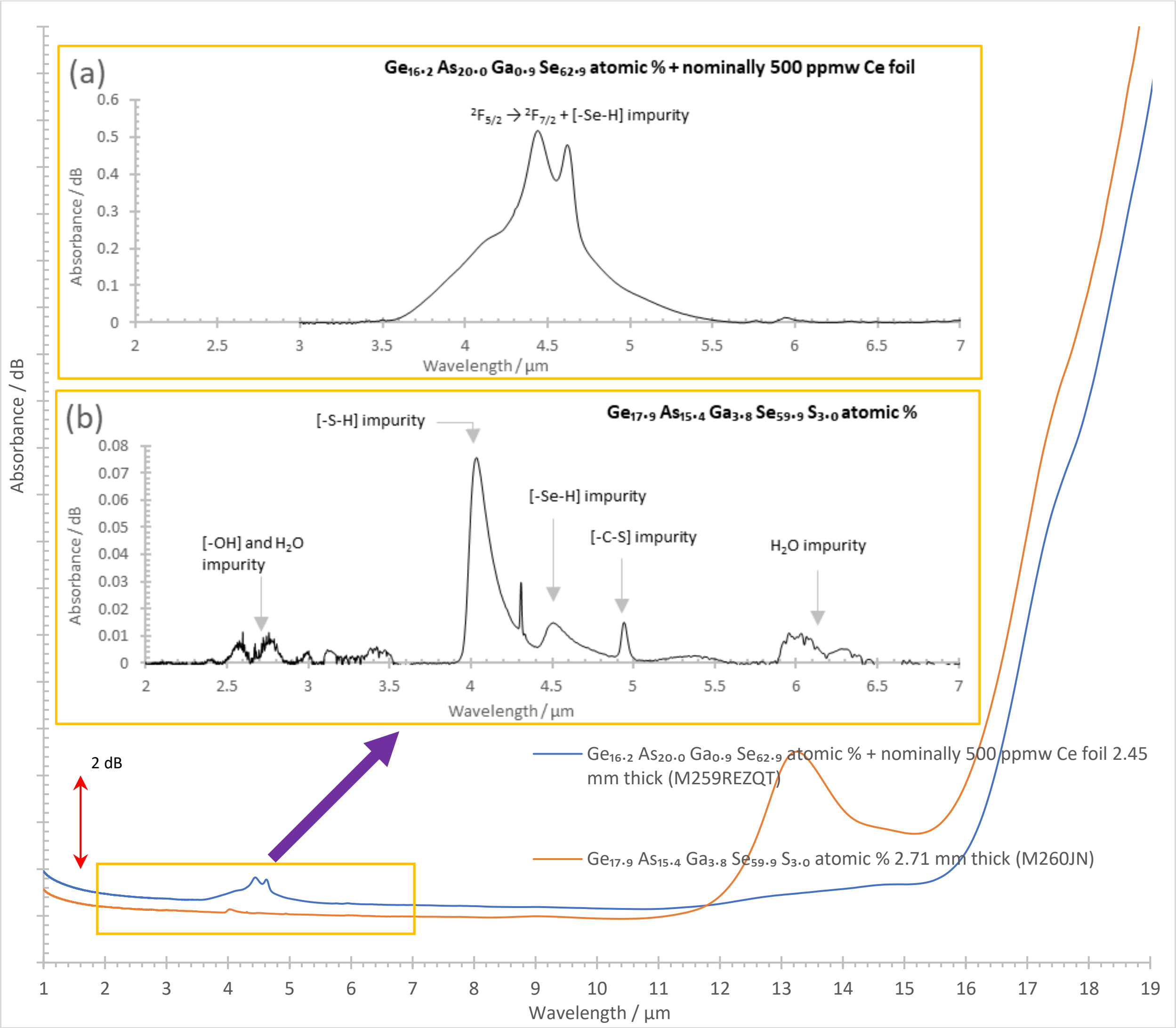

Figure 3-11: Room temperature IR absorption spectrum of undistilled nominally 500 ppmw Ce (foil) doped M259REZQT bulk glass sample, and M260JN bulk glass sample, with insets (a) and (b) showing Ce^{3+} ground-state electronic absorption bands in the 2.0 to 7.0 µm spectral region along with unwanted host glass impurities (see Table 2-4) with the contributions of their respective host glass baselines removed. Note, the as measured glass compositions, using SEM-EDX, for M259REZQT, and M260JN are quoted in the legend.

Figure 3-12 (a) shows the refractive index measurements for the M259REZQT core glass and the M260JN cladding glass, while Figure 3-12 (b) shows the refractive index measurements for the M259REZQT core glass and the M287RC cladding glass.

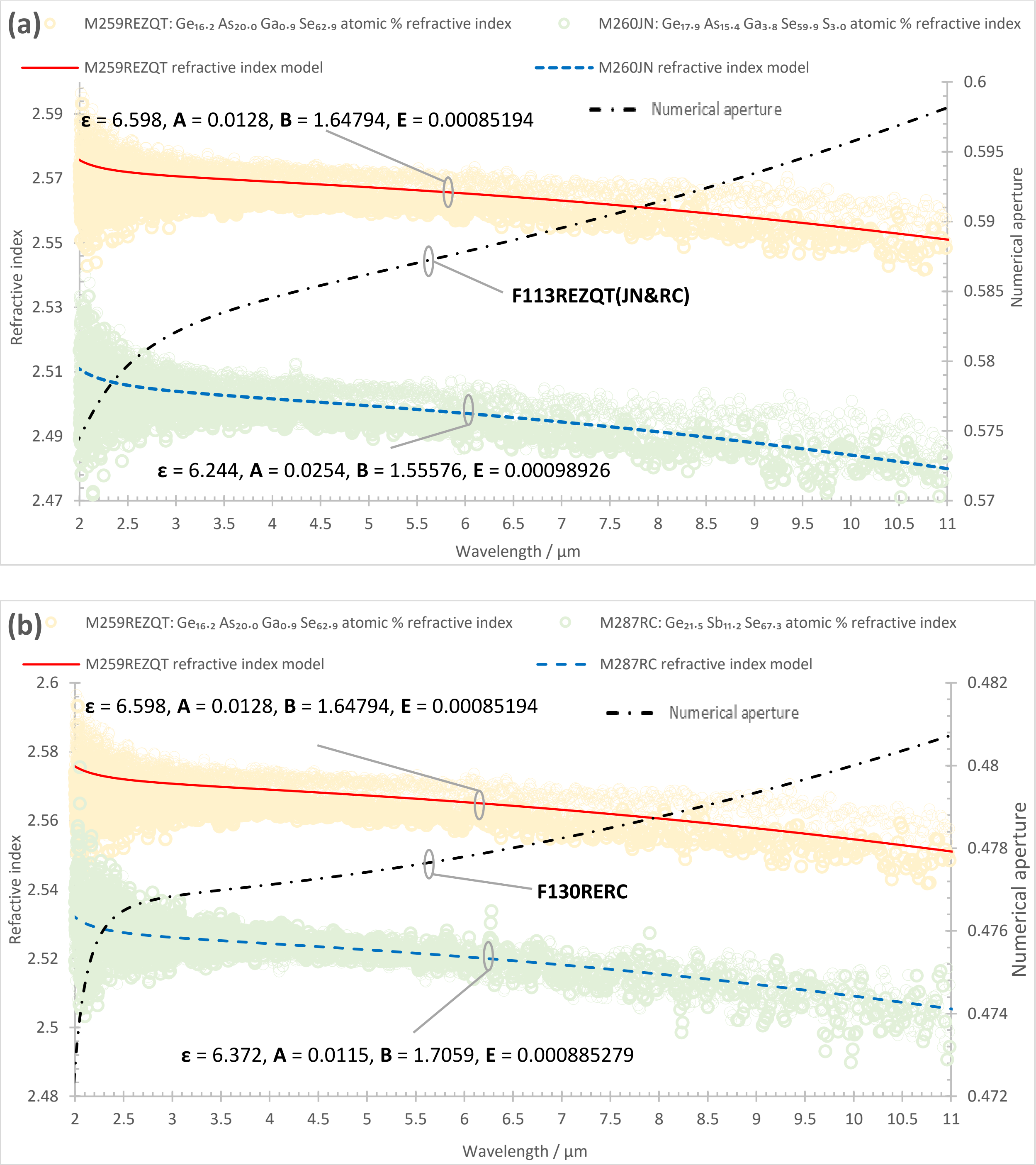

*Figure 3-12: Showing: **(a)** refractive index dispersion of the bulk glass samples M259REZQT and M260JN, along with their calculated numerical aperture. Note, M259REZQT and M260JN constituted the core and cladding glass compositions, respectively, of the SIF F113REZQT(JN&RC), and **(b)** refractive index dispersion of the bulk glass samples M259REZQT and M287RC sample, along with their calculated numerical aperture. Note, M259REZQT and M287RC constituted the core and cladding glass compositions, respectively, of the SIF F130RERC. Note, the as measured glass compositions, using SEM-EDX, for M259REZQT, M260JN, and M287RC samples are quoted in the legend, and the 2-term Sellmeier model coefficients included in annotations for refractive index measurements (see Equation 3-2).*

The core and cladding of the SIF F113REZQT(JN&RC) consisted of the M259REZQT and M260JN glass compositions, respectively, and thus should possess a similar numerical aperture to that calculated in Figure 3-12 (a). Similarly, the core and cladding of the SIF F130RERC consisted of the M259REZQT and M287RC glass compositions, respectively, and thus should possess a similar numerical aperture to that calculated in Figure 3-12 (b).

Considering Figure 3-12 (a), the SIF F113REZQT(JN&RC) likely possessed a numerical aperture of around 0.585 between the 4.00 to 7.00 µm spectral region. Conversely, the SIF F130REC likely possessed a numerical aperture of around 0.476 between wavelengths of 4.00 to 7.00 µm, according to Figure 3-12 (b). However, due to differences in thermal history between the annealed M259REZQT, M260JN, and M287RC bulk glass samples and the unannealed SIF F113REZQT(JN&RC) and F130RERC, the actual numerical aperture of each SIF possibly differed.

3.2.2.2 F109REZQT9RC&JN), F113REZQT(JN&RC) and F130RERC evaluation:

Figure 3-13 shows the attenuation spectrum for a nominally 500 ppmw 'Ce' foil doped, undistilled single material fibre F109REZQT(RC&JN) with a diameter of 245.0 ± 8.3 µm, and a minimum optical loss of 2.23 ± 0.03 dB/m at a wavelength of 6.90 µm (*measured to an 8 cm^{-1} resolution*).

The core of both SIFs, F113REZQT(JN&RC) and F130RERC, probably possessed a similar attenuation spectrum, to that shown in Figure 3-13, by virtue of their cores being comprised of single material cane produced from the same bulk glass rod as the F109REZQT(RC&JN). However, as both SIFs went through different thermal processing there may be additional losses coupled with imperfections at their core/cladding interfaces.

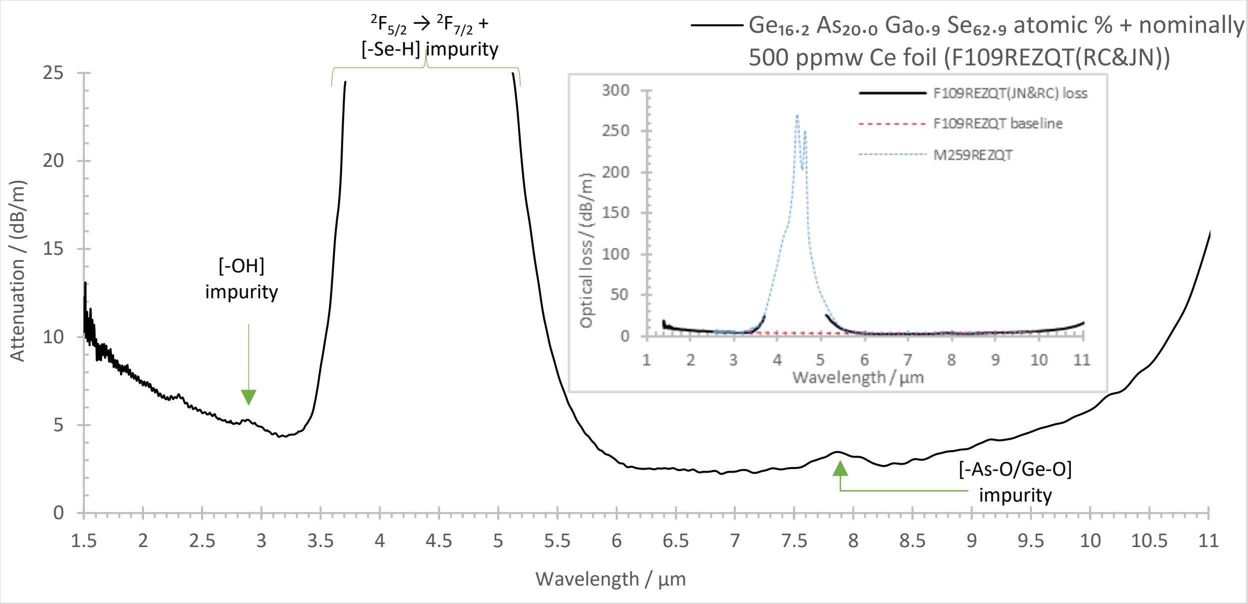

Figure 3-13: Attenuation (dB/m) vs. Wavelength (μm) for a nominally 500 ppmw Ce (foil) doped, undistilled single material fibre F109REZQT(RC&JN) with a diameter of 245.8 ± 8.3 μm, 2.75 m long with a minimum loss of 2.23 ± 0.03 dB/m at 6.90 μm. With inset showing absorption data from M259REZQT sample superimposed onto F109REZQT(RC&JN) loss spectrum. The Ce^{3+} ground-state electronic absorption and extrinsic vibrational absorption loss due to unwanted host glass impurities are identified (see Table 2-4). Note, the as measured glass composition, using SEM-EDX, for F109REZQT(RC&JN) quoted in legend.

The cleaved end face of a F113REZQT(JN&RC) SIF sample was evaluated by means of visible, NIR, and MIR imaging, using the procedures described in Section 3.1.2.2. This SIF exhibited good ovality of both the core and cladding, and concentricity of core, as shown in Figure 3-14. Additionally, this SIF could be handled delicately with little fear of unintentional breakage.

NIR imaging of the F113REZQT(JN&RC) sample shown in Figure 3-14 (b), obtained using the equipment configuration in Figure 3-5 (c) viewed in transmission, revealed the core to be circular and centred within the cladding, it also revealed an unusual dark ring around the core along with striae within the cladding, as shown in Figure 3-14 (b) and (c). The formation of the striae is discussed in Sections 3.2.8.4 and 3.2.8.6.

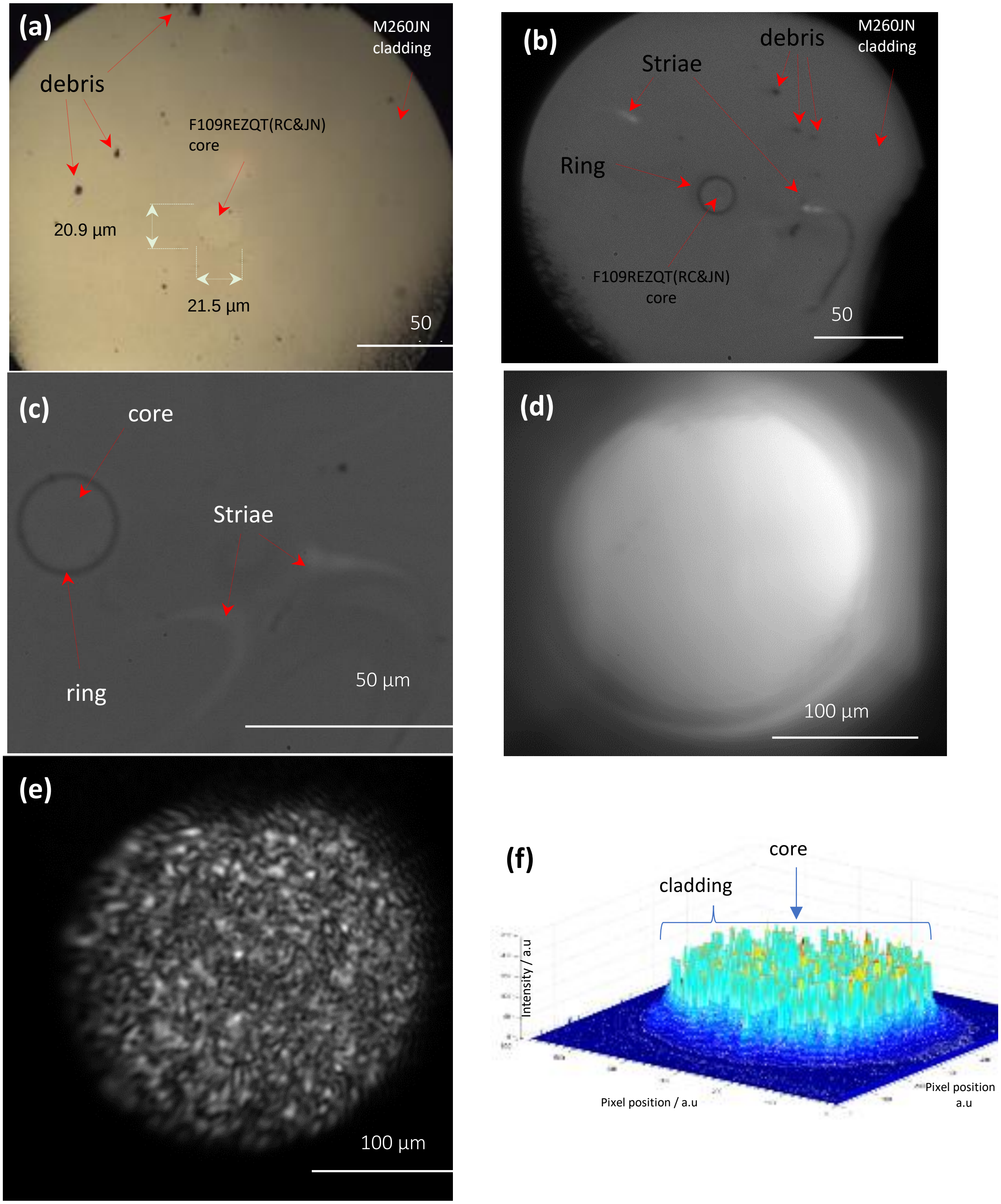

Figure 3-14: Images of the cleaved end of a SIF F113REZQT(JN&RC) sample with a ~21 µm core and 22 cm long, viewed in: ***(a)*** *reflection with visible illumination,* ***(b)*** *transmission with NIR illumination* ***(c)*** *transmission with NIR illumination at higher magnification,* ***(d)*** *reflection through a 4.203 µm LWP filter while under broadband illumination,* ***(e)*** *transmission/emission through a 4.203 µm LWP filter while illuminating the sample from the opposite end with a 4.15 µm laser and* ***(f)*** *Intensity map of Figure (e) with transmitted/emission light > 4.203 µm. Note, all images presented are of the* <u>*same*</u> *SIF sample.*

The ‘ring’ was observed on several different samples, taken from different sections of the SIF drawing drum and thus spanned a significant portion of the total SIF. The ‘ring’ portion of the SIF was evaluated with SEM-EDX and was found to possess a $Ge_{17.9}$ $As_{15.4}$ $Ga_{3.8}$ $Se_{59.9}$ $S_{3.0}$ atomic % composition like the adjacent cladding glass, outside of the ring. MIR imaging of the F113REZQT(JN&RC) sample shown in Figure 3-14 (d) and (e), obtained using equipment configuration in Figure 3-5 (d) with a 4.15 µm pump laser viewed in reflection/transmission, revealed the SIF to be unable to guide light within its core. Troublingly, both 4.15 µm QCL light and Ce^{3+} PL due to the $^2F_{7/2} \rightarrow {}^2F_{5/2}$ radiative transition were found propagating in the cladding, as illustrated by the intensity map in Figure 3-14 (f). Moreover, MIR imaging of additional SIF samples, as short as 2.53 cm long, yielded similar results. Interestingly, the core glass, F109REZQT(RC&JN), was also used in the SIF F130RERC, while the cladding glass M260JN was also used in the SIF F122REJN, and both SIFs were able to guide light in their cores. Thus, the poor optical guiding properties of the SIF F113REZQT(JN&RC) was most likely due to the unusual dark ring at the core/cladding interface, and not due to the composition of either the core or cladding glass. The mechanism for the formation of this ‘ring’ or how it prevented the core from guiding light, while also not guiding light itself, are currently unknown.

The cleaved end face of a F130RERC SIF sample was evaluated by means of visible, and SEM imaging, This SIF exhibited good ovality of the core, good handleability, and concentricity of core, as shown in Figure 3-15. SEM imaging revealed the core to be circular and centred within the cladding, as shown in Figure 3-15 (a) and (b). Additionally, Figure 3-15 (c) shows visible imaging of a F130RERC SIF sample, obtained using the equipment configuration in Figure 3-5 (c) viewed in reflection, which revealed a prominent hole at the core/cladding interface. Several samples were subsequently cleaved from sections of the SIF adjacent to the initial cleave and visible imaging revealed that the initially observed hole spanned over a metre in length inside the fibre. The location of these features, at the core/cladding interface, indicated a void/bubble, between the core and cladding, was elongated during fibre drawing. This void was most likely inadvertently introduced during the 'rod-in-tube' assembly process (see Section 7.1.12).

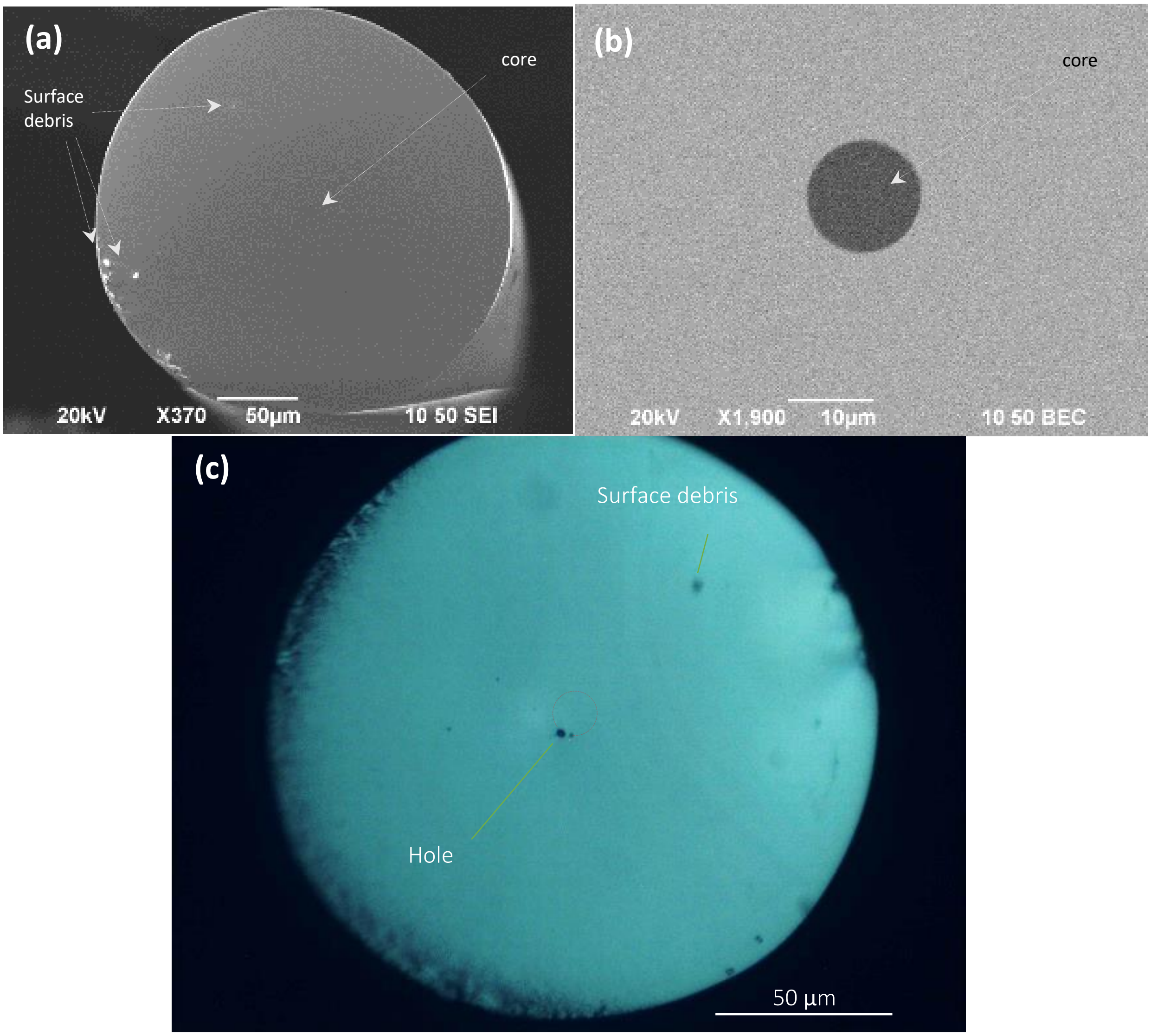

*Figure 3-15: SEM images of cleaved end of SIF F130RERC with 19 μm diameter core **(a)** image of SIF showing extraneous surface debris **(b)** image showing core/cladding interface and **(c)** visible image of SIF F130RERC with approximately 9 μm core showing a prominent hole at core/cladding interface which spanned over a metre in length inside the fibre (Note core/cladding interface has been outlined in red).*

3.2.2.3 Photoinduced refractive-index changes:

The M259REZQT bulk glass sample, used for the room temperature IR absorption spectrum shown in Figure 3-11, had five separate sections of its surface, R1 to R5 shown in Figure 3-16, written into using the parameters described in Table 3-3. Note, this laser writing was kindly carried out by a collaborator of the Mid-Infrared Photonics Group Dr Kaiming Zhou at Aston University. The end face of the M259REZQT bulk glass sample was evaluated by means of visible and NIR imaging, using the procedures described in Section 3.1.2.2. Figure 3-17, shows the written sections of the M259REZQT sample obtained using the equipment configuration in Figure 3-5 (c).

These photoinduced changes were found to be permanent, at room temperature, and the characteristics of these features could be manipulated via the laser writing process (see Table 3-3). Each area evaluated was comprised of lines spaced approximately 6 µm apart, which were comprised of overlapping spots spaced approximately 2 µm apart. Undesirable surface debris was generated due to volatilisation of the glass sample during laser scanning on sections R1, R2 and R3. Conversely, the scanning parameters used for the R4 and R5 sections produced no surface damage, indicating the importance of the scan depth parameter (see Table 3-3). Importantly, these permanent photoinduced changes to the refractive index were intended as a first step towards inscribing grating structures, such as FBG’s, into RE^{3+} doped chalcogenide glass.

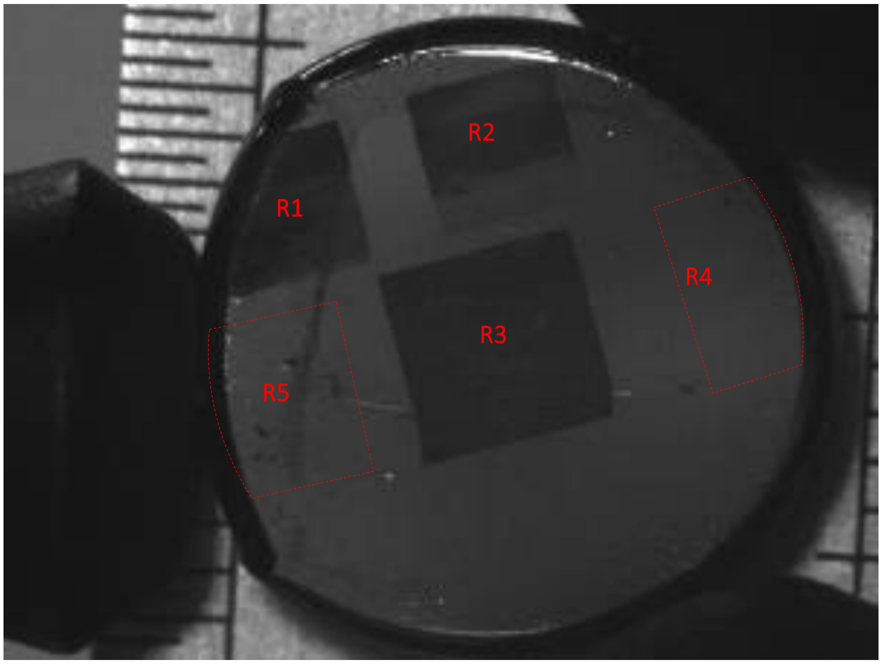

Figure 3-16: Showing visible image of M259REZQT sample, laser writing process, with the sections labelled R1 to R3 visible, along with sections R4 and R5 outlined. Note, image was taken adjacent to a ruler with ½ mm gradations for scale.

Table 3-3: Specification of laser writing process used on M259REZQT glass sample shown in Figure 3-16.

Section	**Area / mm**	**Laser energy /µJ**	**Pulse duration / fs**	**Scan parameters / (mm/sec)**	**Depth / µm**	**Comments**
R1	3×3	1.72	160	2	0	Pattern visible with naked eye due to surface debris.
R2	3×3	2.00	170	2	15	Pattern visible with naked eye due to surface debris.
R3	4×4	1.70	170	2	15	Pattern visible with naked eye due to significant amounts of surface debris.
R4	3×3	2.00	170	1	30	Pattern was not visible to naked eye.
R5	3.7×2.5	1.70	170	1	30	Pattern was not visible to naked eye.

Note, a 6 µm line spacing was used for each section.

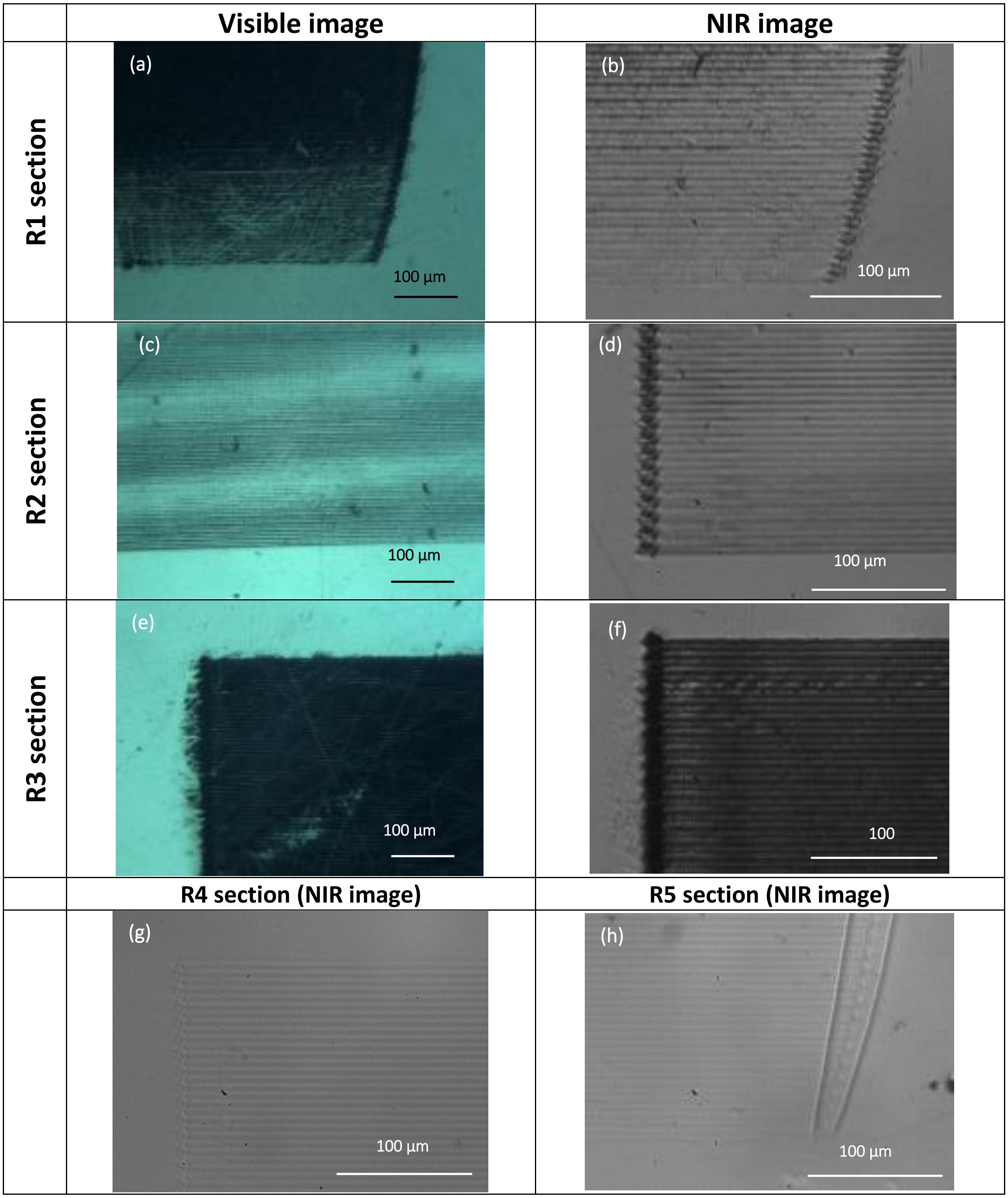

Figure 3-17: Images of sections of M259REZQT bulk glass after laser writing showing images of: ***(a)*** *&* ***(b)*** *R1 section viewed in visible and NIR illumination, respectively,* ***(c)*** *&* ***(d)*** *R2 section viewed in visible and NIR illumination, respectively,* ***(e)*** *&* ***(f)*** *R3 section viewed in visible and NIR illumination, respectively,* ***(g)*** *R4 section viewed under NIR illumination and* ***(h)*** *R5 section viewed under NIR illumination. Note, the pattern in the R4 and R5 sections was not visible, thus visible images were omitted.*

3.2.3 Vacuum distillation of undoped chalcogenide glass:

The undistilled bulk glass M273REJN of nominal composition: $Ge_{15.2}$ $As_{21.2}$ $Se_{63.6}$ + 1000 ppmw $TeCl_4$ was produced by the author, then further purified via vacuum distillation (D046JN). This undoped, distilled glass was then used to produce three separate bulk glass compositions M274REJN, M275REJN, and M276REJN which were evaluated in Sections 3.2.4 and 3.2.5.

During the distillation procedure, eight temperature zones, in the distillation rig were subjected to concurrent heating schedules as shown in Figure 3-18 (a). The heating schedule used for the distillation process, shown in Figure 3-18 (b), was sub-divided into the following subsections:

- Distillation rig bake out: The 'Link 2', 'Distillate 1', 'Distillate 2', 'Coil', 'Link 1A', and 'Link1B' temperature zones of the distillation rig were subjected to a bake-out at ~ 600 °C for ~ 1 hour to remove any undistilled glass dust that may have reached these sections during the batching and sealing steps described in Appendix 7.1.6.
- HCl bake-out: Each temperature zone on the distillation rig was subjected to a bake-out at around 300 °C for ~11 hours to allow outgassing of any HCl gas produced from the $TeCl_4$ getter incorporated into the M273JN chalcogenide glass, see Equation 7-3.
- Distillation of glass: The 'Charge 1' and 'Charge 2' temperature zones were heated to ~ 500 °C for ~ 1.3 hours to bring the glass in the charge chamber above its liquidus and start the distillation process. Concurrently, the 'Link 1A', 'Link 1B' and 'coil' temperature zones were heated to ~ 600 °C to prevent the accumulation of any glass distillate in this region. The 'Distillate 1', and 'Distillate 2' temperature zones were kept ~ 300 °C to allow the distilled chalcogenide glass to deposit in the distillation chamber while being sufficiently hot to discourage volatile impurities from condensing in this section. Additionally, the 'Link 2' was

kept ~ 300 °C to deter volatile impurities from condensing too close to the distillation chamber. The temperature of the 'Charge 1' and 'Charge 2' temperature zones was further increased to 700 °C for ~ 1 hour, to complete the distillation leaving only the Al metal getter residue in the charge chamber.

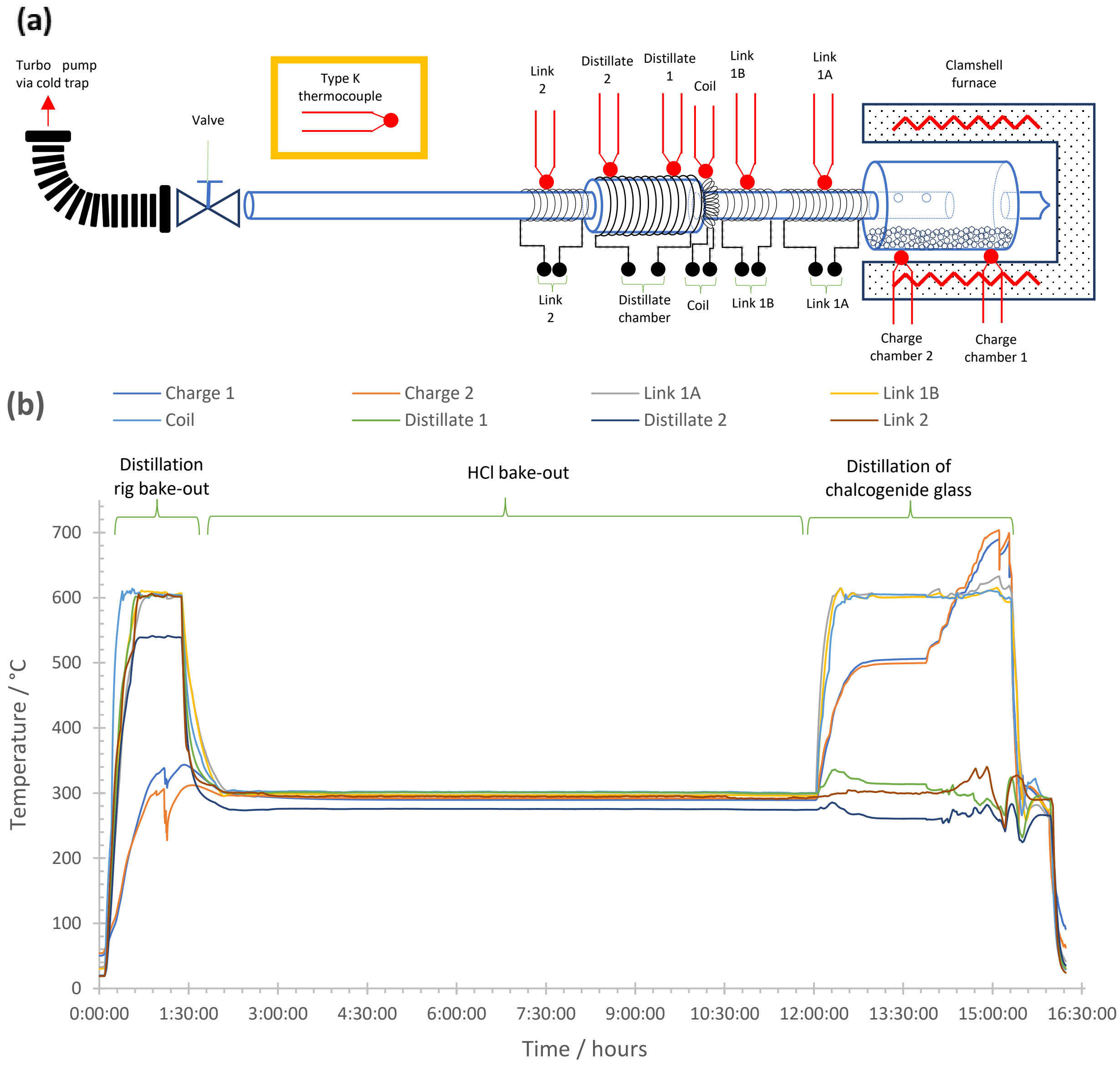

*Figure 3-18: Showing **(a)** Illustration of silica glass distillation rig used for distillation of undoped chalcogenide glass with temperature zones identified, and **(b)** Heating schedule used for the distillation of M273JN, showing eight temperature zones on distillation rig.*

The link 1 and link 2 tubes were sealed, as illustrated in Figure 7-9 (e). The distilled glass was then subjected to the standard melt/quench process to homogenise the glass.

Glass distillation, using the process described in Section 7.1.6, encompassed an approximately 16.5-hour long procedure, as shown in Figure 3-18. This process distilled the Ge-As-Se glass in the charge chamber only once, causing it to be condensed mostly in the distillation chamber, as illustrated in Figure 7-9 (a). Imprecise temperature control made it difficult to completely prevent some of the more volatile constituents of the glass from condensing in the 'link 2' tube, to form an 'Se' rich film (see Table 2-3). The 'link 2' tube was subsequently removed during the oxy propane sealing step (see Appendix 7.1.6). This caused in an 'Se' deficiency in the resulting distilled glass composition, as evident by the SEM-EDX measurements presented in Section 3.2.4. The shortcomings of this equipment configuration are discussed in Section 3.2.8.3. The resulting distilled glass was then broken into cullet and re-batched into three new 10/14 silica glass ampoules, as shown in Figure 3-19. Subjectively, the best chunks of glass were reserved for both M274REJN, and M275REJN, while the remaining glass powder was used for M276REJN.

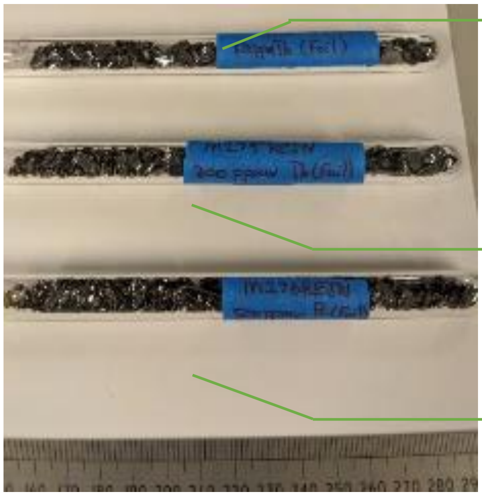

M274REJN: Nominally $Ge_{14.8}$ $As_{20.8}$ $Ga_{2.0}$ $Se_{62.4}$ atomic % + 1000 $TeCl_4$ + 500 ppmw Tb (*foil*). **Note** the best quality pieces of distilled glass were selected and batched into an ampoule.

M275REJN: Nominally $Ge_{15.2}$ $As_{21.2}$ $Se_{63.6}$ atomic % + 1000 $TeCl_4$ + 300 ppmw Tb (*foil*). **Note** good quality pieces of distilled glass were selected and batched into an ampoule.

M276REJN: Nominally $Ge_{14.8}$ $As_{20.8}$ $Ga_{2.0}$ $Se_{62.4}$ atomic % + 1000 $TeCl_4$ + 500 ppmw Pr (*foil*). **Note** small pieces of distilled glass, inclusive of dust selected and batched into an ampoule.

Figure 3-19: Image of M274REJN, M275REJN and M276REJN glass samples prior to remelting.

3.2.4 Distilled terbium cation doped samples:

Table 3-4 lists the specifications for two separate glass compositions, a 'Tb' (*foil*) doped distilled core M274REJN, and an undoped, undistilled cladding glass M260JN. The core glass was drawn to single material fibre F116REJN while the cladding glass was extruded into a tube E090DF(JN). The core and cladding glass were subsequently assembled and drawn into a SIF F122REJN via the 'rod-in-tube' method. Section 3.2.4.1 presents the IR absorption spectrum, and refractive index measurements of polished bulk M274REJN, and M260JN glass samples. Section 3.2.4.2 presents the evaluation of the single material F116REJN, and SIF F122REJN. The 'Tb' cation doped single material fibre produced was subsequently used for the PL emission and ESA measurements presented in Section 4.2.4.

Table 3-4: List of production and fabrication specifications for M274REJN, M260JN, F116REJN and F122REJN. Note, the Tb^{3+} cation concentration calculations assumed several factors (see Section 3.2.8.2) and thus its accuracy should not be relied upon.

Glass type:	**Core**	**Cladding**
Glass melt code:	**M274REJN (D046JN)**	**M260JN**
Nominal composition: (atomic %)	$Ge_{14.8}$ $As_{20.8}$ $Ga_{2.0}$ $Se_{62.4}$ (***distilled***) + 1000 ppmw $TeCl_4$ + 500 ppmw Tb (*foil*)	$Ge_{16.5}$ $As_{16.0}$ $Ga_{3.0}$ $Se_{61.5}$ $S_{3.0}$ (***undistilled***)
Glass density	~ 4.5 g/cm^3	Not evaluated
Tb^{3+} concentration	8.53×10^{18} cations/cm^3	Undoped
Produced by:	The author	The author
Fibre and cane drawing code	**F116REJN**	Not fibre drawn
Cladding tube extrusion code:	Not extruded	**E090DF(JN)**
SIF code:	**F122REJN**	

The glass density was estimated based on density measurements reported in [97,153,154].

SEM-EDX evaluation of the SIF F122REJN revealed the composition of the core (*nominally* $Ge_{14.8}$ $As_{20.8}$ $Ga_{2.0}$ $Se_{62.4}$ *atomic % M274REJN*) was $Ge_{17.0}$ $As_{23.4}$ $Ga_{2.5}$ $Se_{57.1}$ atomic %, while the composition of the cladding (*nominally* $Ge_{16.5}$ $As_{16.0}$ $Ga_{3.0}$ $Se_{61.5}$ $S_{3.0}$ *atomic % M260JN*) was $Ge_{17.9}$ $As_{15.4}$ $Ga_{3.8}$ $Se_{59.9}$ $S_{3.0}$ atomic %. The 'Se' deficiency in the distilled M274REJN glass composition was due to excessive loss of 'Se' rich material within the distillation rig, during distillation.

3.2.4.1 Bulk glass M274REJN and M260JN evaluation:

Figure 3-20 shows the room temperature IR absorption spectrum for a polished bulk M274REJN sample, with an inset showing the Tb^{3+} GSA bands from the 1.5 to 7.0 µm spectral region. Note, the M260JN absorption spectrum can be seen in Figure 3-11.

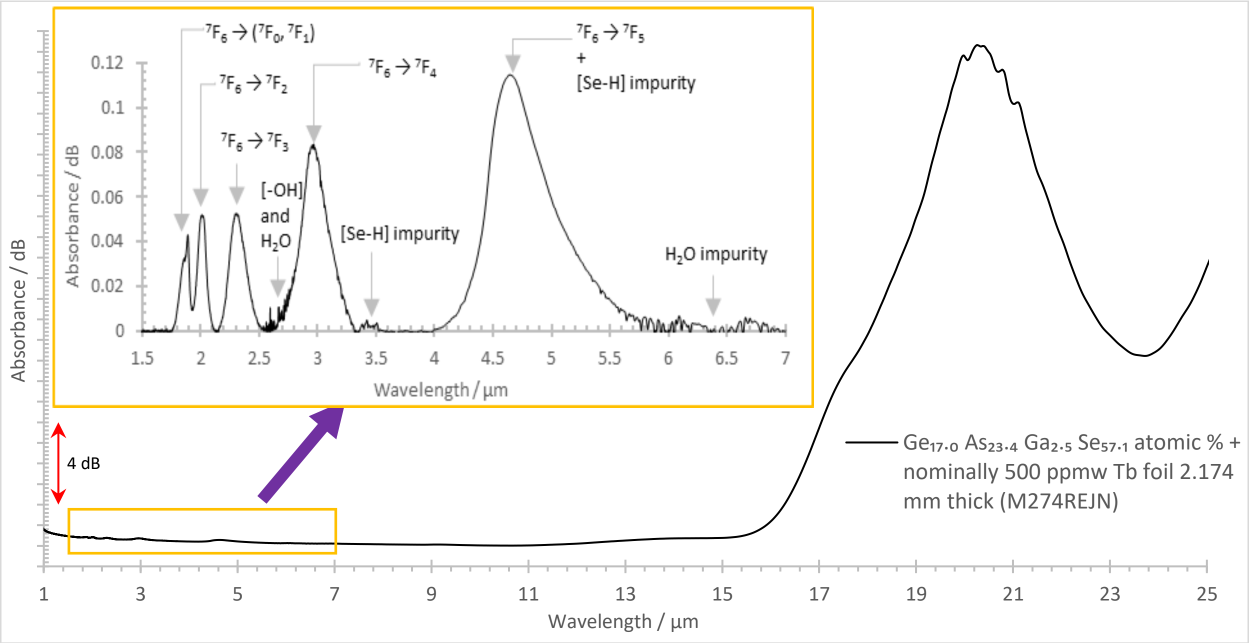

Figure 3-20: Showing room temperature IR absorption spectrum of distilled nominally 500 ppmw Tb (foil) doped bulk M274REJN sample 2.174 mm thick, with inset showing Tb^{3+} ground-state electronic absorption bands from bulk sample in the 1.5 to 7.0 µm spectral region with the contributions of their respective host glass baselines removed. <u>Note</u>, the as measured glass composition, using SEM-EDX, for M274REJN quoted in legend.

The inset in Figure 3-20 shows that the Tb^{3+} doped sample exhibited several NIR and MIR GSA bands along with extrinsic impurity vibrational absorption bands like those observed in Section 3.2.1.1.

Figure 3-21 shows the refractive index measurements for the as measured distilled bulk core glass M274REJN and the undistilled bulk cladding glass M260JN. The core and cladding of the SIF F122REJN consisted of the M274REJN and M260JN glass compositions, respectively, and thus should possess a similar numerical aperture to that calculated in Figure 3-21.

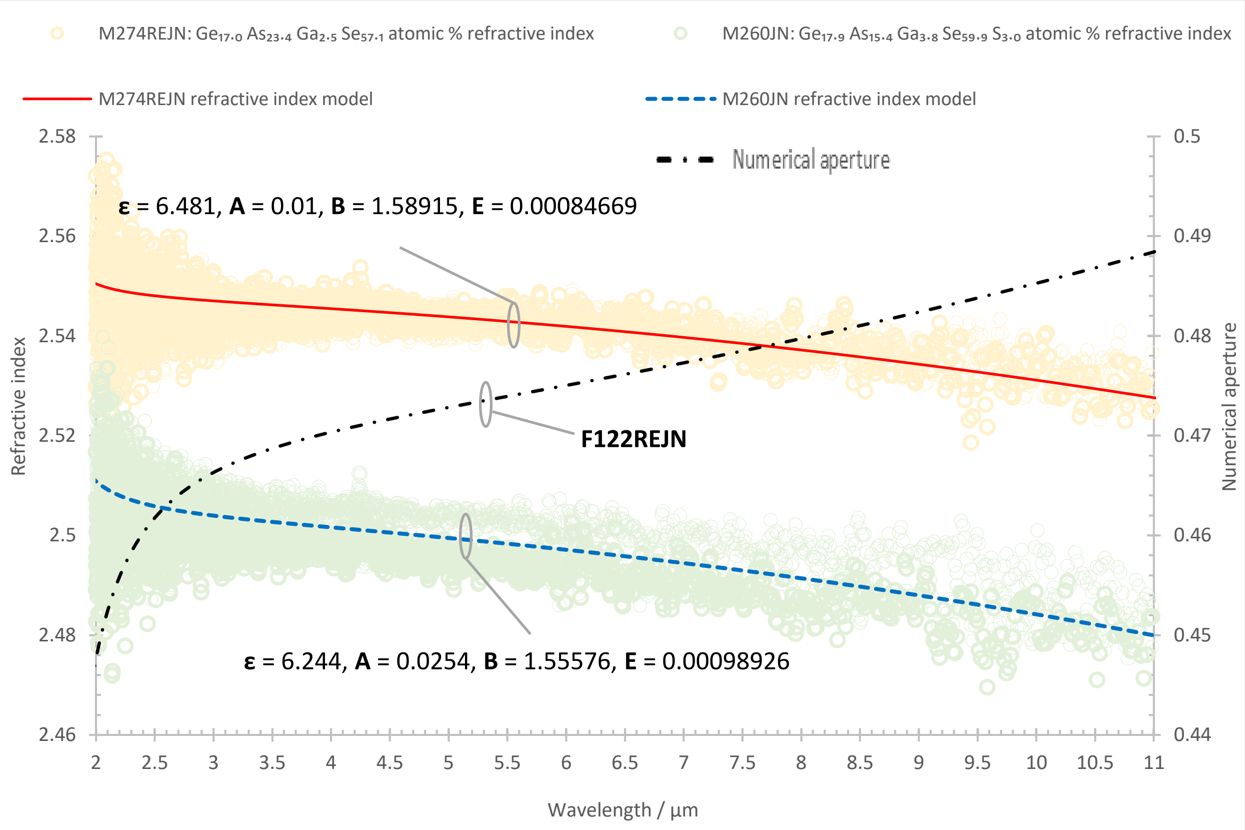

Figure 3-21: Showing refractive index dispersion of the bulk glass samples M274REJN and M260JN, along with their calculated numerical aperture. Note, M274REJN and M260JN constituted the core and cladding glass compositions of the SIF F122REJN. Additionally, the as measured glass composition, using SEM-EDX, for M274REJN, and M260JN quoted in legend, and 2-term Sellmeier model coefficients have been included in annotations for refractive index measurements (see Equation 3-2).

3.2.4.2 F116REJN and F122REJN evaluation:

Figure 3-22 shows the attenuation spectrum for a distilled nominally 500 ppmw 'Tb' foil doped single material fibre F116REJN with a diameter of 220 ± 10 µm with a minimum optical loss of 2.32 ± 0.40 dB/m occurring at 6.67 µm.

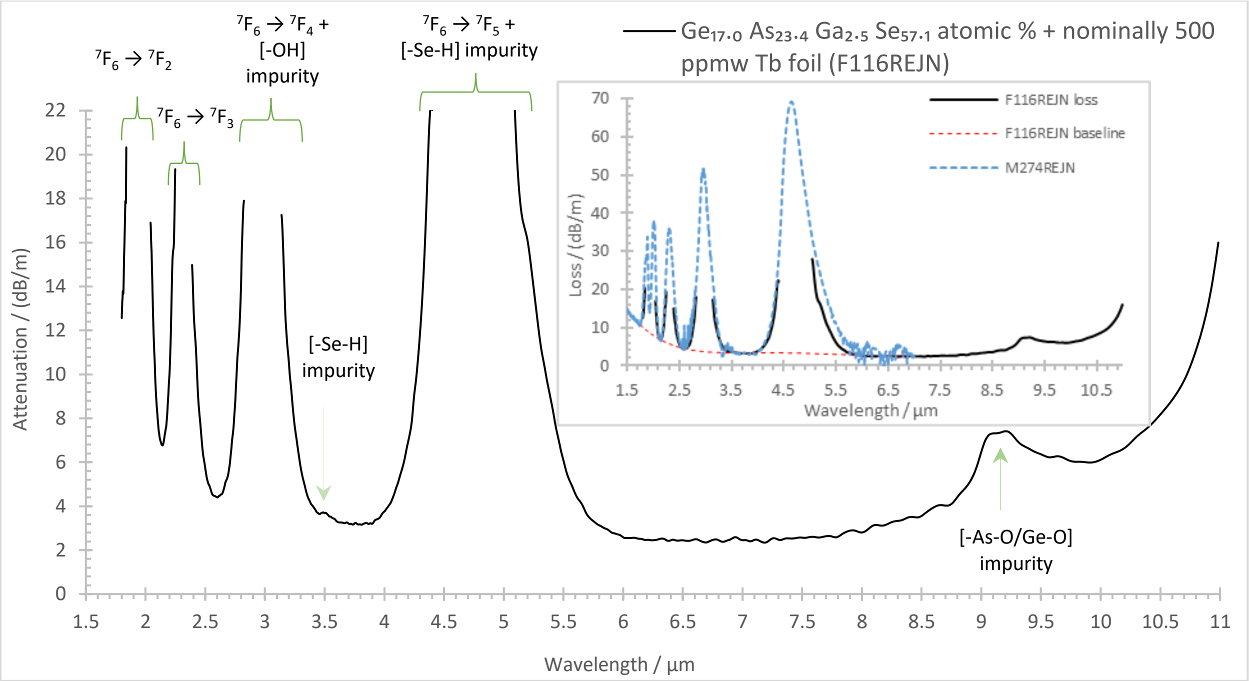

Figure 3-22: Attenuation (dB/m) vs. Wavelength (µm) for a nominally 500 ppmw Tb (foil) doped, distilled single material fibre F116REJN with a diameter of 220 ± 10 µm, 4.26 m long with a minimum loss of 2.32 ± 0.40 dB/m at 6.67 µm. With inset showing absorption data from M274REJN sample superimposed onto F116REJN loss spectrum. The Tb^{3+} ground-state electronic absorption and extrinsic vibrational absorption loss due to unwanted host glass hydride, hydroxide, and oxide impurities are identified (see Table 2-4). Note, the as measured composition, using SEM-EDX, for F116REJN quoted in legend.

Considering Figure 3-21, the SIF F122REJN likely possessed a numerical aperture of around 0.47 between the 4.00 to 7.00 µm spectral region. However, due to differences in thermal history between the annealed M274REJN and M260JN bulk glass samples and the unannealed SIF F122REJN, the actual numerical aperture of the SIF possibly differed. Additionally, the core of the

SIF, F122REJN probably possessed a similar attenuation spectrum to that shown in Figure 3-22, by virtue of its core being comprised of single material cane produced from the same bulk glass rod as the fibre used for F116REJN. However, there may be additional losses in the SIF due to differences in thermal processing and imperfections at its core/cladding interface.

The cleaved end face of a F122REJN SIF sample was evaluated by means of visible, NIR, and MIR imaging, using the procedures described in Section 3.1.2.2. This SIF exhibited good ovality of both the core and cladding, and concentricity of the core, as shown in Figure 3-23. Additionally, this SIF could be handled delicately with little fear of unintentional breakage.

Note, the same SIF sample with a 15 µm core and 27 cm long was evaluated for the images presented in Figure 3-23 (a) to (e). Figure 3-23 (b) and (c) show NIR imaging of the SIF sample, obtained using the equipment configuration in Figure 3-5 (c), viewed in transmission. This imaging revealed cord and striae within the cladding, and the trifold symmetry of the cladding, due to the three-hold spider die used during extrusion (see Appendix 7.1.8), was also observed. Figure 3-23 (d) and (e) show MIR imaging of the SIF sample, obtained using the equipment configuration in Figure 3-5 (d) using a 1.94 µm pump laser, and viewed through a 4.203 long wave pass filter in reflection/transmission, and transmission, respectively. This imaging revealed the F122REJN SIF was capable of guiding light within its core. Tb^{3+} PL due to the $^7F_5 \rightarrow {}^7F_6$ radiative transition, with a wavelength > 4.203 µm was found propagating predominantly in the core, as illustrated by the intensity map in Figure 3-23 (f). Note, visible, NIR and MIR imaging was also performed on other SIF F122REJN samples, with core diameters of ~10 µm, ~20 µm, ~25 µm and ~30 µm, these were all found capable of guiding light within their respective cores. Additionally, several prominent holes at the core/cladding interface were also found in the SIF F122REJN.

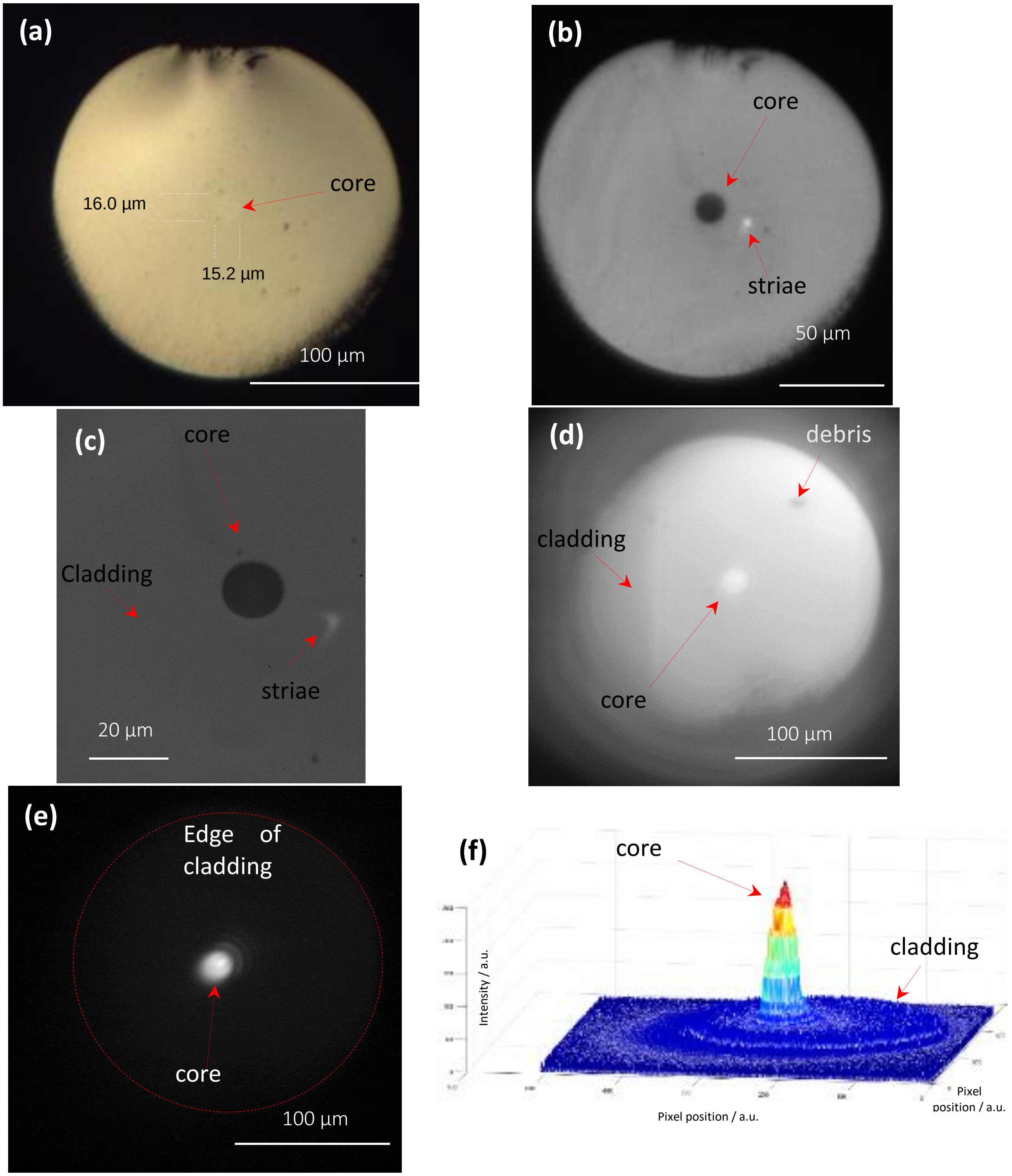

*Figure 3-23: Images of the cleaved end of a SIF F122REJN sample with a ~15 µm core and 27 cm long viewed in: **(a)** reflection with visible illumination, **(b)** transmission under 940 nm NIR illumination, **(c)** transmission under 940 nm NIR illumination at higher magnification, **(d)** through 4.203 µm LWP filter illuminated with both broadband globar, and 1.940 µm pump laser in reflection/ transmission, **(e)** through a 4.203 µm LWP filter while illuminated in transmission with 1.940 µm laser (Note, the circumference of the cladding was outlined in red), and **(f)** showing intensity map of Figure (e) with light transmitted/emitted at wavelengths > 4.203 µm. Note, all images presented are of the same SIF F122REJN sample, also please refer to Section 3.1.2.2 for clarification on imaging configurations employed.*

3.2.5 Distilled terbium and praseodymium cation doped samples:

Table 3-5 lists the specifications for two separate distilled glass rods of differing composition, a 'Tb' (*foil*) doped glass M275REJN, and a 'Pr' (*foil*) doped glass M276REJN. Both glass rods were then individually drawn to single material fibre F120REJN and F119REJN. Section 3.2.5.1 presents the IR absorption spectrum measurements of polished bulk M275REJN and M276REJN glass samples. Refractive index, and SEM-EDX measurements were not performed on these compositions. Section 3.2.5.2 presents the evaluation of the single material fibres F120REJN and F119REJN. Note, both the Pr^{3+} and Tb^{3+} doped single material fibres were used for PL emission measurements presented in Sections 4.2.2 and 4.2.4,respectively.

Table 3-5: List of production and fabrication specifications for M275REJN, M276REJN, F119REJN, and F120REJN. Note, the dopant concentration calculations assumed several factors (see Section 3.2.8.2) and thus its accuracy should not be relied upon.

Glass melt code	**M275REJN (D046JN)**	**M276REJN (D046JN)**
Nominal composition: (atomic %)	$Ge_{15.2}$ $As_{21.2}$ $Se_{63.6}$ (***distilled***) + 1000 ppmw $TeCl_4$ + 300 ppmw Tb (*foil*)	$Ge_{14.8}$ $As_{20.8}$ $Ga_{2.0}$ $Se_{62.4}$ (***distilled***) + 1000 ppmw $TeCl_4$ + 500 ppmw Pr (*foil*)
Glass density	~4.45 g/cm^3	~4.5 g/cm^3
Dopant concentration	5.06×10^{18} cations/cm^3	9.62×10^{18} cations/cm^3
Produced by:	The author	The author
Fibre and cane drawing code	**F120REJN**	**F119REJN**

The glass densities were estimated based on density measurements reported in [97,153,154].

3.2.5.1 Bulk glass M275REJN and M276REJN evaluation:

Figure 3-24 shows the room temperature IR absorption spectra for a polished bulk M275REJN and a M276REJN sample, with an inset showing the Tb^{3+} and Pr^{3+} GSA bands from the respective samples in the 1.0 to 7.0 µm spectral region. Inset (a) in Figure 3-24 shows that the Pr^{3+} doped sample exhibited several NIR and MIR GSA bands between the $^3H_4$ ground state and the $^3H_5$, $^3H_6$, $^3F_2$, $^3F_3$, $^3F_4$ and $^1G_4$ excited state levels each ostensibly peaking at 4.75 µm, 2.44 µm, 2.03 µm, 1.60 µm, 1.49 µm, and 1.03 µm, respectively. The ($^3H_4 \rightarrow {}^3H_6$) and ($^3H_4 \rightarrow {}^3F_2$) GSA bands overlapped each other, while the ($^3H_4 \rightarrow {}^3F_3$) and ($^3H_4 \rightarrow {}^3F_4$) GSA bands overlapped each other.

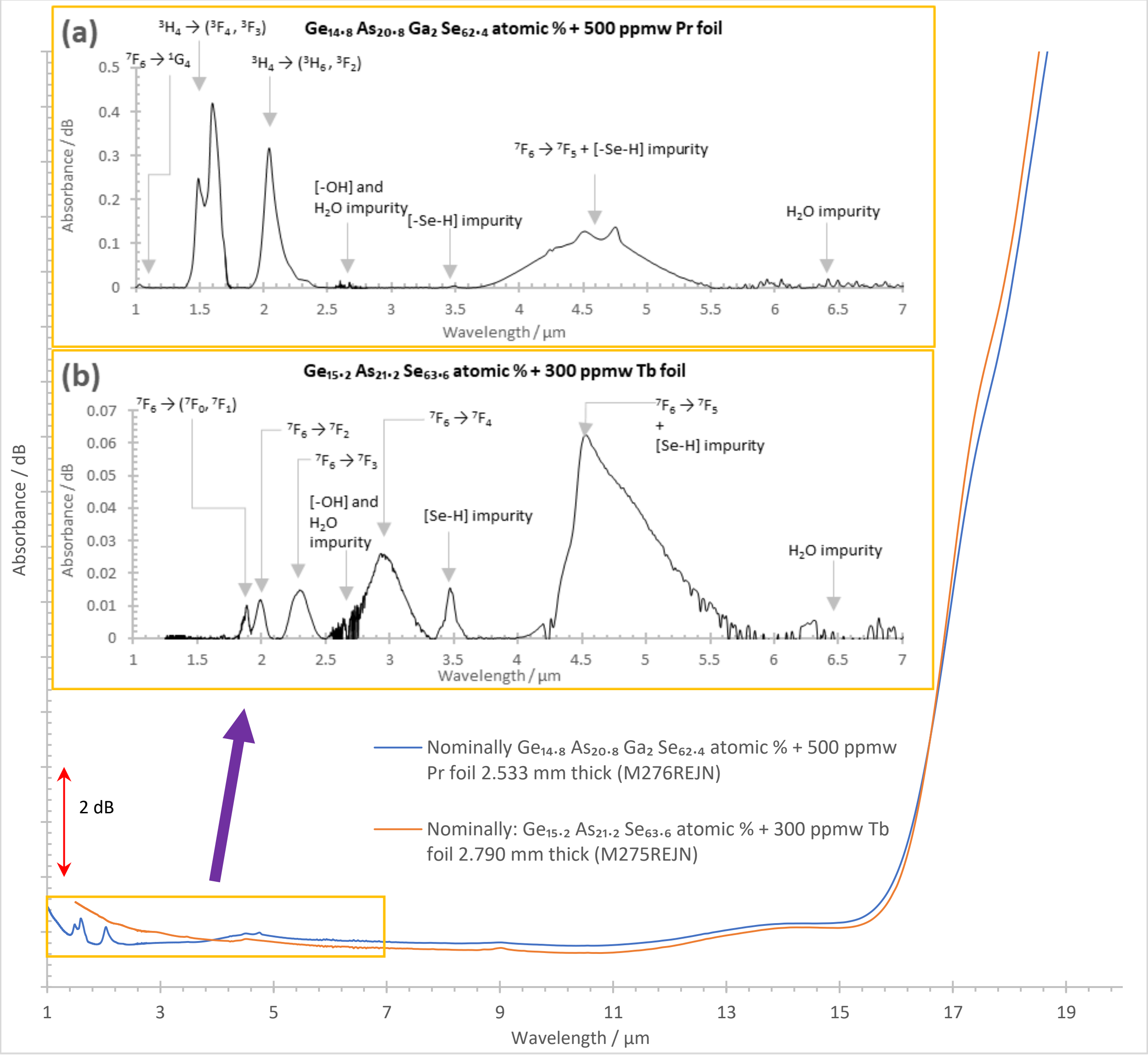

Figure 3-24: Showing room temperature IR absorption spectra of distilled nominally 300 ppmw Tb (foil) doped bulk M275REJN glass sample 2.790 mm thick and a distilled nominally 500 ppmw Pr (foil) doped bulk M276REJN glass sample 2.533 mm thick, with insets (a) & (b) showing the respective Tb^{3+} and Pr^{3+} ground-state electronic absorption bands from each bulk sample in the 1.0 to 7.0 µm spectral region with the contributions of their respective host glass baselines removed.

Inset (b) in Figure 3-24 shows that the Tb^{3+} doped sample exhibited several NIR and MIR GSA bands like those observed in Section 3.2.1.1. Notably, the absence of 'Ga' in the M275REJN composition had negligible effect on the Tb^{3+} GSA peaks, except the apparent shift in the $^7F_6 \rightarrow {}^7F_5$ GSA to 4.52 µm.

3.2.5.2 F119REJN and F120REJN evaluation:

Figure 3-25 (a) shows the attenuation spectrum for the distilled nominally 300 ppmw 'Tb' foil doped single material fibre F120REJN with a diameter of 225.3 ± 4.1 µm with a minimum optical loss of 1.81 ± 0.29 dB/m at a wavelength of 6.58 µm. Note, this is the lowest minimum optical loss of all the single material fibres evaluated in the presented work. However, the attenuation in the NIR spectral region for F120REJN was significantly higher than its F116REJN counterpart (see Figure 3-22), which contained 'Ga' as a co-solubilizer for the 'Tb' dopant. This significant increase in attenuation at shorter wavelengths was most likely due to poor solubility of the 'Tb' dopant in the host glass, owing to the absence of 'Ga' in the glass composition causing additional Rayleigh or Mie scattering. The influence of the 'Ga' co-solubilizer is discussed in Section 3.2.8.1. Figure 3-25 (b) shows the attenuation spectrum for the distilled nominally 500 ppmw 'Pr' foil doped single material fibre F119REJN with a diameter of 215.6 ± 4.0 µm, 1.89 m long, with a minimum optical loss of 6.42 ± 0.20 dB/m at 6.53 µm. This minimum loss was significantly higher than its F116REJN counterpart (see Figure 3-22), which shared an identical nominal host glass composition. This discrepancy was most likely due to the inferior glass cullet and powder used during batching, as shown in Figure 3-19. Additionally, this single material fibre exhibited good ovality and could be handled delicately with little fear of unintentional breakage.

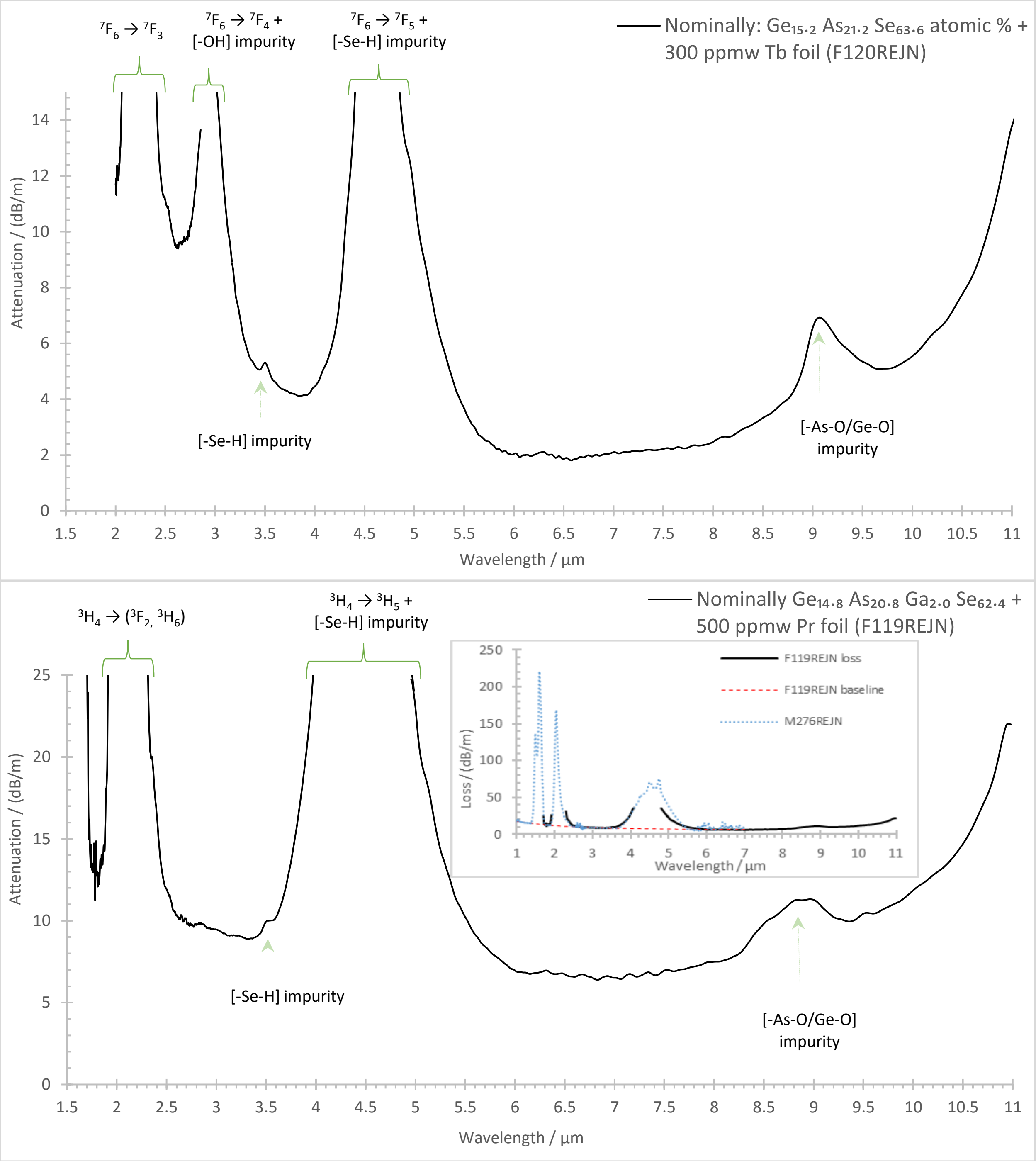

*Figure 3-25: Showing **(a)** the Attenuation (dB/m) vs. Wavelength (µm) for a nominally 300 ppmw Tb foil doped, distilled single material glass fibre F120REJN with a diameter of 225.3 ± 4.1 µm, 3.93 m long with a minimum loss of 1.81 ± 0.29 dB/m at 6.58 µm, and **(b)** shows the MIR attenuation spectrum of a nominally 500 ppmw Pr foil doped, distilled single material glass fibre F119REJN, with a diameter of 215.6 ± 4.0 µm and 1.89 m long with a minimum loss of 6.42 ± 0.20 dB/m at 6.53 µm. With inset showing absorption data from M276REJN sample superimposed onto F119REJN loss spectrum. The Tb^{3+} and Pr^{3+} ground-state electronic absorption and extrinsic vibrational absorption loss due to unwanted host glass impurities are identified (see Table 2-4). Note, nominal glass compositions for each fibre quoted in legend. Note, nominal glass composition quoted in legend.*

3.2.6 Undistilled cerium and dysprosium cation doped co-extrusion:

Table 3-5 lists the specifications for two separate undistilled glass rods of differing composition, a 'Ce' (*foil*) doped core glass M293REJN and a 'Dy' (*foil*) doped cladding glass M295REJN. Polished discs of both the core and cladding glass were then co-extruded into a single step index glass rod E094REDF(JN). Section 3.2.6.1 presents the optical evaluation and IR absorption spectrum measurements of bulk M293REJN and M295REJN glass samples. Refractive index, and SEM-EDX measurements were not performed on these compositions. Section 3.2.6.2 presents the evaluation of the co-extruded rod E094REDF(JN). Note, this co-extruded rod E094REDF(JN) was planned as an intermediary stage in the fabrication of a SIF, however due to time limitations this objective was not fully achieved. This co-extrusion was intended as a first step to produce a high-quality SIF to address several issues encountered during optical cavity experiments (see Section 5.2.2). Additionally, the 'Dy' dopant was included in the cladding to investigate the feasibility of cladding pumping the 'Ce' doped core with Dy^{3+} PL, which is explored in Section 4.2.5.3.a.

Table 3-6: List of production and fabrication specifications for M293REJN and M295REJN. Note, the dopant concentration calculations assumed several factors (see Section 3.2.8.2) and thus its accuracy should not be relied upon.

Glass type:	**Core**	**Cladding**
Glass melt code:	**M293REJN**	**M295REJN**
Nominal composition: (atomic %)	$Ge_{14.8}$ $As_{20.8}$ $Ga_{2.0}$ $Se_{62.4}$ (***undistilled***) + 500 ppmw Ce (*foil*)	$Ge_{16.5}$ $As_{16.0}$ $Ga_{3.0}$ $Se_{61.5}$ $S_{3.0}$ (***undistilled***) + 500 ppmw Dy (*foil*)
Glass density:	~4.5 g/cm^3	~4.5 g/cm^3
Dopant concentration:	9.67 × 10^{18} cations/cm^3	8.34 × 10^{18} cation/cm^3
Produced by:	The author	The author
Co-extruded glass rod code:	**E094REDF(JN)**	

The glass densities were estimated based on density measurements reported in [97,153,154].

3.2.6.1 Bulk glass M293REJN and M295REJN evaluation:

Figure 3-26 shows visible and NIR images of the M293REJN glass rod, gradations were carefully scored into the surface of the glass rod at 5 ± 0.25 mm intervals to act as a rudimentary scale, as shown in Figure 3-26 (a) and (b).

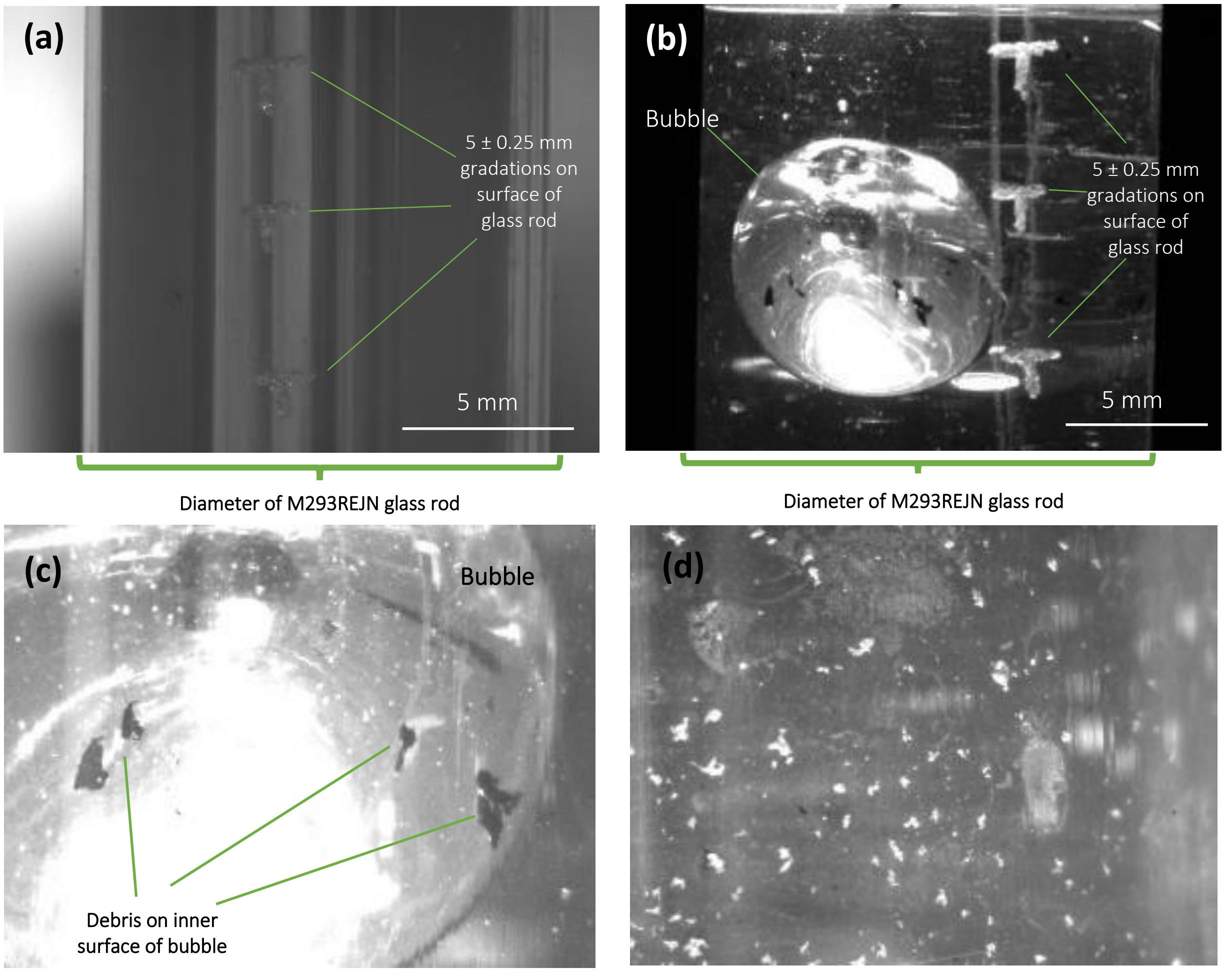

Figure 3-26: Images of M293REJN glass rod showing: ***(a)*** *glass rod surface with 5 ± 0.25 mm gradations scored into surface while viewed under visible illumination,* ***(b)*** *bubble inside of glass rod while viewed under NIR illumination (surface gradations also visible),* ***(c)*** *bubble inside of glass rod viewed under NIR illumination along with debris on inner surface of bubble, and* ***(d)*** *possible crystals formed in the vicinity of the bubble (these crystals are also visible in Figures (b) & (c)). Note, the length scale on Figures (c), and (d) have been intentionally omitted due to the magnification imposed by the cylindrical glass rod.*

NIR evaluation of the M293REJN glass rod, obtained using the equipment configuration in Figure 3-5 (a), revealed a single bubble originally hidden to the naked eye, as shown in Figure 3-26 (b). The formation of bubbles is discussed in Section 3.2.8.4. Under closer examination the bubble appeared to have debris on its inner surface, as shown in Figure 3-26 (c). Additionally, NIR imaging revealed what may have been crystals formed in the vicinity of the bubble, as shown in Figure 3-26 (d). Note, these crystals were visible in Figure 3-26 (b) and (c), and they seem to have formed relatively close to the surface of the glass rod. The magnification imposed by the cylindrical glass rod made it difficult to measure the true dimensions of some of the observed features, thus scale bars were intentionally omitted from Figure 3-26 (c) and (d).

Figure 3-27 shows the room temperature IR absorption spectra for polished bulk M293REJN and M295REJN samples. Inset (a) in Figure 3-27, shows that the Ce^{3+} doped sample exhibited a single broad $^2F_{5/2} \rightarrow {}^2F_{7/2}$ MIR GSA along with extrinsic impurity vibrational absorption bands like those observed in Section 3.2.2.1.

Inset (b) in Figure 3-27, shows that the Dy^{3+} doped sample exhibited several NIR and MIR GSA bands between the $^6H_{15/2}$ ground state and $^6H_{13/2}$, $^6H_{11/2}$, and ($^6H_{9/2}$, $^6F_{11/2}$) excited state levels each ostensibly peaking at 2.85 µm, 1.71 µm, and 1.31 µm respectively. The $^6H_{15/2} \rightarrow {}^6H_{13/2}$ GSA overlapped the extrinsic [-OH] impurity vibrational absorption, while the extrinsic vibrational absorption for; [-S-H] at 4.1 µm, and [-C-S] at 4.96 µm, along with the [-Se-H] absorption bands at 3.5 and 4.5 µm can be observed.

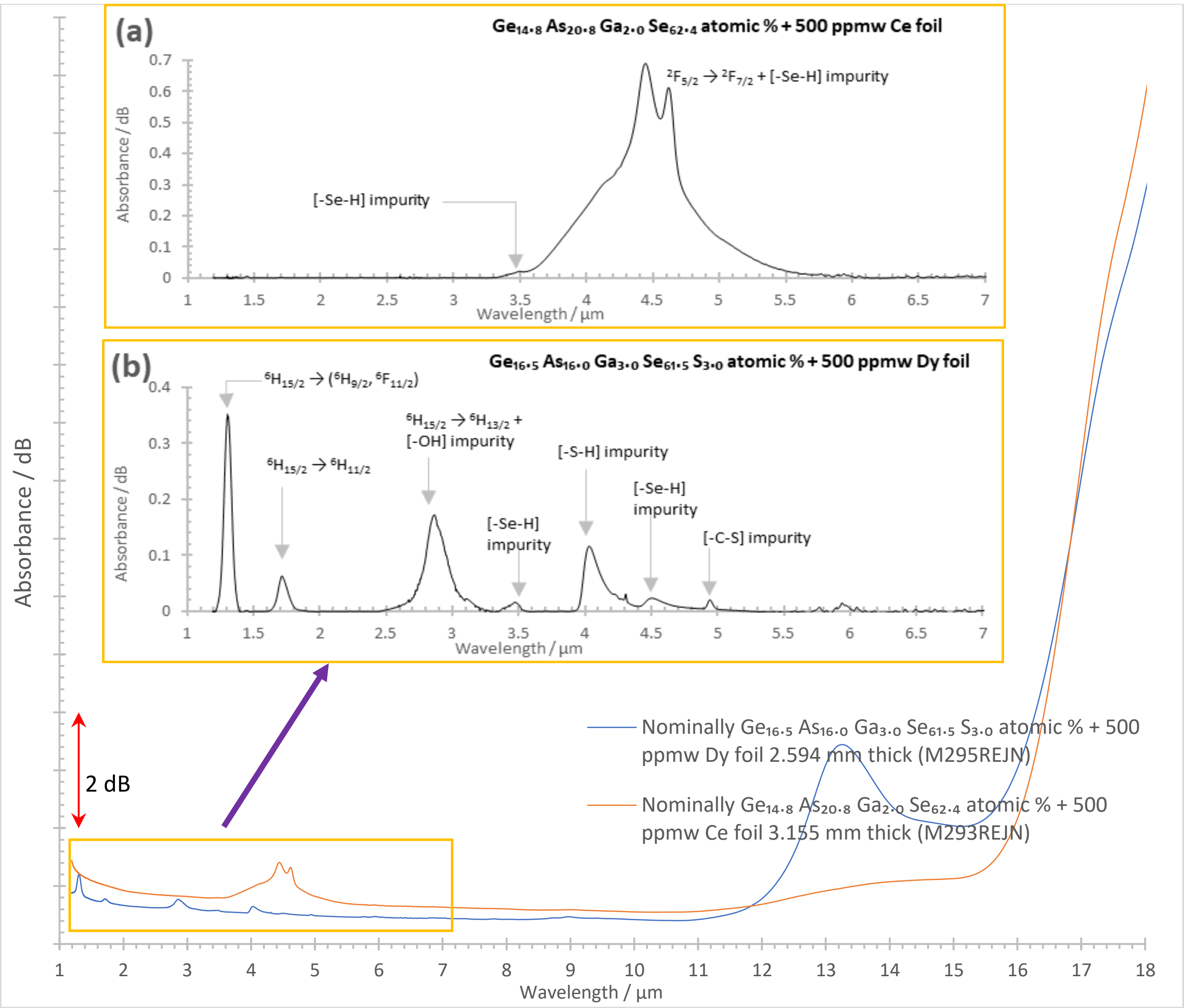

Figure 3-27: Room temperature IR absorption spectra of an undistilled nominally 500 ppmw Ce(foil) doped bulk M293REJN glass sample 2.533 mm thick and an undistilled nominally 500 ppmw Dy (foil) doped bulk M295REJN glass sample 2.594 mm thick, with insets (a) and (b) showing Ce^{3+} and Dy^{3+} ground-state electronic absorption bands from each bulk sample in the 1 to 7.0 µm spectral region with the contributions of their respective host glass baselines removed. Note, the respective Ce^{3+} and Dy^{3+} ground-state electronic absorption bands from each bulk sample are also identified along with unwanted host glass impurities (see Table 2-4).

3.2.6.2 Evaluation of M293REJN and M295REJN co-extrusion:

Polished samples for both the core glass M293REJN (*5.54 mm thick*), and the cladding glass M295REJN (*5.31 mm thick*), were stacked and co-extruded, using the procedure described in Appendix 7.1.9. The resulting co-extruded step-index rod is shown in Figure 3-28.

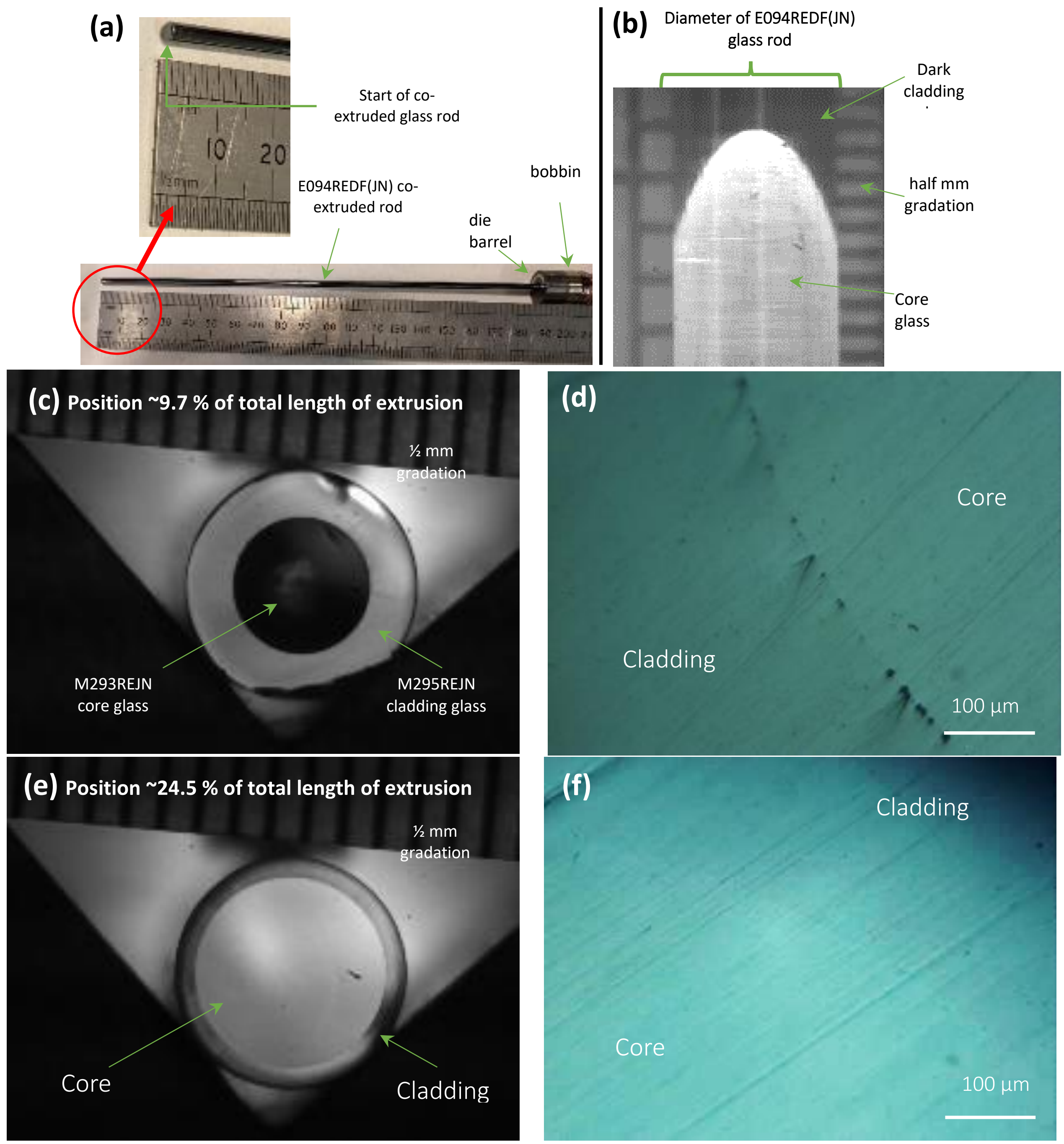

*Figure 3-28: Showing: **(a)** image of co-extruded rod E094REDF(JN) after extrusion (M293REJN was 5.54 mm thick, and M295REJN was 5.31 mm thick prior to co-extrusion), **(b)** NIR image of core ~ 13 mm from start of co-extrusion, **(c)** NIR image of segment cross section originally ~20.1 mm from start of extrusion, **(d)** visible image of segment cross section originally ~20.1 mm from start of extrusion showing holes at core/cladding interface, **(e)** NIR image of segment cross section originally ~50.8 mm from start of extrusion, and **(f)** visible image of segment cross section originally ~50.8 mm from start of extrusion showing core/cladding interface. Note, within Figure (b) the core glass appears to occupy entire diameter of extrusion due to the magnification imposed by the cylindrical glass rod, and NIR images in Figures (b), (c) and (e) were taken adjacent to a ruler with ½ mm gradations for scale.*

The resulting step index co-extruded glass rod E094REDF(JN) had an outer diameter of approximately 3.2 mm, and was approximately 207 mm long, inclusive of material remaining inside the die barrel, as shown in Figure 3-28 (a). NIR evaluation of the E094REDF(JN) glass rod, shown in Figure 3-28 (b), obtained using the equipment configuration in Figure 3-5(a), revealed the introduction of the core glass material into the extrusion around 13 mm from the start of the co-extruded rod. Note, the core glass appeared to have the same 3.2 mm diameter as the extruded rod due to the magnification imposed by the cylindrical glass rod.

The E094REDF(JN) extruded rod was subsequently cut into 10 ± 0.25 mm long segments. Both end faces, of each segment, were then polished to a 1 µm finish. Using NIR imaging, the diameter of the core along the length of the co-extruded rod was measured, as shown in Figure 3-28 (c) and (e), and obtained using equipment configuration in Figure 3-5 (b). These segments were then visually inspected under a microscope to detect holes and any other defects.

Figure 3-29 shows the measured core diameter relative to the cladding diameter for each segment of the co-extruded glass rod plotted against their initial distance from the start of the co-extrusion relative to the total extrusion length. Co-extrusion of the core glass M293REJN and the cladding glass M295REJN produced a straight, step index glass rod E094REDF(JN) with a concentric core and cladding. The measured core/cladding ratio along the length of the extrusion peaked at 88.6 %. Visible evaluation of the glass rod segments revealed the presence of bubbles at the core/cladding interface, see Figure 3-28 (d) and (f), the abundance of these bubbles decreased along the length of the extruded rod. A significant reduction in the number of bubbles between 9.7 % to 18.9 % of the total co-extrusion length was observed, beyond which bubbles were infrequent and small, but were not eliminated. Note, these observations agree with the findings and predictions found in [159,160]. These bubbles were possibly due to residual impurities on the mating surfaces of the core and cladding bulk glass samples prior to extrusion. The Isopropanol used in the final cleaning stage prior to extrusion possibly contributed to the volatile impurities on the mating surfaces. This issue is discussed further in Section 3.2.8.5.

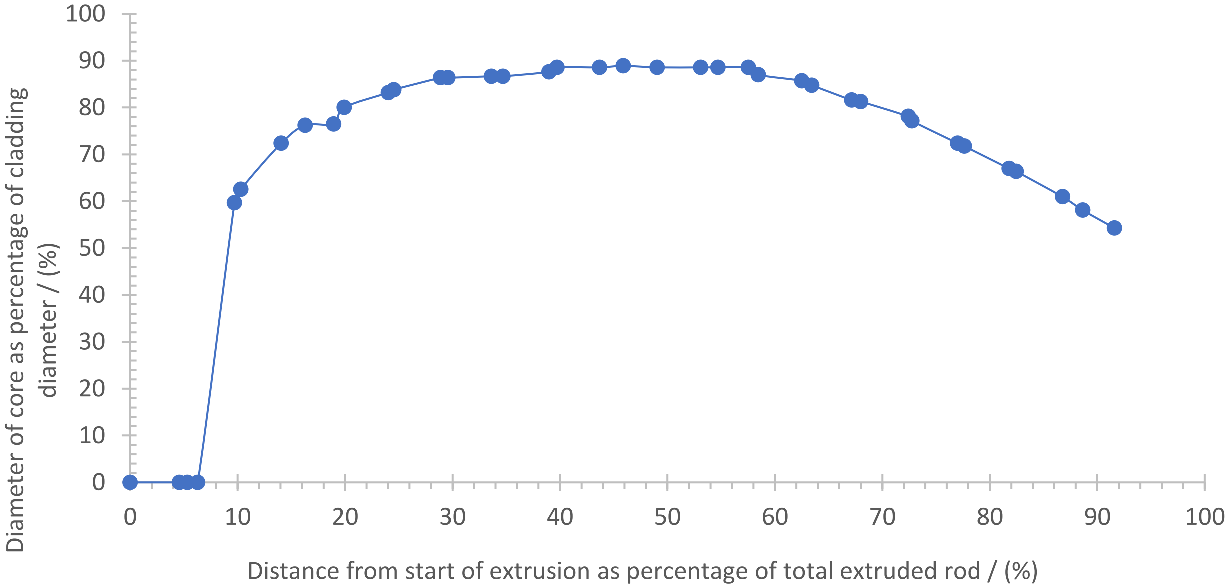

Figure 3-29: Diameter of core as percentage of cladding vs distance from start of extrusion as percentage of total extruded rod for the E094REDF(JN) glass rod. Note quoted distances of segments relative to the start of extrusion measured with an accuracy of ± 0.25 mm or ± 0.12 % of total extrusion length.

3.2.7 Samarium and dysprosium cation doped samples:

Table 3-7 lists the specifications for two separate glass rods of differing glass composition, an undistilled 'Sm' (*foil*) doped glass M227RERC and a distilled 'Dy' (*foil*) doped glass M285REJN. Both glass rods were then individually drawn to single material fibre F099RERC and F125RERC. Section 3.2.7.1 presents the optical evaluation and IR absorption spectrum measurements of bulk M227RERC and M285REJN glass samples. Refractive index, and SEM-EDX measurements were not performed on these compositions. Section 3.2.7.2 presents the evaluation of the single material fibres F099RERC and F125RERC. These two single material fibres were subsequently used for PL emission, and ESA measurements presented in Sections 4.2.3, and 4.2.5, respectively.

Table 3-7: List of production and fabrication specifications for M227RERC and M285RERC. Note, the dopant concentration calculations assumed several factors (see Section 3.2.8.2) and thus its accuracy should not be relied upon.

Glass melt code	**M227RERC**	**M285RERC**
Nominal composition (atomic %)	$Ge_{19.4}$ $Sb_{9.7}$ $Ga_{3.0}$ $Se_{67.9}$ (***undistilled***) + 1000 ppmw Sm (*foil*)	$Ge_{15.0}$ $As_{21.0}$ $Ga_{1.0}$ $Se_{63.0}$ + 850 ppmw $TeCl_4$ (**distilled**) + 500 ppmw Dy (*foil*)
Glass density	~4.6 g/cm^3	4.448 g/cm^3
Dopant concentration	1.84×10^{19} cations/cm^3	8.24×10^{18} cations/cm^3
Produced by:	PhD student Richard Crane	PhD student Richard Crane
Fibre and cane drawing code	**F099RERC**	**F125RERC**

Note:

- The density of M285RERC was based on gas pycnometer measurements reported in [97].
- The M227RERC glass density was estimated based on density measurements reported in [122].

3.2.7.1 Bulk glass M227RERC and M285RERC evaluation:

Figure 3-30 shows an NIR image of the M285RERC glass rod, obtained using the equipment configuration in Figure 3-5 (a).

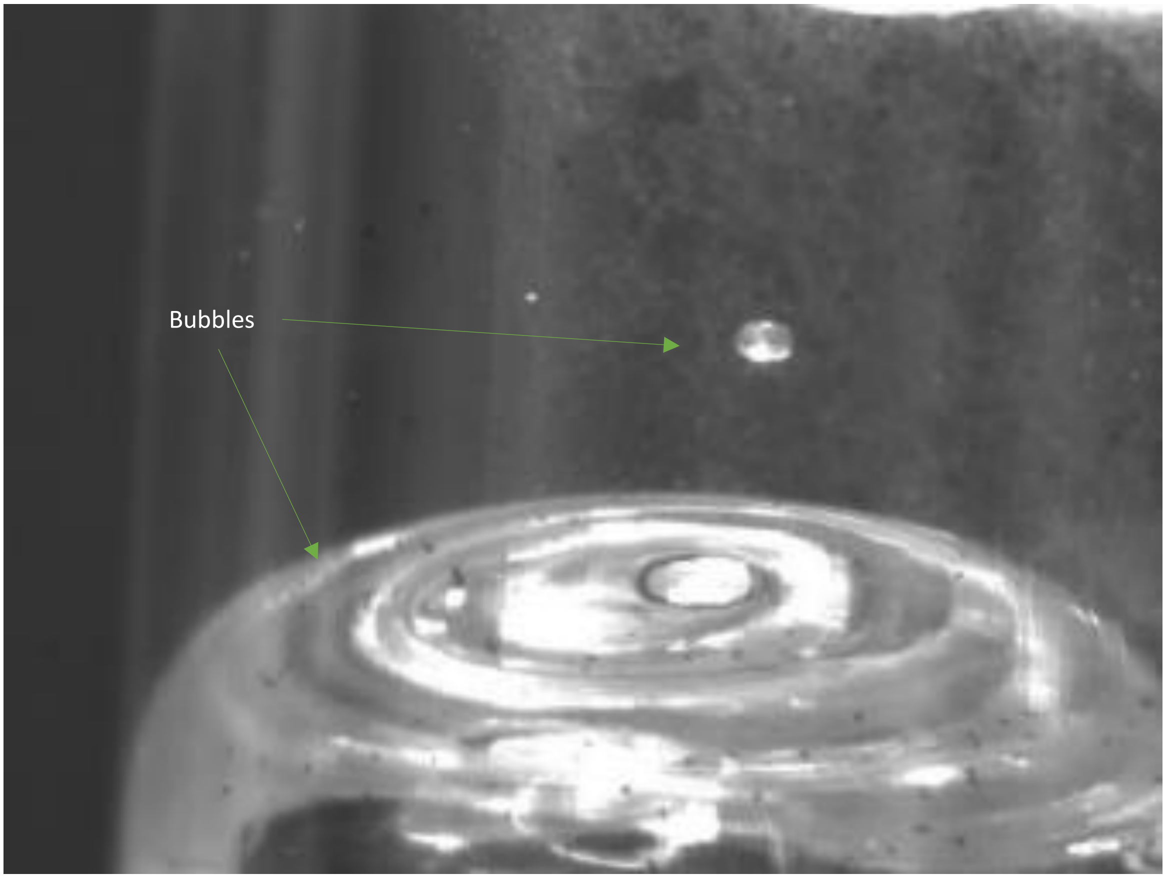

Figure 3-30: NIR images of M285RERC glass rod showing two bubbles, and tiny specks inside of glass rod. Note, the length scale on has been intentionally omitted due to the magnification imposed by the cylindrical glass rod.

NIR imaging revealed two empty spherical inclusions (the formation of bubbles is discussed in Section 3.2.8.4.), and tiny specks originally hidden to the naked eye. These specks seemed to be evenly distributed throughout the interior of the glass rod and appeared like those observed in the M260JN sample, shown in Figure 3-10 (d). This glass rod was drawn to single material fibre F125RERC and used for the presented attenuation spectrum in Figure 3-33.

Figure 3-31 shows the room temperature IR absorption spectra for the polished bulk M227RERC and M285RERC samples, with insets showing the Sm^{3+} and Dy^{3+} GSA bands for each sample, within the 0.5 to 10 µm spectral region. Inset (a) in Figure 3-31, shows that the Sm^{3+} doped sample exhibited several NIR and MIR GSA bands between the $^6H_{5/2}$ ground state and its excited state levels. The $^6F_{5/2}$, $^6F_{3/2}$, $^6F_{1/2}$, and $^6H_{15/2}$ levels exhibited extensive overlapping making identification of the individual GSA unreliable. The ($^6H_{5/2} \rightarrow {}^6H_{9/2}$) GSA overlapped the extrinsic [-Se-H] impurity vibrational absorption, while the ($^6H_{5/2} \rightarrow {}^6H_{11/2}$) GSA overlapped the extrinsic [-OH] impurity vibrational absorption. Inset (b) in Figure 3-31, shows that the Dy^{3+} doped sample exhibited several NIR and MIR GSA bands between the $^6H_{15/2}$ ground state and $^6H_{13/2}$, $^6H_{11/2}$, ($^6H_{9/2}$, $^6F_{11/2}$), ($^6H_{7/2}$, $^6F_{9/2}$), and $^6H_{5/2}$ excited state levels each ostensibly peaking at 2.85 µm, 1.71 µm, 1.31 µm, 1.11 µm, and 0.92 µm respectively. Additionally, the extrinsic vibrational absorption bands [-OH] and H_2O impurity can be observed at ~2.7 and ~6.5 µm, respectively, while the $^6H_{15/2} \rightarrow {}^6H_{13/2}$ GSA overlapped the extrinsic [-OH] impurity vibrational absorption, and the [-Se-H] impurity absorption can be observed at 3.5 and 4.5 µm. Notably, the extrinsic impurity vibrational absorption bands for [-S-H] at 4.030 µm, [-Se-H] at 4.500 µm and [-C-S] at 4.940 µm were unobstructed by any overlapping RE^{3+} absorptions. The [S-H] impurity vibrational absorption was present due to the sulfur contained in the glass composition This was attributed to the sulfur acting as a getter, preferentially sequestering hydride impurities as [-S-H], which would have otherwise resulted in a greater [-Se-H] concentration.

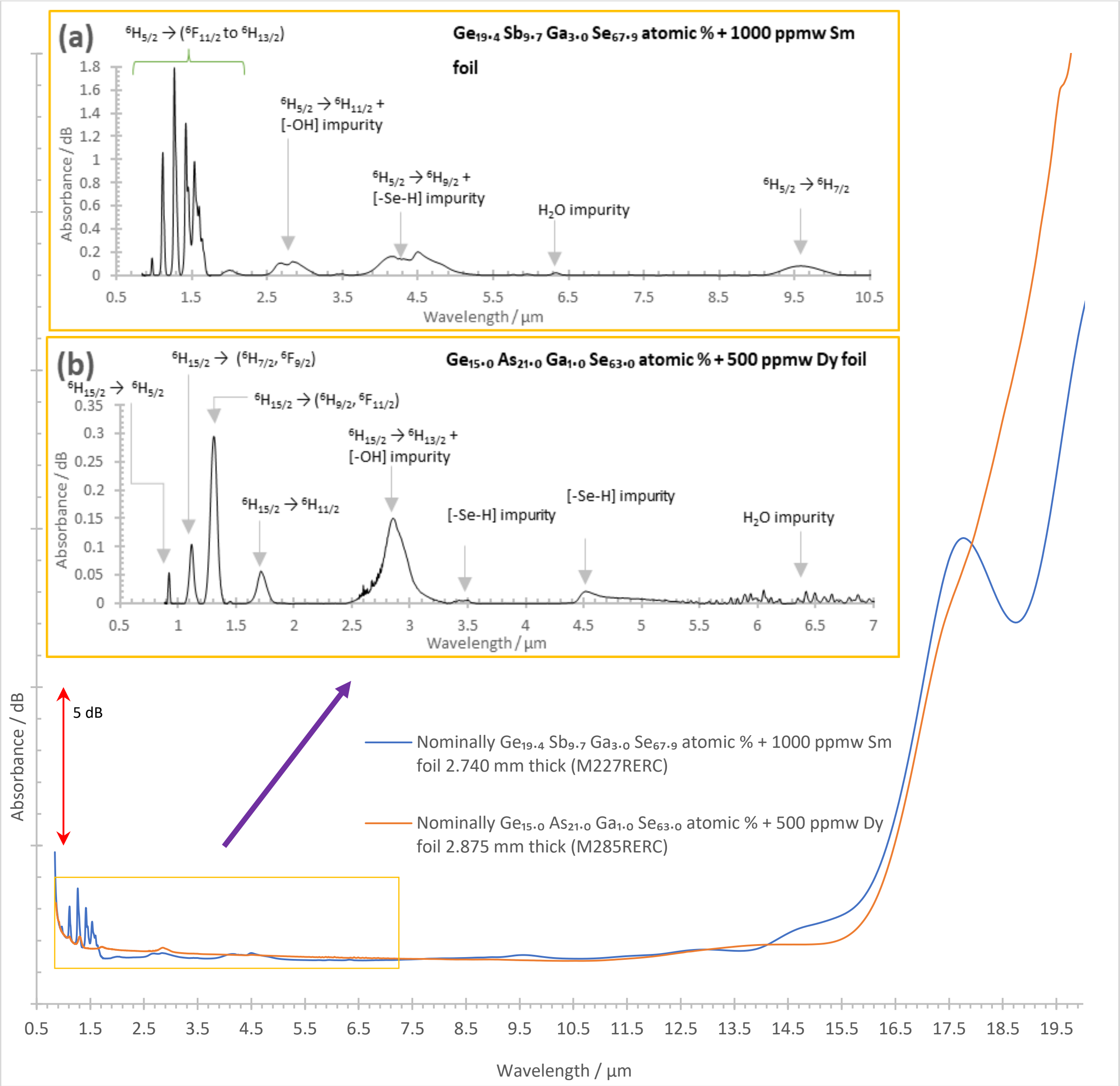

Figure 3-31: Room temperature IR absorption spectra of an undistilled nominally 1000 ppmw Sm (foil) doped bulk M227RERC glass sample 2.74 mm thick and an undistilled nominally 500 ppmw Dy (foil) doped bulk M285RERC glass sample 2.875 mm thick, with inset showing Sm^{3+} and Dy^{3+} ground-state electronic absorption bands from each bulk sample in the 0.5 to 10.0 µm spectral region with the contributions of their respective host glass baselines removed.

3.2.7.2 F099RERC and F125RERC evaluation:

Figure 3-33 shows the attenuation spectrum obtained from an undistilled nominally 1000 ppmw ‘Sm’ foil doped single material fibre F099RERC sample with a diameter of ~ 232 µm, 2.84 m long, with a minimum optical loss of 2.36 ± 0.13 dB/m at 6.03 µm, measured to an 8 cm^{-1} resolution. This single material fibre exhibited reasonable ovality and could be handled delicately however unintentional breakage was common.

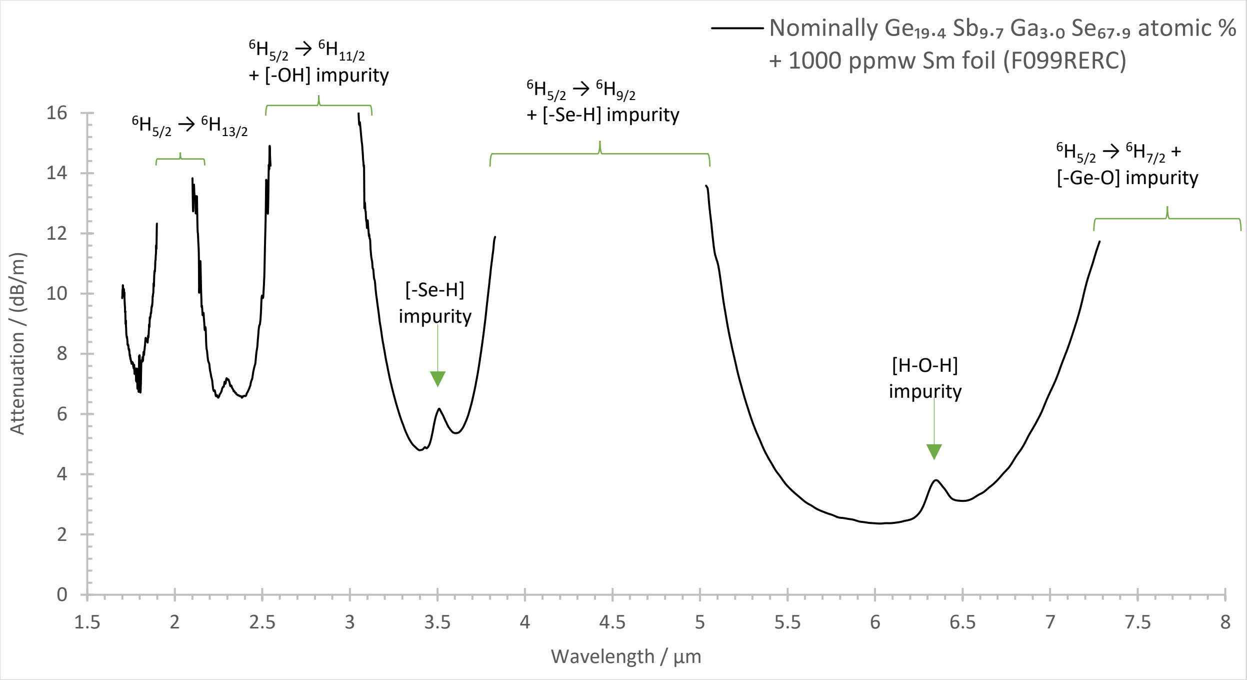

Figure 3-32: Attenuation (dB/m) vs. Wavelength (µm) for a nominally 1000 ppmw Sm (foil) doped F099RERC single material fibre sample with diameter of ~ 232 µm and 2.84 m long with a minimum loss of 2.36 ± 0.13 dB/m at 6.03 µm. The Sm^{3+} ground-state electronic absorption and extrinsic vibrational absorption loss due to unwanted host glass impurities are identified (see Table 2-4). Note, nominal glass compositions quoted in legend.

Figure 3-33 (a) shows the attenuation spectrum obtained from a distilled nominally 500 ppmw ‘Dy’ foil doped single material fibre F125RERC sample with a diameter around 230 µm with a minimum optical loss of 2.07 ± 0.33 dB/m at a wavelength of 6.13 µm, measured to an 8 cm^{-1} resolution. This single material fibre exhibited good ovality and could be handled delicately with little fear of unintentional breakage. Additionally, the specks observed in Figure 3-30 did not appear to influence the attenuation spectrum in the evaluated spectral region. Figure 3-33 (b) shows [-Se-H] absorption spectrum with gaussian fitting, this is used in Section 4.2 to correct absorption cross-sections.

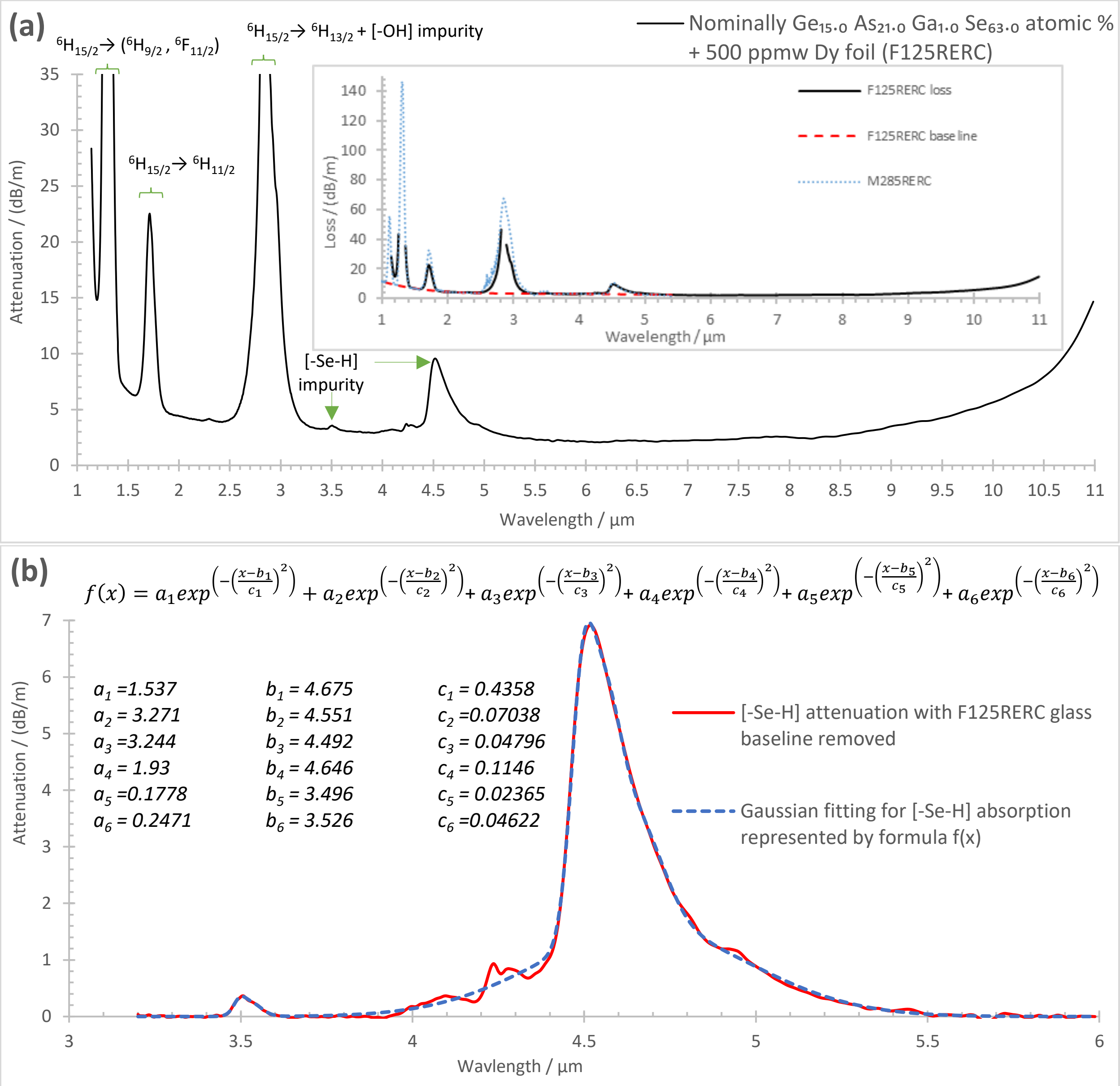

*Figure 3-33: plot **(a)** shows attenuation (dB/m) vs. wavelength (µm) for a 500 ppmw Dy (foil) doped F125RERC single material glass fibre sample with diameter of ~ 230 µm and 5.78 m long with a minimum loss of 2.07 ± 0.33 dB/m at 6.13 µm. With inset showing absorption data from M285RERC sample superimposed onto F125RERC loss spectrum. The Dy^{3+} ground-state electronic absorption and extrinsic vibrational absorption loss due to unwanted host glass impurities are identified (see Table 2-4). Note, nominal glass composition quoted in legend. Plot **(b)** shows the [-Se-H] impurity vibrational absorption from the F125RERC loss spectrum with host glass baseline removed and a gaussian fitting of the absorption.*

3.2.8 Discussion on chalcogenide glass synthesis and fabrication:

An ideal glass composition, intended for use in MIR light sources, should possess a wide glass-forming region so it can be fabricated into low-loss fibre with good optical and mechanical properties. These fibres should be capable of being handled, delicately, without fear of unintentional breakage. The optical loss of the host glass should be as low as possible, and there should be negligible variability of the optical properties, such as refractive index and RE^{3+} dopant concentration, between samples taken from a common host glass. Thus, the production and fabrication steps used for the glass should ensure glass homogeneity while minimising the inclusion of extrinsic impurities and light scattering defects. The presented results show that there is still room for improvement to the chalcogenide glass making and fabrication processes. This section discusses the challenges encountered in the synthesis and fabrication of chalcogenide glass by studying the achievements and finding presented throughout Sections 3.2.1 to 3.2.7.

3.2.8.1 Impurities introduced during glass synthesis:

Table 3-8 compares the purification steps for the constituent elements of three glass samples against their minimum optical loss to highlight where impurities are being introduced.

Excluding the ‘Ge’ precursor (see Appendix 7.1.2.2), each of the elemental precursors used in glass production were purified prior to the initial glass synthesis. Vacuum distillation of undoped glass, using the procedure described in Appendix 7.1.6, allowed for the reduction of oxide, hydride, and carbon impurities in all the constituent elements, inclusive of the ‘Ge’. Thus, lowering the minimum optical loss of the distilled glass when compared to the undistilled glass.

Preparation of the ‘Ga’ and RE foil precursors (see Appendix 7.1.2.3 and 7.1.2.4) focused on removal of surface impurities. Unfortunately, this procedure only scratched the surface, leaving impurities within these precursors, thus allowing for their inclusion into the host glass composition during remelting to incorporate the RE-dopant. Thus, the inclusion of both the ‘Ga’ and RE foil precursors invariably increased the minimum optical loss of the host glass.

Table 3-8: A comparison of the purification steps for each chemical constituents and minimum optical loss of three glass samples:

Glass code	**Nominal composition / atomic %**	**Distilled**	**Bulk purification**				**Tb^{3+} / ppmw**	**Minimum optical loss / (dB/m)**
			‘Ge’	**‘As’**	**‘Ga’**	**‘Se’**		
F103REJN(RC)	$Ge_{14.8}$ $As_{20.8}$ $Ga_{2.0}$ $Se_{62.4}$	No	No	Yes	No	Yes	500	3.61 ± 0.15
F116REJN	$Ge_{14.8}$ $As_{20.8}$ $Ga_{2.0}$ $Se_{62.4}$	Yes	Yes	Yes	No	Yes	500	2.32 ± 0.40
F120REJN	$Ge_{15.2}$ $As_{21.2}$ $Se_{63.6}$	Yes	Yes	Yes	Absent	Yes	300	1.81 ± 0.29

Note, F116REJN and F120REJN were produced from the same host glass M273 (see Section 3.2.3).

Considering Table 3-8, both F103REJN(RC) and F116REJN share the same nominal composition, while F120REJN is the same composition <u>without</u> the 2 atomic % ‘Ga’. Comparing the preparation of F103REJN(RC) to F116REJN the unpurified ‘Ge’ precursor likely contributed to additional optical losses along with any residual impurities in the other elements. Comparing the composition of F116REJN to F130REJN the absence of ‘Ga’ and reduced Tb^{3+} dopant concentration lowered the optical losses. Thus, a trend of lower minimum optical attenuation can be observed with glass compositions containing lower ‘Ga’ and RE-dopant content, this is further corroborated by the optical attenuation literature survey listed in Table 2-5. Regrettably, despite the low optical loss of the F120REJN sample, the lack of 'Ga' caused poor solubility of the RE dopant causing excessive Rayleigh or Mie scattering in the NIR spectral region.

The inclusion of the 'Ga' and RE dopant constituents precluded further purification of the RE-doped glass via typical distillation between 600 to 700 °C, due to their low volatility [85,86,161,162], which would otherwise result in their separation from the host glass during distillation. In hindsight the impurities contained in the 'Ga' and RE-dopant precursors could have potentially been reduced with the inclusion of chemical 'getters' during the batching of the active RE dopant. These getters could either cause the formation of volatile species or preferentially react and sequester anionic impurities. This is expanded upon in Section 6.1.

3.2.8.2 RE dopant concentration:

The optical evaluations presented in Sections 3.2.1 to 3.2.7 allude to some uncertainty in the RE^{3+} dopant concentrations. Considering the relatively small RE dopant concentrations used in the presented work the following confounding factors compromise the accuracy of the MIR active RE^{3+} concentration in the samples investigated:

- Impurities and alternate reaction paths for RE dopants: The RE dopants are the most reactive elements in the host glass composition thus making them an effective chemical 'getter', readily reacting with anionic impurities such as oxide and hydroxide impurities present in the host glass [86]. This could have potentially sequestered a portion of the RE dopant. Additionally, the preparation process for the silica ampoules (see Appendix 7.1.1) resulted in a pristine surface. This potentially made the inner ampoule wall more reactive with the contents of the ampoule, especially the RE dopant when considering the high temperatures and long heating schedule used in the 'melt-quench' process. Hence, the intentional difference in heating schedules between the undoped and RE doped glass employed in the melt-quench process outlined in Appendix 7.1.5.1.

- <u>Heterogeneous inclusions</u>: NIR imaging of both RE^{3+} doped and undoped samples revealed the presence of unwanted microscopic heterogeneous inclusions, or ‘specks’, within the glass (*see Figure 3-10 (d) and Figure 3-30*). The composition of these inclusions was not evaluated however impurities are the most likely cause. It was reported that impurity inclusions within a host glass can act as centres for glass crystallization [104,105]. Considering the poor solubility of the RE dopant, it is conceivable that these inclusions could have had an equivalent or greater solubility of the RE^{3+} dopant than the surrounding chalcogenide host glass. This would result in a non-uniform distribution of RE^{3+} dopant concentration within the samples. The small size of these specks coupled with their sparse but relatively uniform distribution within the glass makes their evaluation challenging because these features are easy to miss.
- <u>Bubbles and voids</u>: NIR imaging of bulk glass samples revealed the presence of bubbles of various sizes in <u>most</u> of the glass rods evaluated. Note, the formation of bubbles is discussed further in Section 3.2.8.4. Due to the opacity of chalcogenide glass, it is conceivable that a hidden bubble or bubbles could be present within a sample used for density measurements. The potential presence of these internal voids would be detrimental to the accuracy of the measurements. Furthermore, this inaccuracy could have afflicted prior chalcogenide host glass density measurements found in literature.

3.2.8.3 Vacuum distillation of glass:

The distillation process presented in Section 3.2.3 undoubtedly improved to quality of the glass produced. However, the entire distillation process exhibited several deficiencies with its setup and operation. The preparation procedure for the distillation rig encompassed several days entailing custom fabrication, glassware preparation (see Section 7.1.1), and setup of heating coils and thermocouples (see Section 7.1.6) resulting in a rig that was expensive, fragile and tedious to setup. The glass distillation process only distilled the chalcogenide glass once and was unsuitable for purification of compositions containing ‘Ga’ or RE-dopants. Furthermore, it was difficult to prevent excessive loss of the volatile constituents of the chalcogenide glass such as ‘Se’ during distillation.

Several of these issues with the distillation process could be addressed by changing the distillation rig to a vertical orientation to improve refluxing by allowing condensed molten glass to flow under gravity into hotter zones to be re-distilled. Additionally, active cooling, around the distillation chamber could have better controlled the condensation of the more volatile constituents of the glass. These improvements are expanded upon further in Section 6.1.1.

3.2.8.4 Glass melt quenching:

Glass quenching, using the process described in Appendix 7.1.5.2, employed a sequence of steps to rapidly cool molten glass inside an ampoule in a controlled manner. The initial air quench resulted in some of the more volatile constituents of the glass evaporating and condensing on the cooler upper portion of the inner wall of the ampoule, as shown in Figure 7-8 (b). This resulted in the glass having a small compositional gradient between its top and bottom. It was postulated that this compositional discrepancy contributed towards the formation of striae during tube extrusions.

Following the initial air quench and furnace quench, ampoules were subjected to an N_2 jet quench (see Appendix 7.1.5.2). Wherein, a N_2 jet was applied to the upper portion of the silica ampoule and progressively moved to the bottom. This allowed for the initial release of the chalcogenide glass from the inner ampoule wall in a controlled manner. This procedure was the simplest and most convenient way to detach the glass, however, this seemingly contributed towards the frequent formation of vacuum bubbles. Two possible explanations for the bubble formation are:

- It was postulated that these bubbles were formed due to a mismatch in contraction rates between the cooler, solidified, upper portion of the chalcogenide glass and the lower molten glass still in contact with the ampoule inner wall. Potentially this thermal gradient prevented the entire chalcogenide glass rod from uniformly contracting, thus causing tension between the solidified glass, and the still contracting liquid, resulting in bubbles which may have initially been filled with a low-pressure vapor derived from the surrounding molten material, this phenomenon was further explored in [163].
- The N_2 jet quench always caused the glass melt meniscus to form a contraction cone. These were funnel shaped depressions at the top of the glass rod (see Figure 3-34 (a)). The depth of the contraction cone varied with glass composition, silica ampoule diameter and quenching rates, contraction cones up to 13 mm deep have been measured. This formation process was often very sudden and violent. This event would sometimes crack the silica ampoule, hence the check for the structural integrity of the ampoule in the process flow chart in Figure 3-1. Thus, it is conceivable that the rapid downward

contraction of the solidified glass could generate a shockwave in the molten glass below. This shockwave could generate cavitation bubbles due to sudden change in momentum of the glass melt [164], like the “exploding beer trick” [165]. These bubbles could then be frozen during the quenching process.

Bubbles were only found in glass rods made in 10/14 silica ampoules. Notably, no bubbles were found in glass rods produced in larger diameter ampoules. The largest bubbles often formed in the middle of the glass rods evaluated while smaller bubbles were sometimes found at the bottom of the glass rods. Bubbles with diameters as large as 2.8 mm were found in samples (see Figure 3-34 (b)).

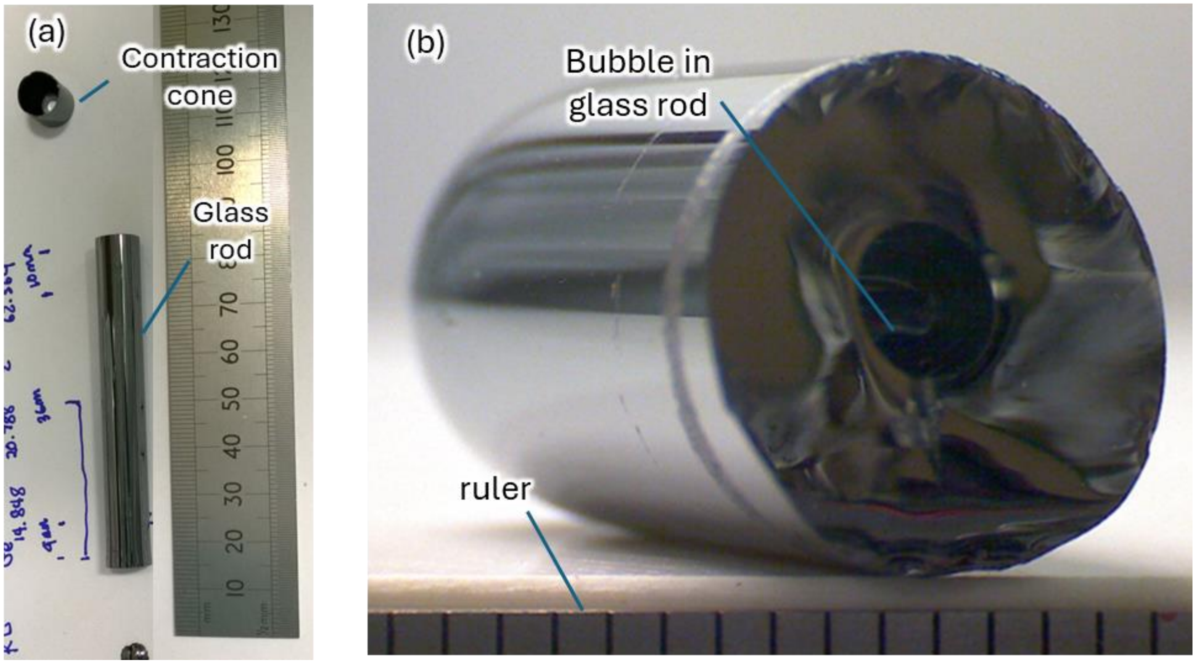

*Figure 3-34:Showing **(a)** image of the contraction cone removed from adjacent glass rod, and **(b)** Image of chalcogenide glass rod with bubble in its centre, this sample was destructively evaluated to determine the true dimensions of the bubble within. Note, image (b) was taken adjacent to a ruler with 1 mm gradations for scale.*

3.2.8.5 *Impurities and defects introduced during glass fabrication:*

Impurities and defects unintentionally introduced during the fabrication of glass extrusions and glass fibres caused additional optical losses. Chalcogenide glasses are typically insoluble in water, and they are not oxidized in air below their 'T_g', beyond a protective oxide nanolayer [151]. However, the impurities introduced to the glass during fabrication were attributed to oxidation, and absorption/adsorption of atmospheric molecules and liquids after the glass was removed from its sealed ampoule. These impurities could cause additional unwanted vibrational absorptions in the glass, and/or form physical defects such as bubbles, and act as nucleation cites for crystals. This was exemplified by the presence of the following:

- Vibrational absorptions due to [-OH] at ~2.8 µm and H_2O centred around 6.5 µm were present in most of the <u>bulk glass</u> absorption measurements presented. Notably, these spectral features were absent from the corresponding fibre optic loss spectra, despite the bulk glass and the single material fibres being comprised of identical glass and the measurements being performed to an identical resolution. Thus, it was postulated that each 'cut-back' during a fibre optical loss measurement (see Appendix 7.2.2) revealed pristine glass to be analysed. Loss measurements were conducted before any appreciable absorptions could occur and the methodology employed precluded any exposure to liquids. Therefore, the methodology used to prepare and handle the bulk samples caused their contamination.
- Etching cause poor surface quality. Glass etching was done to remove surface impurities using procedure in Appendix 7.1.11. Etching time varied from several hours to several days and was dependant on glass composition, sample geometry, and ambient

temperature. This process frequently resulted in a poor surface quality leading to a pitted surface, especially for selenide-based compositions containing ‘As’. This ‘wet etching’ procedure afforded ample opportunity for chemicals such as propylamine, acetone and isopropanol to attach themselves to the glass surface. In hindsight dry etching’ procedures such as plasma etching, and reactive ion etching could avoid adding impurities onto the glass surface, while leaving the surface pristine.

- Physical defects were often present at the core/cladding interface of SIF made using the ‘rod-in-tube’ method (see Appendix 7.1.12) which were likely due to impurities on the mating surfaces. It was postulated that impurities accumulated on the rough surface of the glass cane after propylamine etching. These volatile impurities likely contributed towards the formation of holes at the core/cladding interface during the fibre drawing process (see Appendix 7.1.12). Impurities would form bubbles when heated and regions of were then elongated along within the fibre, often for several metres, as shown in Figure 3-9 (b) and Figure 3-15 (c), thus potentially compromising the usefulness of large sections of the resulting SIF. It was also postulated that the glass co-extrusion demonstrated in Section 3.2.6.2, and described in Section 7.1.9, could be used to avoid the issue of maintaining pristine mating surfaces while using the rod-in-tube method.

Additional impurities could have been introduced during the opening of silica ampoules, as described in Section 7.1.3. Due to these ampoules being under vacuum this step potentially introduced silica glass dust and shards into the content of the ampoule.

3.2.8.6 Glass extrusions and SIF fabrication:

Striae was observed in the cladding on all the SIF samples that utilised an extruded cladding tube. These extruded cladding tubes were produced using a three-hole spider die (see Appendix 7.1.8). Wherein the initial solid glass billet was heated and forced through each of the holes in the die, each of the three streams then recombined upon exiting the die. This flow pattern likely incorporated pre-existing compositional inhomogeneities within the glass billet into the resulting extruded tube. Note, it was postulated the compositional inhomogeneities were introduced between the top and the bottom of the glass rod during the quenching process, see Section 3.2.8.4. Luckily these striae resided in the cladding of SIF's where they were unlikely to affect light guided in the core. However, they presented an issue when launching light into a SIF as these striae extended for the entire SIF and some were capable of be optically guiding light.

During SIF fabrication using the 'rod-in-tube' (see Appendix 7.1.12) it was found that closely matching the OD of the cane to the ID of the cladding tube consistently resulted in good concentricity between the core and cladding, along with a circular core that exhibited good ovality, or 'out-of-roundness' as defined in [166], when fibre drawn.

3.3 Chapter summary

The material preparations stages, shown in Section 3.1, ideally allowed for the prevention or removal of extrinsic impurities during glass production and its fabrication into glass fibres. The techniques introduced in this chapter enabled production of chalcogenide glass compositions that were amenable to both extrusion and fibre drawing, while possessing comparable optical attenuation to that found in literature (see Table 2-5). Additionally, most of these fibres exhibited good ovality and handleability. Table 3-9 summarises the spectroscopic properties of these glass samples. These techniques were also used to demonstrate the following capabilities:

i. Co-processing of two glasses of differing composition. The various RE^{3+} doped core glass compositions and undoped cladding chalcogenide glass compositions could undergo co-processing to fabricate a SIF, as demonstrated with the production of the F105REJN, F130RERC, and F122REJN SIF samples. Additionally, co-extrusion of a step index glass rod with separate RE dopants in both the core and cladding was demonstrated (see Section 3.2.6.2) enabling the fabrication of an SIF with a co extruded core/cladding interface and cladding pumping of the core with RE^{3+} PL from the cladding.
ii. Control the NA of SIF. MIR spectroscopic ellipsometry revealed that SIFs could be fabricated with a range of numerical apertures by controlling the composition of core and cladding glass. Evaluation of the bulk glass used to produce SIF samples revealed the range of numerical aperture achieved, was between 0.210 to 0.585 (see Table 3-9).
iii. The capability to cause permanent photoinduced refractive-index changes in RE^{3+} doped glass was demonstrated, in collaboration with Aston University, (see Section 3.2.2.3), thus enabling FBGs to be written.

Table 3-9: Summary of each chalcogenide glass composition evaluated in Section 3.2. Note, the rows for glass samples with identical nominal compositions were shaded with the same colour to aid with comparison.

<table>
<tr><th>Glass code</th><th>Glass type</th><th>Chalcogenide glass nominal composition (atomic %) and code</th><th>Minimum loss (dB/m)</th><th>SIF fabrication</th><th>SIF (code)</th><th>NA (4 to 7 µm)</th></tr>
<tr><td>M228REJN(RC)
(F103REJN(RC))</td><td>Core glass</td><td>$Ge_{14.8}As_{20.8}Ga_{2.0}Se_{62.4}$ (undistilled) + 500 ppmw Tb (*foil*)</td><td>3.61 ± 0.15
(Figure 3-8)</td><td>↘</td><td rowspan="2">F105REJN</td><td rowspan="2">0.210</td></tr>
<tr><td>M251JN
(E088DF(JN))</td><td>Cladding glass</td><td>$Ge_{14.8}As_{20.8}Ga_{2.0}Se_{61.5}S_{1.0}$ (undistilled)</td><td>Not evaluated</td><td>↗</td></tr>
<tr><td>M287RC
(E093RC)</td><td>Cladding glass</td><td>$Ge_{21.0}Sb_{10.0}Se_{69.0}$ (undistilled)</td><td>Not evaluated</td><td>↘</td><td rowspan="2">F130RERC</td><td rowspan="2">0.475</td></tr>
<tr><td rowspan="2">M259REZQT
(F109REZQT(RC&JN))</td><td rowspan="2">Core glass</td><td rowspan="2">$Ge_{15.0}As_{21.0}Ga_{1.0}Se_{63.0}$ (undistilled) + 500 ppmw Ce (*foil*)</td><td rowspan="2">2.23 ± 0.03
(Figure 3-13)</td><td>↗</td></tr>
<tr><td>↘</td><td rowspan="2">F113REZQT
(JN&RC)</td><td rowspan="2">0.585</td></tr>
<tr><td rowspan="2">M260JN
(E090JN)</td><td rowspan="2">Cladding glass</td><td rowspan="2">$Ge_{16.5}As_{16.0}Ga_{3.0}Se_{61.5}S_{3.0}$ (undistilled)</td><td rowspan="2">Not evaluated</td><td>↗</td></tr>
<tr><td>↘</td><td rowspan="2">F122REJN</td><td rowspan="2">0.470</td></tr>
<tr><td>M274REJN
(F116REJN)</td><td>Core glass</td><td>$Ge_{14.8}As_{20.8}Ga_{2.0}Se_{62.4}$ (distilled) + 1000 ppmw $TeCl_4$ + 500 ppmw Tb (*foil*)</td><td>2.32 ± 0.40
(Figure 3-22)</td><td>↗</td></tr>
<tr><td>M275REJN
(F120REJN)</td><td>Single material fibre</td><td>$Ge_{15.2}As_{21.2}Se_{63.6}$ (distilled) + 1000 ppmw $TeCl_4$ + 300 ppmw Tb (*foil*)</td><td>1.81 ± 0.29
(Figure 3-25 (a))</td><td>None</td><td colspan="2">Not evaluated</td></tr>
<tr><td>M276REJN
(F119REJN)</td><td>Single material fibre</td><td>$Ge_{14.8}As_{20.8}Ga_{2.0}Se_{62.4}$ (distilled) + 1000 $TeCl_4$ + 500 ppmw Pr (*foil*)</td><td>6.42 ± 0.20
(Figure 3-25 (b))</td><td>None</td><td colspan="2">Not evaluated</td></tr>
<tr><td>M293REJN</td><td>Core glass</td><td>$Ge_{14.8}As_{20.8}Ga_{2.0}Se_{62.4}$ (undistilled) + 500 ppmw Ce (*foil*)</td><td>Not evaluated</td><td>↘</td><td rowspan="2">E094REDF(JN)</td><td rowspan="2">0.470*</td></tr>
<tr><td>M295REJN</td><td>Cladding glass</td><td>$Ge_{16.5}As_{16.0}Ga_{3.0}Se_{61.5}S_{3.0}$ (undistilled) + 500 ppmw Dy (*foil*)</td><td>Not evaluated</td><td>↗</td></tr>
<tr><td>M227RERC
(F099RERC)</td><td>Single material fibre</td><td>$Ge_{19.4}Sb_{9.7}Ga_{3.0}Se_{67.9}$ (undistilled) + 1000 ppmw Sm (*foil*)</td><td>2.36 ± 0.13
(Figure 3-32)</td><td>None</td><td colspan="2">Not evaluated</td></tr>
<tr><td>M285RERC
(F125RERC)</td><td>Single material fibre</td><td>$Ge_{15.0}As_{21.0}Ga_{1.0}Se_{63.0}$ + 850 ppmw $TeCl_4$ (distilled) + 500 ppmw Dy (*foil*)</td><td>2.07 ± 0.33
(Figure 3-33)</td><td>None</td><td colspan="2">Not evaluated</td></tr>
</table>

*Note, the NA of the co-extruded rod E094REDF(JN) was estimated to be 0.47 based on the identical composition of the core and cladding glass to SIF F122REJN.

The spectroscopic analysis of these glass compositions showed how the vacuum distillation purification process on the reduced the minimum optical loss. This analysis also revealed the advantages of lower 'Ga' content and simpler glass compositions on the minimum optical loss.

The production of each of RE^{3+} doped glass sample presented in Sections 3.2.1 to 3.2.7 revealed the presence of internal defects such as unwanted impurities, debris, bubbles of various sizes, heterogeneous nucleation, and heterogeneous crystals in each bulk glass sample prepared in a 10/14 silica ampoule. Furthermore, defects such as striae within the cladding and holes at the core/cladding interface were found in each SIF sample prepared using the 'rod-in-tube' method (see Section 7.1.12). These results indicated systemic deficiencies with both the production and fabrication methodologies that were not limited to RE dopant, or glass composition. Notably, the discovery of these flaws initiated the development of the IR imaging described in Section 3.1.2.2. Several modifications to the current methodologies to mitigate these defects were proposed in Section 6.1. Additionally, coextrusion of core and cladding glass was demonstrated (see Section 3.2.6.2) to minimise defects at core/cladding interface in a step-index glass rod.

4. Spectroscopy of trivalent rare-earth doped chalcogenide glasses:

This chapter presents the spectroscopy measurements of five trivalent lanthanide dopants, namely: 'Ce' (*cerium*), 'Pr' (*praseodymium*), 'Sm' (*samarium*), 'Tb' (*terbium*), and 'Dy' (*dysprosium*) each incorporated into a separate chalcogenide host glass. Section 4.1 describes the methodology employed to perform PL (*photoluminescence*) emission measurements, and ESA (*excited state absorption*) measurements on RE^{3+} doped chalcogenide glass samples, along with the procedure for evaluation and interpretation of the empirical results. Section 4.2 presents for each lanthanide dopant, PL emission measurements, and ESA measurements, along with a brief literature survey on RE^{3+} PL emissions and a discussion on the presented results. Section 4.3 summarizes the presented results.

4.1. Measurement methodology.

Section 4.1.1 describes the methodology employed to perform PL emission measurements while Section 4.1.2 introduces ESA measurements which used a novel variation on the 'pump-probe' technique, devised and implemented by the author and the Mid-Infrared Photonics Group, to reveal latent MIR ESA bands in RE^{3+} doped into chalcogenide glass fibre with.

4.1.1 PL (*photoluminescence*) emission spectroscopy.

RE^{3+} PL emission spectroscopy measurements were achieved via photoexcitation of RE^{3+} doped chalcogenide glass samples using an excitation laser with a wavelength overlapping a RE^{3+} GSA band while evaluating the resulting PL. These emission measurements were performed on RE^{3+}

doped glass samples with different geometries primarily to investigate PL emission spectra and lifetimes, while evaluating the effects of reabsorption and up-conversion. Sample types included polished bulk glass, powdered glass, and SIF (*step-index fibre*) and single material fibre.

4.1.1.1 Equipment configuration:

PL emission spectra, and PL emission lifetimes were the two types of measurements performed on RE^{3+} doped samples. This entailed photoexcitation of a sample, with either a CW (*continuous wave*) or a QCW (*quasi-continuous wave*) excitation source, while evaluating the RE^{3+} PL emitted. PL spectra were emission intensity measurements, as a function of wavelength. PL lifetimes were intensity measurements of a decaying PL emission signal, after turning off the pump laser, as a function of time. Figure 4-1 shows a detailed parts list and diagram of the equipment configurations used to perform these measurements. In each configuration the RE^{3+} doped samples were exposed to an excitation source, and the resultant PL emissions, emanating from the sample were collected and evaluated. These PL emission measurements employed different equipment configurations for each combination of sample type and excitation source. Each configuration was sub-divided into four major subsections, namely:

1. Launch optics: The excitation lasers employed in the various equipment configurations were either fibre-coupled or open beam and each type required different supplemental optical components to efficiently excite the sample. Insets **A** to **E**, in Figure 4-1, illustrate how pump light from the different types of lasers was delivered to the sample. Appendix 7.2.4.1 describes the procedure used to achieve this.

2. <u>The Sample</u>: PL emission measurements could be performed on fibres, powdered glass, or bulk glass samples. Each sample type required specific preparation, followed by fixturing and mounting within the equipment configuration. Appendix 7.2.4.2 describes the procedure used to prepare and mount each sample type. Additionally, insets **F** to **H**, in Figure 4-1 illustrates how each sample was mounted. Powdered samples were ground to a mostly uniform particle diameter and sealed, while under an inert N_2 atmosphere, in a 3D printed powder sample holder equipped with CaF_2 windows (*designed by the author and 3D printed by Dr David Furniss*). The powdered glass was kept sealed to avoid oxidation, absorption, and adsorption of water and other atmospheric molecules.
3. <u>Collection/detection</u>: PL emissions emanating from a sample were collected, separated into their constituent wavelengths, and evaluated. Inset **I**, in Figure 4-1, illustrates how this was achieved and Appendix 7.2.4.3 describes in detail how this was done.
4. <u>Control/data acquisition</u>: This shows how the components in the equipment configuration were connected and how measurement parameters such as modulation source/frequency, wavelength selection, and storage of captured data were controlled. Wavelength selection of the emissions emanating from the samples was accomplished using a monochromator, item 15(a) in Figure 4-1, which was controlled by a data acquisition computer, item 18 in Figure 4-1, running MATLAB software written by the author (*see url: https://github.com/joel-nunes/Monochromator-control-and-data-acquisition.git*). This software automated the wavelength selection of the monochromator and storage of captured data. Inset **J**, in Figure 4-1, illustrates these connections, and Appendix 7.2.4.4 describes how this was done.

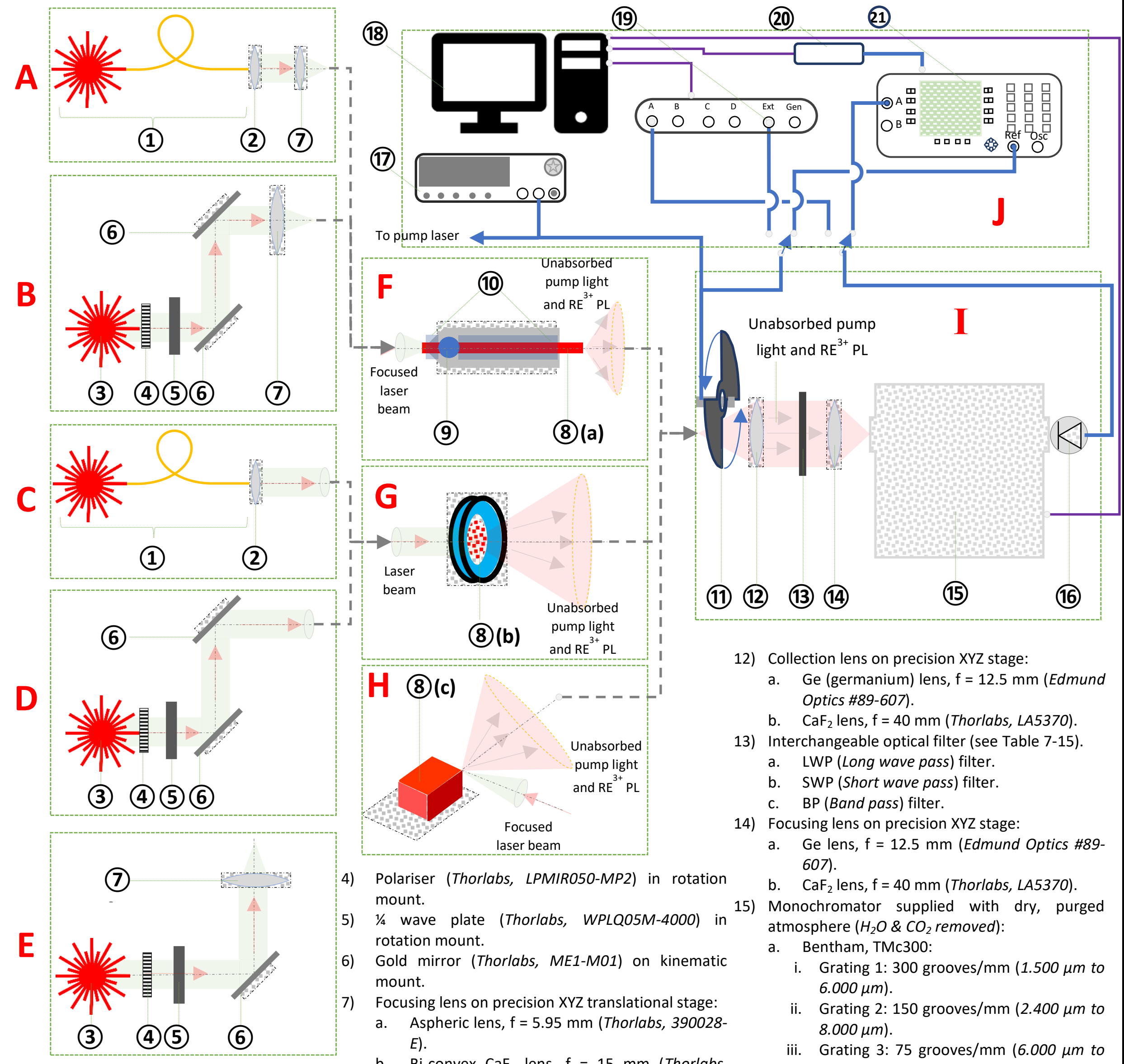

1) Fibre coupled excitation laser:
   a. Tuneable source (*Agilent, 8164B + 8198- tuneable module, with EDFA: IRE-POLUS EAD-2W-C*).
   b. 1.700 µm source (*QPC Lasers Inc. BrightLase® PR-6017-0000*).
   c. 1.940 µm source (*m2K-BA-1940-E0500-MMF200_IG10*).
   d. 2.013 µm source (*LISA lasers products, FG-E 0380*).
   e. 1.310 µm source (*Thorlabs, FPL1053S*)
2) Collimator on a XYZ translational stage:
   a. Thorlabs, F220APC-1550 used with tunable and 1.310 µm sources.
   b. Ocean Optics, 74-VIS used with the 1.700 µm, 1.940 µm, and 2.013 µm sources.
3) Open beam 4.150 µm QCL (*Pranalytica, 1101-42-CW-2500LH*).
4) Polariser (*Thorlabs, LPMIR050-MP2*) in rotation mount.
5) ¼ wave plate (*Thorlabs, WPLQ05M-4000*) in rotation mount.
6) Gold mirror (*Thorlabs, ME1-M01*) on kinematic mount.
7) Focusing lens on precision XYZ translational stage:
   a. Aspheric lens, f = 5.95 mm (*Thorlabs, 390028-E*).
   b. Bi-convex CaF$_2$ lens, f = 15 mm (*Thorlabs, LB5766-E*).
8) RE^{3+} doped chalcogenide glass sample:
   a. Single material fibre or SIF sample, with both ends cleaved on Stainless steel 'V-groove' fibre holder on XYZ stage.
   b. Powdered glass in sample holder fitted with two CaF$_2$ windows (*Crystran, CAFP20-1*) on XYZ stage.
   c. Cuboid shaped, polished bulk glass sample on XYZ stage.
9) Fibre mount:
   a. Magnets.
   b. UV curable polymer.
10) Optional coating of Galinstan (*InGaSn alloy*) for cladding mode-stripping. Note this was only used on SIF samples mounted with UV polymer.
11) Optional optical chopper (*Bentham, S200_218_H*). Note this only used for RE^{3+} PL emission spectra measurements.
12) Collection lens on precision XYZ stage:
    a. Ge (germanium) lens, f = 12.5 mm (*Edmund Optics #89-607*).
    b. CaF$_2$ lens, f = 40 mm (*Thorlabs, LA5370*).
13) Interchangeable optical filter (see Table 7-15).
    a. LWP (*Long wave pass*) filter.
    b. SWP (*Short wave pass*) filter.
    c. BP (*Band pass*) filter.
14) Focusing lens on precision XYZ stage:
    a. Ge lens, f = 12.5 mm (*Edmund Optics #89-607*).
    b. CaF$_2$ lens, f = 40 mm (*Thorlabs, LA5370*).
15) Monochromator supplied with dry, purged atmosphere (*H_2O & CO_2 removed*):
    a. Bentham, TMc300:
       i. Grating 1: 300 grooves/mm (*1.500 µm to 6.000 µm*).
       ii. Grating 2: 150 grooves/mm (*2.400 µm to 8.000 µm*).
       iii. Grating 3: 75 grooves/mm (*6.000 µm to 20.000 µm*).
    b. Spex Minimate with diffraction grating blazed at 6.000 µm.
16) Detector on XYZ stage:
    a. InGaAs (*Thorlabs, PDA10D-EC*) (*1.200 to 2.600 µm spectral range*).
    b. MCT (mercury cadmium telluride) detector (*Vigo Systems, PVI-4TE-6*) (*2.000 to 7.500 µm spectral range*).
    c. Liquid nitrogen cooled MCT detector (*Kolmar Technologies, V100-1B-7/190*) (2.500 *to 11.000 µm spectral range*).
17) Function generator (*GW Instek, SFG-2104*) or (*Picoscope, 5444b*).
18) Control and data acquisition computer.
19) USB oscilloscope (*Picoscope, 5444b*).
20) National Instruments USB-6009 multifunction I/O.
21) Lock-in amplifier (*Ametek Signal Recovery, 7270 DSP*).

Figure 4-1: Equipment configurations used for RE^{3+} PL emission measurements.

4.1.1.2 PL spectrum measurements:

PL spectrum measurements evaluated the emission intensity from the samples, over a user defined spectral range, as a function of wavelength. The PL emission spectrum was obtained by taking intensity measurements on the emitted RE^{3+} PL, at uniform wavelength intervals, using the procedure described in Appendix 7.2.4.5. These intensity measurements were then plotted against wavelength to produce the PL emission spectrum. The resulting PL emission spectrum was then corrected for the system spectral response unless specified otherwise.

4.1.1.3 PL lifetime measurements:

PL lifetime measurements evaluated the PL emission intensity from the samples, at a fixed user defined wavelength, as a function of time. The PL lifetime spectrum was obtained by taking intensity measurements on a narrow spectral range of RE^{3+} PL light (*typically less than 50 nm in spectral width*), at uniform time intervals, using the procedure described in Appendix 7.2.4.6. These intensity measurements were then plotted against time and then fitted to a suitable exponential decay function to determine the PL emission lifetime(s) at a specific wavelength.

Several of the RE^{3+} dopants exhibited multiple PL emission bands having similar or overlapping wavelengths emanating from different energy levels, each with a distinct 'τ_{rad}' (see Figure 2-1 (f)). This resulted in PL emissions at specific wavelength regions comprised of a mixture of radiative lifetimes. Thus, multi-term exponential fitting was applied to empirical PL intensity data using a modified version of Equation 2-2 in MATLAB using the non-linear least squares method for a multi-term exponential function of the following form:

$$I(t) = \left(\sum_{j=1}^{n} A_j \times exp^{\left(\frac{-t}{\tau_j}\right)} \right) + Y_0 \qquad \textit{Equation 4-1}$$

where ‘n’ is the number of exponential terms used to fit the empirical data; ‘A_j’ are the non-zero coefficient(s) of each exponential term that expressed the fraction of the contribution to the overall exponential process; ‘τ_j’ are the radiative lifetimes of each exponential term, and ‘Y_0’ is a constant relating to the SNR of the detection system.

Single-term (*n = 1*), two-term (*n = 2*), and three-term (*n = 3*) exponential functions were individually fitted to the measurement data and the RMSE (*root mean square error*) of these fittings were then compared. The fitting with both the lowest RMSE and lowest number of exponential terms, was then selected as the lifetime to avoid under-fitting or over-fitting. This was done to best fit the lifetime data, while also accounting for confounding factors such as sample geometry, pump power density and any idiosyncrasies in the emission behaviour [32,167].

PL emission ‘rise time’ measurements were carried out on a few samples. These measurements were accomplished in a near identical manner to the lifetime measurement using the procedure described in Appendix 7.2.4.6. The ‘rise time’ was defined as the time for the PL emission intensity to rise from 10 % to 90 % of the peak emission intensity, according to [168].

4.1.2 ESA (excited state absorption) measurements.

Transmission spectroscopy, employing a novel variation on the ‘pump-probe’ technique, was used to investigate the ESA behaviour of RE^{3+} doped chalcogenide glass fibre samples. In this technique, a CW (*continuous wave*) excitation laser, the ‘pump’, and a broadband blackbody light source, the 'probe', were simultaneously launched into a fibre sample. The wavelength of the pump was chosen such that it coincided with a RE^{3+} GSA, resulting in the temporary redistribution of a portion of the ground state electronic population to upper energy levels. This enabled subsequent optical absorption of the probe light by the electron population in these excited levels, resulting in relative changes in the transmission spectrum of the sample during pump excitation. A FTIR (*Fourier transform infrared*) spectrometer was then used to detect changes in the transmission spectrum. Single material fibre samples were used to maximise the changes in the transmission spectrum over the length of the sample. Notably, the equipment configuration described in Section 4.1.2.1 differed from prior equipment configurations found in the literature [42,43], which use a double modulation scheme, because of the inclusion of this FTIR spectrometer. The FTIR spectrometer in the presented equipment configuration affords convenient, rapid, low-noise assessment of the RE^{3+} ESA bands, over a relatively large spectral bandwidth, due to its speed, wide wavelength range, and stability. To the best of my knowledge this is the first example of an FTIR spectrometer being used to evaluate latent ESA in this manner. Note, the advantages and disadvantages of this equipment configuration are discussed further in Section 4.2.6.3. Additionally, a monochromator-based equipment configuration capable of ESA measurements is evaluated in Section 4.2.2.4.

4.1.2.1 FTIR (Fourier transform infrared)-based ESA equipment configuration:

The ESA measurement equipment configuration examined static lengths of RE^{3+} doped fibre by simultaneously exposing it to 'pump' and 'probe' light in a counter-propagating configuration. A detailed parts list and diagram of the ESA measurement equipment configuration are shown in

Figure 4-2. A FTIR spectrometer, item 11 in Figure 4-2, provided and analysed modulated broadband ‘probe light’ transmitted through the fibre sample with and without the application of ‘pump light’ from a CW excitation laser, item 1 in Figure 4-2. A beam of modulated, broadband probe light, from the FTIR spectrometer, was focused on to the ‘probe-launch-end’ of the fibre sample. A LWP (*long wave pass*) filter, item 4 in Figure 4-2, acting as a long-pass dichroic mirror, was used to reflect a collimated beam of CW pump-light, which was then focused onto the opposite, ‘pump-launch-end’ of the fibre sample, which was mounted in a stainless-steel V-groove fibre-holder, item 6 in Figure 4-2. Thermal management of the ‘pump launch end’ of the fibre sample was done by minimising fibre-overhang beyond the edge of the metal V-groove fibre holder, which also acted as a heatsink. The LWP filter, acting as a long-pass dichroic mirror, was selected to reflect at the pump wavelength, while simultaneously passing probe light transmitted through the fibre sample, along with RE^{3+} PL emissions emanating from the fibre sample. A 2.505 µm LWP filter was used to transmit the 2.300 to 6.300 µm spectral region, while a 6.386 µm LWP filter was used for the 7.000 to 11.500 µm spectral region, the 45° incidence angle of these items caused them to operate slightly outside of their specifications. The transmitted probe light and RE^{3+} PL were then focused onto an MCT detector, item 2 in Figure 4-2. A FTIR interferogram based on the intensity of the incident modulated light was measured with a resolution of 4 cm^{-1} using Bruker OPUS software. Unmodulated spontaneous RE^{3+} PL, emanating from the fibre sample during the application of the CW pump, was ostensibly ignored by the FTIR spectrometer due to frequency discrimination afforded by its principles of operation, see [169,170]. However, RE^{3+} PL emissions stimulated by the modulated FTIR ‘probe light’ would still have been detected.

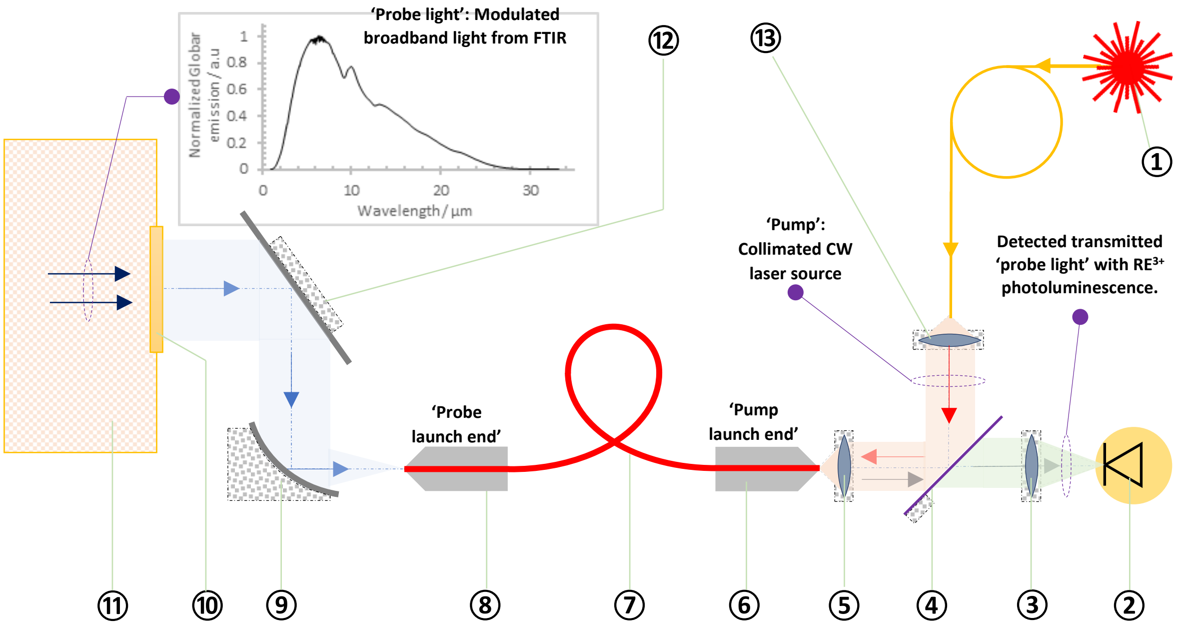

1) CW (*continuous wave*) 'Pump': Fibre coupled excitation laser:
   i. 1.550 µm and 1.535 µm source (*Agilent 8164B + 8198- tuneable module, amplified using an EDFA: IRE-POLUS EAD-2W-C*).
   ii. 1.940 µm source (*m2K-BA-1940-E0500-MMF200_IG10*).
   iii. 1.700 µm source (*QPC Lasers Inc. BrightLase® PR-6017-0000*).
2) Liquid nitrogen cooled MCT (*mercury-cadmium-tellurium 'Hg-Cd-Te'*) detector (*Kolmar Technologies, V100-1B-7/190*), connected to Bruker IFS 66/S FTIR (*Fourier transform infrared*) spectrometer.
3) Aspheric 'Ge' germanium lens, f = 12.5 mm (*Edmund Optics, 89607*) on a translational stage.
4) Dichroic mirror on a kinematic mount:
   i. 2.505 µm LWP (*Long Wave Pass*) filter (*Northumbria Optical Coatings, SLWP-2505-001089*).
   ii. 6.386 µm LWP filter (*Northumbria Optical Coatings, SLWP-6386-000297*).
5) Aspheric lens, f = 5.95 mm (*Thorlabs, 390028-E*) on a XYZ translational stage.
6) Stainless steel 'V-groove' fibre holder, 82 mm long, providing heatsinking.
7) RE^{3+} (*rare-earth)* ion doped chalcogenide glass fibre sample, with both ends cleaved.
8) Stainless steel 'V-groove' fibre holder, 40 mm long.
9) Aluminium 90° 'Off-axis' parabolic mirror, f = 69 mm on a kinematic mount.
10) 'KBr' (*potassium bromide*) window 2 mm thick.
11) Bruker IFS 66/S FTIR spectrometer equipped with Globar© source and 'KBr' beam splitter, using Bruker OPUS software (*version 3.1 build 3,0,19*), (See Figure 7-12).
12) Aluminium mirror on a kinematic mount.
13) Collimator on a XYZ translational stage:
   i. Thorlabs, F220APC-1550 used with 1.550 µm and 1.535 µm sources.
   ii. Ocean Optics, 74-VIS used with the 1.94 µm and 1.700 µm sources.

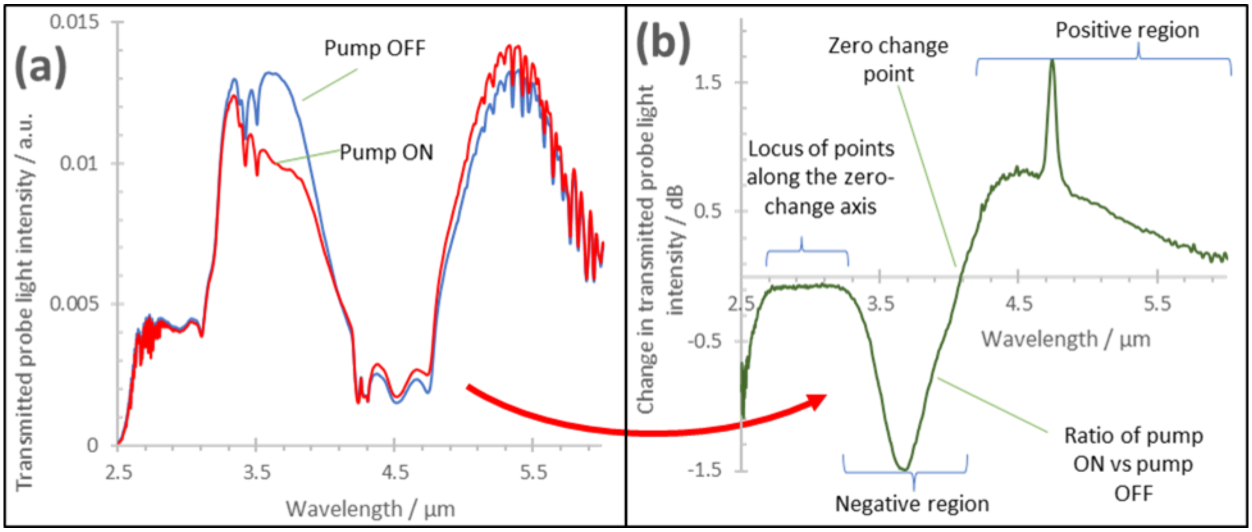

Figure 4-2: Diagram of 'pump and probe' equipment configuration used to investigate ESA (excited state absorption) in RE^{3+} (rare-earth) cation doped, chalcogenide glass fibres, with inset showing emission spectrum of broadband IR source used as the probe light source. Along with plots showing an example of: ***(a)*** *transmitted probe light intensity spectrum obtained from illustrated equipment configuration, and* ***(b)*** *change in transmitted probe light intensity obtained from inset (a) using Equation 4-2.*

Steady state changes in the intensity of transmitted probe light were evaluated by taking the ratio of the measured transmission spectra with, and without, the application of pump light (*see inset (a) in Figure 4-2*), and plotted as 'change in transmitted probe light intensity' versus wavelength, using the following equation (*see inset (b) in Figure 4-2*):

$$Change\ in\ probe\ intensity\ (dB) = 10 \times log_{10}\left(\frac{Probe\ intensity\ with\ pump\ light\ on}{Probe\ intensity\ with\ pump\ light\ off}\right) \qquad \text{Equation 4-2}$$

4.1.2.2 Interpretation of ESA measurements:

The ESA spectra derived from Equation 4-2 plotted the 'change in transmitted probe light intensity' versus wavelength (*see inset (b) in Figure 4-2*). These spectra depict the relative changes in the optical attenuation of doped fibre samples during pumping as experienced by the broadband probe light. The following are some common features in ESA spectra:

- Regions of negative change: These indicated an increase in attenuation. Upward transitions originating from latent ESA bands, occurring only during photoexcitation, increase the attenuation of the RE^{3+} dope sample within specific spectral regions due to the presence of an excited electron population. The RE^{3+} energy levels with the longest radiative lifetimes were postulated as the predominant initial state from which ESA took place because they had a higher probability of possessing an electronic population.
- Regions of positive change: Indicated a decrease in attenuation. It was postulated that **GSD** (*ground state depletion*), a reduction of the ground state electron population, occurring only during photoexcitation (*especially at very high pump powers*), decreased the attenuation of the RE^{3+} doped sample within the GSA bands. Additionally, RE^{3+} **SE** (*stimulated emission*)

caused by modulated probe light resulted in an apparent decrease in attenuation within the RE^{3+} PL emission bands. Note, in this situation while SE occurred during photoexcitation the attenuation of the sample remained unchanged. Additionally, in most situations, ESA measurements were unable to explicitly differentiate GSD from SE due to the decrease in attenuation that they both caused. Thus, GSD and SE transitions were typically proposed together and were represented using the two half arrowheads to indicate the bidirectional nature of both transitions (*"Initial state"* $\rightleftharpoons$ *"Next state"*).

- A locus of points along the zero-change axis: These were spectral regions that lay along the wavelength-axis on the ESA spectra that indicated the probe light only experienced attenuation from the underlying RE^{3+} doped host glass. This indicated a spectral region with no matching RE^{3+} electronic transitions to interact with incident probe light. Thus, within these regions the magnitude of the optical attenuation in dB/m was available by referencing the corresponding attenuation spectrum of the fibre sample.
- Zero-change point: Spectral regions of negative change which partially overlapped spectral region of positive change always resulted in the occurrence of an 'zero-change' point. These conspicuous points were postulated to be due to a balancing, or equilibrium between, competing photoinduced upward and downward RE^{3+} electronic transitions for a static sample length, such that resultant optical attenuation experienced at these wavelengths equalled that of the RE^{3+} doped glass without the application of the pump source. This was due to these points occurring on the zero-change axis.

4.2. Spectroscopy of RE^{3+} dopants in chalcogenide glass host.

This section presents the absorption and emission spectroscopy measurements of five lanthanide dopants namely: ‘Ce’, ‘Pr’, ‘Sm’, ‘Tb’, and ‘Dy’. These are inclusive of absorption measurements, PL emission measurements, and ESA measurements for each lanthanide dopant. Each Section includes a brief literature survey of the reported PL emissions which is used to put the presented results into context. Section 4.2.6 is a discussion on the absorption, PL emission, and ESA measurements presented. Note the following:

- Fibre samples, powdered glass samples and polished bulk glass samples, were prepared using the procedures described in Section 7.2.4.2.
- Absorption and emission cross-section spectra were calculated using procedure shown in Section 7.2.1.1. Additionally, several of the RE^{3+} absorption cross-section spectra had the underlying [-Se-H] impurity absorption bands numerically removed using the [-Se-H] absorption model derived in Figure 3-33 (b) and the procedure described in [116].
- PL emission measurements, and ESA measurements were carried out by the author, at room temperature between 21 to 23 °C. Additionally, the laboratory humidity and CO_2 concentrations were allowed to vary during measurements.
- PL emission measurements were carried out using the procedure described in Section 4.1.1 and PL lifetime data were fitted with a suitable exponential function, using the procedure described in 7.2.4.6. PL emission spectra presented throughout Section 4.2 were normalised to their peak emission wavelength.
- ESA measurements were accomplished using the FTIR-based equipment configuration shown in Figure 4-2 and the procedure described in Section 4.1.2.

4.2.1 Cerium spectroscopy.

Two separate undistilled, glass rods of nominal composition: $Ge_{15.0}$ $As_{21.0}$ $Ga_{1.0}$ $Se_{63.0}$ atomic % + 500 ppmw Ce (*foil*) M259REZQT, and $Ge_{14.8}$ $As_{20.8}$ $Ga_{2.0}$ $Se_{62.4}$ atomic % + 500 ppmw Ce (*foil*) M293REJN, were independently produced by Dr Zhuoqi Tang and the author, respectively. The M259REZQT glass rod was drawn into single material fibre and cane: F109REZQT(RC&JN). See sections 3.2.2 and 3.2.6 for the optical and compositional evaluation of these glasses. The M259REZQT and M293REJN glass rods were individually processed into two separate bulk glass samples and used for the measurements in Section 4.2.1.1. The F109REZQT(RC&JN) cane was subsequently used as the core in the fabrication of the SIF F113REZQT(JN&RC). M293REJN was subsequently co extruded by Dr David Furniss and the author to produce the co-extruded glass rod E094REDF(JN). Section 4.2.1.3 presents PL emission measurement results from single material fibre F109REZQT(RC&JN), powdered glass (*made using single material fibre F109REZQT(RC&JN)*), SIF (F113REZQT(JN&RC)), polished bulk glass (M259REZQT) and a portion of the extruded rod E094REDF(JN). Note, Ce^{3+} ESA measurements were omitted due to the limitations of the current equipment configuration, as discussed in Section 4.2.6.3.

4.2.1.1 Ce cation absorption and emission cross-sections:

Figure 4-3 (a) shows the absorption coefficient for two nominally 500 ppmw Ce (*foil*) doped bulk glass samples M259REZQT, and M293REJN, each ostensibly containing 9.56 × 10^{18} cations/cm^3 and 9.67 × 10^{18} cations/cm^3, respectively. Figure 4-3 (b) shows the corresponding Ce^{3+} preliminary energy level diagram. Figure 4-3 (c) shows the calculated absorption cross-section for the $^2F_{5/2} \rightarrow {}^2F_{7/2}$ GSA and the emission cross-section for the $^2F_{7/2} \rightarrow {}^2F_{5/2}$. Note, the underlying [-Se-H] impurity vibrational absorption bands at 3.5 and 4.5 µm were not numerically removed.

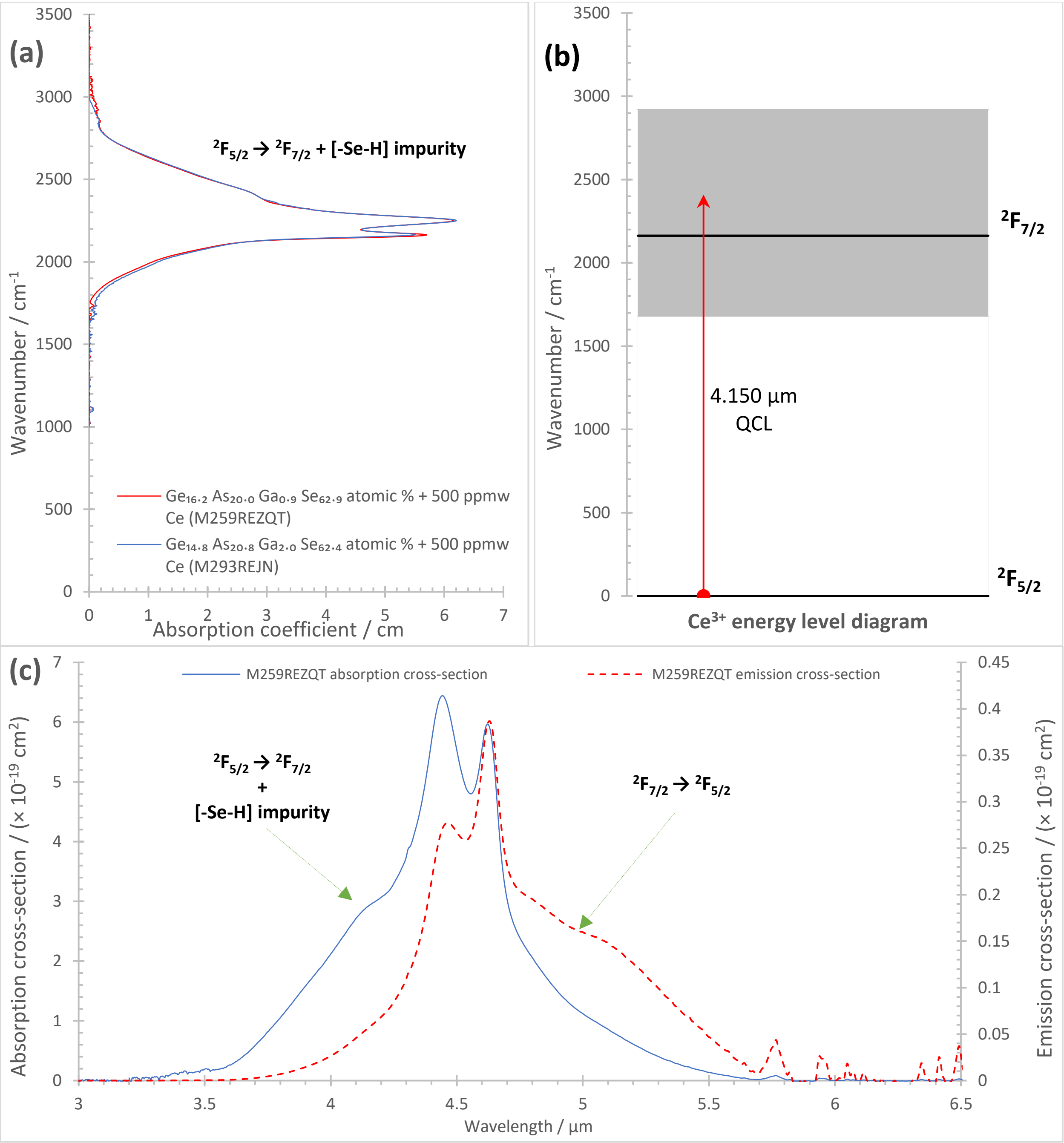

*Figure 4-3: Showing: **(a)** Room temperature absorption spectrum of two undistilled nominally 500 ppmw Ce (foil) doped bulk glass samples along with **(b)** the corresponding energy level diagram for Ce^{3+} cation in glass host showing 4.150 µm QCL, and **(c)** showing the calculated absorption (solid lines) and emission (dashed lines) cross-sections. Note, the Ce^{3+} cross-section calculations assumed several factors (see Section 3.2.8.2 and 4.2.6.1) and thus its accuracy should not be relied upon.*

4.2.1.2 Ce^{3+} literature review:

The Ce^{3+} cation has an electronic configuration consisting of a $^2F_{5/2}$ ground state and a single $^2F_{7/2}$ excited state, both of these manifolds are known to exhibit extensive Stark splitting in a variety of host materials [155–158]. The luminescent properties of 'Ce' compounds often focus on their ultraviolet and visible emissions due to 5d→ 4f radiative transitions [20,155,171–173]. The dearth of affordable pump sources to excite the $^2F_{7/2}$ manifold results in a relative lack of publications on the MIR properties of the 'Ce' dopant. Table 4-1 and Table 4-2 show that the Ce^{3+} cation exhibits only one broad MIR PL emission band peaking at ~ 4.6 µm with a relatively long radiative lifetime in both arsenic-based and antimony-based chalcogenide glass compositions. Notably, the 'Ce' dopant can exhibit a stable tetravalent state, Ce^{4+} [19–21] for example in the form CeO_2. Moreover, 'Ce^{4+}' possesses an electronic configuration of [Xe], with no available '4f' electrons for 4f $\rightleftharpoons$ 4f transitions, thus is unlikely to exhibit MIR PL.

Table 4-1: Ce^{3+} PL emission bands found in literature (see Figure 4-3 (b) for energy level diagram):

Transition	**Composition / sample type**	**Pump λ / µm**	**Emission band range / µm**	**Peak λ / µm**	**Reference**
$^2F_{7/2} \rightarrow {}^2F_{5/2}$	$Ge_{15.0}As_{21.0}Ga_{1.0}Se_{63.0}$ 500 ppmw Ce (*foil*) (*single material fibre*)	4.150	3.4 to 5.9	~ 4.6	[140]
$^2F_{7/2} \rightarrow {}^2F_{5/2}$	$Ge_{20.0}Sb_{10.0}Ga_{5.0}Se_{65.0}$ Ce^{3+} @ 3.1×10^{19} cm^{-3} (*Polished plate*)	2.940 or Dy^{3+} PL	3.5 to 6.0	~ 4.6	[174]

Table 4-2: Ce^{3+}PL emission lifetimes found in literature (see Figure 4-3 (b) for energy level diagram):

Transition		**Host composition / sample type**	**Calculated τ_{rad} / ms**	**Measured τ_{rad} / ms**	**Reference**
From	**To**				
$^2F_{7/2}$	$^2F_{5/2}$	$Ge_{15.0}As_{21.0}Ga_{1.0}Se_{63.0}$ + 500 ppmw Ce (*foil*) (*single material fibre*)	Not reported	3.6	[140]
$^2F_{7/2}$	$^2F_{5/2}$	$Ge_{20.0}Sb_{10.0}Ga_{5.0}Se_{65.0}$ Ce^{3+} @ 3.1×10^{19} cm^{-3} (*Polished plate*)	Not reported	2.5	[174]

4.2.1.3 Ce^{3+} PL emission measurements:

Ce^{3+} PL emission spectrum, PL lifetime and PL rise time measurements were performed using in-band pumping with a 4.150 µm QCL on the samples listed in Table 4-3. The 4.150 µm excitation scheme used the $^2F_{5/2} \rightarrow {}^2F_{7/2}$ GSA, as illustrated in Figure 4-3 (b).

Table 4-3: Sample codes, composition, dimentions, and equipment configurations used for Ce^{3+} PL emission measurements (see Section 7.3 for description of equipment configuration code).

Sample type	Code and nominal composition (atomic %)	Dimensions	Figure and equipment configuration
Bulk glass (*annealed and polished*)	**M259REZQT** ($Ge_{15.0} As_{21.0} Ga_{1.0} Se_{63.0}$ + *500 ppmw Ce (foil)*)	4.54 mm × 3.76 mm × 2.02 mm.	Figure 4-4 (a) and Figure 4-5 (a): **E**[7_b] **H**[] **I**[12_a- $13_{4.203}$ LWP- 14_b -15_b – 16_b]
Single material fibre (*un-annealed*)	**F109REZQT(JN&RC)** ($Ge_{15.0} As_{21.0} Ga_{1.0} Se_{63.0}$ + *500 ppmw Ce (foil)*)	Diameter of 220 ± 5 µm and 93.4 mm long.	Figure 4-4 (a) and Figure 4-5 (c): **B**[7_a] **F**[9_a] **I**[12_a- $13_{4.203}$ LWP- 14_b -15_b – 16_b]
Powdered glass (*single material fibre, un-annealed*)	**F109REZQT(JN&RC)** ($Ge_{15.0} As_{21.0} Ga_{1.0} Se_{63.0}$ + *500 ppmw Ce (foil)*)	Varying granule size < 100 µm in diameter.	Figure 4-4 (a) and Figure 4-5 (e): **D**[] **G**[] **I**[12_a- $13_{4.203}$ LWP- 14_b -15_b – 16_b]
SIF (*un-annealed*)	**F113REZQT(RC&JN)**: (Core: **F109REZQT(JN&RC)**: $Ge_{15.0} As_{21.0} Ga_{1.0} Se_{63.0}$ + *500 ppmw Ce (foil)* Cladding **M260JN**: $Ge_{16.5} As_{16.0} Ga_{3.0} Se_{61.5} S_{3.0}$)	Core diameter of 21 ± 0.5 µm, 237 ± 3.0 µm OD and 90.0 mm long.	Figure 4-4 (a) and Figure 4-5 (b): **B**[7_a] **F**[9_b- 10] **I**[12_a- $13_{4.203}$ LWP- 14_b -15_b – 16_b]
SIF (*un-annealed*)	**F130RERC**: (Core: **F109REZQT(JN&RC)**: $Ge_{15.0} As_{21.0} Ga_{1.0} Se_{63.0}$ + *500 ppmw Ce (foil)* Cladding **M287RC**: $Ge_{21.0} Sb_{10.0} Se_{69.0}$)	Core diameter of 17 µm, OD and 95.0 mm long.	Figure 4-4 (a) and Figure 4-5 (b): **B**[7_a] **F**[9_b- 10] **I**[12_a- $13_{4.203}$ LWP- 14_b -15_b – 16_b]
Co-extruded glass rod (*annealed and polished*)	**E094REDF(JN)**: (Core: **M293REJN:** $Ge_{14.8} As_{20.8} Ga_{2.0} Se_{62.4}$ + *500 ppmw Ce (foil)* Cladding: **M295REJN**: $Ge_{16.5} As_{16.0} Ga_{3.0} Se_{61.5} S_{3.0}$ *+ 500 ppmw Dy (foil)*)	9.1 mm long with a 3.2 mm outer diameter. Maximum core diameter: 1.88 mm.	Figure 4-4 (a) and Figure 4-5 (d): **B**[7_a] **F**[9_{none}] **I**[12_a- $13_{4.203}$ LWP- 14_a -15_{aii} – 16_b]

4.2.1.3.a Ce^{3+} PL emission spectra:

The 4.150 µm excitation scheme used for each sample type, listed in Table 4-3, consistently yielded a broad Ce^{3+} PL emission spectrum between 3.400 to 5.800 µm, and peaked around 4.60 µm, attributed to the $^2F_{7/2} \rightarrow {}^2F_{5/2}$ radiative transition, as shown in Figure 4-4. A portion of the emission spectrum between 3.900 to 4.400 µm in Figure 4-4 was omitted due to the presence of unabsorbed 4.150 µm QCL light. Notably, Figure 4-4 shows that a portion of this emission spectrum exhibited up-conversion, resulting in Ce^{3+} PL emissions at wavelengths as short as 3.400 µm. Additionally, the presented Ce^{3+} PL emission spectra agrees with other MIR Ce^{3+} PL spectra found in [174] and the shape of the calculated emission cross-section in in Figure 4-3 (c).

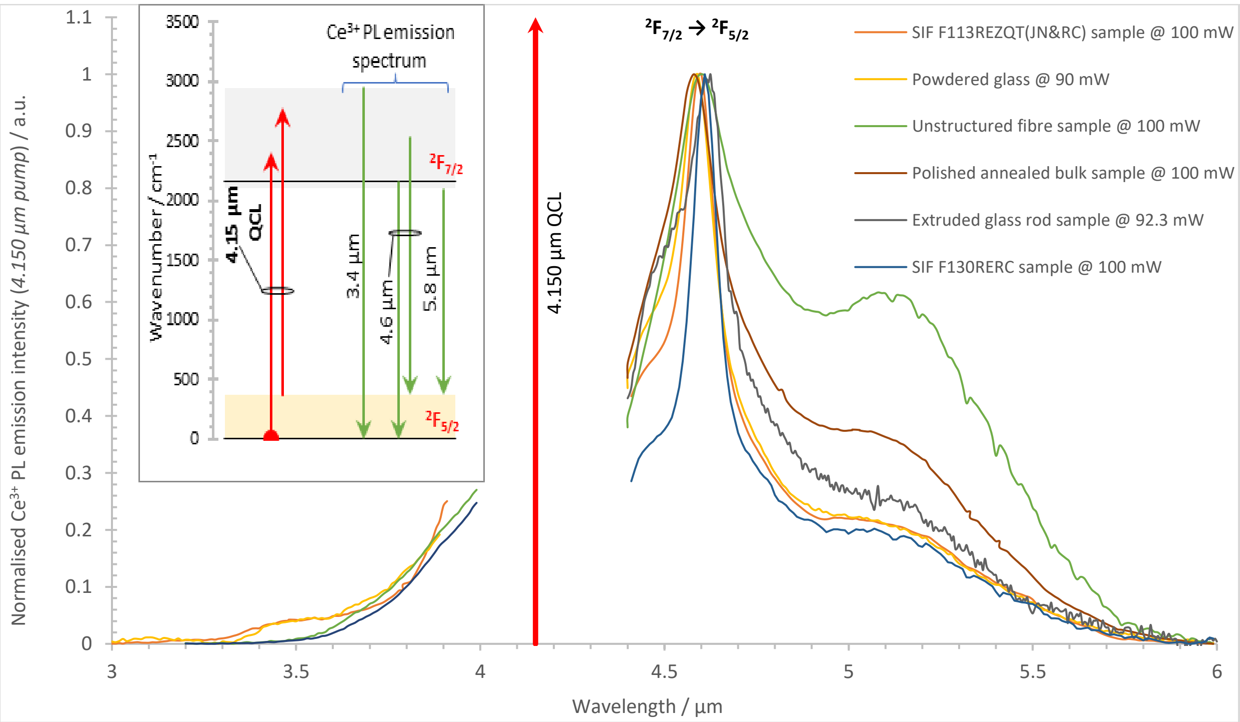

Figure 4-4: Normalised PL emission spectra for nominally 500 ppmw Ce (foil) doped samples, see Table 4-3, each excited with 4.150 µm QCL along with inset showing the corresponding Ce^{3+} energy level diagram showing photoexcitation and subsequent Ce^{3+} PL emission. Not corrected for system spectral response. Note, the bulk glass, single material fibre, powdered glass, and the core of the SIF sample each have the same $Ge_{15.0}As_{21.0}Ga_{1.0}Se_{63.0}$ atomic % composition, while the co-extruded rod had a $Ge_{14.8}As_{20.8}Ga_{2.0}Se_{62.4}$ atomic % composition, for geometry of each sample type.

The Ce^{3+} energy level diagram inset into Figure 4-4 was derived from Ce PL emission spectrum, this was necessary to account for the Stark splitting in the $^2F_{5/2}$ ground state reported in [155–158]. Optical absorption of the 4.150 µm QCL occurred throughout the $^2F_{5/2}$ ground state manifold, causing the upper portions of the $^2F_{7/2}$ manifold to be excited, as illustrated in the inset of Figure 4-4. The 3.400 Ce^{3+} PL µm originated from the uppermost boundary of the $^2F_{7/2}$ manifold. The PL emission around 4.600 µm could occur from the lower portion of the $^2F_{7/2}$ manifold to the $^2F_{5/2}$ ground state. The PL emission around 5.800 µm could occur from the lowest portion of the $^2F_{7/2}$ manifold to the uppermost portion of the $^2F_{5/2}$ ground state. Notably, the presented Ce^3+ energy level diagram differs from the bulk absorption spectrum shown in Figure 4-3, due to the constraints imposed by the width of the $^2F_{5/2}$ ground state, which caused the lower boundary of the $^2F_{7/2}$ manifold to deviate from the bulk absorption measurement.

The shapes of the PL emission spectra in Figure 4-4 obtained from the samples listed in Table 4-3, the samples possessing the $Ge_{15.0}$ $As_{21.0}$ $Ga_{1.0}$ $Se_{63.0}$ atomic % glass composition showed no significant difference with the co-extruded glass rod and its $Ge_{14.8}$ $As_{20.8}$ $Ga_{2.0}$ $Se_{62.4}$ atomic % glass composition. The single material fibre sample showed signs of reabsorption, around 5.100 µm (*1961 cm^{-1}*). Conversely, both the powdered sample and the SIF sample did not exhibit reabsorption in this spectral region due to their short propagation lengths, (*See Section 3.2.2.2 for the shortcomings of the SIF sample*). Interestingly, the polished bulk sample showed signs of reabsorption despite the steps taken to minimise specular reflections described in Appendix 7.1.7. Thus, it was speculated that this reabsorption was due to diffused Fresnel reflections of PL emissions emanating from the interior of the bulk sample.

4.2.1.3.b Ce^{3+} PL lifetime and risetime results:

PL emission lifetime 'τ_{rad}' and PL rise time measurements were performed on the samples listed in Table 4-3, using in-band pumping with a 4.150 µm QCL modulated at 12 Hz. Figure 4-5 shows the normalised Ce^{3+} PL emission decay from each sample type was measured at wavelengths of 3.800 µm, 4.600 µm and 5.200 µm along with a corresponding fitted exponential function. Note, the 'τ_{rad}' at 3.80 µm and 5.2 µm, for the powdered glass sample, was not measured due to poor PL signal intensity. The Ce^{3+} PL 10 % to 90 % rise time measurement procedure was performed on each sample type and Table 4-4 lists both the PL lifetimes and rise times for each sample type. The $^2F_{7/2} \rightarrow {}^2F_{5/2}$ PL lifetimes and rise time, measured at wavelengths of 3.800 µm, 4.600 µm, and 5.200 µm, exhibited little variation with each other when considering only a single sample type at a time, as shown in Figure 4-5 and Table 4-4. This consistency in PL lifetimes and rise times within a single sample type, was present for each sample type, excluding the powdered sample. This indicated a consistent temporal behaviour of optical absorption the various Stark levels in the $^2F_{5/2}$ ground state, and subsequent spontaneous emissions from various Stark levels in the $^2F_{7/2}$ manifold, as illustrated in the inset of Figure 4-4. PL lifetimes and rise times results varied between sample types.

The lifetimes obtained from the bulk glass, SIF, powdered glass, single material fibre, and co-extruded rod samples all differed slightly from one another, while rise times differed significantly between sample types, as shown in Table 4-4. These differences indicated an influence possibly due to differences in stress/strain, composition, and pump energy density in the sample geometry.

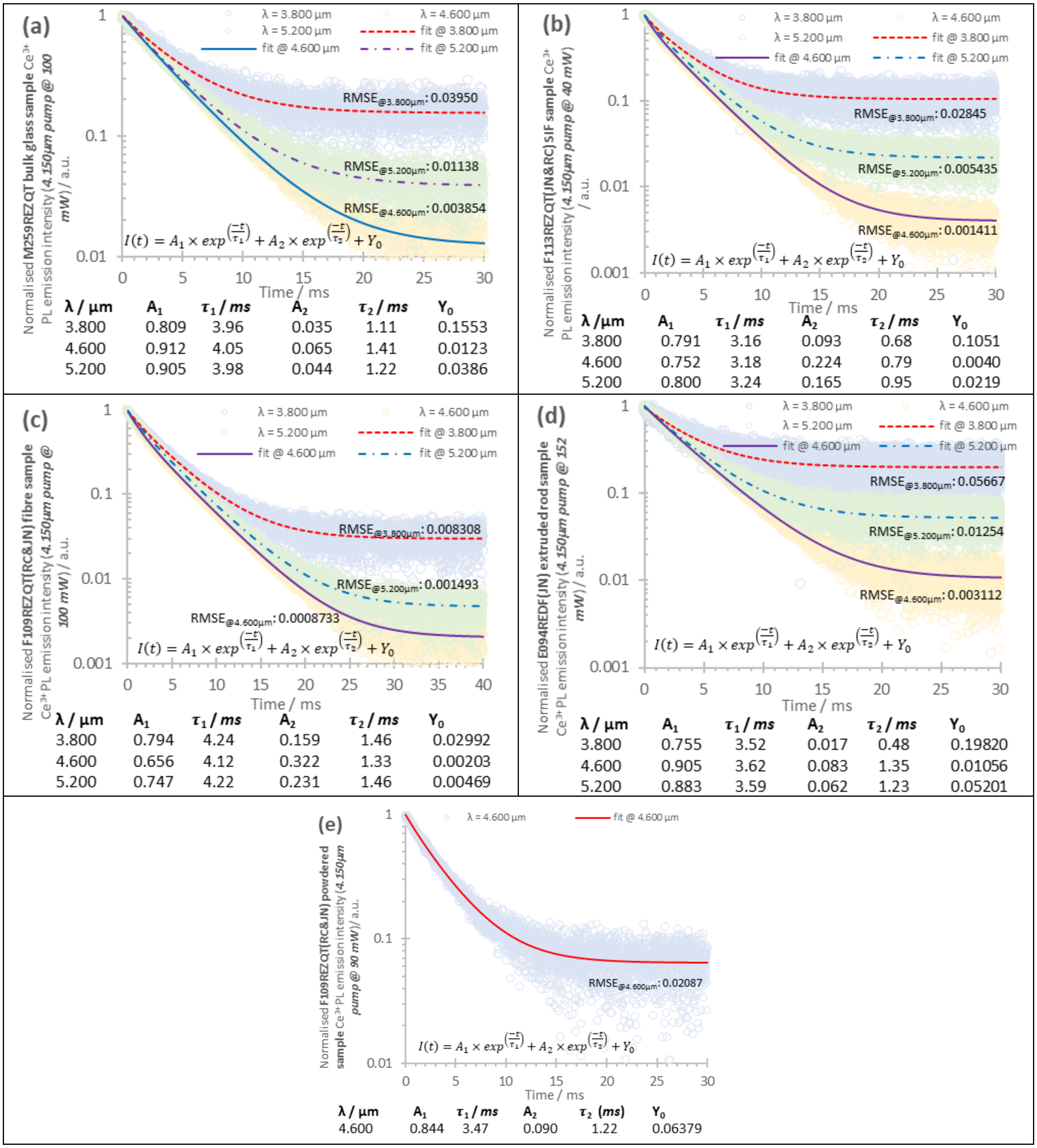

(a)

λ / µm	A_1	τ_1 / ms	A_2	τ_2 / ms	Y_0
3.800	0.809	3.96	0.035	1.11	0.1553
4.600	0.912	4.05	0.065	1.41	0.0123
5.200	0.905	3.98	0.044	1.22	0.0386

(b)

λ / µm	A_1	τ_1 / ms	A_2	τ_2 / ms	Y_0
3.800	0.791	3.16	0.093	0.68	0.1051
4.600	0.752	3.18	0.224	0.79	0.0040
5.200	0.800	3.24	0.165	0.95	0.0219

(c)

λ / µm	A_1	τ_1 / ms	A_2	τ_2 / ms	Y_0
3.800	0.794	4.24	0.159	1.46	0.02992
4.600	0.656	4.12	0.322	1.33	0.00203
5.200	0.747	4.22	0.231	1.46	0.00469

(d)

λ / µm	A_1	τ_1 / ms	A_2	τ_2 / ms	Y_0
3.800	0.755	3.52	0.017	0.48	0.19820
4.600	0.905	3.62	0.083	1.35	0.01056
5.200	0.883	3.59	0.062	1.23	0.05201

(e)

λ / µm	A_1	τ_1 / ms	A_2	τ_2 (ms)	Y_0
4.600	0.844	3.47	0.090	1.22	0.06379

*Figure 4-5: Normalised Ce^{3+} PL lifetime (scatter plot) fitted with exponential decay function (line) for nominally 500 ppmw Ce cation doped samples using 4.150 µm pump laser modulated at 12 Hz with: **(a)** annealed bulk (M259REZQT) sample, **(b)** SIF (F113REZQT(JN&RC)) sample, **(c)** single material fibre (F109REZQT(RC&JN)) sample, **(d)** annealed co-extruded rod (E094REDF(JN)) sample and **(e)** powdered fibre. Note, the M259REZQT and F109REZQT(RC&JN) samples along with the core of F113REZQT(JN&RC) sample each have the same $Ge_{15.0}$ $As_{21.0}$ $Ga_{1.0}$ $Se_{63.0}$ atomic % nominal composition and the core of E094REDF(JN): $Ge_{14.8}$ $As_{20.8}$ $Ga_{2.0}$ $Se_{62.4}$ atomic %. See Table 4-3 for sample specifications and equipment configuration used, and results summarised in Table 4-4.*

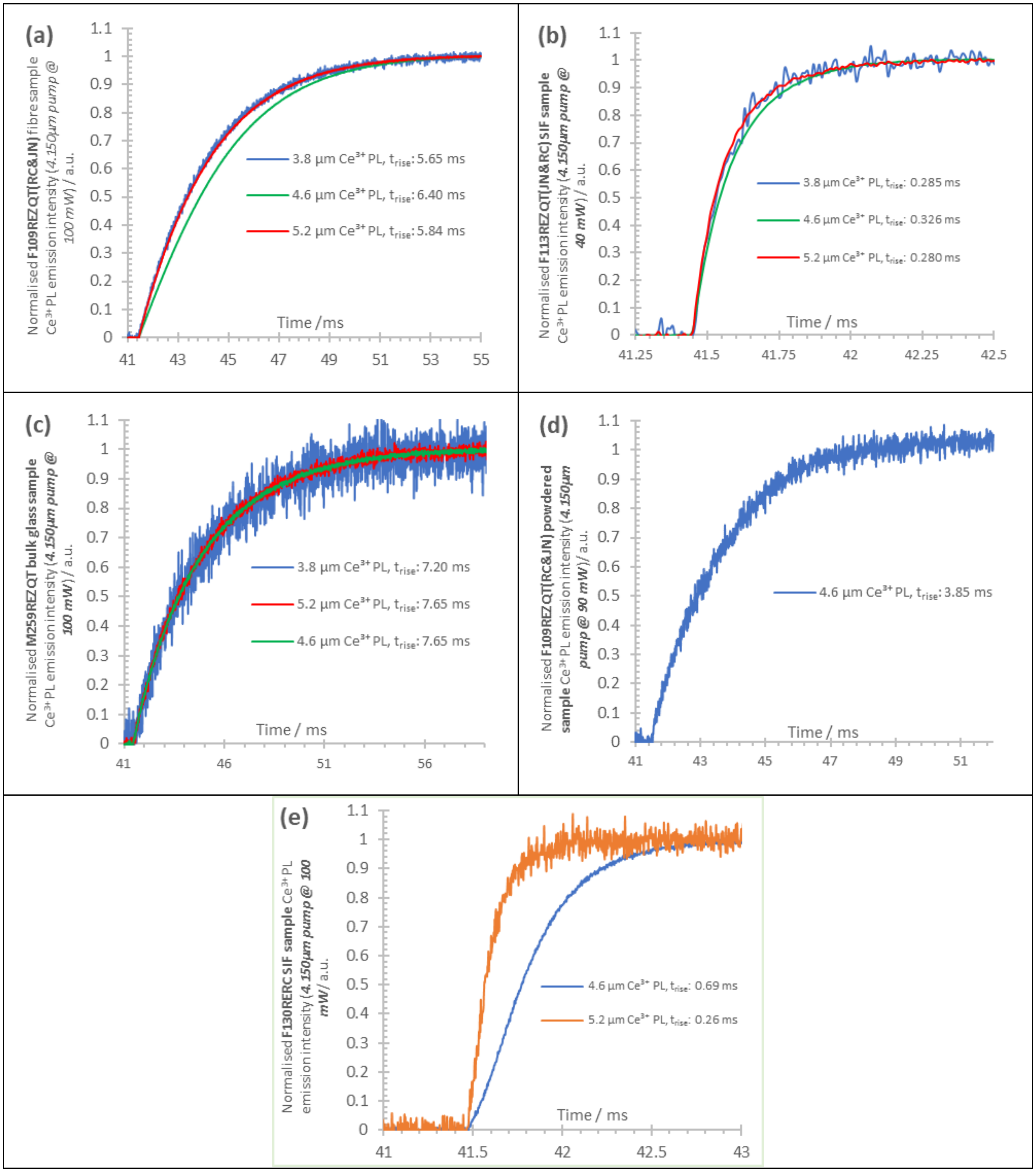

*Figure 4-6: Normalised Ce^{3+} PL rise time for nominally 500 ppmw Ce cation doped samples using 4.150 µm pump laser modulated at 12 Hz with: **(a)** single material fibre (F109REZQT(RC&JN)) sample, **(b)** SIF (F113REZQT(JN&RC)) sample, **(c)** annealed bulk (M259REZQT) sample, **(d)** powdered fibre and **(e)** SIF (F130RERC sample. Note, the M259REZQT and F109REZQT(RC&JN) samples along with the core of the F113REZQT(JN&RC) and the F130RERC samples each have the* <u>*same*</u> *$Ge_{15.0}$ $As_{21.0}$ $Ga_{1.0}$ $Se_{63.0}$ atomic % nominal composition. See Table 4-3 for sample specifications and equipment configuration used.*

Table 4-4: Summary of Ce^{3+} lifetime (Figure 4-5) and rise time measurement results using 4.150 µm excitation source, (see Table 4-3 for sample specifications and equipment configuration):

Sample type and composition (atomic %)	**Measurement λ / µm**	**lifetime coefficients for $^2F_{7/2} \rightarrow {}^2F_{5/2}$**					**10% to 90% rise time for $^2F_{5/2} \rightarrow {}^2F_{7/2}$ / ms**
		A_1	τ_1 / ms	A_2	τ_2 / ms	Y_0	
M259REZQT *Bulk glass (Annealed & polished)* (*$Ge_{15.0}As_{21.0}Ga_{1.0}Se_{63.0}$ + 500 ppmw Ce (foil)*)	3.800	0.809	**3.96**	0.035	1.11	0.15530	7.20
	4.600	0.912	**4.05**	0.065	1.41	0.01230	7.65
	5.200	0.905	**3.98**	0.044	1.22	0.03861	7.65
F113REZQT(JN&RC) *SIF* (*un-annealed*) (Core: **F109REZQT(JN&RC)**: *$Ge_{15.0}As_{21.0}Ga_{1.0}Se_{63.0}$ + 500 ppmw Ce (foil)* Cladding **M260JN**: *$Ge_{16.5}As_{16.0}Ga_{3.0}Se_{61.5}S_{3.0}$*)	3.800	0.791	**3.16**	0.093	0.68	0.10510	0.285
	4.600	0.752	**3.18**	0.224	0.79	0.00401	0.326
	5.200	0.800	**3.24**	0.165	0.95	0.02186	0.280
F109REZQT(RC&JN) *Single material fibre (un-annealed)* (*$Ge_{15.0}As_{21.0}Ga_{1.0}Se_{63.0}$ + 500 ppmw Ce (foil)*)	3.800	0.794	**4.24**	0.159	1.46	0.02992	5.65
	4.600	0.656	**4.12**	0.322	1.33	0.00203	6.40
	5.200	0.747	**4.23**	0.231	1.46	0.00469	5.84
E094REDF(JN) *Co-extruded glass rod (annealed & polished)* (Core: **M293REJN:** *$Ge_{14.8}As_{20.8}Ga_{2.0}Se_{62.4}$ + 500 ppmw Ce (foil)* Cladding: **M295REJN**: *$Ge_{16.5}As_{16.0}Ga_{3.0}Se_{61.5}S_{3.0}$ + 500 ppmw Dy (foil)*)	3.800	0.755	**3.52**	0.017	0.48	0.19820	Not evaluated
	4.600	0.905	**3.62**	0.083	1.35	0.01056	
	5.200	0.883	**3.59**	0.062	1.23	0.05201	
F130RERC *SIF* (*un-annealed*) (Core: **F109REZQT(JN&RC)**: *$Ge_{15.0}As_{21.0}Ga_{1.0}Se_{63.0}$ + 500 ppmw Ce (foil)* Cladding **M287RC**: *$Ge_{21.0}Sb_{10.0}Se_{69.0}$*)	4.60	0.386	**2.41**	0.543	**0.48**	0.01964	0.69
	5.20	0.549	**3.06**	0.268	0.88	0.09074	0.26
F109REZQT(RC&JN) *Powdered glass (single material fibre, un-annealed)* (*$Ge_{15.0}As_{21.0}Ga_{1.0}Se_{63.0}$ + 500 ppmw Ce (foil)*)	4.600	0.844	**3.47**	0.090	1.22	0.06379	3.85

4.2.2 Praseodymium spectroscopy.

A distilled, nominally $Ge_{14.8}$ $As_{20.8}$ $Ga_{2.0}$ $Se_{62.4}$ atomic % + 1000 ppmw $TeCl_4$ + 500 ppmw Pr (*foil*) M276REJN glass rod was produced by the author and subsequently drawn into the single material fibre F119REJN and cane. Note, the optical and compositional evaluation of this glass can be found in Section 3.2.5. A portion of the glass rod was processed into a polished bulk glass sample and used for the presented absorption measurements in Section 4.2.2.1. Another portion of the bulk glass was ground into powdered glass and used along with a section of the single material fibre F119REJN for the PL emission measurements presented in Section 4.2.2.3. A separate section of single material fibre F119REJN was used for the ESA measurements presented in Section 4.2.2.4.

4.2.2.1 Pr^{3+} absorption and emission cross-sections:

Figure 4-7 (a) shows the absorption coefficient for a nominally 500 ppmw Pr (*foil*) doped distilled M276REJN sample, ostensibly containing 9.62 × 10^{18} cations/cm^3. The GSA between the $^3H_4$ ground state and the $^3H_5$, $^3H_6$, $^3F_2$, $^3F_3$, $^3F_4$ and $^1G_4$ excited state levels each ostensibly peaking at 2104 cm^{-1}, 4095 cm^{-1}, 4906 cm^{-1}, 6265 cm^{-1}, 6725 cm^{-1}, and 9710 cm^{-1}, respectively can be seen. Figure 4-7 (b) shows the corresponding the Pr^{3+} energy level diagram. Figure 4-7 (c) shows the calculated absorption cross-sections for each of the observed GSA bands and the emission cross-sections for the ($^3F_4$, $^3F_3$) → $^3H_4$, ($^3F_2$, $^3H_6$) → $^3H_4$, and $^3H_5$ → $^3H_4$ transitions. The underlying [-Se-H] impurity vibrational absorption bands were numerically removed in Figure 4-7 (a) and (c). These results agree with the GLS absorption data presented in [118].

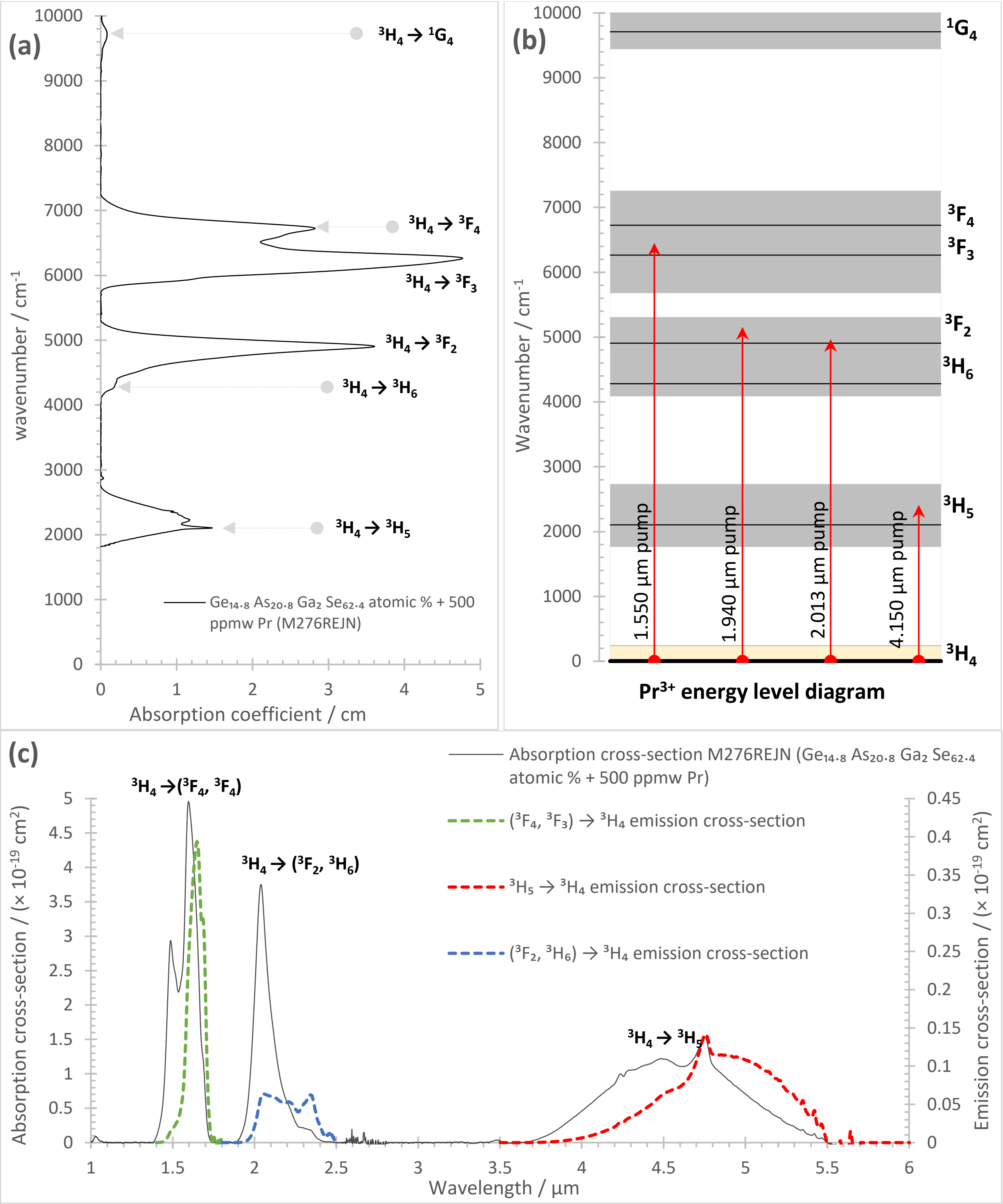

Figure 4-7: Showing: ***(a)*** *room temperature absorption spectrum of a nominally 500 ppmw Pr (foil) doped sample, along with* ***(b)*** *the corresponding energy level diagram for Pr^{3+} in glass host showing 1.550 µm, 1.940 µm, 2.013 µm and 4.150 µm excitation wavelengths which were used in future measurements, and* ***(c)*** *showing the calculated absorption (solid line) and emission (dashed line) cross-sections for the M276REJN sample. Note, the Pr^{3+} cross-section calculations assumed several factors (see Section 3.2.8.2 and 4.2.6.1) and thus its accuracy should not be relied upon.*

4.2.2.2 Pr^{3+} literature review:

The NIR and MIR properties of the 'Pr' dopant have been well investigated in several host glass compositions with different excitation schemes due to the Pr^{3+} dopant exhibiting absorption bands suitable for pumping with readily commercially available sources. Table 4-5 shows the major Pr^{3+} PL emission bands, some of which were comprised of one or more transitions,

Table 4-5: Pr^{3+} cation PL emission bands found in literature (see Figure 4-7 (b) for energy level diagram):

Transition	**Composition/ sample type**	**Pump λ / µm**	**Emission band range / µm**	**Peak λ / µm**	**Reference**
$^3H_5 \to {}^3H_4$ $({}^3F_2, {}^3H_6) \to {}^3H_5$	Ge-As-Ga-Se 500 ppmw Pr^{3+} (*SIF*)	1.550 or 1.940	3.5 to 6.0	~ 4.7	[119]
$^1G_4 \to {}^3F_4$	Ge-As-Ga-Se 1000 ppmw Pr^{3+}	1.060	3.1 to 3.7	~ 3.42	[17]
$^3H_5 \to {}^3H_4$ $({}^3F_2, {}^3H_6) \to {}^3H_5$		1.500	3.5 to > 5.5	~ 4.9	
$^3H_5 \to {}^3H_4$	Ge-As-Ga-Se 500 ppmw Pr^{3+} (*single material fibre*)	4.150	3.5 to 6.0	~ 4.7	[175]
$({}^3F_2, {}^3H_6) \to {}^3H_4$			2.0 to 2.7	~ 2.5	
$^3H_5 \to {}^3H_4$ $({}^3F_2, {}^3H_6) \to {}^3H_5$	Ge-As-Ga-Se 500 ppmw Pr^{3+} (*single material fibre*)	1.470	3.3 to > 6.0	~ 4.7	[176]
$^3F_3 \to {}^3F_2$			6.5 to 8.0	6.5	
$^3H_5 \to {}^3H_4$ $^3H_6 \to {}^3H_5$	Ge-As-Ga-Se 500 ppmw Pr^{3+} (*SIF*)	1.550	3.5 to 6.0	~ 4.7	[149]
$^3F_3 \to {}^3H_5$ $^3F_2 \to {}^3H_4$	$Ge_{36.0}Ga_{5.0}Se_{59.0}$ Pr^{3+} @ 2×10^{19}, 5×10^{19} and 1×10^{20} cm^{-3} (*Polished disc*)	1.480	2.0 to 2.7	~ 2.5	[177]
$^3H_5 \to {}^3H_4$ $^3H_6 \to {}^3H_5$			4.0 to 6.0	~ 5.0	
$^3H_5 \to {}^3H_4$ $^3H_6 \to {}^3H_5$	$Ga_{5.0}Ge_{20.0}Sb_{10.0}S_{65.0}$ 500 and 1000 ppmw Pr^{3+} (*single material fibre*)	2.000	3.4 to 5.5	~ 4.7	[178]
$^3H_5 \to {}^3H_4$ $^3H_6 \to {}^3H_5$	$Ga_{5.0}Ge_{20.0}Sb_{10.0}Se_{65.0}$ 500 and 1000 ppmw Pr^{3+} (*single material fibre*)				
$^3H_5 \to {}^3H_4$ $({}^3F_2, {}^3H_6) \to {}^3H_5$	Ge-As-Ga$_{1.0}$Se 500 ppmw Pr^{3+} (*single material fibre*)	1.550	3.5 to 6.0	~ 4.7	[66]
$^3H_5 \to {}^3H_4$ $({}^3F_2, {}^3H_6) \to {}^3H_5$	Ge-As-In$_{1.0}$Se 500 ppmw Pr^{3+} (*single material fibre*)		3.5 to 6.0	~ 4.7	
$^3H_5 \to {}^3H_4$ $({}^3F_2, {}^3H_6) \to {}^3H_5$	Ge-As-Ga$_{1.0}$Se (*single material fibres*) 500 ppmw Pr foil 500 ppmw PrI$_3$ 500 PrCl$_3$	1.550	3.5 to 6.0	~ 4.7	[32]
$^1G_4 \to {}^3H_6$ $^3F_2 \to {}^3H_4$ $^1G_4 \to {}^3F_2$	Ga-La-S 1.5 mol % Pr$_2$S$_3$ (*bulk glass*)	1.064	1.7 to 2.15	~ 1.85	[118]
$^1G_4 \to {}^3F_3$			2.7 to 3.1	~ 2.77	
$^3H_5 \to {}^3H_4$ $({}^3F_2, {}^3H_6) \to {}^3H_5$		2.000	3.4 to > 5.5	~ 4.7	

Table 4-6 shows the Pr3+ PL lifetimes reported.

Table 4-6: Pr^{3+} PL emission lifetimes found in literature (see Figure 4-7 (b) for energy level diagram):

Transition		**Host composition / sample type**		**Calculated τ_{rad} / ms**	**Measured τ_{rad} / ms**	**Reference**
From	**To**					
$^3H_5$	$^3H_4$	Ge-As-Ga-Se 500 ppmw Pr^{3+} (*SIF*)		10	11.5 ± 0.5	[119]
($^3F_3$, $^3F_4$)	$^3H_4$			0.23	0.272 ± 0.003	
$^3H_6$		Ge-As-Ga-Se 500 ppmw Pr^{3+} (*bulk glass*)		3.7	-	
$^3F_2$				0.44	-	
$^3H_5$	$^3H_4$	Ge-As-Ga-Se 1000 ppmw Pr^{3+}		15	12	[17]
($^3F_2$, $^3H_6$)	$^3H_5$			3.4	4.2	
($^3F_4$, $^3F_3$)	$^3H_6$			0.29	0.25	
($^3F_4$, $^3F_3$)	$^3F_2$					
$^1G_4$	$^3F_4$			0.36	0.22	
$^3F_3$	$^3F_2$	Ge-As-Ga-Se 500 ppmw Pr^{3+} (*single material fibre*)		-	0.3	[176]
$^3H_5$	$^3H_4$			-	6.5	
$^3F_3$	$^3H_4$			-	0.27	
4.7 µm emission		Ge-As-Ga-Se (*SIF sample*)		-	7.8	[149]
4.7 µm emission		Ge-As-Ga$_{1.0}$Se 500 ppmw Pr^{3+} (*single material fibre*)		-	7.8	[66]
		Ge-As-In$_{1.0}$Se 500 ppmw Pr^{3+} (*single material fibre*)		-	10.1	
4.7 µm emission		Ge-As-Ga$_{1.0}$Se (*single material fibre*)	500 ppmw Pr foil	-	10.1 and 3.3	[32]
			500 ppmw PrI$_3$	-	10.4 and 3.2	
			500 PrCl$_3$	-	10.3, 2.4 and 0.21	

4.2.2.3 Pr^{3+} PL emission measurements:

Pr^{3+} PL emission spectrum and PL lifetime measurements were performed sequentially using four separate excitation sources operating at wavelengths of 1.550 µm, 1.940 µm, 2.013 µm and 4.150 µm on the samples listed in Table 4-7. The 1.550 µm excitation scheme used the $^3H_4 \rightarrow (^3F_4, ^3F_3)$ GSA, both the 1.940 µm and 2.013 µm excitation schemes used the $^3H_4 \rightarrow {}^3F_2$ GSA, and the 4.150 µm excitation scheme used the $^3H_4 \rightarrow {}^3H_5$ GSA, as illustrated in Figure 4-7 (b).

Table 4-7: Sample codes, composition, dimentions, and equipment configurations used for Pr^{3+} PL emission measurements (see Section 7.3 for description of equipment configuration code).

Sample type	Code and nominal composition (atomic %)	Dimensions	Figure and equipment configuration
Single material fibre (*un-annealed*)	**F119REJN** (*$Ge_{14.8}$ $As_{20.8}$ $Ga_{2.0}$ $Se_{62.4}$ + 1000 ppmw $TeCl_4$ + 500 ppmw Pr (foil)*)	79.68 mm long, with diameter of 209 ± 2.4 µm.	Figure 4-8: **A**[1_a-7_a] **F**[9_a] **I**[12_a- 13_{none}- 14_a -15_{ai} – 16_a] Figure 4-9 (a), and Figure 4-11 (e): **A**[1_a-7_a] **F**[9_a] **I**[12_b- $13_{2.000\ SWP}$- 14_b -15_{aii} – 16_b] **A**[1_d-7_a] **F**[9_a] **I**[12_b- $13_{2.000\ LWP}$- 14_b -15_{aii} – 16_b] **B**[7_a] **F**[9_a] **I**[12_b- $13_{3.351\ SWP}$- 14_b -15_{aii} – 16_b] Figure 4-10 (a), Figure 4-11 (a) and (b): **A**[1_a-7_a] **F**[9_a] **I**[12_b- $13_{3.407\ LWP}$- 14_b -15_{aii} – 16_b] **A**[1_d-7_a] **F**[9_a] **I**[12_b- $13_{3.407\ LWP}$- 14_b -15_{aii} – 16_b] **B**[7_a] **F**[9_a] **I**[12_b- $13_{4.203\ LWP}$- 14_b -15_{aii} – 16_b]
Powdered glass (*annealed bulk glass*)	**M276REJN** (*$Ge_{14.8}$ $As_{20.8}$ $Ga_{2.0}$ $Se_{62.4}$ + 1000 ppmw $TeCl_4$ + 500 ppmw Pr (foil)*)	Varying granule size, 320.6 ± 80.8 µm diameter.	Figure 4-8: **C**[1_d] **G**[] **I**[12_b- 13_{none}- 14_b -15_{ai} – 16_a] Figure 4-9 (b) and Figure 4-11 (e): **C**[1_a] **G**[] **I**[12_a- 13_{none}- 14_a -15_{aii} – 16_b] **C**[1_d] **G**[] **I**[12_a- 13_{none}- 14_a -15_{aii} – 16_b] Figure 4-10 (b), Figure 4-11 (c) and (d): **C**[1_a] **G**[] **I**[12_a- $13_{3.407\ LWP}$- 14_a -15_{aii} – 16_b] **C**[1_d] **G**[] **I**[12_a- $13_{3.407\ LWP}$- 14_a -15_{aii} – 16_b] **D**[3] **G**[] **I**[12_b- $13_{4.203\ LWP}$- 14_b -15_{aii} – 16_b]

4.2.2.3.a Pr^{3+} PL emission spectra:

Three distinct Pr^{3+} PL emission bands between, 1.600 to 1.740 µm, 2.100 to 2.800 µm, and 3.500 to 6.500 µm were detected and evaluated. Pr^{3+} PL emissions greater than 6.500 µm were not investigated. The three PL emission bands resemble those found in literature (see Table 4-5).

Each of the 2.013 µm or the 4.150 µm excitation sources resulted in a weak emission band between 1.550 µm to 1.750 µm, attributed to the $^3F_3 \rightarrow {}^3H_4$ transition, as shown in Figure 4-8.

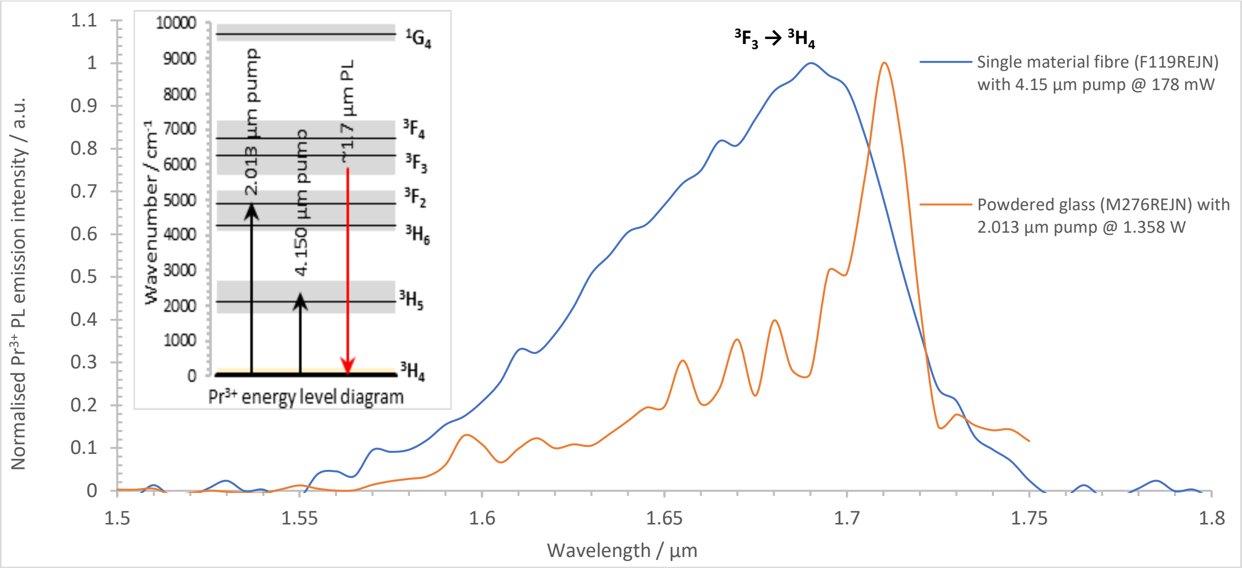

Figure 4-8: Normalised PL emission spectra for nominally 500 ppmw Pr (foil) doped $Ge_{14.8}$ $As_{20.8}$ $Ga_{2.0}$ $Se_{62.4}$ atomic % + 1000 ppmw $TeCl_4$ single material fibre (F119REJN) sample, and powdered glass (M276REJN) sample excited using either a 2.013 µm or a 4.150 µm pump source, with inset showing Pr^{3+} energy level diagram (Arrow lengths ARE TO SCALE). Not corrected for system spectral response. See Table 4-7 for sample specifications and equipment configuration.

Figure 4-8 shows a Pr^{3+} emission spectrum with a shorter wavelength (*higher photon energy*) than either the 2.013 µm or 4.150 µm excitation wavelengths employed, as illustrated in the inset in Figure 4-8. Thus, this emission band could only have occurred due to ESA of either pump source and/or ESA of Pr^{3+} PL. Considering Table 4-5, to the best of my knowledge, this is the first reported instance of up-conversion into the $^3F_3$ manifold. The ~1.6 µm Pr^{3+} PL emission band in Figure 4-8 shows good agreement with the calculated ($^3F_4$, $^3F_3$) → $^3H_4$ emission shape in Figure 4-7 (c).

Application of each excitation source (*1.550 µm, 1.940 µm, 2.013 µm and 4.150 µm*), on the samples listed in Table 4-7, resulted in a Pr^{3+} emission spectrum between 2.100 to 2.800 µm, as shown in Figure 4-9 (a) and (b), and was attributed to both the ($^3F_4$, $^3F_3$) → $^3H_5$ and ($^3F_2$, $^3H_6$) → $^3H_4$ transitions. Interestingly, the shape of the 2.100 to 2.800 µm Pr^{3+} PL emission spectra in

Figure 4-9 (a) and (b) was influenced by the excitation wavelength used, indicating a change in contributions of the radiative transitions comprising the emission band.

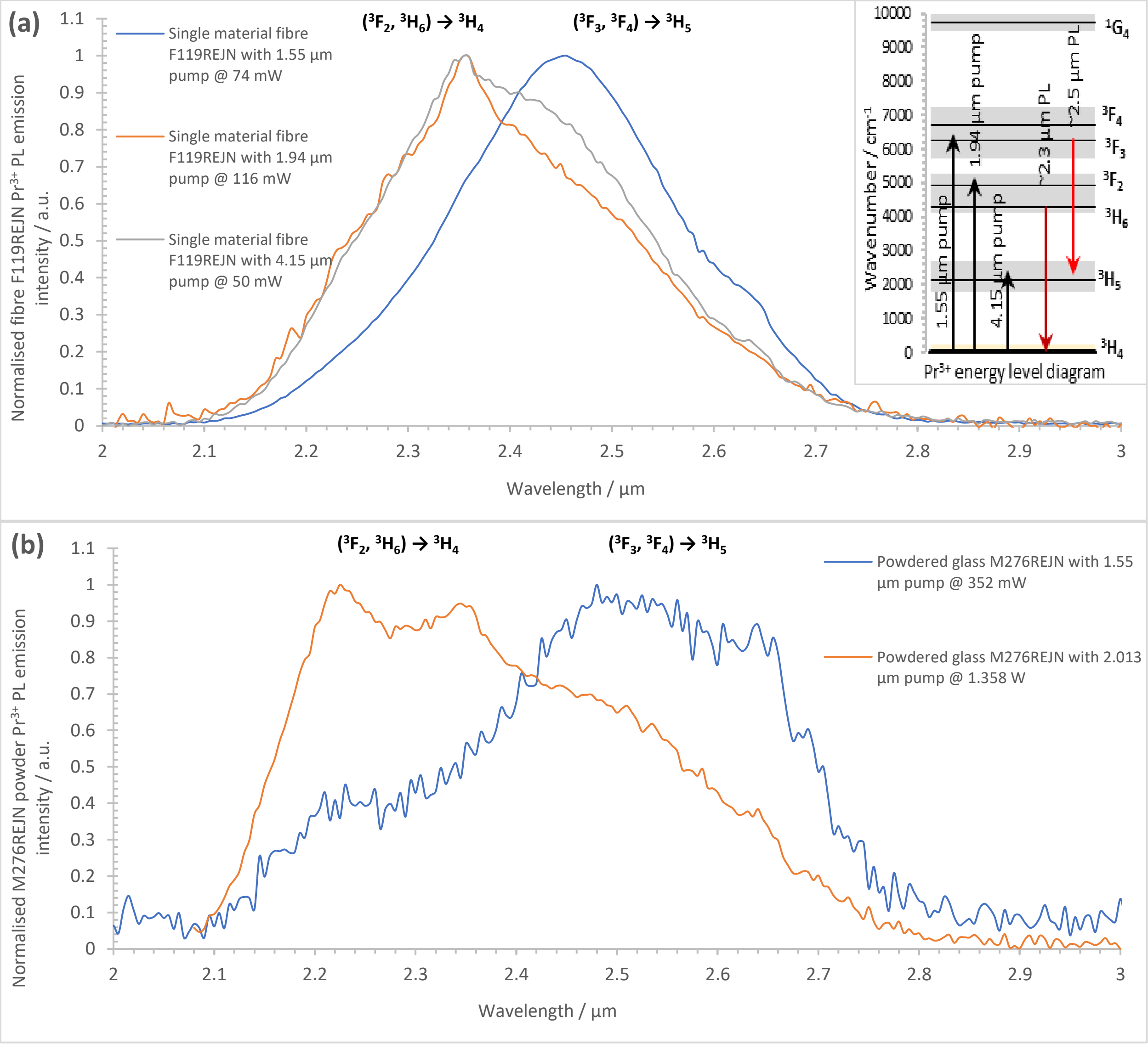

Figure 4-9: Showing normalised PL emission spectra for nominally 500 ppmw Pr (foil) doped Ge$_{14.8}$ As$_{20.8}$ Ga$_{2.0}$ Se$_{62.4}$ atomic % + 1000 ppmw TeCl$_4$ sample of: ***(a)*** *single material fibre (F119REJN) with inset showing Pr^{3+} energy level diagram (Arrow lengths ARE TO SCALE), and* ***(b)*** *Powdered glass (M276REJN). Not corrected for system spectral response. See Table 4-7 for sample dimensions and equipment configuration.*

The 1.550 µm excitation scheme resulted in Pr^{3+} PL emissions peaking around 2.450 µm (*4082 cm^{-1}*), which matched the $^3F_3 \rightarrow {}^3H_5$ transition. While the 1.940 µm, 2.013 µm and 4.150 µm excitation schemes each resulted in Pr^{3+} PL emissions peaking around 2.360 µm (*4237 cm^{-1}*) which matched the $^3H_6 \rightarrow {}^3H_4$ transition, as illustrated in the inset of Figure 4-9 (a). Additionally, in Figure 4-9 (a) the Pr^{3+} emission spectrum produced due to the 4.150 µm excitation scheme could only have occurred due to ESA of the pump and/or Pr^{3+} PL, as illustrated in inset of Figure 4-9 (a).

Each excitation source (*1.550 µm, 1.940 µm, 2.013 µm and 4.150 µm*) resulted in a Pr^{3+} PL emission band between 3.400 to 6.500 µm in wavelength as shown in Figure 4-10 (a) and (b), which could be attributed to the $^3H_5 \rightarrow {}^3H_4$, ($^3F_2$, $^3H_6$) $\rightarrow$ $^3H_5$ and ($^3F_4$, $^3F_3$) $\rightarrow$ ($^3F_2$, $^3H_6$) transitions. The 1.550 µm, 1.940 µm and 2.013 µm excitation schemes each resulted in similarly shaped emission bands, indicating identical radiative transitions. Comparing the emission spectra Figure 4-10 (a) and (b), the powder sample exhibited slightly greater relative intensity at 4.500 µm when compared to the single material fibre sample due to lower [-Se-H] impurity resonantly absorbing and transferring PL into vibrational quanta along the PL propagation path.

The ~4.7 µm PL emission spectrum in Figure 4-10 does not match the calculated $^3H_5 \rightarrow {}^3H_4$ transition shape in Figure 4-7 (c). Unsurprisingly, this is due to the ~4.7 µm PL emission band being comprised of transitions from multiple energy levels, as illustrated within the inset in Figure 4-10.

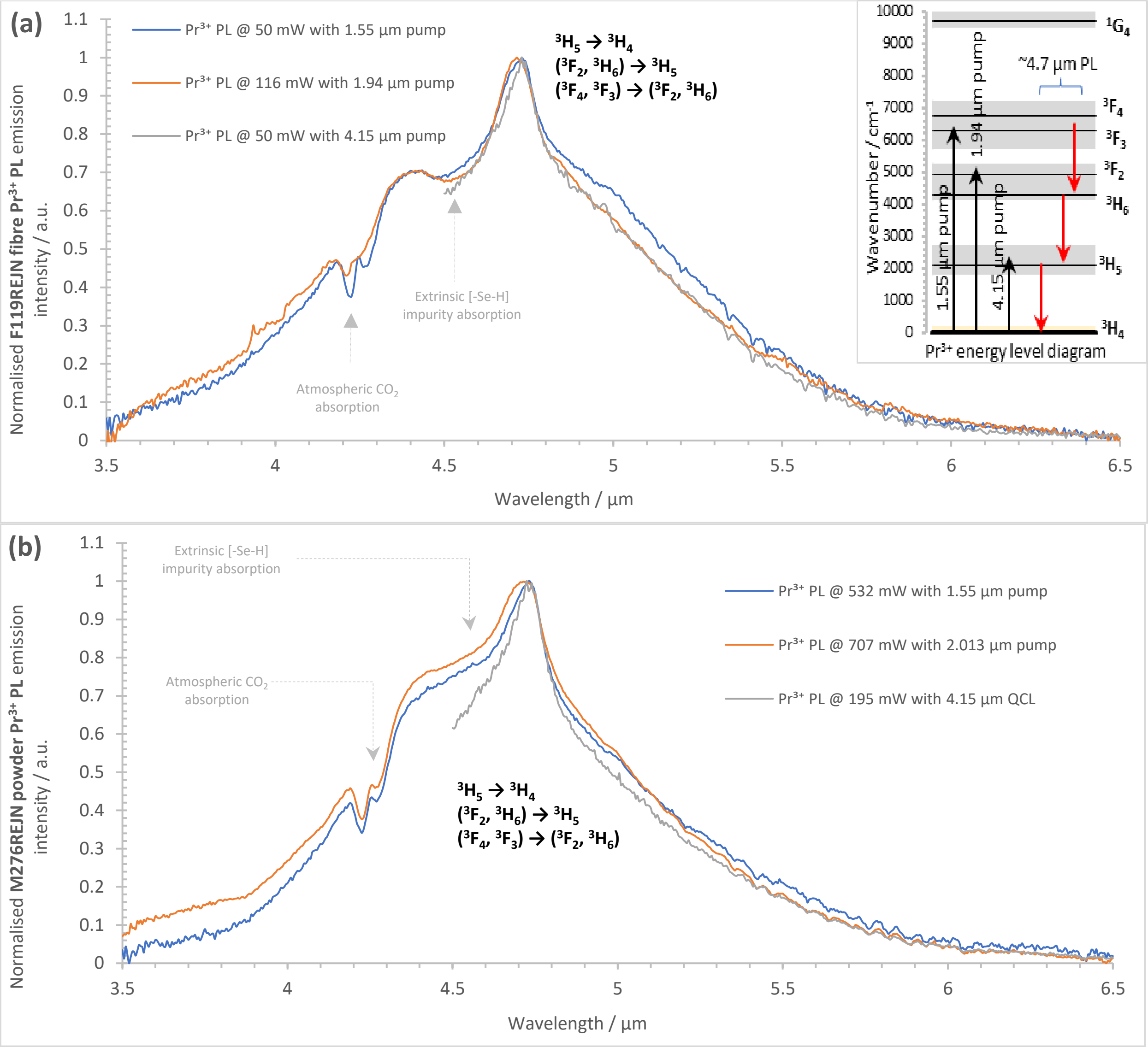

Figure 4-10: Showing normalised PL emission spectra for a nominally 500 ppmw Pr (foil) doped Ge$_{14.8}$ As$_{20.8}$ Ga$_{2.0}$ Se$_{62.4}$ atomic % + 1000 ppmw TeCl$_4$ sample of: ***(a)*** *single material fibre (F119REJN) with inset showing Pr^{3+} energy level diagram (Arrow lengths ARE TO SCALE), and* ***(b)*** *powdered glass (M276REJN). See Table 4-7 for sample dimensions and equipment configuration. Note, a portion of the emission spectrum resulting from the 4.150 µm excitation scheme (grey plot), below 4.500 µm, was omitted due to the presence of unabsorbed 4.150 µm QCL light.*

4.2.2.3.b Pr^{3+} PL lifetime results:

PL emission lifetime 'τ_{rad}' measurements were performed on the samples listed in Table 4-7 using the 1.940 µm 2.013 µm and 4.150 µm excitation sources. These lifetime 'τ_{rad}' measurements focused on the 2.100 to 2.800 µm and the 3.400 to 6.500 µm Pr^{3+} PL emission bands; shorter wavelengths were omitted due to weak PL intensity. Figure 4-11 shows the normalised Pr^{3+} PL emission decay from each sample type, along with a corresponding fitted exponential function. Additionally, Table 4-8 lists the Pr^{3+} PL lifetimes for each sample type.

Lifetime measurements at wavelengths of 4.440 µm, 4.720 µm and 5.000 µm were consistently best fitted with a two-term exponential function, as shown in Figure 4-11 (a) to (d), and Table 4-8. These results predominantly consisted of a longer 'τ_1', at ~ 10.5 ms, attributed to the $^3H_5 \rightarrow {}^3H_4$ transition, along with a less frequent and shorter 'τ_2', at ~ 3.6 ms, attributed to the ($^3F_2$, $^3H_6$) → $^3H_5$ transition, as illustrated in the inset in Figure 4-10 (a). This result indicated consistent contributions from each of these transitions over the entire emission band.

Lifetime measurements for the 2.100 to 2.800 µm Pr^{3+} PL emission band were fitted to a single-term exponential function due to the relatively weak PL intensity, as shown in Figure 4-11 (e). These results principally consisted of 'τ_1', at ~ 3.6 ms, attributed to the ($^3F_2$, $^3H_6$) → $^3H_4$ transition, as illustrated in the inset in Figure 4-9 (a). However, considering Figure 4-9 (a) and (b), these Pr^{3+} PL emission spectrum measurements indicated contributions from the ($^3F_4$, $^3F_3$) → $^3H_5$ transition which would exhibit a 'τ_1' at ~ 0.24, as found in literature and listed in Table 4-6.

Lifetime results measurements varied between fibre and powdered sample types. The fibre sample, which possessed a longer propagation path, exhibited slightly longer lifetimes under similar excitation schemes when compared to the powdered sample.

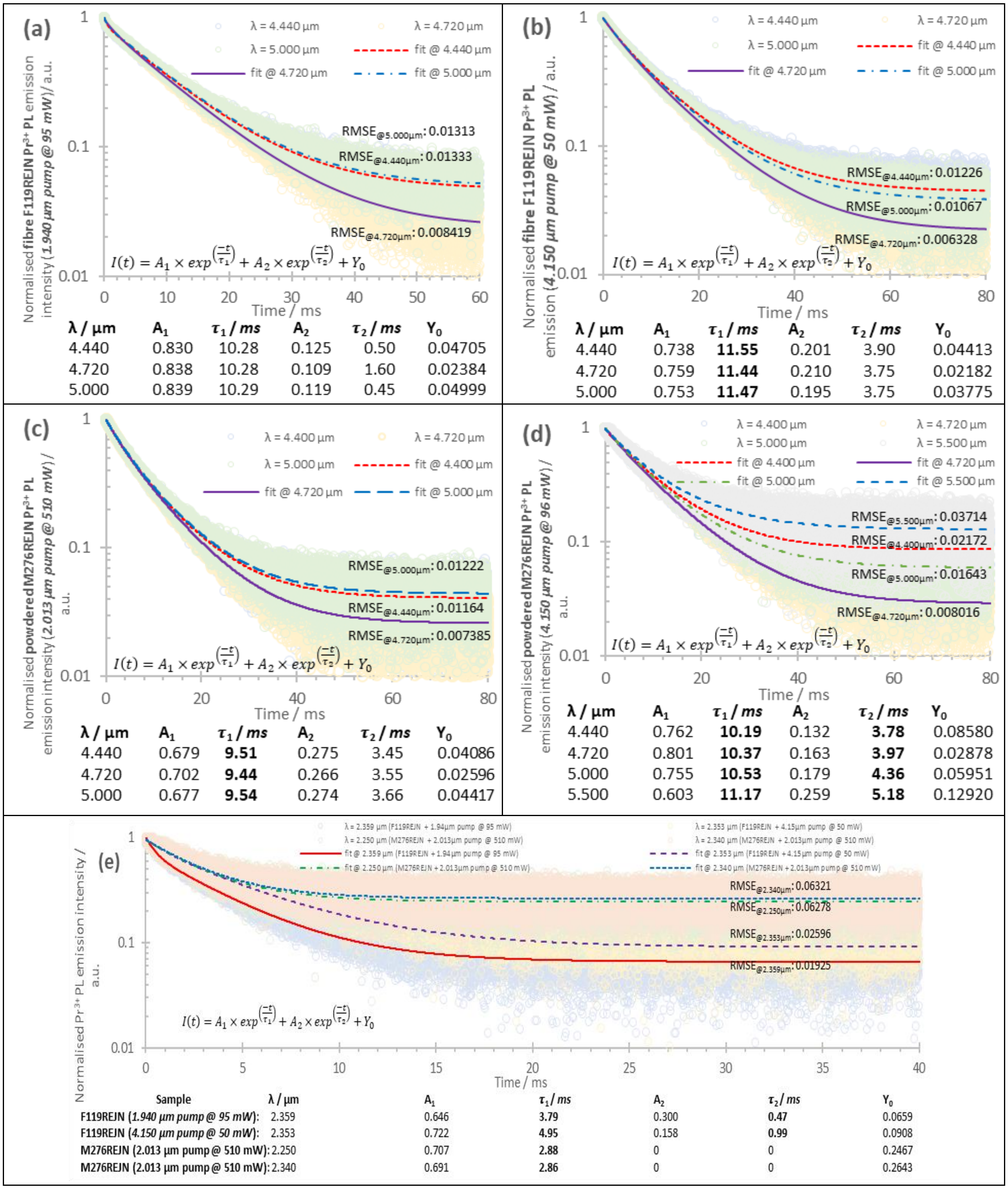

(a)

λ / µm	A_1	τ_1 / ms	A_2	τ_2 / ms	Y_0
4.440	0.830	10.28	0.125	0.50	0.04705
4.720	0.838	10.28	0.109	1.60	0.02384
5.000	0.839	10.29	0.119	0.45	0.04999

(b)

λ / µm	A_1	τ_1 / ms	A_2	τ_2 / ms	Y_0
4.440	0.738	**11.55**	0.201	3.90	0.04413
4.720	0.759	**11.44**	0.210	3.75	0.02182
5.000	0.753	**11.47**	0.195	3.75	0.03775

(c)

λ / µm	A_1	τ_1 / ms	A_2	τ_2 / ms	Y_0
4.440	0.679	**9.51**	0.275	3.45	0.04086
4.720	0.702	**9.44**	0.266	3.55	0.02596
5.000	0.677	**9.54**	0.274	3.66	0.04417

(d)

λ / µm	A_1	τ_1 / ms	A_2	τ_2 / ms	Y_0
4.440	0.762	**10.19**	0.132	**3.78**	0.08580
4.720	0.801	**10.37**	0.163	**3.97**	0.02878
5.000	0.755	**10.53**	0.179	**4.36**	0.05951
5.500	0.603	**11.17**	0.259	**5.18**	0.12920

(e)

Sample	λ / µm	A_1	τ_1 / ms	A_2	τ_2 / ms	Y_0
F119REJN (*1.940 µm pump @ 95 mW*):	2.359	0.646	**3.79**	0.300	**0.47**	0.0659
F119REJN (*4.150 µm pump @ 50 mW*):	2.353	0.722	**4.95**	0.158	**0.99**	0.0908
M276REJN (2.013 µm pump @ 510 mW):	2.250	0.707	**2.88**	0	0	0.2467
M276REJN (2.013 µm pump @ 510 mW):	2.340	0.691	**2.86**	0	0	0.2643

*Figure 4-11: Normalised Pr^{3+} PL lifetime (scatter plot) fitted with exponential decay function (line) for **(a)** single material fibre (F119REJN) sample with 1.940 µm pump, **(b)** single material fibre (F119REJN) with 4.150 µm pump, **(c)** powdered bulk glass (M276REJN) with 1.940 µm pump, **(d)** powdered bulk glass with 4.150 µm pump and **(e)** Both single material fibre sample and powdered bulk glass with 2.013 µm and 4.150 µm pump sources. Note, each pump source was modulated at 10 Hz, and both samples had the same $Ge_{14.8}$ $As_{20.8}$ $Ga_{2.0}$ $Se_{62.4}$ + 1000 ppmw $TeCl_4$ + 500 ppmw Pr (foil) composition. See Table 4-7 for sample dimensions and equipment configurations, and results summarised in Table 4-8.*

Table 4-8: Summary of Pr^{3+} lifetime measurement results in Figure 4-11 (see Table 4-7 for sample specifications and equipment configurations):

Sample type and composition (atomic %)	Pump λ / µm	Measurement λ / µm	Lifetime coefficients				
			A$_1$	τ_1 / ms	A$_2$	τ_2 / ms	Y$_0$
F119REJN *Single material fibre (un-annealed)* (*$Ge_{14.8}$ $As_{20.8}$ $Ga_{2.0}$ $Se_{62.4}$ + 1000 ppmw $TeCl_4$ + 500 ppmw Pr (foil)*)	1.940	4.440	0.830	**10.28**	0.125	**0.50**	0.04705
		4.720	0.838	**10.28**	0.109	**1.60**	0.02384
		5.000	0.839	**10.29**	0.119	**0.45**	0.04999
	4.150	4.440	0.738	**11.55**	0.201	**3.90**	0.04413
		4.720	0.759	**11.44**	0.210	**3.75**	0.02182
		5.000	0.753	**11.47**	0.195	**3.75**	0.03775
M276REJN *Powdered glass (annealed bulk glass)* (*$Ge_{14.8}$ $As_{20.8}$ $Ga_{2.0}$ $Se_{62.4}$ + 1000 ppmw $TeCl_4$ + 500 ppmw Pr (foil)*)	2.013	4.400	0.679	**9.51**	0.275	**3.45**	0.04086
		4.720	0.702	**9.44**	0.266	**3.56**	0.02596
		5.000	0.677	**9.54**	0.274	**3.66**	0.04417
	4.150	4.400	0.762	**10.19**	0.132	**3.78**	0.0858
		4.720	0.801	**10.37**	0.163	**3.97**	0.02878
		5.000	0.755	**10.53**	0.179	**4.36**	0.05951
		5.500	0.603	**11.17**	0.259	**5.18**	0.12920
F119REJN *Single material fibre (un-annealed)* (*$Ge_{14.8}$ $As_{20.8}$ $Ga_{2.0}$ $Se_{62.4}$ + 1000 ppmw $TeCl_4$ + 500 ppmw Pr (foil)*)	1.940	2.359	0.646	**3.79**	0.300	0.47	0.06590
	4.150	2.353	0.722	**4.95**	0.158	0.99	0.09082
M276REJN *Powdered glass (annealed bulk glass)* (*$Ge_{14.8}$ $As_{20.8}$ $Ga_{2.0}$ $Se_{62.4}$ + 1000 ppmw $TeCl_4$ + 500 ppmw Pr (foil)*)	2.013	2.250	0.707	**2.88**	0	0	0.2467
	2.013	2.340	0.691	**2.86**	0	0	0.2643

The predominant 'τ_1' constituent of Pr^{3+} PL lifetimes, measured at wavelengths of 4.400 µm, 4.720 µm, and 5.000 µm, revealed that a longer wavelength pump source (*4.15 µm QCL*) resulted in longer lifetimes when compared to a shorter wavelength pump source (*~2 µm pump laser*), as shown in Figure 4-11 and Table 4-8. This trend was present for each sample type evaluated with the two pump sources.

4.2.2.4 Pr^{3+} ESA measurements

ESA measurements were performed on a distilled, nominally 500 ppmw Pr (*foil*) doped $Ge_{14.8}$ $As_{20.8}$ $Ga_{2.0}$ $Se_{62.5}$ atomic % + 1000 ppmw $TeCl_4$ F119REJN single material fibre sample 304 mm long, with a diameter of 99.4 ± 3.0 µm. This single material fibre sample was exposed to CW pump light from a 1.550 µm excitation laser to induce the $^3H_4 \rightarrow (^3F_3, {}^3F_4)$ GSA, a subsequent ESA measurement using the same sample was performed using a 1.940 µm excitation laser to induce the $^3H_4 \rightarrow {}^3F_2$ transition. Figure 4-12 (a) and (b) show the room temperature, steady state, relative change in intensity of the transmitted probe-light with pump, relative to no pump present. Additionally, the inset within Figure 4-12 (a) shows the attenuation spectrum of a separate F119REJN fibre sample. Note, this attenuation spectrum represents the zero-change axis (*along the wavelength-axis*) in the accompanying ESA spectrum in Figure 4-12 (a) and (b).

Both the 1.550 µm and 1.940 µm excitation schemes resulted in similarly shaped spectra in Figure 4-12 (a) and (b), indicating identical excited state transitions responsible for observed spectral features. However, the shapes of these two ESA spectra are likely to diverge at wavelengths less than 2.300 µm, due to differences in the predominant decay path for each excitation source, as evident by the divergent Pr^{3+} PL emission spectra for the 2.100 to 2.800 µm spectral region seen in Figure 4-9 (a) and (b). The spectral region below 2.300 µm was not evaluated due to the optical filter/dichroic mirror used (see item 4 in Figure 4-2).

Comparing these ESA spectra in Figure 4-12 (a) and (b) to the attenuation spectrum in inset Figure 4-12 (a), no prominent features were observed at 2.400 µm and 3.650 µm in the attenuation spectrum, thus confirming the latent nature of these unobstructed regions of these ESA bands which are present in the ESA spectra.

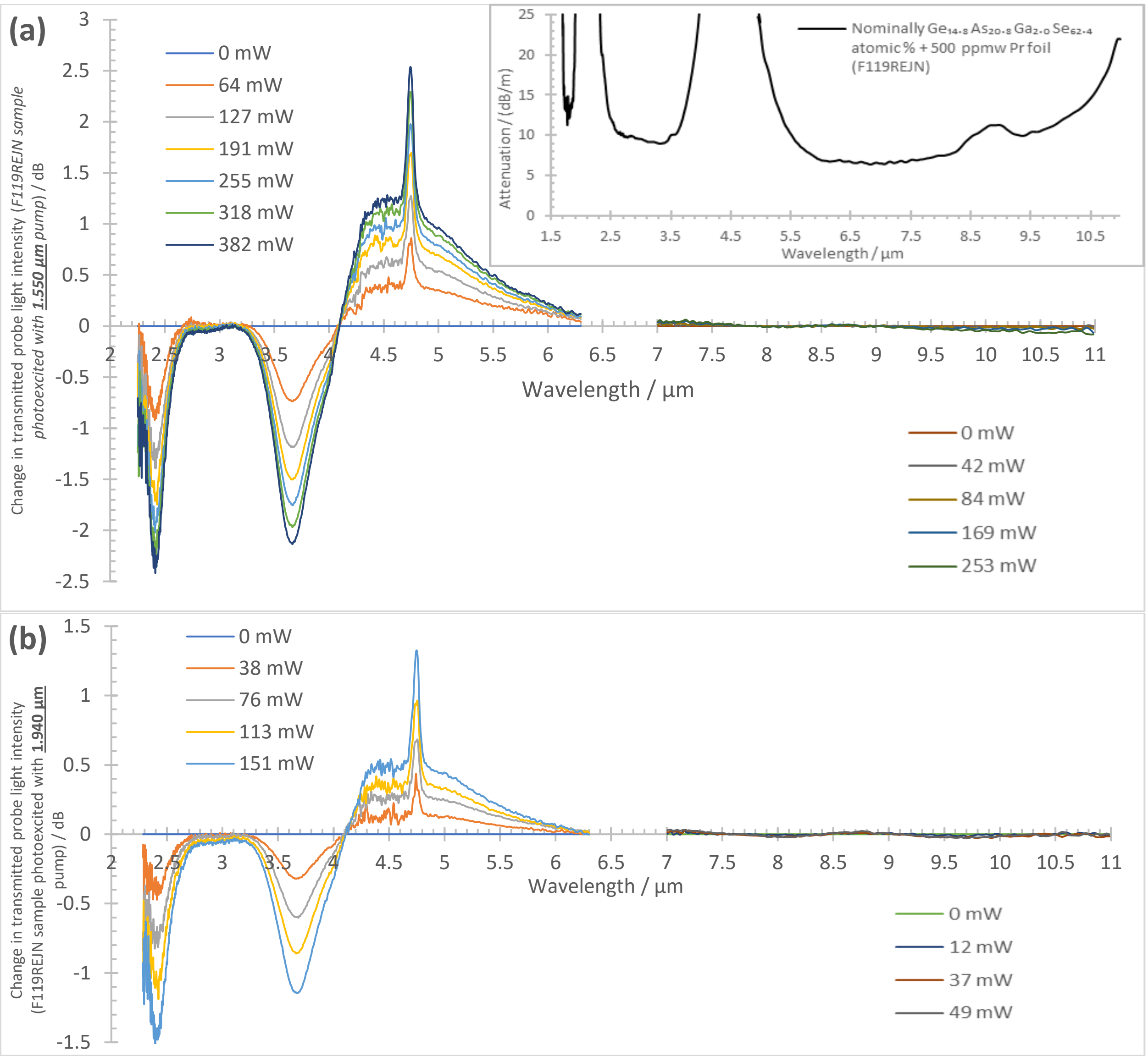

*Figure 4-12: Showing changes in transmitted probe light intensity, under application of continuous wave pump, for a 304 mm long, nominally 500 ppmw Pr (foil) doped $Ge_{14.8}$ $As_{20.8}$ $Ga_{2.0}$ $Se_{62.5}$ atomic % + 1000 ppmw $TeCl_4$ single material fibre (F119REJN) sample of diameter: 99.4 ± 3.0 µm, using: **(a)** 1.550 µm excitation laser with inset showing attenuation spectrum of F119REJN single material fibre (see Figure 3-25 (b) for additional details), and **(b)** 1.940 µm excitation laser. Note, ESA bands listed in Table 4-9.*

Table 4-9 lists each significant spectral feature, observed in Figure 4-12 (a) and (b), along with the corresponding proposed energy level transitions responsible, while Figure 4-13 shows the Pr^{3+} electronic energy level diagram, inclusive of arrows for proposed energy level transitions. The $^3H_5$ energy level was postulated as the predominant initial state from which ESA took place due to its relatively long lifetime of ~ 10.5 ms, as obtained in Section 4.2.2.3.b. These proposed energy level transitions match the corresponding Pr^{3+} energy level spacing. However, it must be noted that additional transitions between alternate energy levels were not ruled out; moreover, these alternate transitions could have also been partially, or completely, obscured by overlapping GSA bands. The ESA band centred around 2.400 µm, in Figure 4-12 (a) and (b), matched the $^3H_5 \rightarrow {}^3F_3$ upward transition, see Figure 4-13. While the ESA band peaking at 3.650 µm matched the $^3H_5 \rightarrow {}^3F_2$ upward transition. Considering the PL lifetime measurements in Section 4.2.2.3.b the 'τ_2', lifetime at ~ 3.6 ms was present throughout the 4.400 to 5.500 µm spectral region, and was attributed to the $(^3F_2, {}^3H_6) \rightarrow {}^3H_5$ transition. This indicated that the $^3H_5 \rightarrow (^3F_2, {}^3H_6)$ ESA band would also be present throughout the 3.500 to 6.500 µm spectral region, as reported in [175], and as evident by the presence of the ~1.7 and ~2.3 µm Pr^{3+} PL emission bands when employing the 4.150 µm pump, and shown in Figure 4-8, Figure 4-9 (a), Figure 4-10 (a) and (b) and Figure 4-11 (b) and (d). This ESA band was obscured by the $^3H_5 \rightarrow {}^3H_4$ GSA. Both the PL lifetime measurements and the presence of this ESA band indicate a dynamic between the $(^3F_2, {}^3H_6)$ and $^3H_5$ manifolds.

The ESA band peaking at 3.650 µm partially overlapped a SE/GSD (*stimulated emission/ground state depletion*) band centred at 4.74 µm, which matched both the $^3H_5 \rightleftharpoons {}^3H_4$ and $^3H_6 \rightarrow {}^3H_5$ transitions. Thus, it was postulated that the spectral overlap of the $^3H_5 \rightarrow {}^3F_2$ against the $(^3H_5 \rightleftharpoons {}^3H_4)$ and $(^3H_6 \rightarrow {}^3H_5)$ transitions resulted in a zero-change point at 4.110 µm, at ~35 dB/m attenuation. Note, these two transitions are further explored via numerical modelling in [179].The weak ESA bands at 8.110 µm and 9.670 µm were speculated to be due to the $^3F_2 \rightarrow {}^3F_3$ transition, due to Pr^{3+} PL emissions measurements reported in [176].

Table 4-9: Proposed Pr^{3+} electronic transitions to account for observed spectral features in Figure 4-12.

λ / µm (*see* *Figure 4-12*)	**Description**	**Proposed electronic transition**
2.400 (*4167 cm^{-1}*)	ESA band	$^3H_5 \rightarrow {}^3F_3$
3.650 (*2740 cm^{-1}*)	ESA band	$^3H_5 \rightarrow {}^3F_2$
4.110 (*2433 cm^{-1}*)	Zero-change point	$^3H_5 \rightarrow {}^3F_2$ and ($^3H_5 \rightleftharpoons {}^3H_4$) + ($^3H_6 \rightarrow {}^3H_5$)
4.740 (*2110 cm^{-1}*)	Either SE and/or GSD	$^3H_5 \rightleftharpoons {}^3H_4$ and $^3H_6 \rightarrow {}^3H_5$
8.110 (*1233 cm^{-1}*)	Weak ESA band	$^3F_2 \rightarrow {}^3F_3$
9.670 (*1034 cm^{-1}*)	Weak ESA band	$^3F_2 \rightarrow {}^3F_3$

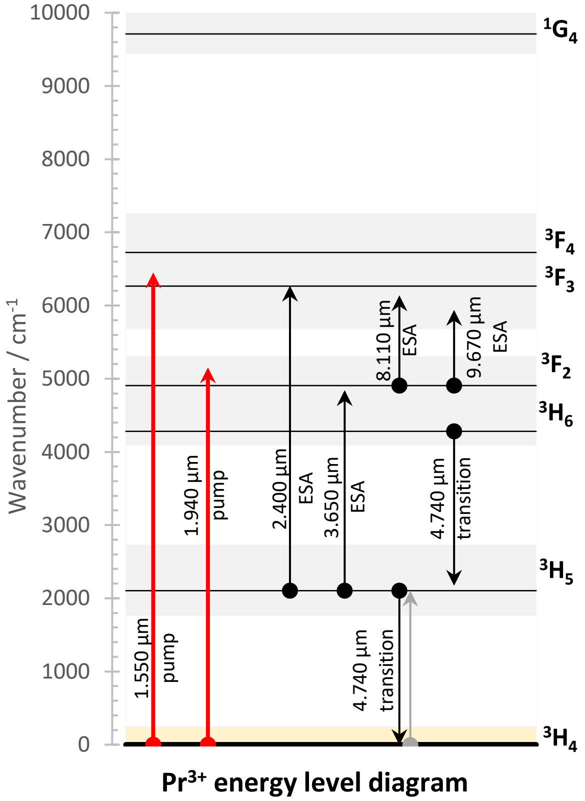

Figure 4-13: Pr^{3+} energy level diagram with possible upward and downward transitions to account for changes observed in Figure 4-12 (a) and (b) (Arrow lengths ARE TO SCALE).

Note, **GSD**- Ground State Depletion, and **SE**- Stimulated emission.

To investigate the influence of ESA transitions on the Pr^{3+} PL intensity during excitation a 'co-propagating' equipment configuration was devised and implemented, as illustrated in Figure 4-14. A nominally 1000 ppmw Pr^{3+} doped single material fibre F087REDJ, produced by Dr Dinuka Jayasuriya, was evaluated. In this configuration beams from the 1.542 µm pump sources and a broadband IR beam were combined using a 50/50 beam splitter filter, item 7 in Figure 4-14. These two beams were then focused into the sample, item 10 in Figure 4-14. The resulting Pr^{3+} PL emissions from the fibre were collected from the opposite end of the fibre and evaluated. The change in RE^{3+} PL emission intensity was calculated using the following equation:

$$Change\ in\ PL\ intensity\ (dB) = 10 \times log_{10}\left(\frac{PL\ intensity\ with\ broadband\ IR\ source\ on}{PL\ intensity\ with\ broadband\ IR\ source\ off}\right) \qquad \text{Equation 4-3}$$

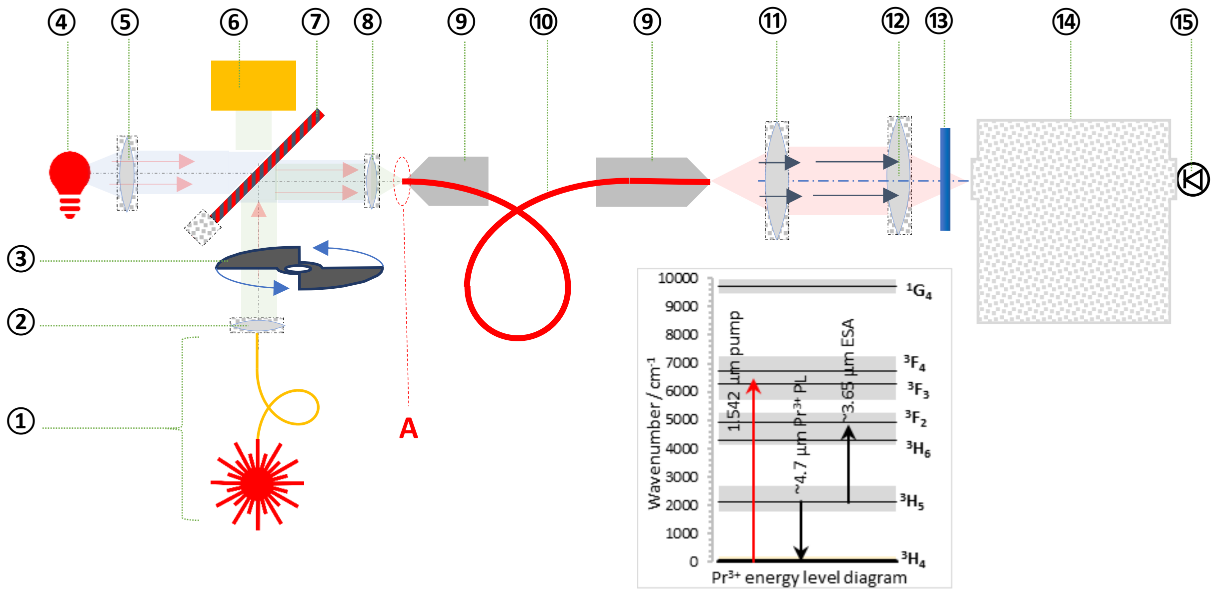

1. Fibre coupled tuneable source (*Agilent, 8164B + 8198- tuneable module, with EDFA: IRE-POLUS EAD-2W-C*) operated at a wavelength of 1.542 µm in CW mode.
2. Collimator (*Thorlabs, F220APC-1550*) mounted on a XYZ translational stage.
3. Optical chopper (*Scitec Instruments*) operated at 200 Hz.
4. Broadband IR light source (*Tungsten carbide filament*), 12 volts at 1.56 ± 0.05 amperes operated in CW mode. With launch power ~ 20 mW at position 'A'.
5. CaF_2 lens, f = 40 mm (*Thorlabs, LA5370*).
6. Thermal power meter (*Thorlabs, C-Series S302C*).
7. CaF_2 50/50 beam splitter (*Thorlabs, BSW520*) mounted in kinematic mount.
8. Focusing lens, aspheric lens, f = 5.95 mm (*Thorlabs, 390028-E*) on XYZ translational stage.
9. Stainless steel V-groove fibre holder used to mount the single material fibre.
10. Single material fibre: **F087REDJ** a nominally 1000 ppmw Pr^{3+} doped $Ge_{15}As_{21}Se_{63}Ga_1$ atomic %, sample 195 mm long, with a 170 µm diameter.
11. CaF_2 lens, f = 20 mm (*Thorlabs, LA5315*) on XYZ translational stage.
12. Ge lens, f = 12.5 mm (*Edmund Optics #89-607*) on XYZ translational stage.
13. 3.407 µm LWP (*long wave pass*) optical filter (see).
14. Monochromator (*Spex Minimate equipped with diffraction grating blazed at 6.000 µm*) with 1 mm entrance and exit slits, supplied with dry, purged atmosphere (*reduced H_2O & CO_2 concentration*).
15. MCT (*mercury cadmium telluride*) detector (*Vigo Systems, PVI-4TE-6*).

Note, quoted launch power estimated at position '**A**'

Figure 4-14: Illustration showing 'co-propagating' equipment configuration used to evaluate a 1000 ppmw Pr^{3+} doped single material fibre F087REDJ sample, along with inset showing the Pr^{3+} energy level diagram. Note, the control/data acquisition configuration used is described in Appendix 7.2.4.4.

Figure 4-15 shows the Pr^{3+} PL emission spectrum and change in Pr^{3+} PL emission intensity spectra obtained from a single material fibre F087REDJ sample, with a 170 µm diameter, 19.5 cm long. A

3.407 µm LWP filter was used as item 13 in Figure 4-14 to prevent the 2nd order diffraction of ~2.4 µm Pr^{3+} PL emission band from influencing the measurement.

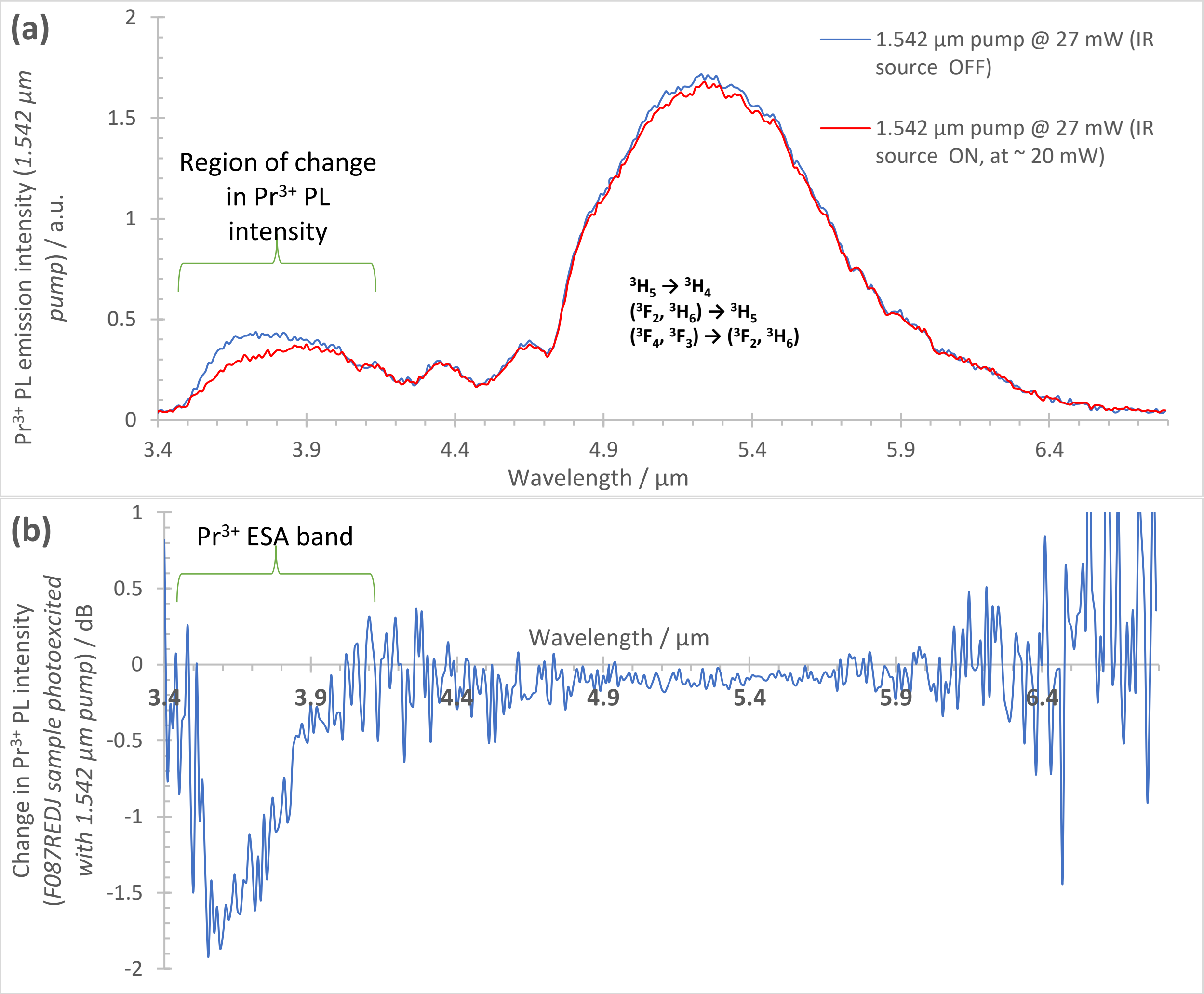

Figure 4-15: A nominally $Ge_{15}As_{21}Se_{63}Ga_{1}$ atomic % doped with 1000 ppmw Pr (foil) single material fibre F087REDJ sample, with 170 µm diameter and 19.5 cm long, excited with 1.542 µm pump source using the equipment configuration shown in Figure 4-14, showing: ***(a)*** *Pr^{3+} PL emission spectra with and without application of broadband IR source, and* ***(b)*** *changes in Pr^{3+} PL intensity due application of broadband IR source.*

Figure 4-15 (a) shows a reduction in Pr^{3+} PL intensity within the 3.4 µm to ~4.0 µm spectral region while the broadband IR source was ON. Additionally, the Pr^{3+} PL emission band shown differed from the Pr^{3+} PL spectra presented in Section 4.2.2.3 due to the underlying [-Se-H] vibrational impurity (see Table 2-4) within the long propagation length of the sample.

Figure 4-15 (b) shows an ESA band spanning the 3.4 µm to ~4.0 µm spectral region influencing the intensity of the Pr^{3+} PL emission intensity. These results were noisy, however the spectral feature spanning the 3.4 µm to ~4.0 µm spectral region agrees with the ESA measurements presented in Section 4.2.2.4. It was postulated that the change in Pr^{3+} PL intensity within the 3.4 µm to ~4.0 µm spectral region was due to ESA from the $^3H_5$ manifold which caused a reduction in $^3H_5 \rightarrow {}^3H_4$ PL intensity.

4.2.3 Samarium spectroscopy.

An undistilled, nominally $Ge_{19.4}Sb_{9.7}Ga_{3.0}Se_{67.9}$ atomic % + 1000 ppmw Sm (*foil*) M227RERC glass rod was made by PhD student Richard Crane and subsequently drawn into single material fibre F099RERC, using the procedure described in [36]. Note, the optical and compositional evaluation of this glass can be found in Section 3.2.7. A portion of the bulk glass M227RERC rod was processed into a bulk glass sample and used for the presented absorption measurements in Section 4.2.3.1. Portions of the single material fibre F099RERC were used for the PL emission measurements and ESA measurements in Sections 4.2.3.3 and 4.2.3.4, respectively.

4.2.3.1 Sm^{3+} absorption and emission cross-sections:

Figure 4-16 (a) shows the absorption coefficient spectrum for an undistilled, nominally 1000 ppmw Sm (*foil*) doped sample M227RERC, ostensibly containing 1.84×10^{19} cations/cm^3. The GSA between the $^6H_{5/2}$ ground state and its excited state levels can be observed. The ($^6H_{5/2} \rightarrow {}^6F_{11/2}$) transition was the shortest observed GSA, centred at 10304 cm^{-1} (*0.970 μm*), shorter absorptions were either very weak or obscured by the high energy optical bandgap absorption edge of the Ge-Sb-Ga-Se host glass. Figure 4-16 (b) shows the corresponding Sm^{3+} energy level diagram. Figure 4-16 (c) shows the calculated absorption cross-sections for each of the observed GSA bands. The underlying [-Se-H] impurity vibrational absorption bands were numerically removed. These results agree with the GLS absorption data presented in [118]. Note, the underlying [-OH] impurity vibrational absorption band was not numerically removed in Figure 4-16 (a) and (c).

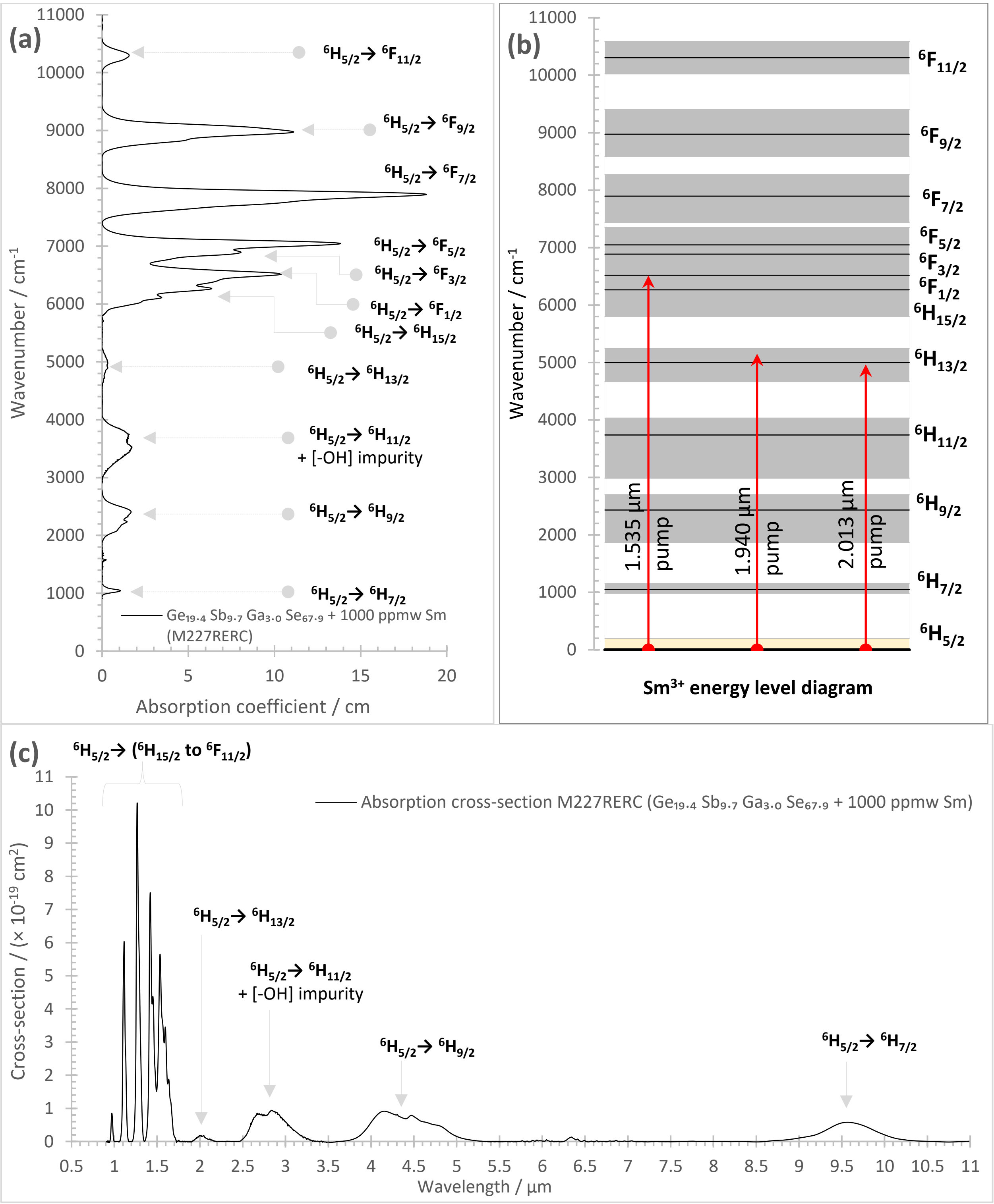

*Figure 4-16: Showing: **(a)** absorption coefficient spectrum of a nominally 1000 ppmw Sm (foil) doped M227RERC sample, along with **(b)** the corresponding energy level diagram for Sm^{3+} in glass host showing 1.535 µm, 1.940 µm, and 2.013 µm excitation wavelengths used in future measurements, and **(c)** showing the calculated M227RERC absorption cross-sections. Note, the Sm^{3+} cross-section calculations assumed several factors (Section 3.2.8.2 and 4.2.6.1) and thus its accuracy should <u>not</u> be relied upon.*

4.2.3.2 Sm^{3+} literature review:

The NIR and MIR properties of the 'Sm' dopant have received relatively little attention, despite exhibiting GSA bands suitable for pumping with readily commercially available sources. This is possibly due to the transitions between the closely spaced levels in the Sm^{3+} energy level (see Figure 4-34) being dominated by non-radiative multi-phonon decay. Table 4-10 shows the PL emission bands exhibited by the Sm^{3+} cation, while Table 4-11 shows the relatively radiative lifetimes of these emission bands.

Table 4-10: Sm^{3+} PL emission bands found in literature (see Figure 4-16 (b) for energy level diagram):

Transition	**Composition / sample type**	**Pump λ / µm**	**Emission band range / µm**	**Peak λ / µm**	**Reference**
$^6F_{1/2} \rightarrow {}^6H_{5/2}$	$Ga_{5.0}Ge_{20.0}Sb_{10.0}Se_{65.0}$ Either 500 or 1000 ppmw Sm^{3+} (*single material fibres*)	1.450 or 2.050	1.5 to 1.8	~1.67	[37]
$^6H_{13/2} \rightarrow {}^6H_{5/2}$			1.8 to 2.1	~1.95	
$^6H_{13/2} \rightarrow {}^6H_{9/2}$			3.2 to 4.5	~ 3.7	
$^6H_{13/2} \rightarrow {}^6H_{11/2}$			6.0 to 9.0	~7.3	
$^6H_{13/2} \rightarrow {}^6H_{7/2}$ $^6H_{11/2} \rightarrow {}^6H_{5/2}$ $(^6F_{1/2}, {}^6F_{3/2}, {}^6H_{15/2}) \rightarrow {}^6H_{9/2}$	$(Ge\text{-}Sb\text{-}Se)_{97.0}Ga_{3.0}$ 1000 ppmw Sm (*foil*) (*single material fibre*)	1.470	2.2 to 3.2	~ 2.7	[36]
$^6H_{13/2} \rightarrow {}^6H_{9/2}$ $^6H_{11/2} \rightarrow {}^6H_{7/2}$ $(^6F_{1/2}, {}^6F_{3/2}, {}^6H_{15/2}) \rightarrow {}^6H_{11/2}$		1.470 or 1.300	3.2 to 4.5	~ 3.6	
$^6H_{13/2} \rightarrow {}^6H_{11/2}$ $^6H_{11/2} \rightarrow {}^6H_{9/2}$			6.3 to 8.7	~ 7.7	

Table 4-11: Sm^{3+} PL emission lifetimes found in literature (see Figure 4-16 (b) for energy level diagram):

Transition		**Composition / sample type**	**Calculated τ_{rad} / ms**	**Measured τ_{rad} / ms**	**Reference**
From	**To**				
$^6F_{1/2} + {}^6F_{3/2} + {}^6H_{15/2}$	$^6H_{5/2}$	$Ga_{5.0}Ge_{20.0}Sb_{10.0}Se_{65.0}$ 500 ppmw Sm^{3+} (*single material fibres*)	0.39	0.005 ± 0.002	[37]
$^6H_{13/2}$	$^6H_{5/2}$		4.34	0.011 ± 0.002	
$^6H_{13/2}$	$^6H_{9/2}$		4.34	0.011 ± 0.002	
$^6H_{11/2}$			6.61	-	
$^6H_{13/2}$ $^6H_{11/2}$	$^6H_{9/2}$ $^6H_{7/2}$	$(Ge\text{-}Sb\text{-}Se)_{97.0}Ga_{3.0}$ 1000 ppmw Sm (*foil*) (*single material fibre*)	-	0.102	[36]
$^6H_{13/2}$ $^6H_{11/2}$ $(^6F_{1/2} + {}^6F_{3/2} + {}^6H_{15/2)}$	$^6H_{11/2}$ $^6H_{9/2}$ $^6H_{11/2}$		-	0.097	

Notably, depending on the host material, fabrication process, and excitation conditions the Sm cation can exhibit two stable valence states, a divalent state, (Sm^{2+}) or the trivalent state (Sm^{3+}) and both valence states can coexist [23,24,118,180]. Moreover, the 'Sm^{2+}' possesses an electronic configuration of [Xe] $4f_4$, like trivalent promethium (Pm^{3+}), with available '4f' electrons for 4f ⇌ 4f transitions, thus is likely to exhibit MIR PL.

4.2.3.3 Sm^{3+} PL emission measurements

Sm^{3+} PL emission spectrum and PL lifetime measurements were performed sequentially using three separate excitation sources operating at wavelengths of 1.535 µm, 1.940 µm and 2.013 µm on the samples listed in Table 4-12. The 1.535 µm excitation scheme used the $^6H_{5/2} \rightarrow {}^6F_{1/2}$ GSA, while both the 1.940 µm and 2.013 µm excitation schemes used the $^6H_{5/2} \rightarrow {}^6H_{13/2}$ GSA, as illustrated in Figure 4-16 (b)

Table 4-12: Sample codes, composition, dimentions, and equipment configurations used for Sm^{3+} PL emission measurements (see Section 7.3 for description of equipment configuration code).

Sample type	Code and nominal composition (atomic %)	Dimensions	Figure and equipment configuration
Single material fibre (*un-annealed*)	**F099RERC** ($\mathit{Ge}_{19.4}\ \mathit{Sb}_{9.7}\ \mathit{Ga}_{3.0}\ \mathit{Se}_{67.9}$ + *1000 ppmw Sm (foil)*)	88.71 mm long, with diameter of 216 ± 21.5 µm.	Figure 4-17: **A**[1_d-7_a] **F**[9_a] **I**[12_a- $13_{2.000\ \mathrm{LWP}}$- 14_a -15_{ai} – 16_b] Figure 4-18 (a): **A**[1_a-7_a] **F**[9_a] **I**[12_a- $13_{2.484\ \mathrm{LWP}}$- 14_a -15_{aii} – 16_b] Figure 4-18 (a) and Figure 4-19: **A**[1_c-7_a] **F**[9_a] **I**[12_a- $13_{2.484\ \mathrm{LWP}}$- 14_a -15_{aii} – 16_b]
Single material fibre (*un-annealed*)	**F099RERC** ($\mathit{Ge}_{19.4}\ \mathit{Sb}_{9.7}\ \mathit{Ga}_{3.0}\ \mathit{Se}_{67.9}$ + *1000 ppmw Sm (foil)*)	~48 mm long, with diameter of ~ 210 µm.	Figure 4-19: **A**[1_a-7_a] **F**[9_a] **I**[12_b- $13_{3.407\ \mathrm{LWP}}$- 14_b -15_{none} – 16_b]

4.2.3.3.a Sm^{3+} PL emission spectra:

Three distinct Sm^{3+} PL emission bands spanning between ~2.00 to 2.300 µm, 2.400 to 3.200 µm, and 3.230 to ~5.000 µm were detected and investigated, like those found in literature (see Table 4-10). Sm^{3+} PL emission greater than 6.500 µm were not investigated.

Application of the 2.013 µm excitation source resulted in two weak emission bands between ~2.00 to 2.300 µm and 2.400 to 3.200 µm, as shown in Figure 4-17, which were attributed to the $^6H_{13/2} \rightarrow {}^6H_{5/2}$, and $^6H_{11/2} \rightarrow {}^6H_{5/2}$ transitions, respectively.

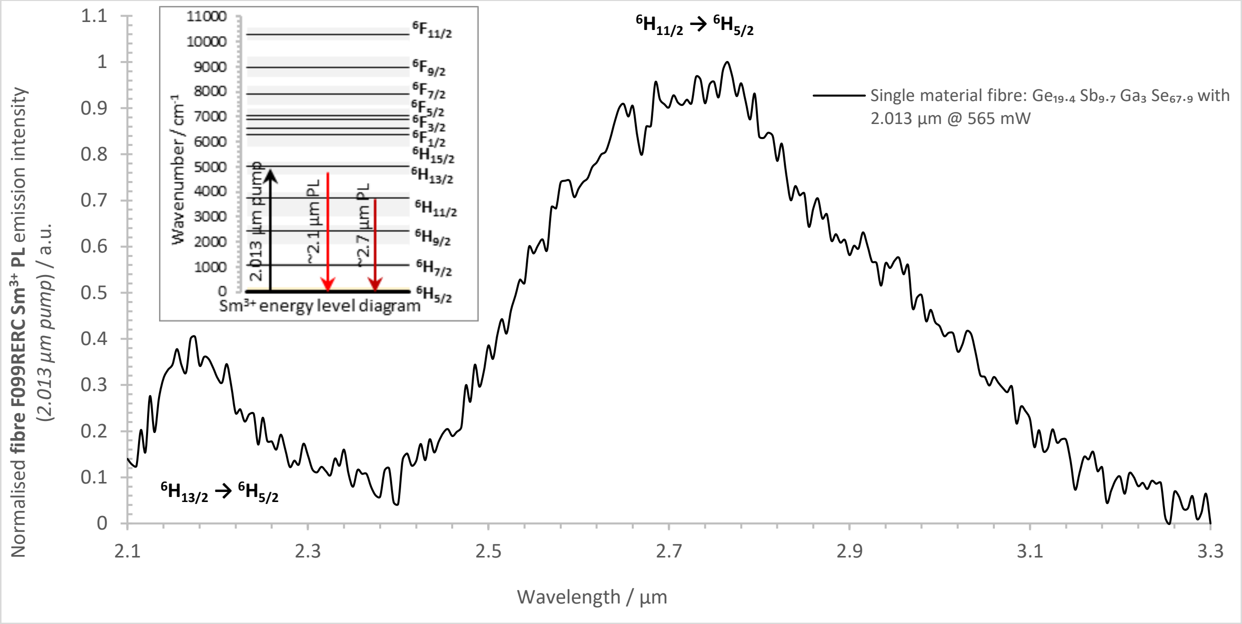

*Figure 4-17: Normalised PL emission spectra for nominally 1000 ppmw Sm (foil) doped $Ge_{19.4}$ $Sb_{9.7}$ $Ga_{3.0}$ $Se_{67.9}$ atomic % single material fibre (**F099RERC**) sample using a 2.013 µm pump source with inset showing Sm^{3+} energy level diagram (<u>Arrow lengths ARE TO SCALE</u>). Not corrected for system spectral response. See Table 4-12 for sample dimensions and equipment configuration used.*

The ~2.00 to 2.300 µm emission band was partially truncated by the 2.00 µm LWP filter used in the equipment configuration to block any unabsorbed 2.013 µm pump light.

Application of either the 1.535 µm or the 2.013 µm excitation source resulted in an emission band between 3.230 to ~5.000 µm, as shown in Figure 4-18. This PL emission band could potentially be attributed to at least three different radiative transitions; ($^6F_{1/2}$, $^6H_{15/2}$) → $^6H_{11/2}$, $^6H_{13/2}$ → $^6H_{9/2}$, and $^6H_{11/2}$ → $^6H_{7/2}$, as illustrated within the inset in Figure 4-18.

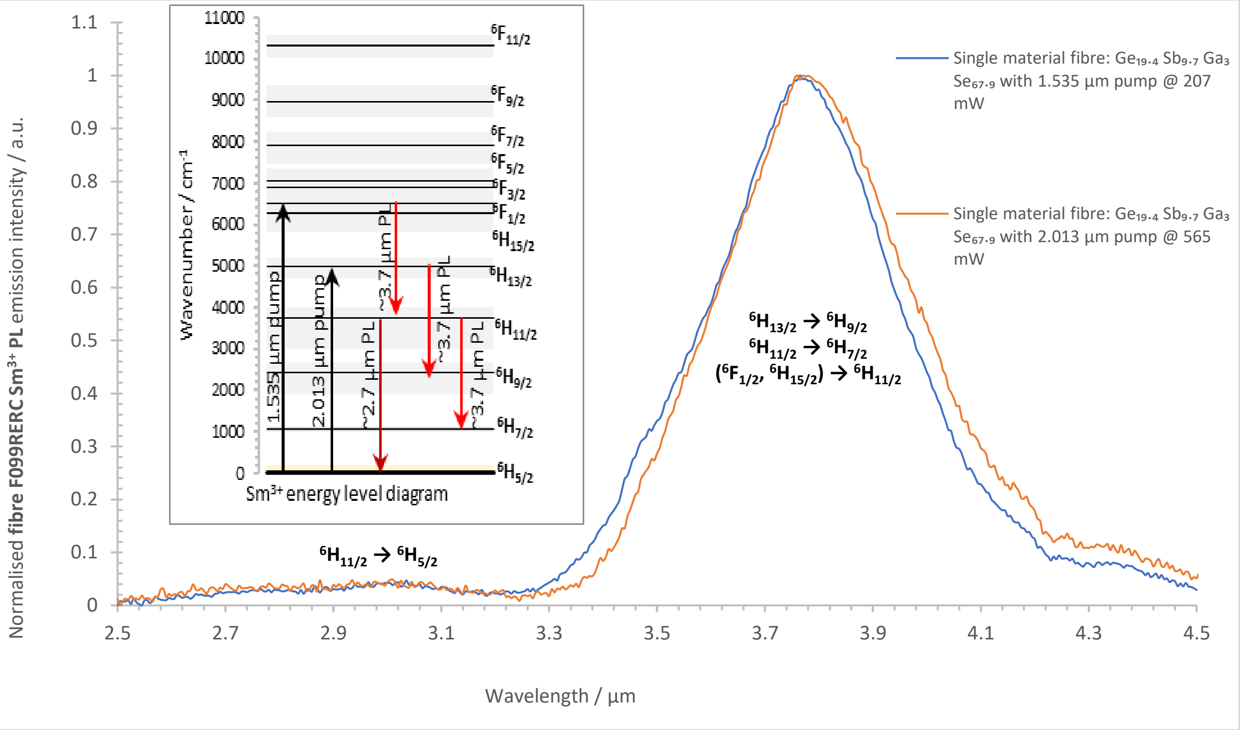

Figure 4-18: Normalised PL emission spectra for nominally 1000 ppmw Sm (foil) doped $Ge_{19.4}$ $Sb_{9.7}$ $Ga_{3.0}$ $Se_{67.9}$ atomic % single material fibre (F099RERC) sample using 1.535µm and 2.013 µm pump sources with inset showing Sm^{3+} energy level diagram (Arrow lengths ARE TO SCALE). Not corrected for system spectral response. See Table 4-12 for sample dimensions and equipment configuration used.

Both the 1.535 µm and the 2.013 µm excitation schemes resulted in similarly shaped emission spectra, as shown in Figure 4-18, indicating that they were comprised of similar radiative transitions, as illustrated within the inset in Figure 4-18.

The weak intensity of the 2.400 to 3.200 µm emission band shown in Figure 4-17 and Figure 4-18, was attributed to reabsorption due to the $^6H_{5/2}$ → $^6H_{13/2}$ GSA, along with the overlapping [-OH] impurity vibrational absorption resonantly absorbing and transferring PL into vibrational quanta. Conversely, the 3.230 to ~5.000 µm emission band, shown in Figure 4-18, exhibited a greater intensity because it did not terminate at the ground state, as illustrated within the inset in Figure 4-18, and overlapped a relatively small [-Se-H] absorption, peaking around 3.5 µm.

4.2.3.3.b Sm^{3+} PL lifetime results:

PL emission lifetime 'τ_{rad}' measurements were performed on the samples listed in Table 4-12 using either a 1.535 µm or a 1.940 µm excitation source. These lifetime measurements focused on the 3.230 to ~5.000 µm Sm^{3+} PL emission band. Evaluation of the ~2.00 to 2.300 µm, and 2.400 to 3.200 µm Sm^{3+} PL emission bands were omitted due to low PL intensity. Figure 4-19 (b) shows the normalised Sm^{3+} PL emission measurement results, along with the corresponding fitted exponential function for each sample. Note, a nonstandard equipment configuration was employed for PL lifetime measurements using the 1.535 µm excitation source to avoid utilizing an EDFA, (*erbium doped fibre amplifier*), which would otherwise be connected to the 1.535 µm source. This limited the maximum output power to less than 30 mW. The equipment configuration is shown in Figure 4-19 (a), employed a 3.407 LWP (*long wave pass*) filter in place of a monochromator to maximise the Sm^{3+} PL intensity detected for wavelengths greater than 3.407 µm.

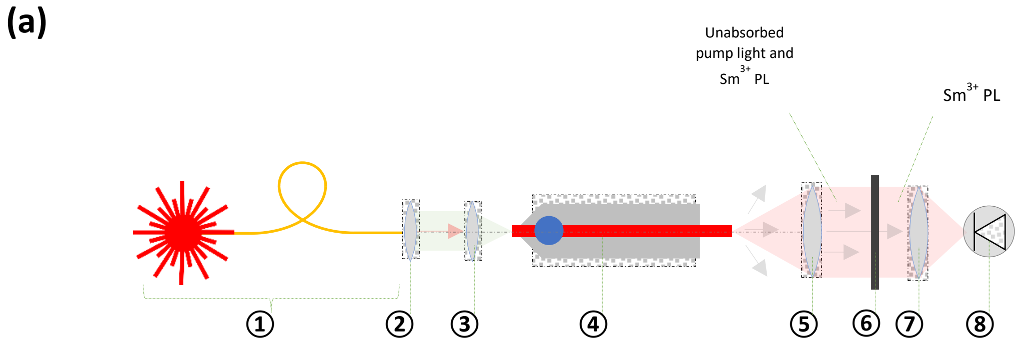

1) 1.535 µm fibre coupled excitation laser (*Agilent, 8164B + 8198- tunable module*).
2) Collimator (*Thorlabs, F220APC-1550*) on a XYZ translational stage:
3) Bi-convex CaF_2 lens, f = 15 mm (*Thorlabs, LB5766-E*) focusing lens on XYZ translational stage:
4) Single material fibre F099RERC sample, with both ends cleaved on Stainless steel 'V-groove' fibre holder on XYZ stage.
5) CaF_2 lens, f = 40 mm (*Thorlabs, LA5370*) collection lens on XYZ stage.
6) 3.407 µm LWP (*Long wave pass*) filter.
7) CaF_2 lens, f = 40 mm (*Thorlabs, LA5370*) collection lens on XYZ stage.
8) MCT (*mercury cadmium telluride*) detector (*Vigo Systems, PVI-4TE-6*)

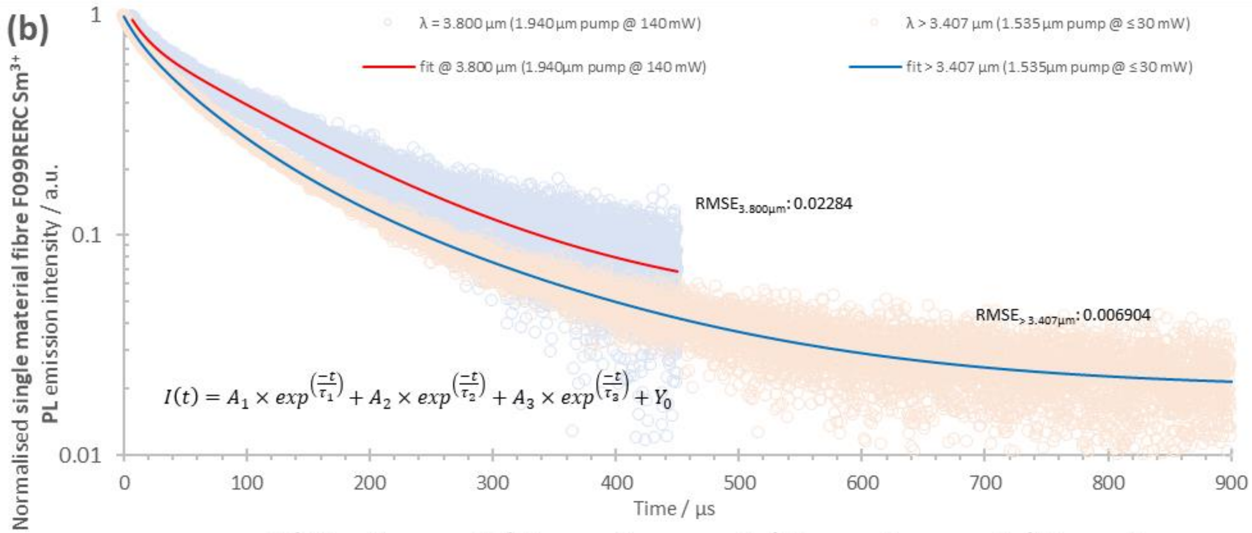

	λ / µm	A_1	τ_1 / µs	A_2	τ_2 / µs	A_3	τ_3 / µs	Y_0
1.940 µm pump (140 mW)	3.800	0	**0**	0.757	**128.19**	0.314	**14.36**	0.04586
1.535 µm pump (≤ 30 mW)	3.407	0.503	**56.09**	0.311	**169.49**	0.159	**12.40**	0.02005

*Figure 4-19: Showing **(a)** Equipment configuration used for lifetime measurements of nominally 1000 ppmw Sm (foil) doped $Ge_{19.4}$ $Sb_{9.7}$ $Ga_{3.0}$ $Se_{67.9}$ atomic % single material fibre (**F099RERC**) sample using a 1.535 µm pump source, and **(b)** Normalised Sm^{3+} PL lifetime (scatter plot) fitted with exponential decay function (line) for two separate single material fibre (**F099RERC**) samples excited with 1.535 µm and 1.940 µm pump sources modulated at 10 Hz. Note, both samples had the same $Ge_{19.4}$ $Sb_{9.7}$ $Ga_{3.0}$ $Se_{67.9}$ atomic % + 1000 ppmw Sm (foil) composition. See Table 4-12 for sample dimensions and equipment configuration used.*

The PL lifetime measurement at 3.800 µm, shown in Figure 4-19 using the 1.940 µm pump source, was best fitted using a two-term exponential function, which predominantly consisted of a longer

'τ_2', at ~ 128.2 µs, along with a less frequent shorter 'τ_3', at ~ 14.4 µs. The PL lifetime measurement for wavelengths greater than 3.407 µm, shown in Figure 4-19 using the 1.535 µm pump source, was best fitted using a three-term exponential function, which predominantly consisted of a 'τ_1', at ~ 56.09 µs, followed by 'τ_2', at ~ 169.49 µs and 'τ_3', at ~ 12.4 µs. Notably, the values of 'τ_2' obtained from the different excitation schemes were close to each other in value and similar in magnitude to lifetime measurements found in [36], this similarity was also present for the 'τ_3' results. This indicated that both excitation schemes shared at least two common radiative transitions, possibly the $^6H_{13/2} \rightarrow {}^6H_{9/2}$, and $^6H_{11/2} \rightarrow {}^6H_{7/2}$ transitions, see inset with Figure 4-18, and as evident by the similarly shaped Sm^{3+} PL emission spectra shown in Figure 4-18.

4.2.3.4 Sm^{3+} ESA measurements

ESA measurements were performed on an undistilled, nominally 1000 ppmw Sm (*foil*) doped $Ge_{19.4}\,Sb_{9.7}\,Ga_{3.0}\,Se_{67.9}$ atomic % F099RERC single material fibre sample 300 mm long, with a diameter of 189.6 ± 8.3 µm. This single material fibre sample was exposed to CW pump light from a 1.535 µm excitation laser to induce the $^6H_{5/2} \rightarrow {}^6F_{1/2}$ GSA. Figure 4-20 show the room temperature, steady state, relative change in intensity of the transmitted probe-light with pump, relative to no pump present, for the fibre sample. Additionally, the inset within Figure 4-20 shows the attenuation spectrum of a separate F099RERC fibre sample. Note, this attenuation spectrum represents the zero-change axis (*along the wavelength-axis*) in the accompanying ESA spectrum in Figure 4-20. Comparing the ESA spectra in Figure 4-20 to the F099RERC attenuation spectrum inset, no prominent features were observed at ~ 2.5 µm, ~ 3.5 µm and ~ 5.0 µm in the attenuation spectrum, thus verifying the latent nature of these unobstructed ESA bands that were present in the corresponding ESA spectrum.

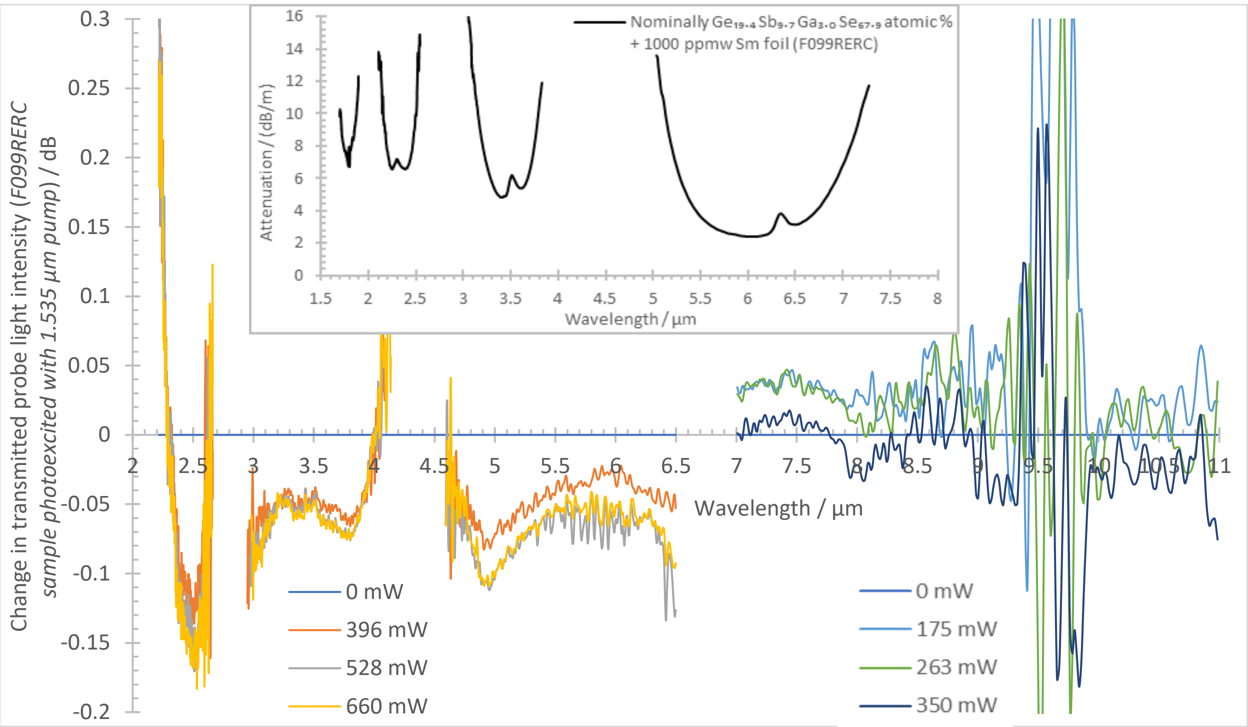

Figure 4-20: Showing changes in transmitted probe light intensity, under application of a 1.535 µm continuous wave pump laser for a 302 mm long, nominally 1000 ppmw Sm (foil) doped $Ge_{19.4}$ $Sb_{9.7}$ $Ga_{3.0}$ $Se_{67.9}$ atomic % single material fibre sample (F099RERC) with diameter of 189.6 ± 8.3 µm, with inset showing attenuation (dB/m) vs. Wavelength (µm) for F099RERC single material fibre sample (see Figure 3-32 for additional details on F099RERC attenuation spectrum). Note, spectral regions between 2.6 to 3.0 µm, and 4.1 to 4.6 µm, were omitted due to the $^6H_{5/2} \rightarrow {}^6H_{11/2}$ GSA + [-OH] impurity absorption, and the $^6H_{5/2} \rightarrow {}^6H_{9/2}$ GSA + [-Se-H] impurity absorption, respectively. Note, ESA bands are listed in Table 4-13.

Table 4-13 lists each significant spectral feature, observed in Figure 4-20, along with the corresponding proposed energy level transitions responsible for these features, while Figure 4-21 shows the Sm^{3+} electronic energy level diagram, inclusive of arrows for proposed energy level transitions. The obtained spectra were very weak and noisy, this, coupled with the inherently complex Sm^{3+} energy level scheme, made speculating the transitions responsible for the observed features uncertain. Hence the presented Sm^{3+} ESA transitions are more tentative than the Pr^{3+}, Tb^{3+}, and Dy^{3+} dopants evaluated.

Table 4-13: Proposed Sm^{3+} electronic transitions to account for observed spectral features in Figure 4-20.

λ / µm (*see Figure 4-20*)	**Description**	**Proposed electronic transition**
~ 2.0 µm (*5000 cm^{-1}*)	Either SE and/or GSD	$^6H_{13/2} \rightleftharpoons {}^6H_{5/2}$
~ 2.5 µm (*4000 cm^{-1}*)	Indistinct ESA	$^6H_{7/2} \rightarrow {}^6H_{13/2}$, $^6H_{9/2} \rightarrow ({}^6H_{15/2}, {}^6F_{1/2})$, $^6H_{11/2} \rightarrow {}^6F_{7/2}$, $^6H_{13/2} \rightarrow {}^6F_{9/2}$, and $({}^6H_{15/2}, {}^6F_{1/2}) \rightarrow {}^6F_{11/2}$
~ 2.7 µm (*3700 cm^{-1}*)	Either SE and/or GSD	$^6H_{11/2} \rightleftharpoons {}^6H_{5/2}$
~ 3.5 µm (*2850 cm^{-1}*)	Indistinct ESA	$^6H_{7/2} \rightarrow {}^6H_{11/2}$, $^6H_{9/2} \rightarrow {}^6H_{13/2}$, $^6H_{11/2} \rightarrow ({}^6F_{1/2}, {}^6H_{15/2})$, $^6H_{13/2} \rightarrow {}^6F_{7/2}$, and $({}^6H_{15/2}, {}^6F_{1/2}) \rightarrow {}^6F_{9/2}$
~ 4.3 µm (*2300 cm^{-1}*)	Either SE and/or GSD	$^6H_{9/2} \rightleftharpoons {}^6H_{5/2}$
~ 5.0 µm (*2000 cm^{-1}*)	Indistinct ESA	$^6H_{13/2} \rightarrow ({}^6F_{5/2}, {}^6F_{3/2})$ and $({}^6F_{3/2}, {}^6F_{5/2}) \rightarrow {}^6F_{9/2}$
~8.0 µm (*1250 cm^{-1}*)	Indistinct ESA	$^6H_{7/2} \rightarrow {}^6H_{9/2}$, $^6H_{9/2} \rightarrow {}^6H_{11/2}$, $^6H_{11/2} \rightarrow {}^6H_{13/2}$ $^6H_{13/2} \rightarrow ({}^6H_{15/2}, {}^6F_{7/2})$, $({}^6H_{15/2}, {}^6F_{1/2}) \rightarrow {}^6F_{7/2}$, $^6F_{7/2} \rightarrow {}^6F_{9/2}$, and $^6F_{9/2} \rightarrow {}^6F_{11/2}$
~ 9.5 µm (*1052 cm^{-1}*)	Either SE and/or GSD	$^6H_{7/2} \rightleftharpoons {}^6H_{5/2}$

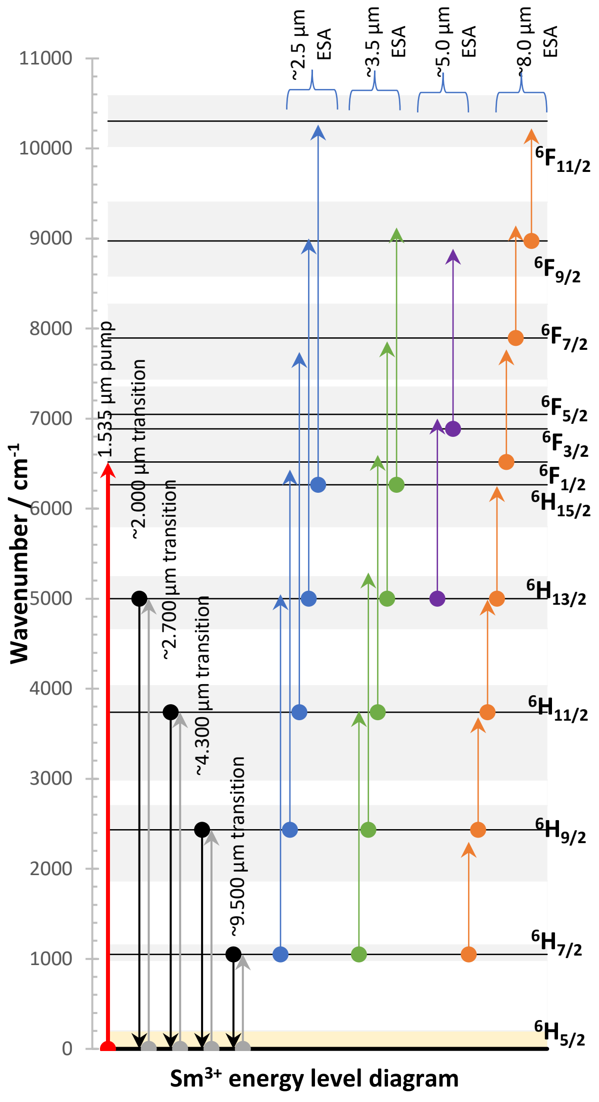

Figure 4-21: Sm^{3+} energy level diagram with possible upward and downward transitions to account for changes observed in Figure 4-20 (Arrow lengths ARE TO SCALE in energy).

Note, **GSD**- Ground State Depletion, and **SE**- Stimulated emission.

The separate SE/GSD bands centred around ~2.0 µm, ~2.7 µm, ~4.3 µm and ~9.5 µm, seen in Figure 4-20, were attributed to the $^6H_{13/2} \rightleftharpoons {}^6H_{5/2}$ transition, $^6H_{11/2} \rightleftharpoons {}^6H_{5/2}$ transition, $^6H_{9/2} \rightleftharpoons {}^6H_{5/2}$ transition, and $^6H_{9/2} \rightleftharpoons {}^6H_{5/2}$ transition, respectively, and shown in Figure 4-21. At least four weak and indistinct broad ESA bands around ~2.5 µm, ~3.5 µm, ~5.0 µm and ~8.0 µm were present in Figure 4-20. Due to the complex Sm^{3+} energy level these ESA features could not easily be attributed to any specific transitions thus, several transitions were proposed and listed in Table 4-13. However, it must be noted that an excited electronic population was assumed present for ESA to originate from these levels. The proposed transitions to account for the ~2.5 µm, ~3.5 µm, ~5.0 µm and ~8.0 µm transitions, listed in Table 4-13 and shown in Figure 4-21, highlighted the potential for the Sm^{3+} cation to up-convert longer wavelengths to several shorter wavelengths simultaneously. Additionally, the numerous of disparate transitions possible could also explain the weak and indistinct nature of the ESA features observed even at ~ 660 mW pump powers.

4.2.4 Terbium spectroscopy.

Two separate distilled, glass rods of nominal composition: $Ge_{14.8}$ $As_{20.8}$ $Ga_{2.0}$ $Se_{62.4}$ atomic % + 1000 ppmw $TeCl_4$ + 500 ppmw 'Tb' (*foil*) M274REJN, and $Ge_{15.2}$ $As_{21.2}$ $Se_{63.6}$ atomic % + 1000 ppmw $TeCl_4$ + 300 ppmw 'Tb' (*foil*) M275REJN, were produced by the author. Both M274REJN and M275REJN glass rods were then individually drawn into single material fibre/cane: F116REJN and F120REJN, respectively. A portion of each M274REJN and M275REJN glass rod was processed into two separate bulk glass samples and used for the presented absorption measurements in Section 4.2.4.1. The cane F116REJN was subsequently used as the core in the fabrication of the SIF F122REJN. A portion of the M274REJN bulk glass was ground into powdered glass and used with sections of single material fibre F116REJN, F120REJN, along with SIF F122REJN for the PL emission measurements presented in Section 4.2.4.3. Additionally, a separate section of single material fibre was used for the ESA measurements presented in Section 4.2.4.4. Note, the M275REJN composition was fabricated to investigate the viability of doping and drawing to fibre a chalcogenide glass without any 'Ga' co-solubilizer. Both the M274REJN, and M275REJN samples are further evaluated in Sections 3.2.4, and 3.2.5.

4.2.4.1 Tb^{3+} absorption and emission cross-sections:

Figure 4-22 (a) shows the absorption coefficient spectra for two nominally 500 ppmw 'Tb' (*foil*) glass samples M228REJN(RC), M274REJN, and a nominally 300 ppmw 'Tb' (*foil*) glass sample M275REJN, each ostensibly containing 8.53×10^{18} cations/cm^3, 8.53×10^{18} cations/cm^3, and 5.06×10^{18} cations/cm^3, respectively.

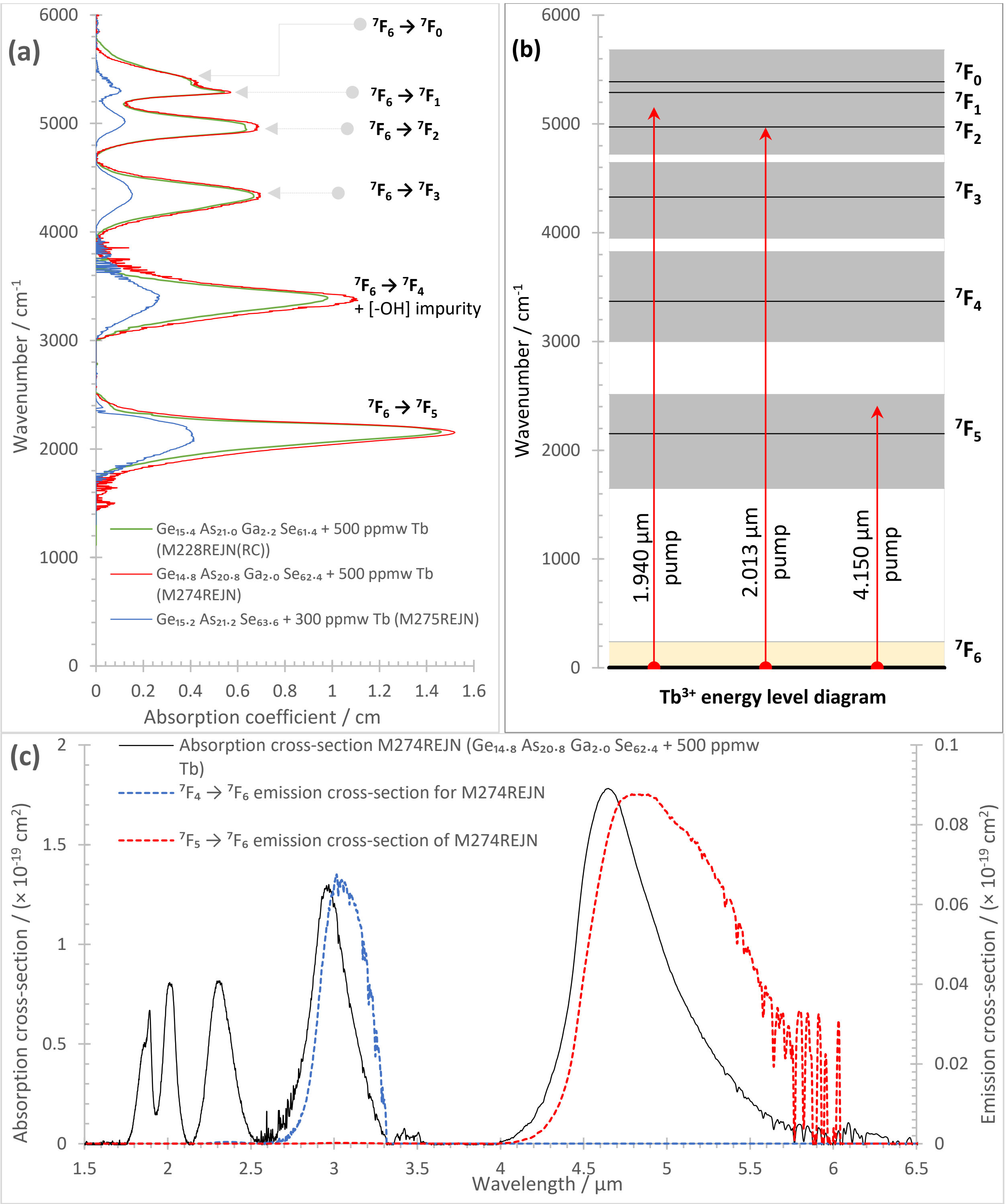

*Figure 4-22: Showing: **(a)** absorption coefficient spectrum of three Tb (foil) doped glass samples: M228REJN(RC), M274REJN, and M275REJN along with **(b)** the corresponding energy level diagram for Tb^{3+} in glass host showing 1.940 µm, 2.013 µm and 4.150 µm excitation wavelengths which were used in future measurements, and **(c)** showing the calculated absorption (solid line) and emission (dashed line) cross-sections for the M274REJN sample. Note, the Tb^{3+} cross-section calculations assumed several factors (see Section 3.2.8.2 and 4.2.6.1) and thus its accuracy should <u>not</u> be relied upon.*

The GSA between the $^7F_6$ ground state and the $^7F_5$, $^7F_4$, $^7F_3$, $^7F_2$, $^7F_1$ and $^7F_0$ excited state levels each ostensibly peaking at 2152 cm^{-1}, 3369 cm^{-1}, 4328 cm^{-1}, 4972 cm^{-1}, 5289 cm^{-1}, and 5388 cm^{-1}, respectively can be observed. Figure 4-22 (b) shows the corresponding Tb^{3+} energy level diagram. Figure 4-22 (c) shows the calculated absorption cross-sections for each of the observed GSA bands and the emission cross-sections for the $^7F_4 \rightarrow {}^7F_6$, and $^7F_5 \rightarrow {}^7F_6$. Note, the underlying [-Se-H] impurity vibrational absorption bands were numerically removed in Figure 4-7 (a) and (c). The shape of these results agree with those found in literature [118,181].

4.2.4.2 Tb^{3+} literature review:

The NIR and MIR properties of the 'Tb' dopant have been investigated in several host glass compositions. Table 4-14 shows the three major MIR emission bands peaking in intensity at ~3.2 µm, ~4.8 µm, and ~7.5 µm that the Tb^{3+} cation exhibited. Curiously, to the best of my knowledge, there are no reports of the $^7F_3 \rightarrow {}^7F_6$ radiative transition, which should occur around 2.3 µm, being detected.

Table 4-15 shows the radiative lifetimes for these emission bands, with notably one of the longest radiative lifetimes of all RE dopants evaluated. The Tb^{3+} $^7F_6$ ground state manifold also exhibits Stark splitting [182–184]. Interestingly, lifetime measurements of the ~3.1 µm Tb^{3+} PL emissions, emanating from the $^7F_4$ manifold, yielded inconclusive results due to "*an overestimated $^7F_4$ fluorescence lifetime of few milliseconds*" as reported in [38]. This peculiarity of the 3.1 µm Tb^{3+} PL emission band is further explored in Section 4.2.4.3.b. The lifetime of the $^7F_5 \rightarrow {}^7F_6$ transition was significantly influenced by the dopant concentration, and the host glass compositions, with Se-based compositions exhibiting longer lifetimes compared to Sb-based compositions.

Table 4-14: Tb^{3+} PL emission bands found in literature (see Figure 4-22 (b) for energy level diagram):

Transition	Composition / sample type	Pump λ / µm	Emission band range / µm	Peak λ / µm	Reference
$^7F_4 \rightarrow {}^7F_6$	$Ga_{5.0}Ge_{20.0}Sb_{10.0}Se_{65.0}$ Either 500 or 1000 ppmw Tb^{3+} (*bulk samples and single material fibres*)	2.050	2.7 to 3.5	~ 3.2	[38]
$^7F_5 \rightarrow {}^7F_6$			4.0 to 6.0	~ 5.0	
$^7F_4 \rightarrow {}^7F_5$			~6.8 to ~9.3	~ 8.1	
$^7F_5 \rightarrow {}^7F_6$	$Ga_{3.2}Ge_{24.9}As_{15.3}Se_{56.6}$ 1050 ppmw Tb^{3+} (*SIF*)	2.000	4.0 to ~6.0	~5.0	[141]
$^7F_4 \rightarrow {}^7F_6$	Ge–As–Ga–Se 500, 1000, and 1500 ppmw Tb^{3+} (*bulk glasses*) and 500 ppmw Tb^{3+} (*single material fibre*)		4.1 to 6.0	4.7	[181]
$^7F_4 \rightarrow {}^7F_6$	Ge–As–Ga–Se 1000-ppmw Tb^{3+}	2.000	3.0 to 3.5	~ 3.2	[17]
$^7F_5 \rightarrow {}^7F_6$			4.0 to 5.8	~ 4.8	
$^7F_4 \rightarrow {}^7F_5$			6.0 to 8.5	~ 7.5	
$^7F_5 \rightarrow {}^7F_6$	$Ge_{5.0}As_{32.0}Ga_{0.5}Se_{57.5}I_{5.0}$ 1000 ppmw Tb^{3+} (*polished disc*)	2.940	4.0 to 5.5	~ 4.9	[40]
$^7F_4 \rightarrow {}^7F_6$	$Ga_{5.0}Ge_{20.0}Sb_{10.0}Se_{65.0}$ 500 ppmw Tb^{3+} (*polished bulk glass and single material fibre*)	2.050	2.7 to 3.5	~ 3.15	[122]
$^7F_5 \rightarrow {}^7F_6$			4.0 to 6.0	~ 5	
$^7F_4 \rightarrow {}^7F_5$			6.8 to 9.4	~ 8.1	
$^7F_4 \rightarrow {}^7F_6$	$Ga_{5.0}Ge_{20.0}Sb_{10.0}Se_{45.0}Te_{20.0}$ 500 ppmw Tb^{3+} (*polished bulk glass and single material fibre*)		2.7 to 3.5	~ 3.15	
$^7F_5 \rightarrow {}^7F_6$			4.0 to 6.0	~ 4.8	
$^7F_4 \rightarrow {}^7F_5$			6.8 to 9.4	~ 8.1	

Table 4-15: Tb^{3+} PL emission lifetimes found in literature (see Figure 4-22 (b) for energy level diagram):

Transition		Host composition / sample type		Calculated τ_{rad} / ms	Measured τ_{rad} / ms	Reference
From	To					
$^7F_5$	$^7F_6$	$Ga_{5.0}Ge_{20.0}Sb_{10.0}Se_{65.0}$ (*bulk samples*)	500 ppmw 1000 ppmw	13.9	8.9 5.6	[38]
$^7F_4$	$^7F_6$		500 ppmw 1000 ppmw	4.9	-	
$^7F_5$		Ge–As–Ga–Se 1000 ppmw Tb^{3+} (*bulk glasses*)		13.1	12.9	[141]
$^7F_5$	$^7F_6$	Ge–As–Ga–Se 1000-ppmw Tb^{3+}		15	11	[17]
$^7F_4$	$^7F_6$			8	0.012	
$^7F_4$	$^7F_5$			8	0.012	
$^7F_3$	$^7F_5$			4.1	-	
$^7F_5$	$^7F_6$	$Ge_{5.0}As_{32.0}Ga_{0.5}Se_{57.5}I_{5.0}$ 1000 ppmw Tb^{3+} (*polished disc*)		-	16.1	[40]
$^7F_5$	$^7F_6$	$Ga_{5.0}Ge_{20.0}Sb_{10.0}Se_{65.0}$ 500 ppmw Tb^{3+}		13.9	8.9	[122]
$^7F_4$	$^7F_5$			4.9	-	
$^7F_4$	$^7F_6$			4.9	-	
$^7F_5$	$^7F_6$	$Ga_{5.0}Ge_{20.0}Sb_{10.0}Se_{45.0}Te_{20.0}$ 500 ppmw Tb^{3+}		14.8	7.8	
$^7F_4$	$^7F_5$			6.5	-	
$^7F_4$	$^7F_6$			6.5	-	
$^7F_4$		$Ge_{16.5}As_{16.0}Ga_{3.0}Se_{64.5}$ 1000-2000 ppmw Tb^{3+} (bulk glass)		5.9	-	[185]
$^7F_5$				11.8	-	

4.2.4.3 Tb^{3+} PL emission measurements

Tb^{3+} PL emission spectrum and PL lifetime measurements were performed sequentially using two separate excitation sources at wavelengths of 2.013 µm and 4.150 µm with the samples listed in Table 4-16. The 2.013 µm excitation scheme used the $^7F_6 \rightarrow {}^7F_2$ GSA, while the 4.150 µm excitation scheme used the $^7F_6 \rightarrow {}^7F_5$ GSA, as shown in Figure 4-22 (b).

Table 4-16: Sample codes, composition, dimentions, and equipment configurations used for Tb^{3+} PL emission measurements (see Section 7.3 for description of equipment configuration code).

Sample type	Code and nominal composition (atomic %)	Dimensions	Equipment configuration and Figure
Single material fibre (*un-annealed*)	**F116REJN** (*$Ge_{14.8}$ $As_{20.8}$ $Ga_{2.0}$ $Se_{62.4}$ + 1000 ppmw $TeCl_4$ + 500 ppmw Tb (foil)*)	Diameter of 207.1 ± 2.8 µm and 89.1 mm long.	Figure 4-23 (a) and Figure 4-25 (f): **A**[1_d-7_a] **F**[9_a] **I**[12_a- $13_{2.484\ \mathrm{LWP}}$- 14_a -15_{ai} – 16_b] Figure 4-23 (b) and Figure 4-25 (a): **A**[1_d-7_a] **F**[9_a] **I**[12_a- $13_{3.981\ \mathrm{LWP}}$- 14_a -15_{aii} – 16_b]
		Diameter of 226 ± 2 µm and 278 mm long.	Figure 4-23 (c): **A**[1_d-7_a] **F**[9_a] **I**[12_a- $13_{6.386\ \mathrm{LWP}}$- 14_a -15_{aiii} – 16_c]
		Diameter of ~220 µm and 98.1 nm long.	Figure 4-24 (a), Figure 4-25 (f) and Figure 4-26: **B**[7_a] **F**[9_a] **I**[12_a- $13_{3.351\ \mathrm{SWP}}$- 14_a -15_{ai} – 16_b] Figure 4-24 (b) and Figure 4-25 (e): **B**[7_a] **F**[9_a] **I**[12_a- $13_{4.630\ \mathrm{LWP}}$- 14_a -15_{aii} – 16_b]
SIF (*un-annealed*)	**F122REJN**: (*Core: **F116REJN**: $Ge_{14.8}$ $As_{20.8}$ $Ga_{2.0}$ $Se_{62.4}$ + 1000 ppmw $TeCl_4$ + 500 ppmw Tb (foil)* *Cladding **M260JN**: $Ge_{16.5}$ $As_{16.0}$ $Ga_{3.0}$ $Se_{61.5}$ $S_{3.0}$*)	27.8 ± 2.1 µm core, 237 ± 0.6 µm cladding diameter and 77.7 mm long	Figure 4-23 (a): **A**[1_d-7_a] **F**[9_b- 10] **I**[12_a- $13_{2.484\ \mathrm{LWP}}$- 14_a -15_{ai} – 16_b] Figure 4-23 (b): **A**[1_d-7_a] **F**[9_b- 10] **I**[12_a- $13_{3.981\ \mathrm{LWP}}$- 14_a -15_{aii} – 16_b]
Single material fibre (*un-annealed*)	**F120REJN** (*$Ge_{15.2}$ $As_{21.2}$ $Se_{63.6}$ + 1000 ppmw $TeCl_4$ + 300 ppmw Tb (foil)*)	Diameter of 218.9 ± 3.2 µm and 90.16 mm long.	Figure 4-23 (a): **A**[1_d-7_a] **F**[9_a] **I**[12_a- $13_{2.484\ \mathrm{LWP}}$- 14_a -15_{ai} – 16_b] Figure 4-23 (b) and Figure 4-25 (c): **A**[1_d-7_a] **F**[9_a] **I**[12_a- $13_{3.981\ \mathrm{LWP}}$- 14_a -15_{aii} – 16_b]
Powdered glass (*annealed bulk glass*)	**M274REJN** (*$Ge_{14.8}$ $As_{20.8}$ $Ga_{2.0}$ $Se_{62.4}$ + 1000 ppmw $TeCl_4$ + 500 ppmw Tb (foil)*)	Varying granule size, 20.5 ± 11.7 µm in diameter.	Figure 4-23 (a): **C**[1_d] **G**[] **I**[12_a- $13_{2.484\ \mathrm{LWP}}$- 14_a -15_{ai} – 16_b] Figure 4-23 (b) and Figure 4-25 (d): **C**[1_d] **G**[] **I**[12_a- $13_{3.981\ \mathrm{LWP}}$- 14_a -15_{aii} – 16_b]

4.2.4.3.a Tb^{3+} PL emission spectra:

Application of the 2.013 µm excitation source on the samples listed in Table 4-16, resulted in the detection of three distinct Tb^{3+} PL emission bands and correspond to those found in literature (see Table 4-14). A relatively weak Tb^{3+} PL emission band between 2.700 to 3.500 µm, shown in Figure 4-23 (a), which was attributed to the $^7F_4 \rightarrow {}^7F_6$ transition. A strong Tb^{3+} PL emission band between 3.800 to 6.200 µm, shown in Figure 4-23 (b), which was attributed to the $^7F_5 \rightarrow {}^7F_6$ and $^7F_3 \rightarrow {}^7F_5$ transitions. A weak Tb^{3+} PL emission band between 7.000 to 9.400 µm, shown in Figure 4-23 (c), and attributed to the $^7F_4 \rightarrow {}^7F_5$ transition.

The weak intensity of the 2.700 to 3.500 µm Tb^{3+} PL emission band, shown in Figure 4-23 (a), was likely due to the underlying [-OH] impurity resonantly absorbing and transferring PL into vibrational quanta, and/or reabsorption via the $^7F_6 \rightarrow {}^7F_4$ GSA. This resulted in emissions ~ 230 times smaller than the peak intensity from the adjacent 3.800 to 6.200 µm emission band. The ~3.1 µm Tb^{3+} PL emission band in in Figure 4-23 (a) shows good agreement with the calculated $^7F_4 \rightarrow {}^7F_6$ emission shape in Figure 4-22 (c).

Comparing the shapes of the PL emission spectra in Figure 4-23 (a) obtained from the samples listed in Table 4-16, showed no significant difference between the samples possessing the $Ge_{14.8}$ $As_{20.8}$ $Ga_{2.0}$ $Se_{62.5}$ atomic % composition and the single material fibre F120REJN and its $Ge_{15.2}$ $As_{21.2}$ $Se_{63.6}$ atomic % composition. This similarity was also present for the PL emission spectra in Figure 4-23 (b) for the 3.800 to 6.200 µm emission band, indicating that the absence of 'Ga' from the F120REJN sample composition did not significantly alter the emission spectra when compared to the spectra of samples containing 'Ga'.

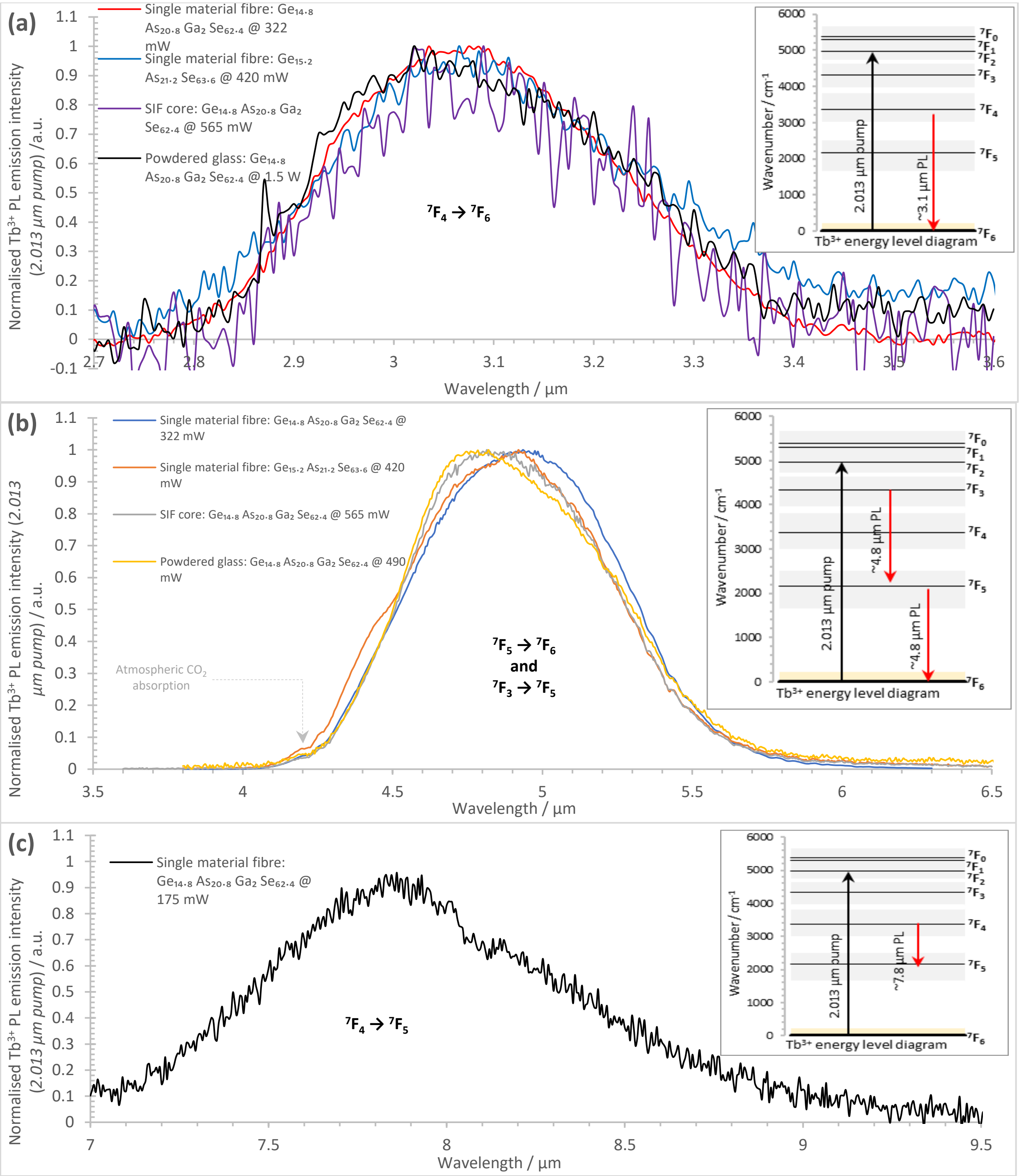

*Figure 4-23: Normalised PL emission spectra for Tb (foil) doped samples listed in Table 4-16 using 2.013 µm pump source: **(a)** 2.700 to 3.600 µm Tb^{3+} PL emission band, **(b)** 3.800 to 6.200 µm Tb^{3+} PL emission band, **(c)** 7.000 to 9.400 µm Tb^{3+} PL emission band. Note, each figure shows Tb^{3+} energy level diagram (Arrow lengths ARE TO SCALE). Not corrected for system spectral response. See Table 4-16 for sample specifications and equipment configuration used. Note, the M274REJN and F116REJN samples, along with the core of F122REJN sample each have the same nominal composition, while F120REJN possessed a different composition.*

The PL emission spectra shown in Figure 4-23 (b), obtained from the samples listed Table 4-16, exhibited only small variations in peak Tb^{3+} PL emission between sample types, with the powdered glass sample showing the least amount of reabsorption. These variations were likely due to differences in PL propagation paths afforded by the sample types affecting the amount of [-Se-H] impurity resonantly absorbing and transferring PL into vibrational quanta, and/or reabsorption via the $^7F_6 \rightarrow {}^7F_5$ GSA. The ~4.9 µm Tb^{3+} PL emission band in in Figure 4-23 (b) shows agreement with the calculated $^7F_5 \rightarrow {}^7F_6$ transition shape in Figure 4-22 (c).

The 7.000 to 9.400 µm Tb^{3+} PL emission band, shown in Figure 4-23 (c), was only evaluated using the single material fibre F116REJN sample, as this sample type yielded the greatest PL intensity of all the samples listed in Table 4-16. The weak intensity of this emission band was attributed to competing non-radiative $^7F_4 \rightarrow {}^7F_5$ transitions and a preferential branching ratio favouring the $^7F_4 \rightarrow {}^7F_6$ transition [17,181] resulting in the ~3.1 µm PL emission band, shown in Figure 4-23 (a).

Photoexcitation with the 4.150 µm QCL resulted in a very broad Tb^{3+} PL emission band between 2.700 to 6.200 µm, shown in Figure 4-24 (a) and (b), and attributed to the $^7F_4 \rightarrow {}^7F_6$, $^7F_5 \rightarrow {}^7F_6$, and $^7F_3 \rightarrow {}^7F_5$ transitions, as illustrated within inset in Figure 4-24 (b). To the best of my knowledge this has not been reported elsewhere in the literature. A 3.351 µm SWP (*short wave pass*) filter was used to block any unabsorbed 4.150 µm QCL light, while passing Tb^{3+} PL emissions at wavelengths shorter than 3.351 µm, as shown in Figure 4-24 (a). Interestingly, these PL emissions shorter than 4.150 µm were exclusively due to ESA of both the pump and $^7F_5 \rightarrow {}^7F_6$ PL, as illustrated within the inset in Figure 4-24 (b). This 3.351 µm SWP filter, while not ideal, was the only suitable filter available in our inventory to block the 4.150 QCL. A 4.630 µm LWP (*long wave pass*) filter was used to block any unabsorbed 4.150 µm QCL light, while passing Tb^{3+} PL emissions at wavelengths longer than 4.630 µm, as shown in Figure 4-24 (b). Additionally, and importantly, a 3.800 band pass filter was used to detect relatively strong Tb^{3+} PL emissions at 3.800 µm.

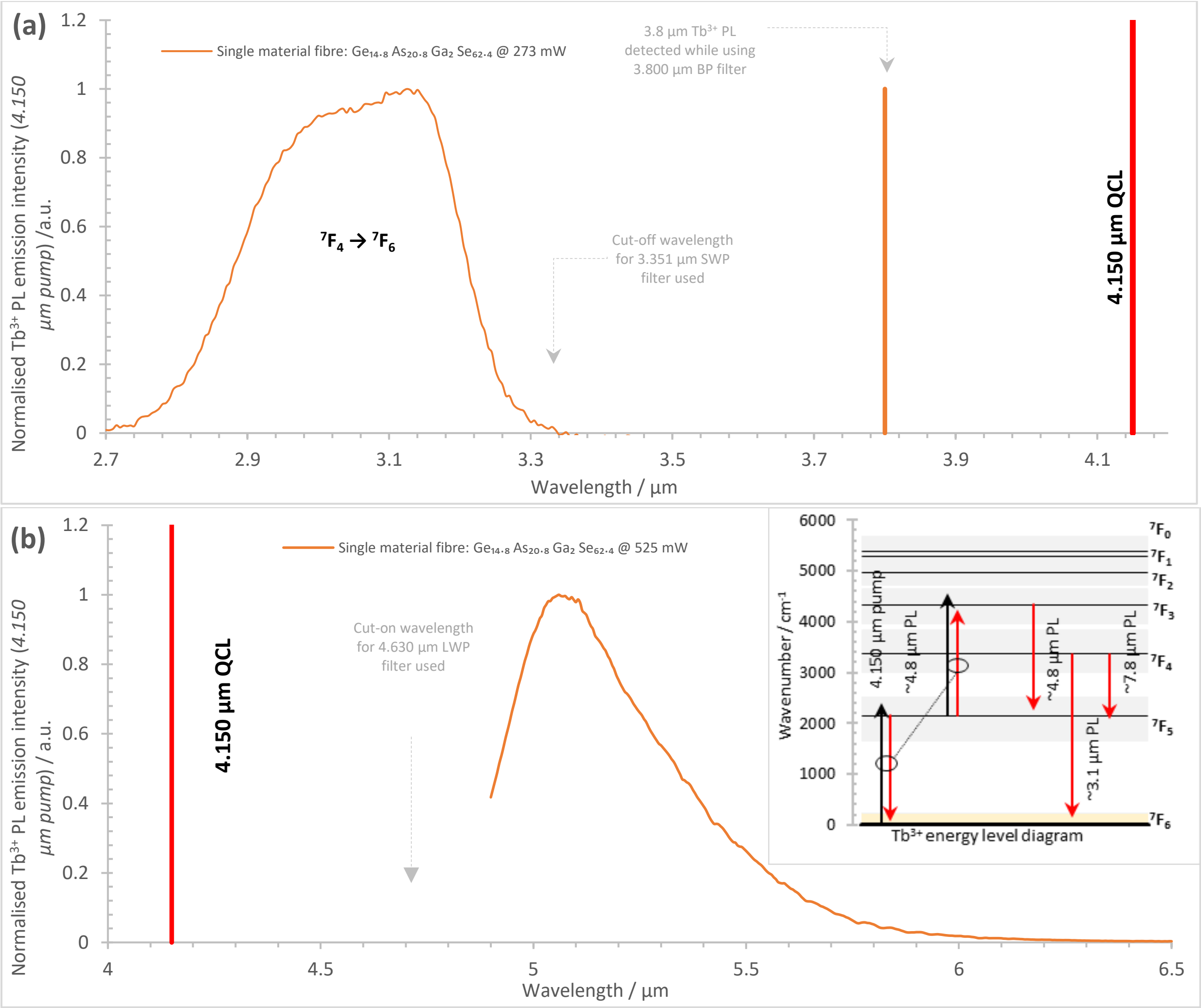

*Figure 4-24: Normalised PL emission spectra for nominally 500 ppmw (foil) cation doped $Ge_{14.8}$ $As_{20.8}$ $Ga_{2.0}$ $Se_{62.4}$ atomic % + 1000 ppmw $TeCl_4$ single material fibre sample using 4.150 µm pump source: **(a)** 2.700 to 3.600 µm Tb^{3+} PL emission band, and **(b)** ~5.000 µm Tb^{3+} PL emission band with inset showing Tb^{3+} energy level diagram (Arrow lengths ARE TO SCALE). See Table 4-16 for sample dimensions and equipment configuration used.*

The cut-off wavelength for the 3.351 µm SWP filter, coupled with the cut-on wavelength of the 4.630 µm LWP filter, resulted in a significant portion of this emission band being omitted. However, the presence of strong Tb^{3+} PL emissions at 3.800 µm, indicated that the 2.700 to 3.500

emission band, shown in Figure 4-23 (a) and the 3.800 to 6.200 µm, shown in Figure 4-23 (b) merged when employing the 4.150 µm pumping scheme.

The 7.000 to 9.400 µm Tb^{3+} PL emission band was not investigated using the 4.150 µm excitation scheme. However, as evident by the presence of the 2.700 to 3.500 µm emission band, shown in Figure 4-24 (a), the branching ratios for the $^7F_4$ manifold decay paths would ensure a corresponding $^7F_4 \rightarrow {}^7F_5$ transition [17,181], thus the 7.000 to 9.400 µm Tb^{3+} PL emission band was likely present when employing the 4.150 µm pumping scheme. To the best of my knowledge this would make it the widest contiguous PL emission band for all the RE dopants, spanning ~2.7 to ~9.4 µm.

Interestingly, application of either the 2.013 µm or the 4.150 µm excitation source yielded no detectable Tb^{3+} PL emission between 2.000 to 2.300 µm, indicating the $^7F_3 \rightarrow {}^7F_6$ transition was quenched by either the $^7F_3 \rightarrow {}^7F_4$ non-radiative transition (*~958 cm*$^{-1}$) or the radiative $^7F_3 \rightarrow {}^7F_5$ transition (~4.8 µm), as illustrated in Figure 4-23 (d) and inset within Figure 4-24 (b).

4.2.4.3.b Tb^{3+} PL lifetime results:

PL emission lifetime 'τ_{rad}' measurements were performed on the samples listed in Table 4-16 using either the 2.013 µm or the 4.150 µm excitation source modulated at 6 Hz. These lifetime measurements focused on the 2.700 to 3.200 µm and the 3.800 to 6.200 µm Tb^{3+} PL emission bands. The 7.000 to 9.400 µm band was omitted due to weak PL intensity. Figure 4-25, and Figure 4-26 shows the normalised Tb^{3+} PL emission decay from each sample type, along with the corresponding fitted exponential function. Table 4-17 lists the PL lifetimes for each Tb^{3+} doped sample type.

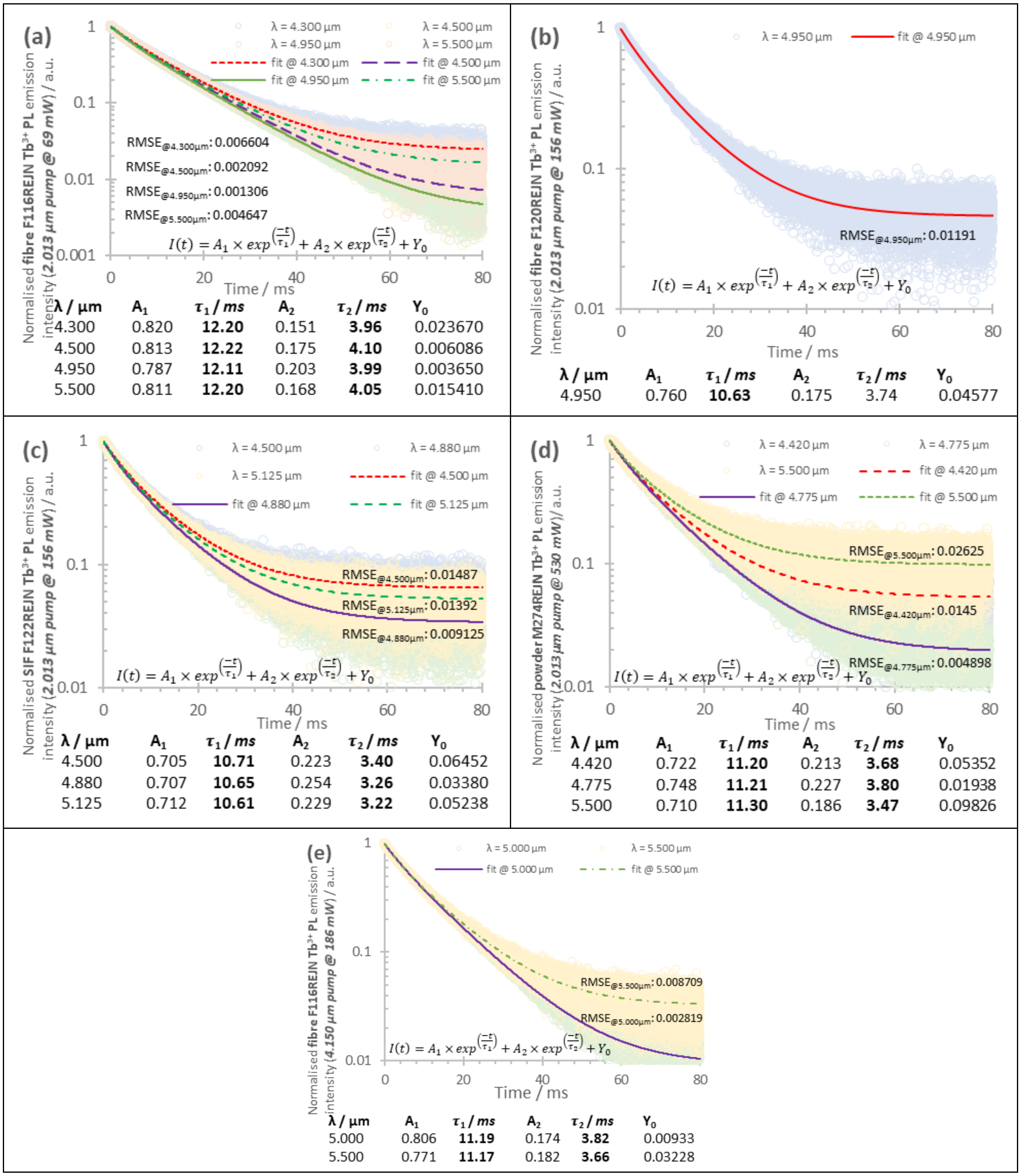

λ / µm	A_1	τ_1 / ms	A_2	τ_2 / ms	Y_0
4.300	0.820	**12.20**	0.151	**3.96**	0.023670
4.500	0.813	**12.22**	0.175	**4.10**	0.006086
4.950	0.787	**12.11**	0.203	**3.99**	0.003650
5.500	0.811	**12.20**	0.168	**4.05**	0.015410

λ / µm	A_1	τ_1 / ms	A_2	τ_2 / ms	Y_0
4.950	0.760	**10.63**	0.175	3.74	0.04577

λ / µm	A_1	τ_1 / ms	A_2	τ_2 / ms	Y_0
4.500	0.705	**10.71**	0.223	**3.40**	0.06452
4.880	0.707	**10.65**	0.254	**3.26**	0.03380
5.125	0.712	**10.61**	0.229	**3.22**	0.05238

λ / µm	A_1	τ_1 / ms	A_2	τ_2 / ms	Y_0
4.420	0.722	**11.20**	0.213	**3.68**	0.05352
4.775	0.748	**11.21**	0.227	**3.80**	0.01938
5.500	0.710	**11.30**	0.186	**3.47**	0.09826

λ / µm	A_1	τ_1 / ms	A_2	τ_2 / ms	Y_0
5.000	0.806	**11.19**	0.174	**3.82**	0.00933
5.500	0.771	**11.17**	0.182	**3.66**	0.03228

*Figure 4-25: Normalised Tb^{3+} PL lifetime (scatter plot) fitted with exponential decay functions (line) for: **(a)** single material fibre (F116REJN) with 2.013 µm pump, **(b)** single material fibre (F120REJN) with 2.013 µm pump, **(c)** SIF (F122REJN) with 2.013 µm pump, **(d)** powdered bulk glass (M274REJN) with 2.013 µm pump, and **(e)** single material fibre (F116REJN) sample with 4.150 µm pump. Note, each pump source was modulated at 6 Hz, the M274REJN and F116REJN samples along with the core of F122REJN sample each have the same $Ge_{14.8}$ $As_{20.8}$ $Ga_{2.0}$ $Se_{62.4}$ atomic % + 1000 ppmw $TeCl_4$ + 500 ppmw Tb (foil) composition, while F120REJN: $Ge_{15.2}$ $As_{21.2}$ $Se_{63.6}$ atomic % + 1000 ppmw $TeCl_4$ + 300 ppmw Tb (foil). See Table 4-16 for sample dimensions and equipment configurations, and results summarised in Table 4-17.*

Lifetime measurements using either excitation source in the 3.800 to 6.200 µm Tb^{3+} PL emission band were best fitted with a two-term exponential function, shown in Figure 4-25 (a) to (e) and listed in Table 4-17. Results predominantly consisted of a distinctively longer 'τ_1' component, at ~ 11.5 ms, which was attributed to the $^7F_5 \rightarrow {}^7F_6$ transition, along with a less frequent, faster 'τ_2' component, at ~ 3.7 ms, which was attributed to the $^7F_3 \rightarrow {}^7F_5$ transition. The 'τ_1' lifetime, from the $^7F_5$ manifold was in agreement with results found in Table 4-15, while the 'τ_2' lifetime, from the $^7F_3$ manifold was close to the calculated radiative lifetime of 4.1 ms found in [17]. This result indicated consistent contributions from each of these transitions over the entire emission band. Lifetime measurements within the 2.700 to 3.200 µm Tb^{3+} PL emission band, using either the 2.013 or the 4.150 µm excitation source, with a single material fibre F116REJN sample, were best fitted with a two-term exponential function once corrected for the pump response, as shown in Figure 4-26 (a) and listed Table 4-17. These results consisted of a long 'τ_1' component, at ~ 12.3 ms, and a shorter 'τ_2' component, at ~ 3.4 ms. Interestingly, the 'τ_1' at ~12.3 ms and 'τ_2', at ~ 3.4 ms components of the fitting match the lifetime measurement results for the 3.800 to 6.200 µm Tb^{3+} PL emission band. Conversely, the identical PL lifetime measurement, uncorrected for the pump sources, as shown in Figure 4-26 (b), revealed an additional fast component to the PL lifetime obscured by the response time of the pump source. It was postulated that this fast PL lifetime component was the true lifetime of the $^7F_4$ manifold. Note, this fast lifetime postulation corresponds to those found in literature (see Table 4-15).

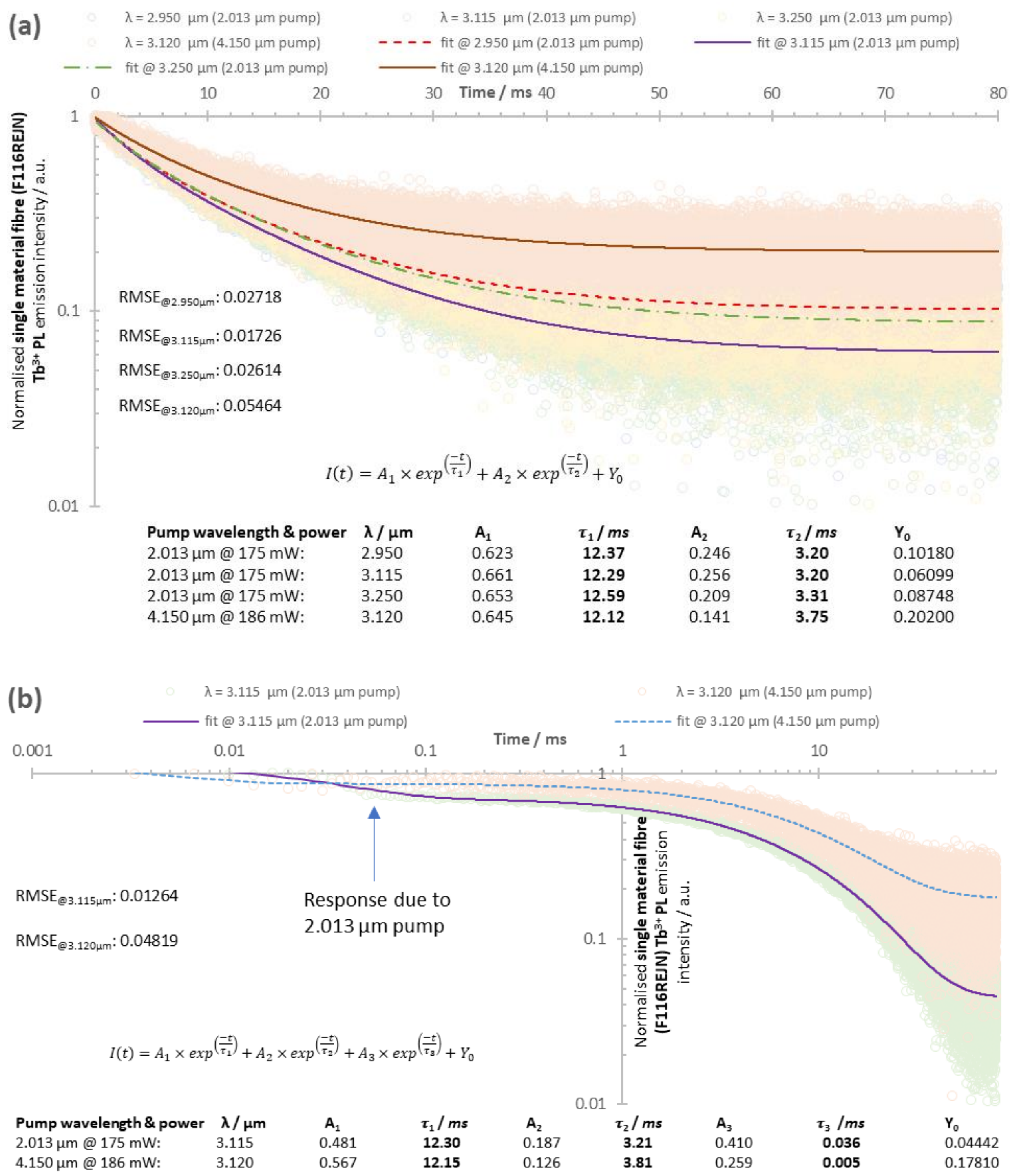

$$I(t) = A_1 \times exp^{\left(\frac{-t}{\tau_1}\right)} + A_2 \times exp^{\left(\frac{-t}{\tau_2}\right)} + Y_0$$

Pump wavelength & power	**λ / µm**	**A_1**	**τ_1 / ms**	**A_2**	**τ_2 / ms**	**Y_0**
2.013 µm @ 175 mW:	2.950	0.623	**12.37**	0.246	**3.20**	0.10180
2.013 µm @ 175 mW:	3.115	0.661	**12.29**	0.256	**3.20**	0.06099
2.013 µm @ 175 mW:	3.250	0.653	**12.59**	0.209	**3.31**	0.08748
4.150 µm @ 186 mW:	3.120	0.645	**12.12**	0.141	**3.75**	0.20200

$$I(t) = A_1 \times exp^{\left(\frac{-t}{\tau_1}\right)} + A_2 \times exp^{\left(\frac{-t}{\tau_2}\right)} + A_3 \times exp^{\left(\frac{-t}{\tau_3}\right)} + Y_0$$

Pump wavelength & power	**λ / µm**	**A_1**	**τ_1 / ms**	**A_2**	**τ_2 / ms**	**A_3**	**τ_3 /ms**	**Y_0**
2.013 µm @ 175 mW:	3.115	0.481	**12.30**	0.187	**3.21**	0.410	**0.036**	0.04442
4.150 µm @ 186 mW:	3.120	0.567	**12.15**	0.126	**3.81**	0.259	**0.005**	0.17810

*Figure 4-26: Normalised Tb^{3+} PL lifetime (scatter plot) fitted with exponential decay functions (line) with either a 2.013 µm or 4.150 µm pump modulated at 6 Hz for a single material fibre (F116REJN) sample with: **(a)** the pump source response removed, and **(b)** uncorrected for pump response (note, a logarithmic time axis was employed to represent the disparate lifetimes comprising the PL emission results). Note, F116REJN has a $Ge_{14.8}$ $As_{20.8}$ $Ga_{2.0}$ $Se_{62.4}$ atomic % + 1000 ppmw $TeCl_4$ + 500 ppmw Tb (foil) composition. Additionally, a 3.351 µm SWP filter was used to block PL emission wavelengths longer the 3.351 µm for these lifetime measurements, see Table 4-16.*

Table 4-17: Summary of Tb^{3+} PL lifetime measurement results in Figure 4-25 an Figure 4-26 (see Table 4-16 for sample specifications and equipment configuration:

Sample type and composition (atomic %)	**pump λ (µm)**	**measurement λ (µm)**	**lifetime coefficients**				
			A_1	**τ_1 (ms)**	**A_2**	**τ_2 (ms)**	**Y_0**
F116REJN *Single material fibre (un-annealed)* (*$Ge_{14.8}$ $As_{20.8}$ $Ga_{2.0}$ $Se_{62.4}$ + 500 ppmw Tb (foil)*)	2.013	4.300	0.820	**12.20**	0.151	**3.96**	0.02367
		4.500	0.813	**12.22**	0.175	**4.10**	0.006086
		4.950	0.787	**12.11**	0.203	**3.99**	0.00365
		5.500	0.811	**12.20**	0.168	**4.05**	0.01541
F120REJN *Single material fibre (un-annealed* (*$Ge_{15.2}$ $As_{21.2}$ $Se_{63.6}$ + 300 ppmw Tb (foil)*)	2.013	4.950	0.760	**10.63**	0.175	**3.75**	0.04577
F122REJN *SIF (un-annealed)* (*Core: **F116REJN**: $Ge_{14.8}$ $As_{20.8}$ $Ga_{2.0}$ $Se_{62.4}$ + 500 ppmw Tb (foil) Cladding **M260JN**: $Ge_{16.5}$ $As_{16.0}$ $Ga_{3.0}$ $Se_{61.5}$ $S_{3.0}$*)	2.013	4.500	0.705	**10.71**	0.223	**3.40**	0.06452
		4.880	0.707	**10.65**	0.254	**3.26**	0.0338
		5.125	0.712	**10.61**	0.229	**3.22**	0.05238
M274REJN *Powdered glass (annealed bulk glass)* (*$Ge_{14.8}$ $As_{20.8}$ $Ga_{2.0}$ $Se_{62.4}$ + 500 ppmw Tb (foil)*)	2.013	4.420	0.722	**11.20**	0.213	**3.68**	0.05352
		4.775	0.748	**11.21**	0.227	**3.80**	0.01938
		5.500	0.710	**11.30**	0.186	**3.47**	0.09826
F116REJN *Single material fibre (un-annealed* (*$Ge_{14.8}$ $As_{20.8}$ $Ga_{2.0}$ $Se_{62.4}$ + 500 ppmw Tb (foil)*)	4.150	5.000	0.806	**12.19**	0.174	**3.82**	0.009329
		5.500	0.771	**12.17**	0.182	**3.66**	0.03228
	2.013	2.950	0.623	**12.37**	0.246	**3.20**	0.10180
		3.115	0.661	**12.29**	0.256	**3.20**	0.06099
		3.250	0.653	**12.59**	0.209	**3.31**	0.08748
	4.150	3.120	0.645	**12.12**	0.141	**3.75**	0.20200

The results shown in Figure 4-26, indicated that the 3.800 to 6.200 µm Tb^{3+} PL emission band directly influenced the 2.700 to 3.200 µm spectral region. Thus, considering the two-term exponential function in Figure 4-26 (a) it was postulated that the 'τ_1' and 'τ_2' constituents were artifacts due to $^7F_5 \rightarrow {}^7F_3$ ESA of the Tb^{3+} PL from the $^7F_3 \rightarrow {}^7F_4$ transition, as illustrated in Figure 4-23 (d) and the inset within Figure 4-24 (b). Consequently, the $^7F_4$ manifold was supplied electrons from the $^7F_5$ and $^7F_3$ manifolds, resulting it mirroring their distinctive lifetimes. This phenomenon was likely due to the use of a single material fibre sample in an 'End-collection' configuration (see Table 4-16), which was necessary to have sufficient PL intensity to perform the lifetime measurement at these wavelengths.

The lifetimes obtained from the SIF, powdered glass, and single material fibre samples all differed slightly from one another, as shown in Table 4-17. Notably, the single material fibre F120REJN and the F122REJN SIF samples both exhibited a lower 'τ_1' lifetime than other samples. In the case of the F120REJN sample this indicated an influence due to a lack of 'Ga' in the glass composition, while in the case of the F122REJN SIF sample in indicated the influence of the SIF fabrication process and pump energy density afforded due to the sample geometry (see Table 4-16).

4.2.4.4 Tb^{3+} ESA measurements

ESA measurements were performed on a distilled nominally 500 ppmw 'Tb' (*foil*) doped $Ge_{14.8}$ $As_{20.8}$ $Ga_{2.0}$ $Se_{62.5}$ atomic % + 1000 ppmw $TeCl_4$ F116REJN single material fibre sample 302 mm long, with a diameter of 110.5 ± 11.8 µm. This single material fibre sample was exposed to a 1.940 µm excitation laser to induce the $^7F_6 \rightarrow {}^7F_2$ GSA. Figure 4-27 (a) shows the room temperature, steady state, relative change in intensity of the transmitted probe-light with pump, relative to no pump present, for the fibre sample. Additionally, the inset within Figure 4-27 shows the attenuation spectrum of a separate F116REJN fibre sample. Note, this attenuation spectrum represents the zero-change axis (*along the wavelength-axis*) in the accompanying ESA spectrum in Figure 4-27.

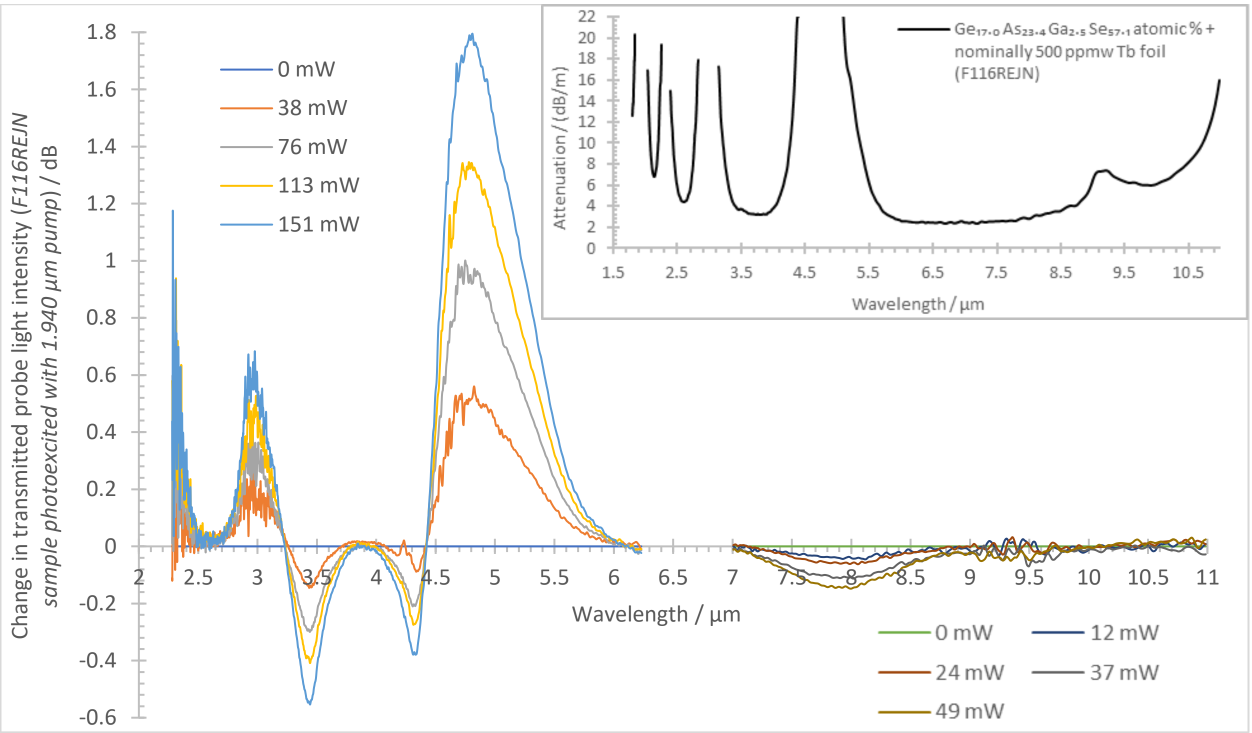

Figure 4-27: Showing changes in transmitted probe light intensity, under application of a 1.940 µm continuous wave pump laser for a 302 mm long, nominally 500 ppmw Tb (foil) doped $Ge_{14.8}$ $As_{20.8}$ $Ga_{2.0}$ $Se_{62.4}$ *atomic % + 1000 ppmw* $TeCl_4$ *glass fibre sample (F116REJN) with diameter of 110.5 ± 11.8 µm, with inset showing attenuation (dB/m) vs. Wavelength (µm) for F116REJN single material glass fibre (see Figure 3-22 for additional details on F116REJN attenuation spectrum). Note, ESA bands listed in Table 4-18.*

Comparing the ESA spectra in Figure 4-27 to the F116REJN attenuation spectrum inset, no prominent features were observed at 3.440 µm, and 7.890 µm in the attenuation spectrum, thus verifying the latent nature of these unobstructed ESA bands, which are present in the ESA spectrum.

Considering the spectral features observed in Figure 4-27 along with the Tb^{3+} absorption and PL emission measurements made in Section 4.2.4.3 the energy level transitions responsible for these features were proposed. Table 4-18 lists each significant spectral feature, observed in Figure 4-27, along with the corresponding proposed energy level transitions accountable for these features, while Figure 4-28 shows the Tb^{3+} electronic energy level diagram, inclusive of arrows for proposed energy level transitions. The $^7F_5$ energy level was postulated as the predominant initial state from which ESA took place due to its relatively long lifetime of ~ 11.5 ms, which was determined in Section 4.2.4.3.b. These proposed energy level transitions match the corresponding Tb^{3+} energy level spacing as shown in Figure 4-28. However, it must be noted that additional transitions between alternate energy levels were not ruled out, moreover these alternate transitions could have also been partially, or completely obscured by overlapping GSA bands.

The SE/GSD (*stimulated emission/ ground state depletion*) feature peaking at 2.330 µm, seen in Figure 4-27, matched the $^7F_3 \rightleftharpoons {}^7F_6$ transition shown in Figure 4-28. This SE/GSD feature was likely mostly GSD due to lack of Tb^{3+} PL detected in this spectral region during the PL emission measurements in Section 4.2.4.3.

The SE/GSD feature peaking at 2.970 µm, seen in Figure 4-27, matched the $^7F_4 \rightleftharpoons {}^7F_6$ transition, while partially overlapping an ESA band centred at 3.440 µm, which matched the $^7F_5 \rightarrow {}^7F_2$ upward transition. Thus, it was postulated that the spectral overlap of the $^7F_4 \rightleftharpoons {}^7F_6$ and $^7F_5 \rightarrow {}^7F_2$ transitions resulted in a zero-change point at 3.210 µm, at ~ 9.9 dB/m of attenuation.

Table 4-18: Proposed Tb^{3+} electronic transitions to account for observed spectral features seen in Figure 4-27.

λ / µm (*see Figure 4-27*)	**Description**	**Proposed electronic transition**
2.330 (*4292 cm^{-1}*)	Either SE and/or GSD	$^7F_3 \rightleftharpoons {}^7F_6$
2.970 (*3367 cm^{-1}*)	Either SE and/or GSD	$^7F_4 \rightleftharpoons {}^7F_6$
3.210 (*3115 cm^{-1}*)	Zero-change point	$^7F_4 \rightleftharpoons {}^7F_6$ and $^7F_5 \rightarrow {}^7F_2$
3.440 (*2906 cm^{-1}*)	ESA band	$^7F_5 \rightarrow {}^7F_2$
4.320 (*2314 cm^{-1}*)	ESA band	$^7F_5 \rightarrow {}^7F_3$
4.420 (*2262 cm^{-1}*)	Zero-change point	$^7F_5 \rightleftharpoons {}^7F_6$ and $^7F_5 \rightarrow {}^7F_3$
4.790 (*2088 cm^{-1}*)	Either SE and/or GSD	$^7F_5 \rightleftharpoons {}^7F_6$
7.890 (*1267 cm^{-1}*)	ESA band	$^7F_5 \rightarrow {}^7F_4$
9.500 (*1053 cm^{-1}*)	Weak ESA band	$^7F_4 \rightarrow {}^7F_3$

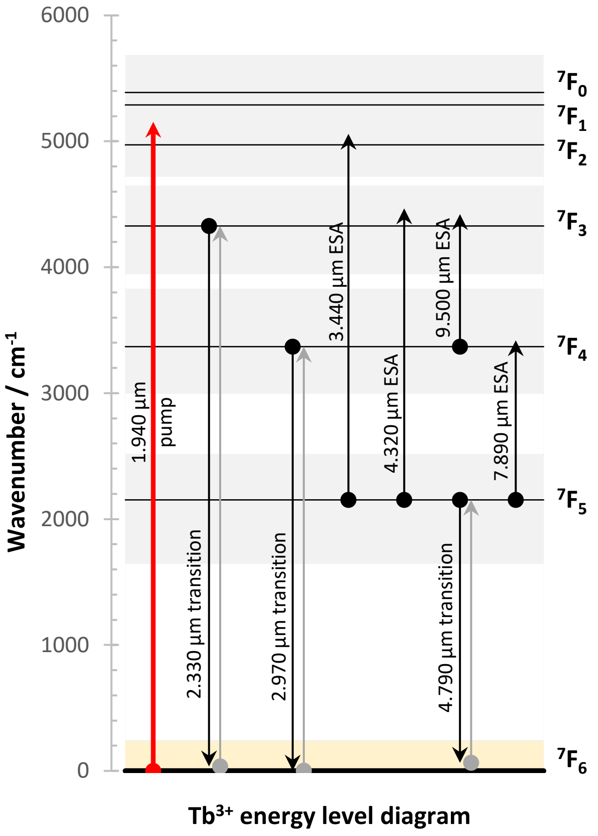

Figure 4-28: Tb^{3+} energy level diagram with possible upward and downward transitions to account for changes observed in Figure 4-27 (Arrow lengths ARE TO SCALE in energy).

Note, **GSD**- Ground State Depletion, **SE**- Stimulated emission.

The ESA band peaking at 4.320 µm, seen in Figure 4-27, matched the $^7F_5 \rightarrow {}^7F_3$ upward transition shown in Figure 4-28. Considering the PL lifetime measurements in Section 4.2.4.3.b, the 'τ_2', lifetime at ~ 3.7 ms was present throughout the 3.800 to 6.200 µm Tb^{3+} PL emission band, and was attributed to the $^7F_3 \rightarrow {}^7F_5$ transition. This indicated that the $^7F_5 \rightarrow {}^7F_3$ ESA would also be present throughout the 3.800 to 6.200 µm spectral region, as evident by the PL emission results while using the 4.150 µm pump, shown in Figure 4-24 (a) and (b), Figure 4-25 (e) and Figure 4-26. This ESA band was partially obscured by the $^7F_6$ → $^7F_5$ GSA. Interestingly, both the PL lifetime measurements and the presence of this ESA band indicate a dynamic between the $^7F_3$ and $^7F_5$ manifolds.

The ESA band peaking at 4.320 µm partially overlapped the SE/GSD band, peaking at 4.79 µm, which matched the $^7F_5 \rightleftharpoons {}^7F_6$ transition. Thus, it was postulated that the spectral overlap of the $^7F_5$ → $^7F_3$ and $^7F_5 \rightleftharpoons {}^7F_6$ transitions resulted in a zero-change point at 4.420 µm, at 23.2 dB/m of attenuation.

The ESA bands centred around 7.890 µm and 9.500 µm, seen in Figure 4-27, matched the $^7F_5$ → $^7F_4$ and $^7F_4$ → $^7F_3$ upward transitions, respectively, as shown in Figure 4-28.

4.2.5 Dysprosium spectroscopy.

Two separate glass rods of nominal composition: a distilled, $Ge_{15.0}$ $As_{21.0}$ $Ga_{1.0}$ $Se_{63.0}$ atomic % + 850 ppmw $TeCl_4$ + 500 ppmw ‘Dy’ (*foil*) M285RERC, and an undistilled $Ge_{16.5}$ $As_{16.0}$ $Ga_{3.0}$ $Se_{61.5}$ $S_{3.0}$ atomic % + 500 ppmw ‘Dy’ (*foil*) M295REJN, were separately produced by PhD student Richard Crane and the author, respectively. The M285RERC glass rod was subsequently drawn into single material fibre and cane: F125RERC. Note, the optical and compositional evaluation of these glasses can be found in Sections 3.2.6 and 3.2.7. A portion of M285RERC and M295REJN was processed into two separate polished bulk glass samples and used for the presented absorption measurements in Section 4.2.5.1. A portion of M295REJN was subsequently co-extruded by Dr David Furniss and the author to produce the co-extruded glass rod E094REDF(JN). Another portion of single material fibre F125RERC was ground into powdered glass and used with a separate section of single material fibre F125RERC and a portion of the extruded rod E094REDF(JN) for the PL emission measurements presented in Section 4.2.5.3. Additionally, a separate section of single material fibre F125RERC was used for the ESA measurements presented in Section 4.2.5.4. The E094REDF(JN) co-extruded glass rod was a step index glass rod with a Ce cation doped core and a Dy^{3+} cation doped cladding.

4.2.5.1 Dy^{3+} absorption and emission cross-sections:

Figure 4-29 (a) shows the absorption coefficient spectra for two nominally 500 ppmw ‘Dy’ (*foil*) doped glass sample M285RERC and M295REJN each ostensibly containing 8.24×10^{18} cations/cm^3, and 8.34×10^{18} cations/cm^3, respectively.

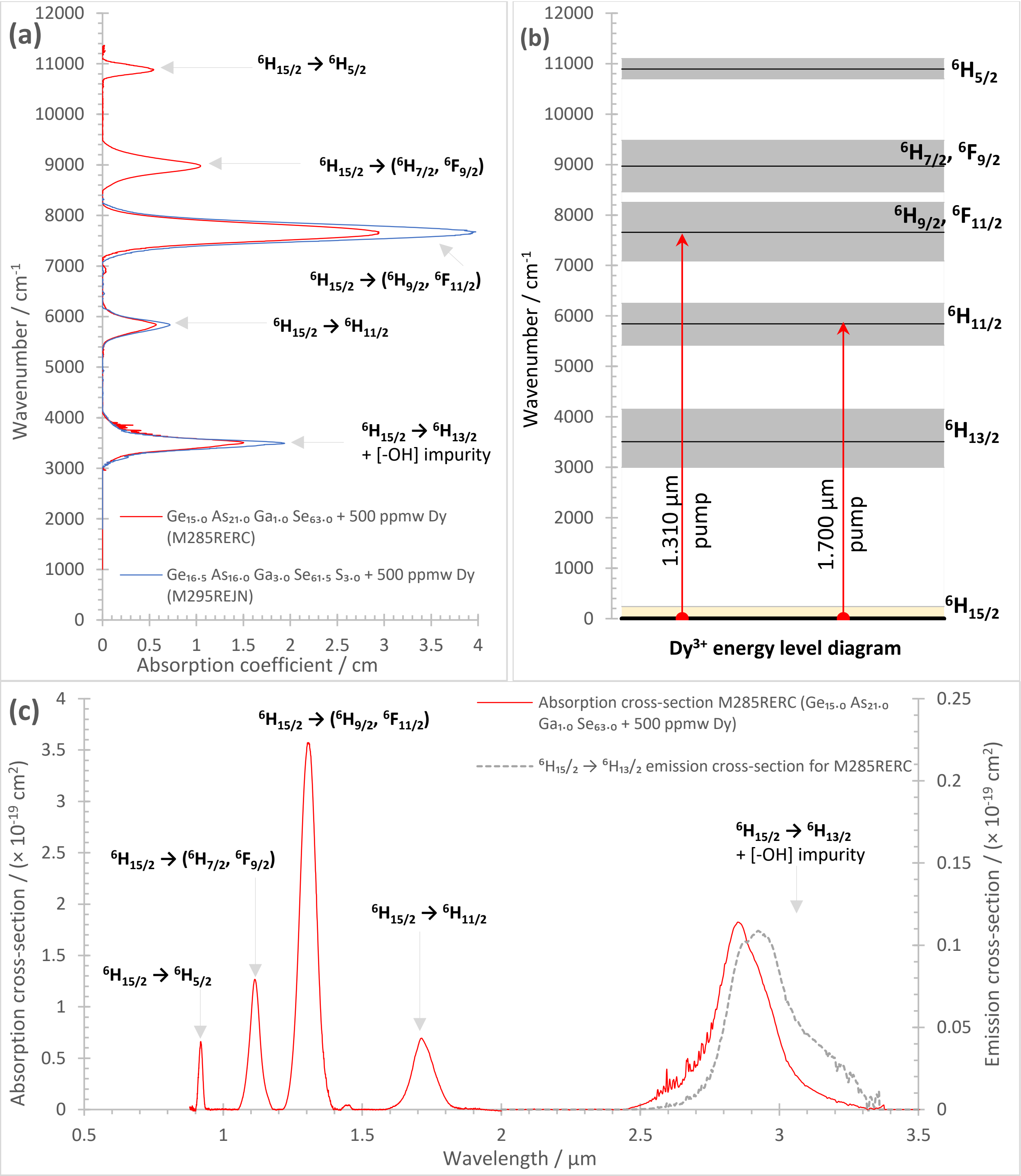

*Figure 4-29: Showing: **(a)** absorption coefficient spectrum of two nominally 500 ppmw Dy (foil) doped glass samples: M285RERC, and M295REJN, along with **(b)** the corresponding energy level diagram for Dy^{3+} in glass host showing 1.310 µm and 1.700 µm pump sources which were used in future measurements, and **(c)** showing the calculated absorption (solid line) and emission (dashed line) cross-sections for the M285RERC sample. Note, the Dy^{3+} cation cross-section calculations assumed several factors (see Section 3.2.8.2 and 4.2.6.1) and thus its accuracy should <u>not</u> be relied upon.*

The GSA between the $^6H_{15/2}$ ground state and $^6H_{13/2}$, $^6H_{11/2}$, ($^6H_{9/2}$, $^6F_{11/2}$), ($^6H_{7/2}$, $^6F_{9/2}$), $^6H_{5/2}$, $^6F_{7/2}$, and $^6F_{5/2}$ excited state levels each ostensibly peaking at 3507 cm^{-1}, 5843 cm^{-1}, 7657 cm^{-1}, 8969 cm^{-1}, 10893 cm^{-1}, 11695 cm^{-1}, and 12423 cm^{-1}, respectively can be observed. The upper most Dy^{3+} energy levels $^6F_{7/2}$, $^6F_{5/2}$ and $^3F_{3/2}$ were too weak to be observed experimentally. Figure 4-29 (b) shows the corresponding Dy^{3+} energy level diagram. Figure 4-29 (c) shows the calculated absorption cross-sections for each of the observed GSA bands and the emission cross-sections for the $^6H_{13/2} \rightarrow {}^6H_{15/2}$ transition.

4.2.5.2 Dy^{3+} literature review:

The NIR and MIR properties of the 'Dy' dopant have been well investigated in several host glass compositions. Table 4-19 lists the IR PL emission bands exhibited by the Dy^{3+} cation.

Table 4-19: Dy^{3+} PL emission bands found in literature (see Figure 4-29 (b) for energy level diagram):

Transition	**Composition / sample type**	**Pump λ / µm**	**Emission band range / µm**	**Peak λ / µm**	**Reference**
($^6F_{11/2}$, $^6H_{9/2}$) → $^6H_{13/2}$	Ge-As-Ga-Se 500 ppmw Dy^{3+} (*single material fibre*)	1.700 or 1.320	2.1 to 2.6	~ 2.4	[186]
$^6H_{13/2} \rightarrow {}^6H_{15/2}$			2.7 to 3.4	~ 2.9	
$^6H_{11/2} \rightarrow {}^6H_{13/2}$			3.5 to 5.0	~ 4.4	
$^6H_{13/2} \rightarrow {}^6H_{15/2}$	Ge-As-Ga-Se 1000 ppmw Dy^{3+}	1.300	2.5 to 3.5	3.05	[17]
$^6H_{11/2} \rightarrow {}^6H_{13/2}$			3.9 to 5.3	4.5	
$^6H_{13/2} \rightarrow {}^6H_{15/2}$	0.9($Ge_{25.0}Ga_{10.0}S_{65.0}$) + 0.1 Br + 500 ppmw Dy^{3+}	0.914	2.6 to 3.4	~ 2.85	[187]
$^6H_{11/2} \rightarrow {}^6H_{13/2}$			4.0 to 4.8	~ 4.45	
$^6H_{7/2} \rightarrow {}^6H_{15/2}$	$Ga_{5.0}Ge_{20.0}Sb_{10.0}Se_{65.0}$ + 1000 ppmw Dy^{3+} (*single material fibre*)	0.920	1.0 to 1.2	~ 1.15	[39]
$^6H_{9/2} \rightarrow {}^6H_{15/2}$			~1.25 to ~1.47	~ 1.38	
$^6H_{11/2} \rightarrow {}^6H_{13/2}$		1.300	3.7 to 4.7	~ 4.4	
	$Ga_{5.0}Ge_{20.0}Sb_{10.0}S_{65.0}$ + 1000 ppmw Dy^{3+} (*single material fibre*)			~ 4.3	
($^6F_{11/2}$, $^6H_{9/2}$) → $^6H_{11/2}$	$Ga_{5.0}Ge_{20.0}Sb_{10.0}Se_{65.0}$ + 1000 ppmw Dy^{3+} (*single material fibre*)		~5.0 to ~6.0	5.4	
($^6H_{7/2}$, $^6F_{9/2}$) → ($^6H_{9/2}$, $^6F_{11/2}$)		1.12	6.5 to ~9.5	~ 7.4	
$^6H_{11/2} \rightarrow {}^6H_{13/2}$	$Ga_{5.0}Ge_{20.0}Sb_{10.0}S_{65.0}$ 0.1 weight % Dy^{3+} (*single material fibre*)	0.920	4.0 to 4.7	~ 4.37	[178]
$^6H_{11/2} \rightarrow {}^6H_{15/2}$	Ga-La-S 9900 ppmw Dy_2S_3	0.815	1.65 to 1.95	~1.76	[188]
$^6H_{13/2} \rightarrow {}^6H_{15/2}$			2.6 to 3.2	~ 2.83	
$^6H_{11/2} \rightarrow {}^6H_{13/2}$			3.8 to 4.8	~ 4.27	

Table 4-20 shows the 'Dy' cation PL lifetimes for IR transitions found in literature.

Table 4-20: Dy^{3+} PL emission lifetimes found in literature (see Figure 4-29 (b) for energy level diagram):

Transition		**Host composition**	**Calculated τ_{rad} / ms**	**Measured τ_{rad} / ms**	**Reference**
From	**To**				
($^6F_{11/2}$, $^6H_{9/2}$)	$^6H_{11/2}$	$Ge_{25}Ga_{10}S_{65}$	0.205	0.034 ± 0.003	[187]
		0.95($Ge_{25}Ga_{10}S_{65}$) + 0.05 Br	0.332	0.045 ± 0.004	
		0.9($Ge_{25}Ga_{10}S_{65}$) + 0.1 Br	0.405	0.051 ± 0.004	
		Ge-As-Ga-Se	0.38	0.31	[17]
		$Ge_{25}Ga_{10}S_{65}$	0.205	0.034	[189]
		$Ge_{30}As_{10}S_{60}$	0.153	-	[190]
		$Ge_{25}Ga_5S_{70}$	0.229	0.038	
		$Ga_5Ge_{20}Sb_{10}S_{65}$		0.034	[39]
		$Ga_5Ge_{20}Sb_{10}Se_{65}$	0.11	0.230	
$^6H_{11/2}$	$^6H_{13/2}$	$Ge_{25}Ga_{10}S_{65}$	2.94	1.09 ± 0.11	[187]
		0.95($Ge_{25}Ga_{10}S_{65}$) + 0.05 Br	3.59	1.53 ± 0.10	
		0.9($Ge_{25}Ga_{10}S_{65}$) + 0.1 Br	4.3	1.39 ± 0.11	
		Ge-As-Ga-Se	2.4	2	[17]
		$Ge_{16.5}As_{16.0}Ga_{3.0}Se_{64.5}$	2.2	-	[185]
		$Ge_{30}As_{10}S_{60}$	2.22	0.728	[190]
		$Ge_{25}Ga_5S_{70}$	3.29	1.13	
		$Ga_8Sb_{28}As_4S_{60}$	2.02	1.38	[191]
		$Ga_5Ge_{20}Sb_{10}S_{65}$		1.30	[39]
		$Ga_5Ge_{20}Sb_{10}Se_{65}$	1.63	1.46	
		Ga-La-S	2.53	1.30	[188]
	$^6H_{15/2}$	Ga-La-S	2.53	1.30	
$^6H_{13/2}$	$^6H_{15/2}$	$Ge_{25}Ga_{10}S_{65}$	6.71	3.92 ± 0.17	[187]
		0.95($Ge_{25}Ga_{10}S_{65}$) + 0.05 Br	10.0	6.12 ± 0.21	
		0.9($Ge_{25}Ga_{10}S_{65}$) + 0.1 Br	11.2	6.31 ± 0.19	
		Ge-As-Ga-Se	6.2	6	[17]
		$Ge_{16.5}As_{16.0}Ga_{3.0}Se_{64.5}$	6.1	-	[185]
		$Ga_8Sb_{28}As_4S_{60}$	4.38	3.15	[191]
		$Ga_5Ge_{20}Sb_{10}S_{65}$	-	5.60	[39]
		$Ga_5Ge_{20}Sb_{10}Se_{65}$	4.17	3.30	
		$Ge_{30}As_{10}S_{60}$	5.29	4.55	[190]
		$Ge_{25}Ga_5S_{70}$	6.63	6.00	
		ZBLAN	-	0.631	[192]
		Ga-La-S	6.29	3.60	[188]

4.2.5.3 Dy^{3+} PL emission measurements

Dy^{3+} PL emission spectrum and PL lifetime measurements were performed sequentially using two separate excitation sources at wavelengths of 1.310 µm and 1.700 µm with the samples listed in Table 4-21. The 1.310 µm excitation scheme used the $^6H_{15/2} \rightarrow (^6H_{9/2}, {}^6F_{11/2})$ GSA, while the 1.700 µm excitation scheme used the $^6H_{15/2} \rightarrow {}^6H_{11/2}$ GSA, as shown in Figure 4-29 (b).

Table 4-21: Sample codes, composition, dimentions, and equipment configurations used for Dy^{3+} PL emission measurements (see Section 7.3 for description of equipment configuration code).

Sample type	Code and nominal composition (atomic %)	Dimensions	Equipment configuration and Figure
Single material fibre (*un-annealed*)	**F125RERC** (*$Ge_{15.0}As_{21.0}Ga_{1.0}Se_{63.0}$ + 850 ppmw $TeCl_4$ + 500 ppmw Dy (foil)*)	Diameter of 186.9 ± 1.8, and 83.34 mm long.	Figure 4-30 (a): **A**[1_{e}-7_{b}] **F**[9_{a}] **I**[12_{b}- $13_{2.000\ \mathrm{LWP}}$- 14_{b} -15_{ai} – 16_{b}] Figure 4-31 (a): **A**[1_{b}-7_{b}] **F**[9_{a}] **I**[12_{b}- $13_{2.484\ \mathrm{LWP}}$- 14_{b} -15_{ai} – 16_{b}] Figure 4-30 (c) and Figure 4-31 (a): **A**[1_{b}-7_{b}] **F**[9_{a}] **I**[12_{b}- $13_{2.484\ \mathrm{LWP}}$- 14_{b} -15_{aii} – 16_{b}]
Powdered glass (*un-annealed single material fibre*)	**F125RERC** (*$Ge_{15.0}As_{21.0}Ga_{1.0}Se_{63.0}$ + 850 ppmw $TeCl_4$ + 500 ppmw Dy (foil)*)	Varying granule size, 129 ± 47 µm µm in diameter.	Figure 4-30 (a): **C**[1_{e}] **G**[] **I**[12_{a}- 13_{none}- 14_{a} -15_{ai} – 16_{b}] Figure 4-30 (b) and Figure 4-31 (b): **C**[1_{b}] **G**[] **I**[12_{a}- $13_{2.484\ \mathrm{LWP}}$- 14_{a} -15_{ai} – 16_{b}] Figure 4-30 (c) and Figure 4-31 (b): **C**[1_{b}] **G**[] **I**[12_{a}- $13_{2.484\ \mathrm{LWP}}$- 14_{a} -15_{aii} – 16_{b}]
Co-extruded glass rod (*annealed and polished*)	**E094REDF(JN)**: (Core: **M293REJN:** *$Ge_{14.8}As_{20.8}Ga_{2.0}Se_{62.4}$ + 500 ppmw Ce (foil)* Cladding: **M295REJN**: *$Ge_{16.5}As_{16.0}Ga_{3.0}Se_{61.5}S_{3.0}$ + 500 ppmw Dy (foil)*)	9.1 mm long with a 3.2 mm outer diameter. Maximum core diameter: 1.88 mm.	Figure 4-30 (b): **A**[1_{b}-7_{b}] **F**[9_{none}] **I**[12_{b}- $13_{2.484\ \mathrm{LWP}}$- 14_{b} -15_{ai} – 16_{b}] Figure 4-30 (c) and Figure 4-31 (c): **A**[1_{b}-7_{b}] **F**[9_{none}] **I**[12_{b}- $13_{2.484\ \mathrm{LWP}}$- 14_{b} -15_{aii} – 16_{b}]

4.2.5.3.a Dy^{3+} PL emission spectra:

Three distinct Dy^{3+} PL emission bands spanning between 2.200 to 2.500 µm, 2.600 to 3.400 µm, and 3.800 to 5.100 µm were detected and investigated and correspond to those found in literature (see Table 4-19). Note, the Dy^{3+} PL emissions with wavelengths less than 2 µm or greater than 5 µm were not investigated.

Application of the 1.310 µm excitation source resulted in the 2.200 to 2.500 µm emission band, shown in Figure 4-30 (a), which was attributed to the ($^6H_{9/2}$, $^6F_{11/2}$) → $^6H_{13/2}$ transition. Application of either the 1.310 µm or the 1.700 µm excitation source resulted in two additional emission bands between 2.600 to 3.400 µm, shown in Figure 4-30 (b), and 3.800 to 5.100 µm, shown in Figure 4-30 (c), which were attributed to the $^6H_{13/2}$ → $^6H_{15/2}$ transition and $^6H_{11/2}$ → $^6H_{13/2}$ transition, respectively. The ~2.9 µm Dy^{3+} PL emission band in in Figure 4-30 (b), agrees with the calculated $^6H_{13/2}$ → $^6H_{15/2}$ emission shape in Figure 4-29 (c).

The 2.200 to 2.500 µm emission band, shown in Figure 4-30 (a), was only accessible using the 1.310 µm excitation scheme. Notably, this emission band was absent, or not detectable, when employing the 1.700 µm pump. This indicated ESA of the 1.700 µm pump between the $^6H_{13/2}$ → ($^6H_{7/2}$,$^6F_{9/2}$) manifolds, shown within the inset in Figure 4-30 (b), was either absent or not efficient. Furthermore, the branching ratios from the ($^6H_{7/2}$,$^6F_{9/2}$) manifolds favour radiative transitions outside of the presented measurement window [17,39].

Comparing the shapes of the PL emission spectra in Figure 4-30 (c) obtained from the samples listed in Table 4-21, showed minor differences between the samples possessing the $Ge_{15.0}$ $As_{21.0}$ $Ga_{1.0}$ $Se_{63.0}$ atomic % composition, against the co-extruded rod E094REDF(JN) with its $Ge_{16.5}$ $As_{16.0}$ $Ga_{3.0}$ $Se_{61.5}$ $S_{3.0}$ atomic % composition. This indicated that the presence of sulfur and additional 'Ga' in the co-extruded glass rod composition did not significantly alter the Dy^{3+} PL emission spectra when compared to the other samples.

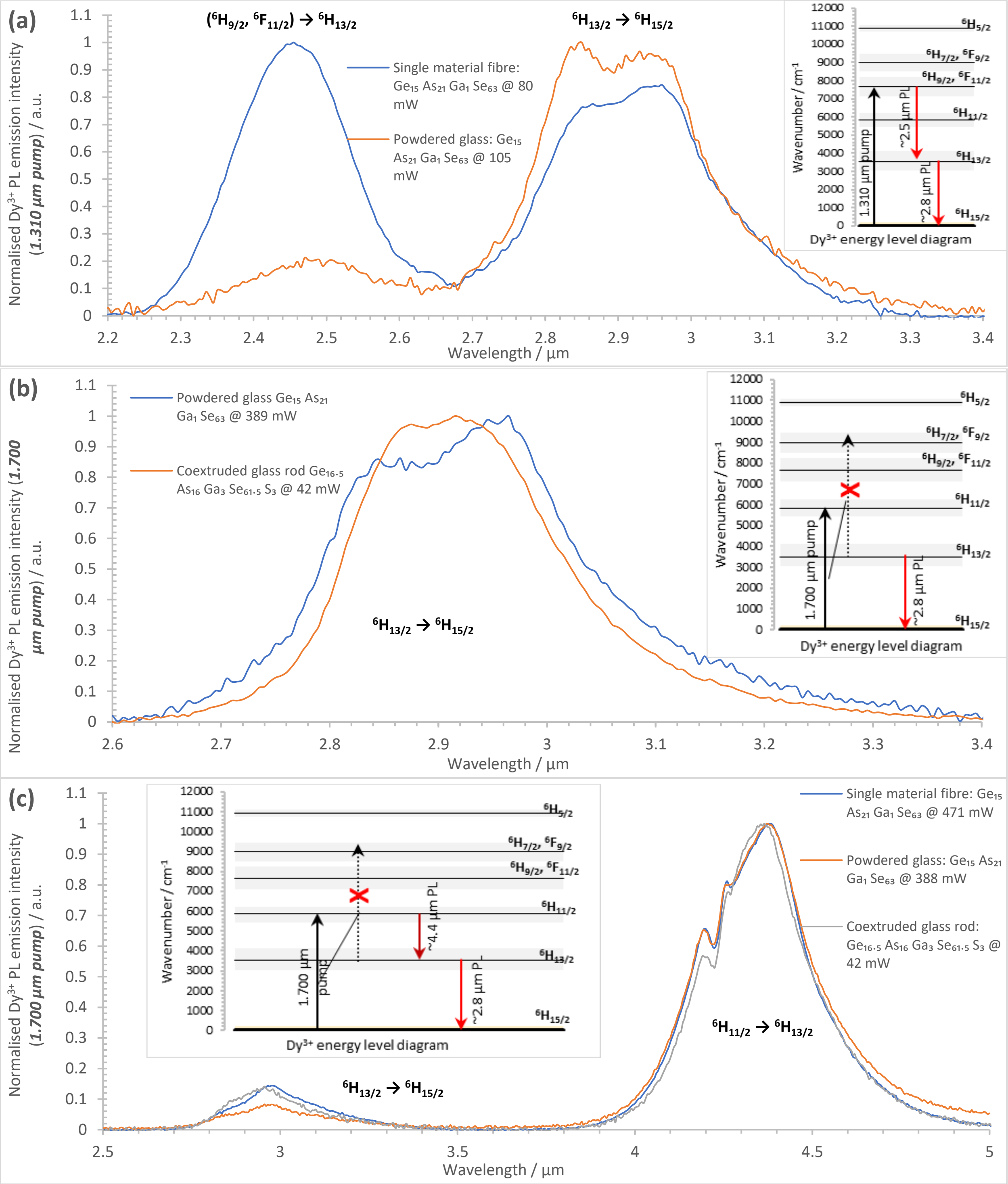

Figure 4-30: Normalised PL emission spectra for nominally 500 ppmw Dy (foil) doped samples, listed in Table 4-21 measured between the wavelengths of: ***(a)*** *2.200 to 3.400 µm using 1.310 µm pump,* ***(b)*** *2.600 to 3.400 µm using 1.700 µm pump,* ***(c)*** *2.500 to 5.000 µm using 1.700 µm pump. Each figure shows the Dy^{3+} energy level diagram (<u>Arrow lengths ARE TO SCALE</u>). Not corrected for system spectral response. See Table 4-21 for sample dimensions and equipment configuration.*

Comparing the intensity between the 2.600 to 3.400 µm, and the 3.800 to 5.100 µm emission bands, shown in Figure 4-30 (a), the $^6H_{13/2} \rightarrow {}^6H_{15/2}$ transition was weaker than the $^6H_{11/2} \rightarrow {}^6H_{13/2}$ transition, as illustrated within the inset in Figure 4-30 (c). This discrepancy was attributed to reabsorption from both the $^6H_{15/2} \rightarrow {}^6H_{13/2}$ GSA and the underlying [-OH] impurity resonantly absorbing and transferring PL into vibrational quanta.

4.2.5.3.b Dy^{3+} PL lifetime results:

PL emission lifetime 'τ_{rad}' measurements were performed on the samples listed in Table 4-21 using the 1.700 µm excitation source modulated at 8 Hz. These lifetime measurements focused on the 2.600 to 3.400 µm and the 3.800 to 5.100 µm Dy^{3+} PL emission bands. The 2.200 to 2.500 µm band was omitted. Figure 4-31 shows the normalised Dy^{3+} PL emission decay from each sample type, along with a corresponding fitted exponential function. Table 4-22 lists the Dy^{3+} PL lifetimes from each sample type. Note, the fitting applied to the 2.600 to 3.400 µm spectral range started at t = 1.5 ms to avoid unwanted transients introduced by the 1.700 µm pump source upon the weak Dy^{3+} PL signal.

Lifetime measurements in the 2.600 to 3.400 µm and the 3.800 to 5.100 µm Dy^{3+} PL emission bands were individually best fitted with a single-term exponential function, shown in Figure 4-31 (a) to (c) and listed in Table 4-22. Results for measurements within the 2.600 to 3.400 µm spectral range consisted of a 'τ_1', at ~ 4.56 ms, which was attributed to the $^6H_{13/2} \rightarrow {}^6H_{15/2}$ transition. Results for measurements within the 3.800 to 5.100 µm spectral range consisted of a 'τ_1', at ~ 1.67 ms which was attributed to the $^6H_{11/2} \rightarrow {}^6H_{13/2}$ transition. These lifetime results roughly match the results found in literature (see Table 4-20).

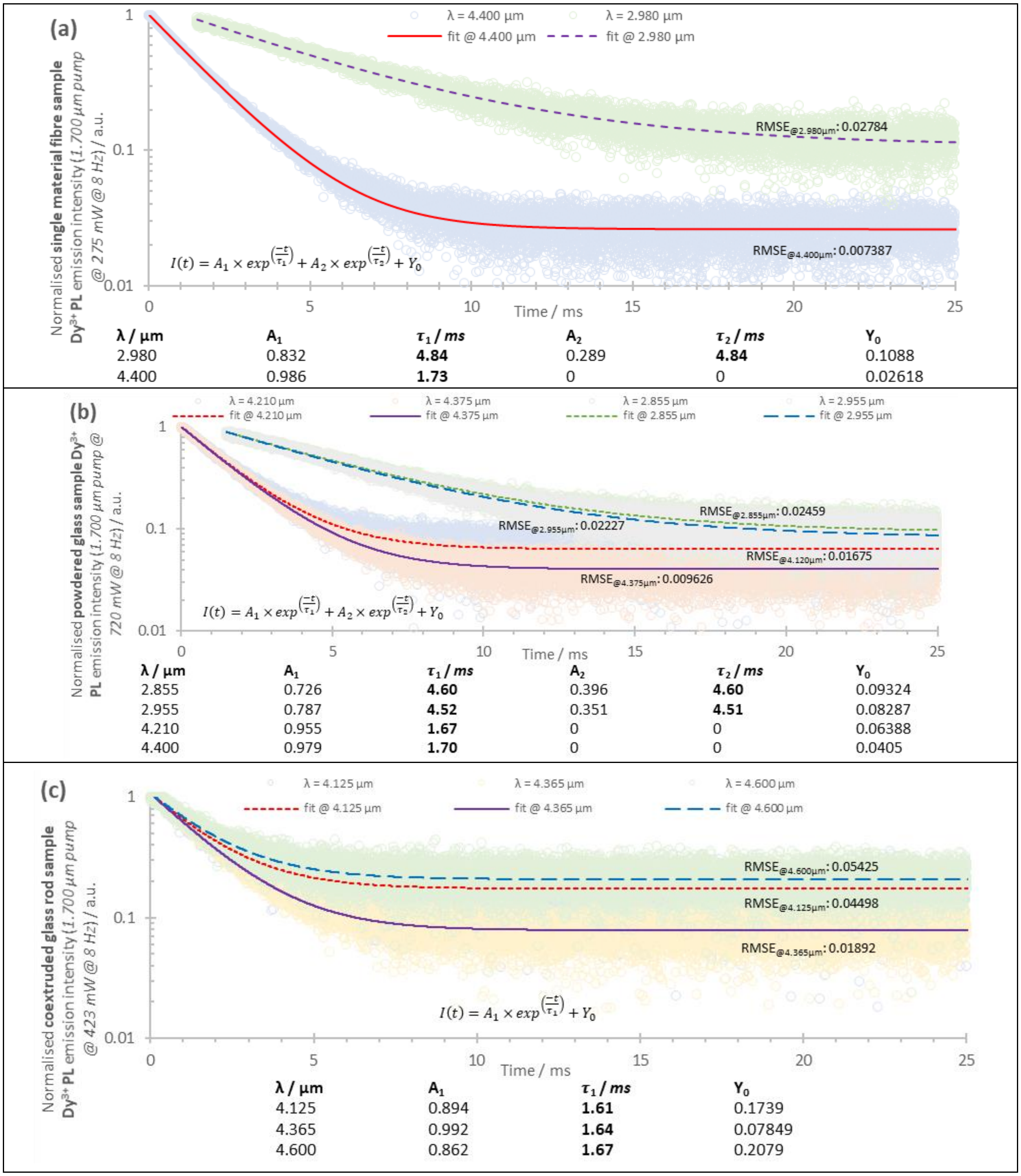

λ / μm	**A_1**	**τ_1 / ms**	**A_2**	**τ_2 / ms**	**Y_0**
2.980	0.832	**4.84**	0.289	**4.84**	0.1088
4.400	0.986	**1.73**	0	0	0.02618

λ / μm	**A_1**	**τ_1 / ms**	**A_2**	**τ_2 / ms**	**Y_0**
2.855	0.726	**4.60**	0.396	**4.60**	0.09324
2.955	0.787	**4.52**	0.351	**4.51**	0.08287
4.210	0.955	**1.67**	0	0	0.06388
4.400	0.979	**1.70**	0	0	0.0405

λ / μm	**A_1**	**τ_1 / ms**	**Y_0**
4.125	0.894	**1.61**	0.1739
4.365	0.992	**1.64**	0.07849
4.600	0.862	**1.67**	0.2079

Figure 4-31: Normalised Dy^{3+} PL lifetime (scatter plot) fitted with exponential decay functions (line) for nominally 500 ppmw Dy^{3+} doped samples using 1.700 μm pump laser for: ***(a)*** *single material fibre (****F125RERC****),* ***(b)*** *Powdered bulk glass (****F125RERC****) sample, and* ***(c)*** *co-extruded glass rod (****E094REDF(JN)****) sample. Note, the pump source modulated at 8 Hz, and the F125RERC samples possessed a: $Ge_{15.0}$ $As_{21.0}$ $Ga_{1.0}$ $Se_{63.0}$ atomic % + 850 ppmw $TeCl_4$ composition while the cladding of E094REDF(JN): $Ge_{16.5}$ $As_{16.0}$ $Ga_{3.0}$ $Se_{61.5}$ $S_{3.0}$ atomic % composition. See Table 4-21 for sample dimensions and equipment configurations, and results summarised in Table 4-22.*

Table 4-22: Summary of Dy^{3+} lifetime measurement shown in Figure 4-31 using 1.700 µm excitation source (see Table 4-21 for sample specifications and equipment configuration)

Sample type and composition (atomic %)	Measurement λ / µm	Lifetime coefficients				
		A_1	τ_1 / ms	A_2	τ_2 / ms	Y_0
F125RERC *Single material fibre (un-annealed)* (*$Ge_{15.0}$ $As_{21.0}$ $Ga_{1.0}$ $Se_{63.0}$ + 850 ppmw $TeCl_4$ + 500 ppmw Dy (foil)*)	4.400	0.987	**1.73**	0	0	0.02618
F125RERC *Powdered glass (un-annealed single material fibre)* (*$Ge_{15.0}$ $As_{21.0}$ $Ga_{1.0}$ $Se_{63.0}$ + 850 ppmw $TeCl_4$ + 500 ppmw Dy (foil)*)	4.120	0.955	**1.67**	0	0	0.06388
	4.375	0.979	**1.71**	0	0	0.0405
E094REDF(JN) *Co-extruded glass rod (annealed and polished)* (Core: **M293REJN:** *$Ge_{14.8}$ $As_{20.8}$ $Ga_{2.0}$ $Se_{62.4}$ + 500 ppmw Ce (foil)* Cladding: **M295REJN**: *$Ge_{16.5}$ $As_{16.0}$ $Ga_{3.0}$ $Se_{61.5}$ $S_{3.0}$ + 500 ppmw Dy (foil)*)	4.125	0.894	**1.61**	0	0	0.1739
	4.365	0.992	**1.64**	0	0	0.07849
	4.600	0.862	**1.68**	0	0	0.2079
F125RERC *Single material fibre (un-annealed)* (*$Ge_{15.0}$ $As_{21.0}$ $Ga_{1.0}$ $Se_{63.0}$ + 850 ppmw $TeCl_4$ + 500 ppmw Dy (foil)*)	2.980	0.832	**4.84**	0.289	**4.84**	0.1088
F125RERC *Powdered glass (un-annealed single material fibre)* (*$Ge_{15.0}$ $As_{21.0}$ $Ga_{1.0}$ $Se_{63.0}$ + 850 ppmw $TeCl_4$ + 500 ppmw Dy (foil)*)	2.855	0.726	**4.60**	0.396	**4.60**	0.09324
	2.955	0.787	**4.52**	0.351	**4.51**	0.08287

Notably, the PL lifetimes in both the 2.600 to 3.400 µm and the 3.800 to 5.100 µm Dy^{3+} PL emission bands varied slightly between the sample types listed in Table 4-21. When comparing the F125RERC composition against the E094REDF(JN) composition, the presence of 'S' (*sulfur*) in the E094REDF(JN) composition did not significantly alter the Dy^{3+} lifetimes as compared to the composition without sulfur (see Table 4-21).

Considering both the absorption results in Section 4.2.5.1, and the PL emission results in Section 4.2.5.3.a, the addition of a relatively small amount of sulfur (≤ 3 atomic %) ostensibly reduced the [Se-H] impurity concentration while having no deleterious effects on the Dy^{3+} cation dopant.

Thus, the addition of sulfur to the glass composition should be a viable option to 'tailor' a host glass composition containing a RE^{3+} cation dopant to minimise the underlying attenuation in the 4.5 µm spectral region, especially for MIR fibre laser applications.

4.2.5.4 Dy^{3+} ESA measurements

ESA measurements were performed on a distilled nominally 500 ppmw 'Dy' (*foil*) doped $Ge_{15.0}$ $As_{21.0}$ $Ga_{1.0}$ $Se_{63.0}$ atomic % + 850 ppmw $TeCl_4$ F125RERC single material fibre sample, 441 mm long, with a diameter of 118.7 ± 18.2 µm. This single material fibre sample was exposed to a 1.700 µm pump laser to induce the $^6H_{15/2} \rightarrow {^6H_{11/2}}$ electronic transition. Figure 4-32 show the room temperature, steady state, relative change in intensity of the transmitted probe-light with pump, relative to no pump present, for the fibre sample. Additionally, the inset within Figure 4-32 shows the attenuation spectrum of a separate F125RERC fibre sample. Note, this attenuation spectrum represents the zero-change axis (*along the wavelength-axis*) in the accompanying ESA spectrum in Figure 4-32.

Comparing the ESA spectra in Figure 4-32 to the F125RERC attenuation spectrum inset, no prominent features were observed at 3.150 µm, 5.420 µm, 8.090 µm and 9.670 µm in the corresponding attenuation spectrum, thus validating the latent nature of these unobstructed ESA bands which are present in the ESA spectra.

Considering the spectral features observed in Figure 4-32 along with the Dy^{3+} absorption and PL emission measurements made in Section 4.2.5.3, the energy level transitions responsible for these features were proposed. Table 4-23 lists each significant spectral feature, observed in Figure 4-32, along with the corresponding proposed energy level transitions responsible for these features, and Figure 4-33 shows the Dy^{3+} electronic energy level diagram, inclusive of arrows for the proposed energy level transitions. Both the $^6H_{11/2}$ and $^6H_{13/2}$ energy levels were postulated as the predominant initial states from which ESA took place due to their ~1.67 ms and ~4.56 ms lifetimes, as determined in Section 4.2.5.3.b. These proposed energy level transitions match the corresponding Dy^{3+} energy level spacing as shown in Figure 4-33. However, it must be noted that additional transitions between alternate energy levels were not ruled out; moreover, these alternate transitions could have also been partially, or completely obscured by overlapping GSA bands.

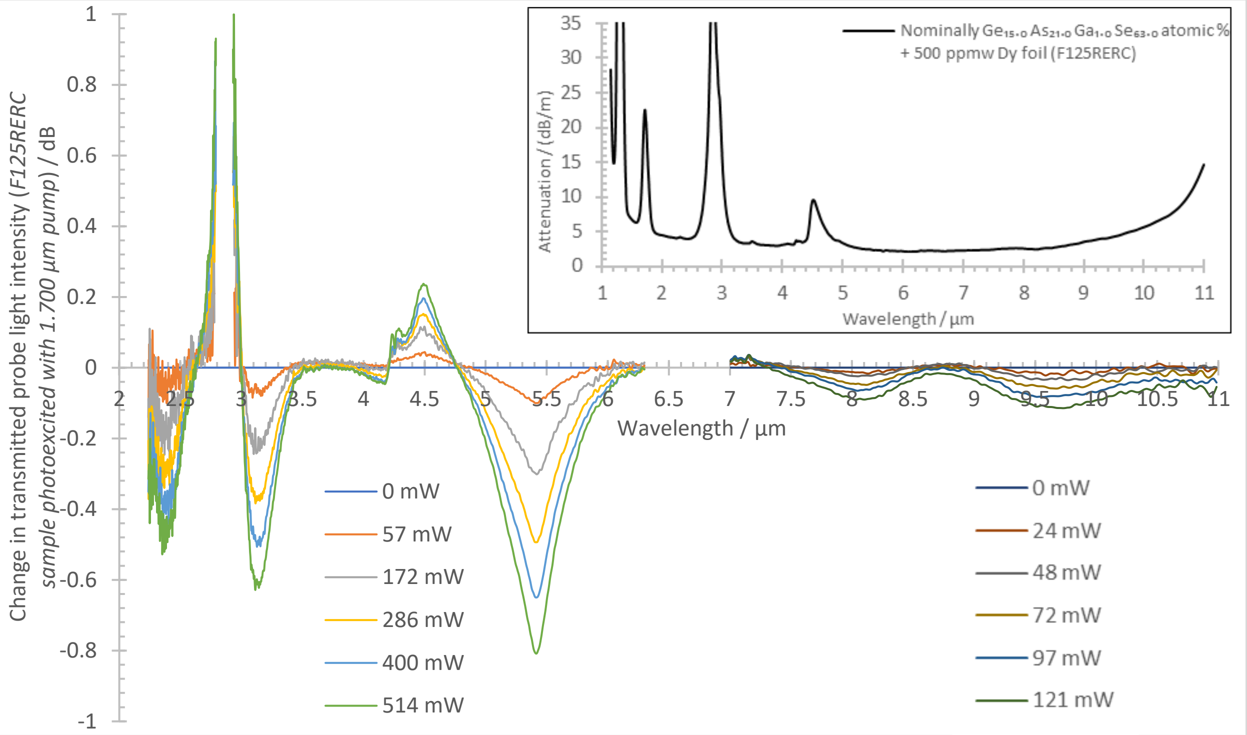

Figure 4-32: Showing changes in transmitted probe light intensity, under application of a 1.700 µm continuous wave pump laser for a 441 mm long, nominally 500 ppmw Dy (foil) doped, distilled $Ge_{15.0}$ $As_{21.0}$ $Ga_{1.0}$ $Se_{63.0}$ atomic % + 850 ppmw $TeCl_4$ glass fibre sample (F125RERC) of diameter 118.7 ± 18.2 µm, with inset showing attenuation (dB/m) vs. wavelength (µm) for F125RERC single material glass fibre sample (see Figure 3-33 for additional details on F125RERC attenuation spectrum). Note, the 2.78 to 2.94 µm spectral region was omitted due to strong absorptions from $^6H_{15/2} \rightarrow {}^6H_{13/2}$ and [-OH] impurity.

Table 4-23: Proposed Dy^{3+} electronic transitions to account for observed spectral features seen in Figure 4-32.

λ / µm (see Figure **4-32)**	**Description**	**Proposed electronic transition**
2.370 (*4219 cm^{-1}*)	ESA band	$^6H_{13/2} \rightarrow (^6H_{9/2}, ^6F_{11/2})$
2.640 (*3788 cm^{-1}*)	Zero-change point	$^6H_{13/2} \rightarrow (^6H_{9/2}, ^6F_{11/2})$ and $^6H_{13/2} \rightarrow {}^6H_{15/2}$
2.840 (*3521 cm^{-1}*)	Either SE and/or GSD	$^6H_{13/2} \rightleftharpoons {}^6H_{15/2}$
3.000 (*3333 cm^{-1}*)	Zero-change point	$^6H_{13/2} \rightarrow {}^6H_{15/2}$ and $^6H_{11/2} \rightarrow (^6H_{7/2}, ^6F_{9/2})$
3.150 (*3175 cm^{-1}*)	ESA band	$^6H_{11/2} \rightarrow (^6H_{7/2}, ^6F_{9/2})$
4.180 (*2392 cm^{-1}*)	ESA band	$^6H_{13/2} \rightarrow {}^6H_{11/2}$
4.210 (*2375 cm^{-1}*)	Zero-change point	$^6H_{13/2} \rightarrow {}^6H_{11/2}$ and $^6H_{11/2} \rightarrow {}^6H_{13/2}$
4.480 (*2232 cm^{-1}*)	**SE only**	$^6H_{11/2} \rightarrow {}^6H_{13/2}$
4.760 (*2101 cm^{-1}*)	Zero-change point	$^6H_{11/2} \rightarrow {}^6H_{13/2}$ and $^6H_{11/2} \rightarrow (^6H_{9/2}, ^6F_{11/2})$
5.420 (*1845 cm^{-1}*)	ESA band	$^6H_{11/2} \rightarrow (^6H_{9/2}, ^6F_{11/2})$
8.090 (*1236 cm^{-1}*)	ESA band	$(^6H_{9/2}, ^6F_{11/2}) \rightarrow (^6H_{7/2}, ^6F_{9/2})$
9.670 (*1034 cm^{-1}*)	ESA band	$(^6H_{9/2}, ^6F_{11/2}) \rightarrow (^6H_{7/2}, ^6F_{9/2})$

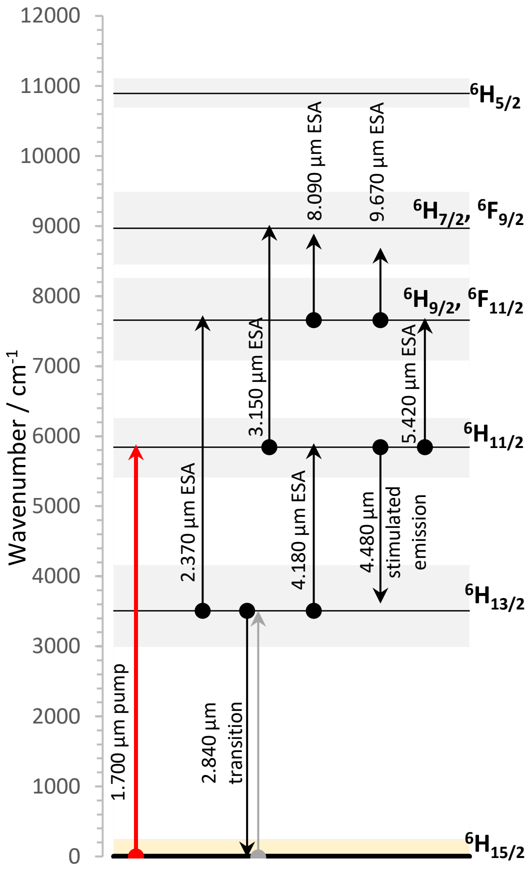

Dy^{3+} energy level diagram

Figure 4-33: Dy^{3+}energy level diagram with possible upward and downward transitions to account for changes observed in Figure 4-32 (Arrow lengths ARE TO SCALE in energy).

Note, **GSD**- Ground State Depletion, and **SE**- Stimulated emission.

The ESA band centred at 2.370 µm matched the $^6H_{13/2} \rightarrow (^6H_{9/2}, ^6F_{11/2})$ upward transition. This ESA band was partially overlapped by the SE/GSD (*stimulated emission/ ground state depletion*) centred at 2.840 µm, which matched the $^6H_{13/2} \rightleftharpoons {}^6H_{15/2}$ transition. Thus, it was postulated that the spectral overlap of the $^6H_{13/2} \rightarrow (^6H_{9/2}, ^6F_{11/2})$ and $^6H_{13/2} \rightleftharpoons {}^6H_{15/2}$ transitions resulted in a zero-change point at 2.640 µm, at 6.9 dB/m of attenuation.

The ESA band around 3.150 µm matched the $^6H_{11/2} \rightarrow (^6H_{7/2}, ^6F_{9/2})$ upward transition. This ESA band also partially overlapped by the SE/GSD centred at 2.840 µm resulting in another zero-change point at 3.000 µm, at ~ 17 dB/m of attenuation. Interestingly, this ESA band around 3.150 µm presents an unexpected issue for the development of 2.8 to 3.4 µm Dy^{3+}-based lasers [138], <u>while employing a 1.70 µm pump laser</u>, as this ESA band partially overlaps the 2.600 to 3.400 µm Dy^{3+} PL emission band, shown in Figure 4-30 (a) and (b). Considering the display of Dy^{3+} lasers operating around 3.1 µm [138], while employing either a 1.064 µm or 1.3 µm pump wavelengths, it was likely that this ~3.1 µm ESA band was likely diminished or absent.

The $^6H_{11/2} \rightarrow {}^6H_{13/2}$ transition was solely responsible for the Dy^{3+} PL emissions between 3.800 to 5.100 µm, shown in Figure 4-30 (c) as revealed during the Dy^{3+} PL emission measurements in Section 4.2.5.3.a. Interestingly, and importantly, the spectral feature peaking at 4.480 µm in Figure 4-32 could only have been due to SE between the $^6H_{11/2} \rightarrow {}^6H_{13/2}$ manifolds because of a lack of any overlapping Dy^{3+} GSA bands to exhibit GSD in this spectral region. This was unexpected considering the $^6H_{13/2}$ manifold has a longer lifetime than the $^6H_{11/2}$ manifold, see Section 4.2.5.3.b, which would cause the excited electron population in the $^6H_{13/2}$ manifold to be larger. Thus, it is postulated that other ESA band originating from the $^6H_{13/2}$ manifold sufficiently depopulated the level to allow SE between the $^6H_{11/2} \rightarrow {}^6H_{13/2}$ manifolds. The extrinsic [-Se-H] impurity vibrational absorption band overlaps this SE band. This SE band alludes the opportunity to achieve lasing at ~ 4.34 µm similar to [135,136,143,193].

The weak ESA band centred at 4.180 µm matched the $^6H_{13/2} \rightarrow {}^6H_{11/2}$ upward transition. This ESA band which was partially overlapped by the SE band centred at 4.480 µm, which was attributed to the $^6H_{11/2} \rightarrow {}^6H_{13/2}$ downward transition, resulting in a zero-change point at 4.210 µm, at 2.7 dB/m of attenuation. The ESA band centred at 5.420 µm matched the $^6H_{11/2} \rightarrow ({}^6H_{9/2}, {}^6F_{11/2})$ upward transition, which partially overlapped by the SE centred at 4.480 µm, resulting in another zero-change point at 4.760 µm, at 4.8 dB/m of attenuation.

The spectral features at 8.090 µm and 9.670 µm were speculated to originate due to the $({}^6H_{9/2}, {}^6F_{11/2}) \rightarrow ({}^6H_{7/2}, {}^6F_{9/2})$ transition, due to Dy^{3+} PL emissions reported in [39].

4.2.6 Discussion on measurement methodology:

This section discusses the measurement methodology used to achieve the finding presented throughout Sections 4.2.1 to 4.2.5.

4.2.6.1 Absorption measurements results:

Absorption measurements were carried out on polished, bulk chalcogenide glass samples (see Appendix 7.2.1). These RE^{3+} GSA spectra were used to produce the corresponding RE^{3+} energy level diagrams and emission and absorption cross-sections. The RE^{3+} GSA within these bulk absorption spectra were obtained by numerically removing the host glass baseline absorption and overlapping extrinsic impurity absorptions. These processes sometime introduced errors:

i. Inaccuracies with the baseline removal process introduced uncertainty into the presented absorption and cross-section spectra. The precise position of the underlying host glass baseline at every point of the absorption spectrum was not always obvious. Spectral regions containing multiple overlapping GSA bands, or regions where GSA bands partially overlapped extrinsic impurities absorptions sometimes made discerning the host glass baseline difficult and subjective. This was further exacerbated by the linear interpolation method commonly used by software packages to ‘fit’ the host glass baseline. Depending on trend in the host glass baseline the fitting could slightly underestimate or overestimate the RE^{3+} GSA absorption.
ii. Extrinsic impurities often exhibit vibrational overlapping absorption bands with the GSA of the RE^{3+} dopant. Thus, necessitating the RE^{3+} GSA bands be deconvolved from the overlapping extrinsic impurity absorptions, using the procedure described in [116]. This

task was made more difficult by approximations of the un-obstructed extrinsic absorption band shape along with uncertainty in the concentration of the unwanted impurity and assumptions about the predictability of these extrinsic absorptions while overlapped by RE^{3+} GSA.

Calculation of the optical cross-sections employed the procedures described in Section 7.2.1.1. Calculation of the emission cross-section employed the Füchtbauer–Ladenburg equation which required the refractive index of the host material. Unfortunately, the MIR ellipsometry measurements, see Section 3.2, only evaluated the 2 to 20 µm spectral region. Thus, estimates of the refractive index outside the evaluated spectral regions were used.

4.2.6.2 PL emission measurements:

PL emission measurements were done to investigate PL from the various decay path(s), while evaluating up-conversion and reabsorption effects by assessing samples with different geometries. Several learnings were uncovered while carrying out these measurements:

<u>Sample geometry</u>:

Reabsorption due to GSA, ESA, and extrinsic impurities could each influence the emission spectrum prior to the PL exiting a sample during PL emission spectrum measurements. Additionally, the volume of the sample, aspect ratio, and the relative position of the PL collection optics each affected the maximum propagation length within the sample. Thus, to investigate the influence of these confounding variables several equipment configurations were employed using samples with different geometries, namely polished bulk glass, powdered glass, and various lengths and diameters of SIF (*step-index fibre*) and single material fibre.

Powdered RE^{3+} doped samples ensured a very short propagation length, due to their small volume and the relatively uniform aspect ratio of each granule, thus they were considered to produce the most faithful representation of the nominal RE^{3+} PL emission spectrum. Conversely, fibres employing the 'End-collection' configuration, see inset **F** in Figure 4-1, afforded significant propagation length within the sample allowing for reabsorption effects to be evaluated when compared with powdered sample results. Hence, powdered samples and fibres where the preferred sample types employed for the PL emission measurements throughout Section 4.2. The small propagation length the powdered sample configuration produced relatively weak intensity, while 'End-collection' enabled greater intensity by collecting emissions propagating along the long axis of the fibre sample.

<u>PL spectrum modulation</u>:

PL emanating from the sample could either be electronically or mechanically modulated. PL emission spectra obtained using an electronically modulated excitation source required consideration of the modulation frequency and the lifetimes of each of the RE^{3+} energy levels contributing to the PL emission band. This was necessary to avoid selecting too high a modulation frequency which could hinder the ability to modulate specific radiative transitions, effectively filtering them by decoupling them from the detection system, thus influencing the resulting PL emission spectrum. Several of the RE^{3+} dopants evaluated throughout Section 4.2 possess disparate lifetimes for their different energy levels, and exhibit PL emission bands comprised of radiative transitions from multiple energy levels. Fortunately, mechanical modulation of PL using an optical chopper with the procedure described in Appendix 7.2.4.5, avoided these potential issues by virtue of employing a CW pump source. Thus, CW excitation of a sample followed by mechanical modulation of PL was the preferred method used for obtaining the RE^{3+} PL emission spectra presented throughout Section 4.2, unless otherwise stated. Note, electronic modulation was exclusively used with the lifetime measurement procedure described in Section 4.1.1.3.

4.2.6.3 ESA measurements:

The FTIR-based ESA equipment configuration (see Section 4.1.2.1) could be used with different types and static lengths of RE^{3+} doped fibres, or conceivably a gas cell, and was amenable to different spectral regions once the selected pump and probe wavelengths were capable of being propagated along the transmission medium. However, the following challenges were encountered:

i. Thermal management: Proper thermal management of the ‘pump launch end’ of the fibre sample (see Figure 4-2), was essential to achieve repeatable results. Otherwise, localised heating within the fibre would alter the host glass loss spectrum resulting in spurious results. This manifested itself as a conspicuous offset from the zero-change axis.

ii. Atmospheric absorptions: Maintaining constant ambient conditions along the optical path between measurements was essential to obtain reliable and repeatable results. This was achieved by restricting laboratory occupancy during measurements to avoid changes in CO_2 and H_2O concentrations and minimising length of sections of the optical path open to the atmosphere.

iii. Spectral range of measurement: The ESA equipment configuration, shown in Figure 4-2, was not capable of performing ESA measurements at the ‘pump’ wavelength, due to the conflicting transmission band requirement of the dichroic mirror in the optical path, item 4, in Figure 4-2. Importantly, this prevented the evaluation of transitions occurring at the pump wavelength, which obscured knowledge of the relative population densities in the uppermost energy manifolds.

iv. RE^{3+} PL emission: The FTIR-based ESA equipment configuration was not capable of evaluating the RE^{3+} PL emanating from fibre samples during photoexcitation, due to the CW pump laser, item 1 in Figure 4-2. This limitation was addressed in Section 4.2.2.4 using an alternate equipment configuration.

v. ‘Cut-back’ measurements: The ‘counter-propagating’ equipment configuration, shown in Figure 4-2, was unsuitable for ‘cut-back’ measurements. This was due to the difficulty in maintaining constant launch conditions for either the pump or probe sources, after cutting back the fibre sample. This prevented a proper assessment of the ‘change in transmitted probe light intensity’ per unit length (dB/m) over the entire measurement window.

Ambiguity of electronic transitions responsible for observed spectral features:

ESA measurements did not clearly differentiate which electronic transitions were responsible for the spectral features observed, as it evaluated only relative changes induced by the application of the ‘pump’ source. Often, when considering an individual RE^{3+} dopant, there were several possible electronic transitions to account for the observed spectral features. Therefore, the corresponding RE^{3+} absorption measurements and PL emission measurements, along with the process of elimination were used, when possible, to corroborate and rationalise the most conservative proposed ESA transitions.

<u>ESA spectra only show relative attenuation or amplification afforded by the RE^{3+} dopant</u>:

The pump-probe measurement technique evaluated only relative changes of the broadband probe source by ratioing the transmitted spectra with, and without, the application of the 'pump' source (*see inset (b) in Figure 4-2*). This had the benefit of showing only the relative changes induced due to the photoexcitation of the RE^{3+} dopant. While the underlying attenuation spectrum of the fibre sample, inclusive of impurity absorptions, was flattened to form the zero-change axis (*the wavelength-axis*) (*compare insets (a) and (b) in Figure 4-2*). This method of representing the ESA spectra was preferred over presenting the otherwise complex absorption spectrum of the fibre with its photoexcited RE^{3+} dopant. The ESA spectra presented throughout Section 4.2, especially in the spectral regions of "positive change" (*see Section 4.1.2.2*) could be misconstrued as 'gain', when in truth they were superimposed on the underlying attenuation spectrum of the fibre. Hence the reason each RE^{3+} ESA spectrum was <u>always</u> accompanied by the corresponding attenuation spectrum. Note, the spectral changes observed during ESA measurements, would likely be exaggerated in a small core SIF due to higher pump and probe intensity in the core.

<u>Zero-change points</u>:

Each RE^{3+} dopant exhibited at least one conspicuous ‘zero-change’ point, situated on, or very close to, the zero-change axis, in their respective ESA spectra (excluding the ‘Sm’ doped sample). The wavelength at which these ‘zero-change’ points occurred appeared to be fixed, within the 4 cm^{-1} resolution of the measurement, regardless of pump power used. It was postulated that each zero-point change was due to the SE and ESA having the same cross-sections. Thus, the ESA and SE/GSD effectively cancelled each other resulting in only the GSA remaining. Thus, at these wavelengths the optical attenuation experienced equalled that of the RE^{3+} doped glass without the application of the pump source and was at least partially comprised of contributions from an ESA band. Interestingly, the ESA spectra within the immediate vicinity of these points always appeared to be linear (straight lines), with their gradients being proportional the pump power, and was at least partially associated with contributions from an ESA band. Notably, this behaviour was also present in the Er^{3+} ESA measurements presented in [45].

4.3. Chapter summary:

The NIR and MIR absorption spectra, PL emission spectra, and PL lifetimes of the Ce^{3+}, Pr^{3+}, Sm^{3+}, Tb^{3+}, and Dy^{3+} cations were each evaluated in Section 4.2. Figure 4-34 summarised the radiative transitions that were detected superimposed on the corresponding RE^{3+} dopant energy level.

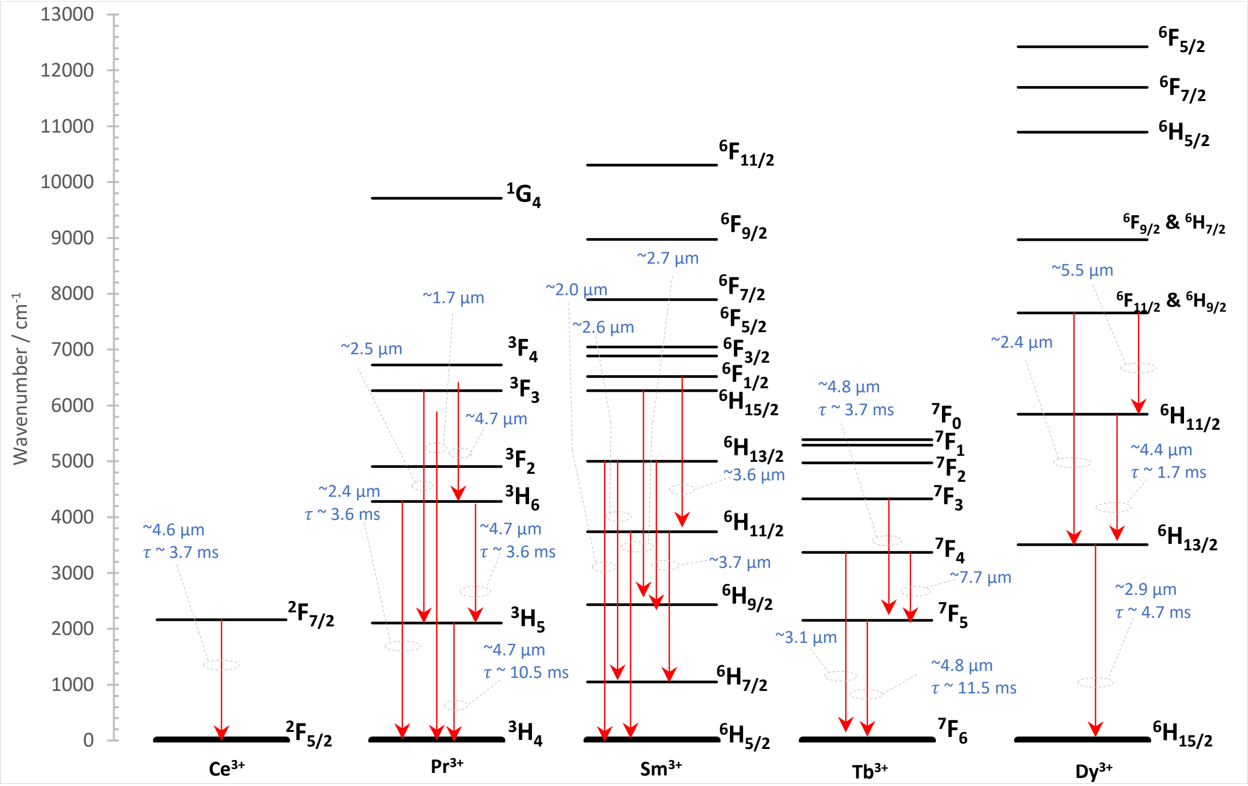

Figure 4-34: Showing a summary of the PL emission wavelengths, and radiative lifetimes detected from the Ce^{3+}, Pr^{3+}, Sm^{3+}, Tb^{3+} and Dy^{3+} dopants evaluated throughout Sections 4.2.1 to 4.2.5 superimposed on their corresponding RE^{3+} energy level diagrams. Arrows in red are to scale.

Encouragingly, several of the PL lifetimes and PL emission bands evaluated agreed with those reported in literature. Some of the PL emission measurement findings included:

i. The amount of 'Ga' in the glass composition seemed to influence the PL lifetime. Considering the Tb^{3+} lifetime measurements, in Section 4.2.4.3.b, the glass composition without 'Ga' exhibited a shorter PL lifetime when compared to its 'Ga' containing counterpart, a difference of ~ 1.55 ms was observed in the 4.9 µm PL emission band, while using a 2 µm pump. Conversely, the Ce^{3+} PL measurements, in Section 4.2.1.3.b, did not exhibit this behaviour. The 1 atomic % 'Ga' containing M259REZQT sample exhibited a longer PL lifetime than its 2 atomic % 'Ga' E094REDF(JN) counterpart, a difference of ~ 0.42 ms was observed.

ii. Pr^{3+} PL lifetime measurements, in Section 4.2.2.3.b, revealed that a longer wavelength pump source resulted in longer lifetimes when compared to a shorter wavelength pump source. A difference of ~1.2 ms was observed for both the 2.3 µm and 4.7 µm emission bands in the Pr^{3+} PL measurements when comparing a 4.15 µm to the 2 µm pump sources. Interestingly, the Tb^{3+} PL measurements did not exhibit this behaviour.

iii. Sample geometry also influenced PL lifetimes, the un-annealed single material fibres samples often exhibited the longest lifetimes, followed by powdered glass samples which were shorter, and SIF samples typically had the shortest lifetimes.

iv. Unsurprisingly, the PL emission spectra from powdered glass samples exhibited the least amount of reabsorption of RE^{3+} PL.

The latent ESA bands for individually Pr^{3+}, Sm^{3+}, Tb^{3+}, and Dy^{3+} doped chalcogenide fibres samples were evaluated. Figure 4-35 summarised the proposed ESA transitions to account for the ESA bands detected. Reassuringly, these proposed transitions presented throughout Section 4.2 match the energy level spacing of their corresponding RE^{3+} dopant.

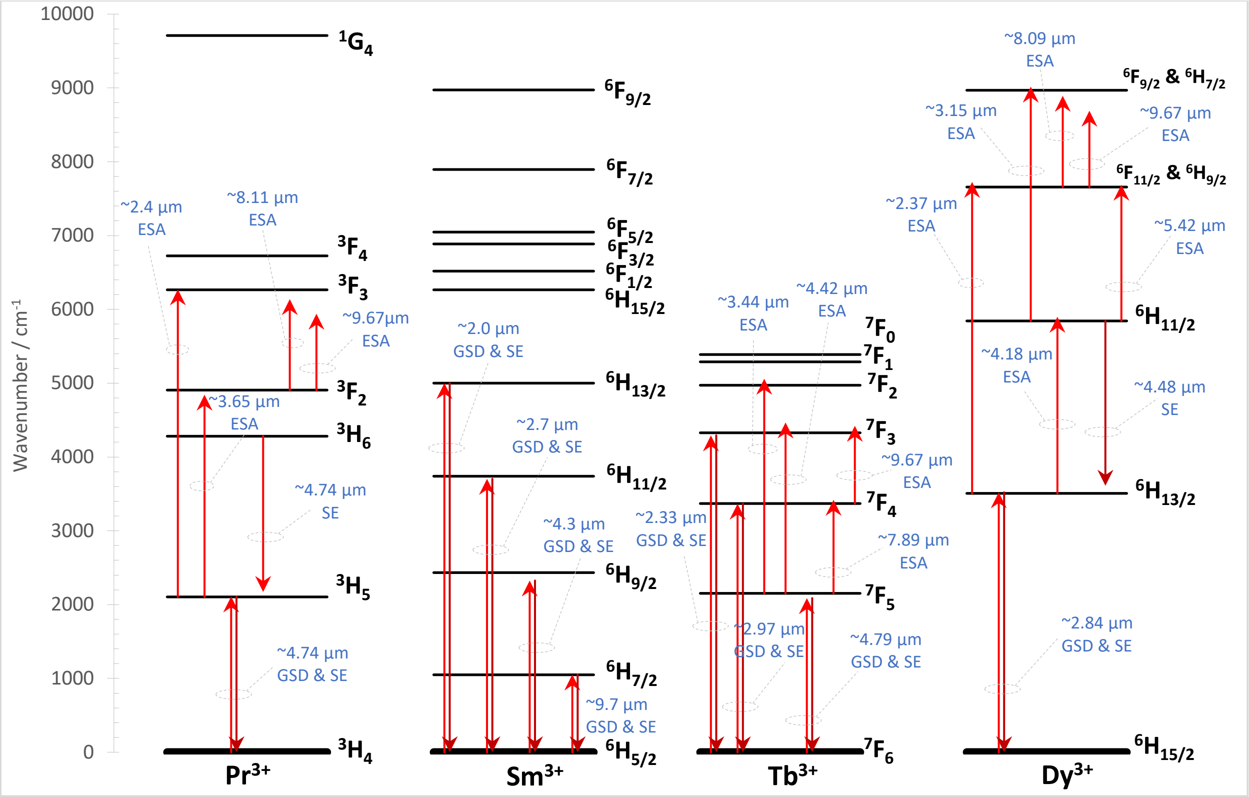

Figure 4-35: Showing a summary of ESA transitions detected from the Pr^{3+}, Sm^{3+}, Tb^{3+} and Dy^{3+} dopants evaluated throughout Sections 4.2.1 to 4.2.5 superimposed on their corresponding energy level diagrams (arrows in red are to scale). Please refer to Section 4.1.2 about ESA measurement.

Each RE^{3+} cation evaluated exhibited PL emission bands that overlapped their ESA bands. Importantly, this resulted in each of these RE^{3+} cations producing PL while simultaneously being capable of absorbing the PL via ESA. Additionally, the Pr^{3+}, Tb^{3+}, and Dy^{3+} ESA measurements show that the transitions occurring from different portions of a single excited state manifold can influence transitions occurring elsewhere within the same manifold. Unfortunately, some of the numerical models used to represent the transitions occurring between the manifolds in RE^{3+} cations, such as those described in [181,194,195], will not faithfully capture the dynamics of these transitions, especially over a range of different excitation powers and sample geometry

Spectroscopic evaluation of each RE dopant revealed the following:

- In-band pumping of 'Ce' cation doped samples with a 4.150 µm source resulted in Ce^{3+} PL spectra between 3.400 to 5.800 µm. A portion of this Ce^{3+} PL emission band exhibited up-conversion, presumably due to phonon-based up-conversion and requires further investigation. The Ce^{3+} PL 'τ_{rad}' was on average ~ 3.7 ms, while rise times differed significantly between sample types ranging from 0.28 ms to 7.65 ms.
- Photoexcitation of Pr^{3+} doped glass samples revealed three PL emission bands peaking at ~ 1.700 µm, ~2.400 µm and ~4.700 µm. The PL emission bands peaking at ~2.400 µm and ~4.700 µm were found to each be comprised of more than one radiative transition overlapping in wavelength. The Pr^{3+} PL emission bands peaking at ~ 1.700 µm, and ~2.400 µm were both capable of occurring due to ESA of either pump source and/or ESA of Pr^{3+} PL. The shape and peak wavelength of the ~2.400 µm PL emission band was influenced by the pump wavelength, indicating a change in contributions of the constituent radiative transitions comprising this emission band. The ~2.400 µm emission band was found to have a ~3.6 ms lifetime, while the ~4.700 µm emission was found to have a lifetime comprised of both ~10.5 ms and ~ 3.6 ms. Pr^{3+} ESA measurements revealed prominent unobstructed latent ESA bands centred at 2.400 µm, and 3.650 µm which were attributed to the ($^3H_5 \rightarrow {}^3F_3$), and ($^3H_5 \rightarrow {}^3F_2$) transitions, respectively, along with smaller ESA bands. The monochromator-based Pr^{3+} ESA measurements revealed an ESA band peaking around 3.65 µm, this result agreed with the Pr^{3+} FTIR-based ESA measurements. Thus, confirming the validity of the FTIR-based ESA equipment configuration. Furthermore, these results showed the effects of ESA on PL intensity within a spectral region occupied by an unobstructed ESA band.

- Photoexcitation of Sm^{3+} doped samples yielded three PL emission bands centred at 2.100 µm, 2.700 µm and 3.800 µm. The Sm^{3+} PL emission band peaking at ~3.800 µm was comprised of more than one radiative transition overlapping in wavelength. Moreover, the 3.800 µm emission band exhibited several lifetimes. Sm^{3+} ESA measurements revealed several weak and very broad ESA bands that could not be easily attributed to a single transition.
- Pumping of Tb^{3+} doped samples with a 2.013 µm pump source yielded three 'Tb' cation PL emission bands peaking at 3.100 µm, 4.700 µm and 7.800 µm. Conversely, in-band pumping of a Tb^{3+} doped sample with a 4.150 µm source ostensibly resulted in a very broad Tb^{3+} PL emission spectrum between 2.700 to 6.200 µm, were emissions occurring above 4.150 µm were due to ESA of either pump source and/or ESA of Tb^{3+} PL. The Tb^{3+} PL emissions in the ~ 4.700 µm spectral region exhibited two lifetimes predominately comprised of ~ 11.5 ms and ~ 3.7 ms. Interestingly, the emissions in the ~ 3.100 µm spectral region exhibited two lifetimes which consisted of ~ 12.0 ms, and ~ 3.4 ms. It was speculated that these two lifetimes were artifacts due to ESA from the ~4.700 emission band. Tb^{3+} ESA measurements revealed three prominent unobstructed latent ESA bands centred at 3.440 µm, 4.320 µm and 7.890 µm which were attributed to the ($^7F_5 \rightarrow {}^7F_2$), ($^7F_5 \rightarrow {}^7F_3$) and ($^7F_5 \rightarrow {}^7F_4$) transitions, respectively, along with smaller ESA bands.
- Pumping Dy^{3+} doped samples yielded four 'Dy' cation PL emission bands peaking at ~2.450 µm, ~2.900 µm, and ~4.400 µm. The 2.900 µm and 4.400 µm emission bands exhibited lifetimes of ~ 4.7 ms and ~ 1.7 ms, respectively. Dy^{3+} ESA measurements revealed five prominent unobstructed latent ESA bands centred at 2.37 µm, 3.15 µm, and 5.42 µm

which were attributed to the ($^6H_{13/2}$ → $^6H_{9/2}$, $^6F_{11/2}$), ($^6H_{11/2}$ → $^6H_{7/2}$, $^6F_{9/2}$), and ($^6H_{11/2}$ → $^6H_{9/2}$, $^6F_{11/2}$) transitions, respectively. Importantly, the Dy^{3+} cation was the only dopant to unequivocally show stimulated emissions at 4.40 µm alluded to the possibility of achieving fibre lasing, like the crystal-based Dy^{3+} lasers listed in Table 2-6. Unfortunately, this ESA was overlapped by the [-Se-H] extrinsic impurity aborption.

Interestingly, the ESA bands exhibited in each RE^{3+} dopant allowed the optical attenuation of specific, relatively narrow, spectral regions within the transmission window of the RE^{3+} doped fibre to be adjusted optically. Importantly, this capability potentially enables the fabrication of an all-optical, relatively narrowband, polarization independent, VOA (*variable optical attenuator*). This capability could be very useful in optical computing or in communications systems employing wavelength-division multiplexing, allowing specific wavelengths to be manipulated, without influencing the optical loss of adjacent wavelength regions, all within in the same transmission medium.

5 Investigation of laser action in RE^{3+} doped chalcogenide glass fibres:

This chapter investigates MIR lasing in SIF (*step index fibre*) samples with RE (*rare-earth*) cation doped cores. Section 5.1 describes the methodology employed in both the preparation of chalcogenide SIF samples and assembly and alignment of the optical cavity used to evaluate SIF samples. Section 5.2 presents results obtained for the room temperature (20 - 24°C) evaluation of SIF samples with either ‘Tb’ (*terbium*) or ‘Ce’ (*cerium*) cation doped cores. Section 5.3 presents a discussion on the methodology employed in the presented work.

5.1 Methodology for sample preparation and optical cavity setup:

Setup of the equipment configuration used entailed alignment of a specially prepared SIF sample to both the pump source and the collection/detection optics, followed by the abutment of discrete mirrors to form an optical cavity. Once the mirrors were abutted there was no perceivable gap, the SIF looked as if it was a continuous fibre extending into the mirror. Figure 5-1 shows the flowchart used in cleaving, inspection, and cleaning of fibre samples along with the mounting, and thermal management of the specially prepared samples. SIF sample preparation entailed the following steps:

i. Cleaving of the fibre sample: SIF samples were cut to a desired length by cleaving both end faces at approximately 90° using a fibre cleaver.
ii. Inspection of cleaved end faces: Each cleaved end was inspected using ‘the end inspection’ equipment configuration shown in Figure 3-5 (c) to evaluate the SIF dimensions and cleave quality. Each cleave angle was evaluated using the equipment configuration shown in Figure 5-2 (a) and (b) (*designed and built by Dr David Furniss*).

iii. Cleaning of any surface debris: Fibre samples were cleaned of any surface debris, using procedure described in Appendix 7.2.4.2, to ensure mirrors could be properly abutted to the surface during optical cavity assembly.

iv. Mounting of sample onto a V-groove fibre holder: Samples were mounted onto a metal V-groove fibre holder using UV curable polymer, see Figure 5-2 (c). The SIF samples were mounted with their cleaved face slightly protruding beyond the edge of the V-groove to facilitate mirror abutment. The 90° ± ≤ 1° end face cleaves on the SIF samples prevented the V-groove fibre holder from impinging the mirrors during their abutment. Additionally, the overhang of the fibre was intentionally minimised to ensure maximum contact with the V-groove to improve heat transfer from the pump launch site.

v. Thermal management of SIF: The SIF sample was coated with the liquid metal InGaSn alloy (*Galinstan*) using a cotton swab. The liquid metal coating allowed excellent thermal conductivity (~$16.5\ W{\cdot}m^{-1}{\cdot}K^{-1}$ [196]) between the SIF sample and the metal V-groove fibre holder which acted as a heat sink. The InGaSn alloy was applied as close as possible to the 'laser launch end' to maximise heat transfer during photoexcitation see Figure 5-2 (c). Additionally, a gentle jet of dry air was directed at the cleaved end face of the laser launch end for additional forced convection cooling.

vi. Cladding mode stripping: The high refractive index of the liquid metal coating (*greater than 2.6*) caused the SIF cladding to be anti-guiding by inhibiting TIR (*total internal reflection*), within the cladding, along the region where it was applied. This ensured that light transmitted through the SIF predominately propagated within the core of the SIF, while light in the cladding was attenuated, thus aiding in the optical alignment.

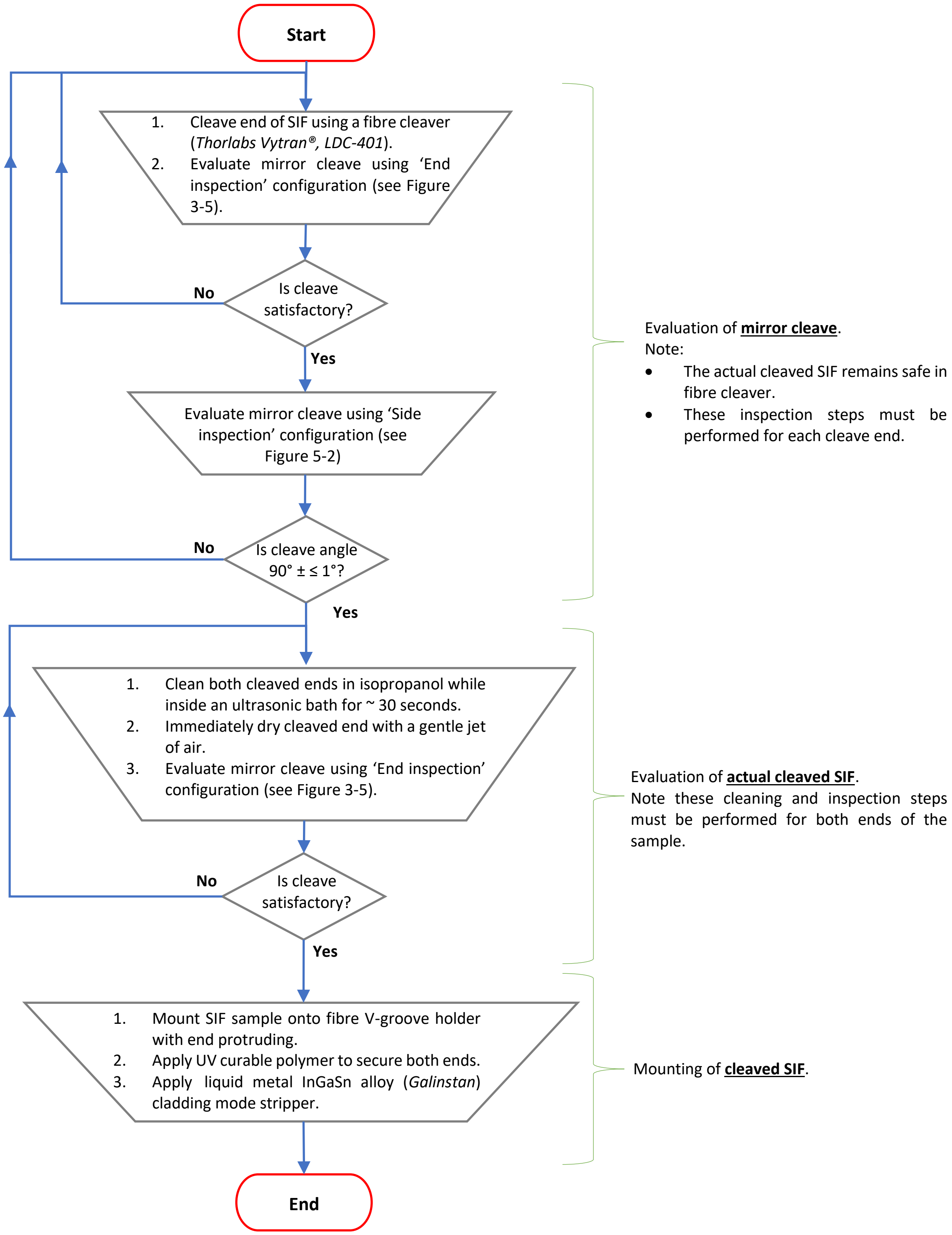

Evaluation of **mirror cleave**.
Note:

- The actual cleaved SIF remains safe in fibre cleaver.
- These inspection steps must be performed for each cleave end.

Evaluation of **actual cleaved SIF**.
Note these cleaning and inspection steps must be performed for both ends of the sample.

Mounting of **cleaved SIF**.

Figure 5-1: Process flow chart for SIF sample preparation.

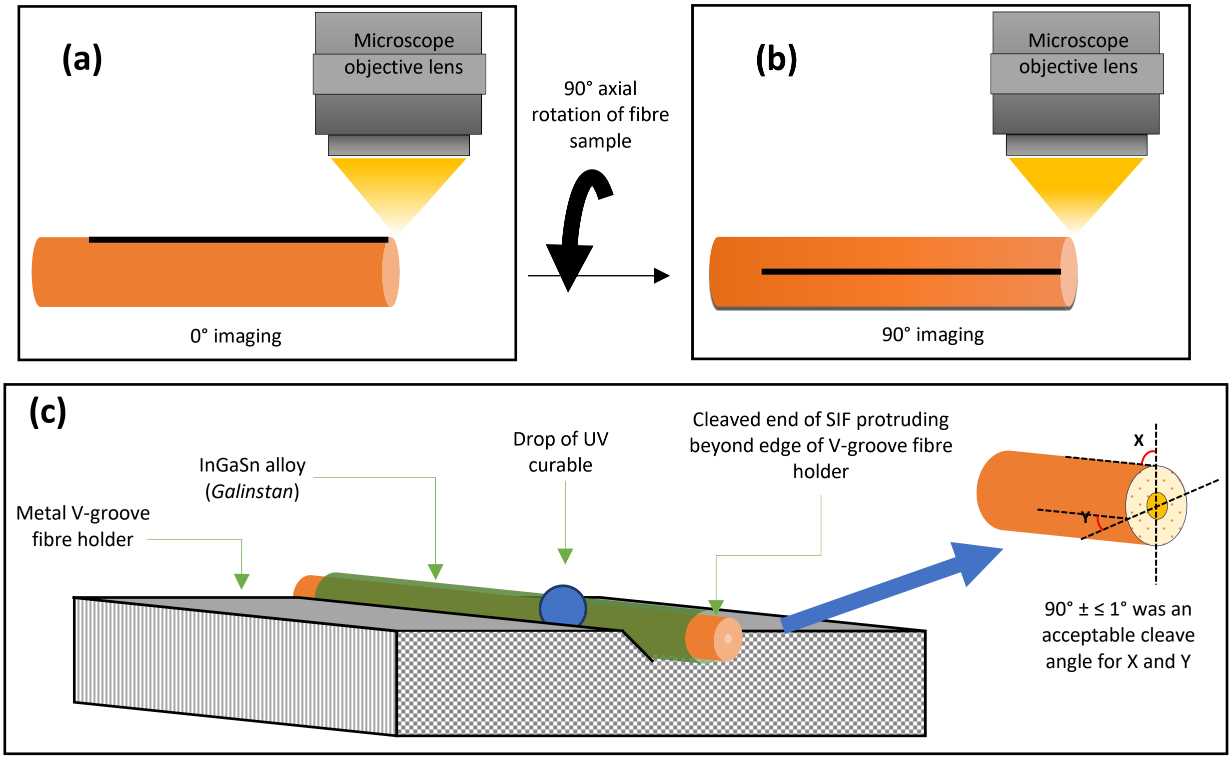

Figure 5-2: Showing: ***(a)*** *&* ***(b)*** *Illustration of measurement procedure for cleave angle (Note, entire imaging equipment configuration shown in Figure 3-5) along with* ***(c)*** *illustration of mounted, prepared SIF sample.*

5.2 Evaluation of MIR lasing in rare-earth ion doped chalcogenide glass fibres:

The dopants ‘Tb’ and ‘Ce’ were each evaluated for their room temperature (*20 -24°C*) MIR lasing potential. In Section 5.2.1, the SIF F105REJN, with its Tb^{3+} doped core, (see Section 3.2.1.2) was evaluated using a 2.825 µm pump source. In Section 5.2.2, the SIF F130RERC, with its Ce^{3+} doped core, (see Section 3.2.2.2) was evaluated using in-band pumping with a 4.150 µm pump source. Notably, MIR lasing at wavelengths greater than 5 µm, due to the $^2F_{7/2} \rightarrow {}^2F_{5/2}$ radiative transition, was demonstrated during this evaluation.

5.2.1 Optical cavity containing Tb^{3+} doped SIF:

The lasing potential of a SIF F105REJN with a nominally 500 ppmw ‘Tb’ cation doped core, and a calculated NA of ~ 0.21, was evaluated in collaboration with Dr Fred Maes and Dr Martin Bernier of the University of Laval, Canada. The impetus for this collaboration was due to the numerical modelling presented in [181] which alluded to the feasibility of MIR lasing, along with the availability of the custom made 2.825 µm pump source provided by the collaborators from the University of Laval. Due to time limitations and technical challenges MIR lasing was not achieved during this collaboration, however several important learnings were uncovered, and subsequently applied to the Ce MIR lasing in Section 5.2.2.

A ‘butt-coupled’ and a ‘backward-pumping’ equipment configuration were both tested. The ‘butt-coupled’ configuration was used to investigate the power dependency of Tb^{3+} PL emissions from a SIF sample. The ‘backward-pumping’ configuration was used to investigate the potential for lasing within a partial optical cavity. In both equipment configurations a 2.825 µm pump laser was selected to engage the Tb^{3+} $^7F_6 \rightarrow {}^7F_4$ ground state absorption.

A ‘butt-coupled’ equipment configuration, shown in Figure 5-3 (a), was used to excite a SIF sample with a Tb^{3+} doped core using a 2.825 µm fibre laser, item 1 in Figure 5-3. In this configuration a beam from the 2.825 µm laser was focused into the launch end of an undoped fluoride fibre, item 7 in Figure 5-3. The opposite end of this fibre was abutted to a SIF sample, item 9 in Figure 5-3. The resulting Tb^{3+} PL emissions from the core of the SIF were collected from the opposite end of the fibre and evaluated. The results of using this equipment configuration are presented in Section 5.2.1.1. Note, the ‘laser launch end’ of the undoped fluoride fibre, item 7 was observed to deteriorate over a few days, possibly due to its hygroscopic properties.

(a) **Butt-coupled equipment configuration**

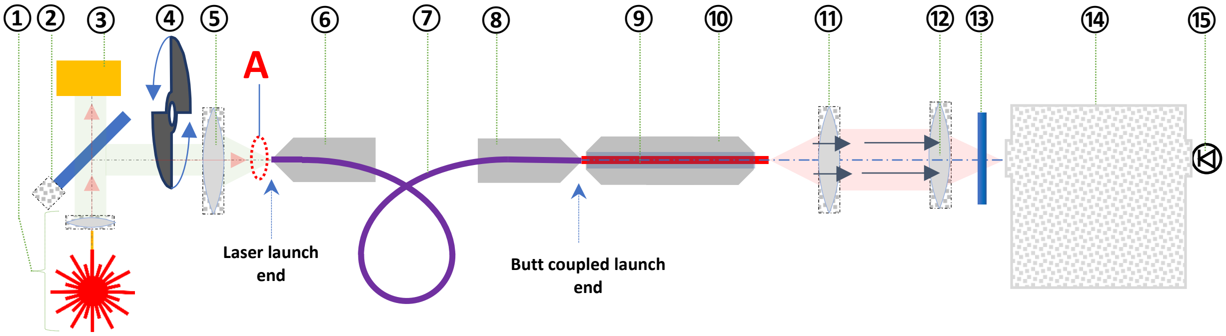

(b) **Backward pumping equipment configuration**

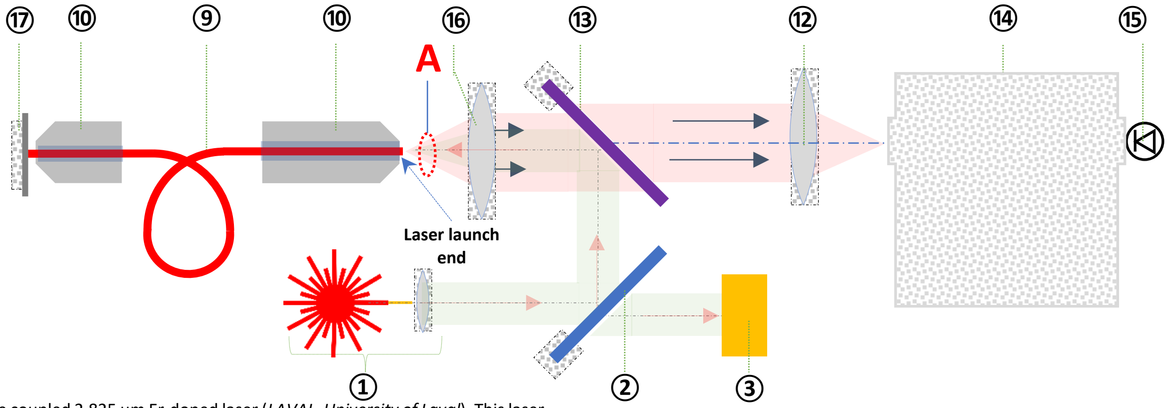

1. Fibre coupled 2.825 µm Er-doped laser (*LAVAL, University of Laval*). This laser was electronically modulated while using the 'backward pumping configuration'.
2. CaF$_2$ 50/50 beam splitter (*Thorlabs, BSW520*) mounted in kinematic mount.
3. Thermal power meter *(Molectron, PM3*).
4. Optional mechanical chopper (*Scitec Instruments*) amplitude modulating the Er fibre laser at frequency of 74 Hz.
5. Bi-convex CaF$_2$ lens, f = 15 mm (*Thorlabs, LB5766-E*) on pan/tilt XYZ translational stage.
6. Copper V-groove fibre holder was used to hold a fluoride fibre at the laser launch end.
7. Fluoride fibre 15 µm core 250 µm OD, NA = 0.12, and ~2.5 m long, with both ends cleaved at ~90° and attached to the V- groove fibre holders at both ends using UV curable, high index, polymer.
8. Stainless steel V-groove fibre holder used to mount fluoride fibre, with cleaved end face protruding, approximately 1 diameter to facilitate 'butt-coupling' launch end.
9. SIF F105REJN sample, with both ends cleaved at ~90° and attached to V-groove fibre holder(s) at both ends using UV curable polymer and coated in of Galinstan (*InGaSn alloy*) for cladding mode-stripping and thermal management.
10. Stainless steel V-groove fibre holder used to mount SIF F105REJN with cleaved launch end face protruding, approximately one fibre diameter to facilitate 'butt-coupling'.
11. Plano convex CaF$_2$ lens, f = 20 mm (*Thorlabs, LA5315*) mounted on XYZ stage.
12. Plano convex CaF$_2$ lens, f = 40 mm (*Thorlabs, LA5370*) mounted on precision XYZ stage.

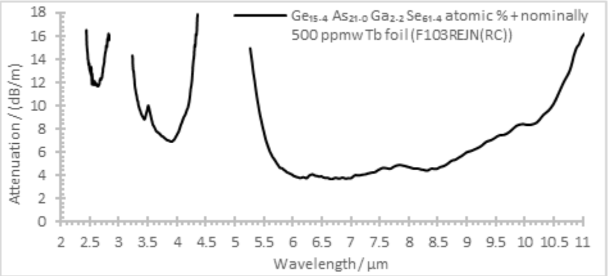

13. 3.981 µm long wave pass filter (*NOC, SLWP-3981-000145*) on kinematic mount.
14. Monochromator (*Spex Minimate equipped with diffraction grating blazed at 6.000 µm*) with 0.25 mm entrance and exit slits, supplied with dry, purged atmosphere (*H$_2$O & CO$_2$ removed*).
15. MCT (*mercury cadmium telluride*) detector (*Vigo Systems, PVI-4TE-6*).
16. Plano convex CaF$_2$ lens f = 50 mm (*Thorlabs, LA5763*) on pan/tilt precision XYZ translational stage (*Newport, 561D*).
17. Interchangeable item:
    a. Gold mirror (*Thorlabs, ME1-M01*) mounted in kinematic mount atop a precision XYZ stage (*Melles Griot*).
    b. Thermal power meter (*Thorlabs, C-Series S302C*).

Note, quoted launch power estimated at position '**A**'

Figure 5-3: Showing equipment configurations used to evaluate SIF F105REJN samples with Tb doped cores and excited with a 2.825 µm pump source: ***(a)*** *'Butt-coupled' equipment configuration and* ***(b)*** *'Backward-pumping' configuration with inset of F103REJN(RC) attenuation spectrum (note this is core of F105REJN sample). Note, the control/data acquisition configuration used for both the 'butt-coupled' and 'backward pumping' configurations is described in Section 7.2.4.4.*

A ’backward-pumping’ equipment configuration, shown in Figure 5-3 (b), was used to excite a SIF sample with a Tb^{3+} doped core as the gain medium while in a partial optical cavity. Note, this configuration was described as a ‘partial optical cavity’ due to the mirrors used namely, a gold mirror (*item 17(a) in Figure 5-3, 95.8 % reflective at 5 µm*) and the Fresnel reflection at the ‘laser launch end’ (~*19 % reflective at 5 µm*). In this configuration a 3.981 µm LWP filter acting as a long pass dichroic mirror, item 18 in Figure 5-3, was used to reflect the 2.825 µm beam towards the SIF sample while nominally allowing emissions in the spectral region greater than 4.0 µm emanating from the SIF to be transmitted towards the detection system. The beam from the 2.825 µm laser was focused into the SIF sample, item 9 in Figure 5-3. The opposite end of this SIF was either abutted to a gold mirror or directed into a thermal power meter to measure the pump power transmitted through the SIF. The resulting Tb^{3+} PL emissions emanating from the core of the SIF at the ‘laser launch end’ were transmitted through the dichroic mirror and collected and evaluated. The results of using this equipment configuration are presented in Section 5.2.1.2 and discussed in Section 5.3.

5.2.1.1 SIF F105REJN evaluation with ‘butt-coupled’ equipment configuration:

Figure 5-4 shows the Tb^{3+} PL emission spectra for a SIF F105REJN sample with a core diameter of approximately 30 µm, 130 mm long, using the ‘butt-coupled’ equipment configuration, shown in Figure 5-3 (a). The Tb^{3+} PL emission band spanned the 4.00 to 6.00 µm spectral region and was predominately attributed to the $^7F_5 \rightarrow {}^7F_6$ radiative transition. Importantly, the intensity of Tb^{3+} PL emissions centred around 4.85 µm was sublinear at higher pump power, with the onset of saturation of Tb^{3+} PL emissions above 400 mW RMS power, as shown on the inset in Figure 5-4.

This sublinear relationship implied saturation of the entire 130 mm long sample and possible population inversion between the $^7F_5$ manifold and the $^7F_6$ ground state. Note, the ostensible ability to saturate the Tb^{3+} PL emission without incurring damage to the sample was the impetus to evaluate an SIF sample inside a partial optical cavity which is expanded on in the next Section.

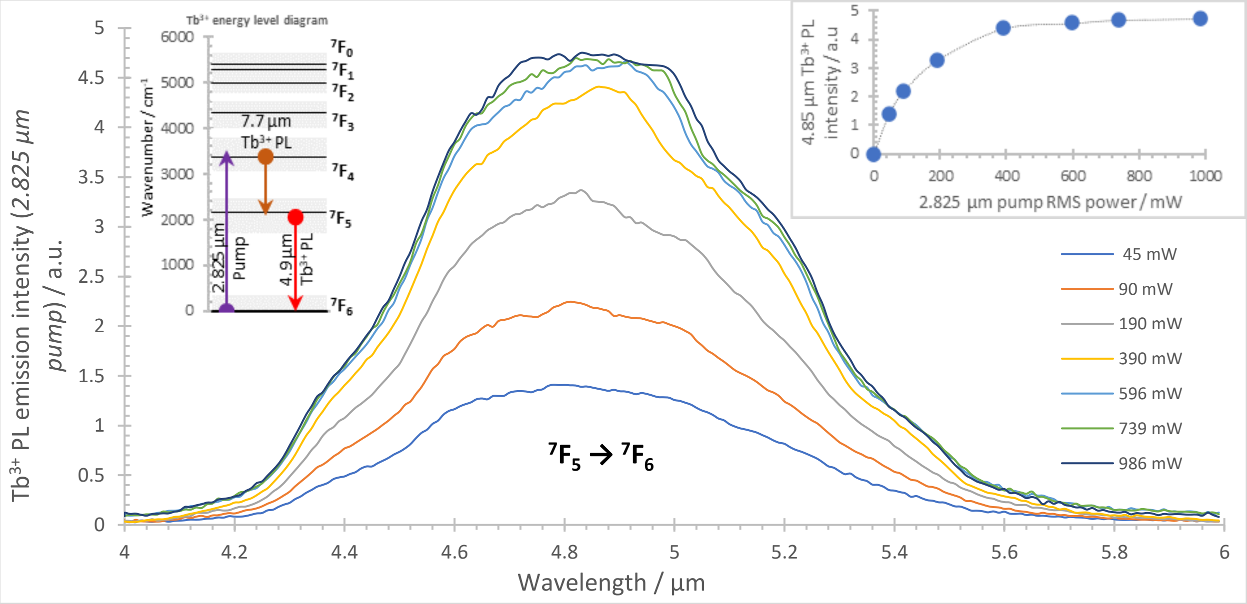

Figure 5-4: PL emission spectra from SIF F105REJN sample with a nominally 500 ppmw Tb (foil) doped core ~ 30 µm core diameter and 130 mm long excited with 2.825 µm pump source using the 'butt-coupled' equipment configuration shown in Figure 5-3 (a), along with inset showing sub-linear Tb^{3+} PL emission intensity at 4.85 µm with increasing pump power. Note, RMS power of 2.825 µm pump source listed in legend and presented spectra have not been corrected for system spectral response.

5.2.1.2 SIF F105REJN evaluation with 'backward pumping' equipment configuration:

Figure 5-5 shows the normalised Tb^{3+} PL emission spectra for a SIF F105REJN sample with a core diameter of approximately 25 µm, 380 mm long, using the 'backward-pumping' equipment configuration, shown in Figure 5-3(b). Note, the Tb^{3+} PL emission spectra were each measured with the gold mirror, item 17(a) in Figure 5-3, abutted to the SIF sample to form a partial optical cavity. The Tb^{3+} PL emission band spanned the 4.00 to 5.80 µm spectral region and was predominantly attributed to the $^7F_5 \rightarrow {}^7F_6$ radiative transition. Notably, the peak PL emission gradually shifted to longer wavelengths with increasing pump power. The features observed within the 4.60 to 5.20 µm spectral region in Figure 5-5 were unexpected, especially when considering the shape of the Tb^{3+} PL emission spectra previously shown in Figure 5-4, thus it was postulated to be due to an absorption band. The strength of this absorption band increased with the 2.825 µm pump power, thus was likely a result of ESA. Note, the spectral feature around 5.62 µm was attributed to the 2nd order diffraction of the 2.825 µm pump laser. This was present due to a portion of the 2.825 µm pump light being reflected off the SIF sample and into the collection optics and detection system.

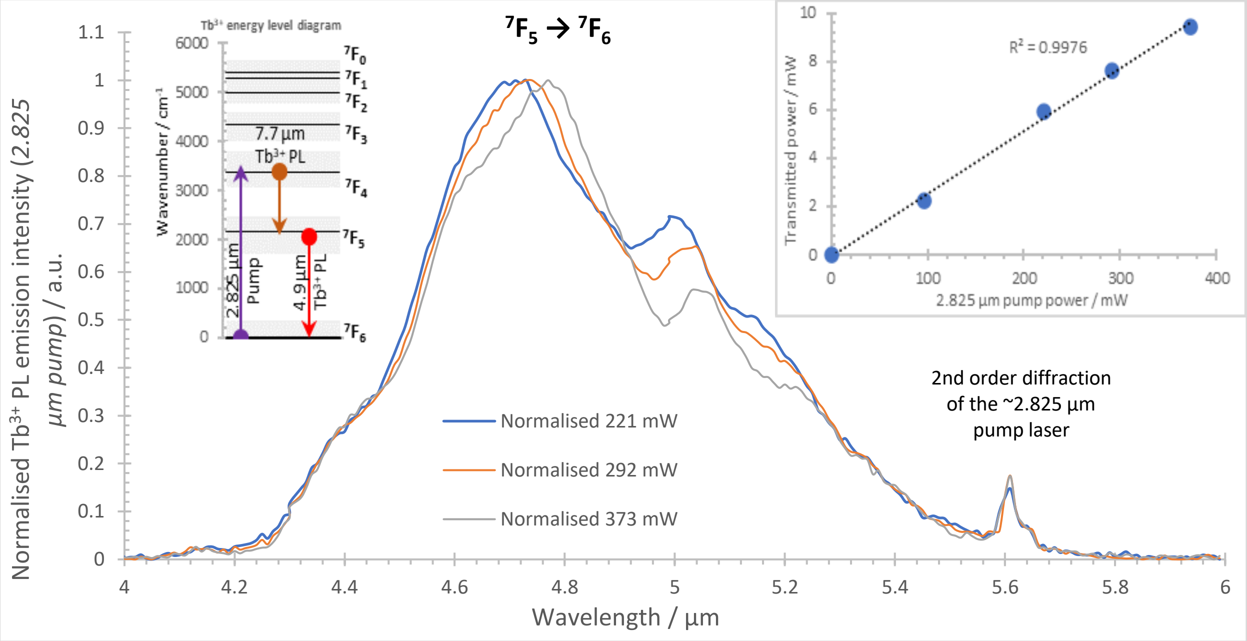

Figure 5-5: Normalised PL emission spectra from SIF F105REJN sample with a nominally 500 ppmw Tb (foil) doped core ~ 25 µm core diameter and 380 mm long excited with 2.825 µm pump source using the 'backward-pumping' equipment configuration shown in Figure 5-3(b) (gold mirror abutted), with inset showing launch pump power vs transmitted power at opposite end of SIF sample measured with thermal power meter. Note, the presented spectra were normalised to their peak emission wavelength to highlight the shift in the peak emission to longer wavelengths with increasing pump power. Additionally, RMS power of 2.825 µm pump source listed in legend and presented spectra have not been corrected for system spectral response.

The inset in Figure 5-5 shows the pump launch power versus the transmitted power at the far end of the SIF F105REJN sample. Note, the transmitted power was measured with the thermal power meter, item 17(b) in Figure 5-3. The relationship between the pump launch power versus the transmitted power was linear up to 373 mW RMS pump power. Regrettably, this SIF F105REJN was permanently damaged at an RMS launch power of ~ 421 mW, which caused a significant decrease in Tb^{3+} PL emission intensity, however there was no visible damage at the laser launch end, indicating possible internal damage further along the SIF. Note, SEM images of the 'laser launch end' of this 'damaged' SIF sample are presented in Chapter 3 in Figure 3-9 (d). Notably, the linear relationship between the pump launch power and the transmitted power indicated that, without the gold mirror abutted, the 380 mm long sample was not entirely saturated for the pump powers tested.

The Tb^{3+} PL emission spectra presented in Figure 5-5 differed from those presented in Figure 5-4 due to the differences in the dimensions of both samples, the equipment configurations used, and the system spectral response of each equipment configuration (see Figure 5-3).

Considering the pump powers employed in Figure 5-5 and the results from the 'butt-coupling' equipment configuration, the portion of the SIF sample closest to the 'laser launch end' was most likely saturated, while the far end of the sample was unsaturated. Thus, to account for the apparent absorption band between 4.60 to 5.20 µm, shown in Figure 5-5, and its variability with pump power, it was postulated that the saturated regions of the SIF afforded ESA of Tb^{3+} PL, especially from the unsaturated regions where the PL was reflected due to the partial optical cavity. In hindsight ESA evaluation of Tb^{3+}-doped samples with a 2.8 µm pump source to exploit the $^7F_6 \rightarrow {}^7F_4$ GSA while using the equipment configuration described in Section 4.1.2.1 could verify the nature of this absorption. Considering the presented Tb^{3+} energy level diagram, illustrated in Figure 5-6, the proposed ESA was most likely due to optical absorption between:

- The $^7F_5 \rightarrow {}^7F_3$ transition centred around 4.63 µm (~*2159 cm^{-1}*). The long ~11.5 ms radiative lifetime of the $^7F_5$ manifold (see Section 4.2.4.3.b) potentially enabled excited electrons to undergo optical absorption with Tb^{3+} PL, to be further excited to the $^7F_3$ manifold.
- The $^7F_4 \rightarrow ({}^7F_0, {}^7F_1)$ transition centred around 5.00 µm (~*2000 cm^{-1}*). Despite the short ~35 µs lifetime of the $^7F_4$ manifold (see Section 4.2.4.3.b), it was postulated that the 2.825 µm pump wavelength enabled an electron population in the $^7F_4$ manifold which could then undergo optical absorption with Tb^{3+} PL, to be further excited to the ($^7F_0$ $^7F_1$) manifolds.

Note, both proposed ESA transitions would potentially manifest themselves as NIR PL emissions from the uppermost energy levels. NIR PL measurements were not carried out to detect these wavelengths due to the specifications of the dichroic mirror, item 18 in Figure 5-3, used in the presented equipment configuration.

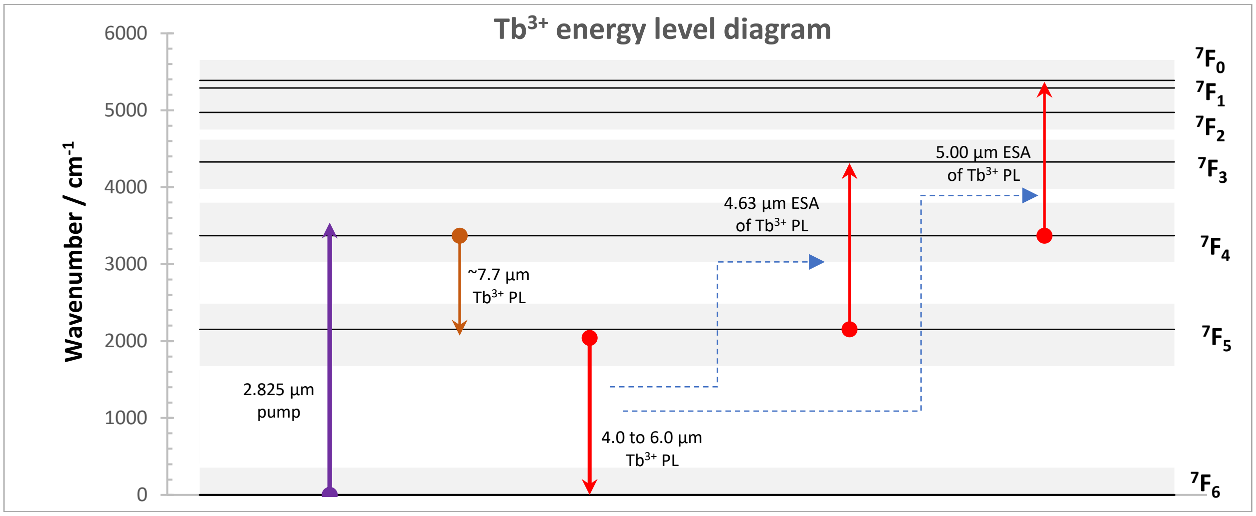

Figure 5-6: Illustration of Tb^{3+} energy level diagram showing two proposed ESA transitions with 2.825 µm pump source to account for spectral features observed in Figure 5-5. Note, arrows are too scale.

5.2.2 Optical cavity containing Ce^{3+} doped SIF:

Trivalent Ytterbium (Yb^{3+}) has an electronic configuration consisting of a $^2F_{7/2}$ ground state and a single $^2F_{5/2}$ excited state. Owing to the similarities between the two-level electronic configurations of both trivalent Ce^{3+}, and Yb^{3+} it was postulated that the Ce^{3+} cation could be used as the gain medium for a MIR laser analogous to the Yb^{3+} dopant used in yttrium aluminium garnet NIR lasers. These Yb^{3+} lasers utilised 'in-band pumping' between the $^2F_{7/2}$ and $^2F_{5/2}$ manifolds to form a quasi-three-level laser system, relying on non-radiative transitions between the Stark splitting within both the ground state and excited state [73,197]. Thus, Yb^{3+} NIR lasers were the impetus to evaluate the MIR lasing potential of the SIF with a nominally 500 ppmw 'Ce' cation doped core, with a calculated NA of ~0.48, using in-band pumping with a 4.150 µm source. Figure 5-7 shows the 'backward-pumping' equipment configuration used to investigate room temperature MIR lasing in SIF F130RERC samples.

The optical cavity used comprised the 'Ce' cation doped gain medium, item 2 in Figure 5-7, with a mirror butt-coupled to each end. A short wave-pass filter (*item 4 in Figure 5-7, acting as a dichroic mirror 87 % reflective at 5.100 µm*) was abutted at the 'laser launch end' and a gold mirror (*item 1 in Figure 5-7*, *95.8 % reflective at 5.10 µm*) was abutted at the opposite end. The 4.150 µm QCL beam was partially reflected off an LWP (*long wave-pass*) filter, item 6 in Figure 5-7, and focused into the 'laser launch end' of the SIF sample through the dichroic mirror (*item 4 in Figure 5-7, 74 % transparent at 4.150 µm*). The resulting optical cavity emissions emanating from the 'laser launch end' were transmitted through the dichroic mirror, item 6 in Figure 5-7, and collected and evaluated.

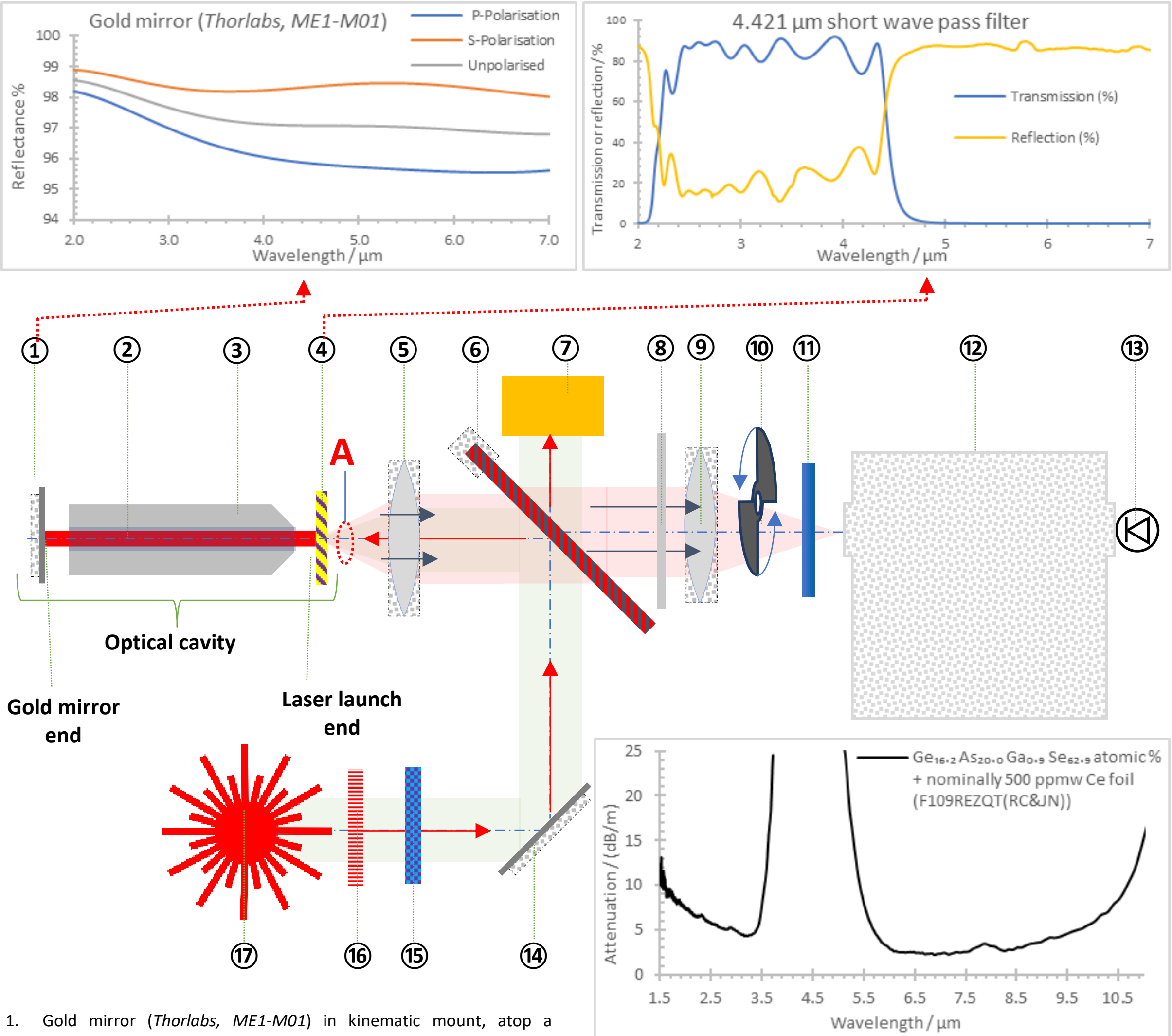

1. Gold mirror (*Thorlabs, ME1-M01*) in kinematic mount, atop a precision XYZ translational stage (*Melles Griot*).
2. SIF F130RERC sample, coated in of Galinstan (*InGaSn alloy*) for cladding mode-stripping and thermal management, a low flow rate of FTIR purge gas was used to actively cool the laser launch end.
3. Stainless steel V-groove fibre holder on XYZ translational stage.
4. 4.421 µm short wave pass filter (*NOC, SWP-17220-1-1-17*) in kinematic mount, atop a precision XYZ translational stage (*Melles Griot*).
5. Bi-convex CaF_2 lens, f = 15 mm (*Thorlabs, LB5766-E*) on pan/tilt, precision XYZ translational stage (*Newport, 561D)*.
6. 4.203 µm LWP (*long wave pass*) filter (*NOC, SLWP-4203-001138*) acting as a dichroic mirror, on kinematic mount.
7. Thermal power meter (*Thorlabs, C-Series S302C*).
8. Optional neutral density filter (*Thorlabs, NDIR10B*).
9. CaF_2 lens, f = 50 mm (*Thorlabs, LA5763*) on pan/tilt, precision XYZ translational stage (*Newport, 561D*).
10. Optional mechanical chopper (*Bentham, S200_218_H*) modulating input to monochromator at **418** Hz. Note this only used for emission spectrum measurements.
11. 4.630 µm LWP filter (*NOC, SLWP-4630-000434*) optical filter:
12. Monochromator (*Spex Minimate equipped with diffraction grating blazed at 6.000 µm*) with **0.25 mm** entrance and exit slits, supplied with dry, purged atmosphere (*reduced H_2O & CO_2 concentration*).
13. MCT (*mercury cadmium telluride*) detector (*Vigo Systems, PVI-4TE-6*).
14. Gold mirror (*Thorlabs, ME1-M01*) on kinematic mount.
15. ¼ wave plate (*Thorlabs, WPLQ05M-4000*) in rotational mount.
16. Polariser (*Thorlabs, LPMIR050-MP2*) in rotational mount.
17. Open beam 4.15 µm QCL (*Pranalytica, 1101-42-CW-2500LH*) either CW mode or electronically modulated.

Note, quoted launch power estimated at position '**A**'.

Figure 5-7: 'Backward-pumping' equipment configuration used to evaluate Ce-doped SIF F130RERC samples with a Ce-doped core and excited with a 4.15 µm QCL, with two insets showing specification of optical cavity mirrors and attenuation of F109REZQT(RC&JN) (this is the core of SIF 130RERC). Note, the control/data acquisition configuration used with the equipment configuration is described in Section 7.2.4.4.

A small portion of the 4.150 µm pump power was transmitted through the LWP filter, item 6 in Figure 5-7, into a thermal power meter, item 7 in Figure 5-7, which was used to monitor the 4.15 µm launch power during operation. A 4.630 µm LWP filter, item 11 in Figure 5-7, was positioned at the entrance of the monochromator to block any 4.150 µm pump light reflected off the SIF sample, and transmitted through the dichroic mirror, item 6 in Figure 5-7, towards the collection optics and detection system.

The dichroic mirror used at the 'laser launch end', (*item 4 in Figure 5-7*) had low transparency, ~0.24 % at ~5.1 µm, as shown in the inset in Figure 5-7. As a result, once the optical cavity was assembled, this dichroic mirror significantly attenuated all transmitted emissions with wavelengths greater than ~4.4 µm, inclusive of laser emissions and Ce^{3+} PL. Thus, resulting in the distinct flat baseline of the emission spectra with conspicuous peaks present at lasing wavelengths presented in the following Sections. Additionally, the resolution of the detection system was determined to be approximately 0.015 µm at a wavelength of 4.150 µm. This characterisation was achieved by evaluating the 4.150 µm QCL output spectrum using the monochromator and detector, items 12 and 13 in Figure 5-7, and comparing that result against the manufacture supplied specifications for the QCL. Note, this 'backward-pumping' equipment configuration is further discussed in Section 5.3.

MIR lasing was observed in four separate SIF F130RERC samples using the equipment configuration shown in Figure 5-7. Table 5-1 lists the specifications for each SIF F130RERC sample, prepared using the procedure described in Section 7.2.4.2.

Table 5-1: Physical dimensions for SIF F130RERC samples that exhibited lasing action:

Parameter	Sample #3	Sample #4	Sample #8	Sample #11
Cladding diameter	245 ± 3.2 µm	247± 4.7 µm	191.5 ± 5.8 µm	235 ± 2 µm
Core diameter	14 µm	13 µm	~ 9 µm	15.3 µm
Sample length	5.5 cm	4.77 cm	6.4 cm	~ 6.4 cm
Cleave angles for cleave for gold mirror end.	90.0° 89.3°	90.3° 89.3°	89.9° 89.6°	89.0° 90.8°
Cleave angles for cleave for laser launch end.	89.9° 89.7°	90.6° 89.0°	89.8° 89.6°	89.1° 90.0°

5.2.2.1 SIF F130RERC samples #3 & #4 evaluation with 'backward pumping' configuration:

Evaluation of SIF F130RERC sample #3 (see Table 5-1) exhibited intermittent lasing action at wavelengths around 4.9 µm and 5.1 µm. The optical cavity output intensity fluctuated significantly for a few minutes before completely stopping on its own.

Evaluation of SIF F130RERC sample #4 (see Table 5-1) generated intermittent lasing action at wavelengths around 4.89 µm and 5.12 µm. The optical cavity output intensity fluctuated for about 5 to 10 minutes before completely stopping on its own. Attempts to restart lasing after repositioning of the 4.421 SWP filter, item 4 in Figure 5-7, were unsuccessful.

Note, that the equipment configuration, and methodology were still undergoing refinement during measurements with sample #3 and #4. Thus, improper mirror abutment and misalignment of the pump laser to the SIF core likely contributed towards the intermittent lasing observed.

5.2.2.2 SIF F130RERC sample #8 evaluation with ‘backward pumping’ equipment configuration:

The evaluation of SIF F130RERC sample #8 (see Table 5-1) yielded a stable CW output from the optical cavity, with emission peaks centred around 5.135 µm ‘Peak A’, 5.175 µm ‘Peak B’, and 5.28 µm ‘Peak C’, as shown in Figure 5-8 (a).

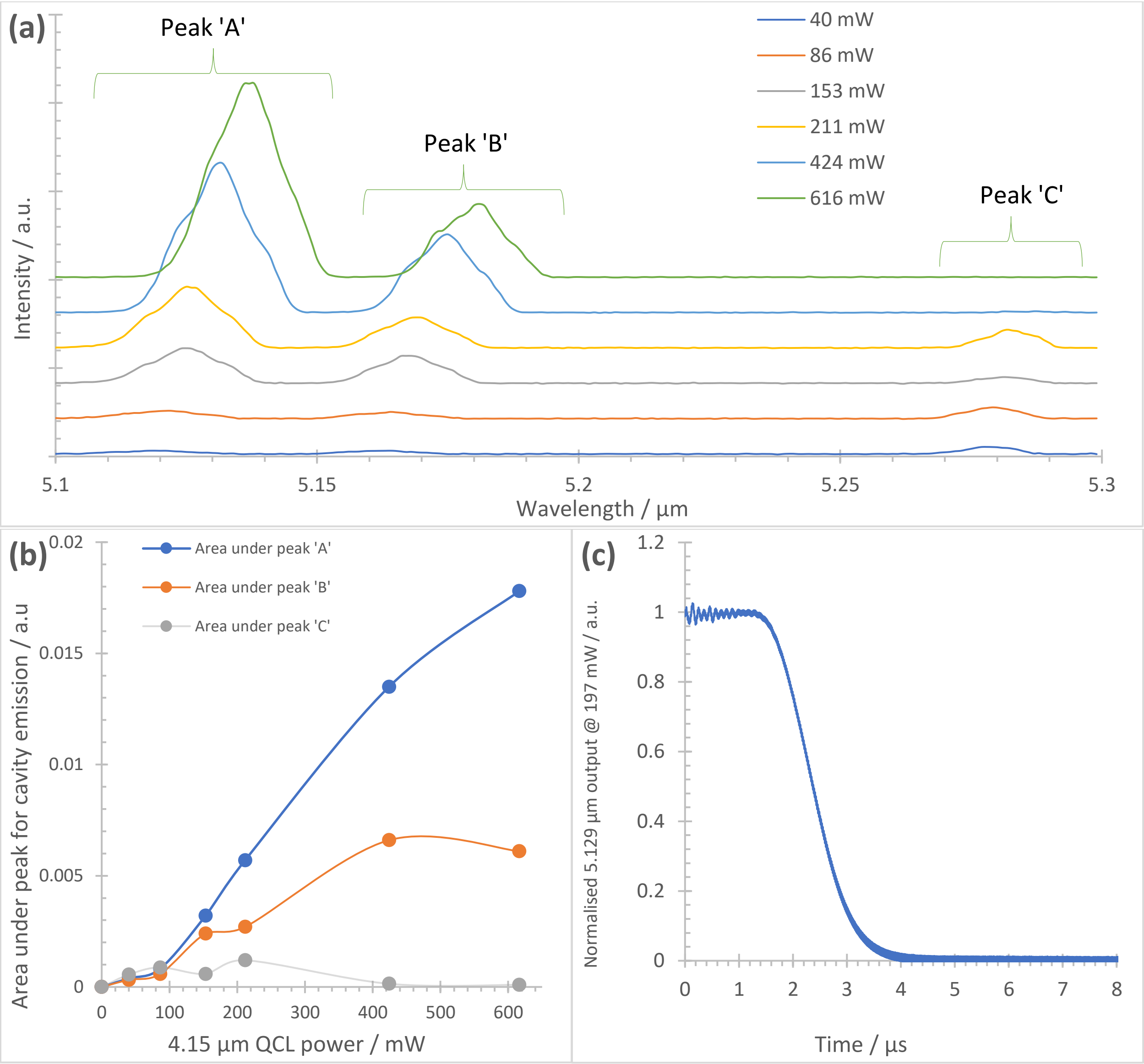

*Figure 5-8: Optical cavity emission measurements for SIF F130RERC sample #8 with a nominally 500 ppmw Ce doped core (see Table 5-1) showing **(a)** intensity (a.u.) vs wavelength (µm) for optical cavity output **Note**, each plot has been intentionally offset on the vertical axis to better show the shift in peak emission wavelength at different pump powers and continuous wave QCL power quoted in legend, **(b)** areas under emission bands seen in Figure (a) vs. 4.150 µm QCL power (mW) **(c)** Switch off time for 5.129 µm emission intensity vs. time (µs) with 4.15 µm QCL at 197 mW RMS launch power.*

The three peaks, shown in Figure 5-8 (a), indicated the presence of at least three modes within the cavity during operation. Notably, each peak gradually shifted to longer wavelengths with increasing 4.15 µm QCL power, this was possibly due to microscopic changes in the dimensions of the optical cavity with changes in QCL power. Due to the spectral resolution of the equipment configuration (*~0.015 µm*) the true shape of these emission peaks likely differed in fine detail from those presented. The output power of the optical cavity was too low to measure with the available thermal power meter, preventing a traditional laser characteristic, (*pump power versus laser output power*) from being evaluated. To address this omission the total area under each emission peak was integrated and plotted against the pump power, as shown in Figure 5-8 (b). Both 'Peak A' and 'Peaks B' exhibited a 'threshold' like feature at ~86 mW pump power, followed by a near linear region with increasing pump power up to 616 mW for peak A. Conversely, both 'Peak B' and 'Peak C' exhibited sublinear behaviour with increasing pump power and notably 'Peak C' completely disappeared at pump powers above 211 mW. The laser launch end of the SIF F130RERC sample #8 was permanently damaged at a launch power of ~ 830 mW, which caused all laser output from the optical cavity to cease. The cavity output was capable of being switched off and on and modulated via the 4.15 µm QCL source. The fall time of the optical cavity was measured at 2.5 µs at 5.129 µm (peak A), as shown in Figure 5-8 (c).

5.2.2.3 F130RERC sample #11 evaluation with 'backward pumping' equipment configuration:

The evaluation of SIF F130RERC sample #11 (see Table 5-1) yielded a stable CW output from the optical cavity roughly centred around 5.1 µm, comprised of a complex series of peaks, as shown in Figure 5-9 (a). Cavity emissions, shown in Figure 5-9 (a), exhibited multiple peaks, especially at higher QCL power, which indicated multimode operation of the cavity. Additionally, the cavity emissions gradually shifted to shorter wavelengths with pump powers greater than 202 mW. Notably, this complex optical cavity emission spectrum measured resembled that found in [130].

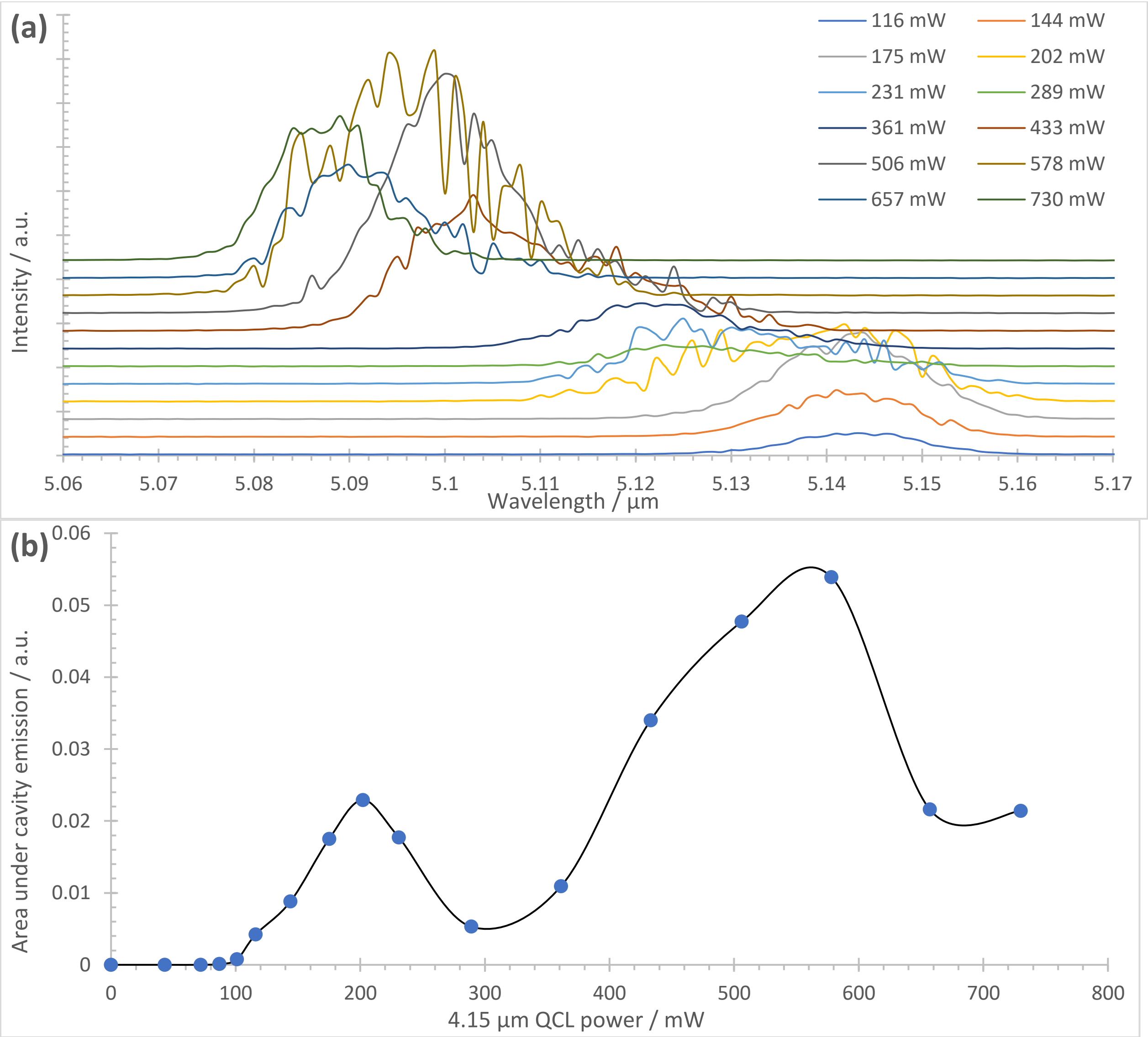

*Figure 5-9: Optical cavity emission measurements for SIF F130RERC sample #11 with a nominally 500 ppmw (see Table 5-1) showing **(a)** Intensity (a.u.) vs wavelength (µm) for optical cavity output **Note**, each plot has been intentionally offset on the vertical axis to better show the shift in peak emission wavelength at different pump powers, and **(b)** area under emission band seen in Figure (a) vs. 4.150 µm QCL power (mW). Note, continuous wave QCL power quoted in legend.*

The output power of the optical cavity was too low to measure with the available thermal power meter, preventing a traditional laser characteristic from being evaluated. Thus, the total area under the cavity emission spectrum was integrated and plotted against the pump power, as shown in Figure 5-9 (b). Notably, a 'threshold' like feature was present at 100 mW pump power, followed by a near linear region with increasing pump power up to 202 mW. This near linear dependence ceased at pump powers above 202 mW, interestingly this coincided with the start in gradual shift to shorter wavelengths for the emission spectrum, shown in Figure 5-9 (a).

5.3 Discussion of methodology and results:

The results presented in Sections 5.2.1 and 5.2.2 highlight the challenges of achieving MIR lasing using chalcogenide SIF samples with RE^{3+} doped cores. Internal defects (holes, and striae) were the most problematic issue encountered during laser experiments, Sections 3.2.1.2 and 3.2.2.2, show some of the defects. Regrettably, this issue limited the maximum usable lengths of SIF samples and made iterating experiments to optimise the ideal sample dimensions and optical cavity configuration difficult. Importantly, the desire to avoid or eliminate these internal defects was the impetus for the following work:

- Development of a non-destructive imaging presented in Section 3.1.2.2 to screen samples for internal defects.
- Co-extrusion of the core and cladding, presented in Section 3.2.6.2 to minimise defects at the core cladding interface.

The backward pumping configuration, shown in both Figure 5-3 (b) and Figure 5-7, was an ad hoc design implemented to capitalise on the available optical components. This equipment configuration conveniently allowed a generic, low cost, gold mirror to be used as part of the optical cavity. Thus, affording for the assembly of a partial optical cavity (shown in Figure 5-39 (b)), when only using the discrete gold mirror, or a full optical cavity (shown in Figure 5-7), when using both the discrete gold mirror and a dichroic mirror. The 'backward pumping' configuration exhibited several short comings due to component choices and equipment configuration layout:

- Optimising the alignment of the 'laser launch end' of the SIF to both the pump laser and the collection optics was difficult and time consuming. The dichroic mirror, item 4 in Figure 5-7, once aligned, provided feedback into the optical cavity. Unfortunately, it was cumbersome and difficult to align, often detrimentally influencing the injection of the pump laser.
- The dichroic mirror used to reflect the pump laser towards the 'laser launch' end of the SIF sample, item 18 in Figure 5-3, and item 6 in Figure 5-7, limited the detectable spectral range of the measurements, while influencing the spectral response of the collection optics.
- A portion of the pump laser light reflected from the SIF sample was invariably directed towards the detection system, as shown with the presence of the harmonics of the 2.825 µm pump laser in Figure 5-5. Thus, necessitating additional optical filtering in the collection optics.
- The detection system lacked the spectral resolution to accurately evaluate the optical cavity emissions.

- The poor transparency of the dichroic mirror, item 4 in Figure 5-7, used to construct the optical cavity was detrimental to the output performance of the laser.

5.3.1 SIF with Tb^{3+} doped core discussion:

The results presented in Section 5.2.1 allude to the challenges of achieving MIR lasing due to the $^7F_5 \rightarrow {}^7F_6$ transition with the Tb^{3+} cation. These issues were potentially due to deficiencies in either the equipment configuration or SIF used. Additionally, evidence of ESA of Tb^{3+} PL, see Figure 5-6, indicated that the 2.825 µm pumping scheme was potentially problematic. This was further corroborated by recent reports of MIR lasing in Tb^{3+} doped samples at wavelengths greater than 5 µm found in literature [121,141,142], while using a 2 µm pump laser.

5.3.2 SIF with Ce^{3+} doped core discussion:

Room temperature lasing at wavelengths greater than 5 µm from a chalcogenide SIF with a 'Ce' cation doped core while using in-band pumping was demonstrated. This achievement was undoubtably enabled by the relative simplicity of the Ce^{3+} cation, along with the relatively low loss and low phonon energy of the chalcogenide host glass. Challenges with the optical component choices employed in the equipment configuration and imperfections in the 'Ce' cation doped samples hampered laser performance and prevented proper laser characterisation and optimisation of the equipment configuration employed. Notably, lasing was achieved with a Ce^{3+} doped sample that was not purified with vacuum distillation. The [-Se-H] vibrational impurity absorption band, spanning the 4.3 to 5.0 µm spectral region (*see Table 2-4 and Figure 3-33*) increased optical attenuation within the gain medium at these wavelengths, resulting in heating within the sample. 'Gain' within the optical cavity was likely only present for wavelengths just beyond the [-Se-H] absorption band wavelengths. This indicated that the optical loss of the glass in this spectral region, was sufficiently low to achieve lasing. Furthermore, presumably if the [-Se-H] impurity was significantly reduced or removed the Ce^{3+} lasing wavelengths could potentially occur at wavelengths below 5.0 µm.

The results presented in Section 5.2.2 also showed variability in their PL emission intensity and lasing ability of SIF sample. The root cause for this variability could have been attributed to internal defects in the SIF samples and possible non-uniform distribution of the Ce^{3+} dopant concentration. To address these issues each core glass compositions produced by the author, excluding F120REJN, (see Table 3-9) was produced with 2 atomic % 'Ga' in its composition to improve RE^{3+} dopant solubility despite its detrimental effects to the minimum optical loss.

The high cost of the 4.15 µm QCL (> £40,000) used in the presented equipment configuration (see item 17 in Figure 5-7) renders it uneconomical. To make this MIR laser commercially viable a more economical pump source is required. Alternate MIR pump sources such as the Fe:ZnSe pulsed lasers operating at 4.1 µm, as described in [130,131], are bulky and require cryogenic cooling. Alternatively, Ce^{3+} cation excitation schemes employing a co-dopant, such as the Dy^{3+} cation, to enable photoexcitation with more economical pump lasers, have been demonstrated in [174]. The Dy^{3+} cation can be efficiently photoexcited with relatively low-cost pump sources (*either a 1.3 µm or 1.7 µm pump source*), the resulting 3.8 to 5.2 µm Dy^{3+} PL emission band (see Figure 4-30) completely overlaps the Ce^{3+} GSA band (see Figure 4-3 (a) and (c)). Thus, the Dy^{3+} PL can efficiently photoexcite the Ce^{3+} cation. Importantly, the Dy^{3+} cation does not have a GSA band that overlaps the 3 - 6 µm spectral range (*unlike the Pr^{3+} cation which also has a PL emission* *bands within the ~4.7 µm spectral range*). Pricing of these alternative pump sources can vary widely commercially available options can be more than 10 times cheaper [198] than the 4.15 QCL used. These pump sources are often fibre-coupled making them suitable for integration with compact MIR-fibre laser designs and importantly they would be insensitive to Ce^{3+} PL (the 4.15 µm QCL was susceptible to output power fluctuations due to the Ce^{3+} PL, see 7.2.4.1) However, unwanted interactions between the desired Ce^{3+} lasing wavelengths and latent ESA bands present in the RE co-dopant, as shown in Section 4.2.5.4 could render these excitation schemes unusable while in an optical cavity. Conceivably, the Ce^{3+} doped core of an SIF could be cladding pumped with RE^{3+} PL to avoid these potential latent ESA bands. Note, this was the impetus for the production and fabrication of the coextruded glass rod presented in Sections 3.2.6.2.

5.4 Chapter summary:

The aim of the work presented in this chapter was to investigate room temperature MIR lasing in chalcogenide SIF samples with RE (*rare-earth*) cation doped cores. Two dopants, Ce^{3+} and Tb^{3+} were separately, evaluated.

MIR lasing was not achieved in the Tb^{3+} doped samples due to time limitations and technical challenges. However, saturation of Tb^{3+} PL from samples without incurring damage while using a 2.825 µm pump source was demonstrated along with ostensible evidence of ESA within in an optical cavity was observed. Fortunately, MIR lasing due to the $^2F_{7/2} \rightarrow {}^2F_{5/2}$ radiative transition in Ce cation doped samples was demonstrated, with emission wavelengths up to 5.28 µm. The intensity of these cavity emissions was too weak to be properly evaluated, hence the omission of a laser characteristic or slope efficiency. However, analysis of the cavity emission spectra revealed ‘threshold-like’ features at pump powers as low as 86 mW. The shortcomings encountered were due to technical challenges with the optical component choices employed in the equipment configuration and imperfections in the ‘Ce’ cation doped samples. Additionally, the poor performance and reliability of the SIF sample evaluated allude to significant room for improvement.

6 Conclusions and possible future work:

A significant milestone of this work was to achieve room temperature MIR (*mid-infrared*) lasing in trivalent lanthanide, RE^{3+} doped chalcogenide glass fibres. This objective was ultimately realised when lasing at wavelengths greater than 5 µm from a SIF (*step-index fibre*), with a 'Ce' cation doped core, was demonstrated for the first time (see Section 5.2.2). In addition to this objective, the spectral properties of individual Ce^{3+}, Pr^{3+}, Sm^{3+}, Tb^{3+}, and Dy^{3+} doped chalcogenide glass samples were evaluated, inclusive of latent ESA (*excited state absorption*) measurements, (see Section 4.2). The production of both undistilled or distilled, undoped or RE^{3+} doped bulk chalcogenide glass compositions was also demonstrated (see Section 3.2). These glass compositions were shown to be amenable to extrusion, co-extrusion, drawing into SIF or drawing into single material fibre/cane, with relatively low optical attenuation. Additionally, improvements to glass production and fibre fabrication were made. These entailed NIR/MIR imaging of glass samples to detect hidden internal defects, and co-extrusion of RE-cation doped glass into a step-index glass rod to minimise defects at the core/cladding interface in SIF samples. However, the presented work alludes to several potential advancements in the areas of chalcogenide glass production, chalcogenide fibre fabrication, and spectroscopic characterisation, and MIR lasing.

6.1 Chalcogenide glass production and fabrication:

Purification of the chemical precursors used in chalcogenide glass production was imperative towards minimising the optical losses of the resulting chalcogenide glass fibre. Additionally, the preparation and cleaning procedures must be improved to eliminate defects and impurities introduced during the fabrication of chalcogenide components.

6.1.1 Purification of chemical precursors and glass:

To minimise optical attenuation both the volatile and non-volatile impurities in <u>each</u> chemical precursor must be removed. However, purifying certain chemical precursors, namely ‘Ge’, ‘Ga’ and RE metal, can be challenging due to their low volatility at temperatures below 1000 °C. The following are some alternate purification methods which could be employed in future work:

<u>Purification of RE metal precursors</u>:

Electrolysis has been demonstrated as a viable method for the bulk purification of actinides [199], thus this concept should be applicable to the purification of lanthanides. Electrolysis of a lanthanide selenide could purify the desirable RE cation by separating it from the unwanted anionic extrinsic impurities. A chalcogen salt was suggested because of the presence of the chalcogen element in the glass composition. Additionally, the amount of RE^{3+} cations within the electrolyte could be measured to a high degree of accuracy by evaluating the current flowing during electrolysis.

<u>Reflux distillation of chalcogenide glass inclusive of non-volatile constituents</u>:

Reflux distillation potentially allows for the purification of each constituent of the glass composition. Figure 6-1 illustrates a very simplified ‘Λ-shaped’ distillation rig that could potentially be used for reflux distillation. By controlling the heating schedule of the different temperature zones, the host glass constituents could be repeatedly distilled between two locations while passing through a non-evaporating chemical getter such as ‘Mg’, ‘Al’ or ‘La’ (*lanthanum*). The low volatility of the ‘Ga’ and RE dopant chemical precursors could be beneficial to their purification in a reflux-distillation system. These elements could conceivably be purified by repeated rinsing/dissolved in molten purified chalcogenide glass. This would cause a small proportion of the oxide and hydride impurities in these precursor chemicals to be leached into the chalcogenide glass melt. The impurities, now contained in the glass melt, could then be separated via distillation and/or sequestered via chemical getters or removed by a vacuum system. This process could conceivably be achieved either within a sealed vessel (as shown in Figure 6-1), or under continuous/dynamic vacuum with some modifications to the presented design. Furthermore, refractory impurities such as ‘C’ could be made volatile with the inclusion of trace amounts of ‘S’ to form the volatile CS_2 gas which could be removed during a ‘bake-out’ under continuous/dynamic vacuum.

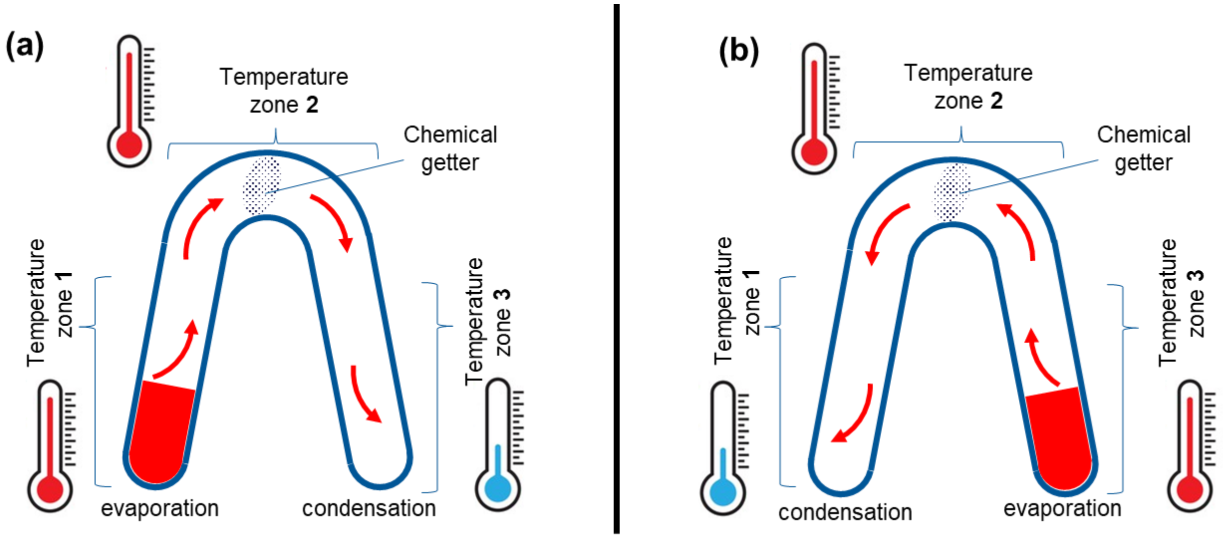

Figure 6-1: Showing a simplified illustrations of a proposed ‘Λ-shaped’ distillation rig with the chalcogenide glass being distilled between the different temperature zones. Note, distillation is intended to occur while the configuration is in a vertical orientation.

6.1.2 Fabrication of chalcogenide glass:

The presence of striae and holes in most of the SIFs, and the glass rod evaluated in Section 3.2 indicated room for improvement. The following are some ways in which these issues can be addressed:

Improvements to multi-stage quenching process:

Optimising the heating schedule during glass production, especially during the glass quenching process, could minimise the formation of compositional inhomogeneities. The current quenching methodology for the ‘3-stage quenching’ process (see Section 7.1.5.2) relies heavily on timing and temperature schedules based on past glass quenching operations for ampoules containing glass of similar mass and composition. Unfortunately, this methodology ostensibly affords opportunities for the formation of voids, and compositional inhomogeneities within the resulting bulk chalcogenide glass. Additionally, the true temperature of the melt/quench ampoule, during each stage of the ‘3-stage’ quenching operation, is poorly defined and subject to a variety of factors. These issues could potentially be alleviated by optimising the temperature and duration of each stage of the quench. This could be done by evaluating the internal dynamics of the chalcogenide glass during the quenching operation with NIR imaging of the molten glass. However, this evaluation requires that the quenching medium be transparent to allow an unobstructed view of the melt/quench ampoule and its contents during each stage of quenching. Additionally, the temperature at each stage of quenching could be better controlled by using a new quenching medium. Ideally, the desirable properties of an alternate quenching medium/media are:

i. Boiling point above 700 °C.
ii. High specific heat capacity (greater than air), to prevent significant changes in temperature of the quenching medium during quench. Thus, ensuring a well-defined quenching temperature.
iii. High thermal conductivity, greater than air, to ensure good heat transfer during each quenching stage.

Potential candidates for a quenching medium could include low melting temperature inorganic salts and molten white sugar. When compared to air as a quenching medium these items can have high boiling points, high specific heat capacity, and good thermal conductivity [200–202]. Additionally, some of these potential candidates can also be 'relatively' safe to handle.

Glass compositions:

Hydride impurities are unlikely to be completely eliminated from the chalcogenide glass despite stringent purification techniques. The [-Se-H] extrinsic impurity exhibits a 3.9 to 5.5 µm vibrational absorption peaking at 4.5 µm (*see Figure 3-33 (b)*). The PL emission bands from the Ce^{3+}, Pr^{3+}, Tb^{3+}, and Dy^{3+} cations each completely overlapped the [-Se-H] extrinsic vibrational absorption within the ~4.5 µm spectral region. Conversely, the [-S-H] extrinsic impurity exhibits a 3.9 to ~4.4 µm vibrational absorption peaking at 4.1 µm (see Figure 3-11). Additionally, it has been observed that the presence of 'S' in the glass composition significantly reduces the [-Se-H] absorption, because the hydride impurities preferentially associated with the 'S' rather than 'Se'. Thus, very small amounts of 'S' could be added to a glass composition to shift [-Se-H] absorption to the ostensibly less critical [-S-H] absorption. This could be especially beneficial for lasing within the 4.5 µm spectral region for the Ce^{3+}, Pr^{3+}, Tb^{3+}, and Dy^{3+} cations.

Plasma etching:

Implementing new stringent surface cleaning procedures for the glass after its exposure to contaminants such as laboratory atmosphere and liquid chemicals. Cleaning after each stage of fabrication would minimise the presence of volatile impurities. Material can be removed from the surface of an object via bombardment from a plasma source, this 'dry-etching' processing can be used for removing organic contaminants on surfaces without the use of liquids. Thus, plasma etching could be employed as the last step in the surface preparation of bulk chalcogenide glass and the items they encounter, prior to its fabrication into optical components and fibre. Additionally, this could also prove useful as the final cleaning stage for the surface of silica glassware, metal utensils and metallic precursors such as RE foil and 'Al' wire.

6.2 Characterisation of chalcogenide glasses and RE dopants:

The PL emission measurements presented throughout Section 4.2 focused on PL emissions in the MIR spectral region, however due to the influence of ESA many of the RE^{3+} dopants evaluated would also benefit from NIR measurements at wavelengths shorter than the pump wavelength. Additionally, temperature-controlled PL emission spectra and PL emission lifetime measurements, at sub-ambient and above ambient temperatures could give insight into the thermal dynamics of the RE^{3+} dopants during excitation.

The ESA measurement results presented in this thesis (see Section 4.2) show the dynamics of transitions occurring between different energy manifolds within RE cations. However, the ESA equipment configuration shown in Figure 4-2 imposed spectral limitations due to optical components used, specifically the dichroic mirror, item 4, in Figure 4-2. This item prevented ESA measurements at the pump wavelength or wavelength shorter than the pump wavelength. Improvements to the ESA equipment configuration could be made by implementing either of the following:

- A ‘co-propagating’ equipment configuration for the pump and probe sources, like that shown in Figure 4-14. This configuration would enable the evaluation of latent ESA over a range of wavelengths, inclusive of the pump wavelength, and could be used to analyse small core SIF samples. Additionally, it would allow the position of ‘zero-change’ points (see Section 4.1.2.2) for different sample lengths to be evaluated via a ‘cut-back’ of the sample. These zero-change points could potentially provide insight into the absorption cross-section, of the excited state transition.
- Orthogonal pump and probe beams, like that illustrated in Figure 6-2. Wherein, both the pump and probe sources are launched orthogonally to one another into a polished bulk cuboid sample. This would allow evaluation of latent ESA over a very wide measurement window (~1 to 25 µm). Additionally, this configuration could be made amenable to measurements at cryogenic temperatures using a ‘cold plate’, by modifying the sample holder (item 9 in Figure 6-2). Several RE^{3+} dopants exhibit very broad energy manifolds a wide ESA measurement window could enable the evaluation of intra-manifold transitions.

Both suggested equipment configurations above, would enable the evaluation of absorptions at the pump wavelength, thus revealing more of the transitions occurring. Furthermore, they could be used to investigate implementing an all-optical VOA (*variable optical attenuator*).

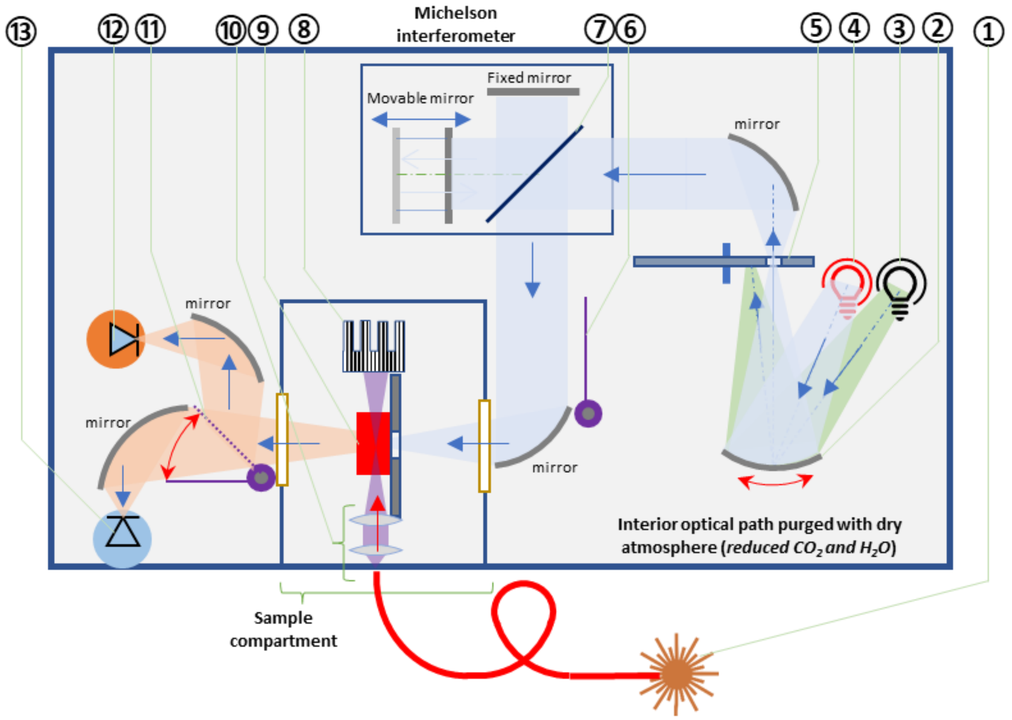

1. Fibre coupled pump laser.
2. Movable mirror to select between two broadband light sources.
3. Tungsten lamp used for the visible/NIR spectral region.
4. Globar® source for the NIR/MIR spectral region.
5. Aperture wheel to select measurement resolution.
6. Movable mirror to direct light between internal sample compartment and external window.
7. Beam splitter for Michelson interferometer:
   a. CaF_2 (*calcium fluoride*) beam-splitter for the visible/NIR spectral region.
   b. KBr beam-splitter for the NIR/MIR spectral region.
8. Beam dump used to absorb transmitted pump laser light.
9. Polished bulk chalcogenide glass sample attached with blu tack putty to a vertical metal sample holder.
10. Collimating and focusing optics for pump laser.
11. Movable mirror to direct light between one of two detector locations.
12. Room temperature InGaAs (*indium gallium arsenic*) detector used for the visible/NIR spectral region.
13. Room temperature DTGS (*deuterated triglycine sulfate*) detector used for the MIR spectral region.

Figure 6-2: Illustration of proposed equipment configuration for ESA measurement employing polished bulk RE^{3+} *doped chalcogenide sample.*

6.3 MIR fibre lasers:

Optimisations to the glass production and SIF fabrication processes would allow for improvements to laser performance and yield greater efficiency by decreasing optical attenuation of the host glass, along with a reduction/elimination of defects and tailoring of NA.

In addition to this, the equipment configuration used for the optical cavity could be optimised in the following ways:

- Improvements to the spectral resolution of the measurement system. This could possibly be done with the use of either an FTIR or a MIR optical spectrum analyser to evaluate optical cavity emissions.
- Employing a traditional optical cavity equipment configuration (see Figure 2-4) using FBGs. Using FBGs would simplify the equipment configuration, enabling greater compactness, efficiency, and reliability while avoiding many of the alignment issues encountered with discrete mirrors, inclusive of being insensitive to mechanical disturbances. This configuration could then be employed to properly characterise laser output for slope efficiency, beam profile, and wavelength tunability, while allowing power scaling experiments.
- A more cost-effective excitation scheme could be employed to excite the Ce^{3+} cation, possibly employing a PL from another RE cation similar to [174]. For example, the Dy^{3+} cation can be efficiently pumped with a relatively low cost 1.3 µm or 1.7 µm laser PL from, which would result in PL emissions spanning 3.80 to 6.00 µm, which completely overlaps the Ce^{3+} GSA. Thus, the Dy^{3+} PL can effectively excite the Ce^{3+} cation or via cladding pumping using PL from another RE cation.

Importantly, each of these suggestions could also be applied towards the development of MIR fibre lasers, operating at wavelengths greater than 7 µm, using either the Tb^{3+} or Dy^{3+} cations.

7 Appendix:

The procedures in Sections 7.1 and 7.2 were either previously developed within the Mid-Infrared Photonics Group, George Green Institute for Electromagnetics Research, at the University of Nottingham or found in literature. Section 7.3 presents an equipment configuration coding system developed by the author.

7.1 Synthesis and production of chalcogenide glass:

The Sections present the procedures used to produce either undistilled or distilled, undoped or RE cation doped bulk chalcogenide glass using the 'melt-quench' technique.

7.1.1 Silica glassware preparation:

Silica glassware was selected and sequentially rinsed with acetone, isopropanol (*see Table 7-3*), and distilled water. The inside of the glassware was then etched with 40 % by volume aqueous hydrofluoric acid for 5 minutes to remove surface roughness then thoroughly rinsed with distilled water. The glassware was then subjected to a 'Bake-Out' under standard atmosphere (~*101 kPa*) to remove any carbonaceous residue. Figure *7-1* along with Table 7-1 and Table 7-2 show the heating schedule applied to commonly used glassware. Glassware intended as the melt/quench vessel, used in Appendix 7.1.2 was then further vacuum baked at ~0.92 Pa to accelerate outgassing of physically or chemically adsorbed water from its interior surfaces. The interior of this vacuum baked glassware was kept under vacuum until needed. Note after each of these stages the glassware was visually inspected for physical imperfections that could cause a catastrophic failure at later stages in the glass making process.

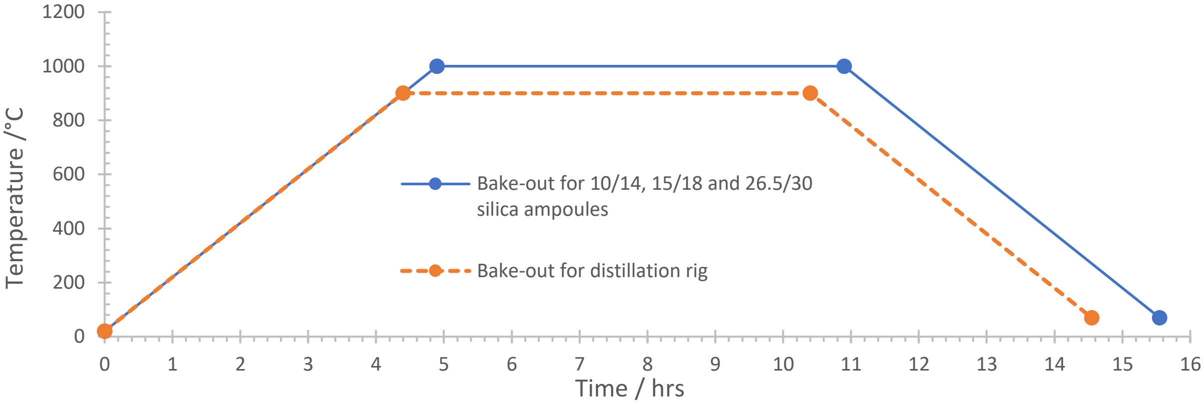

Figure 7-1: Heating schedule for 'bake out' applied to 10/14, 15/18 & 26.5/30 silica glass ampoules (blue line) and custom-made silica distillation rig (orange dotted line). *Note, the peak temperature for the silica distillation rig heating schedule, was lower than the silica glassware, solely due to the constraints of safely connecting a vacuum system to the distillation rig, which was a long, delicate, and unwieldy item.*

Table 7-1: Heating schedule for 10/14, 15/18 & 26.5/30 silica glass ampoules:

Step	Program instruction	Initial temp / °C	Target temp / °C	Rate °C/hrs	Time / hrs
1.	Step	~20	20	0	0
2.	Ramp	20	1000	200	4.9
3.	Dwell	1000	1000	0	6
4.	Ramp	1000	70	200	4.65
5.	Dwell	70	70	0	-
6.	End				

Table 7-2: Heating schedule for silica glass distillation rig:

Step	Program instruction	Initial temp /°C	Target temp / °C	Rate °C/hrs	Time / hrs
1.	Step	~20	20	0	0
2.	Ramp	20	900	200	4.4
3.	Dwell	900	900	0	6
4.	Ramp	900	70	200	4.15
5.	Dwell	70	70	0	-
6.	End				

7.1.2 Purification of precursor materials:

Chemical precursors were purchased at the highest available purity and stored under a dry nitrogen atmosphere inside a glovebox (*MBraun, MB 150B-G < 0.6 ppm* H_2O*, and < 0.3 ppm* O_2). Table 7-3 lists the specifications of the chemicals and equipment frequently referenced throughout the thesis. Precursors were then further purified before being used. This was done to minimise unwanted impurities present in the precursors during their refining/manufacture, or impurities accumulated during their transport and subsequent storage.

Table 7-3: Nominal specifications of chemical precursors used throughout Chapter 3.

Chemical	Description	Nominal purity	Manufacturer	Model #
As (*arsenic*)	1-4 mm pieces	7N5	Furukawa	120354
Ge (*germanium*)	3-6 mm pieces	5N	Materion	122954
Se (*selenium*)	3 mm shot	7N5	Materion	123220
Ga (*gallium*)	liquid	7N	Alfa Aesar	10186
S (*sulfur*)	3-6 mm pieces	5N	Alfa Aesar	S-1037
Sb (*antimony*)	1-4 mm pieces	6N	Materion	122718
$TeCl_4$ (*tellurium tetrachloride*)	anhydrous powder	3N	Alfa Aesar	12284
Al (*aluminium*)	1 mm outer diameter wire	5N	Alfa Aesar	10747
Ce (*cerium*)	0.25 mm thick foil	3N	Alfa Aesar	12377
Pr (*praseodymium*)	0.25 mm thick foil	2N	Alfa Aesar	10305
Sm (*samarium*)	0.1 mm thick foil	3N	Alfa Aesar	12421
Tb (*terbium*)	0.25 mm thick foil	3N	Alfa Aesar	12429
Dy (*dysprosium*)	0.25 mm thick foil	3N	Alfa Aesar	12381
Acetone	Liquid		Puriss	UN1090
Isopropanol	Liquid P/7507/PB17		Fisher Scientific	10641203
N_2 (*nitrogen*)	Gas		BOC	UN1066
O_2 (*oxygen*)	Gas		BOC	UN1072
Propane	Gas		BOC	UN1978
Propylamine	Liquid ≥ 99 % propylamine		ACROS Organics	

Table 7-4: Specifications for laboratory consumables used throughout Chapter 3:

Item	Description	Usage	Manufacturer
10/14	< 0.1 ppm OH, silica ampoule with a 10 mm ID and 14 mm OD	Purification ampoule and/or melt/quench ampoule.	Multilab
26.5/30	< 0.1 ppm OH, silica ampoule with a 26.5 mm ID and 30 mm OD	Purification ampoule and/or melt/quench ampoule.	Multilab
7/9	Silica tube with a 7 mm ID and 9 mm OD	Sacrificial tubing used to collect impurities and condensed distillate.	Multilab
Distillation rig	< 0.1 ppm OH, custom silica rig See Figure 7-9	Used for the vacuum distillation of previously made undoped chalcogenide glass.	Multilab
Weigh boats	85 mL Polystyrene	Used for portioning of material in batching and purification process.	Fisherbrand
Lens tissue	Optical lens tissue, 114 x 127mm	Cleaning of delicate components	PELCO®
Plastic pipette	Extended fine tip transfer pipette 3.3 mL	Used for the purification of 'Ga' metal.	Thermo Scientific™ Samco™
Nichrome wire	Uninsulated Ni80 nichrome resistance wire with an outer diameter of 0.45 mm.	Used to manipulate and handle hot ampoules during quenching and to produce custom heating coils for the distillation rig.	Crazy Wire Company (Kanthal)
Aluminosilicate blanket	Superwool™ 607™ Blanket	Insulation for the melting/rocking furnace and the distillation rig.	Ceramo

All batching was carried out under a dry nitrogen atmosphere, inside a glovebox. Separate laboratory utensils (metal tweezers, spatulas, scissors, etc.) were used for each specific precursor to prevent cross contamination.

The following sections describe the techniques employed in the purification of the chemical precursors used in the production of chalcogenide glass. These techniques include 'Bake-out' (see Section 7.1.2.1) and physically separation (see Sections 7.1.2.3 and 7.1.2.4).

7.1.2.1 Chalcogens and pnictogens 'bake-out':

Chalcogens and pnictogens were purified using a 'bake-out', Figure 7-2 shows an illustration of the equipment configuration used for this process. The precursor material was batched into prepared silica ampoules while in a glovebox. The weight of chemical precursor being purified dictated the type/size of silica glass ampoule used. A sacrificial 7/9 silica tube was sometimes inserted into the ampoule to prevent the accumulation of loosely adhering impurities and condensed distillate on the cooler 10/14 upper portion of the silica glass ampoule during purification, as illustrated in Figure 7-2 (a). A valve was then attached to the ampoule and then closed. The sealed, dry N_2 filled, ampoule was then moved outside of the glovebox, into a fume hood and connected to a vacuum system. The valve was then opened, and the ampoule evacuated to a pressure of ~0.92 Pa. The ampoule was then inserted into a tube furnace, as illustrated in Figure 7-2 (a) and (b) and a heating schedule was applied while under continuous vacuum, as illustrated in Figure 7-3 and Table 7-5 to Table 7-8.

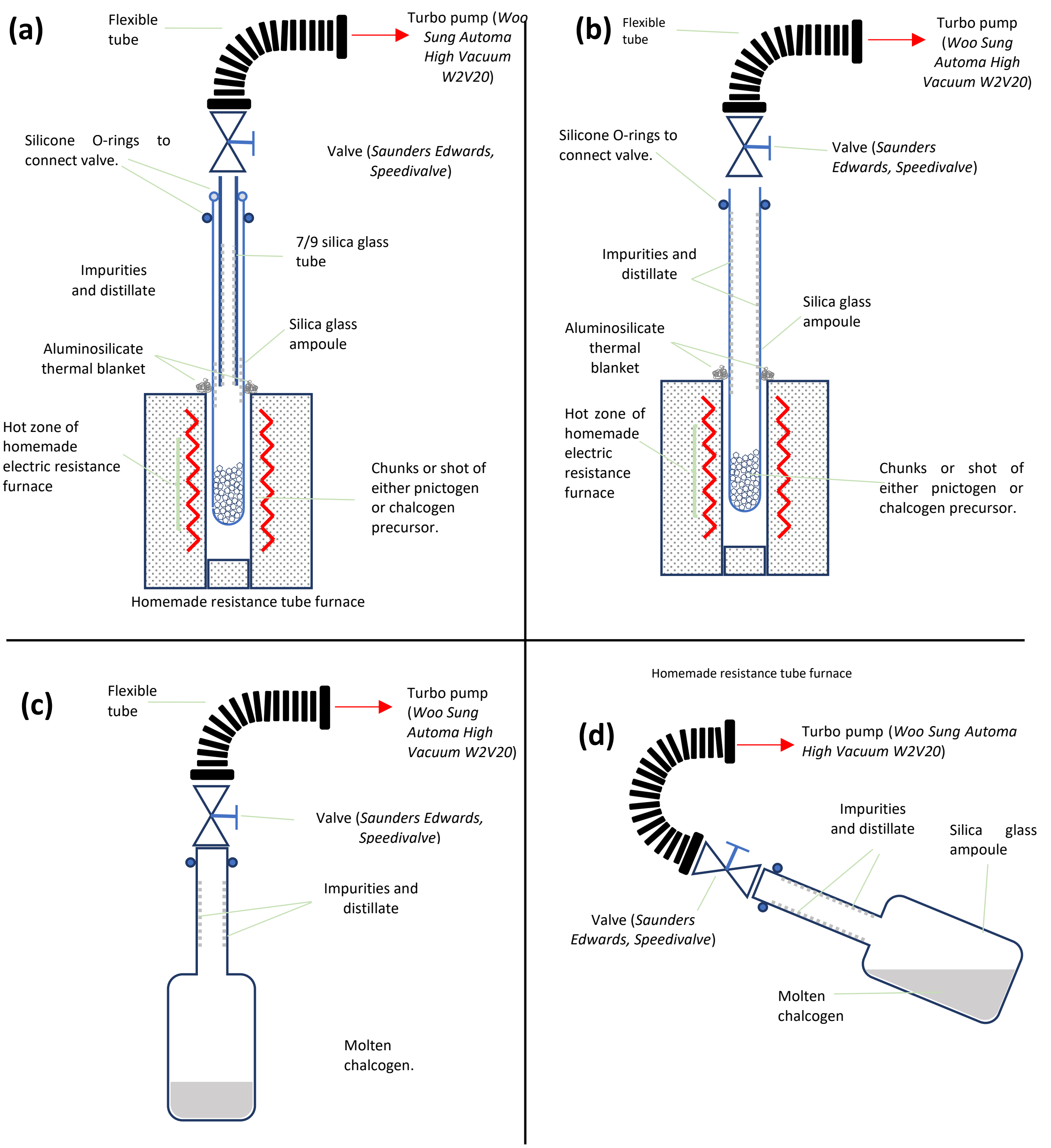

Figure 7-2: Showing illustration of equipment configurations for 'bake-out' ***(a)*** *with 7/9 shield tube inside 10/14 ampoule,* ***(b)*** *10/14 ampoule without shield tube, along with the equipment configuration used with the 26.5/30 ampoule for:* ***(c)*** *vertical cooling, and* ***(d)*** *slanted cooling.*

*Table 7-5: Heating schedule for ‘**S**’ precursor purification:*

Step	Program instruction	Initial temp / °C	Target temp /°C	Rate °C/hrs	Time /hrs
1.	Step	~20	20	0	0.00
2.	Ramp	20	140	200	0.60
3.	Dwell	140	140	0	0.50
4.	Ramp	140	30	300	0.37
5.	End				

*Table 7-6: Heating schedule for ‘**As**’ precursor purification:*

Step	Program instruction	Initial temp / °C	Target temp /°C	Rate °C/hrs	Time /hrs
1.	Step	~20	20	0	0.00
2.	Ramp	20	200	200	0.90
3.	Ramp	200	260	100	0.60
4.	Dwell	260	260	0	0.50
5.	Ramp	260	310	100	0.50
6.	Dwell	310	310	0	1.50
7.	Ramp	310	30	300	0.93
8.	End				

*Table 7-7: Heating schedule for ‘**Se**’ precursor purification:*

Step	Program instruction	Initial temp / °C	Target temp /°C	Rate °C/hrs	Time /hrs
1.	Step	~20	20	0	0.00
2.	Ramp	20	210	200	0.95
3.	Ramp	210	260	100	0.50
4.	Dwell	260	260	0	2.00
5.	Ramp	260	30	300	0.77
6.	End				

*Table 7-8: Heating schedule for ‘**Sb**’ precursor purification:*

Step	Program instruction	Initial temp / °C	Target temp /°C	Rate °C/hrs	Time /hrs
1.	Step	~20	20	0	0.00
2.	Ramp	20	500	250	1.92
3.	Dwell	500	500	0	0.10
4.	Ramp	500	570	100	0.70
5.	Dwell	570	570	0	3.00
6.	Dwell	570	30	300	1.80
7.	End				

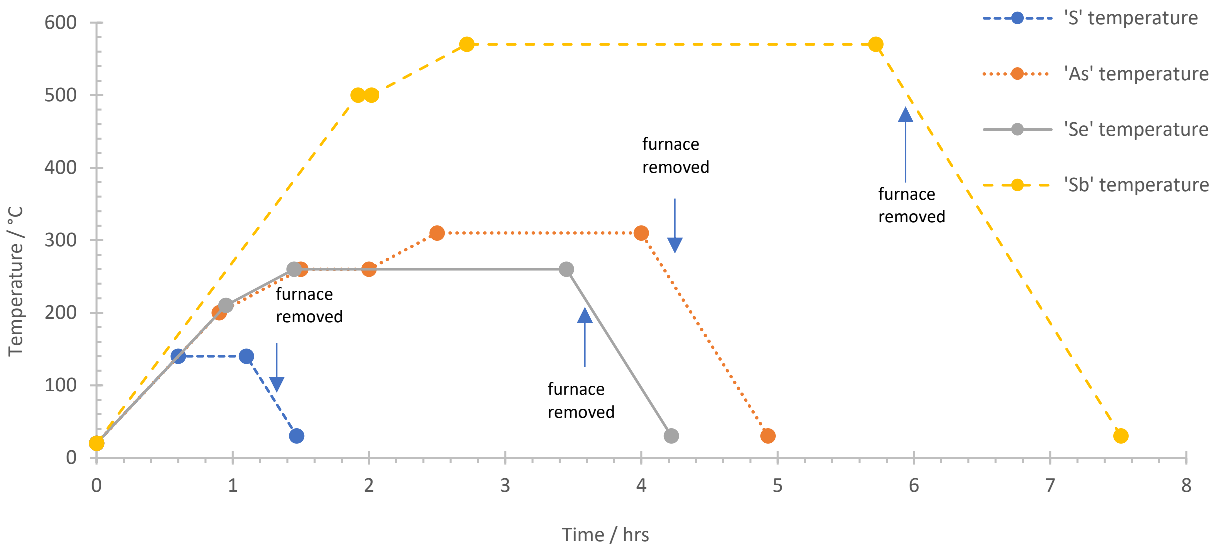

Figure 7-3: Individual heating schedules used for 'S', 'As', 'Se' and 'Sb' precursor purification. Note, ‘furnace removed’ refers to the silica glass ampoule being removed from the furnace, see Figure 7-2 (c) and (d).

Upon completion of the heating schedule the ampoule was allowed to cool in either a vertical or slanted orientation (Figure 7-2 (d)). This was done to prevent any thermal contraction of the contents of the ampoule from damaging the ampoule wall. The valve was then either closed, or the ampoule was sealed with an oxy-propane torch (*see decision flowchart in Figure 7-4*). The outer surface of the silica ampoule was wiped to remove any thermal blanket material. The cool, clean ampoule and its purified contents were then returned to the glovebox, whilst still under vacuum, for batching (*see Appendix 7.1.4*). The 7/9 silica tube, if used, was discarded to prevent this accumulated material from being reintroduced into the purified precursor and/or hamper with the accurate weighing of the purified precursor and any ampoule sealing.

7.1.2.1.1 Purification of pnictogens:

Pnictogens; ‘As’ or ‘Sb’ (*see Table 7-3*) were individually subjected to a ‘bake-out’ below their melting or sublimation point, while under continuous vacuum, as illustrated in Figure 7-2 (a) or (b). Table 7-6 and Table 7-8 show the individual heating schedule used to purify the ‘As’ and ‘Sb’ precursors, respectively. Pnictogens were not purified in the melt/quench ampoule, because after purification they could easily be removed from the ampoule and accurately re-batched. The ‘As’ precursor was purified without a 7/9 glass silica shield tube, as illustrated in Figure 7-2 (b), thus impurities and ‘As’ distillate condensed and adhered as a silvery black and splotchy white, thin film onto the cool upper section of the inner silica ampoule wall. Conversely, the ‘Sb’ precursor was typically purified with a 7/9 shield tube, as illustrated in Figure 7-2 (a), thus impurities and ‘Sb’ distillate condensed as small, silvery, flakes, loosely adhered to the cool portion of the 7/9 tube, along its inner wall. Upon completion of the bake-out, the valve was closed, and the cooled, purified pnictogen at the bottom of the ampoule was returned to the glovebox whilst still under vacuum and opened to be used in the batching process.

7.1.2.1.2 Purification of chalcogens:

Chalcogens; ‘S’ and ‘Se’ (*see Table 7-3*) were individually heated above their melting points while under continuous vacuum in a silica glass ampoule, as illustrated in Figure 7-2(a) or (b). Table 7-5 and Table 7-7 show the individual heating schedules used to purify the ‘S’ and ‘Se’ precursors, respectively. Additionally, Figure 7-4 shows a flowchart used for the purification of ‘S’ or ‘Se’ precursors.

Purification of chalcogens resulted in a solidified mass, which often adhered to the ampoule inner wall, especially with the ‘S’ precursor. Consequently, at least one chalcogen in the glass composition was always purified in the ‘melt/quench ampoule’ to avoid removing this solidified mass. Thus, the ‘S’ precursor was purified in the ‘melt/quench ampoule for glass compositions which contained both ‘S’ and ‘Se’, while the ‘Se’ precursor was purified in a sacrificial ampoule. Conversely, the ‘Se’ precursor was purified in the ‘melt/quench ampoule for glass compositions which did not contain ‘S’. Additionally, for ‘Se’ purifications weighing more than 40 g, a ’slanted quench’, as illustrated in Figure 7-2 (d), was employed to allow the purified ‘Se’ to cool to avoid structural failure of the ampoule due to contraction and/or expansion of its contents. The weight of the empty melt/quench ampoule ‘$\mathbf{W}_{empty}$’ was recorded before batching or purification, this was necessary to calculate the weight of the remaining solidified chalcogen after purification.

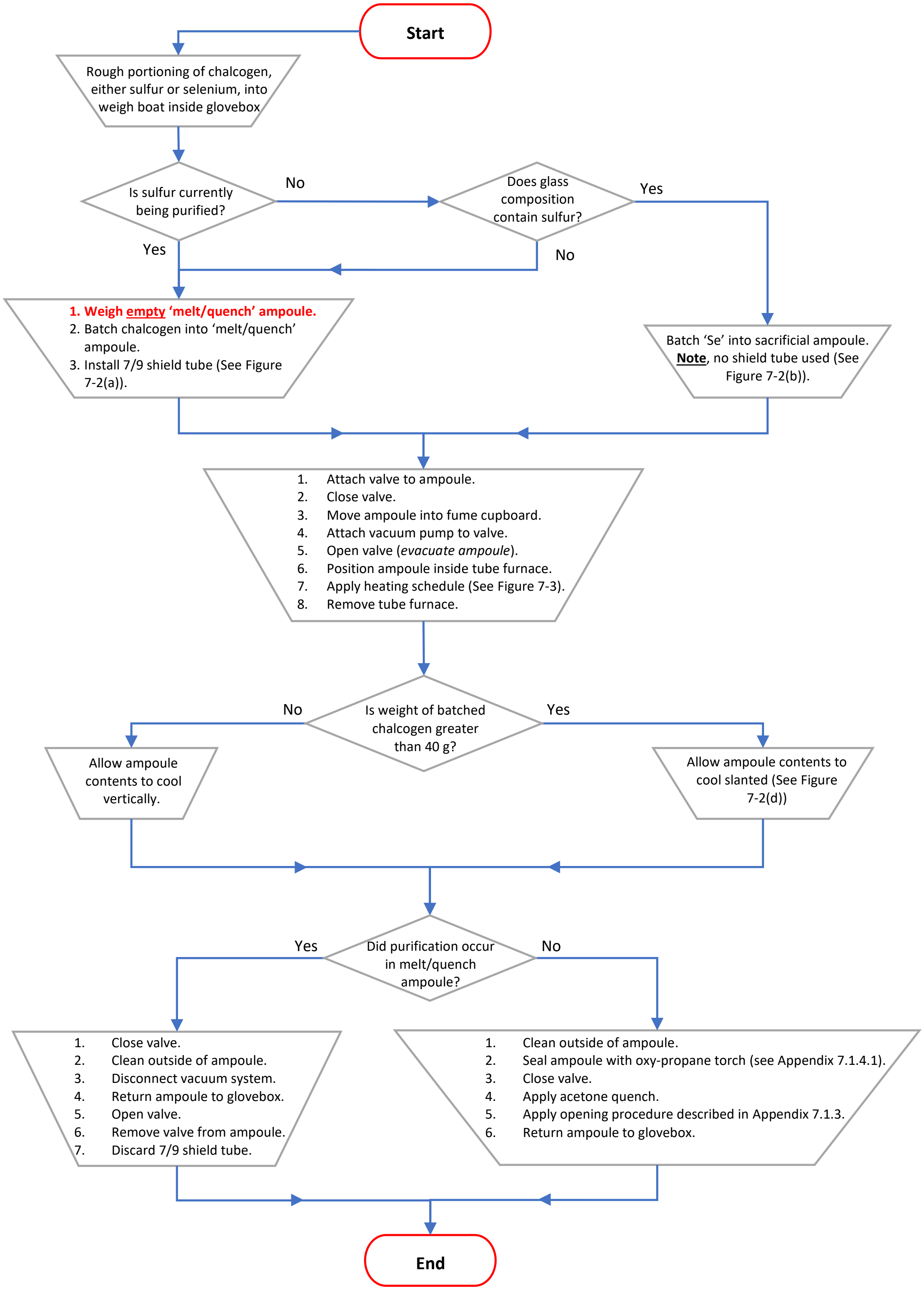

Figure 7-4: Flowchart illustrating the purification steps of either sulfur or selenium precursor.

The final weight of the purified chalcogen in the melt/quench ampoule dictated the weight of each of the other glass constituents added in the precision batching process described in Appendix 7.1.4.

Chalcogen purification occurring in the 'melt/quench' ampoule was always done with a 7/9 silica shield tube, as illustrated in Figure 7-2(a). Conversely, a 7/9 silica shield tube was not used during the purification of chalcogens in a sacrificial ampoule, as these ampoules were sealed with an oxy-propane torch upon completion of the purification process.

Oxy-propane sealing was done on sacrificial ampoules to remove the valve and O-rings (see Figure 7-2 (d)), both of which could be compromised during the opening process described in Section 7.1.3 and contaminate the contents of the ampoule and glovebox. The 'Se' chemical, after being purified in a sacrificial ampoule, was then detached from the ampoule inner wall using an 'acetone quench': wherein, acetone was slowly streamed over the outer surface of the ampoule, while its contents were still under vacuum, reducing its temperature via evaporation, causing the solidified contents of the ampoule to contract inward away from the ampoule inner wall. The opening process, described in Section 7.1.3, was then carried out and the purified 'S' or 'Se' were returned to the glovebox.

7.1.2.2 Challenges of germanium purification:

The metalloid 'Ge' was the only precursor material that was not purified. This was due to its high melting temperature (*see Table 2-3*), along with the relatively low volatility of the 'Ge' and Ge-oxides at temperatures below 1000 °C [84,203]. Note, 1000 °C was the maximum continuous admissible temperature of the silica glassware used. Note, the glass transition of SiO_2 is ~ 1050 °C [48]. Thus, 'Ge' with a 5N purity (*see Table 7-3*) was purchased and subsequently batched.

7.1.2.3 Surface purification of gallium:

The low vapour pressure of the element 'Ga' precluded heat treatment as a purification step (*see Table 2-3*). Thus, the metal 'Ga' (*see Table 7-3*) was purified inside the glovebox by physically separating its surface impurities. The metal was initially melted using a homemade low power electric resistance heater. The liquid metal was then poured into a disposable antistatic weighing boat. A disposable plastic pipette was inserted into the liquid 'Ga' to extract the silvery and lustrous liquid from the centre of the puddle, while separating the dull surface liquid. The contents of the plastic pipette were transferred to a new weighing boat and this process was then repeated 3-4 times before the 'Ga' was ready to be batched.

7.1.2.4 Surface purification of rare earth foils:

For the presented work all the lanthanide precursors were in the form of metal foils typically having a dull surface. Purification of these rare-earth foils entailed mechanical removal of surface contaminants while inside the glovebox. In this mechanical removal process a piece of the metal foil was cut and then scratched with a shard of 'Ge' in a cross hatched pattern to remove surface impurities until it appeared lustrous. 'Ge' was used because of its hardness and presence in the glass composition. Thus, the 'Ge' was considered an acceptable contaminant. Additionally, this surface scraping purification procedure was also applied to the 'Al' metal used in the vacuum distillation process (*see Appendix 7.1.6*).

7.1.3 Opening vacuum sealed ampoules:

The opening process for sealed ampoules entailed weakening the other surface of the silica ampoule and snapping the ampoule open in a controlled manner. This was done by either scoring the surface, or making a series of shallow cuts, around 0.25 mm deep in the outer diameter of the silica ampoule, using an oil lubricated diamond saw (*Buehler, IsoMet equipped with a Leco diamond blade*). Scoring and cutting always occurred outside the glove box to avoid generating extraneous silica dust inside the glovebox. The outer surface of the ampoule was then carefully cleaned, and it was then returned to the glovebox to be cracked open under a dry N_2 atmosphere. These ampoules would often suck silica dust and shards into the content of the ampoule when cracked open due to them initially being under vacuum. Thus, the silica shards were manually removed, while most of the silica dust was removed with a vacuum cleaner (MBraun) installed inside the glovebox.

7.1.4 Precision batching:

The constituents of the chalcogenide glass melt were weighed and batched into either a melt/quench silica glass ampoule or distillation rig, while under a dry nitrogen atmosphere, inside a glovebox. Each constituent to be added was initially portioned into disposable weigh-boats, while being weighed using a digital balance (*Sartorius, BP221S*).

For a typical glass melt the final weight of the purified chalcogen, either ‘S’, or ‘Se’, solidified in the melt/quench ampoule was calculated by subtracting the gross weight of the melt/quench ampoule containing the purified chalcogen, ‘$\mathbf{W}_{full}$’ from its initial empty weight ‘$\mathbf{W}_{\mathbf{empty}}$’.

$$W_{full} - W_{empty} = \text{Weight of purified chalcogen} \qquad \text{Equation 7-1}$$

Using the desired nominal atomic % composition of the final glass, and the weight of the purified, solidified chalcogen in the melt/quench ampoule, the target weight for each of the other constituents to be added to the melt/quench ampoule was calculated. This calculation was done using a custom-made application called 'Batch' written by Dr David Furniss.

Each precursor was initially batched into a disposable weigh-boat according to the batching procedure in Table 7-9, then carefully transferred into the melt/quench ampoule or distillation rig using the procedure illustrated in Figure 7-5. After batching was completed, a valve was attached to the ampoule (*see Figure 7-2 (b)*) or distillation rig (*see Figure 7-9*) and closed.

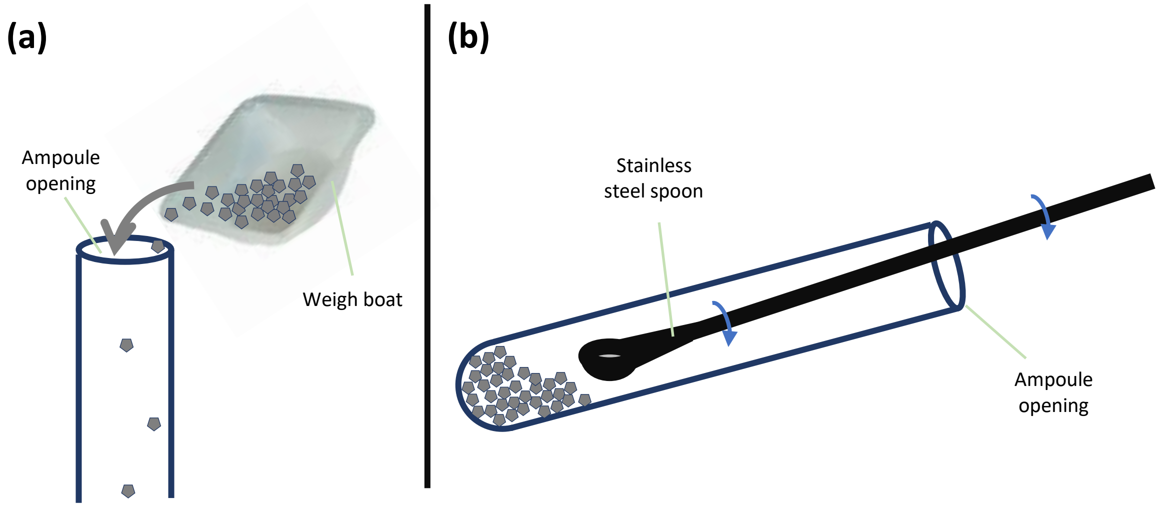

Figure 7-5: Illustration of batching procedure prior to melting a chalcogenide glass for; ***(a)*** *solid chunks, and* ***(b)*** *powder and droplets.*

Table 7-9: List of procedures used for batching purified precursors from Table 7-3 into melt/quench vessel.

Precursor	**Batching precision / ± mg**	**Batching procedure**
‘As’ chunks	1.0	Purified precursor chunks were placed into a disposable weigh-boat and carefully swirled around for a few seconds to allow any fine powder of flakes to electrostatically adhere to the inner surface of the weigh-boat. The larger chunks were poured into a new weigh-boat, and this process was repeated until there was little to no dust between the chunks. The chunks of precursor were then portioned into a new weigh-boat to a precision of ± 1 mg. These chunks were then carefully transferred directly into the melt/quench ampoule or distillation rig using the weigh-boats as a pouring funnel/spout, as illustrated in Figure 7-5 (a).
‘Sb’ chunks	1.0	
‘Ge’ chunks	1.0	
‘Se’ chunks	1.0	‘Se’ purified in a sacrificial ampoule (Appendix 7.1.2.1.2) or previously made chalcogenide glass was firstly removed from the ampoule and broken into chunks with an agate mortar and pestle (Fisher). Any dust adhering to the chunks of ‘Se’ or chalcogenide glass were separated using the procedure described above. These chunks were then carefully transferred directly into the melt/quench ampoule or distillation rig using the weigh-boats as a pouring funnel/spout, as illustrated in Figure 7-5 (a).
Chalcogenide glass chunks	1.0	
‘Ga’ droplets	1.0	Constituents of the glass in the form of droplets and powder were carefully batched into separate weigh-boats to a precision of ± 1 mg. These precursors were transferred to the melt/quench vessel using a long stainless-steel spoon. Care was taken to deposit these items towards the bottom of the ampoule to prevent them from adhering to the inner wall of the ampoule in the upper regions where oxy propane sealing occurred, as illustrated in Figure 7-5 (b).
$TeCl_4$ powder	~1.0	
‘Al’ wire	1.0	Purified metals were initially batched into a weigh-boat to the specified precision. These pieces of metal were then carefully transferred to the melt/quench vessel using stainless-steel tweezers.
‘Ce’ foil	0.3	
‘Pr’ foil	0.3	
‘Sm’ foil	0.3	
‘Tb’ foil	0.3	
‘Dy’ foil	0.3	

Note, the precursor sulfur was not included above because it was always purified inside the melt/quench vessel, for glass compositions which contained it, where it adhered to the ampoule inner wall.

7.1.4.1 Oxy propane sealing of ampoule:

After batching the sealed, dry N_2 filled, ampoule was then moved outside of the glovebox, into a fume hood, and connected to a vacuum system and evacuated to a pressure of ~0.92 Pa, (*see Figure 7-2 (b) or Figure 7-9)* then sealed using an oxy-propane torch. The sealing time was kept as short as possible (< *5 minutes*) to minimise the dissociation of silica to silicon monoxide [204] on the inner surface of the ampoule as described by the following reaction:

$$2SiO_2 \rightarrow 2SiO + O_{2\,(gas)} \qquad \text{Equation 7-2}$$

7.1.5 Melting, quenching, and annealing:

Figure 7-6 shows a parts list and illustrates the equipment configuration used to subject the melt/quench vessel to a melting and rocking schedule. In preparation for the melt/quench process, oxy-propane sealed ampoules were partially wrapped in nichrome wire to aid with handling and manipulation during the quenching process, as illustrated in Figure 7-6 (a). These ampoules were then carefully inserted into the hot zone of a resistance, rocking furnace, and surrounded with aluminosilicate blanket to promote uniform heating, as illustrated in Figure 7-6 (b) and (c). Ampoules were then subjected to a simultaneous heating and rocking schedule (see Appendix 7.1.5.1) followed by a multi-stage quenching process (see Appendix 7.1.5.2) and finally an annealing stage (see Appendix 7.1.5.3).

7.1.5.1 Melting/rocking:

Melting and rocking schedules were applied to the melt/quench vessel and its content. The heating and rocking schedules were specific to the glass composition being produced and was comprised of several stages. Table 7-10 and Table 7-11 ,lists the heating and rocking schedules applied to undoped and doped Se-based glass compositions, respectively, while Table 7-12 and Table 7-13 listed the schedules applied to undoped and doped Sb-based glass compositions, respectively.

The furnace was initially oriented in a horizontal configuration, see Figure 7-6 (a) with its rocking action disabled, while the temperature was increased as per the heating schedule of the glass composition (*see program step 2 in Table 7-10 to Table 7-13*). This stationary heating was done to prevent any loose content from scratching the inner wall of the ampoule and allowed the chalcogen(s) to melt. Upon reaching target temperature, the horizontal rocking action was enabled using a 10 second interval between rocking motion, while the temperature was further ramped as per the specific heating schedule of the glass composition (*see program step 4 in Table 7-10 to Table 7-13*). The horizontal orientation of the ampoule improved mixing by sloshing molten materials from end to end during rocking, causing a washing action inside the ampoule and encouraging the dissolution of the more refractory precursors.

Upon reaching a predefined setpoint temperature, depending on the glass composition (*see program step 5 in Table 7-10 to Table 7-13*), the furnace temperature was dwelled for a period ranging from 2 to 12 hours, while horizontally rocking. This temperature dwell was done to try to ensure sufficient mixing and homogeneity of the molten glass. The furnace was then re-oriented to a vertical rocking configuration, as illustrated in Figure 7-6(b), while the temperature dwelled for a 1-hour period (*see program step 6 in Table 7-10 to Table 7-13*). Vertical rocking was employed to allow bubbles (fining) and less dense impurities (refining) to rise to the surface of the molten glass. The rocking was then disabled, and the ampoule cooled to 700 °C (*see program steps 7 to 8 in Table 7-10 to Table 7-13*).

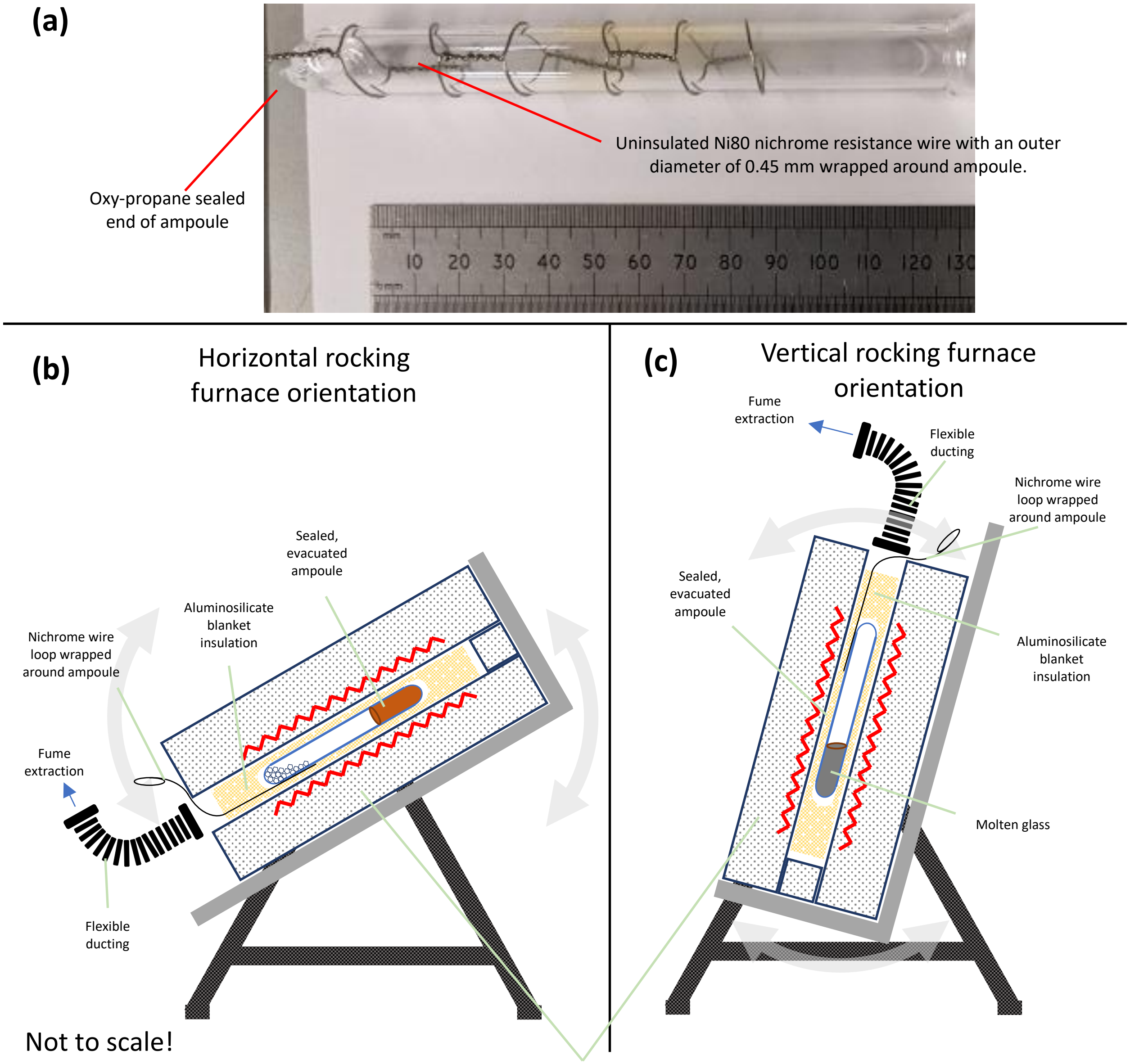

Rocking furnace (TF105/4.5/1ZF, tube ID 86 mm) mounted on homemade platform and operated with temperature controller (Instron, Eurotherm 2408 controller equipped with Type-K thermocouple).

Figure 7-6: ***(a)*** *Image of wire wrapping attached to ampoule prior to melting,* ***(b)*** *cross-sectional illustration of horizontal rocking furnace configuration and* ***(c)*** *cross-sectional illustration of vertical rocking furnace orientation.*

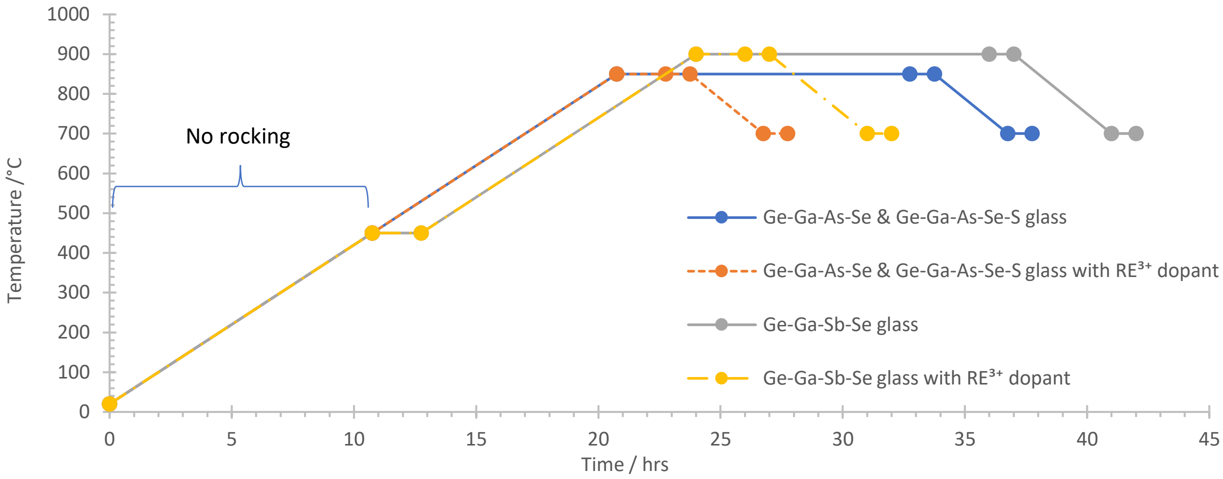

Figure 7-7: Individual heating schedules for melting and homogenisation of (Ge-Ga-As-Se), (Ge-Ga-As-Se-S), and (Ge-Ga-Sb-Se) glass compositions with and without RE^{3+} dopant.

Table 7-10: Heating schedule used for Ge-Ga-As-Se, & Ge-Ga-As-Se-S glass compositions:

Program step	Program instruc	Initial temp /	Target temp	Rate °C/hrs	Duration /hrs	Furnace motion	Furnace orientation
1.	Step	20	20	0	0	stationary	horizontal
2.	Ramp	20	450	40	10.75	stationary	horizontal
3.	Dwell	450	450	0	0	stationary	horizontal
4.	Ramp	450	850	40	10	rocking	horizontal
5.	Dwell	850	850	0	12	rocking	horizontal
6.	Dwell	850	850	0	1	rocking	vertical
7.	Ramp	850	700	50	3	stationary	vertical
8.	Dwell	700	700	0	1	stationary	vertical
9.	End					stationary	vertical

Table 7-11: Heating schedule used for Ge-Ga-As-Se, & Ge-Ga-As-Se-S glass compositions with RE^{3+} dopant:

Program step	Program instruction	Initial temp / °C	Target temp /°C	Rate °C/hrs	Duration /hrs	Furnace motion	Furnace orientation
1.	Step	20	20	0	0	stationary	horizontal
2.	Ramp	20	450	40	10.75	stationary	horizontal
3.	Dwell	450	450	0	0	stationary	horizontal
4.	Ramp	450	850	40	10	rocking	horizontal
5.	Dwell	850	850	0	2	rocking	horizontal
6.	Dwell	850	850	0	1	rocking	vertical
7.	Ramp	850	700	50	3	stationary	vertical
8.	Dwell	700	700	0	1	stationary	vertical
9.	End					stationary	vertical

Table 7-12: Heating schedule used for Ge-Ga-Sb-Se glass compositions:

Program step	Program instructio	Initial temp / °C	Target temp /°C	Rate °C/hrs	Duration /hrs	Furnace motion	Furnace orientation
1.	Step	20	20	0	0.00	stationary	horizontal
2.	Ramp	20	450	40	10.75	stationary	horizontal
3.	Dwell	450	450	0	2.00	stationary	horizontal
4.	Ramp	450	900	40	11.25	rocking	horizontal
5.	Dwell	900	900	0	12.00	rocking	horizontal
6.	Dwell	900	900	0	1.00	rocking	vertical
7.	Ramp	900	700	50	4.00	stationary	vertical
8.	Dwell	700	700	0	1.00	stationary	vertical
9.	End					stationary	vertical

Table 7-13: Heating schedule used for Ge-Ga-Sb-Se glass compositions with RE^{3+} dopant:

Program step	Program instruction	Initial temp / °C	Target temp /°C	Rate °C/hrs	Duration /hrs	Furnace motion	Furnace orientation
1.	Step	20	20	0	0.00	stationary	horizontal
2.	Ramp	20	450	40	10.75	stationary	horizontal
3.	Dwell	450	450	0	2.00	stationary	horizontal
4.	Ramp	450	900	40	11.25	rocking	horizontal
5.	Dwell	900	900	0	2.00	rocking	horizontal
6.	Dwell	900	900	0	1.00	rocking	vertical
7.	Ramp	900	700	50	4.00	stationary	vertical
8.	Dwell	700	700	0	1.00	stationary	vertical
9.	End					stationary	vertical

7.1.5.2 Quenching:

The quenching process entailed rapidly cooling the molten contents of the melt/quench ampoule to form an amorphous solid. Firstly, the ampoule was removed from the rocking furnace at 700 °C and suspended from nichrome wire (*see Figure 7-6 (a) or Figure 7-8 (b)*) then subjected to an air quench, immediately followed by a furnace quench and finally a nitrogen jet quench.

- Air quench: Immediately upon removal from the furnace, the 700 °C ampoule was intentionally quenched in room temperature air (21 - 23 °C) for between a few seconds to 1 minute, depending on the glass composition and weight of chalcogenide glass (*see* Table 7-14). During this phase of the quench volatile constituents of the glass composition often condensed on the cool upper portions of the inner wall of the ampoule as shown in Figure 7-8(b).
- Furnace quench: Immediately following the air-quench, the ampoule was carefully placed into a homemade tube resistance furnace, as illustrated in Figure 7-8 (a). The furnace temperature was initially set to the glass 'T_g'. The tube furnace allowed the ampoule and its contents to cool in a controlled manner preventing the temperature from falling below the glass 'T_g'. The ampoule was kept in the furnace for between a few seconds to 1 minute depending on the mass and composition of the glass.
- Nitrogen jet: Immediately following the furnace quench, the silica ampoule was lifted from the homemade tube resistance furnace while a gentle jet of room temperature N_2 gas was directed at its surface to detach the chalcogenide glass from the inner wall in a controlled manner, as illustrated in Figure 7-8 (a). The chalcogenide glass was progressively detached,

starting from the top of the silica ampoule to the bottom, as quickly as possible to avoid reducing the temperature of the glass rod below its ‘T_g’.

Table 7-14: Chalcogenide bulk glass quenching.

Glass weight / g	Air quench time / s	Furnace quench time / s
15 to 35	~ 35	~ 45
35 to 45	~ 45	~ 55
> 100	60 to 90	75 to 100

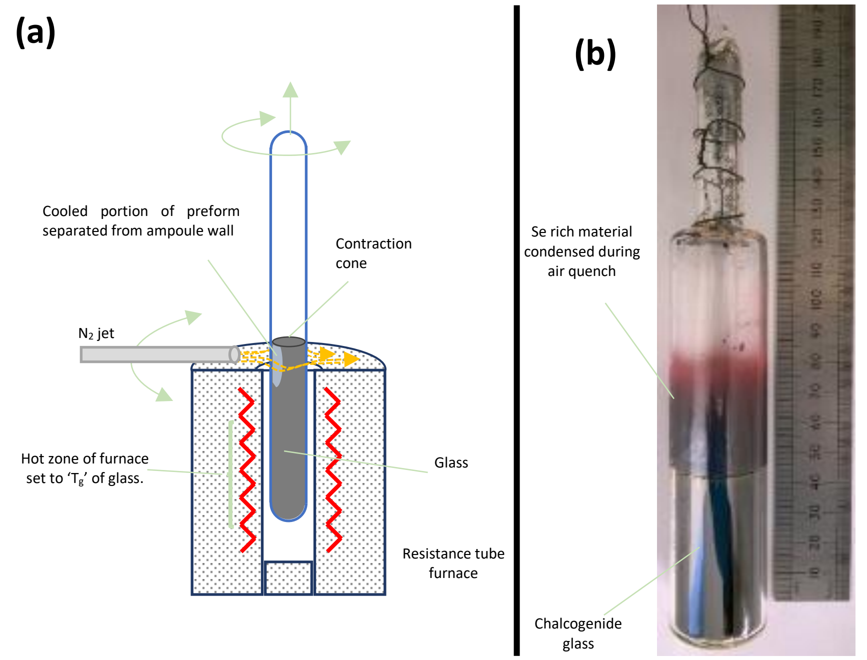

Figure 7-8: (a) N_2 jet quench of silica ampoule process and (b) image of silica after quenching process.

7.1.5.3 Annealing:

Immediately after quenching, the melt/quench silica ampoule containing the chalcogenide glass was placed vertically into a stationary, electric resistance furnace (*Instron, TF105/4.5/1ZF, equipped with a type-K thermocouple and Eurotherm 2408 temperature controller*) to anneal at the glass ‘T_g’ for 1 hour before being allowed to slowly cool to room temperature. This annealing step was a heat-treatment process to release stress from the glass by bringing it to thermal equilibrium at the glass ‘T_g’, then very slowly decreasing the temperature.

7.1.6 Vacuum distillation of undoped glass:

Undoped chalcogenide glass was purified via distillation, using the equipment configuration shown in Figure 7-9. Wherein chalcogenide glass in the ‘charge chamber’ was distilled into the ‘distillation chamber’ at temperatures between 600 to 700 °C, while under continuous/dynamic vacuum. Distillation was performed in a horizontal configuration, and the design of the distillation rig used was based on [99]. Gettering agents were employed during distillation to minimise impurities inadvertently incorporated into the chalcogenide glass during its synthesis. 'Al' metal was used to remove oxide impurities [205] while $TeCl_4$ was used to remove hydride impurities [93,98,100,101]. Oxide impurities reacted with ‘Al’ to form non-volatile Al_2O_3, which was then separated from the glass melt through distillation. The $TeCl_4$ getter reacted with hydride impurities to form volatile HCl [100], which was released as a gas during the distillation process, the following equation is an example of the reaction with the [-Se-H] impurity:

$$TeCl_4 + 4[\text{-Se-H}] \rightarrow 4HCl_{(gas)}\uparrow + [\text{-Te-}]_{(glass)} + 4[\text{-Se-}]_{(glass)} \qquad \text{Equation 7-3}$$

The vacuum distillation process was applied to previously made <u>undoped</u> Ge-As-Se chalcogenide glass cullet produced using the standard melt/quench technique, containing $TeCl_4$ and <u>without</u> ‘Ga’. This chalcogenide glass was batched into the ‘Charge chamber’ of the distillation rig via the ‘charge chamber tube’, see Figure 7-9 (a), along with 1000 ppmw ‘Al’ metal. An end cap was attached to the ‘charge chamber tube’ while a valve was affixed to the ‘Link 2’ tube of the distillation rig, as illustrated in Figure 7-9 (a), the valve was then closed. The ‘charge chamber tube' was then sealed, using the procedure described in Appendix 7.1.4.1 and illustrated in Figure 7-9 (b).

Heating coils, made from uninsulated nichrome wire were individually wrapped around sections of the distillation rig to allow multi-zone temperature control during distillation as illustrated in Figure 7-9 (c). Each custom heating-coil was connected to a DC power supply, (*TENMA, dual output DC bench power supply*) and during the distillation its temperature was controlled by manually adjusting the voltage and current supplied to the coil. At each subsequent stage of the assembly of the equipment configuration, electrical continuity checks were performed between the heating coils to detect and address any electrical short circuits.

Thermocouples (*RS PRO, Type K Thermocouple*) were carefully attached to the distillation rig to monitor different temperature zones, as illustrated in Figure 7-9 (d). Ceramic tubes were used to prevent the thermocouples from causing short-circuits in the custom heating coils. In the presented equipment configuration eight temperature zones, namely, 'Charge chamber 1', 'Charge chamber 2', 'Link 1A', 'Link 1B', 'Coil', 'Distillate 1', 'Distillate 2' and 'Link 2' were monitored.

The 'Charge chamber' on the distillation rig was positioned inside a clam-shell furnace to control the 'Charge chamber 1' and 'Charge chamber 2' temperature zones, as illustrated in Figure 7-9(d). The temperature for the 'Link 1' tube was controlled by the 'Link 1A', 'Link 1B', and 'Coil' custom heating coils.

The temperature for the 'distillate chamber' was controlled by the 'Coil', 'Distillate 1', and 'Distillate 2' custom heating coils. The temperature for the 'Link 2' tube was controlled by the 'Link 2' custom heating coil.

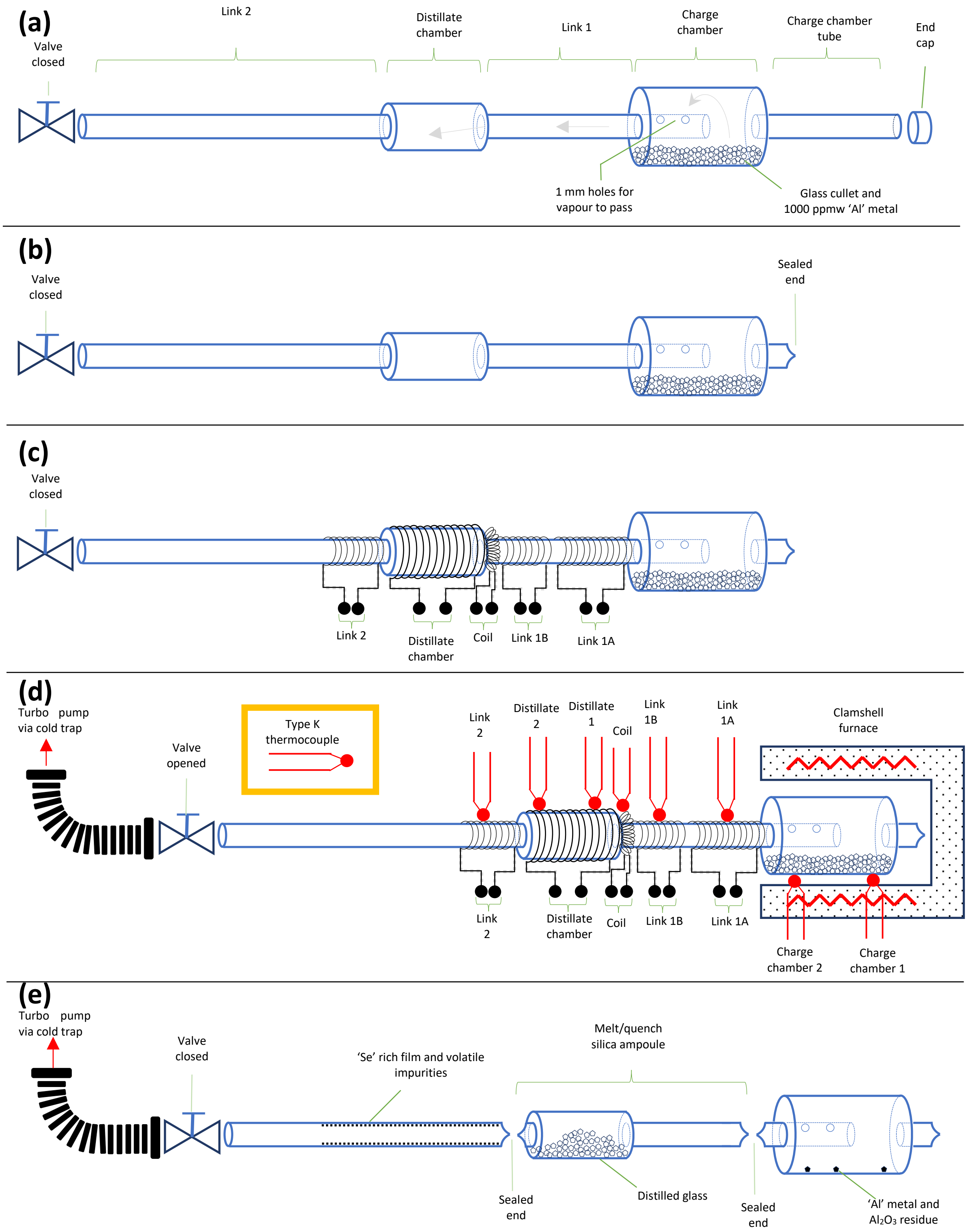

*Figure 7-9: Diagrams showing stages of assembly for silica glass distillation rig used for distillation of undoped chalcogenide glass: **(a)** initial configuration of rig, **(b)** sealed rig, **(c)** heating coils connected to rig, **(d)** type-K thermocouples and vacuum system connected to rig, and **(e)** sealed rig after distillation.*

The distillation rig was then covered with pieces of aluminosilicate thermal blanket to insulate the rig during the distillation process while aiding temperature control of the heating coils. These blanket sections were affixed such that they could be briefly removed to observe the distillation progress without hampering the heating coils.

During the distillation procedure, the eight temperature zones were subjected to concurrent heating schedules while under continuous vacuum. Upon completion of the distillation process the distillation rig was allowed to cool to room temperature, the insulation, thermocouples, and heating coils were then removed.

During the distillation process volatile impurities would condense onto the cool inner wall of the ‘Link 2’ section (*see Figure 7-9 (e)*), while the ‘Link 1’ section tube would remain clear. Thus, the distillation rig was flame sealed using an oxy-propane torch between the distillate chamber and the link tube to form a melt/quench ampoule, as illustrated in Figure 7-9 (e). This sealed ampoule was then subjected to the standard melt/quench procedure to homogenise the distilled glass (*see Appendix 7.1.5*).

7.1.7 Polished bulk glass preparation:

Bulk glass samples were disc shaped pieces of glass cut from larger annealed glass rods, using an oil lubricated diamond saw (*Buehler, IsoMet equipped with a Leco diamond blade*). After cutting, the rough piece of glass was affixed to a polishing jig using paraffin wax, each side was then ground and polished with progressively finer polishing compounds until the desired surface finish was achieved. After polishing each side of the sample was rigorously cleaned to remove any paraffin wax residue using isopropanol (see Table 7-3) in an ultrasonic bath for ~ 60 seconds followed by a gentle drying with lens tissue (see Table 7-4).

The polishing process resulted in two parallel polished faces each with a slightly convex surface, which was desirable for the co-extrusion process in Appendix 7.1.9, and acceptable for bulk glass absorption measurements in Appendix 7.2.1. However, samples intended for MIR ellipsometry, in Section 3.1.2.4, had both sides flattened in a vacuum hot press, between two tungsten carbide anvils (*nominal flatness of* $< \lambda/10$ *at 632 nm*). Additional details on polishing and vacuum hot pressing process can be found in [77]. After vacuum-hot pressing, one side of the sample was intentionally roughened with 120 grit sandpaper, to try to eliminate any specular reflections.

Samples intended for bulk PL emission measurements (see Section 7.2.4.3) had three adjacent faces of a cuboid shaped bulk samples were prepared to a 1 µm surface finish. The remaining three faces were roughened with 120 grit sandpaper to reduce specular Fresnel reflections.

7.1.8 Cladding tube extrusion:

A cylindrical chalcogenide glass rod was inserted into a homemade hydraulic hot press fitted with a three holed ‘spider die’, as shown in Figure 7-10 (a). The glass sample was heated above its ‘T_g’ before pressure was applied to avoid causing a fracture. The cylindrical glass-melt was then forced through the spider die, into three separate streams, before recombining into a tube with an inner diameter ~1 mm and an outer diameter ~10 mm on exiting the die as illustrated in Figure 7-10 (b). Tube extrusions were performed under a flowing dry N_2 atmosphere. The resulting cladding tubes were used as the ‘*tube*’ in the ‘rod in tube’ method for the fabrication of a SIF.

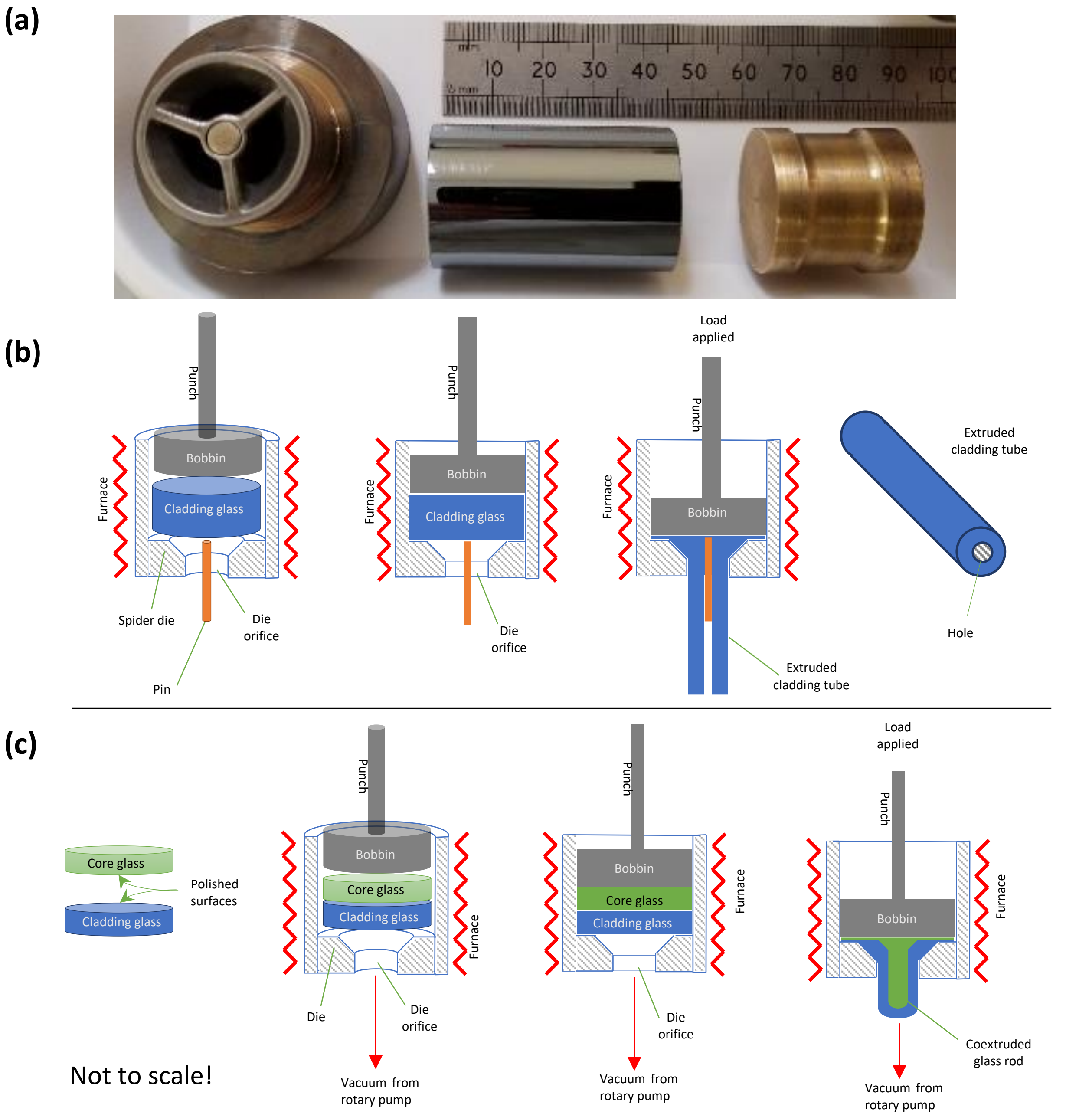

Figure 7-10: Showing ***(a)*** *image of spider die cladding glass billet and bobbin,* ***(b)*** *illustration of tube extrusion process to produce cladding tube, and* ***(c)*** *illustration of co-extrusion process to produce a step-index glass rod.*

7.1.9 Co-extrusion core and inner cladding rod:

Co-extrusion of two chalcogenide glass samples to form a step index glass rod followed a similar procedure to that found in [159,206] and illustrated in Figure 7-10 (c). Wherein, two separate chalcogenide glass rods were prepared for co-extrusion. The mating surfaces of the two polished bulk samples were meticulously cleaned in an ultrasonic bath with isopropanol. The cleaned glass billets were then carefully stacked vertically together in the extruder barrel, core glass on top and cladding glass below, with their convex surfaces touching at a single location, as illustrated in Figure 7-10 (c).

This stacked configuration was done to evacuate the laboratory atmosphere or any outgassing, between the stacked samples during co-extrusion. The stacked glass assembly was placed into a homemade hydraulic hot press fitted with a die with a single circular orifice (*3.2 mm inner diameter*). During co-extrusion a heating schedule was applied while under a continuous vacuum. Force was applied to the glass charge stack only above the glass 'T_g' to avoid causing a fracture. The cylindrical now supercooled-melt was forced through the die, into a single step-index glass rod comprised of both the core and cladding glass (see Figure 7-10 (c)).

7.1.10 Glass fibre drawing:

Glass rods were drawn to either fibre or cane using a customised Heathway draw-tower fitted with a radio frequency furnace, housed in a class 10,000 clean room, using a general configuration like that found in [120,146,102]. This process entailed heating a narrow region of the glass rod above its 'T_g', using a graphite susceptor. The glass rod in a 'supercooled liquid' state was initially pulled into a stream under the influence of gravity (*see inset (a) in* Figure 7-11).

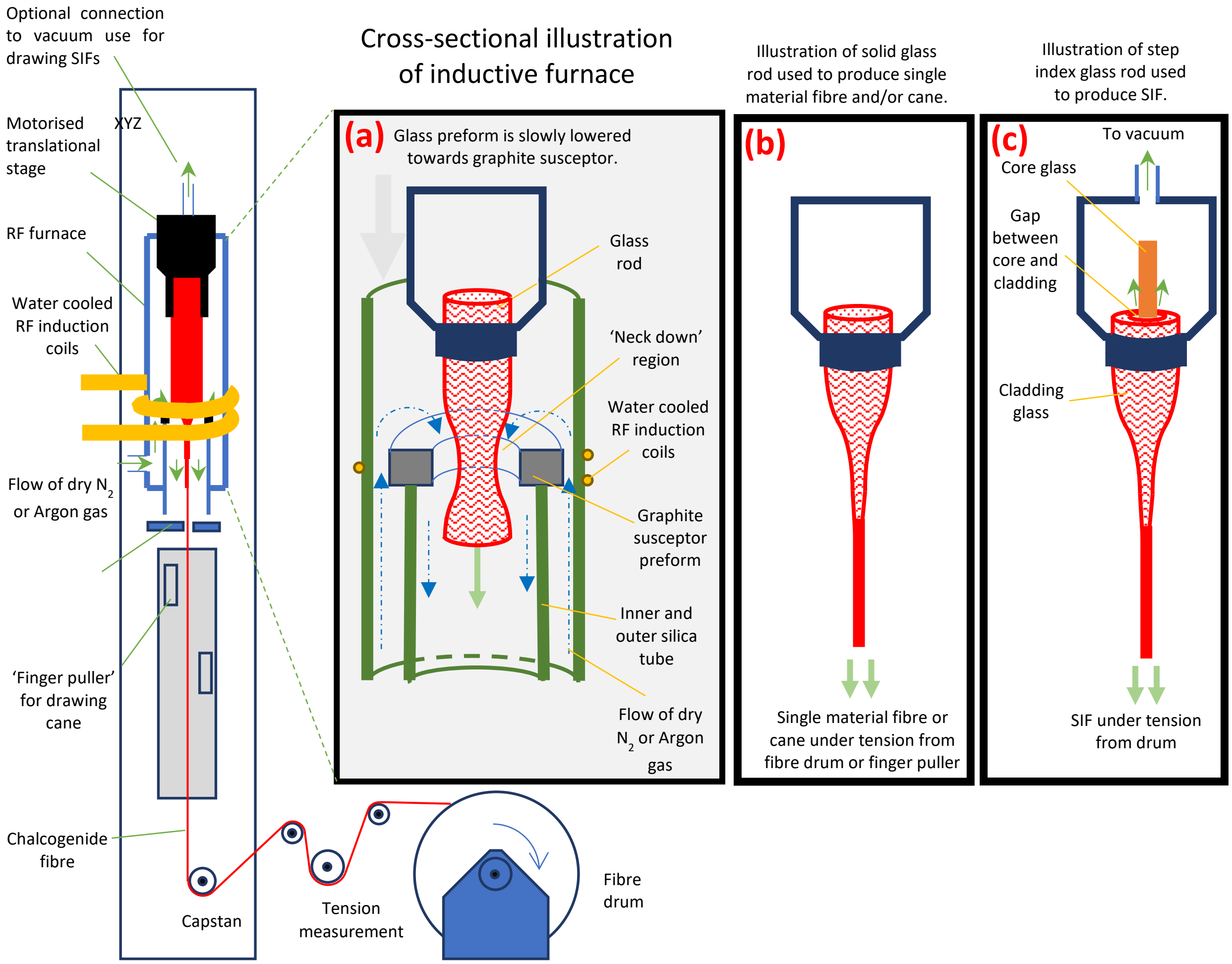

*Figure 7-11: Illustration of equipment configuration used for fibre drawing process, with insets showing **(a)** initial neckdown of glass rod, **(b)** single material fibre drawing, and **(c)** SIF drawing.*

Axial tension was then applied to form a continuous stream of glass which rapidly solidified upon exiting the induction furnace, as illustrated in either inset (b) or (c) in Figure 7-11. The outer diameter of the glass exiting the furnace was controlled by varying the amount of heat applied to the glass rod and axial tension on the solidified glass exiting the induction furnace. Fibre was spooled onto a drum, and cane was stored as short straight lengths (~*0.7 m long*). For SIF drawing the assembled core and cladding rod were co-drawn to a SIF while a vacuum was applied to the region between the core and cladding to prevent the formation of unwanted gaps / holes at the core/cladding interface as illustrated in inset (c) in Figure 7-11.

7.1.11 Propylamine etching:

Propylamine etching was carried out on either annealed glass rods (~ *10 mm outer diameter*), or un-annealed cane (*between 500 µm to 1500 µm outer diameter*). Chalcogenide glass samples were etched in propylamine at room temperature (*20-27 °C*) and 1 atmosphere (~*101 kPa*) in either a silica glass ampoule or plastic covered soda-lime-silica glass vial, while in a fume hood. Etched samples were then rinsed in acetone followed by isopropanol then kept under vacuum awaiting fibre drawing. Note, further information on propylamine etching process employed can be found in [97].

7.1.12 SIF fabrication and drawing:

SIF were drawn from specially prepared glass rods comprised of two materials of differing refractive index. These glass rods were assembled using the ‘rod in tube’ method. Prior to assembly of the ‘rod in tube’ to obtain suitable lengths of cane and cladding tube, these were scored and fractured. Cutting using a diamond saw was not done to avoid introducing additional contaminants on the mating surfaces. The cane (*500 µm ≤ OD ≤ 980 µm*) was then inserted into the extruded cladding tube (ID ~1 mm and OD ~10 mm), while under laboratory atmosphere, prior to fibre drawing. The assembled glass rod was affixed to a special glass rod holder, similar to that described in [146] and illustrated in inset (c) of Figure 7-11, prior to fibre drawing, to allow the space between the core and the cladding to be under continuous vacuum (~40 kPa) during the fibre drawing.

7.1.13 Glass sample description code:

A coding system was previously developed within the Mid-Infrared Photonics Group, George Green Institute for Electromagnetics Research to identify each glass sample and fibre produced. Each sample code was divided into four data fields; the first field described the sample type and was represented by a single letter. Samples starting with the letter '**M**' denoted a bulk glass melt, while the letter '**F**' referred to fibre or cane, and the letter '**E**' referred to an extruded glass rod or tube. The second field was a three-digit number. The next field indicated if the sample was RE^{3+} doped. Note, if the sample was doped the letters '**RE**' would be present immediately after the three-digit number. Conversely, the letters '**RE**' would be absent after the three-digit number if the sample was undoped. The final field identified the initials of the individual(s) responsible for producing the sample.

The following are some examples of the sample coding system:

- M228REJN(RC) referred to; bulk glass melt number 228, RE-cation doped, produced by JN and RC.
- F130RERC referred to fibre number 130, RE^{3+} doped, produced by RC.
- E090DF(JN) referred to extrusion number 90, undoped, produced by DF and JN.
- E094REDF(JN) referred to extrusion number 94, RE^{3+} doped, produced by DF and JN.

7.2 Measurement methodology:

The following sections outline how the various spectroscopic measurements were performed.

7.2.1 Bulk glass absorption measurements:

An FTIR spectrometer was used for bulk glass absorption measurements, it was used to generate, and analyse broadband IR light transmitted through a chalcogenide glass sample. Figure 7-12 shows a simplified internal layout of the FTIR spectrometer. The FTIR spectrometer was equipped with two broadband IR light sources, items 3 and 4 in Figure 7-12, which were selected based on the spectral region under evaluation. A Michelson interferometer, equipped with an interchangeable beam splitter, item 7 in Figure 7-12, was used to modulate the selected broadband IR light source. The FTIR spectrometer was equipped with two internal detectors, items 10 and 11 in Figure 7-12, for measurements using the internal sample compartment. Additionally, the FTIR was equipped with two external detectors for the optical loss measurements, described in Section 7.2.2. NIR and MIR bulk glass absorption measurements were each accomplished using an identical two-step process. The sample compartment of the FTIR spectrometer was purged with dry air to maintain a consistent atmospheric concentration throughout each portion of the absorption measurement.

A ‘background’ absorption spectrum, with no glass sample in the FTIR spectrometer was first collected. Upon completion of the background measurement, a polished bulk glass sample was inserted into the sample compartment, in the path of a broad band IR beam, and the compartment was close, then allowed to purge (*typically for ~20 minutes*) to reduce atmospheric absorptions to a value consistent with the background measurement. The absorption spectrum was then collected, and any 'background' absorptions were then removed using Bruker OPUS (*version 3.1 build*) control and data acquisition software. The host glass contributions for bulk absorption spectra presented throughout Section 4.2 were numerically removed using the 'Baseline Fit' function in Matlab.

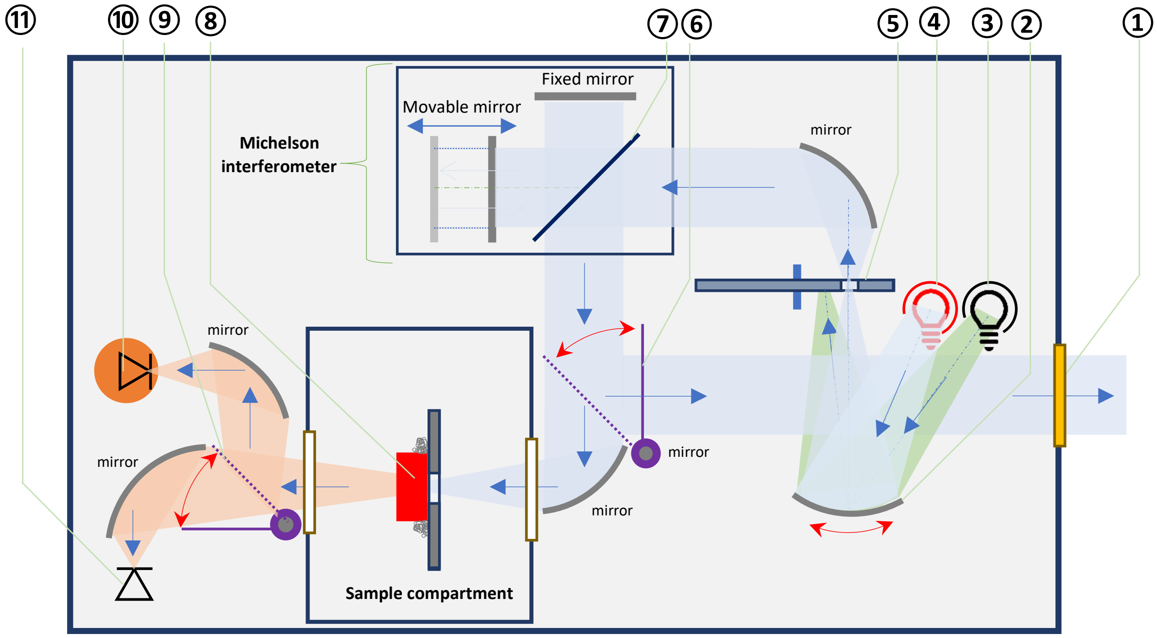

1. 'KBr' (*potassium bromide*) window, 2 mm thick.
2. Movable mirror to select between two broadband light sources.
3. Tungsten lamp used for the visible/NIR spectral region.
4. Globar© source for the NIR/MIR spectral region.
5. Aperture wheel to select measurement resolution.
6. Movable mirror to direct light between internal sample compartment and external window.
7. Beam splitter for Michelson interferometer:
    a. CaF_2 (*calcium fluoride*) beam-splitter for the visible/NIR spectral region.
    b. KBr beam-splitter for the NIR/MIR spectral region.
8. Polished bulk chalcogenide glass sample attached with blu tack putty to a vertical metal sample holder with a clear aperture.
9. Movable mirror to direct light between one of two detector locations.
10. Room temperature InGaAs (*indium gallium arsenic*) detector used for the visible/NIR spectral region.
11. Room temperature DTGS (*deuterated triglycine sulfate*) detector used for the MIR spectral region.

Note, optical path inside the FTIR spectrometer was purged with dry air from an FTIR purge gas generator (*Parker Filtration, #75-52*) to reduce both CO_2 and H_2O.

Figure 7-12: Simplified internal layout of the FTIR spectrometer (Bruker, IFS66/S), and configuration used for bulk glass absorption measurements. Note, this diagram does ***not*** *illustrate all the internal components of the FTIR spectrometer.*

7.2.1.1 Optical cross-sections:

Optical cross sections are used to characterise the probability of an electron undergoing either optical absorption or stimulated emission, wherein a larger cross-sectional area denotes a greater probability of interaction. The 'absorption cross-section' '$\sigma_a(\nu)$' refers to the probability of an electron optically absorbing a photon of specific energy. Conversely, the 'emission cross-section' '$\sigma_e(\nu)$' refers to the probability of an electron undergoing stimulated emission with a specific wavelength of incident light. Absorption cross-sections were obtained by calculating the absorption coefficient 'α' using the following equation derived from the Lambert-Beer law:

$$\Rightarrow \ \alpha = \frac{2.302 \times absorbance}{l}$$

Equation 7-4

Where 'l' is the path length of the sample. Additionally, a sanity check was performed by comparing the absorption coefficient / m to fibre loss measurement. Notably, the presence of overlapping impurity absorptions hamper with the accuracy of these calculations. Thus, these overlapping absorptions are sometimes numerically removed to improve the accuracy of subsequent cross-section calculations [116]. The '$\sigma_a(\nu)$' (*absorption cross-section*) was then calculated as follows:

$$\sigma_a(\nu) = \frac{\alpha(\nu)}{N}$$

Equation 7-5

where ‘N’ is the RE dopant concentration. The corrected measured ‘$\sigma_a(\nu)$’ was transformed into relative ‘$\sigma_{em}(\nu)$’ (*emission cross-section*) spectra using the McCumber method [33,207,208] using the following equation:

$$\sigma_{em}(\nu) = \sigma_{abs}(\nu) \times exp^{\left(\frac{E_0 - h\upsilon}{k_b T}\right)}$$ *Equation 7-6*

where ‘E_0’, is as the net free energy required to excite RE^{3+} cation from the initial relaxed state to an excited state at temperature ‘T’ (Kelvins) [209,210]. The Füchtbauer–Ladenburg equation was then used to convert the relative emission cross-section spectra into absolute cross sections [209] by means of the following equation:

$$\sigma_{em}(\lambda) = \frac{\bar{\lambda}^4}{8\pi c n^2 \tau_{rad}} \times \frac{I(\lambda)}{\int I(\lambda).d\lambda}$$ *Equation 7-7*

Where ‘τ_{rad}’ is the spontaneous emission lifetime of the transition, ‘c’ is the speed of light in a vacuum, ‘n’ is the refractive index, and $\bar{\lambda}$ is the central wavelength of the emission [211–213].

7.2.2 Fibre optical loss measurement:

An FTIR spectrometer, item 1, in Figure 3-3, was utilised to generate modulated broadband IR light, mirrors were then used to focus this light into the cleaved ‘launch-end’ of a fibre sample. The ‘cut-back’ method was employed to compare the intensity of broadband light transmitted through the fibre sample as it was incrementally cleaved towards the ‘launch end’. The position of the ‘launch-end’ was kept constant throughout the measurement to ensure a constant insertion loss for the modulated broadband IR light. At the opposite end of the fibre, the transmitted light was focused onto one of two detectors, items 10 and 11 in Figure 3-3, using mirrors. Each detector measured the intensity of transmitted light for a specific spectral region. Both detectors were installed on a sliding platform, item 12 in Figure 3-3, to switch between detectors during measurements to avoid disrupting the equipment and sample alignment.

A test piece of fibre was used to align the equipment configuration shown in Figure 3-3. The starting length of the evaluated sample was decided by finding the maximum length of fibre through which transmitted IR light was detectable by both detectors (*typically around 3 m for* RE^{3+} *doped fibres*). Once the sample piece was installed the alignment was re-optimised and the position of the ‘launch-end’ was left undisturbed for the remainder of the measurement.

The fibre sample was progressively cleaved back toward the ‘launch-end’ using a fibre cleaver (*Thorlabs Vytran®, LDC-401*) using a procedure similar to that described in [214]. After each ‘cut-back’ the ‘mirror cleave’, the cleaved end removed from the sample fibre, was inspected using an optical microscope (*Vickers Instruments, model M171484*) to judge ‘cleave quality’ and measure fibre diameter (*viewed in reflection with visible illumination, see Figure 3-5 (c)*). The cleaving parameters used prioritised ‘cleave quality’, that is, it maximised the ‘mirror’ region of the cleave fibre end, while the cleave angle was ignored, (see *Section 7.2.3 for fibre cleave angle measurement*). The cleaving process exposed pristine glass at the ‘cut-back’ end of the fibre importantly this surface was not cleaned with any chemicals after cleaving. Furthermore, measurements were typically taken within minutes of cleaving. The ‘cut-back’ procedure was repeated several times, typically around 9 to 12 ‘cut-backs’ each between 60 to 100 cm long for

RE^{3+} doped fibres, unless otherwise stated. The attenuation spectrum was then calculated using Equation 3-2 and the process flow chart shown in Figure 3-4.

7.2.3 Cleaved SIF sample preparation:

The preparation SIF samples with approximately 90° cleaved end faces employed the flowchart in Figure 5-1. SIF samples were cut to a desired length by cleaving both end faces at approximately 90° using a fibre cleaver (*Thorlabs Vytran®, LDC-401*) while following a procedure similar to that described in [214]. The cleaving parameters used prioritised 90° cleave angle. Additionally, the cleaving parameters used were specific to the SIF composition and diameter and were obtained via trial and error and then optimised to minimise cleave angle variation. The 'mirror cleave' for each end was inspected under an optical microscope, using 'the end inspection' equipment configuration shown in Figure 3-5 (c) to evaluate SIF dimensions, cleave quality, and cleave angle. The cleaved end faces were each inspected for defects.

The angles of each 'mirror cleave' were then evaluated under an optical microscope, using 'the side inspection' equipment configuration shown in Figure 3-5, viewed parallel to the cleaved end, using a homemade 3D printed jig (*designed by Dr David Furniss*), which allowed the cleaved SIF to be rotated axially, as illustrated in Figure 5-2 (a) and (b). The cleave was imaged at 0° then the SIF was rotated axially 90° and imaged again. The cleave angle at 0° and 90° rotation were then measured using ImageJ software. Cleave angles within the range of 90° ± ≤ 1° were deemed acceptable.

Note, the 'mirror cleave' was used for the initial optical inspection and the cleave angle measurement to avoid any potential damage to the actual SIF sample. Additionally, mist and hackle in the cladding region were considered acceptable assuming the cleave angle was satisfactory.

SIF samples were cleaned of any surface debris using isopropanol (see Table 7-3) in an ultrasonic bath for ~ 30 seconds followed by a gentle jet of air directed at the cleaved end from an FTIR purge gas generator (*Parker Filtration, #75-52, with reduced concentrations of* CO_2 *and* H_2O). After cleaning the cleaved ends of the SIF sample were inspected under an optical microscope, using 'the end inspection' equipment configuration shown in Figure 3-5 (c) to ensure the absence of debris or residue.

7.2.4 PL (photoluminescence) emission spectroscopy measurement:

PL emission measurements could use a variety of equipment configurations for each combination of sample type and excitation source. Each configuration could be sub-divided into four major subsections, namely launch optics (see Section 7.2.4.1), sample preparation (see Section 7.2.4.2), collection/detection (see Section 7.2.4.3), and control/data acquisition (see Section 7.2.4.4). With all these subsections working together PL emission spectra (see Section 7.2.4.5), and PL emission lifetimes measurements (see Section 7.2.4.6) can be performed.

7.2.4.1 Launch optics:

Each type of excitation laser used for PL emission measurements required different supplemental optical components to efficiently excite the sample as shown in Figure 4-1, insets **A** to **E**. The open beam laser, a 4.150 µm QCL (*quantum cascade laser*), item 3 shown in Figure 4-1, insets **B**, **D** and **E**, required mirrors on kinematic mounts to accurately steer the beam towards the sample.

The beam was passed through a polariser and a quarter wave plate, items 4 and 5 shown in Figure 4-1, to prevent reflections and unpolarised PL emanating from the sample from influencing QCL output power.

The fibre-coupled sources, item 1 within insets **A**, and **C** in Figure 4-1, delivered the laser light to the sample, at which point it was collimated using a fibre collimation package, item 2 in Figure 4-1. A collimated beam was used to excite powdered samples, item 8 (b) in Figure 4-1, due to the large surface area, see insets **C** and **D** in Figure 4-1. Fibre samples, item 8 (a) in Figure 4-1, were excited/illuminated with a beam focused onto a cleaved end face, shown in Figure 4-1, insets **A** and **B**.

7.2.4.2 Sample preparation and mounting:

Samples for PL emission measurements could be fibres, powdered glass, or bulk glass, items 8(a), 8(b) and 8(c), respectively, shown in Figure 4-1. The following gives a description of how each sample type was prepared and mounted:

- Cleaved fibre samples were prepared using process described in Appendix 7.2.3. Cleaved fibre samples were then mounted on a V-groove fibre holder using either magnets or UV curable polymer, item 9 in Figure 4-1, inset **F**. SIF samples were sometimes also coated with the liquid metal InGaSn alloy (*Galinstan*), item 10 in Figure 4-1, for cladding mode-stripping and thermal management, using the procedure described in Section 7.2.3. Fibre samples were excited/illuminated in a co-linear, ‘End-collection’, configuration relative to the launch laser and collection optics.

- Powdered chalcogenide glass samples were prepared by grinding either pieces of bulk glass or single material fibre in an agate mortar and pestle inside a glovebox (*MBraun, MB 150B-G*) while under a dry nitrogen atmosphere (*< 0.7 ppm H_2O and < 0.3 ppm O_2*). The glass was ground to a mostly uniform particle diameter and sealed, while under an inert N_2 atmosphere, in an in-house made 3D printed powder sample holder equipped with CaF_2 windows shown in Figure 4-1, inset **G**. The powdered glass was kept sealed to avoid oxidation, absorption, and adsorption of water and other atmospheric molecules during PL emission measurements. Note, powdered samples were excited in a co-linear configuration relative to the launch laser and collection optics.
- Polished bulk glass samples were prepared using process described in Appendix 7.1.7. The polished bulk sample was mounted in a 'Side-collection' configuration as shown in Figure 4-1, inset **H**, wherein a focused beam was directed at an edge between two polished sides on the bulk sample, while PL was collected orthogonally to minimise reabsorption.

7.2.4.3 Collection/detection equipment configuration:

Figure 4-1, inset **I**, shows how RE^{3+} PL emanating from a sample was modulated, collected, filtered, focused then separated into its constituent wavelengths and evaluated.

An optional optical chopper, item 11 in Figure 4-1, was positioned as close as possible to the sample to amplitude modulate any emitted RE^{3+} PL emissions at a user defined modulation frequency. Note, this mechanical chopper was used only for PL emission spectrum measurements, PL lifetime measurements exclusively employed electronic modulation of the excitation source, using the procedure described in Section 4.1.1.3.

Lenses made of either CaF_2 or Ge were used for the collection optics, items 11 and 14 in Figure 4-1. CaF_2 lenses were used for the visible/NIR/MIR spectral range, while Ge lenses were preferentially used for the MIR (*greater than 3 µm*) spectral range, as per their respective specifications [215,216].

An optional interchangeable optical filter, item 13 in Figure 4-1, was positioned to either transmit or attenuate specific spectral ranges. The type of filter selected, LWP (*long wave pass*), SWP (*short wave pass*) and BP (*band pass*) was based on the spectral range of the desired measurement. Table 7-15 lists the filters used. Note, the choice of collection optics, items 11 and 14 in Figure 4-1, could also act as an optical filter, with 'Ge' lenses effectively acting as 2.000 µm LWP filters.

Table 7-15: List of individual optical filters, item 13 in Figure 4-1, used for PL emission measurements.

Filter type	Cut on, cut off or centre wavelength (µm)	Manufacturer	Model
BP	3.800	Spectrogon	BP-3800-180nm
LWP	2.000	Unknown	-
LWP	2.484	Northumbria Optical Coatings Ltd	SLWP-2484-001086
LWP	2.505	Northumbria Optical Coatings Ltd	SLWP-2505-001089
LWP	2.945	Northumbria Optical Coatings Ltd	SLWP-2945-000743
LWP	3.407	Northumbria Optical Coatings Ltd	SLWP-3407-000189
LWP	3.981	Northumbria Optical Coatings Ltd	SLWP-3981-000145
LWP	4.203	Northumbria Optical Coatings Ltd	SLWP-4203-001138
BP	4.136	Northumbria Optical Coatings Ltd	SBP-4136-001508
LWP	4.630	Northumbria Optical Coatings Ltd	SLWP-4630-000434
LWP	6.386	Northumbria Optical Coatings Ltd	SLWP-6386-000297
SWP	3.351	Northumbria Optical Coatings Ltd	SSWP-3351-001063
SWP	4.421	Northumbria Optical Coatings Ltd	SWP-17220-1-1-17

Note, **BP** (*Band pass*), **LWP** (*long wave pass*) and **SWP** (*short wave pass*).

A monochromator, item 15 in Figure 4-1, based on a 'Czerny-Turner' design with interchangeable diffraction gratings was used to spatially separate the incoming broadband RE^{3+} PL into its constituent wavelengths while directing selected wavelengths to the monochromator exit. The diffraction grating used was selected based on the spectral range of the measurement.

A detector, item 16 in Figure 4-1, was positioned at the exit of the monochromator to measure the intensity of the wavelength selected by the monochromator. The choice of detector was based on the spectral range of the measurement and measurement type. The detector output was sent to either a lock-in amplifier for emission spectrum measurements or a USB oscilloscope for PL lifetime measurements, items 21 and 19, respectively, in Figure 4-1.

7.2.4.4 Control/data acquisition equipment configuration:

Figure 4-1, inset **J**, shows how the electronic components in the equipment configuration were interconnected and controlled. Amplitude modulation of emissions emanating from a sample was done at a fixed user defined frequency. Modulation was accomplished either by using an optical chopper, item 11 in Figure 4-1, or via electronic modulation of the excitation source using a waveform generator, either item 17 or 19 in Figure 4-1. The modulation frequency was dependent on the type of measurement being performed and is discussed further in Section 4.2.6.2. Wavelength selection of the emissions emanating from the samples was accomplished using a monochromator, item 15 in Figure 4-1, which was controlled by a data acquisition computer, item 18 in Figure 4-1. PL lifetime measurements were accomplished using PicoScope6™ software also running on the data acquisition computer. This was used to record intensity measurements as a function of time while time averaging measurements to improve the overall SNR (*signal to noise ratio*) of the measurement by decreasing the variance of the noise associated with the signal and detection system.

7.2.4.5 PL emission spectrum measurements:

The sample was exposed to either a CW source while the resultant RE^{3+} PL was modulated by an optical chopper, or the sample was exposed to an electronically modulated pump source, causing the resulting RE^{3+} PL to be modulated. The resulting amplitude modulated emissions emanating from the sample were collected and evaluated using the collection/detection subsection described in Section 7.2.4.3. Intensity measurements of detected RE^{3+} PL were made using a lock-in amplifier, item 21 in Figure 4-1, with the modulation frequency of the RE^{3+} PL as a reference signal, thus improving the SNR by ignoring incoherent noise [217,218]. The PL emission spectrum was obtained by taking intensity measurements on the emitted RE^{3+} PL, at uniform wavelength intervals, using the control/data acquisition equipment described in Section 7.2.4.4, were measurement parameters such as wavelength interval, and dwell time were specified. These intensity measurements were then plotted against wavelength to produce the PL emission spectrum.

System spectral response: Wavelength-dependent variations introduced to PL emission spectrum measurements, specifically due to the collection/detection subsection described in Section 7.2.4.3, were evaluated for each equipment configuration used. The spectral response of each collection/detection configuration was characterised by recording the IR spectrum emitted from a Globar situated where a photoexcited RE^{3+} doped sample would otherwise be in the equipment configuration (*see insets* ***F****,* ***G****, and* ***H*** *in Figure 4-1*) without the launch optics subsection. A Globar source was used as its IR emission spectrum could be approximated to a blackbody source [219–221]. The theoretical spectral radiance ‘I(λ)’ of the Globar, was calculated by measuring its temperature ‘T (°K)’ with a pyrometer (*Minolta/Land, Cyclops 152A*), and using Planck’s law [219], given in the following equation.

$$B_{\lambda}(\lambda, T) = \frac{2hc^2}{\lambda^5} \times \frac{1}{exp^{\left(\frac{hc}{\lambda k_b T}\right)} - 1} \qquad \text{Equation 7-8}$$

where ‘h’ is Planck’s constant, ‘k_b’ is the Boltzmann constant and ‘c’ speed of light in a vacuum. The calculated spectral radiance ‘I(λ)’ and the measured Globar intensity spectrum ‘L(λ)’ were then normalised to their respective peak intensities. The wavelength dependent sensitivity ‘S(λ)’ of the detection system was then given by the normalised spectral radiance ‘I(λ)’ divided by the normalised measured intensity spectrum ‘L(λ)’ as given in the following equation.

$$S(\lambda) = \frac{I(\lambda)}{L(\lambda)} \qquad \text{Equation 7-9}$$

Transformation of uncorrected emission spectra to corrected emission spectra, presented in Section 4.2 was achieved by multiplying the wavelength dependent sensitivity ‘S(λ)’ by the uncorrected measured spectrum.

7.2.4.6 PL lifetime measurements:

An electronically modulated pump source, with a 50 % duty cycle, was used to excite a sample resulting in amplitude modulated PL emissions. These emissions were collected and evaluated at a fixed user defined wavelength using the collection/detection subsection described in Section

7.2.4.3. The collection/detection subsection allowed a narrow spectral range of PL light (*typically less than 50 nm in spectral width*) to be selected and evaluated by the detector.

PL Intensity measurements were made using a USB oscilloscope, item 19 in Figure 4-1. During the switch off portion of the 50 % duty cycle for the pump source, the decaying PL emission intensity from the sample was recorded as a function of time, using a USB oscilloscope. The modulation frequency of the pump was selected to allow the longest constituent τ_{rad} (*PL lifetime*), exhibited in the RE^{3+} dopant, to decay to approximately zero intensity during the off portion of the 50 % duty cycle. Thus, half of the modulation period was set to be at least eight times the longest τ_{rad} of the RE^{3+} dopant. The repetitive nature of the electronic modulation of the pump source allowed the decaying PL emission intensity, from each off portion of the 50 % duty cycle, to be averaged over several thousand iterations (*typically between 5000 to 10000 averages, depending on PL intensity*).

System response time: This characterisation entailed a lifetime measurement at the pump source wavelength without a RE^{3+} doped sample. Due to the small value of these system response times the presented lifetimes in Section 4.2 were not corrected unless otherwise stated. Table 7-16 shows the response time of the collection system with each pump source listed in Figure 4-1.

Table 7-16: Response times of pump sources listed as item 1 or 3, in Figure 4-1:

Pump source	Response time / µs		Pump source	Response time / µs
Tuneable source (without EDFA)	< 1		1.940 µm	< 1
Tuneable source (with EDFA)	∞ (Does not switch off)		2.013 µm	< 100
1.700 µm	not evaluated		4.150 µm	< 1

7.3 Equipment configuration code:

A coding system was developed by the author to efficiently describe the various equipment configurations employed was implemented. This coding was necessary to describe the multitude of equipment configurations employed to obtain the presented results throughout Section 4.2. The coding system was divided into three data fields each based around one of the three major subsections, which comprise the optical circuit in the equipment configuration, namely, the 'launch optics', 'sample' and 'collection/detection' subsections, see insets **A** to **I** in Figure 4-1 and their associated interchangeable items. Each equipment configuration code comprised:

1) Choice of 'Launch optics' subsection: Options included insets **A** to **E** in Figure 4-1, along with the option of interchangeable items within the selected subsection. Note, each subsection, excluding subsection **D**, contained interchangeable items such as the laser source and the focusing lens, items 1 and 7, respectively, in Figure 4-1.
2) Choice of 'Sample' subsection: Selections included insets **F** to **H** in Figure 4-1, along with the choice of interchangeable items within the selected subsection. Note, only subsection **F**, contained interchangeable items relating to the fibre mounting options and cladding mode stripper, items 9 and 10, respectively, in Figure 4-1.
3) The 'Collection and detection' subsection, shown as inset **I** in Figure 4-1. The choice of interchangeable items within this subsection included the collection optics, optical filter, monochromator, and detector, items 12 to 16 in Figure 4-1.

The following are three examples of this equipment configuration coding:

	Launch optics	**The sample**	**Collection/detection**
Example 1:	**A[1_a- 7_a]**	**F[9_b- 10]**	**I[12_a- $13_{3.407\ LWP}$- 14_a- 15_{aii}- 16_b]**
Description of example 1 code:	A: Refers to 'inset A' in Figure 4-1. **1_a**: Refers to 'item 1(a)', Tuneable source. **7_a**: Refers to 'item 7(a)', Aspheric lens, f = 5.95 mm focusing lens on XYZ translational stage.	F: Refers to 'inset F' in Figure 4-1. **9_b**: Indicated 'item 9(b)', UV curable polymer, was used. **10**: Indicated that 'item 10', Galinstan cladding mode-stripper was used.	I: Refers to 'inset I' in Figure 4-1. **12_a**: Refers to 'item 12(a)', Ge lens, f = 12.5 mm collection lens on XYZ stage. **$13_{3.407\ LWP}$**: Refers to 'item 13', an optical filter, specifically a 3.407 µm LWP filter listed in Table 7-15. **14_a**: Refers to 'item 14(a)', Ge lens, f = 12.5 mm focusing lens on XYZ stage. **15_{aii}**: Refers to 'item 15(a)(ii)', Bentham monochromator, equipped with grating 2. **16_b**: Refers to 'item 16(b)', an MCT detector on an XYZ stage.
Example 2:	**A[1_d- 7_a]**	**F[9_a]**	**I[12_a- $13_{3.351\ SWP}$- 14_a- 15_{ai}- 16_b]**
Description of example 2 code:	A: Refers to 'inset A' in Figure 4-1. **1_d**: Refers to 'item 1(d)', 2.013 µm source. **7_a**: Refers to 'item 7(a)', Aspheric lens, f = 5.95 mm focusing lens on XYZ translational stage.	F: Refers to 'inset F' in Figure 4-1. **9_a**: Indicated 'item 9(a)', magnets, were used. **10**: Indicated that 'item 10', Galinstan cladding mode-stripper was used.	I: Refers to 'inset I' in Figure 4-1. **12_a**: Refers to 'item 12(a)', Ge lens, f = 12.5 mm collection lens on XYZ stage. **$13_{3.351\ LWP}$**: Refers to 'item 13', an optical filter, specifically a 3.351 µm SWP filter listed in Table 7-15. **14_a**: Refers to 'item 14(a)', Ge lens, f = 12.5 mm focusing lens on XYZ stage. **15_{ai}**: Refers to 'item 15(a)(i)', Bentham monochromator, equipped with grating 1. **16_b**: Refers to 'item 16(b)', an MCT detector on an XYZ stage.
Example 3:	**D[]**	**G[]**	**I[12_b- 13_{none}- 14_b- 15_{ai}- 16_a]**
Description of example 3 code:	D: Refers to inset 'D' in Figure 4-1. Note, this subsection has no interchangeable items.	G: Refers to 'inset G' in Figure 4-1. Note, this subsection has no interchangeable items.	I: Refers to 'inset I' in Figure 4-1. **12_b**: Refers to 'item 12(b)', CaF_2 lens, f = 40 mm collection lens on XYZ stage. **13_{none}**: Refers to 'item 13', an optical filter, specifically no optical filter was used. **14_b**: Refers to 'item 14(b)', CaF_2 lens, f = 40 mm focusing lens on XYZ stage. **15_{ai}**: Refers to 'item 15(a)(i)', Bentham monochromator, equipped with grating 1. **16_b**: Refers to 'item 16(a)', an InGaAs detector on an XYZ stage.

8 Bibliography:

[1] J.S. Sanghera, L. Brandon Shaw, I.D. Aggarwal, Chalcogenide Glass-Fiber-Based Mid-IR Sources and Applications, IEEE J. Sel. Top. Quantum Electron. 15 (2009) 114–119. https://doi.org/10.1109/JSTQE.2008.2010245.

[2] B. Bureau, C. Boussard, S. Cui, R. Chahal, M.L. Anne, V. Nazabal, O. Sire, O. Loréal, P. Lucas, V. Monbet, J.-L. Doualan, P. Camy, H. Tariel, F. Charpentier, L. Quetel, J.-L. Adam, J. Lucas, Chalcogenide optical fibers for mid-infrared sensing, Opt. Eng. 53 (2014) 027101. https://doi.org/10.1117/1.OE.53.2.027101.

[3] G. Bellisola, C. Sorio, Infrared spectroscopy and microscopy in cancer research and diagnosis, Am. J. Cancer Res. 2 (2012).

[4] A.B. Seddon, Mid-infrared (IR) - A hot topic: The potential for using mid-IR light for non-invasive early detection of skin cancer *in vivo*, Phys. Status Solidi B 250 (2013) 1020–1027. https://doi.org/10.1002/pssb.201248524.

[5] T. Hocotz, O. Bibikova, V. Belikova, A. Bogomolov, I. Usenov, L. Pieszczek, T. Sakharova, O. Minet, E. Feliksberger, V. Artyushenko, B. Rau, U. Zabarylo, Synergy Effect of Combined Near and Mid-Infrared Fibre Spectroscopy for Diagnostics of Abdominal Cancer, Sensors 20 (2020) 6706. https://doi.org/10.3390/s20226706.

[6] U. Willer, M. Saraji, A. Khorsandi, P. Geiser, W. Schade, Near- and mid-infrared laser monitoring of industrial processes, environment and security applications, Opt. Lasers Eng. 44 (2006) 699–710. https://doi.org/10.1016/j.optlaseng.2005.04.015.

[7] B.M. Walsh, H.R. Lee, N.P. Barnes, Mid infrared lasers for remote sensing applications, J. Lumin. 169 (2016) 400–405. https://doi.org/10.1016/j.jlumin.2015.03.004.

[8] E. Larson, M. Hines, M. Tanas, B. Miller, M. Coleman, F. Toor, Mid-infrared absorption by soft tissue sarcoma and cell ablation utilizing a mid-infrared interband cascade laser, J. Biomed. Opt. 26 (2021). https://doi.org/10.1117/1.JBO.26.4.043012.

[9] N.S. Prasad, Optical Communications in the mid-wave IR spectral band, in: A.K. Majumdar, J.C. Ricklin (Eds.), Free-Space Laser Commun. Princ. Adv., Springer New York, New York, NY, 2008: pp. 347–391. https://doi.org/10.1007/978-0-387-28677-8_8.

[10] L. Flannigan, L. Yoell, C. Xu, Mid-wave and long-wave infrared transmitters and detectors for optical satellite communications—a review, J. Opt. 24 (2022) 043002. https://doi.org/10.1088/2040-8986/ac56b6.

[11] P. Corrigan, R. Martini, E.A. Whittaker, C. Bethea, Quantum cascade lasers and the Kruse model in free space optical communication, Opt. Express 17 (2009) 4355. https://doi.org/10.1364/OE.17.004355.

[12] A. Soibel, M. Wright, W. Farr, S. Keo, C. Hill, R.Q. Yang, H.C. Liu, Free space optical communication utilizing mid-infrared interband cascade laser, in: H. Hemmati (Ed.), San Francisco, California, USA, 2010: p. 75870S. https://doi.org/10.1117/12.845788.

[13] D.H. Titterton, A review of the development of optical countermeasures, in: D.H. Titterton (Ed.), London, United Kingdom, 2004: p. 1. https://doi.org/10.1117/12.610112.

[14] Mid-Infrared Advanced Chemical Laser (MIRACL), Http://Www.Fas.Org/Spp/Military/Program/Asat/Miracl.Htm (1999). https://web.archive.org/web/20070607185251/http://www.fas.org/spp/military/program/asat/miracl.htm (accessed June 8, 2022).

[15] D. Jayasuriya, C.R. Petersen, D. Furniss, C. Markos, Z. Tang, Md.S. Habib, O. Bang, T.M. Benson, A.B. Seddon, Mid-IR supercontinuum generation in birefringent, low loss, ultra-high numerical aperture Ge-As-Se-Te chalcogenide step-index fiber, Opt. Mater. Express 9 (2019) 2617. https://doi.org/10.1364/OME.9.002617.

[16] C.R. Petersen, U. Møller, I. Kubat, B. Zhou, S. Dupont, J. Ramsay, T. Benson, S. Sujecki, N. Abdel-Moneim, Z. Tang, D. Furniss, A. Seddon, O. Bang, Mid-infrared supercontinuum covering the 1.4–13.3 μm molecular fingerprint region using ultra-high NA chalcogenide step-index fibre, Nat. Photonics 8 (2014) 830–834. https://doi.org/10.1038/nphoton.2014.213.

[17] L.B. Shaw, B. Cole, P.A. Thielen, J.S. Sanghera, I.D. Aggarwal, Mid-wave IR and long-wave IR laser potential of rare-earth doped chalcogenide glass fiber, IEEE J. Quantum Electron. 37 (2001) 1127–1137. https://doi.org/10.1109/3.945317.

[18] R. Frerichs, New Optical Glasses with Good Transparency in the Infrared*, J. Opt. Soc. Am. 43 (1953) 1153–1157. https://doi.org/10.1364/JOSA.43.001153.

[19] S. Cotton, Lanthanide and Actinide Chemistry, John Wiley & Sons, Ltd, West Sussex, UK, 2006.

[20] G.H. Dieke, H.M. Crosswhite, The Spectra of the Doubly and Triply Ionized Rare Earths, Appl. Opt. 2 (1963) 675. https://doi.org/10.1364/AO.2.000675.

[21] F.M.A. Sroor, F.T. Edelmann, Lanthanides: Tetravalent Inorganic, in: R.A. Scott (Ed.), Encycl. Inorg. Bioinorg. Chem., John Wiley & Sons, Ltd, Chichester, UK, 2012: p. eibc2033. https://doi.org/10.1002/9781119951438.eibc2033.

[22] T. Li, P. Li, Z. Wang, S. Xu, Q. Bai, Z. Yang, Coexistence phenomenon of Ce^{3+} –Ce^{4+} and Eu^{2+} –Eu^{3+} in Ce/Eu co-doped $LiBaB_9O_{15}$ phosphor: luminescence and energy transfer, Phys. Chem. Chem. Phys. 19 (2017) 4131–4138. https://doi.org/10.1039/C6CP07494D.

[23] K. Oh, U.-C. Paek, T.F. Morse, L. Reinhart, A. Kilian, Photoinduced refractive-index change in Sm^{+2}/Sm^{+3} codoped aluminosilicate fiber by irradiation of an Ar-ion laser, Opt. Lett. 22 (1997) 1192. https://doi.org/10.1364/OL.22.001192.

[24] J. Qiu, K. Miura, T. Suzuki, T. Mitsuyu, K. Hirao, Permanent photoreduction of Sm^{3+} to Sm^{2+} inside a sodium aluminoborate glass by an infrared femtosecond pulsed laser, Appl. Phys. Lett. 74 (1999) 10–12. https://doi.org/10.1063/1.123117.

[25] J. Ueda, M. Katayama, K. Asami, J. Xu, Y. Inada, S. Tanabe, Evidence of valence state change of Ce^{3+} and Cr^{3+} during UV charging process in $Y_3Al_2Ga_3O_{12}$ persistent phosphors, Opt. Mater. Express 7 (2017) 2471. https://doi.org/10.1364/OME.7.002471.

[26] L. Arbelaez, P.-M. Geffroy, A. Aimable, K. Fukuda, E. Béchade, High-purity synthesis of La_2SiO_5 by solid-state reaction between La_2O_3 and different characteristics of SiO_2, Ceram. Int. 46 (2020) 25546–25555. https://doi.org/10.1016/j.ceramint.2020.07.026.

[27] C.E. Moran, G.D. Hale, N.J. Halas, Synthesis and Characterization of Lanthanide-Doped Silica Microspheres, Langmuir 17 (2001) 8376–8379. https://doi.org/10.1021/la0109922.

[28] I. Del Rosal, I.C. Gerber, R. Poteau, L. Maron, Grafting of Lanthanide Complexes on Silica Surfaces: A Theoretical Investigation, J. Phys. Chem. A 114 (2010) 6322–6330. https://doi.org/10.1021/jp101495n.

[29] R.A. Meyers, ed., Encyclopedia of Physical Science and Technology, Academic Press, 2002.

[30] K. Jousten, ed., Handbook of Vacuum Technology, 2nd ed., Wiley-VCH, Germany, 2016.

[31] N. Bohr, *On the constitution of atoms and molecules*, Lond. Edinb. Dublin Philos. Mag. J. Sci. 26 (1913) 1–25. https://doi.org/10.1080/14786441308634955.

[32] Z. Tang, L. Sojka, D. Furniss, J. Nunes, H. Sakr, E. Barney, S. Sujecki, T.M. Benson, A.B. Seddon, Comparative study of praseodymium additives in active selenide chalcogenide optical fibers, Opt. Mater. Express 8 (2018) 3910. https://doi.org/10.1364/OME.8.003910.

[33] P.C. Becker, N.A. Olsson, J.R. Simpson, Erbium-Doped Fiber Amplifiers Fundamental and Technology, in: 1st ed., Academic Press, San Diego, 1999: pp. 5–9, 87–123, 131–137.

[34] L. Sojka, T.M. Benson, D. Furniss, Z. Tang, H. Sakr, A.B. Seddon, S. Sujecki, The Modelling of Fibre Lasers for Mid-Infrared Wavelengths, in: A. Agrawal, T. Benson, R.M. De La Rue, G.A. Wurtz (Eds.), Recent Trends Comput. Photonics, Springer International Publishing, Cham, 2017: pp. 39–75. https://doi.org/10.1007/978-3-319-55438-9_2.

[35] M.J.F. Digonnet, ed., Rare-Earth-Doped Fiber Lasers and Amplifiers, Revised and Expanded, 2nd ed., CRC Press, Boca Raton, FL, 2001.

[36] R.W. Crane, Ł. Sójka, D. Furniss, J. Nunes, E. Barney, M.C. Farries, T.M. Benson, S. Sujecki, A.B. Seddon, Experimental photoluminescence and lifetimes at wavelengths including beyond 7 microns in Sm^{3+} -doped selenide-chalcogenide glass fibers, Opt. Express 28 (2020) 12373. https://doi.org/10.1364/OE.383033.

[37] F. Starecki, A. Braud, N. Abdellaoui, J.-L. Doualan, C. Boussard-Plédel, B. Bureau, P. Camy, V. Nazabal, 7 to 8 µm emission from Sm^{3+} doped selenide fibers, Opt. Express 26 (2018) 26462. https://doi.org/10.1364/OE.26.026462.

[38] F. Starecki, N. Abdellaoui, A. Braud, J.-L. Doualan, C. Boussard-Plédel, B. Bureau, P. Camy, V. Nazabal, 8 µm luminescence from a Tb^{3+} GaGeSbSe fiber, Opt. Lett. 43 (2018) 1211–1214. https://doi.org/10.1364/OL.43.001211.

[39] F. Starecki, G. Louvet, J. Ari, A. Braud, J.-L. Doualan, R. Chahal, I. Hafienne, C. Boussard-Plédel, V. Nazabal, P. Camy, Dy^{3+} doped GaGeSbSe fiber long-wave infrared emission, J. Lumin. 218 (2020) 116853. https://doi.org/10.1016/j.jlumin.2019.116853.

[40] M.F. Churbanov, I.V. Scripachev, V.S. Shiryaev, V.G. Plotnichenko, S.V. Smetanin, E.B. Kryukova, Yu.N. Pyrkov, B.I. Galagan, Chalcogenide glasses doped with Tb, Dy and Pr ions, J. Non-Cryst. Solids 326–327 (2003) 301–305. https://doi.org/10.1016/S0022-3093(03)00417-4.

[41] S. Zemon, G. Lambert, W.J. Miniscalco, R.W. Davies, B.T. Hall, R.C. Folweiler, T. Wei, L.J. Andrews, M.P. Singh, Fiber Laser Sources and Amplifiers II, SPIE, 1991.

[42] J. Koetke, G. Huber, Infrared excited-state absorption and stimulated-emission cross sections of Er^{3+}-doped crystals, Appl. Phys. B Laser Opt. 61 (1995) 151–158. https://doi.org/10.1007/BF01090936.

[43] P.R. Morkel, M.C. Farries, S.B. Poole, Spectral variation of excited state absorption in neodymium doped fibre lasers, Opt. Commun. 67 (1988) 349–352. https://doi.org/10.1016/0030-4018(88)90025-9.

[44] N.A. Tolstik, G. Huber, V.V. Maltsev, N.I. Leonyuk, N.V. Kuleshov, Excited state absorption, energy levels, and thermal conductivity of Er^{3+}:YAB, Appl. Phys. B 92 (2008) 567–571. https://doi.org/10.1007/s00340-008-3101-8.

[45] M. Pollnau, C. Ghisler, W. Lüthy, H.P. Weber, Cross sections of excited-state absorption at 800 nm in erbium-doped ZBLAN fiber, Appl. Phys. B 67 (1998) 23–28. https://doi.org/10.1007/s003400050469.

[46] L. Fornasiero, T. Kellner, S. Kück, J.P. Meyn, P.E.-A. Möbert, G. Huber, Excited state absorption and stimulated emission of Nd^{3+} in crystals III: $LaSc_3(BO_3)_4$, $CaWO_4$, and $YLiF_4$, Appl. Phys. B Lasers Opt. 68 (1999) 67–72. https://doi.org/10.1007/s003400050587.

[47] D.F. De Sousa, V. Peters, G. Huber, A. Toncelli, D. Parisi, M. Tonelli, Pump modulation frequency resolved excited state absorption spectra in Tm^{3+} doped YLF, Appl. Phys. B 77 (2003) 817–822. https://doi.org/10.1007/s00340-003-1293-5.

[48] H. Rawson, Properties and applications of glass (Glass science and technology), Elsevier, North-Holland, 1980.

[49] A. Zakery, S.R. Elliott, Optical properties and applications of chalcogenide glasses: a review, J. Non-Cryst. Solids 330 (2003) 1–12. https://doi.org/10.1016/j.jnoncrysol.2003.08.064.

[50] I. Inagawa, R. Iizuka, T. Yamagishi, R. Yokota, Optical and Thermal Properties of Chalcogenide Ge-As-Se-Te Glasses for IR Fibers.pdf, J. Non-Cryst. Solids 95–96 (1987) 801–808. https://doi.org/10.1016/S0022-3093(87)80684-1.

[51] A. Kinoshita, Characterization of glass transition in a-As_2Se_3 by heat of vaporization, J. Non-Cryst. Solids 42 (1980) 447–454. https://doi.org/10.1016/0022-3093(80)90043-5.

[52] J.D. Musgraves, S. Danto, K. Richardson, Thermal properties of chalcogenide glasses, in: Chalcogenide Glas., Elsevier, 2014: pp. 82–112. https://doi.org/10.1533/9780857093561.1.82.

[53] E. Roeder, Extrusion of glass, J. Non-Cryst. Solids 5 (1971) 377–388. https://doi.org/10.1016/0022-3093(71)90039-1.

[54] J.S. Sanghera, V.Q. Nguyen, P.C. Pureza, R.E. Miklos, F.H. Kung, I.D. Aggarwal, Fabrication of Long Lengths of Low-Loss IR Transmitting $As_{40}S_{(60-X)}Se_x$ Glass Fibers, J. Light. Technol. 14 (1996) 743–748. https://doi.org/10.1109/50.495154.

[55] M.S. Maklad, R.K. Mohr, R.E. Howard, P.B. Macedo, C.T. Moynihan, Multiphonon absorption in $As_2S_3As_2Se_3$ glasses, Solid State Commun. 15 (1974) 855–858. https://doi.org/10.1016/0038-1098(74)90679-6.

[56] D. Lezal, Chalogenide glasses - Survey and progess, J. Optoelectron. Adv. Mater. 5 (2003) 23–34.

[57] J. Málek, Dilatometric study of structural relaxation in arsenic sulfide glass, Thermochim. Acta 311 (1998) 183–198. https://doi.org/10.1016/S0040-6031(97)00466-8.

[58] F. Maes, V. Fortin, S. Poulain, M. Poulain, J.-Y. Carrée, M. Bernier, R. Vallée, Room-temperature fiber laser at 392 µm, Optica 5 (2018) 761. https://doi.org/10.1364/OPTICA.5.000761.

[59] R.M. Almeida, J.C. Pereira, Y. Messaddeq, M.A. Aegerter, Vibrational spectra and structure of fluoroindate glasses, J. Non-Cryst. Solids 161 (1993) 105–108. https://doi.org/10.1016/0022-3093(93)90678-Q.

[60] R.M. Nor, S.N.M. Halim, M.F.M. Taib, A.B.M.A. Ibrahim, M.K. Abd-Rahman, First Principles Study on Phonon Energy in SiO_2 Glass with the Incorporation of Al_2O_3, Solid

State Phenom. 268 (2017) 160–164. https://doi.org/10.4028/www.scientific.net/SSP.268.160.

[61] D.R. Swiler, A.K. Varshneya, R.M. Callahan, Microhardness, surface toughness and average coordination number in chalcogenide glasses, J. Non-Cryst. Solids 125 (1990) 250–257. https://doi.org/10.1016/0022-3093(90)90855-G.

[62] J.-P. Guin, T. Rouxel, J.-C. Sanglebœuf, I. Melscoët, J. Lucas, Hardness, Toughness, and Scratchability of Germanium-Selenium Chalcogenide Glasses, J. Am. Ceram. Soc. 85 (2002) 1545–1552. https://doi.org/10.1111/j.1151-2916.2002.tb00310.x.

[63] P.H. Shipway, I.M. Hutchings, The role of particle properties in the erosion of brittle materials, Wear 193 (1996) 105–113. https://doi.org/10.1016/0043-1648(95)06694-2.

[64] B.G. Aitken, C.W. Ponader, R.S. Quimby, Clustering of rare earths in GeAs sulfide glass, Comptes Rendus Chim. 5 (2002) 865–872. https://doi.org/10.1016/S1631-0748(02)01458-3.

[65] T.H. Lee, S.I. Simdyankin, J. Hegedus, J. Heo, S.R. Elliott, Spatial distribution of rare-earth ions and GaS_4 tetrahedra in chalcogenide glasses studied via laser spectroscopy and *ab initio* molecular dynamics simulation, Phys. Rev. B 81 (2010) 104204. https://doi.org/10.1103/PhysRevB.81.104204.

[66] H. Sakr, D. Furniss, Z. Tang, L. Sojka, N.A. Moneim, E. Barney, S. Sujecki, T.M. Benson, A.B. Seddon, Superior photoluminescence (PL) of Pr^{3+}-In, compared to Pr^{3+}-Ga, selenide-chalcogenide bulk glasses and PL of optically-clad fiber, Opt. Express 22 (2014) 21236. https://doi.org/10.1364/OE.22.021236.

[67] S.Q. Gu, S. Ramachandran, E.E. Reuter, D.A. Turnbull, J.T. Verdeyen, S.G. Bishop, Photoluminescence and excitation spectroscopy of Er-doped As_2S_3 glass: Novel broad band excitation mechanism, J. Appl. Phys. 77 (1995) 3365–3371. https://doi.org/10.1063/1.358624.

[68] Y. Guimond, J.-L. Adam, A.-M. Jurdyc, H.L. Ma, J. Mugnier, B. Jacquier, Optical properties of antimony-stabilised sulphide glasses doped with Dy^{3+} and Er^{3+} ions, J. Non-Cryst. Solids 256–257 (1999) 378–382. https://doi.org/10.1016/S0022-3093(99)00477-9.

[69] J.S. Sanghera, L.B. Shaw, L.E. Busse, V.Q. Nguyen, P.C. Pureza, B.C. Cole, B.B. Harrison, I.D. Aggarwal, R. Mossadegh, F. Kung, D. Talley, D. Roselle, R. Miklos, Development and Infrared Applications of Chalcogenide Glass Optical Fibers, Fiber Integr. Opt. 19 (2000) 251–274. https://doi.org/10.1080/01468030050058811.

[70] J. Schneider, C. Carbonnier, U.B. Unrau, Characterization of a Ho^{3+}-doped fluoride fiber laser with a 3.9-µm emission wavelength, Appl. Opt. 36 (1997) 8595–8600. https://doi.org/10.1364/AO.36.008595.

[71] F. Maes, V. Fortin, M. Bernier, R. Vallée, 5.6 W monolithic fiber laser at 3.55 µm, Opt. Lett. 42 (2017) 2054–2057. https://doi.org/10.1364/OL.42.002054.

[72] O. Henderson-Sapir, S.D. Jackson, D.J. Ottaway, Versatile and widely tunable mid-infrared erbium doped ZBLAN fiber laser, Opt. Lett. 41 (2016) 1676–1679. https://doi.org/10.1364/OL.41.001676.

[73] D.C. Hanna, R.M. Percival, I.R. Perry, R.G. Smart, P.J. Suni, J.E. Townsend, A.C. Tropper, Continuous-wave oscillation of a monomode ytterbium-doped fibre laser, Electron. Lett. 24 (1988) 1111–1113. https://doi.org/doi:10.1049/el:19880755.

[74] A.V. Kiryanov, M.C. Paul, Y.O. Barmenkov, S. Das, M. Pal, L. Escalante-Zarate, Yb^{3+} Concentration Effects in Novel Yb Doped Lanthano-Alumino-Silicate Fibers: Experimental Study, IEEE J. Quantum Electron. 49 (2013) 528–544. https://doi.org/10.1109/JQE.2013.2259143.

[75] G.E. Snopatin, V.S. Shiryaev, V.G. Plotnichenko, E.M. Dianov, M.F. Churbanov, High-purity chalcogenide glasses for fiber optics, Inorg. Mater. 45 (2009) 1439–1460. https://doi.org/10.1134/S0020168509130019.

[76] N. Prasad, D. Furniss, H.L. Rowe, C.A. Miller, D.H. Gregory, A.B. Seddon, First time microwave synthesis of $As_{40}Se_{60}$ chalcogenide glass, J. Non-Cryst. Solids 356 (2010) 2134–2145. https://doi.org/10.1016/j.jnoncrysol.2010.08.006.

[77] N. Prasad, Microwave assisted synthesis of chalcogenide glasses, Ph.D thesis, University of Nottingham, 2010.

[78] Y. Zhang, J.R.G. Evans, S. Yang, Corrected Values for Boiling Points and Enthalpies of Vaporization of Elements in Handbooks, J. Chem. Eng. Data 56 (2011) 328–337. https://doi.org/10.1021/je1011086.

[79] W.A. West, A.W.C. Menzies, The Vapor Pressures of Sulphur between 100° and 550° with related Thermal Data, J. Phys. Chem. 33 (1929) 1880–1892. https://doi.org/10.1021/j150306a002.

[80] H. Rau, Vapour composition and critical constants of selenium, J. Chem. Thermodyn. 6 (1974) 525–535. https://doi.org/10.1016/0021-9614(74)90039-1.

[81] J.J. Doolan, J.R. Partington, The vapour pressure of tellurium, Trans. Faraday Soc. 20 (1924) 342–344. https://doi.org/10.1039/TF9242000342.

[82] R. Celmer, M. Yamamoto, J.M. Toguri, Vapour Pressure of Arsenic, Can. Metall. Q. 23 (1984) 169–172. https://doi.org/10.1179/cmq.1984.23.2.169.

[83] G.M. Rosenblatt, C.E. Birchenall, Vapor Pressure of Antimony by the Torsion-Effusion Method, J. Chem. Phys. 35 (1961) 788. https://doi.org/10.1063/1.1701217.

[84] A.W. Searcy, The Vapor Pressure of Germanium [1], J. Am. Chem. Soc. 74 (1952) 4789–4791. https://doi.org/10.1021/ja01139a019.

[85] R. Speiser, H.L. Johnston, Vapor Pressures of Inorganic Substances. IX. Gallium [1], J. Am. Chem. Soc. 75 (1953) 1469–1470. https://doi.org/10.1021/ja01102a057.

[86] D.R. Lide, ed., CRC Handbook of Chemistry and Physics, 87th ed., CRC Press/Taylor and Francis Group, Boca Raton, FL, 2006.

[87] T. Katsuyama, S. Satoh, H. Matsumura, Fabrication of high-purity chalcogenide glasses by chemical vapor deposition, J. Appl. Phys. 59 (1986) 1446–1449. https://doi.org/10.1063/1.336496.

[88] T. Katsuyama, K. Ishida, S. Satoh, H. Matsumura, Low loss Ge-Se chalcogenide glass optical fibers, Appl. Phys. Lett. 45 (1984) 925–927. https://doi.org/10.1063/1.95462.

[89] L.A. Mochalov, M.F. Churbanov, A.P. Velmuzhov, A.S. Lobanov, R.A. Kornev, G.P. Sennikov, Preparation of glasses in the Ge–S–I system by plasma-enhanced chemical vapor deposition, Opt. Mater. 46 (2015) 310–313. https://doi.org/10.1016/j.optmat.2015.04.037.

[90] Evgenii M Dianov, M Yu Petrov, V G Plotnichenko, V K Sysoev, Estimate of the minimum optical losses in chalcogenide glasses, Sov. J. Quantum Electron. 12 (1982) 498. https://doi.org/10.1070/QE1982v012n04ABEH012237.

[91] J.S. Sanghera, I.D. Aggarwal, Development of chalcogenide glass fiber optics at NRL, J. Non-Cryst. Solids 213–214 (1997) 63–67. https://doi.org/10.1016/S0022-3093(97)00051-3.

[92] D.W. Hewak, J.A. Medeiros Neto, B.N. Samson, J. Wang, H.J. Tate, A. Pearson, W.S. Brocklesby, G. Wylangowski, R.I. Laming, D.N. Payne, A. Jha, M. Naftaly, S. Jordery, M. Poulain, Spectroscopy of Pr^{3+} -doped low-phonon-energy glasses based on halides and sulfides, in: M.J.F. Digonnet (Ed.), Proc SPIE 2073 Fiber Laser Sources Amplif. V, Boston, MA, 1994: p. 102. https://doi.org/10.1117/12.168596.

[93] L. Dimitrij, P. Jitka, G. Jan, V. Rudolf, The preparation of chalcogenide glasses in chlorine reactive atmosphere, Ceram. - Silik. 40 (1996) 55–59.

[94] M.F. Churbanov, G.E. Snopatin, V.S. Shiryaev, V.G. Plotnichenko, E.M. Dianov, Recent advances in preparation of high-purity glasses based on arsenic chalcogenides for fiber optics, J. Non-Cryst. Solids 357 (2011) 2352–2357. https://doi.org/10.1016/j.jnoncrysol.2010.11.057.

[95] M.F. Churbanov, High-purity chalcogenide glasses as materials for fiber optics, J. Non-Cryst. Solids 184 (1995) 25–29. https://doi.org/10.1016/0022-3093(94)00688-1.

[96] H. Rowe, Infrared transmitting optical fibres with potential use in medical diagnosis and treatment, Ph.D thesis, University of Nottingham, 2008.

[97] Z. Tang, RARE EARTH ION DOPED SELENIDE-BASED CHALCOGENIDE GLASSES AND FIBRES TOWARDS MID-INFRARED FIBRE LASERS, Thesis (Doctoral), University of Nottingham, 2012.

[98] V.Q. Nguyen, J.S. Sanghera, P. Pureza, F.H. Kung, I.D. Aggarwal, Fabrication of Arsenic Selenide Optical Fiber with Low Hydrogen Impurities, J. Am. Ceram. Soc. 85 (2004) 2849–2851. https://doi.org/10.1111/j.1151-2916.2002.tb00541.x.

[99] V.Q. Nguyen, J.S. Sanghera, I.D. Aggarwal, Low loss chalcogenide glass and process for making same using arsenic monochalcogenide, US 2005/0229636A1, 2005.

[100] V.Q. Nguyen, J.S. Sanghera, B.J. Cole, P.C. Pureza, F.H. Kung, I.D. Aggarwal, Fabrication of As-S and As-Se optical fiber with low hydrogen impurities using tellurium tetrachloride ($TeC1_4$), in: Y.S. Sidorin, A. Tervonen (Eds.), San Jose, CA, 2003: p. 274. https://doi.org/10.1117/12.473172.

[101] V.Q. Nguyen, G. Drake, G. Villalobos, D. Gibson, S. Bayya, W. Kim, C. Baker, G. Chin, F.H. Kung, M.I. Kotov, L. Busse, J.S. Sanghera, Effect of aluminum and tellurium tetrachloride addition on the loss of arsenic selenide optical fiber, Opt. Mater. 64 (2017) 327–333. https://doi.org/10.1016/j.optmat.2016.12.038.

[102] V.S. Shiryaev, J.-L. Adam, X.H. Zhang, C. Boussard-Plédel, J. Lucas, M.F. Churbanov, Infrared fibers based on Te–As–Se glass system with low optical losses, J. Non-Cryst. Solids 336 (2004) 113–119. https://doi.org/10.1016/j.jnoncrysol.2004.01.006.

[103] Z. Tang, V.S. Shiryaev, D. Furniss, L. Sojka, S. Sujecki, T.M. Benson, A.B. Seddon, M.F. Churbanov, Low loss Ge-As-Se chalcogenide glass fiber, fabricated using extruded preform, for mid-infrared photonics, Opt. Mater. Express 5 (2015) 1722. https://doi.org/10.1364/OME.5.001722.

[104] L.A. Ketkova, A.V. Kurilin, M.F. Churbanov, Characterization of heterophase inclusions in glasses opaque in the visible range, Inorg. Mater. 44 (2008) 773–777. https://doi.org/10.1134/S0020168508070170.

[105] V.S. Shiryaev, L.A. Ketkova, M.F. Churbanov, A.M. Potapov, J. Troles, P. Houizot, J.-L. Adam, A.A. Sibirkin, Heterophase inclusions and dissolved impurities in $Ge_{25}Sb_{10}S_{65}$ glass, J. Non-Cryst. Solids 355 (2009) 2640–2646. https://doi.org/10.1016/j.jnoncrysol.2009.08.022.

[106] I.E. Gordon, L.S. Rothman, C. Hill, R.V. Kochanov, Y. Tan, P.F. Bernath, M. Birk, V. Boudon, A. Campargue, K.V. Chance, B.J. Drouin, J.-M. Flaud, R.R. Gamache, J.T. Hodges, D. Jacquemart, V.I. Perevalov, A. Perrin, K.P. Shine, M.-A.H. Smith, J. Tennyson, G.C. Toon, H. Tran, V.G. Tyuterev, A. Barbe, A.G. Császár, V.M. Devi, T. Furtenbacher, J.J. Harrison, J.-M. Hartmann, A. Jolly, T.J. Johnson, T. Karman, I. Kleiner, A.A. Kyuberis, J. Loos, O.M. Lyulin, S.T. Massie, S.N. Mikhailenko, N. Moazzen-Ahmadi, H.S.P. Müller, O.V. Naumenko, A.V. Nikitin, O.L. Polyansky, M. Rey, M. Rotger, S.W. Sharpe, K. Sung, E. Starikova, S.A.

Tashkun, J.V. Auwera, G. Wagner, J. Wilzewski, P. Wcisło, S. Yu, E.J. Zak, The HITRAN2016 molecular spectroscopic database, J. Quant. Spectrosc. Radiat. Transf. 203 (2017) 3–69. https://doi.org/10.1016/j.jqsrt.2017.06.038.

[107] J.E. Bertie, Z. Lan, Infrared Intensities of Liquids XX: The Intensity of the OH Stretching Band of Liquid Water Revisited, and the Best Current Values of the Optical Constants of $H_20(l)$ at 25 °C between 15,000 and 1 cm^{-1}, Appl. Spectrosc. 50 (1996) 1047–1057. https://doi.org/10.1366/0003702963905385.

[108] J. Kobelke, J. Kirchhof, K. Schuster, A. Schwuchow, Effects of carbon, hydrocarbon and hydroxide impurities on praseodymium doped arsenic sulfide based glasses, J. Non-Cryst. Solids 284 (2001) 123–127. https://doi.org/10.1016/S0022-3093(01)00390-8.

[109] W. Chen, J. Cheng, G. Chen, Formation and properties of chalcohalide glasses in the As_2Se_3–GeTe–CuI system, J. Non-Cryst. Solids 221 (1997) 274–280. https://doi.org/10.1016/S0022-3093(97)00337-2.

[110] W.A. King, A.G. Clare, W.C. LaCourse, Laboratory preparation of highly pure As_2Se_3 glass, J. Non-Cryst. Solids 181 (1995) 231–237. https://doi.org/10.1016/S0022-3093(94)00512-5.

[111] A.M. Reitter, A.N. Sreeram, A.K. Varshneya, D.R. Swiler, Modified preparation procedure for laboratory melting of multicomponent chalcogenide glasses, J. Non-Cryst. Solids 139 (1992) 121–128. https://doi.org/10.1016/S0022-3093(05)80813-0.

[112] J.A. Savage, P.J. Webber, A.M. Pitt, The potential of Ge-As-Se-Te glasses as 3–5 µm and 8–12 µm infrared optical materials, Infrared Phys. 20 (1980) 313–320. https://doi.org/10.1016/0020-0891(80)90045-7.

[113] D.S. Ma, P.S. Danielson, C.T. Moynihan, Bulk and impurity infrared absorption in 0.5 As_2Se_3-0.5 $GeSe_2$ glass, J. Non-Cryst. Solids 37 (1980) 181–190. https://doi.org/10.1016/0022-3093(80)90149-0.

[114] P.J. Webber, J.A. Savage, SOME PHYSICAL PROPERTIES OF Ge-As-Se INFRARED OPTICAL GLASSES, J. Non-Cryst. Solids 20 (1976) 271–283. https://doi.org/10.1016/0022-3093(76)90136-8.

[115] C.T. Moynihan, P.B. Macedo, M.S. Maklad, R.K. Mohr, R.E. Howard, Intrinsic and impurity infrared absorption in As_2Se_3 glass, J. Non-Cryst. Solids 17 (1975) 369–385. https://doi.org/10.1016/0022-3093(75)90127-1.

[116] A.B. Seddon, D. Furniss, Z.Q. Tang, L. Sojka, T.M. Benson, R. Caspary, S. Sujecki, True mid-infrared Pr^{3+} absorption cross-section in a selenide-chalcogenide host-glass, in: 2016 18th Int. Conf. Transparent Opt. Netw. ICTON, IEEE, Trento, Italy, 2016: pp. 1–6. https://doi.org/10.1109/ICTON.2016.7550709.

[117] S.-M. Tsai, E.K.H. Lee, D. Powell, P. Gao, X. Zhang, J. Moses, E. Hébrard, O. Venot, V. Parmentier, S. Jordan, R. Hu, M.K. Alam, L. Alderson, N.M. Batalha, J.L. Bean, B. Benneke, C.J. Bierson, R.P. Brady, L. Carone, A.L. Carter, K.L. Chubb, J. Inglis, J. Leconte, M. Lopez-Morales, Y. Miguel, K. Molaverdikhani, Z. Rustamkulov, D.K. Sing, K.B. Stevenson, H.R. Wakeford, J. Yang, K. Aggarwal, R. Baeyens, S. Barat, M. de V. Borro, T. Daylan, J.J. Fortney, K. France, J.M. Goyal, D. Grant, J. Kirk, L. Kreidberg, A. Louca, S.E. Moran, S. Mukherjee, E. Nasedkin, K. Ohno, B.V. Rackham, S. Redfield, J. Taylor, P. Tremblin, C. Visscher, N.L. Wallack, L. Welbanks, A. Youngblood, E.-M. Ahrer, N.E. Batalha, P. Behr, Z.K. Berta-Thompson, J. Blecic, S.L. Casewell, I.J.M. Crossfield, N. Crouzet, P.E. Cubillos, L. Decin, J.-M. Désert, A.D. Feinstein, N.P. Gibson, J. Harrington, K. Heng, T. Henning, E.M.-R. Kempton, J. Krick, P.-O. Lagage, M. Lendl, M. Line, J.D. Lothringer, M. Mansfield, N.J. Mayne, T. Mikal-Evans, E. Palle, E. Schlawin, O. Shorttle, P.J. Wheatley, S.N. Yurchenko, Photochemically-produced SO_2 in the atmosphere of WASP-39b, Nature 617 (2023) 483–487. https://doi.org/10.1038/s41586-023-05902-2.

[118] T. Schweizer, Rare-Earth-Doped Gallium Lanthanum Sulphide Glasses for Mid-Infrared Fibre Lasers, Thesis (Doctoral), Optoelectronics Research Centre, University of Southampton and Institut für Laser-Physik, Universität Hamburg, 1998. https://eprints.soton.ac.uk/15494/1/Schweizer_2000_thesis_1510T.pdf.

[119] L. Sójka, Z. Tang, D. Furniss, H. Sakr, A. Oladeji, E. Bereś-Pawlik, H. Dantanarayana, E. Faber, A.B. Seddon, T.M. Benson, S. Sujecki, Broadband, mid-infrared emission from Pr^{3+} doped GeAsGaSe chalcogenide fiber, optically clad, Opt. Mater. 36 (2014) 1076–1082. https://doi.org/10.1016/j.optmat.2014.01.038.

[120] B. Cole, J. Sanghera, B. Shaw, B. Harbison, I.D. Aggarwal, LOW PHONON ENERGY GLASS AND FIBER DOPED WITH A RARE EARTH, 6,128,429, 2000.

[121] M.F. Churbanov, B.I. Denker, B.I. Galagan, V.V. Koltashev, V.G. Plotnichenko, M.V. Sukhanov, S.E. Sverchkov, A.P. Velmuzhov, First demonstration of ~ 5 µm laser action in terbium-doped selenide glass, Appl. Phys. B 126 (2020) 117. https://doi.org/10.1007/s00340-020-07473-w.

[122] N. Abdellaoui, F. Starecki, C. Boussard-Pledel, Y. Shpotyuk, J.-L. Doualan, A. Braud, E. Baudet, P. Nemec, F. Cheviré, M. Dussauze, B. Bureau, P. Camy, V. Nazabal, Tb^{3+} doped Ga_5 Ge_{20} Sb_{10} Se_{65-x} Te_x (x = 0-375) chalcogenide glasses and fibers for MWIR and LWIR emissions, Opt. Mater. Express 8 (2018) 2887. https://doi.org/10.1364/OME.8.002887.

[123] B. Cole, L.B. Shaw, P.C. Pureza, R. Mossadegh, J.S. Sanghera, I.D. Aggarwal, Rare-earth doped selenide glasses and fibers for active applications in the near and mid-IR, (1999) 7.

[124] G. Gould R, The LASER, Light Amplification by Stimulated Emission of Radiation, in: Ann Arbor Conf. Opt. Pump. Univ. Mich. 1959 Peter Alden Frank. Richard H Sands, The University of Michigan, 1959.

[125] A. Einstein, Strahlungs-emission und -absorption nach der Quantentheorie, Verhandlungen Dtsch. Phys. Ges. 18 (1916) 318–323.

[126] A. Einstein, Zur Quantentheorie der Strahlung, Phys. Z. 18 (1917) 121–128.

[127] J.P. Gordon, H.J. Zeiger, C.H. Townes, The Maser—New Type of Microwave Amplifier, Frequency Standard, and Spectrometer, Phys. Rev. 99 (1955) 1264–1274. https://doi.org/10.1103/PhysRev.99.1264.

[128] T. Maiman, Stimulated Optical Radiation in Ruby, Nature 187 (1960) 493–494. https://doi.org/10.1038/187493a0.

[129] A. Sincore, J. Cook, F. Tan, A. El Halawany, A. Riggins, L. Shah, A. Abouraddy, M. Richardson, K. Schepler, High Power 2053 nm Transmission through Single-mode Chalcogenide Fiber, in: Laser Congr. 2017 ASSL LAC OSA Tech. Dig. Online Opt. Publ. Group 2017 Pap. ATu5A5, OSA Technical Digest (online) (Optica Publishing Group, 2017), Nagoya, Aichi Japan, 2017. https://doi.org/10.1364/ASSL.2017.ATu5A.5.

[130] P. Fjodorow, M.P. Frolov, S.O. Leonov, B.I. Denker, B.I. Galagan, S.E. Sverchkov, V.V. Koltashev, V.G. Plotnichenko, M.V. Sukhanov, A.P. Velmuzhov, Mid-infrared laser performance of Ce^{3+}-doped selenide glass, Opt. Express 29 (2021) 27674. https://doi.org/10.1364/OE.433828.

[131] M.P. Frolov, Y.V. Korostelin, V.I. Kozlovsky, V.V. Mislavskii, Y.P. Podmar'kov, S.A. Savinova, Y.K. Skasyrsky, Study of a 2-J pulsed Fe:ZnSe 4-μm laser, Laser Phys. Lett. 10 (2013) 125001. https://doi.org/10.1088/1612-2011/10/12/125001.

[132] Y. Cui, W. Huang, Z. Wang, M. Wang, Z. Zhou, Z. Li, S. Gao, Y. Wang, P. Wang, 4.3 μm fiber laser in CO_2 -filled hollow-core silica fibers, Optica 6 (2019) 951. https://doi.org/10.1364/OPTICA.6.000951.

[133] F.B.A. Aghbolagh, V. Nampoothiri, B. Debord, F. Gerome, L. Vincetti, F. Benabid, W. Rudolph, Mid IR hollow core fiber gas laser emitting at 4.6 μm, Opt. Lett. 44 (2019) 383. https://doi.org/10.1364/OL.44.000383.

[134] M.F. Churbanov, B.I. Denker, B.I. Galagan, V.V. Koltashev, V.G. Plotnichenko, G.E. Snopatin, M.V. Sukhanov, S.E. Sverchkov, A.P. Velmuzhov, Laser potential of Pr^{3+} doped chalcogenide glass in 5-6 μm spectral range, J. Non-Cryst. Solids 559 (2021). https://doi.org/10.1016/j.jnoncrysol.2020.120592.

[135] N.P. Barnes, R.E. Allen, Room Temperature Dy :YLF Laser Operation at 4.34 μm, IEEE J. Quantum Electron. 27 (1991) 277–282. https://doi.org/10.1109/3.78231.

[136] M.C. Nostrand, R.H. Page, S.A. Payne, W.F. Krupke, P.G. Schunemann, Room-temperature laser action at 4.3–4.4 mm in $CaGa_2S_4$:Dy^{3+}, Opt. Lett. 24 (1999) 1215–1217. https://doi.org/10.1364/OL.24.001215.

[137] R.I. Woodward, M.R. Majewski, G. Bharathan, D.D. Hudson, A. Fuerbach, S.D. Jackson, Watt-level dysprosium fiber laser at 3.15 μm with 73% slope efficiency, Opt. Lett. 43 (2018) 1471–1474. https://doi.org/10.1364/OL.43.001471.

[138] R.I. Woodward, M.R. Majewski, S.D. Jackson, Dysprosium mid-infrared lasers: Current status and future prospects, Laser Photonics Rev. 14 (2020) 1900195. https://doi.org/10.1002/lpor.201900195.

[139] X. Xiao, Y. Xu, H. Guo, P. Wang, X. Cui, M. Lu, Y. Wang, B. Peng, Theoretical Modeling of 4.3 µm Mid-Infrared Lasing in Dy^{3+}-Doped Chalcogenide Fiber Lasers, IEEE Photonics J. 10 (2018) 1–11. https://doi.org/10.1109/JPHOT.2018.2803155.

[140] J.J. Nunes, Ł. Sojka, R.W. Crane, D. Furniss, Z.Q. Tang, D. Mabwa, B. Xiao, T.M. Benson, M. Farries, N. Kalfagiannis, E. Barney, S. Phang, A.B. Seddon, S. Sujecki, Room temperature mid-infrared fiber lasing beyond 5 µm in chalcogenide glass small-core step index fiber, Opt. Lett. 46 (2021) 3504. https://doi.org/10.1364/OL.430891.

[141] V.S. Shiryaev, M.V. Sukhanov, A.P. Velmuzhov, E.V. Karaksina, T.V. Kotereva, G.E. Snopatin, B.I. Denker, B.I. Galagan, S.E. Sverchkov, V.V. Koltashev, V.G. Plotnichenko, Core-clad terbium doped chalcogenide glass fiber with laser action at 5.38 µm, J. Non-Cryst. Solids 567 (2021) 120939. https://doi.org/10.1016/j.jnoncrysol.2021.120939.

[142] B.I. Denker, B.I. Galagan, V.V. Koltashev, V.G. Plotnichenko, G.E. Snopatin, M.V. Sukhanov, S.E. Sverchkov, A.P. Velmuzhov, Continuous Tb-doped fiber laser emitting at ∼5.25 µm, Opt. Laser Technol. 154 (2022) 108355. https://doi.org/10.1016/j.optlastec.2022.108355.

[143] H. Jelínková, M.E. Doroshenko, M. Jelínek, J. Šulc, V.V. Osiko, V.V. Badikov, D.V. Badikov, Dysprosium-doped $PbGa_2S_4$ laser generating at 4.3 µm directly pumped by 1.7 µm laser diode, Opt. Lett. 38 (2013) 3040–3043. https://doi.org/10.1364/OL.38.003040.

[144] P. Schlosser, L. Isaenko, A. Tarasova, V. Savitski, Diode-pumped Dy:KPb_2Cl_5 laser in the middle-infrared spectral region, Opt. Lett. 47 (2022) 1553. https://doi.org/10.1364/OL.454156.

[145] H. Többen, CW Lasing at 3.45 µm in Erbium-doped Fluorozirconate Fibres, Frequenz 45 (1991) 250–252. https://doi.org/10.1515/FREQ.1991.45.9-10.250.

[146] M. Suzuki, T. Kato, S. Watabe, Rod in tube method of forming a fiber preform, with maintaining a gas supply until after an end is stretched, US6425270B1, 1998.

[147] C. Strutynski, J. Picot-Clémente, A. Lemiere, P. Froidevaux, F. Désévédavy, G. Gadret, J.-C. Jules, B. Kibler, F. Smektala, Fabrication and characterization of step-index tellurite fibers with varying numerical aperture for near- and mid-infrared nonlinear optics, J. Opt. Soc. Am. B 33 (2016) D12. https://doi.org/10.1364/JOSAB.33.000D12.

[148] J. Troles, Y. Niu, C. Duverger-Arfuso, F. Smektala, L. Brilland, V. Nazabal, V. Moizan, F. Desevedavy, P. Houizot, Synthesis and characterization of chalcogenide glasses from the system Ga–Ge–Sb–S and preparation of a single-mode fiber at 1.55 µm, Mater. Res. Bull. 43 (2008) 976–982. https://doi.org/10.1016/j.materresbull.2007.04.029.

[149] Z. Tang, D. Furniss, M. Fay, H. Sakr, L. Sójka, N. Neate, N. Weston, S. Sujecki, T.M. Benson, A.B. Seddon, Mid-infrared photoluminescence in small-core fiber of praseodymium-ion doped selenide-based chalcogenide glass, Opt. Mater. Express 5 (2015) 870. https://doi.org/10.1364/OME.5.000870.

[150] G.C. Chern, I. Lauks, A.R. McGhie, Spin coated amorphous chalcogenide films: Thermal properties, J. Appl. Phys. 54 (1983) 4596–4601. https://doi.org/10.1063/1.332614.

[151] P. Lucas, A.A. Wilhelm, M. Videa, C. Boussard-Plédel, B. Bureau, Chemical stability of chalcogenide infrared glass fibers, Corros. Sci. 50 (2008) 2047–2052. https://doi.org/10.1016/j.corsci.2008.04.020.

[152] CompleteEASE® Software Manual, (2011). https://wiki.nanotech.ucsb.edu/w/images/2/2e/CompleteEASE_Manual.pdf (accessed July 23, 2022).

[153] T. Wang, INVESTIGATIONS ON STRUCTURE AND PROPERTIES OF, Thesis (Doctoral), The Australian National University, 2017.

[154] R.A. Loretz, T.J. Loretz, K.A. Richardson, Predictive method to assess chalcogenide glass properties: bonding, density and the impact on glass properties, Opt. Mater. Express 12 (2022) 2012. https://doi.org/10.1364/OME.455523.

[155] M.J. Weber, Optical spectra of Ce^{3+} and Ce^{3+}-sensitized fluorescence in $YAlO_3$, J. Appl. Phys. 44 (1973) 3205–3208. https://doi.org/10.1063/1.1662735.

[156] A. White, H.J. Williams, J.H. Wernick, R.C. Sherwood, Observation of a Possible Large Crystalline Stark Splitting in Metallic Ce: $LaAl_2$, Phys. Rev. 131 (1963) 1039–1042. https://doi.org/10.1103/PhysRev.131.1039.

[157] S.N. Lukin, A.D. Prokhorov, P. Teslya, Spectroscopic investigation of the Schottky anomaly in cerium ethyl sulfate, J. Exp. Theor. Phys. 73 (1991) 1072.

[158] W.T. Carnall, G.L. Goodman, K. Rajnak, R.S. Rana, A systematic analysis of the spectra of the lanthanides doped into single crystal LaF_3, J. Chem. Phys. 90 (1989) 3443–3457. https://doi.org/10.1063/1.455853.

[159] S.D. Savage, C.A. Miller, D. Furniss, A.B. Seddon, Extrusion of chalcogenide glass preforms and drawing to multimode optical fibers, J. Non-Cryst. Solids 354 (2008) 3418–3427. https://doi.org/10.1016/j.jnoncrysol.2008.01.032.

[160] K. Bhowmick, H.P. Morvan, D. Furniss, A.B. Seddon, T.M. Benson, Co-Extrusion of Multilayer Glass Fiber-Optic Preforms: Prediction of Layer Dimensions in the Extrudate, J. Am. Ceram. Soc. 96 (2013) 118–124. https://doi.org/10.1111/jace.12003.

[161] C.N. Cochran, L.M. Foster, Vapor Pressure of Gallium, Stability of Gallium Suboxide Vapor, and Equilibria of Some Reactions Producing Gallium Suboxide Vapor, J. Electrochem. Soc. 109 (1962) 144.

[162] Vapor pressures of the elements (data page), Wikipedia (2022). https://en.wikipedia.org/wiki/Vapor_pressures_of_the_elements_(data_page).

[163] J.J. Nunes, R.W. Crane, D. Mabwa, D. Furniss, M. Farries, T.M. Benson, A.B. Seddon, Internal examination of mid-infrared chalcogenide glass optical fiber preforms and fiber using near-infrared imaging [Invited], Opt. Mater. Express 11 (2021) 1353. https://doi.org/10.1364/OME.415518.

[164] Z. Pan, A. Kiyama, Y. Tagawa, D.J. Daily, S.L. Thomson, R. Hurd, T.T. Truscott, Cavitation onset caused by acceleration, Proc. Natl. Acad. Sci. 114 (2017) 8470–8474. https://doi.org/10.1073/pnas.1702502114.

[165] Explosive Beer Trick Explained by Physics, Https://Www.Livescience.Com/ (2013). https://www.livescience.com/41514-beer-tapping-physics.html.

[166] Ar. Veerappan, S. Shanmugam, S. Soundrapandian, The Accepting of Pipe Bends With Ovality and Thinning Using Finite Element Method, J. Press. Vessel Technol. 132 (2010) 031204. https://doi.org/10.1115/1.4001423.

[167] H. Przybylińska, C.-G. Ma, M.G. Brik, A. Kamińska, P. Sybilski, A. Wittlin, M. Berkowski, Yu. Zorenko, V. Gorbenko, H. Wrzesinski, A. Suchocki, Electronic structure of Ce^{3+}

multicenters in yttrium aluminum garnets, Appl. Phys. Lett. 102 (2013) 241112. https://doi.org/10.1063/1.4812190.

[168] W.S. Levine, The Control Handbook, in: Control Handb., CRC Press, Boca Raton, FL, 1996: p. 158.

[169] Scientific, Thermo Fisher, Introduction to FTIR spectroscopy, (2022). https://www.thermofisher.com/tt/en/home/industrial/spectroscopy-elemental-isotope-analysis/spectroscopy-elemental-isotope-analysis-learning-center/molecular-spectroscopy-information/ftir-information/ftir-basics.html.

[170] O. Faix, Fourier Transform Infrared Spectroscopy, in: S.Y. Lin, C.W. Dence (Eds.), Methods Lignin Chem. Springer Ser. Wood Sci., Springer, Berlin Heidelberg, 1992.

[171] A.P. Kozlova, V.M. Kasimova, O.A. Buzanov, K. Chernenko, K. Klementiev, V. Pankratov, Luminescence and vacuum ultraviolet excitation spectroscopy of cerium doped $Gd_3Ga_3Al_2O_{12}$ single crystalline scintillators under synchrotron radiation excitations, Results Phys. 16 (2020) 103002. https://doi.org/10.1016/j.rinp.2020.103002.

[172] A. Herrmann, H.A. Othman, A.A. Assadi, M. Tiegel, S. Kuhn, C. Rüssel, Spectroscopic properties of cerium-doped aluminosilicate glasses, Opt. Mater. Express 5 (2015) 720. https://doi.org/10.1364/OME.5.000720.

[173] V.B. Pawade, S.J. Dhoble, Spin–Orbit Splitting Difference and Stokes Shift in Cerium^{3+}-Activated Aluminate Phosphors, Spectrosc. Lett. 46 (2013) 472–475. https://doi.org/10.1080/00387010.2012.731025.

[174] M.F. Churbanov, B.I. Denker, B.I. Galagan, V.V. Koltashev, V.G. Plotnichenko, M.V. Sukhanov, S.E. Sverchkov, A.P. Velmuzhov, Cascade sensitization of mid-infrared Ce^{3+} luminescence by Dy^{3+} ions in selenide glass, J. Lumin. 231 (2021) 117809. https://doi.org/10.1016/j.jlumin.2020.117809.

[175] M. Shen, D. Furniss, M. Farries, D. Jayasuriya, Z. Tang, L. Sojka, S. Sujecki, T.M. Benson, A.B. Seddon, Experimental observation of gain in a resonantly pumped Pr^{3+}-doped chalcogenide glass mid-infrared fibre amplifier notwithstanding the signal excited-state absorption, Sci. Rep. 9 (2019) 11426. https://doi.org/10.1038/s41598-019-47432-w.

[176] L. Sojka, Z. Tang, D. Jayasuriya, M. Shen, J. Nunes, D. Furniss, M. Farries, T.M. Benson, A.B. Seddon, S. Sujecki, Milliwatt-Level Spontaneous Emission Across the 3.5–8 µm Spectral Region from Pr^{3+} Doped Selenide Chalcogenide Fiber Pumped with a Laser Diode, Appl. Sci. 10 (2020) 539. https://doi.org/10.3390/app10020539.

[177] M.F. Churbanov, B.I. Denker, B.I. Galagan, V.V. Koltashev, V.G. Plotnichenko, S.E. Sverchkov, M.V. Sukhanov, A.P. Velmuzhov, Peculiarities of 1.6-7.5 µm Pr^{3+} luminescence in Ge_{36} Ga_5 Se_{59} glass, Opt. Mater. Express 9 (2019) 4154. https://doi.org/10.1364/OME.9.004154.

[178] F. Charpentier, F. Starecki, J.L. Doualan, P. Jóvári, P. Camy, J. Troles, S. Belin, B. Bureau, V. Nazabal, Mid-IR luminescence of Dy^{3+} and Pr^{3+} doped $Ga_5Ge_{20}Sb_{10}S(Se)_{65}$ bulk glasses and fibers, Mater. Lett. 101 (2013) 21–24. https://doi.org/10.1016/j.matlet.2013.03.062.

[179] J. Hu, C.R. Menyuk, C. Wei, L. Brandon Shaw, J.S. Sanghera, I.D. Aggarwal, Highly efficient cascaded amplification using Pr^{3+}-doped mid-infrared chalcogenide fiber amplifiers, Opt. Lett. 40 (2015) 3687. https://doi.org/10.1364/OL.40.003687.

[180] M. Nogami, Y. Abe, Sm^{2+}doped silicate glasses prepared by a solgel process, Appl. Phys. Lett. 65 (1994) 1227. https://doi.org/10.1063/1.112078.

[181] L. Sojka, Z. Tang, D. Furniss, H. Sakr, Y. Fang, E. Beres-Pawlik, T.M. Benson, A.B. Seddon, S. Sujecki, Mid-infrared emission in Tb^{3+}-doped selenide glass fiber, J. Opt. Soc. Am. B 34 (2017) A70. https://doi.org/10.1364/JOSAB.34.000A70.

[182] S. Shintoyo, K. Murakami, T. Fujinami, N. Matsumoto, N. Mochida, T. Ishida, Y. Sunatsuki, M. Watanabe, M. Tsuchimoto, J. Mrozinski, C. Coletti, N. Re, Crystal Field Splitting of the Ground State of Terbium(III) and Dysprosium(III) Complexes with a Triimidazolyl Tripod Ligand and an Acetate Determined by Magnetic Analysis and Luminescence, Inorg. Chem. 53 (2014) 10359–10369. https://doi.org/10.1021/ic501453h.

[183] U.V. Valiev, J.B. Gruber, D.K. Sardar, B. Zandi, I.S. Kachur, A.K. Mukhammadiev, V.G. Piryatinskaya, V.Yu. Sokolov, I.S. Edelman, Zeeman effect and stark splitting of the electronic states of the rare-earth ion in the paramagnetic terbium garnets $Tb_3Ga_5O_{12}$ and $Tb_3Al_5O_{12}$, Phys. Solid State 49 (2007) 91–98. https://doi.org/10.1134/S1063783407010167.

[184] J.A. Koningstein, Energy Levels and Crystal-Field Calculations of Europium and Terbium in Yttrium Aluminum Garnet, Phys. Rev. 136 (1964) A717–A725. https://doi.org/10.1103/PhysRev.136.A717.

[185] Ł. Sójka, Z. Tang, H. Zhu, E. Bereś-Pawlik, D. Furniss, A.B. Seddon, T.M. Benson, S. Sujecki, Study of mid-infrared laser action in chalcogenide rare earth doped glass with Dy^{3+}, Pr^{3+} and Tb^{3+}, Opt. Mater. Express 2 (2012) 1632. https://doi.org/10.1364/OME.2.001632.

[186] L. Sojka, Z. Tang, D. Jayasuriya, M. Shen, D. Furniss, E. Barney, T.M. Benson, A.B. Seddon, S. Sujecki, Ultra-broadband mid-infrared emission from a Pr^{3+} /Dy^{3+} co-doped selenide-chalcogenide glass fiber spectrally shaped by varying the pumping arrangement [Invited], Opt. Mater. Express 9 (2019) 2291. https://doi.org/10.1364/OME.9.002291.

[187] Y.B. Shin, J. Heo, Mid-infrared emissions and multiphonon relaxation in Dy^{3+}-doped chalcohalide glasses, J. Non-Cryst. Solids 253 (1999) 23–29. https://doi.org/10.1016/S0022-3093(99)00403-2.

[188] T. Schweizer, D.W. Hewak, B.N. Samson, D.N. Payne, Spectroscopic data of the 1.8-, 2.9-, and 4.3-µm transitions in dysprosium-doped gallium lanthanum sulfide glass, Opt. Lett. 21 (1996) 1594–1596. https://doi.org/10.1364/OL.21.001594.

[189] J. Heo, 1.3-µm-emission properties and local structure of Dy^{3+} in chalcohalide glasses, Comptes Rendus Chim. 5 (2002) 739–749. https://doi.org/10.1016/S1631-0748(02)01442-X.

[190] J. Heo, Y.B. Shin, Absorption and mid-infrared emission spectroscopy of Dy^{3+} in Ge-As(or Ga)-S glasses, J. Non-Cryst. Solids 196 (1996) 162–167. https://doi.org/10.1016/0022-3093(95)00579-X.

[191] A. Yang, J. Qiu, M. Zhang, H. Ren, C. Zhai, S. Qi, B. Zhang, D. Tang, Z. Yang, Mid-infrared luminescence of Dy^{3+} ions in modified Ga-Sb-S chalcogenide glasses and fibers, J. Alloys Compd. 695 (2017) 1237–1242. https://doi.org/10.1016/j.jallcom.2016.10.251.

[192] L. Gomes, A.F.H. Librantz, S.D. Jackson, Energy level decay and excited state absorption processes in dysprosium-doped fluoride glass, J. Appl. Phys. 107 (2010) 053103. https://doi.org/10.1063/1.3311561.

[193] M.E. Doroshenko, T.T. Basiev, V.V. Osiko, V.V. Badikov, D.V. Badikov, H. Jelínková, P. Koranda, J. Šulc, Oscillation properties of dysprosium-doped lead thiogallate crystal, Opt. Lett. 34 (2009) 590–592. https://doi.org/10.1364/OL.34.000590.

[194] S. Sujecki, L. Sojka, E. Beres-Pawlik, H. Sakr, Z. Tang, E. Barney, D. Furniss, T.M. Benson, A.B. Seddon, Numerical modelling of Tb^{3+} doped selenide-chalcogenide multimode fibre based spontaneous emission sources, Opt. Quantum Electron. 50 (2018) 416. https://doi.org/10.1007/s11082-017-1255-5.

[195] J. Hu, C.R. Menyuk, C. Wei, L. Brandon Shaw, J.S. Sanghera, I.D. Aggarwal, Highly efficient cascaded amplification using Pr^{3+}-doped mid-infrared chalcogenide fiber amplifiers, Opt. Lett. 40 (2015) 3687. https://doi.org/10.1364/OL.40.003687.

[196] Gallium Indium Tin Alloy | AMERICAN ELEMENTS®, (2022). https://www.americanelements.com/gallium-indium-tin-alloy (accessed May 8, 2022).

[197] P. Lacovara, H.K. Choi, C.A. Wang, R.L. Aggarwal, T.Y. Fan, Room-temperature diode-pumped Yb:YAG laser, Opt. Lett. 16 (1991) 1089. https://doi.org/10.1364/OL.16.001089.

[198] 1310 nm, 130 mW, Butterfly Laser Diode, PM Fiber, FC/APC, Thorlabs (n.d.). https://www.thorlabs.com/thorproduct.cfm?partnumber=FPL1053P (accessed May 13, 2024).

[199] J.G. Reavis, Experimental studies of actinides in molten salts, 1985. https://doi.org/10.2172/5492312.

[200] A.T. Golam Mostafa, J.M. Eakman, M.M. Montoya, S.L. Yarbro, Prediction of Heat Capacities of Solid Inorganic Salts from Group Contributions, Ind. Eng. Chem. Res. 35 (1996) 343–348. https://doi.org/10.1021/ie9501485.

[201] Ch.D. Chliatzou, M.J. Assael, K.D. Antoniadis, M.L. Huber, W.A. Wakeham, Reference Correlations for the Thermal Conductivity of 13 Inorganic Molten Salts, J. Phys. Chem. Ref. Data 47 (2018) 033104. https://doi.org/10.1063/1.5052343.

[202] A. Borucka, Survey & Selection Of Inorganic Salts For Application To Thermal Energy Storage, US Energy Res. Dev. Adm. (1975).

[203] E. Shimazaki, N. Matsumoto, K. Niwa, The Vapor Pressure of Germanium Dioxide, Bull. Chem. Soc. Jpn. 30 (1957) 969–971. https://doi.org/10.1246/bcsj.30.969.

[204] D. Starodub, E.P. Gusev, E. Garfunkel, T. Gustafsson, SILICON OXIDE DECOMPOSITION AND DESORPTION DURING THE THERMAL OXIDATION OF SILICON, Surf. Rev. Lett. 06 (1999) 45–52. https://doi.org/10.1142/S0218625X99000081.

[205] V.Q. Nguyen, C. Pureza, H. Kung, D. Aggarwal, Fabrication of Low-Loss IR-Transmitting $Ge_{30}As_{10}Se_{30}Te_{30}$ Glass Fibers, J. Light. Technol. 12 (1994) 737–741. https://doi.org/10.1109/50.293962.

[206] C. Jiang, X. Wang, M. Zhu, H. Xu, Q. Nie, S. Dai, G. Tao, X. Shen, C. Cheng, Q. Zhu, F. Liao, P. Zhang, P. Zhang, Z. Liu, X. Zhang, Preparation of chalcogenide glass fiber using an improved extrusion method, Opt. Eng. 55 (2016) 056114. https://doi.org/10.1117/1.OE.55.5.056114.

[207] W.B. Fowler, D.L. Dexter, Relation between Absorption and Emission Probabilities in Luminescent Centers in Ionic Solids, Phys. Rev. 128 (1962) 2154–2165. https://doi.org/10.1103/PhysRev.128.2154.

[208] D.E. McCumber, Einstein Relations Connecting Broadband Emission and Absorption Spectra, Phys. Rev. 136 (1964) A954–A957. https://doi.org/10.1103/PhysRev.136.A954.

[209] W.J. Miniscalco, R.S. Quimby, General procedure for the analysis of Er^{3+} cross sections, Opt. Lett. 16 (1991) 258. https://doi.org/10.1364/OL.16.000258.

[210] M.J.F. Digonnet, E. Murphy-Chutorian, D.G. Falquier, Fundamental limitations of the McCumber relation applied to Er-doped silica and other amorphous-host lasers, IEEE J. Quantum Electron. 38 (2002) 1629–1637. https://doi.org/10.1109/JQE.2002.805111.

[211] B. Aull, H. Jenssen, Vibronic interactions in Nd:YAG resulting in nonreciprocity of absorption and stimulated emission cross sections, IEEE J. Quantum Electron. 18 (1982) 925–930. https://doi.org/10.1109/JQE.1982.1071611.

[212] W.B. Fowler, D.L. Dexter, Relation between Absorption and Emission Probabilities in Luminescent Centers in Ionic Solids, Phys. Rev. 128 (1962) 2154–2165. https://doi.org/10.1103/PhysRev.128.2154.

[213] W. Krupke, Induced-emission cross sections in neodymium laser glasses, IEEE J. Quantum Electron. 10 (1974) 450–457. https://doi.org/10.1109/JQE.1974.1068162.

[214] Thorlabs LDC Cleavers: Flat Cleave with Tension-and-Scribe Method, Youtube (2021). https://youtu.be/_mEMlYUCYfs.

[215] Calcium Fluoride Plano-Convex Lenses, Uncoated, Substrate Transm. Calcium Fluoride Plano-Convex Lenses (n.d.). https://www.thorlabs.com/newgrouppage9.cfm?objectgroup_id=4354&pn=LA5370#2153 (accessed January 8, 2022).

[216] 25mm Dia x 12.5mm FL 3-12µm Coated, Ge Aspheric Lens, Edmund Opt. (n.d.). https://www.edmundoptics.com/p/25mm-dia-x-125mm-fl-3-12mum-coated-ge-aspheric-lens/32068/ (accessed January 8, 2022).

[217] P. Temple, An introduction to phase-sensitive amplifiers: An inexpensive student instrument, Am. J. Phys. 43 (1975). https://doi.org/10.1119/1.9690.

[218] P. Dixon, L. Wu, Broadband digital lock-in amplifier techniques, Rev. Sci. Instrum. 60 (1988). https://doi.org/10.1063/1.1140523.

[219] M. Planck, M. Masius, The Theory of Heat Radiation, P. Blakiston's Son & Co., Philadelphia, 1914.

[220] R. Loudon, The Quantum Theory of Light (3rd ed), Oxford University Press, 2000.

[221] J.R. Lakowicz, B.R. Masters, Principles of Fluorescence Spectroscopy, Third Edition, J. Biomed. Opt. 13 (2008) 029901. https://doi.org/10.1117/1.2904580.